WOODHEAD PUBLISHING IN MATERIALS

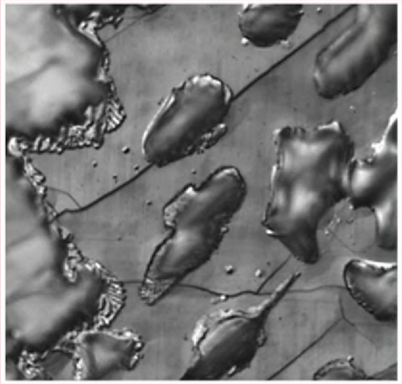

High-temperature superconductors

Edited by X. G. Qiu

WP
WOODHEAD
PUBLISHING

VISIT…

LANZAROTE

Caliente.COM

High-temperature superconductors

Related titles:

Silicon–germanium (SiGe) nanostructures: Production, properties and applications in electronics
(ISBN 978-1-84569-689-4)
Nanostructured silicon–germanium (SiGe) provides the prospect of novel and enhanced electronic device performance. This book will provide a thorough review of the materials science and technology of SiGe nanostructures, including crystal growth and fabrication of nanostructures, material properties and applications in electronics.

Optical switches: Materials and design
(ISBN 978-1-84569-579-8)
Optical components are increasingly important in communication networks and significant technological advances have been made in recent years. *Optical switches: Materials and design* provides a comprehensive review of this interesting and commercially significant field of research. Written by an international team of expert contributors, the major optical switch technologies are discussed with particular emphasis on the materials, design and associated issues. In addition to introductory material and perspective on research results, topics reviewed include acousto-optical switches, thermo-optical switches, magneto-optical switches, MEMs based optical switches, liquid crystal optical switches and photonic crystal optical switches.

Advanced piezoelectric materials: Science and technology
(ISBN 978-1-84569-534-7)
Advanced piezoelectric materials provides an up-to-date comprehensive review of piezoelectrics. Written by a distinguished team of international contributors, this book focuses on the most promising piezoelectric materials and their applications. In the first part of the book, the properties of key piezoelectrics are discussed. Materials include: PZT, relaxor ferroelectrics, Pb free ceramics, quartz, lithium niobate and tantalate, single crystals, polymers and composites. Part II reviews the preparation techniques of piezoelectrics during manufacturing and in the laboratory. Applications-oriented materials development is discussed in Part III, focusing on actuators, high-power applications and performance under stress.

Details of these and other Woodhead Publishing materials books can be obtained by:

- visiting our web site at www.woodheadpublishing.com
- contacting Customer Services (e-mail: sales@woodheadpublishing.com; fax: +44 (0) 1223 832819; tel.: +44 (0) 1223 499140 ext. 130; address: Woodhead Publishing Limited, 80 High Street, Sawston, Cambridge CB22 3HJ, UK)

If you would like to receive information on forthcoming titles, please send your address details to: Francis Dodds (address, tel. and fax as above; e-mail: francis.dodds@woodheadpublishing.com). Please confirm which subject areas you are interested in.

High-temperature superconductors

Edited by
X. G. Qiu

WOODHEAD
PUBLISHING

Oxford Cambridge Philadelphia New Delhi

Published by Woodhead Publishing Limited,
80 High Street, Sawston, Cambridge CB22 3HJ, UK
www.woodheadpublishing.com

Woodhead Publishing, 1518 Walnut Street, Suite 1100, Philadelphia, PA 19102-3406, USA

Woodhead Publishing India Private Limited, G-2, Vardaan House, 7/28 Ansari Road,
Daryaganj, New Delhi – 110002, India
www.woodheadpublishingindia.com

First published 2011, Woodhead Publishing Limited
© Woodhead Publishing Limited, 2011
The authors have asserted their moral rights.

This book contains information obtained from authentic and highly regarded sources. Reprinted material is quoted with permission, and sources are indicated. Reasonable efforts have been made to publish reliable data and information, but the authors and the publisher cannot assume responsibility for the validity of all materials. Neither the authors nor the publisher, nor anyone else associated with this publication, shall be liable for any loss, damage or liability directly or indirectly caused or alleged to be caused by this book.

Neither this book nor any part may be reproduced or transmitted in any form or by any means, electronic or mechanical, including photocopying, microfilming and recording, or by any information storage or retrieval system, without permission in writing from Woodhead Publishing Limited.

The consent of Woodhead Publishing Limited does not extend to copying for general distribution, for promotion, for creating new works, or for resale. Specific permission must be obtained in writing from Woodhead Publishing Limited for such copying.

Trademark notice: Product or corporate names may be trademarks or registered trademarks, and are used only for identification and explanation, without intent to infringe.

British Library Cataloguing in Publication Data
A catalogue record for this book is available from the British Library.

ISBN 978-1-84569-578-1 (print)
ISBN 978-0-85709-103-1 (online)

The publisher's policy is to use permanent paper from mills that operate a sustainable forestry policy, and which has been manufactured from pulp which is processed using acid-free and elemental chlorine-free practices. Furthermore, the publisher ensures that the text paper and cover board used have met acceptable environmental accreditation standards.

Typeset by RefineCatch Limited, Bungay, Suffolk
Printed by TJI Digital, Padstow, Cornwall, UK

Contents

Contributor contact details *ix*
Preface *xi*

Part I Fundamentals of high-temperature superconductors 1

1 Deposition technologies, growth and properties of high-T_c films 3
R. Wördenweber, Jülich Research Centre GmbH, Germany
1.1 Introduction 3
1.2 Deposition techniques 10
1.3 HTS film growth characterisation 23
1.4 Concluding remarks 32
1.5 Acknowledgement 32
1.6 References 33

2 Transport properties of high-T_c cuprate thin films as superconductive materials 38
J. Vanackan and V. V. Moshchalkov, Leuven Catholic University, Belgium
2.1 Introduction 38
2.2 Temperature dependence of the zero-field resistivity in superconducting $La_{2-x}Sr_xCuO_4$ thin films 39
2.3 Magnetoresistivity in superconducting $La_{2-x}Sr_xCuO_4$ thin films 54
2.4 Hall effect 79
2.5 General conclusion 96
2.6 References 96

3 The optical conductivity of high-temperature superconductors 103
R. P. S. M. Lobo, ESPCI, UPMC, CNRS, France
3.1 Introduction 103

3.2 The phase diagram of cuprate superconductors 104
3.3 Optical response of conducting media 108
3.4 The normal state 117
3.5 The superconducting state 127
3.6 Future trends 135
3.7 References 139

Part II Growth techniques and properties of particular high-temperature superconductors 147

4 Sputter deposition of large-area double-sided YBCO superconducting films 149
J. Xiong, B. Tao and Y. Li, University of Electronic Science and Technology of China, China
4.1 Introduction 149
4.2 Sputter deposition technique 152
4.3 Epitaxial YBCO thin films 155
4.4 Issues related to scale-up 156
4.5 Thickness-dependent superconductivity behavior 162
4.6 Challenges 168
4.7 Conclusions 169
4.8 References 169

5 BSCCO high-T_c superconducting films 174
H. Raffy, South Paris University, France
5.1 Growth techniques of BSCCO thin films 174
5.2 Physical properties of BSCCO thin films and multilayers 182
5.3 Concluding remarks and future trends 199
5.4 Acknowledgements 200
5.5 References 201

6 Electron-doped cuprates as high-temperature superconductors 208
M. Naito, Tokyo University of Agriculture and Technology, Japan
6.1 Introduction 208
6.2 Structure 211
6.3 Solid-state chemistry 220
6.4 Sample preparation 226
6.5 Electronic phase diagram 229
6.6 Physical properties (1) – normal-state properties 237
6.7 Physical properties (2) – superconducting properties 244
6.8 Electronic structure and spectroscopy 254
6.9 Summary 263

6.10 Acknowledgements 266
6.11 References 266

7 Liquid phase epitaxy (LPE) growth of high-temperature superconducting films 275
X. Yao and Y. Chen, Shanghai Jiao Tong University, China
7.1 Introduction 275
7.2 Fundamental study on LPE growth 277
7.3 LPE growth mechanism of REBCO films 283
7.4 Conclusion 310
7.5 References 311

Part III Applications of high-temperature superconductors 315

8 High-T_c Josephson junctions 317
P. Seidel, Friedrich-Schiller University Jena, Germany
8.1 Introduction 317
8.2 Types of high-T_c Josephson junctions 325
8.3 Grain boundary junctions 333
8.4 Artificial barrier junctions 341
8.5 Intrinsic Josephson junctions 348
8.6 Hybrid junctions 357
8.7 Future trends 359
8.8 References 362

9 d-Wave YBCO dc superconductive quantum interference devices (dc SQUIDs) 370
F. Lombardi and T. Bauch, Chalmers University of Technology, Sweden
9.1 Introduction 370
9.2 Grain boundary Josephson junctions 372
9.3 Dynamics of a current biased SQUID in the presence of an unconventional current phase relation 376
9.4 Probing the second harmonic component in the current phase relation by the magnetic field response of the SQUID 380
9.5 Quantum circuit applications: HTS SQUIDs as ‘silent’ quantum bit 383
9.6 Conclusions 386
9.7 References 387

10 Microwave filters using high-temperature superconductors 390
Y. S. He and C. G. Li, Chinese Academy of Sciences, China

10.1 Introduction 390
10.2 Superconductivity at microwave frequency 390
10.3 Superconducting transmission lines and related passive devices 396
10.4 Superconducting filter and receiver front-end subsystem 403
10.5 Superconducting meteorological radar 415
10.6 Summary 421
10.7 References 422

Index *424*

Contributor contact details

(* = main contact)

Editor

X. G. Qiu
National Laboratory for Superconductivity
Institute of Physics
Chinese Academy of Sciences
Zhongguancun nansanjie 8
Beijing 100190
China
Email: xgqiu@aphy.iphy.ac.cn

Chapter 1

R. Wördenweber
Institute of Bio- and Nanosystems (IBN) and JARA-Fundamentals of Future Information Technology
Jülich Research Centre GmbH
D-52425 Jülich
Germany
Email: r.woerdenweber@fz-juelich.de

Chapter 2

J. Vanacken* and V. V. Moshchalkov
Institute for Nanoscale Physics and Chemistry
Leuven Catholic University
Celestijnenlaan 200 D
B-3001 Leuven
Belgium
Email: Johan.Vanacken@fys.kuleuven.be; victor.moshchalkov@fys.kuleuven.be

Chapter 3

R. P. S. M. Lobo
Laboratoire de Physique et d'Etude des Materieux
CNRS – UMR 8213
10 Rue Vauquelin
75231 Paris
Cedex 5
France
Email: lobo@espci.fr

Chapter 4

J. Xiong*, Bowan Tao and Yanrong Li
State Key Lab of Electronic Thin Films and Integrated Devices
University of Electronic Science and Technology of China
Chengdu 610054
China
Email: jiexiong@uestc.edu.cn

Chapter 5

H. Raffy
Solid-State Physics Laboratory
South Paris University
91405 Orsay
France
Email: raffy@lps.u-psud.fr

Chapter 6

M. Naito
Department of Applied Physics
Tokyo University of Agriculture and Technology
Naka-cho 2-24-16
Koganei
Tokyo 184-8588
Japan
Email: minaito@cc.tuat.ac.jp

Chapter 7

X. Yao* and Y. Chen
Department of Physics
Shanghai Jiao Tong University
800 Dongchuan Road
Shanghai 200240
China
Email: xyao@sjtu.edu.cn

Chapter 8

P. Seidel
Institute of Solid-State Physics
Friedrich-Schiller University Jena
D-07743 Jena
Germany
Email: paul.seidel@uni-jena.de

Chapter 9

F. Lombardi* and T. Bauch
Mc2-Quantum Device Physics Laboratory
Chalmers University of Technology
Göteborg
Sweden
Email: floriana.lombardi@chalmers.se

Chapter 10

Yusheng He* and Chunguang Li
Institute of Physics
Chinese Academy of Sciences
Zhongguancun nansanjie 8
Beijing 100190
China
Email: yshe@aphy.iphy.ac.cn

Preface

Almost 25 years have passed since the celebrated discovery of high temperature superconductors (HTSCs) by G. Bednorz and K. A. Müller in 1986. HTSCs opened a new era for research on superconductivity, from both fundamental physics and materials science perspectives. In the field of fundamental physics, the research on HTSCs has greatly enriched our understanding of the physics in strongly correlated electron systems, although many crucial issues remain to be understood. In the materials arena, great achievements have been made over the last two decades, both in single crystals and in thin films. It is important to acknowledge that the advances are not limited to the sample quality itself, but also include new methods and techniques developed to grow HTSC thin films. For example, it is because of the research on HTSC thin films that the fabrication techniques for oxide thin films have been able to be developed so fast; facilitating the growth of oxide thin films other than HTSC, such as the $SrTiO_3/LaAlO_3$ system used in interfacial conductivity studies. As time has passed, the fervour over HTSCs has gradually faded away. Now, therefore, is the right time to consider what has been achieved and to summarize the information that will be of help to students and colleagues working at the frontiers of research into oxide thin films in general and superconducting thin films in particular. Therefore, we invited researchers from all over the world, who have been working for many years on different aspects of HTSC thin films, to contribute their cutting edge knowledge on the fabrication and physics of HTSC thin films, reviewing the fabrication techniques and physical properties, as well the applications, of HTSC thin films.

The objective of this book is to serve as a handbook for those who are interested in the growth of HTSC thin films as well as their characterization and applications. It aims to give newcomers such as students a fast track means of understanding what has been achieved in the past and to provide an overview of the status of current research on HTSC thin films. The book will also be a valuable source of references for their research. It is also aimed at the veterans in this field; providing a convenient and consolidated source of information, so avoiding the necessity to search through the numerous references that have been published over the last two decades.

This book is organized into three parts. The first three chapters cover the fundamentals of the materials and physical aspects of HTSCs. Chapter 1 overviews the different deposition techniques used for thin film processes as well as the characterization techniques. Chapters 2 and 3 summarize the transport and optical properties of HTSC, focusing mainly on the results obtained on thin films. Part II covers the fabrication and characterization of different HTSC thin films. As we know, HTSCs can be categorized into hole-doped and electron-doped thin films. Depending on the material and properties of interest, different deposition techniques such as magnetron sputtering and laser ablation are utilized. In Chapters 4 to 7, deposition techniques for several representative hole-doped and electron-doped HTSC thin films are reviewed in detail. The characterization and physical properties of those films is also discussed. Part III of the book describes the application of HTSC thin films. After more than 20 years of development, there has been much progress in HTSC applications, especially in the area of weak signal detecting using thin films. In Chapters 8 to 10, Josephson junctions, SQUIDs and microwave filters based on HTSC thin films are introduced and discussed in detail.

At the time when we started to prepare this book, a new family of HTSCs, i.e. iron pnictide superconductors, had just been discovered. It is anticipated that the thin film fabrication techniques developed for HTSC cuprates can also be applied to the growth of iron pnictide superconductors. Of course, the thin film fabrication techniques described in this book will also be helpful for those working on oxide thin films other than superconductors.

Finally, we would like to thank Woodhead Publishing Limited who have made it possible to have such a handbook published at a time when the superconductivity community is wondering what to do next with HTSCs; we hope that readers will find this book of help to their researches.

Xianggang Qiu

1

Deposition technologies, growth and properties of high-T_c films

R. WÖRDENWEBER, Jülich Research Centre GmbH, Germany

Abstract: Due to the extreme demands of high-temperature superconductor (high-T_c HTS) materials – especially the extremely complex structure, small coherence length and large anisotropy – existing deposition technologies have been greatly improved and novel technologies have been developed in the last decade. This article presents an overview on the deposition and deposition techniques of high-T_c material. The major technological approaches are discussed and compared in the light of the demands of the different superconductor and substrate materials. Nucleation and film growth of ceramic superconducting material are sketched, and consequences of the heteroepitaxial growth are discussed. Finally, a classification of the state of the art and the pros and cons of the different technologies are given.

Key words: high-temperature superconductor thin film deposition, ceramic films, epitaxial growth of oxide films, critical thickness.

1.1 Introduction

Since the discovery of the first high-temperature superconductor (HTS) (Bednorz and Müller, 1986), a significant effort has been put into the research and realisation of textured and epitaxial HTS films. This effort is motivated largely by the potential applications of thin HTS films in a number of cryoelectronic devices and by the possibility of using epitaxial single or multilayer HTS films to study new physical properties of these unique 2D layered materials. The technology of devices and integrated circuits fabricated from low-temperature superconductors (LTS) capable of operating at or near the temperature of liquid helium (4.2K) is by now well established. However, the future application of HTS in cryoelectronic devices which are capable of operating at temperatures between 20–77K will strongly depend on the development of reproducible deposition technologies for high-quality single and multilayer HTS thin films. Nevertheless, a number of technical applications of HTS thin films (mainly passive (linear) and active (nonlinear) devices or circuits) already have a firm implementation base for the next few years, while others represent tentative ‘dreams’ for a more distant future. Typical application areas include: metrology and electronic instrumentation, radioastronomy and environmental spectroscopy (atmosphere and space), neurology and medical diagnostics, electronic warfare (radar, electronic countermeasures (ECM), magnetic anomaly detection); non-destructive materials evaluation (NDE/NDT), geological and environmental prospecting, telecommunication, ultrafast digital signal and data processing.

In this chapter the deposition of HTS thin films and film systems is reviewed. Starting with a sketch of the requirements of HTS material and substrates, with brief introductions to the most commonly used deposition techniques, a number of important issues and problems related to a reproducible fabrication of high quality HTS thin film devices for technical applications and basic research are addressed.

1.1.1 HTS materials and requirements

The most commonly examined HTS material with superconducting transition temperatures T_c above the temperature of liquid nitrogen are $ReBa_2Cu_3O_{7-\delta}$ (Re = Y or rare earth element, typical transition temperature $T_c = 90–95K$), $Bi_2Sr_2Ca_1Cu_2O_8$ ($T_c = 90K$), $Bi_2Sr_2Ca_2Cu_3O_{10}$ ($T_c = 120K$), $Tl_2Ba_2Ca_1Cu_2O_8$ ($T_c = 110K$), $Tl_2Ba_2Ca_2Cu_3O_{10}$ ($T_c = 127K$), $HgBa_2Ca_1Cu_2O_8$ ($T_c = 134K$), MgB_2 ($T_c = 39K$), and, lately, the so-called ferropnictide superconductors (e.g. $Sm_{0.95}La_{0.05}O_{0.85}F_{0.15}FeAs$ with $T_c = 57.3K$) (Zheng Wie *et al.*, 2008). For HTS cryoelectronic devices, thin films are mainly grown from $YBa_2Cu_3O_{7-\delta}$ (YBCO) material. Reasons for this choice are, among others, the phase stability, high crystalline quality, high flux pinning level, low surface resistance, the possibility of using a single deposition step with *in-situ* oxidation, and the absence of poisonous components that are present in Tl, Hg, or As containing HTS films.

In general, the improvement of the superconducting properties (e.g. increase of T_c and energy gap ΔE) is accompanied by an enhancement of (i) the number of elements, (ii) structural complexity, and (iii) anisotropy (Fig. 1.1).

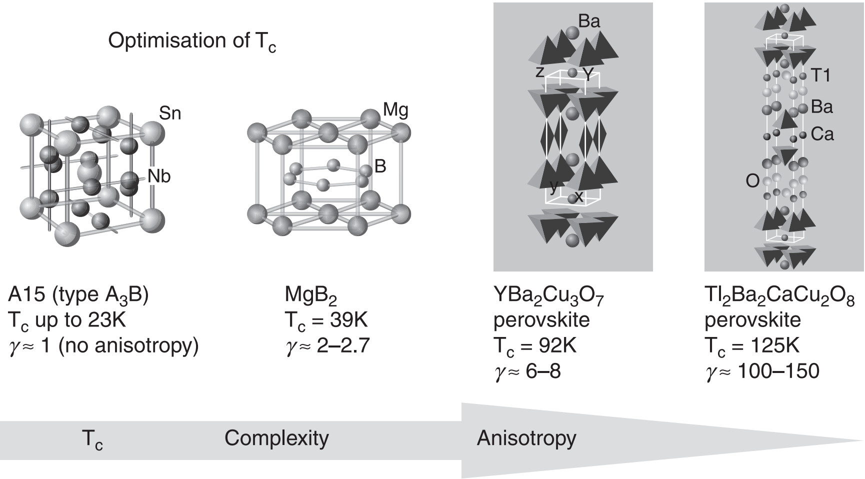

A15 (type A_3B)
T_c up to 23K
$\gamma \approx 1$ (no anisotropy)

MgB_2
$T_c = 39K$
$\gamma \approx 2–2.7$

$YBa_2Cu_3O_7$
perovskite
$T_c = 92K$
$\gamma \approx 6–8$

$Tl_2Ba_2CaCu_2O_8$
perovskite
$T_c = 125K$
$\gamma \approx 100–150$

1.1 The improvement of the superconducting properties (e.g. increase of T_c and energy gap) is achieved via an enhancement of complexity (structural and stoichiometric) and anisotropy of the superconductor.

First, the quasi two-dimensional (2D) nature of the oxide superconductors related to their layered structure leads to a large anisotropy in nearly all parameters. Anisotropy factors of $\gamma = \xi_{ab}/\xi_c = \lambda_c/\lambda_{ab} \approx 6–8$ in YBCO, $\gamma \approx 55–122$ in Bi compounds, and $\gamma \approx 100–150$ in Tl compounds are reported for the anisotropy between the crystallographic c and a-b direction (Farrell *et al.*, 1988, 1989, 1990; Okuda *et al.*, 1991). Furthermore, extremely small coherence lengths are determined for the HTS. For Bi_{2212} values of $\xi_c = 0.02–0.04$ nm and $\xi_{ab} = 2–2.5$ nm, for YBCO $\xi_c = 0.3–0.5$ nm and $\xi_{ab} = 2–3$ nm are measured, which, furthermore, strongly depend on sample quality and oxygen content (Ossandon *et al.*, 1992). Therefore, local variations in the sample properties on the scale of ξ will automatically result in a spatial variation of the superconducting properties. Due to the extremely small coherence length along the crystallographic c-axis, only the current directions along the a–b direction (i.e., along the CuO-planes) can be used in most applications. Since even misalignments in the a–b plane lead to grain boundaries that strongly affect the critical properties (see Fig. 1.2), a perfect biaxial c-axis orientated epitaxial film growth including the avoidance of anti-phase boundaries is necessary for most applications.

Second, the superconducting properties strongly depend upon variations in stoichiometry, especially in the oxygen concentration. Due to the complex crystallographic structure and the small coherence length, extreme requirements are imposed upon the uniformity and stability of the deposition process.

Finally, in a number of applications HTS films are grown on less ideal carriers, e.g. single crystals with large lattice misfit, or, in the case of coated conductors, tapes with crystalline buffer layers. In these cases, polycrystalline or

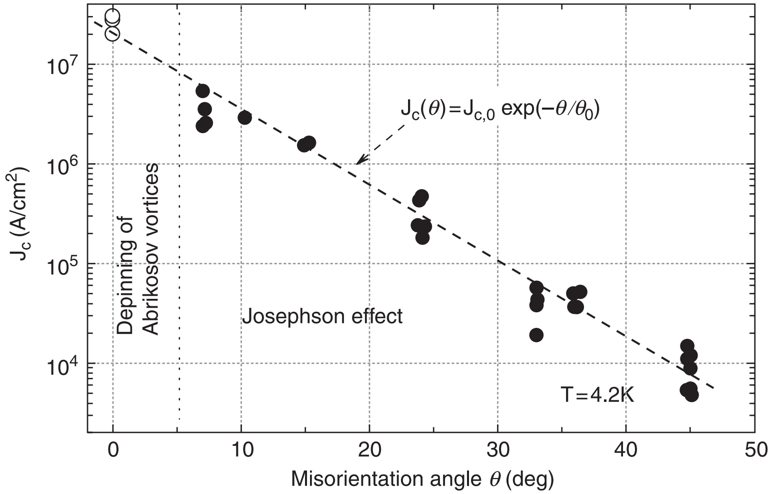

1.2 Critical current density of YBCO bicrystals as a function of misorientation angle at 4.2K (Dimos *et al.*, 1990; Hilgenkamp *et al.*, 1998). Open symbols represent J_c values of epitaxial films on single crystals.

textured HTS films are obtained in which the intergranular properties (i.e., grain boundaries) clearly dominate the superconducting properties like the transport current density J_c or microwave surface resistances R_s. The effect of the grain boundaries upon the J_c is demonstrated in Fig. 1.2. On the one hand, J_c decreases with increasing misorientation angle. On the other hand, at large angles the grain boundary imposes a Josephson-type behaviour that can be utilised for the engineering of Josephson contacts, e.g. by deposition of HTS thin films on bicrystalline substrates with perfectly defined grain boundaries (Divin *et al.*, 2008).

In conclusion, the extraordinary properties of HTS material – the large anisotropy, small coherence length and strong dependence of the superconducting parameters on local modifications – set extremely high requirements for the deposition of HTS thin films:

- perfect stoichiometry and structure
- perfect biaxial epitaxial orientation
- avoidance of defects that hamper the superconducting properties and
- avoidance of grain boundaries.

1.1.2 Substrate requirements

The choice of the substrate material is of vital importance for the performance of a superconducting device. For example microwave applications require substrates with low microwave losses (typically $\tan\delta < 10^{-5}$), whereas coated conductors are based on metallic tapes. As a consequence, large lattice misfits or even non-crystalline carriers with complex crystalline buffer systems have to be taken into account (see Fig. 1.3). Therefore, the impact of the substrate has to be taken into account for the development of a reliable deposition technology for high-quality HTS thin-films. The basic requirements for the substrates (including buffer layer) can be summarised as follows:

- reasonable crystallographic lattice match between HTS film and substrate,
- similar thermal expansion coefficient of HTS and substrate,
- no chemical interaction at the interface between HTS and substrate, and
- surface properties (e.g. polished surface), stability, robustness and size of the substrate suitable for film deposition and application.

Depending upon the application of the films, specific requirements are imposed upon the substrate. For a number of applications twinned substrates should be avoided, or the available size of the substrate and/or its cost are of importance. For example, for microwave applications the dielectric properties, surface quality and available size of the substrate are relevant. Generally we can distinguish between different classes of substrates:

- ‘perfectly compatible’ substrates onto which HTS material can be deposited without buffer layer,

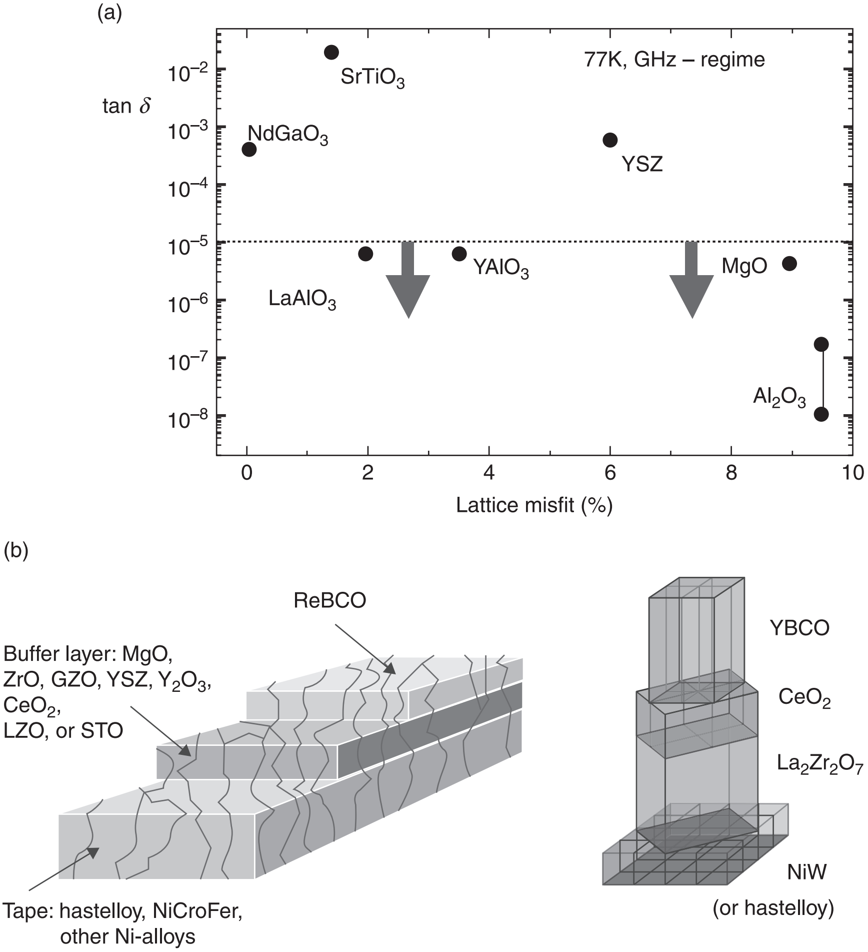

1.3 Substrate material for microwave applications and coated conductors. (a) For microwave applications substrate material with low losses (tan $\delta < 10^{-5}$) are required. Ideal candidates (e.g. MgO, Al_2O_3) suffer from large lattice misfit $(a_{film} - a_{substrate})/a_{film}$, where 'a' represents the in-plane lattice parameter. (b) Coated conductors are based on metallic tapes (e.g. hastelloy, NiCroFer, Ni-alloy). The crystalline structure is generated in the oxide buffer system (e.g. $La_2Zr_2O_7$ plus CeO_2 or Nb-doped titanates $Sr_{1-x}(Ca,Ba)_xTi_{1-y} - Nb_yO_3$).

- 'less compatible' substrates that require an optional buffer layer, and
- 'non-compatible' substrate materials, which have to be covered with an epitaxial buffer layer prior to the deposition of the HTS film due to large lattice mismatch and/or chemical interaction between substrate and HTS material or due to missing in-plane orientation (e.g. for deposition of biaxial oriented YBCO on polycrystalline substrates), respectively.

Deposition on to compatible substrates is generally easier. Typical candidates are $LaAlO_3$, $SrTiO_3$ and MgO for YBCO deposition. Nevertheless, buffer layers can be added, e.g. a CeO_2 buffer layer on $LaAlO_3$ substrates reduce the probability of a-axis growth. Important properties of different material that represent suitable substrate materials as well as buffer or interlayer are summarised in Table 1.1.

In contrast, the deposition of HTS material onto a number of technically interesting substrate materials (e.g. Si, Al_2O_3, or metal tapes for HTS coated conductors) requires a previous coating with an adequate buffer layer that enables epitaxial growth (by reducing the lattice mismatch between substrate and HTS material or, even providing the crystalline structure for epitaxy in the case of coated conductors) and provides a sufficient barrier against chemical interdiffusion between substrate and HTS material. As an example, one of the most interesting substrate candidates for microwave applications is $(1\underline{1}02)$ oriented Al_2O_3 (*r*-cut sapphire), which possesses high crystalline perfection, mechanical strength, and low dielectric permittivity ($\varepsilon \approx 10$) and losses ($\tan\delta$ (77K,10GHz) $\approx 10^{-7}$–10^{-8} (Braginsky *et al.*, 1987). However, the complex crystalline structure of sapphire which is comprised of consecutive planes of oxygen and aluminium hexagons with each third site vacant, provides two planes of rectangular (*m* or $(10\underline{1}0)$ plane) or pseudo-rectangular (*r* or $(1\underline{1}02)$ plane) surface structure. Both planes possess a rather poor lattice match to the rectangular basal plane of the *c*-oriented YBCO structure. Due to smaller mismatch, *r*-cut sapphire is preferentially used for the deposition of YBCO films. The lattice mismatch is accompanied by chemical interaction between YBCO and Al_2O_3 taking place at elevated deposition temperatures (Gao *et al.*, 1992, Davidenko *et al.*, 1992). This yields substantial diffusion of Al into the HTS film and formation of an uncontrolled $BaAl_2O_4$ interfacial layer.

Two different approaches have been considered for the choice of buffer layers. In one approach, material is chosen which is similar to YBCO with respect to chemical and structural properties. One of the few promising candidates for such a buffer is the semiconducting perovskite $PrBa_2Cu_3O_7$ (PBCO) (Gao *et al.*, 1992; Jia *et al.*, 1990). PBCO layers are also good candidates for YBCO multilayers (see, e.g. Triscone and Fischer, 1997). The specific resistance can be improved by partial substitution of Cu by Ga without loss of chemical and structural compatibility. Although the Al diffusion into the YBCO film is blocked by the PBCO buffer layer, YBCO films on PBCO/sapphire exhibit higher R_s and lower J_c values than observed for YBCO films of reasonable quality on compatible substrate materials (Hammond and Matthaei, 1993).

In the second approach, oxides with a cubic structure and lattice parameters comparable to the diagonal of both *r*-plane sapphire and (001) plane orthorhombic YBCO are chosen. Among a large number of candidates MgO, YSZ (ZrO_2 stabilised with ~9 mol % of Y_2O_3), and CeO_2 are the most attractive candidates. Whereas the lattice parameter of MgO is closer to that of sapphire, YSZ and CeO_2

Table 1.1 Properties of crystalline substrate materials suitable for the preparation of YBCO thin films (metallic tapes for coated conductors are not listed)

	Attainable dielectric properties					Crystallinity				
Substrate materials	ε	tan δ at 10GHz, 77K	Thermal exp. coeff. (10^{-6}/°C)	Melting temp. (°C)	Available substrate size (mm)	Lattice misfit to YBCO (%)	Twinning	Chemical stability	Mechanical strength	Remarks
$SrTiO_3$	300	~2×10^{-2}	9.4	2080	30–50	1.4				
YSZ	27–33	> 6×10^{-4}	11.4	2550	Ø100	6				
$NdAlO_3$				2070						
MgO	9.6–10	6.2×10^{-6}	14	2825	> 30	9	No	Good	Poor	Hygroscopic
α–Al_2O_3 (sapphire)	9.4–11.6 anisotropic	10^{-8}	9.4	2049	Ø100	6–11 (*r* cut) 18 (*m* cut)	No	Poor	Good	Requires buffering
YSZ buffered *r*-cut sapphire	27–33 (for YSZ)	> 6×10^{-4} (for YSZ)		2550 (for YSZ)		6	No	Good	Good	
CeO_2 buffered *r*-cut sapphire	21.2 (for CeO_2)			2600 (for CeO_2)	Ø100	0.7	No	Good	Good	
Y_2O_3	14			2400	Ø30	3	No	Expected to be good	Fair	
$YAlO_3$	16	10^{-5}		1875	Ø30	3.5	No	Fair	Fair	
$LaAlO_3$	20.5–27	7.6×10^{-6} to 3×10^{-4}	10–13	2100	Ø100	2	Yes	Good	Fair	
$LaGaO_3$	25		9	1715	Ø40	2	Yes	Good	Fair	
$NdGaO_3$	23	4×10^{-4}	9–11	1670	Ø50	0.04	No	Good	Fair	
$PrGaO_3$	24		7–8	1680	Ø10	0.3	Yes	Good		

Note: the lattice misfit is normalised to the YBCO lattice for c-axis orientation $(a_{film}-a_{substrate})/a_{film}$, the thermal expansion coefficient of c-axis oriented YBCO is ~(1–1.3) × 10^{-5}/K, YSZ refers to yttrium (~9 mol % of Y_2O_3) stabilised ZrO_2. Other candidates, which are not listed here, are, e.g., $CaNdAlO_4$ or $XAlO_3$ (with X = SrLa, Y, Gd, Eu, Sm, Nd or Pr).

matches that of YBCO. CeO_2 has proven to be one of the most effective buffer layers due to its favourable thin film growth characteristics, minimal chemical interaction and good lattice match with most HTS materials. For instance, (001) CeO_2 buffer layers reduce the lattice mismatch between $(1\underline{1}02)$ sapphire and (001) YBCO and provide a sufficient barrier against diffusion of Al into the YBCO film (Zaitsev *et al.*, 1997b). (001) CeO_2 itself has a high lattice mismatch with respect to $(1\underline{1}02)$ sapphire. This can cause insufficient structural perfection of the CeO_2 and YBCO layers despite the very high structural perfection of sapphire substrates. In general, the lattice mismatch between sapphire, buffer and ceramic film leads to large stress induced strain in the film. As a consequence, defects will develop and, finally, films that exceed a critical thickness will crack (Zaitsev *et al.*, 1997a; Hollmann *et al.*, 2009). This will be discussed in section 1.3.2. Nevertheless, YBCO films with high quality with respect to morphology, critical properties and microwave properties can be grown onto technical substrates like sapphire as long as the critical thickness is not surpassed (Lahl and Wördenweber, 2005).

Another example for the need of buffer layers is given by the HTS coated conductors (see Fig. 1.3b). One of the main obstacles to the manufacture of commercial lengths of YBCO wire or tapes has been the phenomenon of weak links, i.e., grain boundaries formed by any type of misalignment of neighbouring YBCO grains are known to form obstacles to current flow. Therefore HTS deposition on metallic tapes require carefully aligning the grains, as low-angle boundaries between superconducting YBCO grains allow more current to flow. For instance, below a critical in-plane misalignment angle of 4°, the critical current density approaches that of YBCO films grown on single crystals (see Fig. 1.2).

The schematics of a typical architecture of a HTS coated conductor is shown in Fig. 1.3b. Coated conductors are based on metallic tapes (e.g. hastelloy, NiCroFer, Ni-alloy). The crystalline structure is generated in a complex oxide buffer system (e.g. $La_2Zr_2O_7$ plus CeO_2 or Nb-doped titanate $Sr_{1-x}(Ca,Ba)_xTi_{1-y} - Nb_yO_3$) onto which the HTS film is deposited. The HTS is normally protected by an additional metallic shunt, typically an Au or Ag layer. Several methods have been developed to obtain biaxially textured buffer layers suitable for high-performance YBCO films. These are ion-beam-assisted deposition (IBAD), the rolling-assisted biaxially textured substrate (RABiTS) process, and inclined substrate deposition (ISD). For more details on these different deposition technologies for HTS coated conductors one should refer to overview articles like Paranthaman and Izumi, 2004.

1.2 Deposition techniques

There exist a large variety of techniques for growing HTS films and multilayers ranging from physical vapour deposition (PVD) to all chemical deposition processes. In all cases, the actual process of deposition can be divided into three steps which are sketched in Fig. 1.4:

1 The *particle source* can be a stoichiometric HTS compound (e.g. for sputtering and PLD), an assembly of different components (e.g. for evaporation), a mixture of organic molecules (e.g. for MOCVD) or a chemical solution (e.g. for CSD or MOD).
2 The *particle transport* is initiated by phonons (evaporation), photons (PLD) or ion bombardment (sputtering) in the case of PVD deposition. In these processes the initial particle energy at the source, the scatter events between particles and process gas, and the resulting energy of the particles impinging on the substrates play an important role. This will be discussed in detail in the section 'Comparison of the different PVD techniques', p. 18. For CVD, CSD and MOD, evaporation and spray-, spin- or dip-coating define the particle transport, respectively.
3 Finally, the *nucleation, phase formation, and film growth* represents the most important step of the deposition process, i.e., the actual formation of the HTS film. It strongly depends on all process parameters (e.g. substrate temperature, process pressure, density of particles) and, obviously, on the configuration of particles (i.e., atoms, (organic) molecules, chemical solution).

Whereas processes (1) and (2) are reasonably well understood, the actual nucleation, phase formation and film growth is difficult to analyse, theoretically

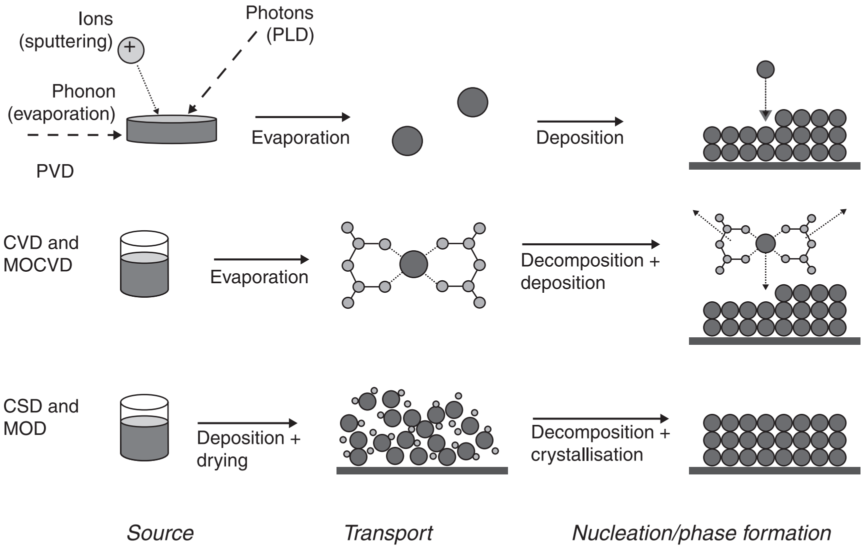
Ions
(sputtering)
+
Photons
(PLD)
Phonon
(evaporation)
PVD
Evaporation
Deposition
CVD and
MOCVD
Evaporation
Decomposition +
deposition
CSD and
MOD
Deposition +
drying
Decomposition +
crystallisation
Source
Transport
Nucleation/phase formation

1.4 Schematic sketch of PVD, (MO)CVD and CSD/MOD technologies.

as well as experimentally. Even simple parameters like the actual temperature at the surface of the substrate are difficult to determine. Therefore, this part of the process is subject to theoretical models and experimental estimates. Nevertheless, there is a reasonably good understanding of the basic principles.

In the following we will discuss the deposition in exactly these three different steps, starting with the description of the different deposition processes used for HTS thin film deposition.

1.2.1 Physical vapour deposition techniques

Physical vapour deposition (PVD) involves purely physical processes, and describes all methods to deposit films via condensation of a vaporised form of the material onto a surface. PVD deposition of HTS involves high-temperature vacuum evaporation, pulsed lased deposition (PLD) or plasma sputter bombardment (sputter technology).

Thermal co-evaporation and molecular beam epitaxy

The thermal evaporation is based on particle sources in the form of thermal boats (typically resistively heated), e-guns, or Knudsen cells. As a consequence and in contrast to sputter and PLD technologies, in evaporation or molecular beam epitaxy (MBE) each material is supplied individually from metallic sources and small gas pressures (especially of reactive components like oxygen) have to be chosen.

In principle, this approach is more flexible since the stoichiometry can be easily changed. Examination of stoichiometric dependent effects of the superconducting film or the preparation of artificial superlattices seems to be easier with this method. However, the difficulty lies in the fact that calibration and rate control is rather complex and difficult, especially since reactive gas (oxygen) is involved in the deposition process of HTS material. Therefore, a very accurate rate control for all components has to be guaranteed and the problem of low oxygen partial pressures has to be solved.

First, by using active rate control utilising (collimated) quartz-crystal monitors or atomic absorption monitors, metal stoichiometry control down to ~1% repeatability seems to be achievable (Matijasevic *et al.*, 1997). Second, the oxygen background pressure at source should not exceed ~10^{-4} mbar during deposition. Therefore, reactive oxygen sources like atomic oxygen, ozone, or NO_2 can be used to increase the oxidation efficiency and allow the formation of the superconducting phase at a lower oxygen pressure. Alternatively, differentially pumped evaporation devices have been developed that provide low pressure at the source and high pressure at the substrate. This can among others, be established by rotation of the substrate in a heater which is partially open facing the evaporation sources (typically 650°C at 10^{-5}mbar for YBCO) and partially closed forming an 'oxygen pocket' with a 100 times higher oxygen partial pressure (Utz *et al.*, 1997) (see Fig. 1.5). Thus, in the closed part of the heater the oxygen partial pressure is increased providing the oxygenation of each deposited layer. This method has lately been adopted for the growth of high-quality large-area MgB_2 thin films ($T_c \approx$ 38–39K) using the 'heater pocket' for the Mg-incorporation (Moeckly and Ruby, 2006).

Alternatively, both problems are solved in differentially pumped MBE systems. For instance, via atomic layer-by-layer MBE a variety of heterostructures based on BSCCO compounds also including DyBaCuO, LaSrCuO and several titanates have been prepared (Bozovic *et al.*, 1994), ultrathin films of $La_{2-x}Sr_xCuO_{4+y}$ have been grown via MBE (Jaccard *et al.*, 1994), and novel superconductors have been designed (Logvenov and Bozovic, 2008).

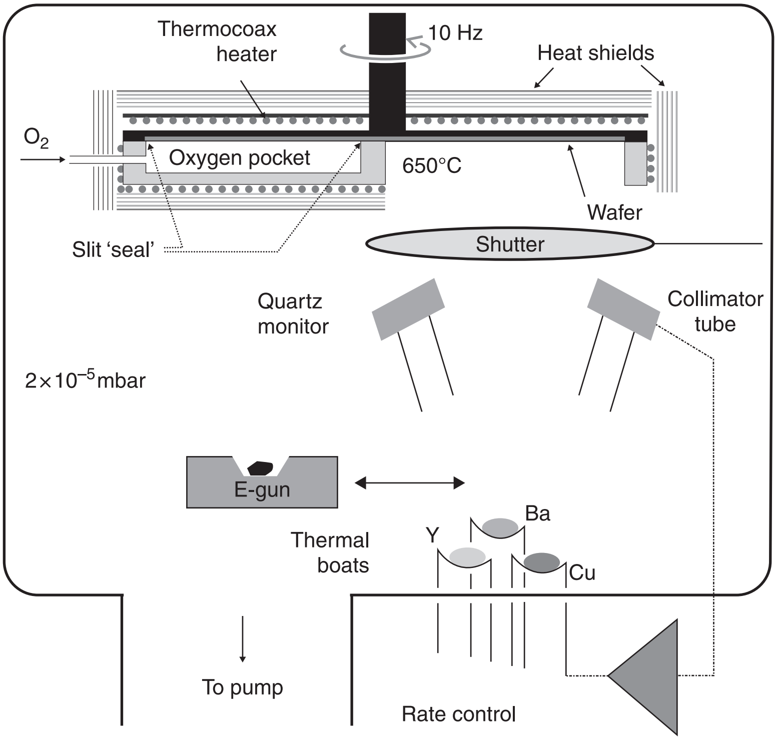
Thermocoax heater
10 Hz
Heat shields
O_2
Oxygen pocket
650°C
Wafer
Slit 'seal'
Shutter
Quartz monitor
Collimator tube
2×10⁻⁵mbar
E-gun
Ba
Y
Thermal boats
Cu
To pump
Rate control

1.5 Schematic sketch of a thermal co-evaporation system (Utz *et al.*, 1997). An oxidation pocket encloses part of the heater. The substrate is rotated continuously through the pocket, enabling intermittent deposition and oxygenation and providing better uniformity during evaporation.

Pulsed laser deposition technique and Laser MBE

The PLD technology represents a special type of evaporation. Due to its flexibility, it has become an important technique to fabricate layers of novel compounds. It is used for the deposition of HTS, ferroelectric and ferromagnetic oxide materials. Film deposition by PLD is based on the irradiation of a single target by a focused laser beam (e.g. excimer ($\lambda = 308$ nm, 248 nm) or Nd:YAG (355 nm); energy density 1–3 J/cm^2/shot; frequency of several Hz). The laser beam removes material from the target and this material is transferred to the substrate (Fig. 1.6). During ablation a luminous cloud (plume) is formed along the normal of the target. Due to the short wavelength, the photons of the laser beam interact only with the free electrons of the target material. The subsequent electron–phonon interaction leads to a sudden increase of the local temperature, surface or subsurface vaporisation (depending on energy of the laser beam) and an explosive removal of material. Laser-induced thermal evaporation or congruent PLD takes place for lower and high ($> 10^7$–10^8 W/cm^2) energy densities, respectively. These ablation processes can be explained in various models (see, for example, Morimoto and Shimizu (1995)) as:

- shock wave caused by rapid surface evaporation,
- subsurface explosion caused by rapid evaporation-induced cooling of the surface,
- formation of Knudsen layer due to collision of ejected atoms, and
- superheating of the surface by suppression due to the recoil pressure for evaporated material.

PLD deposition has a number of advantages. In contrast to most other deposition processes, the energy at the target can be controlled independent of the process pressure and gas mixture. Thus, reactive processes can easily be conducted, and stoichiometric deposition for high energy densities, high rates and high process flexibility are characteristic features of PLD. However, traditionally PLD is limited to small areas (typically 1 cm^2), the pulsed deposition has a large impact upon the morphology of the sample and usually droplets of submicrometer size (boulders) are formed on the surface of the deposited film. Via off-axis PLD and rotation of the substrate, HTS films can be deposited on substrates up to 2" in diameter; utilising rotation and translation in on-axis configuration, films have been deposited even onto 3" wafer (Lorenz *et al.*, 2003). Much effort has been invested into eliminating the boulders on HTS-film surfaces including optimising the laser power (Dam *et al.*, 1994) and masking the ablation plume.

Finally, sophisticated PLD systems have been developed for the deposition of multilayer, complex or perfect film systems by combining the advantages of PLD and MBE (see for instance Blank *et al.*, 2000). In the so-called Laser-PLD (L-PLD) a 'target carousel' allows the subsequent deposition of different components or systems and an *in-situ* characterisation such as low energy electron

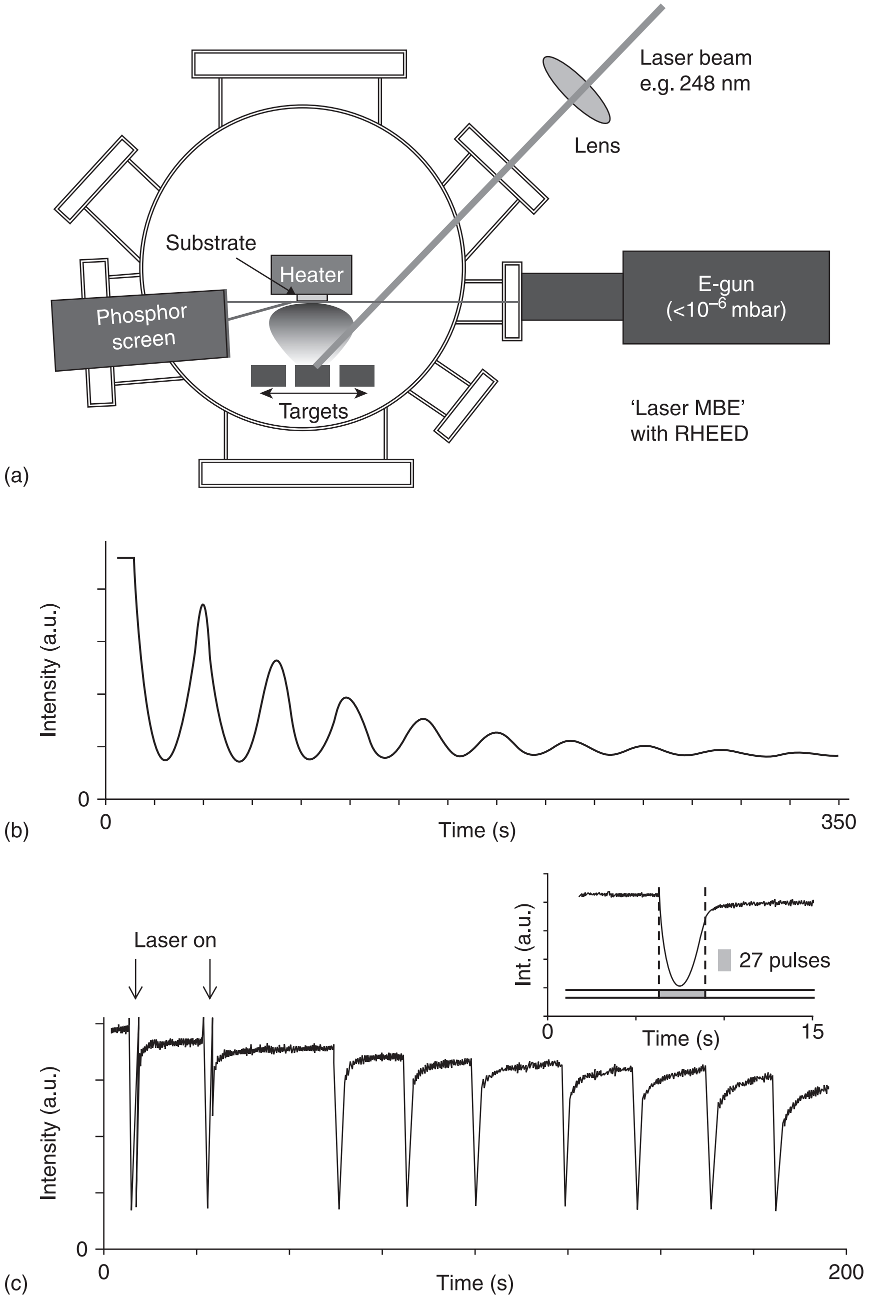
Laser beam
e.g. 248 nm
Lens
Substrate
Heater
Phosphor screen
E-gun
(<10^{-6} mbar)
Targets
'Laser MBE' with RHEED
(a)
Intensity (a.u.)
0
Time (s)
350
(b)
Laser on
Int. (a.u.)
27 pulses
0
Time (s)
15
Intensity (a.u.)
0
0
Time (s)
200
(c)

1.6 Schematic sketch of a Laser-MBE (a), and *in-situ* RHEED characterisation of a continuous (b) and layer-by-layer (c) growth of oxide films via Laser-PLD according to Koster *et al.* (1999).

diffraction (LEED) or reflection high energy diffraction (RHEED) allows a perfectly controlled film growth. Figure 1.6 shows a Laser-PLD and the layer-by-layer growth of oxide films.

Sputter techniques

Sputter deposition has the deserved reputation of being the technique for preparing thin films of alloys and complex materials for industrial application. It is based on a discharge involving free ions and electrons in a gaseous atmosphere (see Fig. 1.7). Three different kinds of discharges can be distinguished: arcs, glow discharges and dark discharges. They can be distinguished by their luminescence but also by their current-voltage characteristic, the current density and breakdown voltage (Fig. 1.7c). These main characteristics depend on the geometry of the electrodes and the vessel, the gas used, the electrode material.

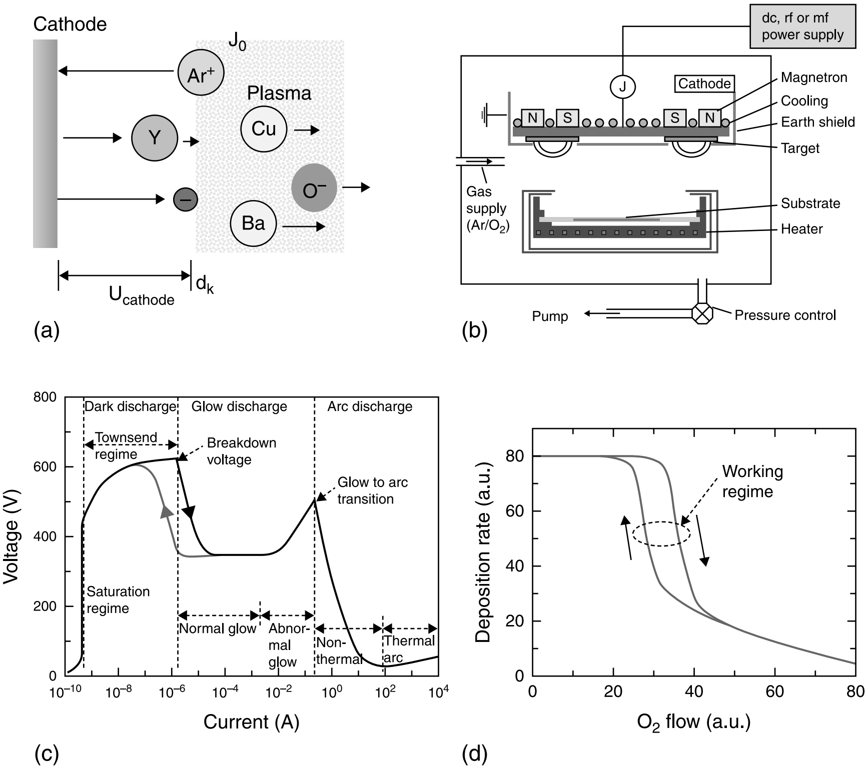
Cathode
J0
Ar+
Plasma
Y
Cu
O−
Ba
Ucathode
dk
(a)
dc, rf or mf power supply
J
Cathode
N S S N
Magnetron
Cooling
Earth shield
Target
Gas supply (Ar/O2)
Substrate
Heater
Pump
Pressure control
(b)
Dark discharge
Glow discharge
Arc discharge
Townsend regime
Breakdown voltage
Glow to arc transition
Saturation regime
Normal glow
Abnormal glow
Non-thermal
Thermal arc
Voltage (V)
Current (A)
800
600
400
200
0
10−10
10−8
10−6
10−4
10−2
10^0
10^2
10^4
(c)
Working regime
Deposition rate (a.u.)
O2 flow (a.u.)
80
60
40
20
0
0
20
40
60
80
(d)

1.7 Schematic sketches of the sputter deposition process: (a) plasma generation and particle removal at the target, (b) sketch of a magnetron sputter device for HTS deposition, (c) voltage-current characteristic of the discharge, and (d) deposition rate as function of reactive gas content during the sputter process.

Dark discharge

Under the force of the electrical field, ions and electrons migrate to the electrodes producing a weak electric current. The current increases with increasing voltage in a highly non-linear way. The region of exponential current increase (Townsend discharge) ends in the electrical breakdown when the ions reaching the cathode start to possess sufficient energy to generate secondary electrons. The breakdown voltage for a particular gas and electrode material depends on the product of the pressure and the distance between the electrodes, it is expressed by Paschen's law (Paschen, 1889).

Glow discharge

The glow discharge regime owes its name to the plasma gas emitting light. In this regime a stable plasma is present. The secondary electrons will generate ions in the plasma that are accelerated towards the target. At the target electrons and particles are removed (Fig. 1.7a). The latter will form the film at the substrate placed opposite to the target (Fig. 1.7b). In the normal glow regime an increase of the energy leads to an increase of the current due to increase of the plasma area. A complete coverage of the target with the plasma is obtained in the abnormal discharge. The abnormal discharge represents the regime of homogeneous sputter deposition, and the energy of the particles can be modified by modifying the potential at the cathode. The cathode fall potential increases rapidly with current, and the dark space shrinks.

Arc discharge

The bombardment with ions ultimately heats the cathode causing thermionic emission. Once the cathode is hot enough to emit electrons thermionically, the discharge will change to the arc regime. Arcing will lead to destruction of the target. In spectro chemistry arc discharges are used in spark OES and DC arc spectroscopy.

Sputter deposition was the natural method to try when HTS materials were first discovered. However, the problem of large particle energies leading to defects and resputtering (see next section) was already recognised in this class of materials some 18 years before the discovery of YBCO for $Ba(PbBi)O_3$ deposition (Gilbert *et al.*, 1980) and has been thoroughly investigated since (Rossnagel and Cuomo, 1988). A method to avoid this problem is the thermalisation of the energetic species (mainly the negatively charged oxygen that is accelerated in the electric field) either by working at very high pressure (which also provides a particularly rich oxygen environment) or by 'off-axis' configuration at a modestly high sputtering pressure which forces all atoms emanating from the target to undergo a few energy reducing collisions before approaching the substrate.

Several different combinations and techniques using fully oxygenated stoichiometric targets are established, i.e. off-axis techniques using a cylindrical magnetron (Liu *et al.*, 2000), facing magnetrons (Newman *et al.*, 1991) or a single magnetron (Eom *et al.*, 1989), and on-axis techniques using non-magnetron sputtering at very high pressure (Divin *et al.*, 2008) or magnetron sputtering at high pressure (Wördenweber *et al.*, 2003, see Fig. 1.7b). Furthermore, the cathodes can be charged with dc, rf (16.56 MHz) or mf (medium frequency ranging from 20–200 kHz) power or a combination of these (Schneider *et al.*, 1997).

Generally, sputter techniques are usually highly reproducible. Furthermore, due to the use of a single stoichiometric target the process is compatible with high oxygen pressure, and calibration and rate control are readily obtained. Homogeneous composition can be obtained over a rather large area (typically 1–2" for off-axis sputtering and 4" and more for on-axis sputtering). However, drawbacks are the relatively small deposition rate (ranging between 0.1 nm/min and 20 nm/min for non-magnetron sputtering and magnetron sputtering, respectively), the presence of a plasma and high deposition pressures that hamper the use of *in-situ* characterisation such as low energy electron diffraction (LEED) or reflection high energy electron diffraction (RHEED), and the tendency of an instable plasma for variation of the local oxygen partial pressure (Fig. 1.7d).

Comparison of the different PVD techniques

PVD technologies are vacuum technologies. The particles are removed from the source via heating (evaporation and PLD) or ion bombardment (sputtering). The resulting energy of the particles at the substrate is one of the most important parameters that determines the nucleation and growth of resulting film.

At the source the particle energy is described by the Thomson relation $N(E) \propto E/(E + E_B)^3$ (Thompson, 1968, 1981) and the Maxwell-Boltzmann distribution $N(E) \propto E.\exp(-E/kT_e)$ for sputtering and evaporation, respectively. The resulting average particle energy is given by ½ of the binding energy E_B for sputtering and the (local) temperature T_e for evaporation, PLD, and CVD. Table 1.2 displays typical initial (i.e., at the source) particle energies that are characteristic for the different deposition technologies. On the one hand, the smallest energy is

Table 1.2 Typical energy of particles leaving the 'source' for the different PVD technologies

	Typical particle energy (eV)
Sputtering	6–8
PLD	1–2
Evaporation	0.06–0.08
CVD	0.005–0.01

associated with CVD followed by evaporation. This is one of the reasons for using these processes for the fabrication of defect-free layers, e.g. in the semiconductor industry. On the other hand, the largest particle energy is provided in the sputter technologies. Due to the high particle energy, sputter deposited films have a good mechanical stability and adhesion, but they are usually loaded with defects. This is of advantage for applications for which the mechanical properties and film adhesion play a major role, e.g. mechanical hardening, optical coating or CD fabrication. However, in the case of structurally perfect HTS films, defect generation due to high energy represents a problem for sputtering as well as for PLD. A solution to this problem is given by the so-called thermalisation of the particles, i.e., the reduction of the particle energy due to interaction of the particles with the process gas during the particle transport from the source to the substrate.

The transport process and, thus, the thermalisation of particles is simulated in Hollmann *et al.*, 2005 and illustrated in Plate I in the colour section between pages 244 and 245. The simulation is based on the *Monte Carlo* method for describing the energy and angular distributions of particles leaving the source. The initial angular distribution of particles is $dN(\vartheta)/d\vartheta \propto \cos^n(\vartheta)$ with typically $n = 1$ for evaporation and sputtering, $n = 5$–10 for PLD (explosion-like removal of material in overcritical liquid state). The mean-free path of the particles can be evaluated. The result is comparable with the text book expression for the mean free path for atmosphere and room temperature

$$\lambda_{\text{lit}} \cong 0.063\ \text{mm}/p, \qquad [1.1]$$

with p representing the pressure in mbar (see Plate I(a) in colour section).

In the simulation (Hollmann *et al.*, 2005), the scatter events are described via a quasi-hard-sphere (QHS) model for the interactions between atom particles. Atoms leaving the target are characterised by their (randomised) initial energy E_0 and direction of motion. During the transport the atoms move straight over a (randomised) distance δr before colliding with a process gas atom. The motion of the gas atoms is chaotic, i.e. position and directions of motion of the colliding atoms are randomised. The scattering process is repeated until the atom reaches either a surface of the chamber or the substrate. The microscopic cross-section σ_{qhs} of the elastic interaction of two particles within the framework of the obtained QHS-model depends on the energy E_c of their relative motion:

$$\sigma_{\text{qhs}} = \pi \cdot r^2_{\min}(E_C), \qquad [1.2]$$

where $r_{\min}$ represents the minimum distance between two atomic particles in case of ‘head-on’ collision, i.e., impact parameter $b = 0$ (see colour Plate I(c)). Using Born-Mayer interatomic interaction potential (Born and Mayer, 1932) for interatomic distances r, the expression for $r_{\min}$ is given by

$$r_{\min} = -b_{BM}(Z_1, Z_2) \cdot \ln \frac{E_C}{A_{BM}(Z_1 \cdot Z_2)^{3/4}}. \qquad [1.3]$$

Here Z_1 and Z_2 represent the atomic numbers, and A_{BM} and b_{BM} the different constants of the Born-Mayer expression (Petrov *et al.*, 1999; Born and Mayer, 1932). Accordingly, the mean free path λ_{qhs} of atomic particles in a gas medium is given by:

$$\lambda_{qhs} = \frac{1}{N\pi \cdot r^2_{min}(E_C)}, \qquad [1.4]$$

where N is the number density of the gas atoms.

Plate I(a) shows the pressure dependence of λ_{lit} and λ_{qhs}. It demonstrates that for 'classical deposition techniques' that work at low pressure, scatter processes between the particles and the process gas need not be considered. However, for the high-pressure processes scatter events have to be considered. The number of scatter events per particle arriving at the substrate increase dramatically in the pressure regime of 1 mbar which is the pressure regime for the deposition of HTS films via sputter and PLD (see Plate I(b)). As result of the scatter events:

- the particle energy is reduced (thermalisation),
- the deposition rate is reduced, and
- the stoichiometry is modified.

Whereas the first effect is intended and necessary for the deposition of HTS material, the latter two effects lead to problems for HTS deposition. For potential industrial applications, the rate is of importance, and for large-area deposition (where usually large target-substrate distances are necessary) the deviation of the stoichiometry causes problems (see Plate I(d), Wördenweber *et al.*, 2003). Nevertheless, sputtering and PLD provide the possibility of inducing defects that could be used to engineer mechanical as well as electronic properties (Einfeld *et al.*, 2001).

Finally, the different pressure regimes used for the different PVD technologies automatically define the preparation regime in the pressure-temperature phase diagram (Fig. 1.8). In order to provide a high mobility of the adsorbed adatoms at the substrate, usually the highest temperature is chosen for which the YBCO phase (1–2–3 phase) is still stable. This is typically the tetragonal phase $YBa_2Cu_3O_y$ with y close to 6. The transition to the orthorhombic phase is performed after deposition (see Fig. 1.8). Using activated oxygen or special temperature-pressure, process steps are usually included in order to improve or speed up the uptake of oxygen (Ockenfuss *et al.*, 1995).

1.2.2 CVD and MOCVD methods

Attempts to use MOCVD to grow HTS films began soon after the discovery of YBCO in 1987 (Yamane *et al.*, 1988). However, MOCVD of YBCO, an oxide compound composed of multiple heavy-metal elements, turned out to be quite difficult. The lack of gas-phase or liquid-phase metalorganic precursors for the

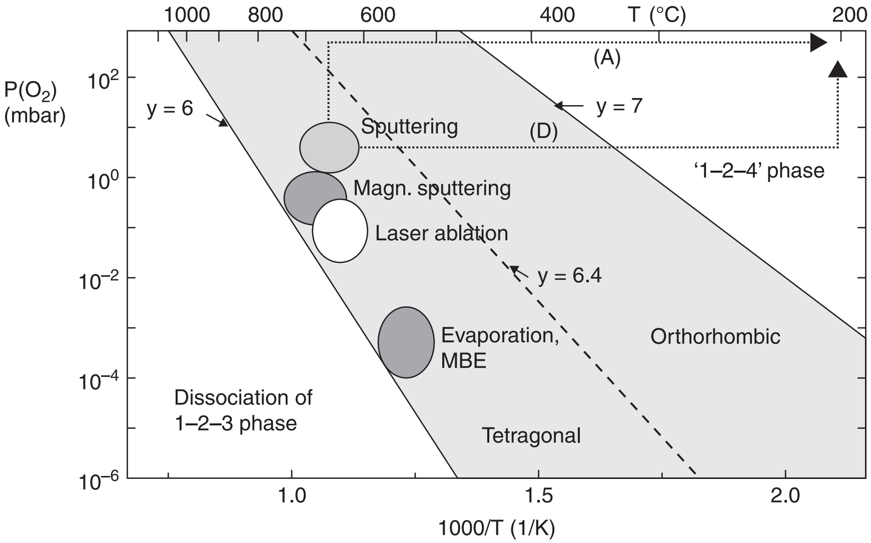

1.8 Pressure–temperature phase diagram for YBCO according to Bormann *et al.* (1989) and Hammond *et al.* (1989). The 1–2–3 phase is stable in the regime indicated by the shaded area, which is divided into the tetragonal and orthorhombic phase. The deposition typically takes place in the tetragonal regime. *In-situ* post-deposition treatments typically follow routes (A) or (D), here indicated for high-pressure sputtering.

heavy-metal elements restricted MOCVD of HTS to the use of solid precursors. These solid precursors turned out to be unstable in the vapour-phase composition, e.g. the commonly used precursors for YBCO deposition (the so-called thd precursors: 2,2,6,6,-tetramethyl-3,5-heptanedionate for Y, Ba, and Cu, respectively) exhibit a high melting point and a low vapour pressure. This instability is strongest of the Ba component, as demonstrated for $Ba(thd)_2$ (Becht, 1996; Richards *et al.*, 1995; Nagai *et al.*, 1997; Burtman *et al.*, 1996; Busch *et al.*, 1993). In order to stabilise the vapour-phase composition of YBCO, alternative precursors or/and novel concepts had to be developed.

For example, the successful use of a fluorinated barium precursor ($Ba(tdfnd)_2$·tetraglyme, where tdfnd is tetradecafluorononanedione) has been reported that is stable at its operating vaporisation temperature of ~145°C (Richards *et al.*, 1995). Using the precursors $Ba(tdfnd)_2$·tetraglyme, $Y(thd)_3$·4tBuPyNO, and $Cu(tdfnd)_2 \cdot H_2O$, which are all evaporated from the liquid phase, a high reproducibility of the film composition was reported (Busch *et al.*, 1993). However, these fluorinated precursors required the addition of water vapour in the deposition process to avoid the formation of BaF_2, which in turn led to problems associated with the removal of HF. Nagai *et al.* (1997) and Yoshida *et al.* (1996) reported that high-crystalline quality MOCVD YBCO films are obtained by liquid-state nonfluorinated sources of $Y(thd)_3{\cdot}4tBuPyNO$, $Ba(thd)_2{\cdot}2tetraene$, and $Cu(thd)_2$. Other adducts that have been used to stabilise the Ba-thd precursor include triglyme and phenanthroline.

Another approach of improved stability is given by the transition from solid-source precursor delivery to liquid-source precursor delivery. These concepts include: (i) liquid-source precursor delivery systems, (ii) direct injection of the precursor in a flash vaporiser (Onabe *et al.*, 2001) or (iii) a two-step evaporation process in a belt-driven system, where the solvent is evaporated in the first step and the precursor is subsequently vaporised in the second step (Stadel *et al.*, 2000).

Irrespective of whether solid- or liquid-phase precursors were used, the traditional method of vapour delivery, with each precursor delivered from a separate vessel, had limited the application of MOCVD to short time runs for YBCO wafer fabrication. Single-source liquid delivery systems (Zhang *et al.*, 1992) are more attractive, especially for the continuous deposition of YBCO films, for instance for coated conductors (Stadel *et al.*, 2003; Selvamanickam *et al.*, 2003). Recent developments in MOCVD precursors and their delivery schemes have been responsible for the dramatic progress in using the MOCVD technique for short time runs and continuous deposition of HTS material.

1.2.3 CSD techniques

Chemical solution deposition (CSD) of HTS material represents all chemical deposition methods ranging from sol-gel to metal-organic decomposition (MOD). Since CSD is no vacuum technology, the major advantage of this process lies in the low investment costs and low energy consumption. Among the different *ex-situ* techniques, CSD is nowadays one of the most promising candidates for deposition of HTS coated conductors including both buffer layer and YBCO (Pomar *et al.*, 2006). On the one hand, it has been demonstrated that high-quality epitaxial YBCO can be grown by PVD onto MOD buffer layers (Rupich *et al.*, 1999; Jarzina *et al.*, 2005). On the other hand, it has been shown that high critical currents can be achieved in YBCO thin films grown by the trifluoroacetates (TFA, $(OCOCF_3)$) route on single crystals or on vacuum deposited buffer layers (Araki and Hirabayashi, 2003; Castano *et al.*, 2003; Rupich *et al.*, 2004; Obradors *et al.*, 2004).

Although different chemical solutions can be chosen (e.g. TFA route, fluorine-free route, water or water-free routes) the basic steps of the CSD processes are fairly similar (Fig. 1.9). Starting with the different educts, the precursor is synthesised. The resulting solution is deposited onto the substrate via spray, spin or dip coating. Depending on the process a consolidation starts due to chemical reaction (sol-gel) or evaporation of the solvent (MOD). Drying steps and pyrolysis (typically at 150–400°C) lead to an amorphous layer. Finally this layer is crystallised at elevated temperature (typically 600–1000°C).

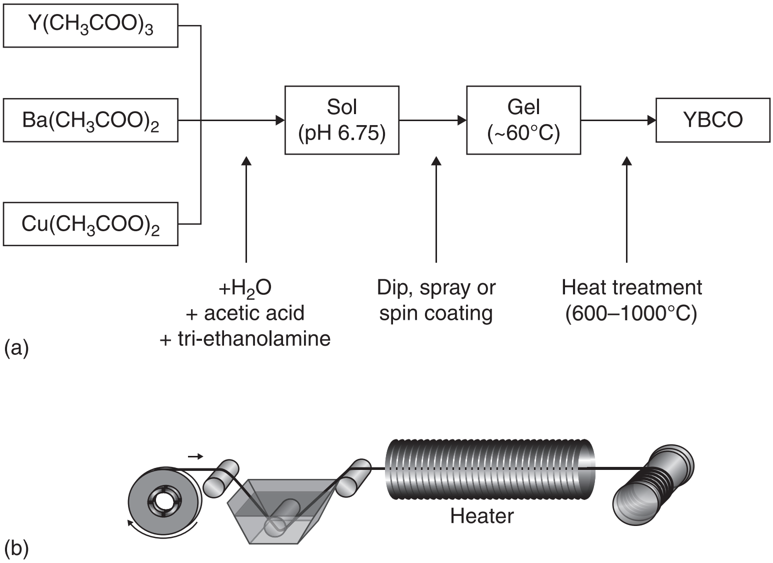

1.9 Schematic sketch of a CSD technology according to Bäcker (2008). (a) Diagram of the AWAT process based on acetates ($C_2H_4O_2$) and (b) continuous dip-coating process for the production of HTS coated conductors.

1.3 HTS film growth characterisation

Growth of cuprate films has remained at best a complicated matter due to its rather complex multicomponent crystal structures of the layered cuprates, which are prone to a variety of defects and growth morphologies, and the extreme deposition parameters (high process pressure and temperature), which furthermore have to be controlled very accurately. A brief sketch of growth mechanisms, in general, and HTS thin film growth, in particular, is given in this section. The general outline of the description is given in Fig. 1.10, detailed information is given in Wördenweber (1999). The emphasis of the following brief description is on PVD processes and the specific problems of adsorption of particles, oversaturation, epitaxy, lattice mismatch, defect generation, stress and strain that represent (a) important problems and (b) options for engineering the properties of oxide films, especially HTS thin films.

1.3.1 Nucleation and phase formation

After transport, particles impinge on the substrate. Chemical adsorption is only possible if the chemical adsorption potential $E_a > 0$, i.e., if the system is chemically

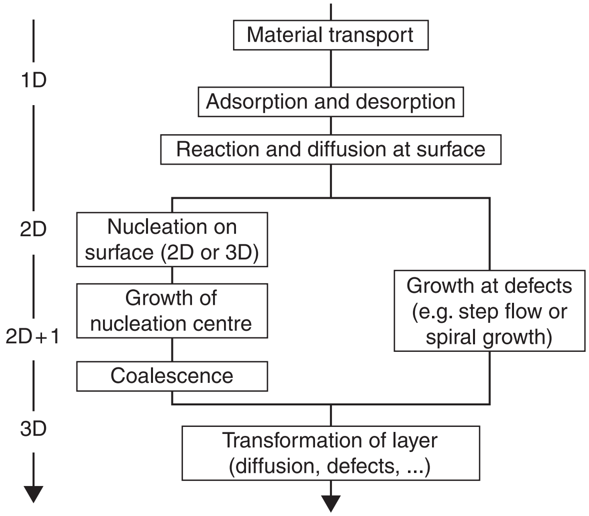
1D
2D
2D+1
3D
Material transport
Adsorption and desorption
Reaction and diffusion at surface
Nucleation on surface (2D or 3D)
Growth of nucleation centre
Coalescence
Growth at defects (e.g. step flow or spiral growth)
Transformation of layer (diffusion, defects, ...)

1.10 Schematic sketch of the adsorption, nucleation, and thin film growth on ideal substrates (left route) and dominated by defects of the substrate's surface (right route). The nucleation and growth process of films can be considered to be a transition from a '1D' particle to a 3D layer (arrow left side).

not inert (Fig. 1.11). The adsorption rate is defined by the number of adatoms per area and time:

$$R = \frac{dn}{dt} \qquad [1.5]$$

and the adatom average migration is given by:

$$\lambda = \sqrt{2D\tau} = \sqrt{2}a_o \exp\left(\frac{E_a - E_d}{2kT_s}\right) \qquad [1.6]$$

respectively. $D = D_o \exp(-E_d/kT_s)$ describes the diffusion, $a_o = (D_o/v)^{1/2}$ is the hopping rate, $\tau = (1/v)\exp(E_a/kT_s)$ is the average resident time, $\upsilon \approx 10^{12}$–10^{14} Hz is the attempt frequency, and T_s, D_o, E_a and E_d represent substrate temperature, diffusion constant, chemical adsorption potential and desorption potential, respectively. During growth from melt (e.g. liquid phase epitaxy) or solution the adatom can easily be desorbed from the surface, i.e. the residence time is relatively short. During growth from vapour (PVD and CVD techniques) the activation energy for desorption is typically larger, resulting in a larger migration length and a larger sticking coefficient.

Nevertheless, inserting typical values for E_a, E_d and D_o for oxides and PVD yields extremely small values for the resident time and migration of $\tau \ll 1$ps and $\lambda < 1$ nm. Experimentally much larger values of $\tau \approx 0.2$–0.5 s and $\lambda \approx 100$–500 nm are reported (Koster *et al.*, 1998). This difference is explained by the particle transport via the gas phase (Wördenweber, 1999). For this mechanism, a

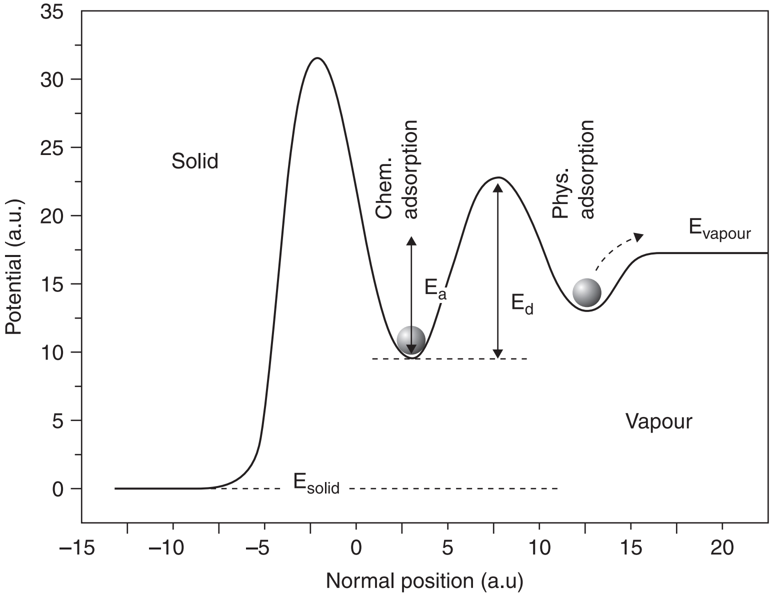

1.11 Schematic sketch of the adsorption potentials the impinging atom experiences at the film surface.

supersaturated gas phase has to be established at the substrate. Desorbed atoms will be re-adsorbed and, therefore, they can migrate larger distances than theoretically expected (Fig. 1.12). As a consequence supersaturated gas phases are vital for the phase formation and deposition. This represents a problem for a number of deposition devices, especially for large-area PVD.

During growth of lattice-matched layers, a layer-by-layer (Frank-van der Merwe) growth mechanism is usually observed. However, even in a layer-by-layer growth the resulting heterojunction interfaces are not perfectly planar. This is especially important in devices (e.g. Josephson junctions) where a monolayer change or defects can strongly affect the electronic properties. Layer-by-layer growth is generally limited by the surface morphology of the underlying substrate (see Fig. 1.13):

- As long as the surface migration length λ of the oncoming adatoms is clearly smaller than substrate features (e.g. l_s defined by terraces separated by step edges in vicinally cut single crystal substrates) growth occurs due to the nucleation of two-dimensional (2D) islands.
- If the migration length is larger than surface terrace size (i.e. $\lambda > l_s$), growth is dominated by attachment of adatoms to the step edges of the terraces. The step edges then propagate at a velocity depending on the step density and growth rate. This limit is called step-flow growth. The difference between these two regimes can be observed by RHEED oscillations (see Fig. 1.13(a)).

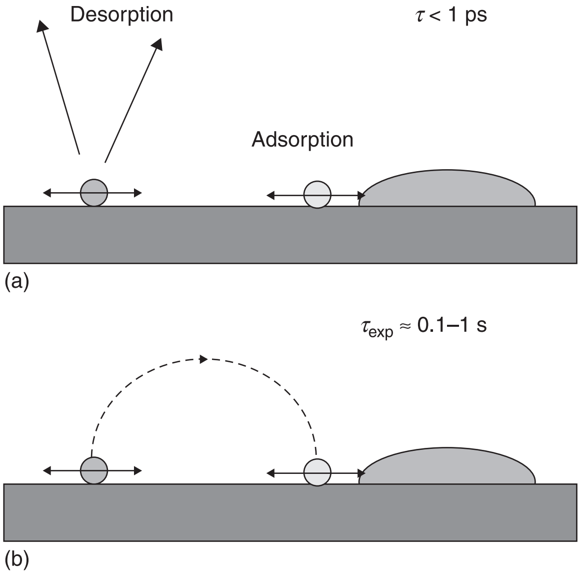
Desorption
τ < 1 ps
Adsorption
(a)
τ_exp ≈ 0.1–1 s
(b)

1.12 Schematic sketch of the phase formation without (a) and with (b) particle transport via the supersaturated gas phase.

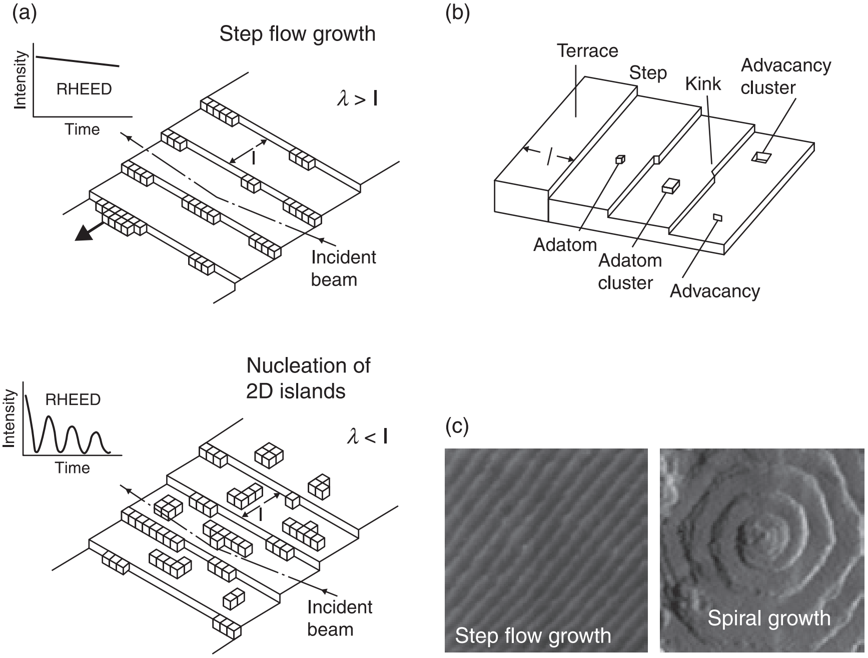
(a)
Step flow growth
Intensity
RHEED
Time
λ > l
l
Incident beam
(b)
Terrace
Step
Kink
Advacancy cluster
l
Adatom
Adatom cluster
Advacancy
Nucleation of 2D islands
Intensity
RHEED
Time
λ < l
l
Incident beam
(c)
Step flow growth
Spiral growth

1.13 (a) Schematic sketch of step flow growth and nucleation of 2D islands, (b) sketch of various topographical structures of real single crystalline substrates, and (c) atomic force microscopy micrographs of YBCO step flow growth on a vicinal cut $SrTiO_3$ substrate and spiral growth (Matijasevic *et al.*, 1996).

- Finally, since ‘real substrates’ are usually cut in slight vicinal ways in both in-plane directions, kinks are usually present at the steps (Fig. 1.13(b)). These kinks can be the starting point for spiral growth mode (Fig. 1.13(c)).

Thus, the growth (heteroepitaxial nucleation and homoepitaxial growth) are strongly determined by the competition between the mobility of the oncoming particles, which can be affected by the preparation method and conditions, and the surface morphology of the substrate, which is among others defined by the cut of the substrate. By modifying the preparation process or the miscut (vicinal) angle of the substrate, the growth mode can be changed from 2D island growth to step flow growth or spiral growth.

1.3.2 Heteroepitaxial growth, stress and defects in HTS films

Heteroepitaxial layer growth represents a major technology for advanced thin film electronic – e.g. for semiconductor and oxide electronics – and for basic solid state research. The most fundamental questions in this automatically strained-layer growth nevertheless are:

- Up to what thickness are heteroepitaxial layers stable?
- In which type of misfit do defects develop?
- What happens upon modification of the misfit for instance due to cooling of the film?

Generally, it is believed that below a critical thickness the strained state is the thermodynamic equilibrium state, and above a critical thickness a strained layer may be metastable or it may relax (Downes *et al.*, 1994). Different critical thicknesses might be associated to different types of misfit defects, e.g. dislocations, misalignments, or even cracks (Zaitsev *et al.*, 1997a). Stress σ in heteroepitaxially grown films results from both an intrinsic and temperature-dependent component. The main reason for the development of intrinsic stress in heteroepitaxially grown films is given by the nominal lattice mismatch

$$\varepsilon_o\left(T\right)=\left|\frac{a_{film}(T)-a_{substrate}(T)}{a_{film}(T)}\right|, \qquad [1.7]$$

at growth condition, where ‘a’ represents the different in-plane lattice parameters. The thermal contribution is due to the difference in thermal expansion coefficient between the film and the underlying substrate resulting in a temperature modified strain $\varepsilon_0(T)$ for instance during cooling of the sample (Ohring, 1991; Hoffman, 1976; Taylor *et al.*, 2002). Due to these two contributions, the resulting generation of defects in our films is discussed in two steps:

(1) generation of lattice misfit dislocations during the growth of HTS films at elevated temperature (typically 700–900°C for YBCO), and

(2) generation of cracks that are most likely generated during the cooling down after deposition.

During deposition, defect-free films grow up to a critical thickness d_c from whereon defects develop in the layer. This situation is most generally described initially by van der Merwe (1962) and later by Matthews and Blakeslee (1974). In these theories, the line tension of a misfit dislocation of finite length is balanced by the force due to the strain in the layer on the termination of the misfit dislocation. Alternatively and equivalently, the energy of the system with and without the misfit dislocation may be considered (Hu, 1991; Fitzgerald, 1991; Freund, 1990). Although in either approaches several approximations of uncertain effect are made, reasonable values for the critical thickness d_c are obtained that are comparable to experimental values (People and Bean, 1985) and provides the basis for the discussion of defect development in semiconducting thin films. For instance the Matthews theory predicts a critical thickness for the development of dislocation lines (Matthews and Blakeslee, 1974):

$$d_c = \frac{C}{\varepsilon_{\text{Intrinsic}}} \ln\left[O\left(d_c\right)\right], \qquad [1.8]$$

where C contains the details of the crystal and the dislocation. Different versions of the term $O(d_c)$ have been discussed by different authors (Downes *et al.*, 1994; Matthews and Blakeslee, 1974; Hu, 1991; People and Bean, 1985), the resulting predictions of critical thickness can vary by at least a factor of two. For instance the development of misfit dislocation lines has been described with this approach by People and Bean, (1985):

$$d_c \cong \left(\frac{b}{4\pi\left(1+\nu\right)\varepsilon_{\text{Intrinsic}}}\right)\left(\ln\left(\frac{d_c}{b}\right)+1\right), \qquad [1.9]$$

where b and ν represent the extension of the dislocation line, and Poisson's ratio, respectively.

Typical predictions for the critical thickness describing the development of misfit dislocations in YBCO are given in Fig. 1.14. Inserting reasonable values and taking into account that the theories are estimates of the critical thicknesses within a factor of about 2, for YBCO on $SrTiO_3$ a critical thickness $d_c < 10$ nm is predicted (Fig. 1.14(c)). Thus, misfit dislocations will be generated already for extremely thin films.

After deposition of the HTS layer at elevated temperature (e.g. 600–900°C for different PVD technologies) the sample is cooled down to room temperature. Due to the mismatch of the thermal expansion coefficient, additional stress is imposed on the HTS layer (see eq. [1.7]). Taking into account the presence of misfit dislocations generated during the growth process, the resulting strain imposed on the film can be described (Zaitsev *et al.*, 1997a; Fitzgerald, 1991) by:

$$\varepsilon_{\text{film}} = \varepsilon_o - \delta = \left|\frac{a_{\text{film}}(T) - a_{\text{substrate}}(T)}{a_{\text{film}}(T)}\right| - \delta, \qquad [1.10]$$

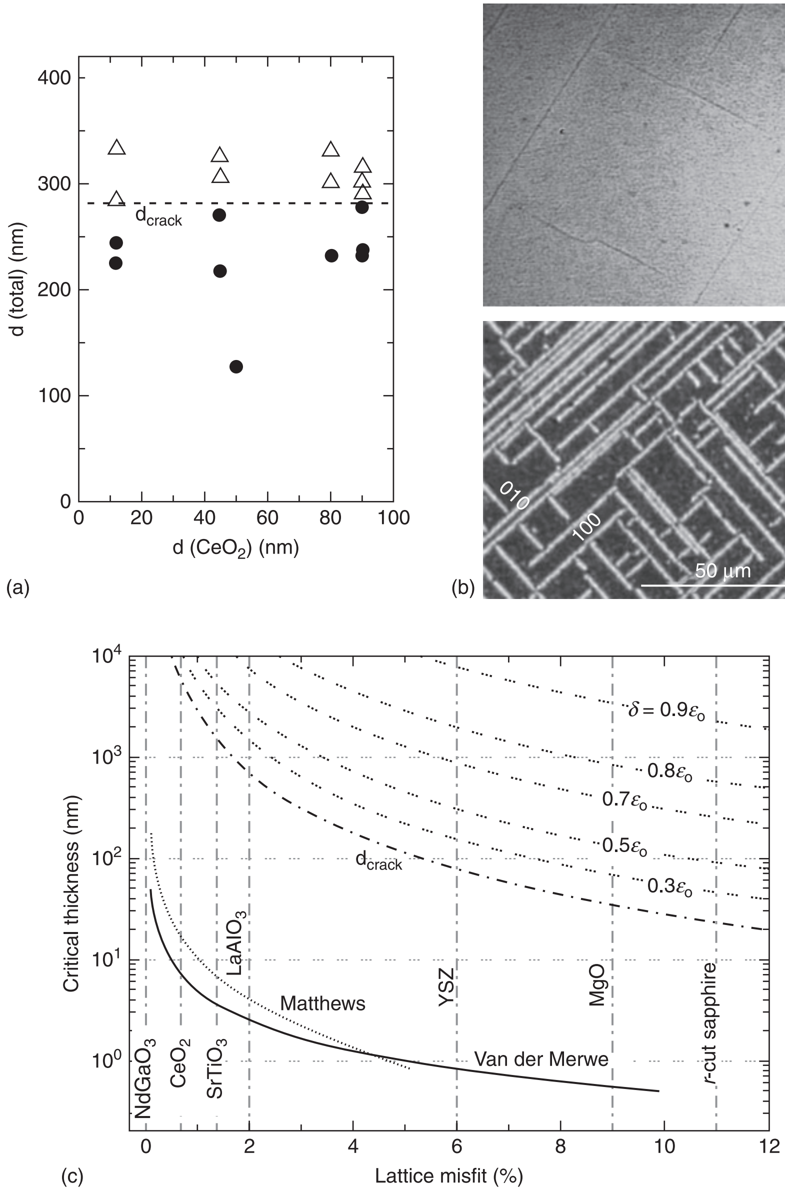

1.14 (a) Experimentally determined critical thickness d_{crack} for YBCO/CeO_2 on *r*-cut sapphire, (b) images of cracks in YBCO on sapphire (Kästner *et al.*, 1995), and (c) theoretical prediction of different critical thicknesses as function of lattice misfit. In (c), the critical thickness for the generation of misfit dislocations according to van der Merwe (1962) (black line) and Matthews theory (dotted line, eq. [1.9]), and the critical thickness for crack generation according to eq. [1.10] and different values of δ is plotted. The lines indicate the lattice misfit of YBCO with respect to various substrates.

where δ describes the release of stain due to the presence of defects or misalignments. While defects and misalignments have developed during growth, cracks are expected to develop during cooling down if this is energetically favourable. According to the theory of fracture of solids, the amount of strain energy that is released per unit length of a two-dimensional crack (Zaitsev *et al.*, 1997a; Cottrell, 1975) is given by:

$$E_{crack} = \pi Y \varepsilon^2 \left(\frac{a}{2}\right)^2, \qquad [1.11]$$

where a represents the height of the crack (a = d, if the crack is normal to the film surface) and Y is the Young's modulus of the material. The Young's modulus of bulk YBCO amounts to Y ≈ 300 (Fitzgerald, 1991). The formation of a crack is energetically favourable, if E_{crack} exceeds the energy $E_{surface}$ (energy per unit crack length) required for the (initial) formation of the two new surfaces of the crack. Therefore, the critical film thickness for crack formation is given for $E_{crack} = 2E_{surface}$:

$$d_{crack} = \frac{8E'_{surface}}{\pi Y \varepsilon^2}, \qquad [1.12]$$

with $E'_{surface} = E_{surface}/d$. The energy of the crack's surfaces is estimated by summation of the binding energies E_B of all atoms at these surfaces. Generally binding energies of oxides are of the order of 15 eV. The resulting surface energy for crack along [100], [010] or [001] axes of YBCO results in a surface formation energy $E'_{surface} \approx 31$–34 J/m^2 (Zaitsev *et al*, 1997a; Hollmann *et al.*, 2009).

Figure 1.14 shows the resulting critical thickness d_{crack} for different values of δ (in units of ε_o). The theoretical values of d_{crack} are comparable with experimental observation for epitaxial HTS layers in general. Ideal, defect-free films show the smallest critical thickness. For a misfit of ~10–11% (e.g. YBCO on sapphire) crack-free layers are limited by $d_{crack} < 30$ nm. With increasing δ the critical thickness increases.

All heteroepitaxially grown HTS films have the following.

- They possess misfit defects that are generated during the growth unless they are quite thin ($d < d_c$). As a result, $\delta > 0$ and the critical thickness for crack formation is enhanced with respect to the critical thickness of defect-free HTS films.
- The critical thickness for crack formation d_{crack} is large for small lattice mismatch, it decreases strongly for larger mismatch, e.g. YBCO on YSZ, MgO or sapphire.
- The critical thickness d_{crack} can be enhanced by artificially inducing adequate defects that take up the stress in the layer. This has been demonstrated for YBCO on sapphire used for microwave applications (Einfeld *et al*, 2001). The generation of defects (e.g. Y_2O_3 precipitates in YBCO) represents one way to engineer the mechanical and electronic properties of HTS films.

1.3.3 Characteristic film properties

In spite of the differences in the growth technologies, deposition parameters and resulting growth mechanisms, a number of characteristic values for the electronic, structural, and morphologic properties of HTS films can be given, that might serve as a kind of benchmark for high-quality HTS films. For YBCO these are: a surface roughness of $r_{\text{peak-to-peak}} \approx 10$–20 nm, a FWHM of the XRD rocking curve of the (005) reflex $\Delta\omega \approx 0.1$–0.3°, a RBS minimum channelling yield of $\chi_{\min} \approx 2$–3 %, a resistivity at 300K of ρ (300K) ≈ 3.5–4 μΩm, a resistance ratio of $\rho(300\text{K})/\rho(100) \approx 3$–3.3, a critical temperature (offset, inductive measurement) of $T_{c,\text{off}} \approx 88$–92 K, a transition width (inductive measurement) of $\Delta T_c \approx 0.5$–0.8 K, a critical current value (resistive measurement) of J_c(77K, 0T) ≈1–5MA/cm^2, and a microwave surface resistance of R_s(77K, 10GHz) ≈ 400 μΩ (Fig. 1.15). Similar sets of data are available for other HTS superconducting films.

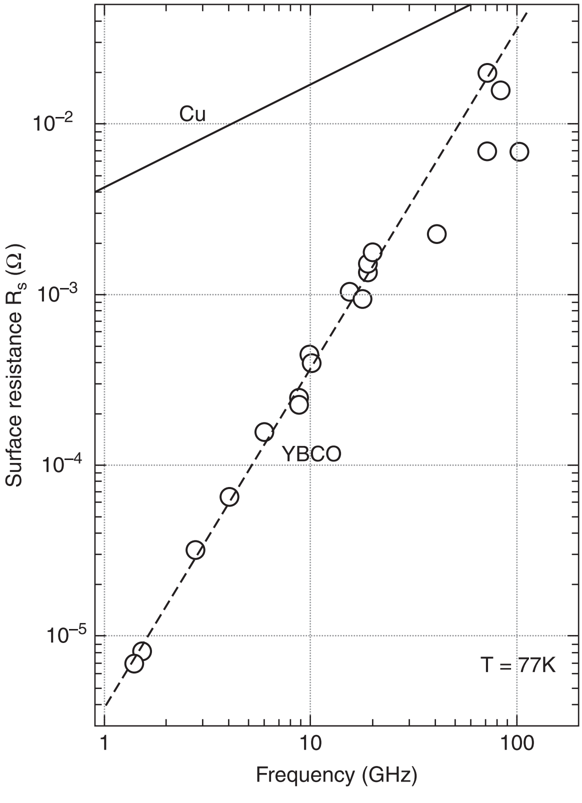

1.15 Comparison of the frequency dependence of the microwave surface resistances of YBCO films on various substrates and Cu at 77K (Wördenweber, 1999).

1.4 Concluding remarks

Due to the extraordinary properties of HTS material – especially the extremely complex structure, small coherence length, and large anisotropy – the preparation of high-quality HTS thin film requires extremely demanding deposition technologies. Different technological approaches have been sketched in this contribution. Each technique has its own advantages and disadvantages, and its own ultimate potential:

- Evaporation represents the classical approach. The development of rotating heaters opens the field towards high-pressure and reactive processes. With this innovation, evaporation turned out to be a reliable tool for the deposition of HTS films.
- PLD seems to be the most flexible technology. Especially, due to the development of laser-MBE, it has the potential to produce complex oxide film systems and multilayers, including layer-by-layer grown HTS films. The drawback of this technology is the small deposition area and the tendency to produce droplets due to the explosive-like removal of material at the target.
- Sputter deposition represents a well established technology. The high energy of the particles can be overcome via thermalisation. Therefore, this technology allows for a variation of the particle energy. Layers with optimised Josephson contacts have been grown with high-pressure cathodic sputtering at a pressure of several mbar (Divin *et al.*, 2008), whereas the high particle energy has been utilised in low-pressure sputtering at 0.5 mbar for microwave suitable YBCO films on sapphire for which the generation of defects leads to an enhancement of the critical thickness d_{crack} (Einfeld *et al*, 2001). Furthermore, sputtering has the advantage to be scalable to meter sizes. Its major drawback is the instability in the reactive mode, which becomes a problem with the size of the target.
- CSD is probably the technology most suitable for continuous HTS deposition, e.g. for HTS coated conductors. This technology has recently improved strongly and the financial argument might be another reason for its use in large-scale industrial application.

Due to the extreme demands of the HTS material, existing deposition technologies have been strongly improved and novel technologies have been developed. This procedure has been beneficial for the deposition technology not only of HTS material but also for the deposition of complex oxide material.

1.5 Acknowledgement

Valuable support from and discussions with E. Hollmann, J. Schubert, R. Kutzner, M. Bäcker, A.G. Zaitsev and A. Offenhäuser are greatly acknowledged.

1.6 References

Araki T and Hirabayashi I, 2003, 'Review of a chemical approach to $YBa_2Cu_3O_7$-x-coated, superconductors – metalorganic deposition using trifluoroacetates', *Supercond. Sci. Technol.* **16**, R71–R94.

Bäcker M, 2008, International Workshop on 'Nanostructured Superconductors: From fundamentals to applications', Freudenstadt-Lauterbad (Germany) 13–17 September.

Becht M, 1996, 'Metal-organic chemical vapor deposition as an emerging technique for the fabrication of $YBa_2Cu_3O_x$ tapes', *Appl. Supercond.* **4**, 465–474.

Bednorz J G and Müller K A, 1986, 'Possible high-T_c superconductivity in the Ba-La-Cu-O system', *Z. Phys.* **B64**, 189–193.

Blank D H A, Rijders G J H M, Koster G, and Rogalla H, 2000, 'A new approach in layer-by-layer growth of oxide materials by pulsed laser deposition', *J. Electroceramics* **4**, 311–318.

Born M and Mayer J E, 1932, 'Zur gittertheorie der Ionenkristalle', *Z. Phys.* **75**, 1–18.

Bozovic I, Eckstein J N, and Virshup G F, 1994, 'Superconducting oxide multilayers and superlattices – physics, chemistry, and nanoengineering', *Physica C* **235–140**, 178–181.

Braginsky V B, Ilchenko V S, and Bagdassarov Kh S, 1987, 'Experimental observation of fundamental microwave absorption in high-quality dielectric crystals', *Phys. Lett.* **120A**, 300–305.

Burtman V, Schieber M, Brodsky I, Hermon H, and Yaroslavsky Y, 1996, 'Raman and infrared spectroscopy and transport properties of aged organometallic precursors used for the deposition of high-T_c superconducting films', *J. Cryst. Growth* **166**, 832–835.

Busch H, Fink A, Müller A, and Samwer K, 1993, 'Beta-diketonate precursors for the chemical vapour deposition of YBaCuO', *Supercond. Sci. Technol.* **6**, 42–45.

Castaño O, Cavallaro A, Palau A, González J C, Rossell M, *et al.*, 2003, 'High quality $YBa_2Cu_3O_7$ thin films grown by trifluoroacetates metalorganic deposition', *Supercond. Sci. Technol*. **16**, 45–53.

Cottrell A H, 1975, in *Physics of Metals. 2. Defects* (ed. P B, Hirsch), Cambridge University Press: Cambridge, London, New York, Melbourne.

Dam B, Rector J, Chang M F, Kars S, de Groot D G, and Griessen R, 1994, 'Laser ablation threshold of $YBa_2Cu_3O_{6+x}$', *Appl. Phys. Lett.* **65**, 1581–1583.

Dimos D, Chaudari P, and Mannhardt J, 1990, 'Superconducting transport properties of grain boundaries in $YBa_2Cu_3O_7$ bicrystals', *Phys. Rev. B* **41**, 4038–4049.

Divin Y, Poppe U, Gubankov V, and Urban K, 2008, 'High-T_c Josephson square-law detectors and Hilbert spectroscopy for security applications', *IEEE Sensors Journal*, **8**, 750–757.

Dovidenko K, Oktyabrsky S, Tokarchuk D, Michaltsov A, and Ivanov A, 1992, 'The influence of the native $BaAl_2O_4$ boundary layer on the microstructure and properties of $YBa_2Cu_3O_{7-x}$ thin films grown on sapphire', *Mater. Sci. Eng. B* **15**, 25–31.

Downes J R, Dunstan D J and Faux D A, 1994, 'Numerical calculation of equilibrium critical thickness in strained-layer epitaxy', *Semicond. Sci. Technol.* **9**, 1265–1267.

Einfeld J, Lahl P, Kutzner R, Wördenweber R, and Kästner G, 2001, 'Reduction of the surface resistance in YBCO films by microscopic defects', *Physica C* 351, 103–117.

Eom C B, Sun J Z, Yamamoto K, Marshall A F, Luther K E, *et al.*, 1989, 'In situ grown $YBa_2Cu_3O_{7-d}$ thin films from single-target magnetron sputtering', *Appl. Phys. Lett.* **55**, 595–597.

Farrell D E, Williams C M, Wolf S A, Bansal N P, and Kogan V G, 1988, 'Experimental evidence for a transverse magnetization of the Abrikosov lattice in anisotropic superconductors', *Phys. Rev. Lett.* **61**, 2805–2808.

Farrell D E, Bonham S, Foster J, Chang Y C, Jiang P Z, *et al.*, 1989, 'Giant superconducting anisotropy in $Bi_2Sr_2Ca_1Cu_2O_{8+\delta}$', *Phys. Rev. Lett.* **63**, 782–785.

Farrell D E, Beck R G, Booth M F, Allen C J, Bukowski E D, and Ginsberg D M, 1990, 'Superconducting effective-mass anisotropy in $Tl_2Ba_2CaCu_2O_x$', *Phys. Rev. B* **42**, 6758–6761.

Fitzgerald E A, 1991, 'Dislocations in strained-layer epitaxy: theory, experiment, and applications', *Mater. Sci. Rep.* **7**, 87.

Freund L B, 1990, 'The driving force for glide of a threading dislocation in a strained epitaxial layer on a substrate', *J. Mech. Phys. Sol.* **38**, 657–679.

Gao J, Klopman B B G, Aarnink W A M, Reitsma A E, Geritsma G J, and Rogalla H, 1992, 'Epitaxial $YBa_2Cu_3O_x$ thin films on sapphire with a $PrBa_2Cu_3O_x$ buffer layer', *J. Appl. Phys.* 71, 2333–2337.

Gilbert L R, Messier R, and Krishnaswamy S V, 1980, 'Resputtering effects in Ba(Pb, Bi) O_3 perovskites', *J. Vac. Sci. Technol.* **17**, 389–391.

Hammond R B and Matthaei G L, 1993, 'Designing with superconductors', *IEEE Spectrum* **30**, 34–39.

Hilgenkamp H and Mannhardt J, 1998, 'Superconducting and normal-state properties of $YBa_2Cu_3O_{7-\delta}$-bicrystal grain boundary junctions in thin films', *Appl. Phys. Lett.* **73**, 265.

Hoffman R W, 1976, 'Stresses in thin films: The relevance of grain boundaries and impurities', *Thin Solid Films* **34**, 185–190.

Hollmann E K, Vol'pyas V A, and Wördenweber R, 2005, 'Monte-Carlo simulation of the particle transport during physical vapor deposition of ceramic superconductors', *Physica C* **425**, 101–110.

Hollmann E, Schubert J, Kutzner R, and Wördenweber R, 2009, 'Stress generated modifications of epitaxial ferroelectric $SrTiO_3$ films on sapphire', *J. Appl. Phys.* **105**, 114104 (6 pages).

Hu S M, 1991, 'Misfit dislocations and critical thickness of heteroepitaxy', *J. Appl. Phys.* **69**, 7901–7903.

Jaccard Y, Cretton A, Williams E J, Locquet J P, Machler E, *et al.*, 1994, 'Characterization of MBE-grown ultrathin films in the La_2-XSRXCu$O_{4+\delta}$ system', *Oxide Supercond. Phys. and Nano-Engineering* **2158**, 200–210.

Jarzina H, Sievers S, Jooss C, Freyhardt H C, Lobinger P, and Roesky H W, 2005, 'Epitaxial MOD-YSZ buffer layers on IBAD-YSZ substrates', *Supercond. Sci. Technol.* **18**, 260–263.

Jia C I, Kabius B, Soltner H, Poppe U, and Urban K, 1990, 'Interfacial defects in $YBa_2Cu_3O_7$/ $PrBa_2Cu_3O_7$-heterostructures on $SrTiO_3$ substrates', *Physica C* **172**, 81–89.

Kästner G, Hesse D, Lorenz M, Scholz R, Zakharov N D, and Kopperschmidt P, 1995, 'Microcracks observed in epitaxial thin films of $YBa_2\ Cu_3O_{7-\delta}$ and $GdBa_2Cu_3O_{7-\delta}$', *Phys. Stat. Sol. a*, **150**, 381–394.

Koster G, Rijnders G J H M, Blank D H A, and Rogalla H, 1998, 'In situ initial growth studies of SrTiO3 on SrTiO3 by time resolved high pressure RHEED', *Advances in Laser Ablation of Materials* **526**, 33–37.

Lahl P and Wördenweber R, 2005, 'Fundamental microwave-power-limiting mechanism of epitaxial high-temperature superconducting thin-film devices', *J. Appl. Phys.* **97**, 113911.

Liu X Z, Li Y R, Tao B W, Luo A, and Geerk J, 2000, 'The crystal perfection improvement of $Y_1Ba_2Cu_3O_{-x}$ thin films by afterglow plasma process', *Thin Solid Films* **371**, 231–234.

Logvenov G and Bozovic I, 2008, 'Artificial superlattices grown by MBE: Could we design novel superconductors?', *Physica C* **468**, 100–104.

Lorenz M, Hochmuth H, Grundmann M, Gaganidze E, and Halbritter J, 2003, 'Microwave properties of epitaxial large-area Ca-doped $YBa_2Cu_3O_{7-\delta}$ thin films on r-plane sapphire', *Sol. State Electr.* **47**, 2183–2186.

Matijasevic V C, Ilge B, Stäuble-Pümpin B, Rietveld G, Tuinstra F, and Mooij J E, 1996, 'Nucleation of a complex oxide during epitaxial film growth: $SmBa_2Cu_3O_y$ on $SrTiO_3$', *Phys. Rev. Lett.* **76**, 4765–4768.

Matijasevic V, Lu Z, Kaplan T, and Huang C, 1997, 'Atomic-absorption controlled reactive evaporation of HTS wafers for microwave applications', *Inst. Phys. Conf. Ser.* **158**, 189–192.

Matthews J W and Blakeslee A E, 1974, 'Defects in epitaxial multilayers: 1. Misfit dislocations', *J. Crystal Growth* **27**, 118–125.

Moeckly B H and Ruby W S, 2006, 'Growth of high-quality large-area MgB_2 thin films by reactive evaporation', *Supercond. Sci. Technol.* **19**, L21–L24.

Morimoto A and Shimizu T, 1995, Handbook of Thin Film Process Technology, ed. D A Glocker and S I Shah, IOP Publishing Ltd., A1.5.

Nagai H, Yoshida Y, Ito Y, Taniguchi S, Hirabayashi I, *et al.*, 1997, 'Preparation of $YBa_2Cu_3O_{7-y}$ films by metal organic chemical vapour deposition using liquid-state nonfluorinated sources', *Supercond. Sci. Technol.* **10**, 213–217.

Newman N, Cole B F, Garrison S M, Char K, and Taber R C, 1991, 'Double gun off-axis sputtering of large area $YBa_2Cu_3O_{7-\delta}$ superconducting films for microwave applications', *IEEE Trans. Magn.* **27**, 1276–1279.

Obradors X, Puig T, Pomar A, Sandiumenge F, Piñol S, *et al.*, 2004, 'Chemical solution deposition: a path towards low cost coated conductors', *Supercond. Sci. Technol.* **17**, 1055–1064.

Ockenfuss G, Wördenweber R, Scherer T A, Unger R, and Jutzi W, 1995, 'In-situ low pressure oxygen annealing of $YBa_2Cu_3O_{7-\delta}$ single- and multilayer systems', *Physica C* **243**, 24–28.

Ohring M., 1991, *The Materials Science of Thin Films*, Academic Aer, New York.

Okuda K, Kawamata S, Noguchi S, Itoh N, and Kadowaki K, 1991, 'Torque study of layered superconducting oxide $Bi_2Sr_2CaCu_2O_{8+\delta}$ single-crystal', *J. Phys. Soc. Japan* **60**, 3226–3229.

Onabe K, Akata H, Higashiyama K, Nagaya S, and Saitoh T, 2001, 'Superconducting property of $Y_1Ba_2Cu_3O_x$ films formed on silver substrates by continuous chemical vapor deposition technique', *IEEE Trans. Appl. Supercond.* **11**, 3150–3153.

Ossandon J G, Thompson J R, Christen D K, Sales B C, Kerchner H R, *et al.*, 1992, 'Influence of oxygen deficiency on the superconductive properties of grain-aligned $YBa_2Cu_3O_{7-\delta}$', *Phys. Rev. B* **45**, 12534–12547.

Paranthaman M P and Izumi T, 2004, 'High-performance YBCO-coated superconductor wires', *MRS Bulletin*, 533–536.

Paschen F, 1889, 'Über die zum Funkenübergang in Luft, Wasserstoff und Kohlensäure bei verschiedenen Drucken erforderliche Potentialdifferenz', *Annalen der Physik* **273**, 69–96.

People R and Bean J C, 1985, 'Calculation of critical layer thickness versus lattice mismatch for Ge_xSi_1-x/Si strained-layer heterostructures', *Appl. Phys. Lett.* **47**, 322–324.

Petrov, P K, Volpyas, V A, and Chakalov, R A, 1999, 'Three-dimensional Monte Carlo simulation of sputtered atom transport in the process of ion-plasma sputter deposition of multicomponent thin films', *Vacuum* **52**, 427–434.

Pomar A, Cavallaro A, Coll M, Gàzquez J, Palau A, *et al.*, 2006, 'All-chemical $YBa_2Cu_3O_7$ coated conductors on IBAD-YSZ stainless steel substrates', *Supercond. Sci. Technol.* **19**, L1–L4.

Richards B C, Cook S L, Pinch D L, Andrews G W, Lengeling G, *et al.*, 1995, 'MOCVD of high quality $YBa_2Cu_3O_{7-\delta}$ thin films using a fluorinated barium precursor', *Physica C* **252**, 229–236.

Rossnagel S M, and Cuomo J J, 1988, 'Ion-bombardment effects during film deposition', *Vacuum* **38**, 73–81.

Rupich M W, Palm W, Zhang W, Siegal E, Annavarapu S, *et al.*, 1999, 'Growth and characterization of oxide buffer layers for YBCO coated conductors', *IEEE Trans. Appl. Supercond.* **9**, 1527–1530.

Rupich M W, Verebelyi D T, Zhang W, Kodenkandath T, and Li X P, 2004, 'Metalorganic deposition of YBCO films for second-generation high-temperature superconductor wires', *MRS Bull.* **29**, 572–578.

Schneider J, Einfeld J, Lahl P, Königs T, Kutzner R, and Wördenweber R, 1997, 'Large area YBCO films deposited by unipolar pulsed magnetron sputtering', *Inst. Phys. Conf. Ser.* **158**, 221–224.

Selvamanickam V, Lee HG, Li Y, Xiong X, Qiao Y, *et al.*, 2003, 'Fabrication of 100 A class, 1 m long coated conductor tapes by metal organic chemical vapor deposition and pulsed laser deposition', *Physica C* 392–396, 859–862.

Stadel O, Schmidt J, Wahl G, Jimenez C, Weiss F, *et al.*, 2000, 'Continuous YBCO deposition onto moved tapes in liquid single source MOCVD systems', *Physica C* **341–348**, 2477–2478.

Stadel O, Schmidt J, Liekefett M, Wahl G, Gorbenko OYu, and Kaul AR, 2003, 'MOCVD techniques for the production of coated conductors', *IEEE Trans. Appl. Supercond.* **13**, 2528–2531.

Taylor T R, Hansen P J, Acikel B, Pervez N, York R A, *et al.*, 2002, 'Impact of thermal strain on the dielectric constant of sputtered barium strontium titanate thin films', *Appl. Phys. Lett.* **80**, 1978–1980.

Thompson M W, 1968, 'Energy spectrum of ejected atoms during high energy sputtering of gold', *Phil. Mag.* **18**, 377–414.

Thompson M W, 1981, 'Physical-mechanism of sputtering', *Physics Reports* **69**, 335–371.

Triscone J and Fischer Ø, 1997, 'Superlattices of high-temperature superconductors: synthetically modulated structures, critical temperatures and vortex dynamics', *Reports on Progress in Physics* **60**, 1673–1721.

Utz B, Semerad R, Bauer M, Prusseit W, Berberich P, and Kinder H, 1997, 'Deposition of YBCO and NBCO films on areas of 9 inches in diameter', *IEEE Trans. on Appl. Supercond.* **7**, 1272–1277.

Van der Merwe J H, 1963, 'Crystal interfaces – part II: finite overgrowths', *J. Applied Phys.* **34**, 123–127.

Wei Z, Li H, Hong W L, Lv Z, Wu H, *et al.*, 2008, 'Superconductivity at 57.3 K in La-doped iron-based layered compound $Sm_{0.95}La_{0.05}O_{0.85}F_{0.15}FeAs$', *J Supercond. Nov. Magn.* **21**, 213–215.

Wördenweber R, 1999, 'Growth of high-Tc thin films', *Supercond. Sci. Technol.* **12**, R86–R102.

Wördenweber R, Hollmann E, Poltiasev M, and Neumüller H W, 2003, 'Low-pressure large-area magnetron sputter deposition of $YBa_2Cu_3O_{7-\delta}$ films for industrial applications', *Supercond. Sci. Technol.* **16**, 584–589.

Yamane H, Masumoto H, Hirai T, Iwasaki H, Watanabe K, *et al.*, 1988, 'Y-Ba-Cu-O superconducting films prepared on $SrTiO_3$ substrates by chemical vapor deposition', *Appl. Phys. Lett.* **53**, 1548–1550.

Yoshida Y, Ito Y, Hirabayashi I, Nagai H, and Takai Y, 1996, 'Surface morphology and growth mechanism of $YBa_2Cu_3O_{7-y}$ films by metalorganic chemical vapor deposition using liquid sources', *Appl. Phys. Lett.* **69**, 845–847.

Zaitsev A G, Ockenfuss G, and Wördenweber R, 1997, 'Critical thickness of YBCO films on CeO_2 buffered sapphire', *Applied Superconductivity* **158**(1/2), 25–28.

Zaitsev A G, Wördenweber R, Ockenfuss G, Kutzner R, Königs T, *et al.*, 1997, 'Microwave losses and structural properties of large-area $YBa_2Cu_3O_7$ films on r-cut sapphire buffered with (001)/(111) oriented CeO_2', *IEEE Trans. on Appl. Supercond.* **7**, 1482–1485.

Zhang J, Gardiner R A, Kirlin P S, Boerstler R W, and Steinbeck J, 1992, 'Single liquid source plasma-enhanced metalorganic chemical vapor deposition of high-quality $YBa_2Cu_3O_{7-x}$ thin films', *Appl. Phys. Lett.* **61**, 2884–2886.

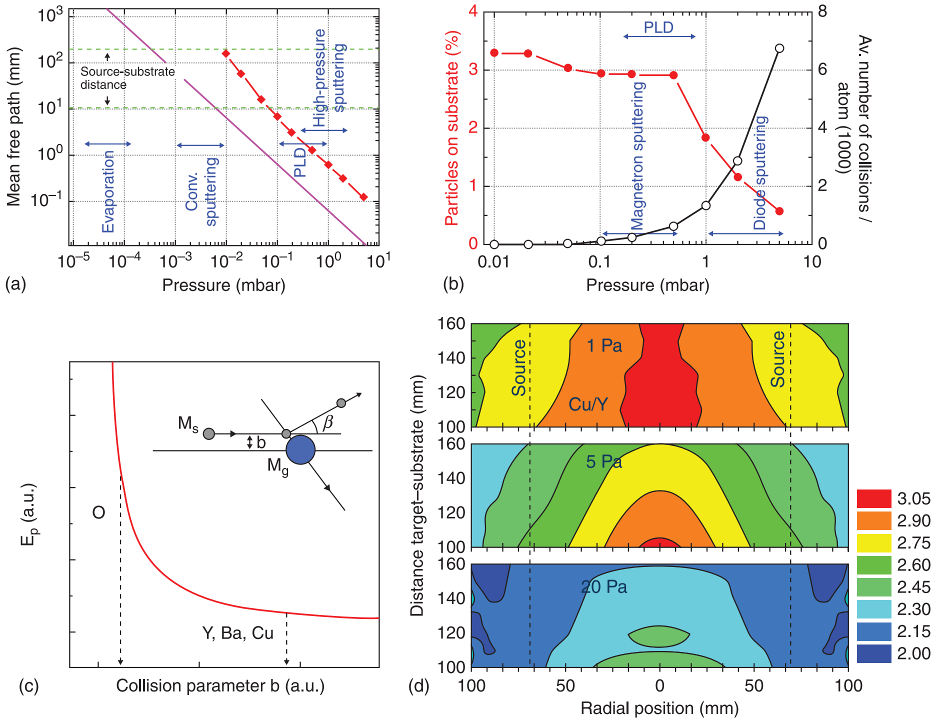

Plate I Sketch and data of the simulated particle flux from the source to the substrate according to Hollmann *et al.*, 2005. In (a) the simulated (Cu in $Ar/O_2 = 4:1$) and literature values (eq. [1.1] in this chapter) of the mean free path are compared. In (b) the pressure dependence of the percentage of particles arriving at the substrate and the average number of scatter events that these particles undergo during the process of traversing the distance between source and substrate are shown. The data are simulated for a sputter process (2″ Cu target, 1 cm^2 substrate, target–substrate distance of 5 cm, and gas mixture of $Ar/O_2 = 1$). The relation between particle energy and collision parameter b (eq. [1.2]) that is used in the QHS-model is shown in (c). The QHS-model is sketched in the inset with the impact parameter b, the process gas atom M_g, the sputtered atom M_s, and the scattering angle β relative to initial direction of motion of the sputtered atom due to the collision. In (d) the particle flux distribution Cu/Y is given as function of the position above a YBCO magnetron target. The position of the magnetrons is marked. The gas mixture is $Ar/O_2 = 4:1$.

2

Transport properties of high-T_c cuprate thin films as superconductive materials

J. VANACKEN and V. V. MOSHCHALKOV, Leuven Catholic University, Belgium

Abstract: In this chapter, the systematic evolution with doping of the normal state properties (resistivity and Hall effect) of the $La_{2-x}Sr_xCuO_4$ thin film cuprates is analyzed. This analysis reveals convincing evidence in favor of the presence of the charge-rich 1D features (stripes), which eventually determine the 1D character of the transport properties at temperatures below the so-called 'spin-gap' temperature T*(x). Measurements of the fluctuation conductivity show how stripe coupling close to T_c recovers the 2D character of the Cu-O planes which is responsible for the 2D Aslamasov–Larkin fluctuations at $T \sim T_c$ and the superconducting state itself at $T < T_c$. Stripes decoupling at low temperature, via strong magnetic fields, induces again a 1D stripe behavior, which, in the presence of impurity centers, leads to blocking of the 1D intra-stripe transport and consequently to the formation of the insulating state in underdoped $La_{2-x}Sr_xCuO_4$ at $T \rightarrow 0$.

Key words: in-plane resistivity, scattering mechanisms, scaling behavior, stripe coupling, Drude model, Hall effect.

2.1 Introduction

The close connection between the electrical resistivity and the scattering mechanisms of charge carriers is already well known from the Drude model, which treats the electrons in a metal as free non-interacting particles:

$$\rho = \frac{m^*}{ne^2\tau} \qquad [2.1]$$

where m* represents the effective mass, n the density and τ the scattering time of the electrons. Expression [2.1], based on a simple single electron picture, implies that the study of the resistivity of a material can give key information about the nature of the electronic scattering. According to the Bloch theory, electrons in a periodic scattering potential of a perfect crystal, are not scattered at all. The finite resistance to electron flow in normal metals is only exhibited because of the thermal vibrations of the ions (phonons), resulting in a resistivity ρ_{ph}, and crystal defects, giving a residual resistivity ρ_D. While ρ_D remains constant, ρ_{ph} varies with temperature. The Debye temperature Θ_D, which is a measure for the stiffness of a crystal, separates two temperature regions where $\rho_{ph}(T)$ reveals a different temperature dependence (Ashcroft 1976). At low temperatures, $T << \Theta_D$, phonon modes with a high excitation energy are frozen out. By increasing the temperature, more and more phonon modes get excited, thus strongly enhancing the electron–phonon scattering. In this temperature region, the resistivity ρ_{ph} increases fast with increasing temperature, obeying a T^5 law. At high temperatures, $T >> \Theta_D$, all phonon modes are already excited and the resistivity ρ_{ph} varies linearly with temperature. Finally, when the inelastic mean-free path approaches the lattice spacing at even higher temperatures, the resistivity ρ_{ph} saturates (Ioffe-Regel criterion). Aside from the scattering mechanisms due to deviations from perfect periodicity, another source of scattering arises from the interactions among electrons, giving rise to a resistivity ρ_{el}. However, this electron–electron scattering usually plays a minor role. At high temperatures, it is much less important than the phonon scattering, and at low temperatures, it is usually dominated by impurity or defect scattering. We conclude that the total resistivity ρ in ordinary metals is given by:

$$\rho = \rho_D + \rho_{ph} + \rho_{el} \qquad [2.2]$$

with ρ_{ph} the dominant term.

In high-T_c cuprates, however, the nominally metallic temperature dependence of the resistivity $\rho(T)$ has been explored at various levels of hole doping and for different geometrical configurations between the applied current and the crystallographic axes (Takagi *et al.* 1992a, Kimura *et al.* 1992, Bucher 1994, Ito *et al.* 1993, Batlogg *et al.* 1994, Hwang *et al.* 1994, Wuyts *et al.* 1996, Ando *et al.* 1996, Trappeniers 2000, Vanacken *et al.* 2001). From the slightly doped up to the strongly overdoped regime, the resistivity of these materials reveals a very anomalous behavior.

We will focus in this chapter on the in-plane resistivity $\rho_{ab}(T)$ of c-axis oriented epitaxial films, which impose by their geometry, a configuration where the current is applied parallel to the ab-plane. The shape of the $\rho_{ab}(T)$-curves for the different doping regimes is, in fact, universal for all high-T_c compounds. As a result, the analysis of the transport properties of a particular cuprate system, $La_{2-x}Sr_xCuO_4$, is also valid for other high T_c cuprates.

2.2 Temperature dependence of the zero-field resistivity in superconducting $La_{2-x}Sr_xCuO_4$ thin films

A clear insight into the scattering processes, which are responsible for the non-Fermi liquid behavior of the normal state in high-T_c cuprates, may provide a clue to the understanding of high-T_c superconductivity itself. The normal state electronic transport properties have been investigated because they give direct information about the scattering mechanisms, which are relevant for the systems. In the following section, the temperature dependence of the in-plane resistivity at zero magnetic field is presented for $La_{2-x}Sr_xCuO_4$ thin films with different doping levels. A remarkable scaling behavior of the temperature dependent in-plane resistivity is observed in the underdoped and slightly overdoped region, leading to the important conclusion that the scattering in these regimes is determined by the same underlying mechanism, independent of the Sr-content *x* or the carrier concentration.

2.2.1 Identification of the different types of ρ–T dependencies defines a generic phase diagram

In a narrow composition range in the overdoped superconducting region (the exact range may depend on the superconducting system), the in-plane resistivity ρ_{ab}(T) shows a robust linear behavior that extends from the critical temperature T_c up to temperatures as high as 1000 K [Takagi *et al.* 1992a] (Fig. 2.1, left side). The Debye temperature Θ_D for high-T_c compounds lies between 300 K and 450 K (Poole *et al.* 1995). If the observed linear temperature dependence of the resistivity would be a consequence of ordinary electron–phonon interactions, a tendency towards a T^5 dependence should certainly show up in the resistivity at $T \leq 0.2\ \Theta_D$ (Poole *et al.* 1995). Clearly, this is not the case with the $La_{2-x}Sr_xCuO_4$ cuprates.

Upon increasing the Sr content, the functional dependence of ρ_{ab} versus T evolves gradually from a linear into a T^2 law, the former being extended over a very broad temperature range (Fig. 2.1, left side). Since electrons in high-T_c compounds are not free but strongly correlated, one may argue that this dependence

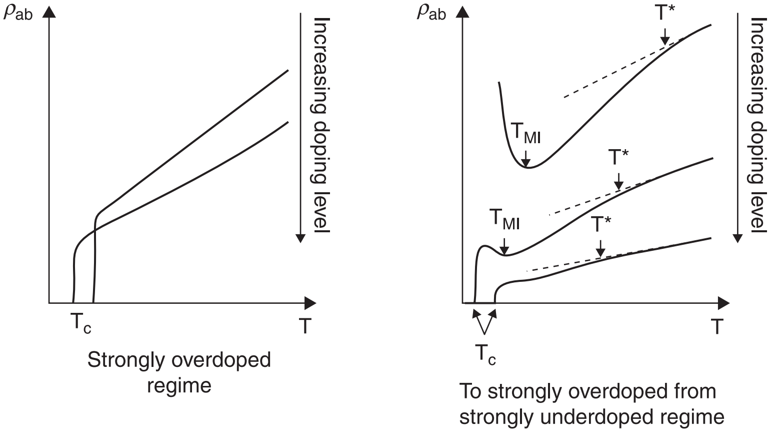

2.1 Schematic overview of the behavior of the in-plane resistivity ρ_{ab} of high-T_c cuprates in the strongly overdoped superconducting regime (left) and the strongly underdoped to the slightly overdoped regime (right). T* is the temperature below which the pseudogap opens. The temperature T_{MI} marks the crossover between metallic ($d\rho/dT > 0$) and insulator-like ($d\rho/dT < 0$) temperature dependencies.

is due to dominant electron–electron scattering, which eventually gives rise to scattering proportionally to T^2. However, the carrier concentration has to be increased deeply into the overdoped region ($x \sim 0.4$) to observe the T^2 law, considered as usual Fermi liquid behavior (Batlogg *et al.* 1994). At lower doping levels, the experimentally obtained powers are considerably below two. These powers cannot be explained as an artifact of the coexistence of electron–phonon and electron–electron scattering because the resistivity would then be dominated by the T^2 term at low temperatures where the electron–phonon contribution can be neglected. This has, however, never been reported.

From the slightly overdoped down to the strongly underdoped regime, the presence of a pseudogap (described below) leads to deviations from the aforementioned behavior for overdoped systems. Although a linear behavior turns up in the in-plane resistivity $\rho_{ab}(T)$ at high temperatures $T > T^*$, an S-shaped superlinear behavior emerges at temperatures $T < T^*$ (Fig. 2.1, right side). This excess conductivity below T*, caused by the opening of a pseudogap, is studied extensively in $YBa_2Cu_3O_{6+\delta}$ (Ito *et al.* 1993, Wuyts *et al.* 1996, Trappeniers 2000, Vanacken *et al.* 2001), $La_{2-x}Sr_xCuO_4$ (Suzuki and Hikita 1991, Kimura *et al.* 1992, Takagi *et al.* 1992b, Batlogg *et al.* 1994) and other high-T_c systems. Moreover, samples with a pseudogap reveal a negative slope $d\rho/dT$ at very low temperatures, a sign for the onset of localization (Fig. 2.1). The temperature T_{MI}, at which the resulting minimum in the $\rho_{ab}(T)$-curve occurs, marks a metal to insulator-like transition. Since T_{MI} decreases with increasing hole concentration, it is masked by the appearance of the superconducting phase at elevated doping with $T_{MI} < T_c$.

In normal Fermi liquids, a saturation of the resistivity occurs at high temperatures when the inelastic mean-free path approaches the lattice spacing (Ioffe–Regel criterion) (Ioffe and Regel 1960). Since high-T_c cuprates are strongly anisotropic, one needs to adopt the simple Drude picture to a layered two-dimensional system with the electrical transport in the a–b plane. This implementation immediately gives

$$\rho = \frac{h|a_c|}{k_F l e^2} \qquad [2.3]$$

where $|a_c|$ is the length of the unit cell in the c-direction, k_F is the Fermi wave vector and l is the mean free path. For the $La_{2-x}Sr_xCuO_4$ system, $|a_c|$ is 13.2 Å and the minimum value for the scattering length l is the CuO bond length $a/(2\sqrt{2})$ (a being the lattice constant in the a-direction). A 'large Fermi surface' is expected from ARPES data (Ino *et al.* 1999). When we assume a Fermi-surface with $k_F \sim \pi/a$, which agrees with a half-filled band, expression 2.3 yields a resistivity that should be saturated at 2 mΩcm. No sign of saturation has been observed in $La_{2-x}Sr_xCuO_4$ systems around this value. A saturating resistivity has never been detected in the superconducting cuprates, although they have been studied up to temperatures as high as 1000 K (Takagi *et al.* 1992a). This observation strongly suggests the inadequacy of the normal Fermi liquid approach.

In that respect, it is clear that the main microscopic mechanism for scattering of charge carriers in high-T_c cuprates strongly deviates from the mechanisms present in ordinary metals. Important progress in the understanding of the peculiar scattering mechanisms in high-T_cs has been achieved based on the universality of the anomalous features observed in the temperature dependent normal state resistivity. A successful scaling analysis has been performed in the underdoped regime, on the $YBa_2Cu_3O_{6+\delta}$ (Wuyts *et al.* 1996, Trappeniers 2000, Vanacken *et al.* 2001) and on the $Y_{0.6}Pr_{0.4}Ba_2Cu_3O_{6+\delta}$ systems (Trappeniers 2000, Vanacken *et al.* 2001). By scaling linearly both the temperature and the resistivity, the $\rho_{ab}(T)$-curves measured on underdoped samples with a different doping level, coincide well with each other, leading to the important conclusion that the transport properties in the different samples are dominated by the same scattering mechanisms, with characteristic parameters being dependent on the hole concentration (oxygen content).

Below we show that this scaling of the normal state resistivity is also applicable to the $La_{2-x}Sr_xCuO_4$ system. Our results will offer a more complete picture of the scaling behavior of the normal state resistivity in high-T_c compounds since they also treat, besides the underdoped superconducting regime ($0.055 < x < 0.15$), the underdoped non-superconducting ($x < 0.055$) and the slightly overdoped region ($x > 0.15$).

The thin films presented in this study cover both the under- and overdoped regime (Fig. 2.2). For each of these samples, the temperature dependence, magnetoresistivity and Hall effect are studied in detail, and presented within the scope of this chapter.

The plots in Fig. 2.3(a) show the temperature dependence of the resistivity for the $La_{2-x}Sr_xCuO_4$ thin films at various levels of hole doping (current drive 10 μA, sample thicknesses: see Table 2.1). A more detailed view on the temperature dependencies of the resistivity for the superconducting samples is presented in Fig. 2.3(b). The fact that the magnitude of ρ_{ab} is better (lower) or comparable with the values reported for single crystals (Kambe *et al.* 1989, Ito 1993, Takagi *et al.* 1992a, Kimura *et al.* 1996), reflects the excellent quality of the studied thin films. For instance, a ρ(300 K) of 420 $\mu\Omega$cm is revealed by our optimal doped $La_{1.85}Sr_{0.15}CuO_4$ thin film; a result, which should be compared to ρ(300 K) = 400 $\mu\Omega$cm, reported for single crystals (Kimura *et al.* 1996). Although a lowering of the resistivity with increasing Sr-content is natural, due to a rising charge carrier concentration, it is worth mentioning that the onset of superconductivity, as x is increased above 0.055, coincides with a very strong drop in the resistivity as can be seen in the inset of Fig. 2.3(a), which shows ρ_{ab}(200 K) for the different samples. The curves in Fig. 2.3(a,b) contain a rich variety of features described in the previous paragraph. We will now discuss the applied scaling in more details.

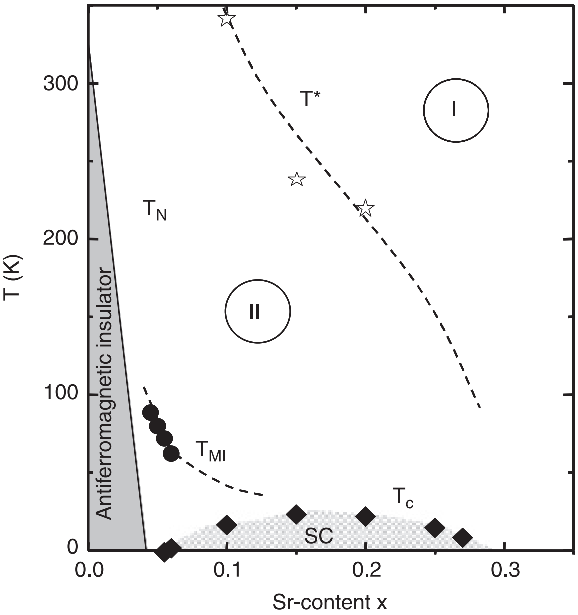

2.2 (T,x)-phase diagram of the $La_{2-x}Sr_xCuO_4$ samples. The antiferromagnetic and superconducting regions are indicated. The crossover temperature T* separates linear ρ-T (region I) from superlinear ρ-T (region II). T_{MI} marks the metal to insulator-like transition. The lines and shaded areas are purely suggestive for the (T,x)-phase diagram of the $La_{2-x}Sr_xCuO_4$ samples. The insulating antiferromagnetic region is indicated as well as the underdoped and overdoped regime.

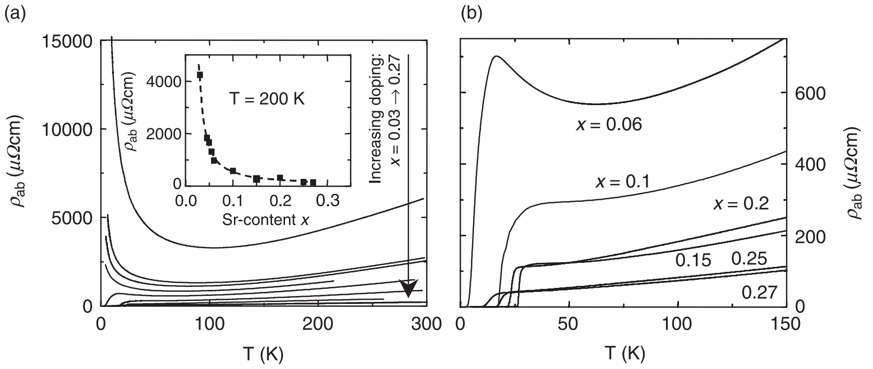

2.3 (a) The in-plane resistivity ρ_{ab}(T) in zero magnetic field for the $La_{2-x}Sr_xCuO_4$ films with $x = 0.03$, 0.045, 0.05, 0.055, 0.06, 0.1, 0.15, 0.2, 0.25 and 0.27, selected for this work. The inset shows the ρ_{ab}(200 K)-values for the different samples. (b) A more detailed view of the temperature dependencies of the resistivity ρ_{ab} for the superconducting samples.

2.2.2 Scaling of the zero-field resistivity for different doping levels

Based on the universality of the anomalous features, found in the temperature dependent normal state resistivity, a scaling analysis is possible. In Fig. 2.4, the rescaled $\rho_{ab}(T)$ curves are plotted for the underdoped $La_{2-x}Sr_xCuO_4$ samples with $x = 0.055$, 0.06, 0.1 and 0.15. The temperature is scaled with a parameter Δ and the resistivity plotted as $(\rho_{ab}(T) - \rho_0)/(\rho_{2\Delta/3} - \rho_0)$ where $\rho_{2\Delta/3}$ is the in-plane resistivity at $T = 2\Delta/3$ (the relevance of the factor 2/3 is discussed later) and ρ_0 the residual resistivity. The rescaled $\rho_{ab}(T)$ curves reveal a very nice overlap for temperatures $T > T_c$. The thin films with $x = 0.055$ and 0.06 show a negative slope $d\rho/dT$ at low temperatures, associated with the onset of the localization effects. The scaling persists in this insulator-like region as well, although in a narrow temperature range.

The used scaling parameters Δ for the different samples are presented in Table 2.1. They define the only energy scale that controls the behavior of the resistivity in the complete temperature range: the linear behavior above T*, the superlinear behavior between T_{MI} and T*, and the insulator-like behavior below T_{MI}. It should be noted that every set of numbers, equal to our set of gap-values Δ multiplied with an arbitrary factor, can serve as a good set of scaling parameters as well. We have chosen to scale our data with the specific values given in Table 2.1 because these values are very meaningful in view of the used

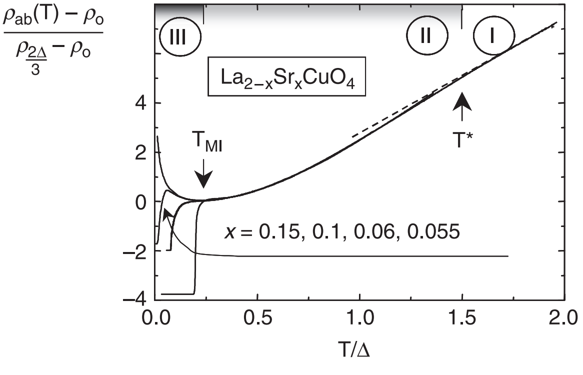

2.4 Scaling of the in-plane resistivity $\rho_{ab}(T)$ for the $La_{2-x}Sr_xCuO_4$ thin films with $x = 0.055$, 0.06, 0.1 and 0.15. The temperature is scaled with a parameter Δ (an energy scale) and the resistivity is given by $(\rho_{ab}(T) - \rho_o)/(\rho_{2\Delta/3} - \rho_o)$ where ρ_o is the residual resistivity and $\rho_{2\Delta/3}$ is the resistivity at $T = 2\Delta/3$. T* marks the transition from region I to region II where the samples show a pseudogap behavior. The metal to insulator transition temperature T_{MI} is indicated. The area below T_{MI} is referred to as region III.

Table 2.1 Overview of the $La_{2-x}Sr_xCuO_4$ thin films selected for this work with their Sr-content x, critical temperature T_c, an estimate of the width ΔT_c of the normal-to-superconducting transition, thickness t, metal to insulator transition temperature T_{MI} and the crossover temperature T*, below which the pseudogap opens (for definitions of the scaling parameters Δ and ρ_0 see section 2.2.3)

$La_{2-x}Sr_xCuO_4$							
x (± 0.005)	T_c (K) (± 1 K)	ΔT_c (K) (± 2 K)	t (nm) (± 10 nm)	T_{MI} (K) (± 0.5 K)	T* (K) (± 50 K)	Δ (K) (± 20 K)	ρ_0 ($\mu\Omega$cm)
0.03	0	–	140	104	460	288	3282
0.045	0	–	106	90	492	308	1226
0.05	0	–	116	80	454	284	1120
0.055	< 2.0	–	165	73	504	315	814
0.06	2.4	14	167	63	432	270	556
0.10	17.5	12	162	56	366	229	293
0.15	25.7	6	178	52*	217	136	118
0.20	21.8	4	190	40*	208	130	134
0.25	15.6	8	119	–	–	–	–
0.27	9.2	11	136	–	–	–	–

one-dimensional even-chain Heisenberg AF spin-ladder model (Moshchalkov *et al.* 1999, 2001), presented in the next paragraph. The scaling behavior is, however, very general and not restricted to any specific theoretical model describing the temperature dependent resistivity. The results, presented in Fig. 2.4, are limited to $x = 0.15$, 0.1, 0.06 and 0.055, but other films ($x = 0.030$, 0.045 or 0.050) scale also well (not shown for clarity of the figure).

2.2.3 Dimensionality of the electronic transport

In the previous section, different regions in the (T,x)-phase diagram have been identified based on the analysis of the ρ_{ab}(T)-data. These different regions are further discussed in this section, bearing in mind the experimental observation of one-dimensional spin-fluctuations in high-T_c cuprates (Tranquada *et al.* 1995). The resistivity data of our $La_{2-x}Sr_xCuO_4$ thin films are compared with the transport data of the doped double leg spin-ladder compound $Sr_{2.5}Ca_{11.5}Cu_{24}O_{41+\delta}$ (Nagata *et al.* 1997). The remarkable similarities in temperature dependencies of resistivity of these two compounds suggest the presence of one-dimensional electronic transport in our underdoped and slightly overdoped samples. Finally, a model for quantum transport in doped 1D and 2D Heisenberg systems ([Moshchalkov 1993; Moshchalkov *et al.* 1999, 2001), is preposed, leading to explicit expressions for the temperature dependent in-plane resistivity ρ_{ab}(T) both above and below T*.

Cuprate spin ladders

A two-leg cuprate spin ladder is an antiferromagnet, consisting of two coupled parallel CuO chains with an interchain bond $J_\perp$ along the rungs comparable in strength to the coupling J along the chains. Figure 2.5 shows schematically a two-leg cuprate compound. The black dots denote Cu atoms, the intersections of the solid lines are the O locations, the dashed lines are Cu-O bonds and the thick gray lines highlight the ladder structure. Along the rungs, 180° Cu-O-Cu bonds occur. These bonds are strongly antiferromagnetic, because the two holes, belonging to neighboring Cu^{2+}-ions, share the same 2p-O orbital in the dominant intermediate state. The ladders are linked by edge sharing of the CuO_4-squares. This gives rise to a different superexchange process, since now there are 90° Cu-O-Cu bonds and

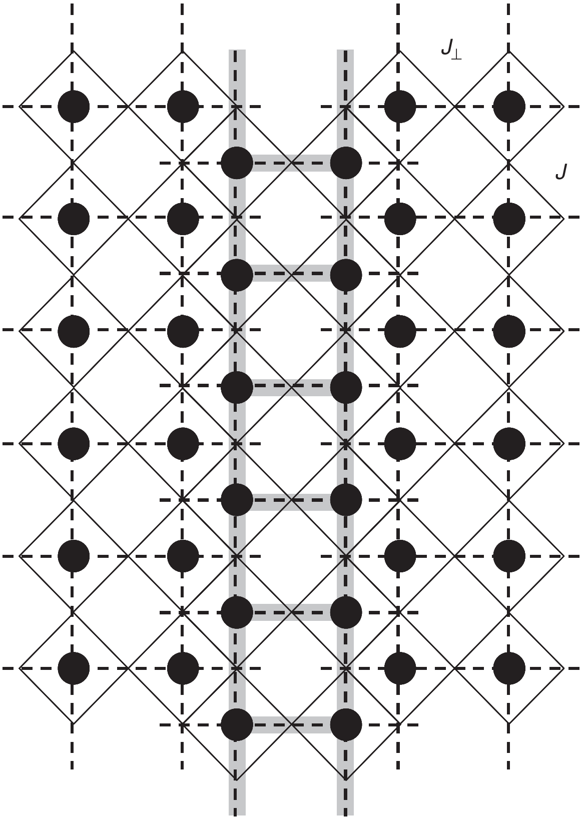

2.5 Schematic representation of a two-leg ladder cuprate. The black dots denote Cu atoms, the intersections of the solid lines are O locations, the dashed lines are Cu-O bonds and the gray lines highlight the ladder structure. $J_\perp$ is the coupling along the rungs, J is the coupling along the chains. (After Azuma *et al.* (1994).)

the two holes in the intermediate state reside on orthogonal 2p-O orbitals: a configuration favoring ferromagnetic alignment of the spins (Zhou 1997), which results in spin frustration at the interface. The ferromagnetic exchange interaction is weak (White 1996) compared to the antiferromagnetic interactions along the rungs and chains of the ladder. The large difference between the superexchange across corner sharing and edge sharing CuO_4-squares offers chemists a large flexibility in creating cuprates with different magnetic structures. For example, one can assemble chains to make ladders of increasing width. Surprisingly, both experiments and numerical calculations show that this crossover between one and two dimensions is not at all smooth (for relevant reviews see (Dagotto 1996, Rice 1998)).

While a ladder with an odd number of legs retains the properties of a purely 1D single Heisenberg chain, namely gapless spin excitations and a power-law decay of the antiferromagnetic correlations, a ladder made of an even number of chains reveals short-range spin correlations that have an exponential decay. These even chain spin ladders exhibit a spin gap Δ_{spin} in the energy spectrum in the absence of hole carriers, which means that it costs a finite amount of energy to create spin excitations above the spin singlet ground state. This property resembles the spin gap feature that has been observed below a temperature T* in the high-T_c cuprates, especially in the underdoped regime. However, for high-T_c cuprates, 'pseudogap' is a better term than spin gap since low-energy spin excitations exist, although with low spectral weight in neutron scattering experiments (Dagotto 1999).

Double leg spin ladders not only share with high-T_c superconductors the corresponding spin gap property, but secondly, theories predict that the ground state of the ladder compounds becomes dominated by superconducting correlations upon doping them with holes (Dagotto *et al.* 1992, Sigrist *et al.* 1994, Gazza *et al.* 1999). The reason leading to these correlations can be best understood in the strong coupling limit where the Heisenberg coupling is taken to be much larger along the rungs ($J_\perp$) than along the legs (J). In this case, the ground state of the two-leg Heisenberg system corresponds to the direct product of spin singlets, one per rung, as schematically represented in Fig. 2.6(a). The overall spin of the system is zero, since each pair of spins on a rung is itself in a singlet state. In order to produce a spin excitation, a rung singlet must be promoted to a rung triplet, and this costs energy $J_\perp$ ($=\Delta_{\text{spin}}$ in the $J_\perp >> J$ limit). If a spin S = ½ is removed from the system by introducing a hole, the other spin of the original singlet becomes free and no longer reduces its energy by singlet formation. If two holes, a large distance apart from each other, are added to the system, each one will produce substantial energy damage to the spin background, since both break a singlet (Fig. 2.6(b)). However, if the two holes are placed nearby, then they can share a common rung, thus reducing the number of damaged spin singlets from two to one. This idea, illustrated in Fig. 2.6(c) (Dagotto *et al.* 1992, Dagotto 1996), leads in a natural way to the concept of hole binding on two-leg ladders and to superconductivity. The idea may hold in the 'isotropic' limit $J_\perp = J$ too, because

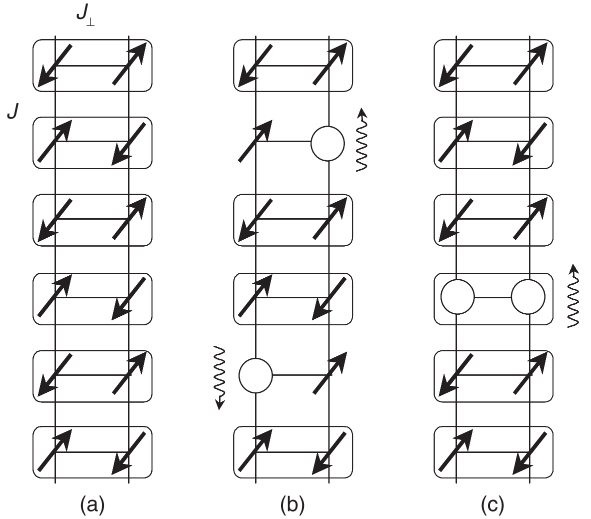

2.6 (a) Schematic representation of the ground state of a two-leg ladder. Pairs of spins along the same rung tend to form a spin singlet. (b) Individual holes added to the ladders destroy spin singlets. (c) To minimize the energy damage caused by the addition of holes, these holes tend to share the same rung forming hole bound-states. (After Hiroi *et al.* (1996).)

numerical calculations have predicted a spin gap in this limit as well ($\Delta \approx 0.5\, J$) (Barnes *et al.* 1993, Dagotto *et al.* 1992). Moreover, a variety of calculations (Riera 1994, Asai 1994, Yamaji and Shimoi 1994, Tsunetsugu *et al.* 1995, Hayward *et al.* 1995) show that the above-described superconductivity for ladders should be in the d-wave channel, currently the most accepted channel for superconductivity in the high-T_c cuprates. We can conclude that ladder compounds might serve as a 'playground' for studies of high-T_c superconductors, as Dagotto stated in (Dagotto 1999).

Up to now, superconductivity has only been observed in one ladder compound: $(La,Sr,Ca)_{14}Cu_{24}O_{41}$. Uehara *et al.* first found superconductivity in the Ca doped compound $Sr_{0.4}Ca_{13.6}Cu_{24}O_{41}$ under a high pressure of 3 GPa (Uehara *et al.* 1996). The optimal pressure is around 5 GPa, with a maximum T_c of 14 K (Isobe *et al.* 1998). While this critical temperature is obviously lower than those reached in two-dimensional high-T_c cuprates, it is nevertheless higher than that of typical metallic superconductors in spite of the low carrier density in $Sr_{0.4}Ca_{13.6}Cu_{24}O_{41}$. X-ray diffraction measurements (Isobe *et al.* 1998) indicate that no serious structural changes take place in this compound under high pressure. As a consequence, it is safe to conclude that the superconducting phase is related to the original ladder structure. The comparative study between the resistivities along the rungs and along the legs, performed by Nagata *et al.* (Nagata 1997), indicate that the carriers are confined on ladders at low pressure, while they become deconfined as the pressure increases. Most probably, the role of high pressure in the realization of superconductivity consists of enhancing the two-dimensional characteristics of the ladder compound.

The open circles in Fig. 2.7 represent the resistivity data $\rho(T)$ of $Sr_{2.5}Ca_{11.5}Cu_{24}O_{41}$ at 8 GPa, taken from (Nagata *et al.* 1997), linearly rescaled both in temperature and resistivity. Remarkably, the resistivity of the double leg ladder compound reveals exactly the same temperature dependence as the pseudogapped $La_{2-x}Sr_xCuO_4$ samples under investigation. This good scaling suggests that the scattering in the even-leg spin ladders may have the same nature as the scattering in the high-T_c compounds in the pseudogap regime at $T < T^*$. The scaling indicates that the transport in high-T_c cuprates in the pseudogap regime may be quasi one-dimensional, in excellent agreement with stripe models.

Charge ordering as a function of doping

The scaling analysis of the $\rho_{ab}(T)$ data obtained on the $La_{2-x}Sr_xCuO_4$ thin films, presented in the previous section, indicates that a unique scattering mechanism dominates the electronic transport in the doping regime, where pseudogap features are found. At the same time, neutron scattering experiments revealed the existence of dynamic 1D charge-rich and charge-poor regions in high-T_c compounds, situated in the same doping regime. The similarities between the behavior of the resistivity of our $La_{2-x}Sr_xCuO_4$ samples and those of the quasi one-dimensional ladder cuprate

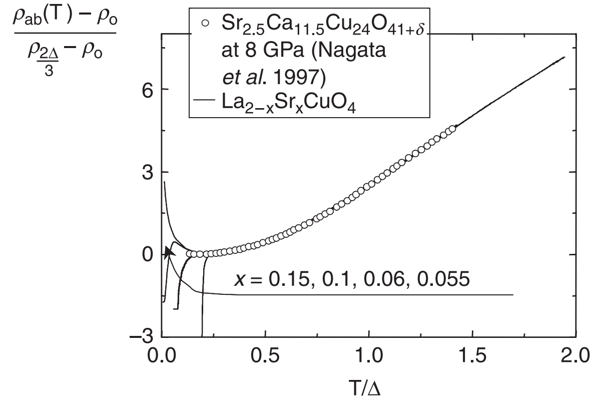

2.7 Temperature dependence of the resistivity $\rho(T)$ of a $Sr_{2.5}Ca_{11.5}Cu_{24}O_{41}$ even-chain spin-ladder single crystal at 8 GPa (experimental data points after Nagata *et al.* (1997)) together with the in-plane resistivity $\rho_{ab}(T)$ of $La_{2-x}Sr_xCuO_4$ thin films with $x = 0.15$, 0.1, 0.06 and 0.055. The temperature is scaled with a parameter Δ (an energy scale) and the resistivity is given by $(\rho_{ab}(T) - \rho_o)/(\rho_{2\Delta/3} - \rho_o)$ where ρ_o is the residual resistivity and $\rho_{2\Delta/3}$ is the resistivity at $T = 2\Delta/3$.

$Sr_{2.5}Ca_{11.5}Cu_{24}O_{41}$, presented in the previous section, suggested moreover that the electronic transport in $La_{2-x}Sr_xCuO_4$, at temperatures $T < T^*$, has a 1D character. The idea of a close connection between the microscopic dynamic 1D charge ordering and the non-Fermi liquid scattering mechanism, acting in high-T_c compounds in the pseudogap regime, therefore becomes very promising. The sensitivity of the charge transport to the expulsion of charge carriers from the surrounding antiferromagnetic regions into 1D stripes, static or dynamic, is very instructive.

In view of the interpretation of the different regions in the (T,x) phase diagram, it is important to discuss the evolution of the charge ordering as a function of doping. Neutron diffraction measurements on $La_{2-x}Sr_xCuO_4$ (Yamada *et al.* 1997) showed that the packing of the charge stripes becomes denser with increasing charge carrier concentration (max. around $x \approx 0.125$), essentially keeping the same doping level within a stripe.

Figure 2.8 shows the inverse inter-stripe distance $1/d_s$ as a function of the charge carrier concentration x, reproduced from (Yamada *et al.* 1997). Frames, which give a schematic view of the configuration of the charge stripes in the CuO_2 planes, are added to the figure at selected x-values. The inverse inter-stripe distance $1/d_s$ becomes noticeable beyond $x = 0.05$, increases approximately linearly with the Sr-content and starts to saturate around $x = 0.125$ (= 1/8), where the distance between the stripes equals $4a$, with a the crystallographic lattice parameter (see also Fig 2.6). In the overdoped region, the inter-stripe distance is almost constant upon doping (Yamada *et al.* 1997): the holes enter the antiferromagnetic regions between the stripes and the doping contrast of the stripes with respect to the surrounding space between them decreases. It is, however, important to stress that Yamada *et al.*

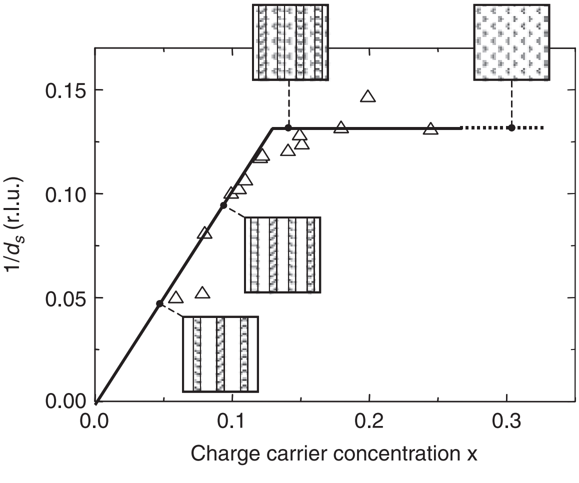

2.8 The reverse inter-stripe distance $1/d_s$ is shown as a function of the charge carrier concentration x (data points from Yamada *et al.* (1997)). The frames give a schematic view of the stripe configurations in the CuO_2 plane at selected x-values. The lines are guides to the eye.

observed well-defined incommensurate spin fluctuations up to the highest Sr-content $x = 0.25$, investigated in their study. Recent (FT-)STM (Hoffman *et al.* 2002, Howald *et al.* 2003, Kohsahak *et al.* 2007, Wise *et al.* 2008) and neutron scattering (Tranquada *et al.* 1995) studies have convincingly demonstrated the existence of stripes in high-T_c cuprates, especially in the underdoped region. This effective reduction of the dimensionality from 2D to 1D should be definitely taken into consideration in the analysis of transport properties of high-T_c cuprates.

A model for quantum transport in doped 1D and 2D Heisenberg systems

In the strongly anisotropic high-T_c cuprates, the role of the CuO_2 planes is crucial. The confinement of the charge carriers to the CuO_2 planes reduces the dimensionality for charge transport to 2D or even to 1D, if stripes are formed. The similarities between high-T_cs and ladder cuprates underline the extreme importance of the microscopic magnetic structure of the Cu^{2+} spins. Any model for high-T_c superconductivity, attempting to explain the unusual non-Fermi liquid behavior of the normal state, should therefore account for both the magnetic structure and the dimensionality. We will present here a model (Moshchalkov 1993, Moshchalkov *et al.* 1999, 2001) based on three assumptions:

1 The dominant scattering mechanism in high-T_c superconductors, in the whole temperature range, is of magnetic origin.
2 The specific temperature dependence of the resistivity $\rho(T)$ can be described by the inverse quantum conductivity σ^{-1} with the inelastic scattering length L fully controlled by the magnetic correlation length ξ_m.
3 The proper 1D or 2D expressions, depending on the effective dimensionality, should be used for calculating the quantum conductivity.

The quantum conductivity σ_{1D} of a single 1D wire is a linear function of the inelastic scattering length L whereas the 2D quantum conductivity σ_{2D} is proportional to *ln*(L) (Abrikosov 1988). They are represented by:

$$\rho_{1D}^{-1}(T) = \sigma_{1D}(T) \propto \frac{1}{b^2}\frac{e^2}{\hbar}L \qquad [2.4]$$

$$\rho_{2D}^{-1}(T) = \sigma_{2D}(T) \propto \frac{1}{b}\frac{e^2}{\hbar}\ln\left(\frac{L}{l}\right) \qquad [2.5]$$

with b the diameter of the 1D wire or the thickness of the 2D layer and l the elastic scattering length. These expressions for the resistivity of 1D wires and 2D layers can be used to calculate $\rho(T)$ by inserting the magnetic correlation length ξ_m, which is schematically presented in Fig 2.9, in the place of the inelastic scattering length L. Hence, the determination of the precise behavior of the resistivity requires the knowledge of the magnetic correlation lengths in the 1D (ξ_{m1D}) and the 2D (ξ_{m2D}) case.

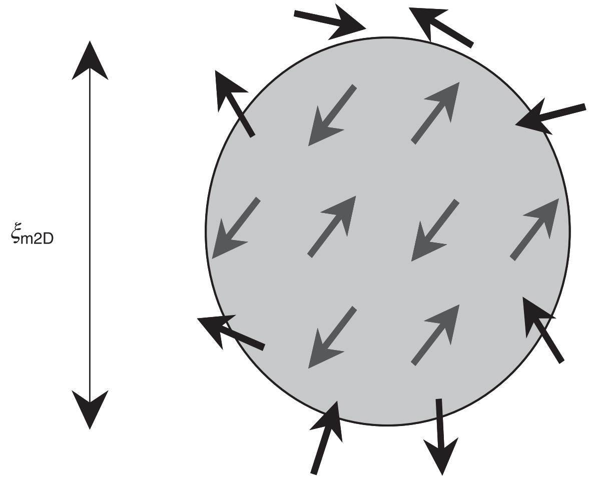

2.9 Schematic representation of the 2D magnetic correlation length ξ_{m2D}.

Following the striking similarities between the ρ(T) curves of pseudo-gapped high-T_c cuprates and spin ladders, the spin-correlation length for even-chain Heisenberg antiferromagnetic spin ladders, found by Monte Carlo simulations (Greven *et al.* 1996), is chosen as ξ_{m1D} (Moshchalkov *et al.* 1999, 2001):

$$\xi_{m1D}(T) = \left(\frac{2\Delta}{\pi} + AT\exp\left(\frac{-\Delta}{T}\right)\right)^{-1} \qquad [2.6]$$

where A ≈ 1.7 and Δ is the spin gap. The correlation length ξ_{m1D}, given by expression [2.6] is derived for undoped ladders. It is assumed in (Moshchalkov *et al.* 1999) that it can still be applied for weakly doped ladders as well.

In the framework of the 2D Heisenberg model, which is certainly applicable for the doped CuO_2 planes without any stripes present, the temperature dependence of the correlation length ξ_{m2D} is expressed as (Hasenfratz and Niedermayer 1991):

$$\xi_{m2D}(T) = \frac{e\hbar c}{8.2\pi F^2}\left(1 - \frac{T}{2.2\pi F^2}\right)\exp\left(\frac{2\pi F^2}{T}\right) \qquad [2.7]$$

with c the spin velocity and F a parameter that can be directly related to the exchange interaction J in accordance with $2\pi F = J$. Equation [2.7] has been derived for undoped 2D Heisenberg systems but numerical Monte Carlo simulations (Reefman 1993) demonstrated its validity also for weakly doped systems.

The combination of the expressions for the 1D and 2D spin correlation length with the proper expressions for the quantum resistivity gives the temperature dependence of the resistivity. The 1D spin ladder resistivity can be described by equation 1.8, with $J_{||}$ the spin-coupling along the chains and a the spacing between the conducting ladders ($J_{||}$ comes in, to recalculate the theorist units) (Moshchalkov *et al.* 1999, 2001):

$$\rho_{1D}(T)=\frac{\hbar b^2}{e^2 a}\left(\frac{2\Delta}{\pi J_{||}}+A\frac{T}{J_{||}}\exp\left(\frac{-\Delta}{T}\right)\right) \qquad [2.8]$$

In the 2D Heisenberg regime, remarkably, the resistivity is a linear function of the temperature (Moshchalkov *et al.* 1999, 2001) due to the mutual cancellation of the logarithmic $\rho(\xi_m)$ and the exponential $\xi_m(T)$ dependencies in the limit $T << 2J$ (J is typically 1600 K):

$$\begin{aligned}\rho_{2D}(T) &\propto (\ln(\xi_m))^{-1}\\ &\propto \left[\ln\left(\exp\left(\frac{J}{T}\right)\right)\right]^{-1}\\ &\propto \frac{b\hbar T}{e^2 J}\end{aligned} \qquad [2.9]$$

The validity of the proposed 1D quantum conductivity model has been extensively tested. The model is, for example, perfectly applicable for the ladder compound $Sr_{2.5}Ca_{11.5}Cu_{24}O_{41}$, earlier mentioned. A fit of the temperature dependent resistivity $\rho(T)$ of this compound with expression [2.8] does not only demonstrate an excellent fit quality over a wide temperature range ($25\ K < T < 300\ K$), but it also offers a reasonable value for the spin gap $\Delta \sim (216 \pm 20)$ K (at 8 GPa) (Trappeniers 2000). Inelastic neutron scattering experiments (Takano *et al.* 1997) determined a gap $\Delta \sim 320$ K for the undoped spin ladder $SrCu_2O_3$. Since the spin gap is expected to be reduced upon doping, both results are in fair agreement. Moreover, the ideas brought up by the model, lead to an excellent description of the temperature dependent Knight shift $K_s(T)$ of the superconducting $YBa_2Cu_3O_8$ system. Troyer *et al.* (Troyer *et al.* 1994) calculated that the Knight shift of a double leg spin-ladder (undoped) should obey the expression:

$$K_s(T) \propto T^{-1/2}\exp\left(-\frac{\Delta}{T}\right) \qquad [2.10]$$

Fitting the $K_s(T)$ data of $YBa_2Cu_3O_8$ (Bucher *et al.* 1994) with this expression leads to a spin-gap $\Delta = (222 \pm 20)$ K. Note that this value is in an excellent agreement with $\Delta = (224 \pm 10)$ K derived from the resistivity measurements on the same compound using the quantum conductivity model (Moshchalkov *et al.* 1999).

Turning back to the $La_{2-x}Sr_xCuO_4$ system, we can compare the NMR knight shift fit using equation [2.10] with the resistivity fit using equation [2.8]. If we fit the Knight shift above T_c (see Fig. 2.10) with expression [2.10] for the temperature dependent $K_s(T)$, a gap $\Delta = (131 \pm 20)$ K is obtained. This value agrees very well with the pseudogap $\Delta = (136 \pm 20)$ K obtained by fitting the resistivity data for the $La_{1.85}Sr_{0.15}CuO_4$ thin film.

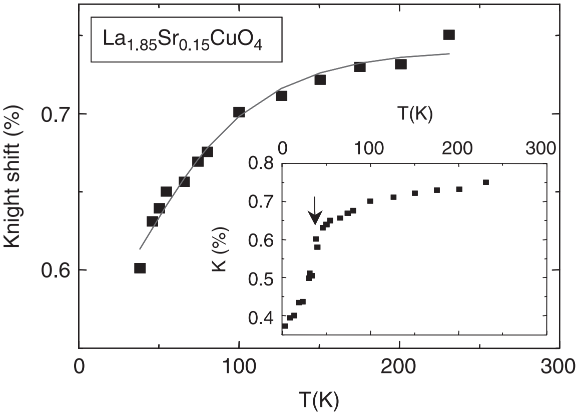

2.10 The inset depicts the temperature dependence of the Knight shift of ^{63}Cu for $La_{1.85}Sr_{0.15}CuO_4$ (Ishida *et al.* 1991). In the main frame, the normal state Knight shift is shown in more detail, together with a fit with the expression $K(T) = K(0) + K_{1D}T^{-1/2} \exp(\Delta/T)$. The fitting parameters are $K(0) = (0.60 \pm 0.0)\%$, $K_{1D} = (3.9 \pm 0.2)\ \%$ and $\Delta = (131 \pm 20)$ K.

It should, however, be mentioned that experimental techniques probing charge excitations (like ARPES and tunneling experiments) give pseudogap values Δ_p that are higher (about a factor 2) than the spin excitation gap Δ_S as observed in NMR knight shift experiments. Since it is assumed in the 1D quantum transport model, that the magnetic correlation length dominates the inelastic length, the agreement of our data with the gap-values determined from the NMR experiments seems to be natural.

In summary of this section we can state that:

- At T > T*, the resistivity reveals a linear temperature dependence (region I). This regime is well described by equation [2.9] for quantum transport in a 2D Heisenberg system with the inelastic length determined by the magnetic (2D) correlation length.
- At T < T*, where charge stripes can develop, the resistivity is observed to have a superlinear temperature dependence (region II). This regime can then be accurately described by equation [2.8], which represents the temperature dependence of the quantum resistivity in a 1D striped material with the inelastic length again determined by the magnetic (1D) correlation length.

2.3 Magnetoresistivity in superconducting $La_{2-x}Sr_xCuO_4$ thin films

In what follows, two phenomena are introduced which are crucial for understanding of the physics behind the magnetoresistivity of the cuprates. First, the main ideas behind the Kohler plot are introduced and secondly, there is a description of the superconducting fluctuations. Both effects influence the ρ(H) behavior, and it is sometimes quite hard to make a clear difference between these effects. Nevertheless, in what follows we will develop a method which shows the separation between these effects and a detailed study of the fluctuation behavior.

2.3.1 Kohler's rule

When a metal is placed in a magnetic field *H*, its resistance usually increases. For low magnetic fields, it is easy to see that the resistance will depend quadratically on *H*. The orbit of an electron in a uniform magnetic field is a spiral whose projection on a plane perpendicular to the field is a circle (of radius *r*). The angular frequency ω_c (cyclotron frequency) is determined by the condition that the centrifugal acceleration $r\omega_c^2$ is provided by the Lorentz force $e\omega_c r\mu_o H$:

$$\omega_c = \frac{e\mu_o H}{m^*} \qquad [2.11]$$

(m^* is the effective mass of the charge carriers). The curving of the electron trajectories in a magnetic field causes the effective mean free path *l* to decrease, as visualized in Fig. 2.11. The difference in length between the arc and the chord is equal to $2r\varphi - 2r\sin\varphi \approx \frac{1}{3}r\varphi^3$, where 2φ is the angular size of the arc. If we assume that $r\varphi \sim l$, then the difference in length is of the order of $l(l/r)^2$, i.e., the relative order of the correction to the resistance is:

$$\Delta\rho \propto \rho\,(l/r)^2 \qquad [2.12]$$

Since $l \sim v\tau$, with v the electron velocity and τ the scattering time, we find that:

$$\Delta\rho \sim \rho\,(\omega_c\tau)^2 \qquad [2.13]$$

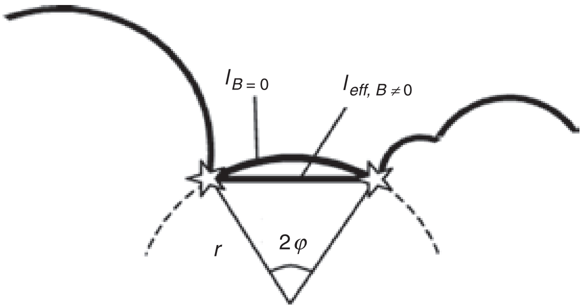

2.11 Schematic representation of the decrease of the effective mean free path due to an applied magnetic field; *r* is the radius of the curved electron trajectory and *2φ* is the angular size of the arc defined by two collisions (stars). The mean free paths at zero and non-zero magnetic field are indicated.

leading to the expected quadratic variation of the resistivity with respect to an applied magnetic field.

Exact calculations of the magnetoresistivity are very complicated. Due to the assumption that every electron has the same thermal speed, the simple Drude model leads to a resistivity that is independent of the magnetic field. The Boltzmann transport equation, on the other hand, departs from a distribution of electron velocities. Solving this equation is, however, far from evident. In low magnetic fields ($\omega_c\tau < 1$), the Boltzmann equation leads to the usual quadratic field dependence of the resistivity (Ziman 1964). In the intermediate field region ($\omega_c\tau \sim 1$), few (if any) theories of magnetoresistivity exist. In high fields ($\omega_c\tau >> 1$), the electrons are able to complete many cyclotron orbits between collisions. In this case, it is the topology of the Fermi surface and not the details of the scattering mechanisms that dominates the character of the magnetoresistance. Solving the Boltzmann transport equation, it can be found that the transverse magnetoresistance tends to saturate in high fields, or increases as H^2, depending on whether the charge carriers are situated on closed or open orbits (Ziman 1964, Abrikosov 1988).

To overcome the problems in describing the magnetoresistance of metals in the different field regimes, one often uses the so-called Kohler's rule (Kohler 1938, Abrikosov 1988). This rule, based on the Boltzmann equation, departs from the idea of a universal mean free path l. The resistance must be inversely proportional to this path length. As the magnetic field increases, the role of the mean free path is gradually taken over by the radius $r \sim v/\omega_c$. It may therefore be assumed that $\rho(\mathrm{H,T})/\rho(0,\mathrm{T})$ depends only on the ratio l/r. But, since $r \sim H^{-1}$ and $l \sim [\rho(0,\mathrm{T})]^{-1}$, we may consider $\rho(\mathrm{H,T})/\rho(0,\mathrm{T})$ to be dependent only on the combination $\mathrm{H}/\rho(0,\mathrm{T})$. Subtracting unity from $\rho(\mathrm{H,T})/\rho(0,\mathrm{T})$, we get (Kohler 1938):

$$\frac{\Delta\rho}{\rho(0,T)} = f\left(\frac{H}{\rho(0,T)}\right) \qquad [2.14]$$

where f is a function that is independent of the temperature. This is what is called Kohler's rule. In the case that the magnetoresistance depends on the quadratic on the field, data are often presented in a 'Kohler plot':

$$\frac{\Delta\rho}{\rho(0,T)} = f\left(\left(\frac{H}{\rho(0,T)}\right)^2\right) \qquad [2.15]$$

Obviously, this rule is only an approximation. For example, deviations may occur in anisotropic metals in the presence of open orbits, or in metals on which the field has other effects besides the curving of the electron trajectories.

2.3.2 Superconducting fluctuations

Within the phenomenological Ginzburg-Landau (GL) model, a superconducting material is determined by the lowest energy eigenfunction ψ of the GL equation.

While this is indeed the most probable state, the presence of thermal energy k_BT implies that the system will fluctuate into other low-lying excited states with a finite probability. Above T_c, the free energy $F(\psi)$ is at its minimum when $|\psi| = 0$. There is however a probability $\exp[-F(\psi)/k_BT]$ that thermal fluctuations drive $|\psi|$ from 0 to a finite value $|\psi| > 0$. These superconducting fluctuations $|\psi| > 0$ above T_c ($\alpha > 0$) can be described in the framework of the Ginzburg-Landau formalism (Tinkham 1996). We will consider the case far enough above T_c so that the effects of the quartic term in the free energy can be neglected. In the absence of any field (A = 0), the Ginzburg-Landau free energy, relative to the normal state, is given by:

$$F = \alpha|\psi|^2 + \frac{\hbar^2}{2m^*}\left|\left(\frac{\nabla}{i}\right)\psi\right|^2 \qquad [2.16]$$

We can expand $\psi(r)$ in Fourier series, so that:

$$\psi(r) = \sum_k \psi_k e^{ik\cdot r} \qquad [2.17]$$

Inserting this into [2.16] and using the orthogonality of the terms in a Fourier series, we find:

$$F = \sum_k \left(\alpha + \frac{\hbar^2 k^2}{2m^*}\right)|\psi_k|^2 \qquad [2.18]$$

This immediately gives us the probability P that the fluctuations realize a particular configuration $\psi(r)$. It is proportional to:

$$P\ \mu\ \exp\left[\frac{-1}{k_B\mathrm{T}}\sum_k\left(\left(\alpha + \frac{\hbar^2 k^2}{2m^*}\right)|\psi_k|^2\right)\right] \qquad [2.19]$$

The average contribution $\langle|\psi_k|^2\rangle$ of each mode to the free energy can be calculated with standard Boltzmann statistical mechanics:

$$\left\langle|\psi_k|^2\right\rangle = \frac{\int|\psi_k|^2 \exp\left[-\frac{1}{k_B\mathrm{T}}\left(\alpha + \frac{\hbar^2k^2}{2m*}\right)|\psi_k|^2\right]d\psi_k}{\int\exp\left[-\frac{1}{k_B\mathrm{T}}\left(\alpha + \frac{\hbar^2k^2}{2m*}\right)|\psi_k|^2\right]d\psi_k} = \frac{2m*}{\hbar^2}\frac{k_B\mathrm{T}}{k^2 + 1/\xi^2} \qquad [2.20]$$

with $(2m\alpha/\hbar^2)^{1/2} = 1/\xi$, the inverse coherence length. Please notice that expression [2.20] defines the spatial variation of the fluctuations. We see that Fourier components with $k > 1/\xi$ come in with reduced weight. In other words, the fluctuations occur on a scale larger than ξ.

Of course, if we want to describe a property such as electrical conductivity, we also need a model of the time dependence since the contribution of a given fluctuation to the conductivity above T_c is proportional to its lifetime. Such a model is provided by the linearized time-dependent Ginzburg-Landau equation. In this case, the parameter τ_o is the temperature-dependent relaxation time of the ($k = 0$) mode:

$$\tau_o = \frac{\pi\hbar}{8k_B(T - T_c)} \tag{2.21}$$

The higher-energy modes with $k > 0$ decay more rapidly with the relaxation rates:

$$\frac{1}{\tau_k} = \frac{1 + k^2\xi^2}{\tau_o} \tag{2.22}$$

In analogy with the Drude model:

$$\sigma = \frac{ne^2\tau}{m} \tag{2.23}$$

which provides the simplest description of the normal conductivity, we might expect the fluctuations to contribute an extra term:

$$\Delta\sigma \approx \frac{(2e)^2}{m^*}\sum_k \frac{\left\langle\left|\Psi_k\right|^2\right\rangle\tau_k}{2} \tag{2.24}$$

It means that ordinary scattering processes are ineffective until a given fluctuation relaxes. The factor ½ comes in, because $|\psi_k|^2$ relaxes twice as fast as ψ_k. Inserting relations [2.20] and [2.22] into [2.24], we obtain:

$$\Delta\sigma \approx \frac{2e^2k_B T\tau_o\xi^2}{\hbar^2}\sum_k \frac{1}{\left(1 + k^2\xi^2\right)^2} \tag{2.25}$$

The summation over k can be converted to an appropriate integration depending on the dimensionality of the electron motion:

$$\text{In 3D: } \sum_k \to \int_0^\infty \frac{4\pi k^2 dk}{(2\pi)^3} \tag{2.26}$$

$$\text{In 2D: } \sum_k \to \int_0^\infty \frac{2\pi k dk}{(2\pi)^2 b}, \quad \text{where } b \text{ is the layer thickness} \tag{2.27}$$

$$\text{In 1D: } \sum_k \to \int_{-\infty}^\infty \frac{dk}{(2\pi)S}, \quad \text{where } S \text{ is the cross-sectional area} \tag{2.28}$$

Following this prescription, we obtain the result, which differs from the exact calculations only by small numerical factors. In particular, the temperature dependence of $\Delta\sigma$ is correctly found to be $(T - T_c)^{-(4-d)/2}$, where d (= 1, 2, 3) is the dimensionality of the system. A more precise result was derived by Aslamazov and Larkin (Aslamazov and Larkin 1968):

$$\Delta\sigma_{3D} = \frac{1}{32}\frac{e^2}{\hbar\xi(0)}\left(\frac{T_c}{T - T_c}\right)^{1/2} \qquad [2.29]$$

$$\Delta\sigma_{2D} = \frac{e^2}{16\hbar b}\frac{T_c}{T - T_c} \qquad [2.30]$$

$$\Delta\sigma_{1D} = \frac{\pi e^2\xi(0)}{16\hbar S}\left(\frac{T_c}{T - T_c}\right)^{3/2} \qquad [2.31]$$

These expressions, referred to as the paraconductive or Aslamazov-Larkin contribution, describe the excess conductivity caused by non-equilibrium Cooper pairs above T_c. The critical exponents obtained in the framework of the theory of Aslamasov and Larkin turn out to be very robust. Later revisions of the theory of paraconductivity (Bulaevski *et al.* 1986, Narozhny 1994, Damianov and Mishonov 1997, Sadovski 1997, Larkin and Varlamov 2005) resulted in the same critical exponents. Only the overall coefficients depend on the characteristics of the model.

Ginzburg (Ginzburg 1968, Abrikosov 1988, Levanyuk 1959) estimated the temperature range where the fluctuations are relevant in a bulk isotropic superconductor (3D):

$$\frac{\partial T}{T_c} \approx \left(\frac{a_o}{\xi}\right)^4 \qquad [2.32]$$

where a_o is the interatomic distance. In conventional superconductors, for which this ratio takes values around 10^{-12}–10^{-14}, fluctuation phenomena are thus barely visible. Ratio equation [2.32] is much larger for high-T_c superconductors because their coherence length is typically comparable to the atomic distance. Moreover, Aslamasov and Larkin (Aslamasov and Larkin 1968) calculated that the exponent v of the ratio (a_o/ξ), which enters in [2.32], drastically decreases as the effective dimensionality of the electron motion diminishes: $v = 4$ for 3D, but $v = 1$ for 2D. The latter is a more appropriate choice with respect to the layered cuprates. We conclude that fluctuation phenomena are prominently present in high-T_c compounds because of their extreme anisotropy and short coherence length. These fluctuations lead to visible precursor effects of the superconducting phase, occurring while the system is still in the normal phase far from T_c.

The Aslamazov-Larkin (AL) fluctuations described above and, caused by the appearance of fluctuating Cooper pairs above T_c, contribute directly to the conductivity. Two other mechanisms are known which affect the conductivity in an indirect way: the density of states (DOS) and the Maki-Thompson (MT) contribution. The first indirect fluctuation correction follows from a decrease of the one-electron density of states at the Fermi level. Indeed, if some electrons are involved in pairing above T_c, they cannot simultaneously participate in normal state charge transfer as one-particle excitations. Since the total number of the electronic states cannot be changed by the Cooper interaction, the energy is redistributed over the levels. The resulting decrease in the one-electron density of states at the Fermi level leads to a reduction of the normal state conductivity. It should be noted that the DOS has an opposite effect on the conductivity, compared to the AL contribution. The DOS correction to the paraconductive fluctuations can usually be neglected (Varlamov *et al.* 1999), certainly when the in-plane conductivity is studied (our case) for which the paraconductive contribution is expected to be very high.

The so-called anomalous Maki-Thompson (MT) contribution is a purely quantum phenomenon. Its physical nature has remained mysterious since 1968, when Maki [1968] calculated it on the basis of Feynman diagrams. It is related to the pairing correlations between electrons of opposite spin moving in opposite directions along a self-intersecting trajectory in real space and has a positive effect on the conductivity. The Maki-Thompson term is small and can usually be neglected with respect to the AL contribution (Kimura *et al.* 1996, Abe *et al.* 1999). Actually, the MT term is expected to be completely absent in d-wave superconductors like high-T_c compounds (Yip 1990).

2.3.3 Experimental magnetoresistivity results: separating fluctuation and normal state contribution

High external magnetic fields can be used to probe the normal state properties and to separate the contribution to the conductivity from fluctuations. Figures 2.12 to 2.19 present the $\rho_{ab}(\mu_o H)$ curves measured at temperatures varying from T >> T_c down to 4.2 K for the $La_{2-x}Sr_xCuO_4$ thin films with Sr content $x = 0.045$, 0.050, 0.055, 0.060, 0.100, 0.200, 0.250 and 0.270.

$La_{1.955}Sr_{0.045}CuO_4$ ($x = 0.045$, highly underdoped, non-superconducting)

The $La_{1.955}Sr_{0.045}CuO_4$ sample (Fig. 2.12) shows a very weak magnetoresistivity (less than 2% at 45 T) in the whole temperature range. This is clearly demonstrated by the graphs A, B, C and D in the middle part of Fig. 2.12, which present the weak, in a first approximation, quadratic magnetoresistivity at the selected temperatures 16 K, 20 K, 32 K and 176 K. No smoothing has been applied to the data, and both raising and lowering field branches are given. The magnetoresistivity, indicated in the graphs is defined as MR = $(\rho_{ab}(50\ T) - \rho(0, T))/\rho(0,T)$.

The in-plane resistivity $\rho_{ab}(T)$ as a function of temperature at zero magnetic field is shown in Fig. 2.12 at the right side of the upper frame; it serves as a guide to see at which temperature the magnetoresistivity measurements have been carried out. The open circles denote the values of the resistivity at zero magnetic field as derived from pulsed field measurements (before and after the pulse). Since $La_{1.955}Sr_{0.045}CuO_4$ exhibits, below T_{MI} ~ 100 K, a resistivity that strongly diverges when lowering the temperature (e.g. $d\rho/dT$ (4.2 K) ≈ –800 $\mu\Omega$cm/K), even minor heating effects in the pulsed field experiment can artificially lead to negative

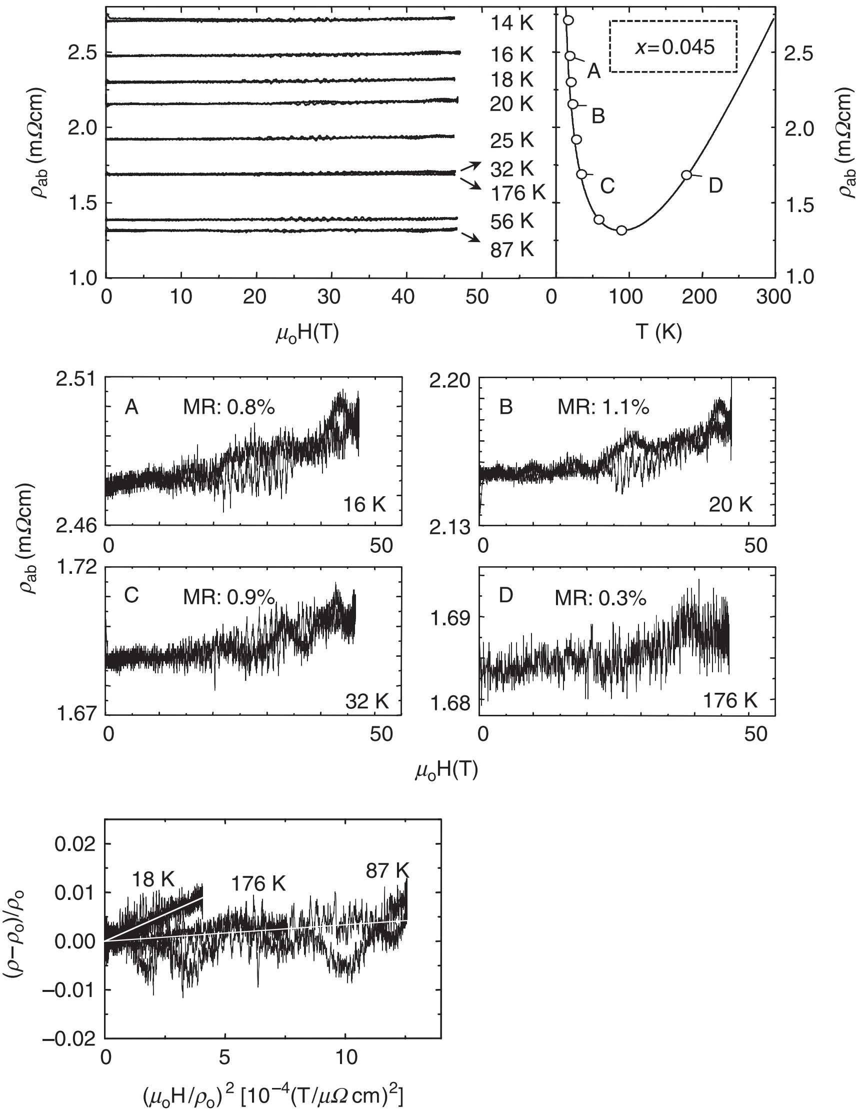

2.12 The left side of the upper frame gives an overview of the field dependence of the in-plane resistivity $\rho_{ab}(\mu_0H)$ of $La_{1.955}Sr_{0.045}CuO_4$ at different temperatures. The right side of the upper frame depicts the temperature dependence of the in-plane resistivity $\rho_{ab}(T)$ at zero magnetic field (solid line). The open circles mark the positions where the magnetoresistivity has been measured. For the positions labeled A, B, C and D, the magnetoresistivity is shown in more detail in the middle part of the figure. The magnetoresistivity at 45 T (MR) is indicated in percent. The lower frame shows the Kohler plots at temperatures T = 18 K, T = 87 K and T = 176 K for the 47 T pulsed field.

magnetoresistivity effects at low temperatures. We judged that the magnetoresistivity of $La_{1.955}Sr_{0.045}CuO_4$ at temperatures T > 14 K could be adequately measured up to 50 T in our setup. Indeed, no discrepancies between data taken during the rising and the lowering branch of the field pulse could be found in this temperature range, a strong indication that heating effects do not influence the results. Additional measurements in DC fields up to 8 T (not shown in this article), convincingly proved that the resistivity of the sample is only slightly magnetic field dependent below 14 K as well.

The lower frame of Fig. 2.12 shows the in-plane magnetoresistivity data for the non-superconducting $La_{1.955}Sr_{0.045}CuO_4$ sample in a Kohler plot ($(\rho - \rho_0)/\rho_0$ vs B^2). The figure suggests that its resistivity is proportional to H^2 at all temperatures. Kohler's rule (Kohler 1938) is however only valid when all the curves coincide. We see that the curves at 87 K and 176 K nicely overlap but that the low temperature data deviate. A violation of Kohler's rule at low temperatures can be expected for this compound since its low temperature region is characterized by variable range hopping conductivity.

$La_{1.95}Sr_{0.05}CuO_4$ ($x = 0.050$, highly underdoped, non-superconducting)

Upon approaching the insulator-superconductor transition in the (T,x)-phase diagram ($x = 0.055$), a considerable positive magnetoresistivity appears (Fig. 2.13). A magnetic field of 45 T causes an excess resistivity of 10% in $La_{1.95}Sr_{0.05}CuO_4$ at a temperature of 10 K. With increasing temperature, the magnetoresistivity of the sample at 45 T goes down to a final decrease below 2% around 40 K. Note that $La_{1.95}Sr_{0.05}CuO_4$ does not show a sign of superconductivity at zero magnetic field down to 1.5 K, the lowest temperature investigated. In contrast, the sample demonstrates an insulator-like behavior ($d\rho_{ab}/dT < 0$) from 80.5 K (T_{MI}) down to the lowest temperature. For clarity, only the data taken during rising magnetic field are shown in graphs A, B, C and D of Fig. 2.13. The overview graph in the upperframe of Fig. 2.13 depicts, at the different temperatures, the data at zero field (open circles) and at 45 T (solid circles).

$La_{1.945}Sr_{0.055}CuO_4$ ($x = 0.055$, highly underdoped, non-superconducting)

Figure 2.14 illustrates that $La_{1.945}Sr_{0.055}CuO_4$, situated at the border of the superconducting phase, manifests strong magnetoresistivity effects. At 4.2 K, the magnetoresistivity at 45 T is already 33%; its value at 9.4 K is 18%. Although situated very close to the insulator-superconductor transition, $La_{1.945}Sr_{0.055}CuO_4$ has a robust insulator-like behavior from 72.7 K (T_{MI}) down to 1.5 K at zero magnetic field, seemingly not to be correlated with the occurrence of superconductivity. The graphs A, B, C, D, E and F in the lower part of Fig. 2.14 give a clear presentation of the evolution of the resistivity with magnetic field for the $La_{1.945}Sr_{0.055}CuO_4$ sample. At low temperatures (4.2 K), a saturating $\rho(\mu_0 H)$ behavior is observed. For

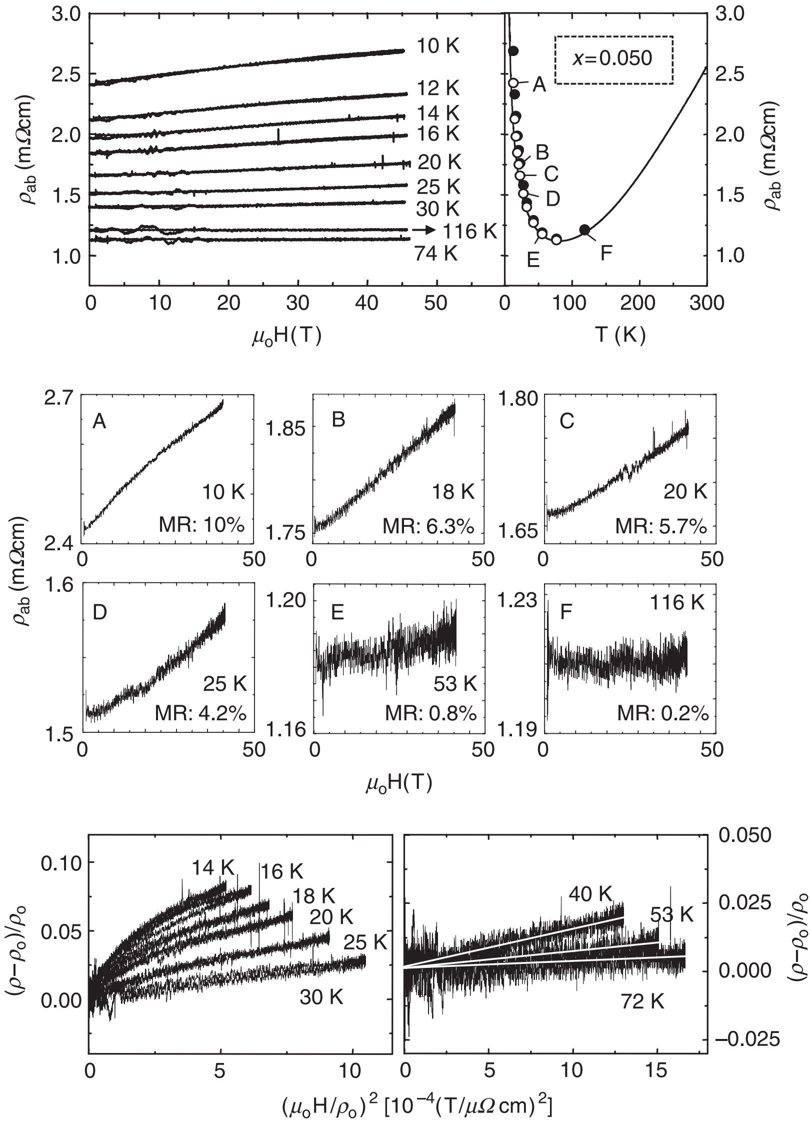

2.13 The left side of the upper frame gives an overview of the field dependence of the in-plane resistivity $\rho_{ab}(\mu_0 H)$ of $La_{1.950}Sr_{0.050}CuO_4$ at different temperatures. The right side of the upper frame depicts the temperature dependence of the in-plane resistivity $\rho_{ab}(T)$ at zero magnetic field (solid line). The open circles denote the values of the resistivity in zero field, derived from pulsed field measurements; filled circles mark the resistivity values at 45 T. For the positions labeled A, B, C, D, E and F, the magnetoresistivity is shown in more detail in the middle part of the figure. The magnetoresistivity at 45 T (MR) is indicated in percent. The lower frame shows the Kohler plots for the $La_{1.950}Sr_{0.050}CuO_4$ sample at selected temperatures 14 K < T < 72 K for the 45 T pulsed field data.

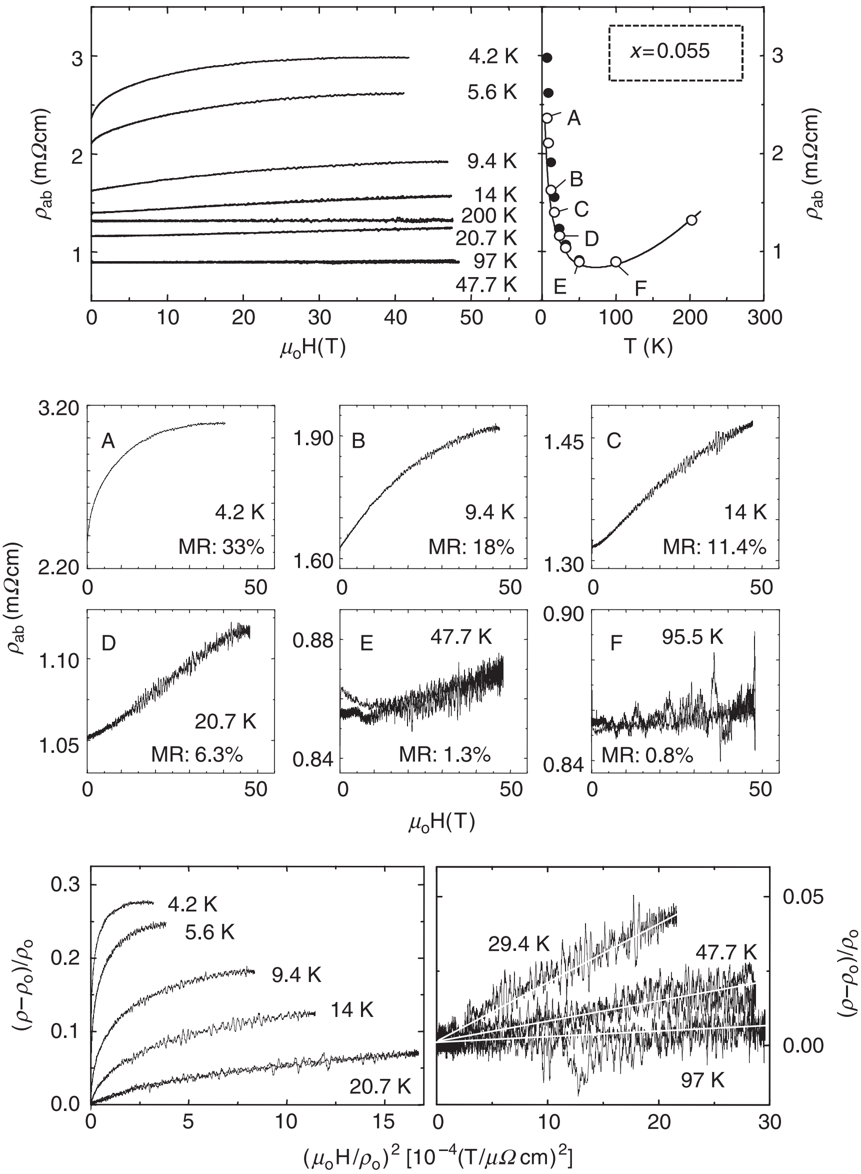

2.14 The magnetoresistivity data of $La_{1.945}Sr_{0.055}CuO_4$ are presented in the same way as in Fig. 2.12 (or 2.13). The filled circles at the right side of the upper frame mark the resistivity values at 45 T. For the positions labeled A, B, C, D, E and F, the magnetoresistivity is shown in more detail in the middle part of the figure. The magnetoresistivity at 45 T (MR) is indicated in percent. The lower frame shows the Kohler plots for the $La_{1.945}Sr_{0.055}CuO_4$ sample at selected temperatures (4.2 K < T < 97 K) for the 47 T pulsed field data.

intermediate temperatures (20.7 K), a quadratic magnetoresistivity at low fields evolves into a behavior that tends to saturate at higher fields. Only a quadratic behavior of the magnetoresistivity remains at sufficiently high temperatures (47.7 K). Graphs A, B, C and D only show the data taken during the increasing branch of the magnetic field pulse.

$La_{1.94}Sr_{0.06}CuO_4$ (*x* = 0.060, underdoped, superconducting)

In the $La_{1.94}Sr_{0.06}CuO_4$ compound (Fig. 2.15), the insulating phase at low temperatures gives way to superconductivity below $T_c = 2.4$ K. The rather low critical temperature $T_c = 2.4$ K implies that the sample is located very close to the insulator-superconductor transition. From Fig. 2.15 it is clear that the magnetoresistivity effects become very pronounced upon increasing the charge carrier concentration through the superconducting phase. At 4.2 K, which is nearly two times T_c, a field of 45 T causes a magnetoresistivity of 330% in $La_{1.94}Sr_{0.06}CuO_4$. Note that the resistivity is not even fully saturated at 45 T. Upon increasing the temperature, the impact of the magnetic field on the resistivity diminishes, resulting in a crossing of the $\rho_{ab}(\mu_o H)$ curves taken at temperatures below $T_{MI} = 63$ K. The fact that the $\rho_{ab}(\mu_o H)$ curves cross each other reflects that the ground state at low temperatures, obscured below T_c by the superconducting phase, has an insulating character in $La_{1.94}Sr_{0.06}CuO_4$. This observation is in agreement with the results reported previously (Ando *et al.* 1995, Boebinger *et al.* 1996) for underdoped superconducting $La_{2-x}Sr_xCuO_4$ single crystals. The temperature dependence of the resistivity at 45 T is shown at the right side of the upper frame of Fig. 2.15 by black circles. Below the metal-to-insulator transition at $T_{MI} = 63$ K, the resistivity at 45 T exhibits insulating properties ($d\rho_{ab}/dT < 0$). The graphs A, B, C, D, E and F show the functional dependence of the resistivity versus field in detail. The magnetoresistivity tends to saturate at low temperatures (4.2 K). Similar to the $La_{1.945}Sr_{0.055}CuO_4$ compound (Fig. 2.14), this behavior gradually evolves into a quadratic dependence (50 K) upon increasing the temperature. To a lower extent, this behavior can be seen as well in the $La_{1.95}Sr_{0.05}CuO_4$ sample presented in Fig. 2.13.

$La_{1.9}Sr_{0.1}CuO_4$ (*x* = 0.100, underdoped, superconducting)

The magnetoresistivity in $La_{1.9}Sr_{0.1}CuO_4$ ($T_c = 17.5$ K) is shown in Fig. 2.16. Again, the study in high magnetic fields reveals an insulating ground state ($d\rho_{ab}/dT < 0$) behind the superconducting phase, which is hidden in zero magnetic fields. The use of high magnetic fields allows us to determine the metal to insulator transition temperature $T_{MI} = 56$ K. Below $T_{MI} = 56$ K, the $\rho_{ab}(\mu_o H)$ curves cross each other. It looks like the curves have a single intersection point in the graph at the left side of the upper frame of Fig. 2.16. However, an enlarged view of this field region indicates that the crossing shifts slightly but quite systematically to

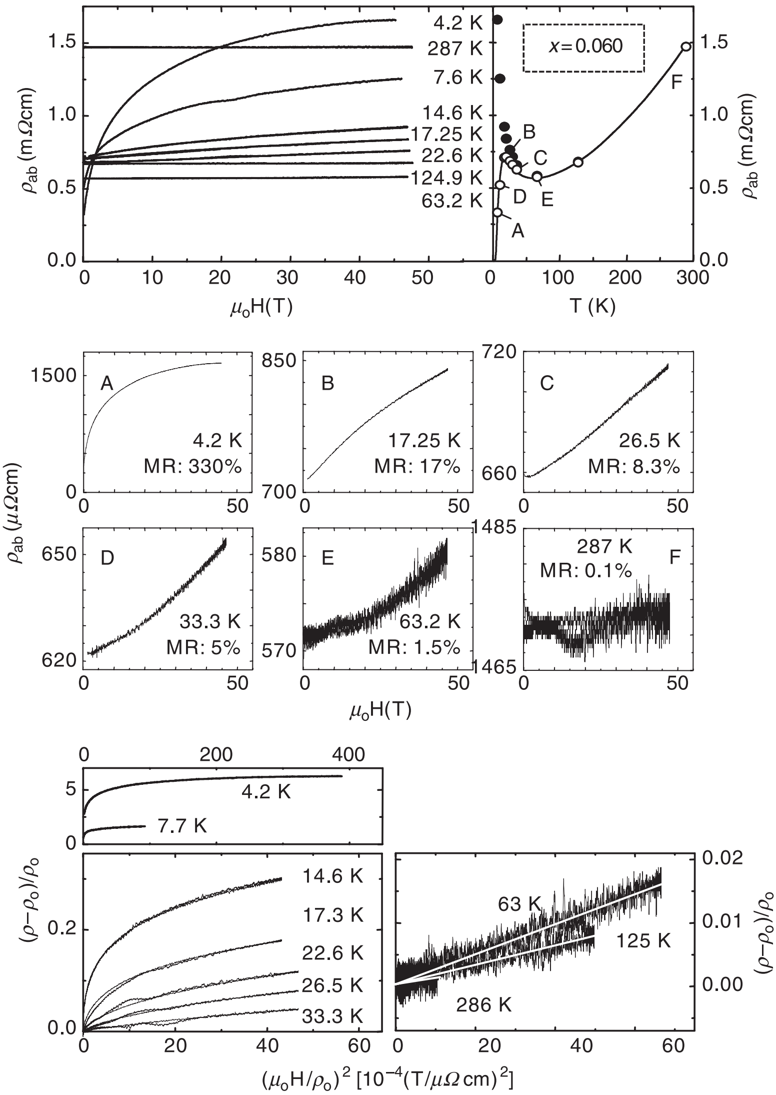

2.15 The left side of the upper frame gives an overview of the field dependence of the in-plane resistivity $\rho_{ab}(\mu_0 H)$ of $La_{1.94}Sr_{0.06}CuO_4$ at different temperatures. The right side of the upper frame depicts the temperature dependence of the in-plane resistivity $\rho_{ab}(T)$ at zero magnetic field (solid line). The open circles denote the values of the resistivity in zero field, derived from pulsed field measurements; filled circles mark the resistivity values at 45 T. For the positions labeled A, B, C, D, E and F, the magnetoresistivity is shown in more detail in the lower part of the figure. The magnetoresistivity at 45 T (MR) is indicated in percent. The lower frame shows the Kohler plots for the $La_{1.94}Sr_{0.06}CuO_4$ sample at selected temperatures used for the 47 T pulsed field data.

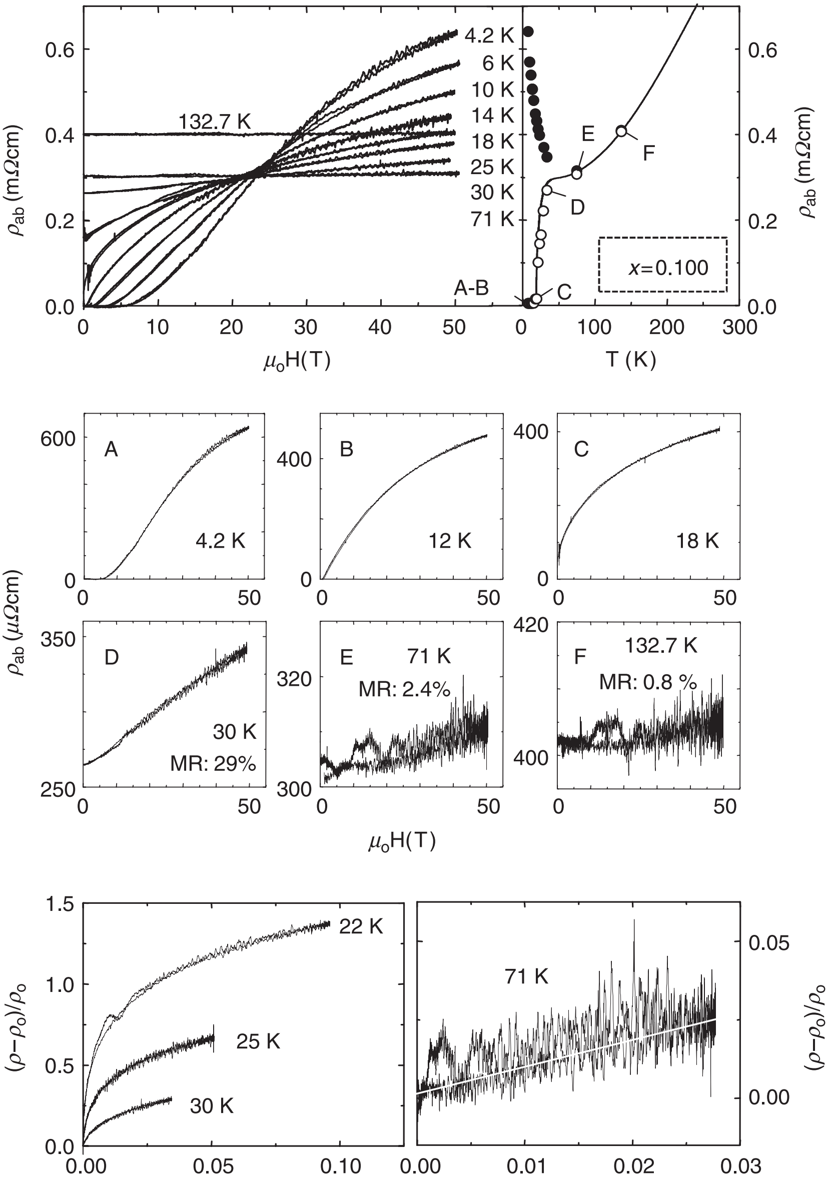

2.16 The magnetoresistivity data of $La_{1.9}Sr_{0.1}CuO_4$ are presented in the same way as in Fig. 2.12. The filled circles at the right side of the upper frame mark the resistivity values at 50 T. For the positions labeled A, B, C, D, E and F, the magnetoresistivity is shown in more detail in the middle part of the figure. The magnetoresistivity at 50 T (MR) is indicated in percent. The lower frame shows the Kohler plots for the $La_{1.9}Sr_{0.1}CuO_4$ sample at selected temperatures used for the 50 T pulsed field data.

higher fields when lowering the temperature. Graphs A, B, C, D, E and F in Fig. 2.16 provide a closer look at the field dependence of the resistivity in $La_{1.9}Sr_{0.1}CuO_4$ at the selected temperatures 4.2 K, 12 K, 18 K, 30 K, 71 K and 132.7 K. Below $T_c = 17.5$ K, the magnetoresistivity tends to saturate. Nevertheless, a complete saturation is still absent at all temperatures. At the same time, the $\rho_{ab}(\mu_0 H)$ curves do not exhibit a knee-shaped feature, marking the position of the second critical field (H_{c2}). Above $T_c = 17.5$ K, the magnetoresistivity shows a familiar behavior: it tends to saturate at low temperatures (18 K), a quadratic dependence at low fields bends down with increasing field at intermediate temperatures (30 K) and a weak quadratic dependence remains at high temperatures (71 K). The magnetoresistivity at 45 T decreases from 30% at 30 K down to below 2% above 71 K. At high temperatures, for example 132.7 K, the magnetoresistivity for the superconducting $La_{1.9}Sr_{0.1}CuO_4$ sample is comparable to that of the distinctly non-superconducting $La_{1.955}Sr_{0.045}CuO_4$ (Fig. 2.12).

Magnetoresistivity of $La_{2-x}Sr_xCuO_4$ close to the insulator – superconductor transition

The lower frames of Fig. 2.13 and 2.14, show the Kohler plots for the $La_{2-x}Sr_xCuO_4$ samples with $x = 0.05$ and 0.055, situated very close to the insulator to superconductor transition. A considerable excess magnetoresistivity, which depends not quadratically on the magnetic field but rather tends to saturate, appears at low temperatures. This contribution becomes more pronounced when increasing the charge carrier concentration through the superconducting phase, as evidenced by the Kohler plots for $La_{1.94}Sr_{0.06}CuO_4$ ($T_c = 2.4$ K) and $La_{1.9}Sr_{0.1}CuO_4$ ($T_c = 17.5$ K), presented in Fig. 2.15 and 2.16, respectively. This evolution strongly suggests that the non-quadratic contribution to the magnetoresistivity can be attributed to superconducting fluctuations.

In zero magnetic field, $La_{1.95}Sr_{0.05}CuO_4$ and $La_{1.945}Sr_{0.055}CuO_4$ demonstrate an insulator-like behavior ($d\rho_{ab}/dT > 0$) at low temperatures down to at least 1.5 K. Nevertheless, the contribution from the superconducting fluctuations appears up to tens of Kelvin. For the superconducting samples $La_{1.94}Sr_{0.06}CuO_4$ and $La_{1.9}Sr_{0.1}CuO_4$, the fluctuations extend over a temperature range, which exceeds several times T_c. For example: the $La_{1.94}Sr_{0.06}CuO_4$ compound shows at 25 K (seven times T_c!) a magnetoresistivity of 8% at 50 T, which is substantially higher than the ~1% for the non-superconducting $La_{1.955}Sr_{0.045}CuO_4$ sample. The fluctuations are moreover of an unusual strength: typical fields for a complete suppression of fluctuations in conventional BCS bulk superconductors should not exceed the paramagnetic limiting field $\mu_o H = 1.38\ T_c$. However, the $La_{1.94}Sr_{0.06}CuO_4$ system shows, at 4.2 K, a magnetoresistivity that is not even saturated at 50 T, a value which is more than a decade higher than the conventional paramagnetic limit of $\mu_o H = 4$ T expected for the sample with $T_c \sim 2.4$K.

$La_{1.8}Sr_{0.2}CuO_4$ ($x = 0.200$, overdoped, superconducting)

In contrast to the underdoped samples, the overdoped $La_{1.8}Sr_{0.2}CuO_4$ ($T_c = 22.8$ K) demonstrates clear knee-shaped features in its field-dependent resistivity curves $\rho_{ab}(\mu_o H)$ at temperatures $T < T_c$ (see graphs A, B and C of Fig. 2.17). As a consequence, the superconducting transitions and the second critical field $H_{c2}(T)$ can be determined for $La_{1.8}Sr_{0.2}CuO_4$. Above $H_{c2}(T)$, the resistivity still depends on the magnetic field. At the same time, the overdoped $La_{1.8}Sr_{0.2}CuO_4$ shows magnetoresistivity, far above T_c, dying out with increasing temperature, similar to the superconducting underdoped samples $La_{1.94}Sr_{0.06}CuO_4$ and $La_{1.9}Sr_{0.1}CuO_4$. However, the functional dependence of the magnetoresistivity changed while crossing the threshold of optimal doping. No tendency towards saturation has been observed in the magnetoresistivity of $La_{1.8}Sr_{0.2}CuO_4$, at temperatures well above the superconducting to normal transition. This is illustrated by graphs D and E in Fig. 2.17. A linear dependence of the resistivity with respect to the field is found at low temperatures (30.6 K). At higher temperatures (79.6 K), a quadratic behavior is predominant. $La_{1.8}Sr_{0.2}CuO_4$ exhibits a minimum in $\rho_{ab}(T)$ at $T_{MI} = 40$ K and a crossover from metallic to insulator-like behavior upon a temperature decrease, in a high magnetic field of 45 T. A low temperature insulating behavior persisting up to optimal doping is reported both for $La_{2-x}Sr_xCuO_4$ single crystals (Boebinger *et al.* 1996) and for the electron-doped superconductor $Pr_{2-x}Ce_xCuO_4$ (Fournier *et al.* 1998). In Bi_2Sr_{2-x}–$La_xCuO_{6+\delta}$, it disappears at 1/8 hole doping, in the underdoped regime (Ono *et al.* 2000). The results on the thin films presented here, on the other hand, show a metal to insulator-like transition in $La_{1,8}$ $Sr_{0.2}CuO_4$, stretching well into the overdoped regime.

$La_{1.75}Sr_{0.25}CuO_4$ ($x = 0.250$, highly overdoped, superconducting)

The resistivity data for the strongly overdoped $La_{1.75}Sr_{0.25}CuO_4$ compound ($T_c =$ 15.6 K) is shown in Fig. 2.18 as a function of the magnetic field. The data for both branches of the field pulse are presented and no smoothing has been applied. The $La_{1.75}Sr_{0.25}CuO_4$ sample shows various kinds of superconducting transitions. While close to T_c, the $\rho_{ab}(\mu_o H)$ transition is narrow, but it broadens significantly when lowering the temperature. This indicates that the irreversibility line $H_{irr}(T)$ and the second critical field $H_{c2}(T)$ gradually separate from each other. The graphs A, B and C of Fig. 2.18 illustrate that the resistivity of $La_{1.75}Sr_{0.25}CuO_4$ is linearly depending on the field above the critical fields. Above T_c (= 15.6 K), $La_{1.75}Sr_{0.25}CuO_4$ still demonstrates a considerable quadratic magnetoresistivity but the $\rho_{ab}(\mu_o H)$ curves lack any sign of saturation. Surprisingly, the high field studies disclose a metal to insulator transition around 10 K (T_{MI}) in $La_{1.75}Sr_{0.25}CuO_4$. Although this sample is situated quite deeply in the overdoped regime, the resistivity values at 50 T demonstrate a distinct upturn when lowering the temperature below TMI. This insulator-like behavior at low temperatures

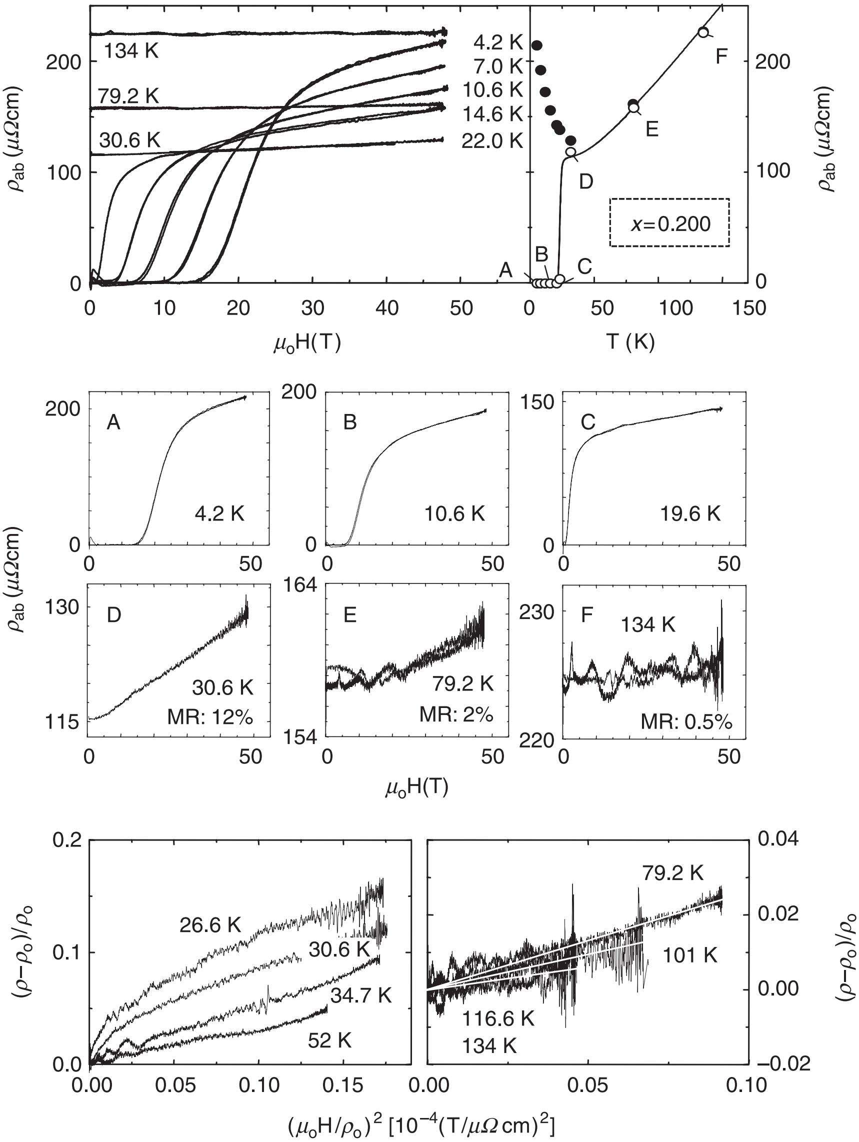

2.17 The left side of the upper frame gives an overview of the field dependence of the in-plane resistivity $\rho_{ab}(\mu_0 H)$ of $La_{1.8}Sr_{0.2}CuO_4$ at different temperatures. The right side of the upper frame depicts the temperature dependence of the in-plane resistivity $\rho_{ab}(T)$ at zero magnetic field (solid line). The open circles denote the values of the resistivity at zero field, derived from pulsed field measurements; filled circles mark the resistivity values at 45 T. For the positions labeled A, B, C, D, E and F, the magnetoresistivity is shown in more detail in the middle part of the figure. The magnetoresistivity at 45 T (MR) is indicated in percent at $T > T_c$. The lower frame shows the Kohler plots for the $La_{1.8}Sr_{0.2}CuO_4$ sample at selected temperatures used for the 48 T pulsed field data.

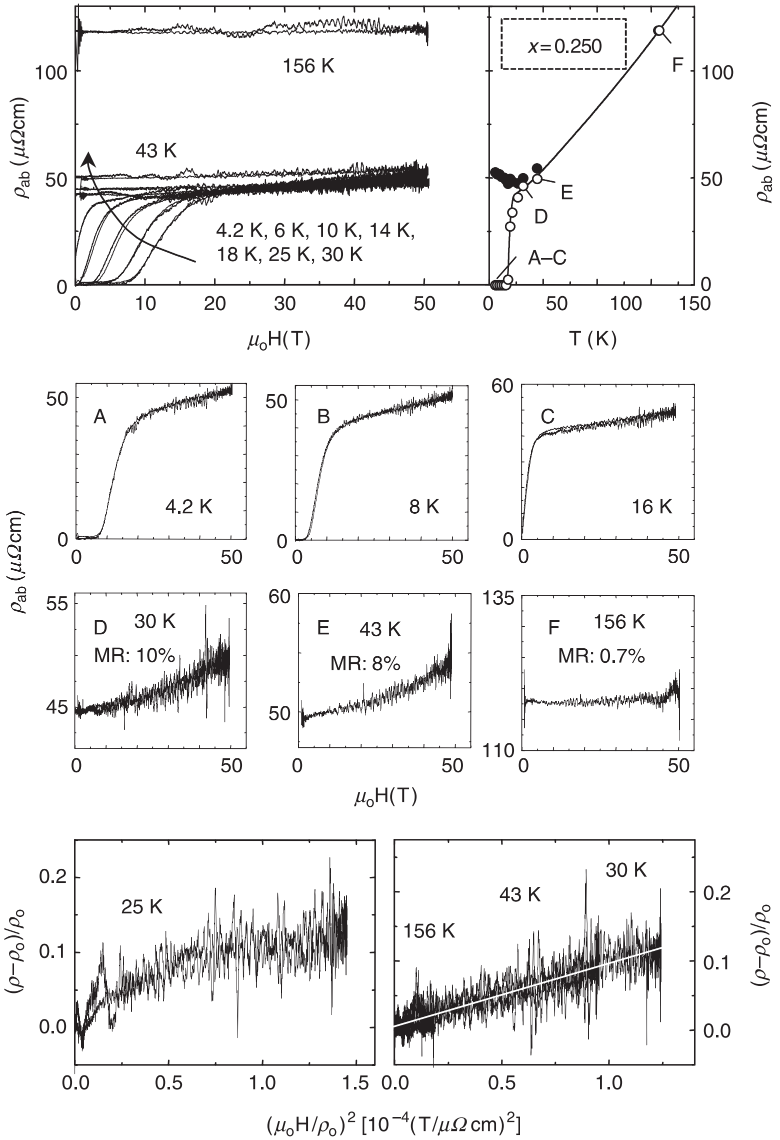

2.18 The left side of the upper frame gives an overview of the field dependence of the in-plane resistivity $\rho_{ab}(\mu_0 H)$ of $La_{1.75}Sr_{0.25}CuO_4$ at different temperatures. The right side of the upper frame depicts the temperature dependence of the in-plane resistivity $\rho_{ab}(T)$ at zero magnetic field (solid line). The open circles denote the values of the resistivity at zero field, derived from pulsed field measurements; filled circles mark the resistivity values at 45 T. For the positions labeled A, B, C, D, E and F, the magnetoresistivity is shown in more detail in the middle part of the figure. The magnetoresistivity at 50 T (MR) is indicated in percent at $T > T_c$. The lower frame shows the Kohler plots for the $La_{1.75}Sr_{0.25}CuO_4$ sample at selected temperatures used for the 50 T pulsed field data.

could be related to a weak pseudogap feature, present even in this compound, and to disorder effects.

$La_{1.73}Sr_{0.27}CuO_4$ (*x* = 0.270, highly overdoped, superconducting)

Finally, Fig. 2.19 gives the field dependent in-plane resistivity data of $La_{1.73}Sr_{0.27}CuO_4$ ($T_c = 9.2$ K), our strongest overdoped sample in this study. The superconducting transitions are clear and sharp, just like in $La_{1.75}Sr_{0.25}CuO_4$. Since $La_{1.73}Sr_{0.27}CuO_4$ has, of all our samples, the lowest normal state resistivity, the mechanical vibrations, caused by the high field-pulses, have a stronger impact on its resistivity data. The effects of the vibrations, particularly present during the lowering branch of the pulse, are clearly visible in the data taken at 12 K and 54 K, respectively, shown in graphs B and D in Fig. 2.19. The other magnetoresistivity curves presented in Fig. 2.19 contain only the data taken during increasing magnetic field for clarity. In contrast with the previous samples, the $\rho_{ab}(\mu_o H)$-curves of $La_{1.73}Sr_{0.27}CuO_4$ do not cross each other at fields below 45 T. Above T_c, the magnetic field dependencies of the resistivity are essentially quadratic, thus without tendency towards saturation.

In the field and temperature range used in our experiments, the magnetoresistivity is positive for all our films, in agreement with the results of (Harris *et al.* 1995, Kimura *et al.* 1996, Malinovski *et al.* 1997). Our data on thin films differ from the results of references (Ando *et al.* 1995, Boebinger *et al.* 1996) on single crystals of $La_{2-x}Sr_x$–CuO_4 with $x = 0.08$ and $x = 0.13$, where the magnetoresistivity in the limit of high fields was found to be negative.

Influence of the normal state magnetoresistivity for (strongly) overdoped $La_{2-x}Sr_xCuO_4$

The lower frames of Fig. 2.17–2.19 present the Kohler plots for the overdoped samples $La_{1.8}Sr_{0.2}CuO_4$ ($T_c = 22.8$ K), $La_{1.75}Sr_{0.25}CuO_4$ ($T_c = 15.6$ K) and $La_{1.73}Sr_{0.27}CuO_4$ ($T_c = 9.2$ K). We see that the part of the magnetoresistivity, which has no quadratic behavior with respect to the applied field diminishes upon increasing the charge carrier concentration and finally becomes undetectable in the $La_{1.73}Sr_{0.27}CuO_4$ sample.

This observation can be consistently interpreted in the context of our previous results that the one-dimensional character of the charge transport (stripes) fades away upon doping (Vanacken *et al.* 2001). As the effective dimensionality of the electrical transport increases from 1D to 2D (or 3D), the fluctuations become indeed less pronounced.

So far, we have ignored the part of the magnetoresistivity that appears in a Kohler plot as a straight line. In Fig. 2.19, we see that magnetic field dependencies of the $La_{1.73}Sr_{0.27}CuO_4$ data are essentially H^2 up to 45 T. Moreover, the straight lines coincide, which implies that H/ρ_o scales the magnetoresistivity and hence

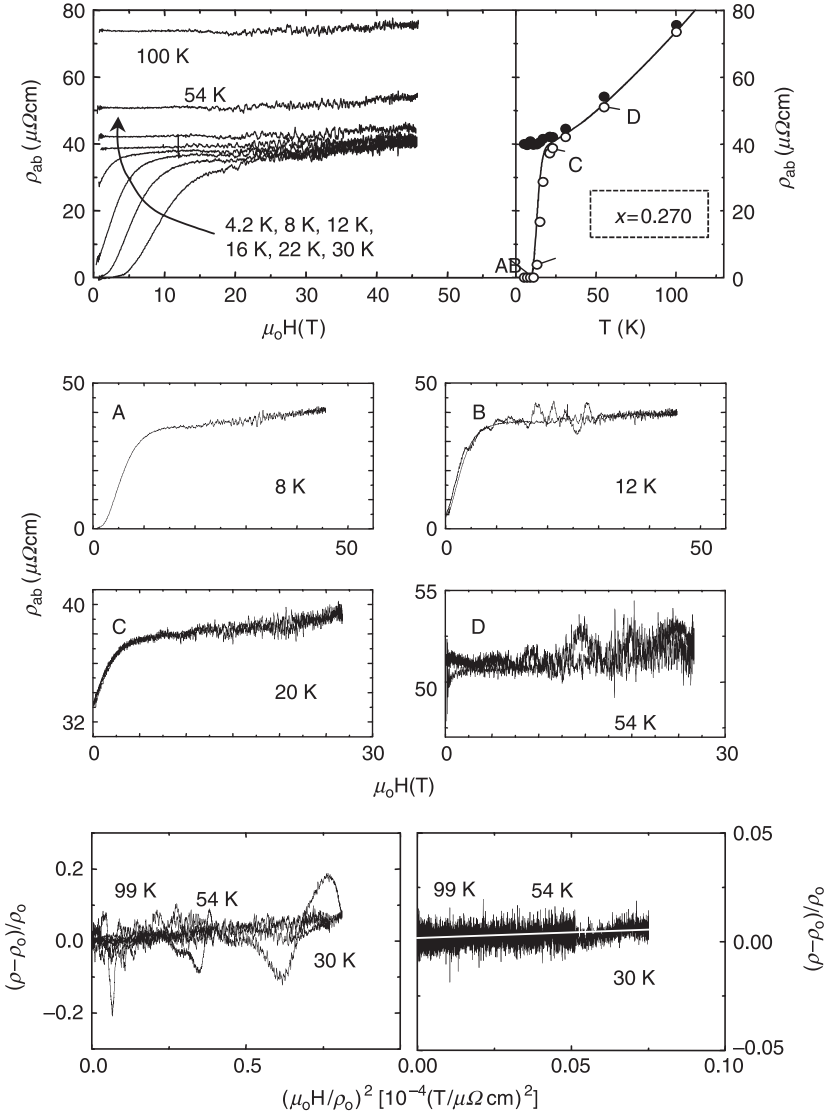

2.19 The left side of the upper frame gives an overview of the field dependence of the in-plane resistivity $\rho_{ab}(\mu_0 H)$ of $La_{1.73}Sr_{0.27}CuO_4$ at different temperatures. The right hand side of the upper frame depicts the temperature dependence of the in-plane resistivity $\rho_{ab}(T)$ at zero magnetic field (solid line). The open circles denote the values of the resistivity at zero field, derived from pulsed field measurements; filled circles mark the resistivity values at 45 T. For the positions labeled A, B, C and D, the magnetoresistivity is shown in more detail in the middle part of the figure. The lower frame shows the Kohler plots for the $La_{1.73}Sr_{0.27}CuO_4$ sample at selected temperatures used for the 45 T pulsed field data (left side) and the 12 T pulsed field data (right side).

that the classical Kohler's rule is valid in $La_{1.73}Sr_{0.27}CuO_4$. Its magnetoresistivity can safely be attributed to the normal state. The data for the other strongly overdoped sample, $La_{1.75}Sr_{0.25}CuO_4$, follows Kohler's rule above 30 K. For the superconducting samples with a lower Sr content (Fig. 2.13 to 2.17, lower frames), the dependence with $(H/\rho_o)^2$ remains linear over a wide temperature range (far above T_c) but the slopes increase when lowering the temperature. The deviations are more pronounced in the underdoped samples. Many authors observed this apparent violation of Kohler's rule in high-T_c systems and speculated on its origin (Lacerda *et al.* 1994, Harris *et al.* 1995, Kimura *et al.* 1996, Semba and Matsuda 1997, Balakirev *et al.* 1998, Abe 1999). In early reports, it was assumed that the violation of Kohler's rule reflected the influence of superconducting fluctuations (Kimura *et al.* 1996, Semba and Matsuda 1997). However, the observed temperature and field dependencies could not be reproduced by any fluctuation theory.

Since the contrast of the stripes with respect to their surrounding decreases upon doping (Fig. 2.8), the dimensionality of the charge-transport in the overdoped samples is not well defined. Although $La_{1.8}Sr_{0.2}CuO_4$ and $La_{1.75}Sr_{0.25}CuO_4$ reveal distinct pseudogap features, they partially recover a 2D (or 3D) character. It is therefore not surprising that the magnetoconductivity of the overdoped samples could not be fitted with a simple power law with respect to the temperature. Moreover, as follows from the data on $La_{1.73}Sr_{0.27}CuO_4$, the normal-state contribution to the magnetoresistivity cannot be neglected in samples with a high doping level. At the moment, however, there is no theory available showing an accurate evaluation of this normal-state background. It is even not 'a priori' clear whether the violation of Kohler's rule should be attributed to fluctuations or to the normal state (or to both). For example, if the mobile stripes bend in a magnetic field, they may influence the normal state magnetoresistivity in an unconventional way. In this context, we would like to mention the result of Ando and co-workers (Ando *et al.* 1999), who have reported a possible influence on the striped structure in non-superconducting underdoped cuprates by a magnetic field, in the configuration where the magnetic field is applied parallel to the ab-plane. Kimura *et al.* (Kimura *et al.* 1996) found a strong suppression of the magnetoresistivity in $La_{2-x}Sr_xCuO_4$ around the hole concentration with $x = 1/8$, a concentration that is related to a more static nature of the stripes (Tranquada *et al.* 1995). Their results underline the importance of the striped structure in the analysis of magnetoresistivity measurements.

Role of the pseudogap and pre-formed pairs

The pseudogap is emerging as an important indicator revealing the nature of the superconductivity as well as the normal state in high-T_c samples. A possible scenario relates the pseudogap with the presence of electronic pair states far above T_c (Tranquada *et al.* 1995, Randeria 1997, Bianconi *et al.* 1998, Maly *et al.* 1998, Emery 1999, Zaanen 1999, Moshchalkov *et al.* 1999, Vanacken *et al.* 2001). The idea is that Cooper pairs are already formed at a temperature T* far above T_c, but bulk phase coherent superconductivity is only established when long-range phase coherence is achieved below T_c. The models, which are based on this precursor superconductivity scenario, get experimental growing support. Scanning tunneling spectroscopy measurements clearly demonstrate that the pseudogap evolves into the superconducting gap at low temperatures (Kugler *et al.* 2001). Moreover, ARPES data indicate that the pseudo- and the superconducting gap both have d-wave symmetry (Loeser *et al.* 1996). Our experimental observation of a close relation between the pseudogap and the superconducting fluctuations (= precursor pairs) strongly favor these models as well. Altshuler *et al.* (Altshuler *et al.* 1996) questioned the interpretation of the pseudogap as the superconducting gap because a large fluctuation diamagnetism has not been observed between T_c and T*. Emery *et al.* [1999] stated however that the absence of strong diamagnetic effects is expected if the superconducting fluctuations are one-dimensional, and if the Josephson coupling between stripes is weak. In this case, an applied magnetic field does not cause any significant orbital motion until full phase coherence develops, close to T_c.

The magnetoresistivity data for $La_{1.9}Sr_{0.1}CuO_4$, presented in Fig. 2.16, do not show either clearly marked second critical fields $H_{c2}(T)$ or saturation at high fields. Fluctuating Cooper pairs seem to exist up to very high fields, most probably above the field range accessible by our pulsed field setup. Following the ideas outlined in (Emery 1999, Kugler *et al.* 2001), T* is the mean-field critical temperature of the superconductor rather than T_c. When T* is used to obtain the paramagnetic limiting field for sample $La_{1.9}Sr_{0.1}CuO_4$ ($T^* \approx 400$ K, $T_c = 17.5$ K) instead of T_c, a value of $\mu_o H_p \approx 700$ T is obtained, illustrating that a field of 50 T is indeed not high enough to destroy completely the preformed pairs. The ARPES study by Loeser *et al.* of the pseudogap state in $Bi_2Sr_2CaCu_2O_{8+\delta}$ (Loeser *et al.* 1996) revealed a binding energy of 75 meV in the precursor pairs. Thus a magnetic field of about 130 T ($\mu_o \mu_B H = k_B T$) would be needed to destroy them completely. If the idea of precursor pairs is correct, the temperature seems to be a much more critical parameter for the existence of the pairs than a magnetic field up to 50 T. The 'resistive upper critical field', as defined by a line construction, is certainly a questionable concept with respect to the underdoped high-T_c compounds. It is possible that the magnetoresistivity data of the samples, which show a pseudogap behavior, just reflect the behavior maybe even the localization, and of the precursor pairs in a magnetic field.

Superconductivity in metals is the result of two distinct quantum phenomena, pairing and long-range phase coherence. The influence of the stripes on superconductivity is therefore two-fold. First of all, the one-dimensional character of the charge transport favors pair formation as follows from the similarities between the pseudogap in high-T_c superconductors and the spin-gap in ladder cuprates and from experiments that demonstrate a connection between the superconducting- and the pseudogap properties. On the other hand, the low dimensionality hinders the long-range phase coherence needed to establish bulk superconductivity. It is a well-known fact that long-range phase coherence is impossible in a purely one-dimensional system. This is in agreement with the observation that $(La,Sr,Ca)_{14}Cu_{24}O_{41}$, the only known superconducting ladder compound, becomes superconducting under high pressure when the interactions between the ladders are enhanced.

As already stated above, the broadening of the superconducting transitions in underdoped cuprates, both in field and temperature, is most probably due to sample inhomogeneities. However, in this case the inhomogeneities do not reflect a bad sample quality but rather an intrinsic property, related to a low charge carrier concentration and the presence of stripes (intrinsic phase separation).

Generic phase diagram including fluctuation area

The pulsed field transport measurements at temperatures $T > T_c$ revealed a sudden appearance of a large positive in-plane magnetoresistivity in $La_{2-x}Sr_xCuO_4$ close to the insulator-superconductor transition at $x = 0.055$. This suggests that the effect can be attributed to superconducting fluctuations. The fluctuations appear at temperatures which exceed T_c by several times. It is therefore reasonable to speak about precursory pairing far above T_c. By presenting the magnetoresistivity data in the form of classical Kohler-plots, we found that the superconducting fluctuations are very pronounced in underdoped samples. At the same time, the normal-state contribution to the magnetoresistivity dominates in overdoped samples. The region where we observed superconducting fluctuations is schematically shown in the phase diagram of Fig. 2.20 by the shaded area. In order to evaluate this region exactly, an adequate theory is needed which allows the separation of fluctuations and normal-state contributions to conductivity. However, it is clear from our data that there is a close link between the presence of strong superconducting fluctuations and the pseudogap phase. Since fluctuations are expected to become more pronounced in systems with a reduced dimensionality, the following section will deal with this analysis.

Fluctuation analysis of underdoped $La_{2-x}Sr_xCuO_4$

To find the correct fluctuation dimensionality of our system, a typical plot can be used (Fig. 2.21). On the x-axis, $\varepsilon = \ln(T/T_c)$ is plotted and on the y axis the log of the difference in conductivity, the paraconductivity $= \sigma_{50T} - \sigma_{0T}$. If ε is small, i.e. near the transition temperature, then ε is equal to $(T - T_c)/T_c$. For the 2D fluctuations, in accordance with the Lawrence-Doniach model (Lawrence and Doniach 1971), a distance between the Cu-O planes is chosen, $d = 6.6Å$. This distance is almost doping independent. For both the 1D and 3D fluctuations, a zero level adjustment can be done by choosing the correct ξ. It can be seen that $\Delta\sigma$

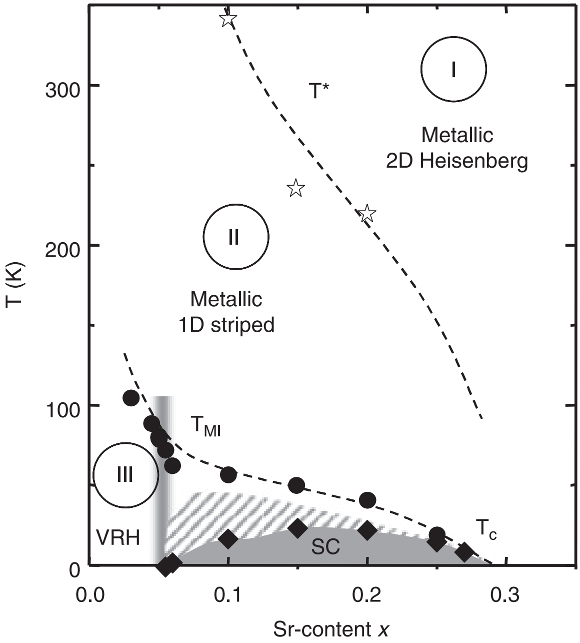

2.20 The same (T,*x*)-phase diagram of the $La_{2-x}Sr_xCuO_4$ samples as shown in Fig. 2.2. The Néel phase is omitted for clarity. Region III, bordered by the T_{MI} line, labels the insulating region of the phase diagram. Region III is divided into two parts by a gray line. On the left side of the gray line, variable range hopping conductivity characterizes the insulating phase. On the right side of the gray line the diverging resistivity upon a temperature decrease can be described by $\rho(T) \sim \ln(1/T)$ or a power law. The shaded region above the superconducting region (SC) depicts the fluctuation area.

data show a good agreement with the 2D AL-fluctuations, not only with the slope, but also the exact value between $\varepsilon = 0.02$ and $\varepsilon = 0.2$ is obtained. In the original paper (Aslamazov and Larkin 1968), the coherence length ξ is considered to be larger than the sample thickness. This is, however, not the case in the samples we used. What could happen is that the superconducting carriers only flow completely inside the Cu-O planes if the temperature is low enough ($\xi \leq t$ and $\xi \leq d$). Then, the coherence length should be bigger than the thickness where the superconducting carriers flow and the 2D formula should be valid. Indeed, taking the results presented in Fig. 2.21, the experimental data fit quite well to the 2D AL formula, indicating the fluctuations are of the two-dimensional type. This might look like a contradiction to the fact that we rather expect the normal state transport mechanism in these underdoped material to be 1D, but when superconductivity occurs, the 1D normal conductivity paths (stripes) seem to couple to allow the appearance of the 2D superconductivity.

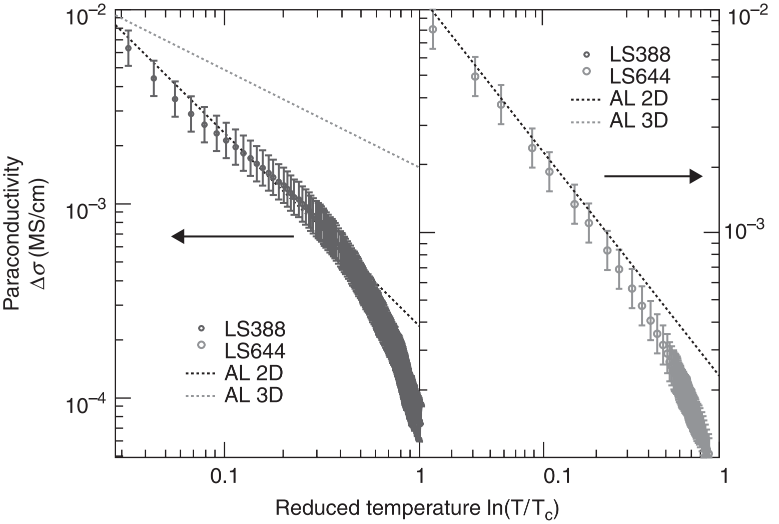

2.21 The paraconductivity as a function of the reduced temperature for samples with $x = 0.08$ and $x = 0.09$. Both samples closely follow the dotted AL 2D lines, and are distinctly different from the dashed 3D AL line.

2.3.4 Conclusion: temperature dependence of the resistivity

After studying the field induced normal state conductivity and the superconducting fluctuations, we are now able to describe the effective dimensionality of the normal state conductivity and the superconducting state. In Fig. 2.22, we show schematically the different charge order states in the Cu-O planes at different temperature regions. The resistivity $\rho(T)$ shows a transition at $T^*(x)$ from a linear to a superlinear temperature dependence. In the model proposed by Moshchalkov *et al.* (Moshchalkov 1999; Moshchalkov *et al.* 1999, 2001; Vanacken *et al.* 2001), this corresponds, respectively, to a two- and a one-dimensional conductivity. At low temperatures $T < T^*$, a stripe structure (1D) is observed, while at high temperatures $T > T^*$, the charges have enough thermal energy to also flow in the interstripe region (2D). When the temperature is close to T_c, the stripes become coupled, resulting in 2D-superconductivity. In the vicinity of T_c, the superconducting fluctuations show a two-dimensional Aslamasov–Larkin behavior (AL). At temperatures lower than T_c, a magnetic field has to be applied to investigate the field-induced normal state. This magnetic field also suppresses the inter-stripe coupling. Hence the stripe structure is recovered, but due to the low temperatures and the impurities, the charges become localized. An insulating-like behavior is thus found for $\rho(T \rightarrow 0)$ (IN) in high magnetic fields.

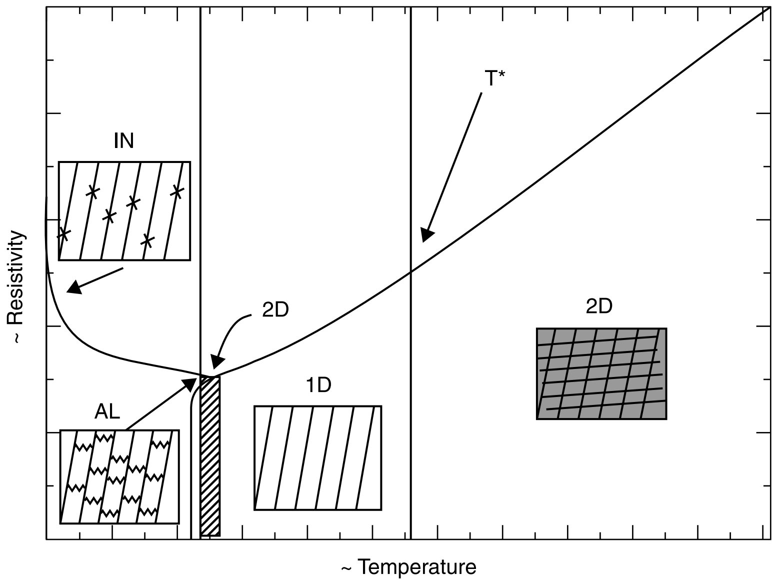

2.22 The different effective dimensionalities of high T_c cuprates in the resistivity–temperature plane.

2.4 Hall effect

In this section, the Hall number and its field and temperature dependencies are investigated. The Hall coefficient data are discussed and the magnetic field dependence of the Hall coefficient is analyzed. The carrier concentration will be derived, followed by derivations of Hall mobility, Hall angle and Hall conductivity. Then, a scaling with the pseudogap energy is used to analyze the temperature dependence of the Hall coefficient data for different doping levels in a similar way as is done for the resistivity.

2.4.1 Introduction

The Hall effect (Hall 1879) can provide valuable information about the electronic structure of the high-T_c superconductors. In this introduction, the origin of the Hall effect is reviewed both in the normal state at temperatures T >> T_c and in the mixed state at temperatures close to T_c. We describe below the field dependence of the Hall resistivity $\rho_H(\mu_o H)$ of our $La_{2-x}Sr_xCuO_4$ thin films in steady magnetic fields up to 10 T and in pulsed magnetic fields up to 50 T. The data obtained on the underdoped samples reveal clear evidence for the presence of strong superconducting fluctuations, in agreement with the results presented in section 2.4.2.

The Hall effect employs crossed electric and magnetic fields to obtain information on the sign, concentration and mobility of the charge carriers. The typical experimental arrangement is illustrated in Fig. 2.23. An electric field E_x, extending in the x-direction, is applied to a conductor. As a consequence, a current density j_x flows through the sample. In addition, a magnetic field B, pointing in the positive z-direction, is applied. The resulting Lorentz force deflects the charge carriers to one side of the conductor, giving rise to the appearance of an electric field, known as the Hall field, E_H, in a direction perpendicular to both the direction of the current and that of the magnetic field. In equilibrium, this transverse electric field E_H exactly opposes the further accumulation of charge carriers. Therefore, the electric current will only flow parallel to the x-axis. Since E_H balances the Lorentz force in the steady state, it will generally be proportional both to the magnetic induction B and to the current j_x. The constant of proportionality, R_H, is called the Hall coefficient or Hall constant.

$$R_H = \frac{E_H}{j_x\, B} \qquad [2.33]$$

In a free electron system, the Hall coefficient is related to the charge carrier density $n.q$:

$$R_H = \frac{1}{nq} \qquad [2.34]$$

where q is the elementary charge, positive or negative. Hence, a measurement of the Hall constant determines the sign of the charge carriers in the free electron model. A more general expression for R_H can be derived within the Bloch-Boltzmann theory (Popovic 1991), and has a much more complicated form. Essentially, it defines that the Hall coefficient is determined by the velocity of the charge carriers, their effective mass, and the anisotropic relaxation time at each point on the Fermi surface. Since the Hall coefficient depends in a complicated manner on very subtle electronic features, its interpretation is not straightforward. However, in many practical cases, the complicated expression for R_H may be simplified to expression [2.34] so that it essentially provides information about the density and sign of the carriers.

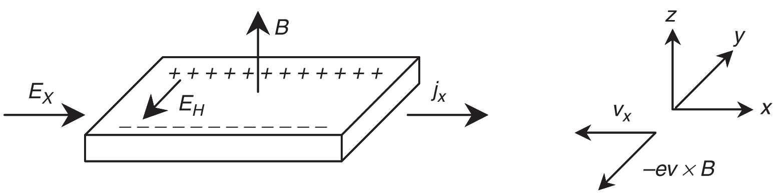

2.23 Schematic view of the Hall effect. The applied electric field E_x and current density j_x, the magnetic induction B and the Hall field E_H, generated by the Lorentz force $-ev \times B$ are indicated.

The Hall angle θ_H is a parameter that is closely related to the Hall coefficient R_H. This quantity characterizes the relation between the parallel and the transverse electric field and can be computed as follows:

$$\cot \vartheta_H = \frac{E_x}{E_H} = \frac{\rho_{ab}}{\rho_H} = \frac{\rho_{ab}}{R_H\, B} \approx \frac{\rho_{ab}}{R_H\, \mu_0 H} \qquad [2.35]$$

The mobility μ of the charge carriers is the drift velocity per unit electric field:

$$\mu = \frac{v_x}{E_x} = \frac{R_H}{\rho_{ab}} \qquad [2.36]$$

The Hall effect described above holds for both fermion and boson charge carriers. However, in the mixed state of superconductors, an extra Hall voltage appears, which originates from the electric field induced by the flux line motion (Poole *et al.* 1995).

When an electric current density j flows through a high-T_c superconducting sample in the presence of an applied magnetic field the vortices arising from the field interact with the current. This interaction can lead to vortex motion and heat dissipation. The result is a resistive term called flux-flow resistance. When the Lorentz force exceeds the pinning force F_p on a flux line ϕ_0,

$$\left| \vec{j} \times \vec{\phi}_0 \right| > F_p \qquad [2.37]$$

the flux line starts to move with a velocity v_ϕ. Two velocity-dependent forces come into play: the frictional drag force βv_ϕ and the Magnus force $- \alpha\, n_s /e/ (v_\phi \times \phi_0)$, with α and β constants and n_s the super electron density. The Magnus force is the force exerted on a spinning object in a fluid medium and it is a direct consequence of the law of Bernoulli for ideal flowing fluids. The Magnus force shifts the direction of vortex motion through an angle Θ_ϕ away from the direction perpendicular to j, as shown in Fig. 2.24. Following Faraday's law of induction, the motion of the vortices transverse to the current density induces a time-averaged macroscopic electric field E, given by:

$$\vec{E} = -\vec{v}_\Phi \times \vec{B}_{av} \qquad [2.38]$$

as indicated in Fig. 2.24, where B_{av} is the average internal field due to the presence of the vortices. The component of this electric field E_y perpendicular to the current-flow direction,

$$E_y = E \sin \Theta_\phi \qquad [2.39]$$

produces a 'vortex dynamics Hall effect'.

The Hall effect in cuprate superconductors has been reported in the literature, both in the normal state ($T \gg T_c$) (Harris *et al.* 1992, Xiong *et al.* 1993, Almasan *et al.* 1994, Hwang *et al.* 1994, Wuyts 1994, Wuyts *et al.* 1996, Ando *et al.* 1997, Konstantinović *et al.* 2000, Hirayama and Nakagawa 2000, Trappeniers 2000) as in the mixed state close to T_c (Iye *et al.* 1989; Hagen *et al.* 1990, 1993; Matsuda *et al.*

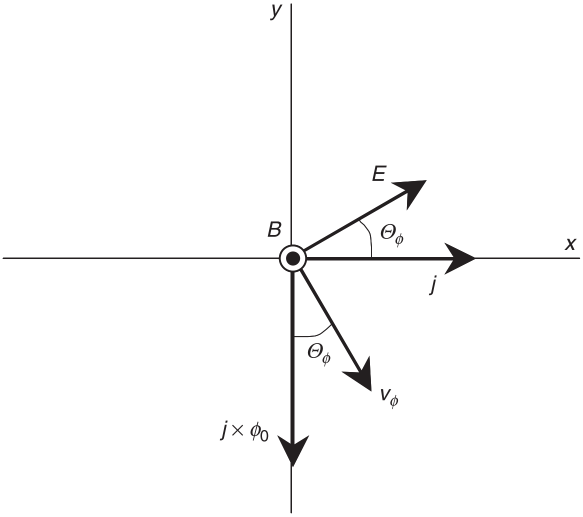

2.24 Electric field *E* induced by the motion of a vortex ϕ_0 moving at a velocity v_ϕ through an applied magnetic induction *B* directed upward from the page. The vectors *E*, v_ϕ and *B* are mutually perpendicular. The vectors for the current density *j* and the Lorentz force $j \times \phi_0$ are also indicated. *E* has an angle of Θ_ϕ with respect to *j*.

1995; Nagaoka *et al.* 1998; Kopnin *et al.* 1999). One of the striking observations is the anomalous temperature dependence of the Hall coefficient far above T_c. In the mixed state close to T_c, most of the underdoped and slightly overdoped high-T_c superconductors reveal a sign change in the Hall effect. Section 2.4.2 will demonstrate the unusual character of the Hall signal in our $La_{2-x}Sr_xCuO_4$ thin films.

2.4.2 Observation of field induced sign reversal in the Hall coefficient

In the set of pristine $La_{2-x}Sr_xCuO_4$ thin films, the Hall voltage sign reversal is observed clearly in the $x = 0.125$ (1/8) film at temperatures T = 13K – T = 19 K (Fig. 2.25). Panel (b) shows the position of the minimum in the Hall voltage as a function of the temperature. The latter graph resembles an *H-T* phase line, similar to the irreversibility line, for instance.

This sign reversal of the Hall resistivity is reported in the literature in moderate magnetic fields close to T_c for several underdoped and slightly overdoped high-T_c samples (Hagen *et al.* 1990, 1991, 1993; Wang *et al.* 1991; Almasan *et al.* 1994; Matsuda *et al.* 1995; Nagaoka *et al.* 1998; Nakao *et al.* 1998). In the low field range close to T_c, the sign of the Hall resistivity often appears to be electron-like in the underdoped and the slightly overdoped range and hole-like in the overdoped regime. The sign reversal of the Hall resistivity is not a new phenomenon for the

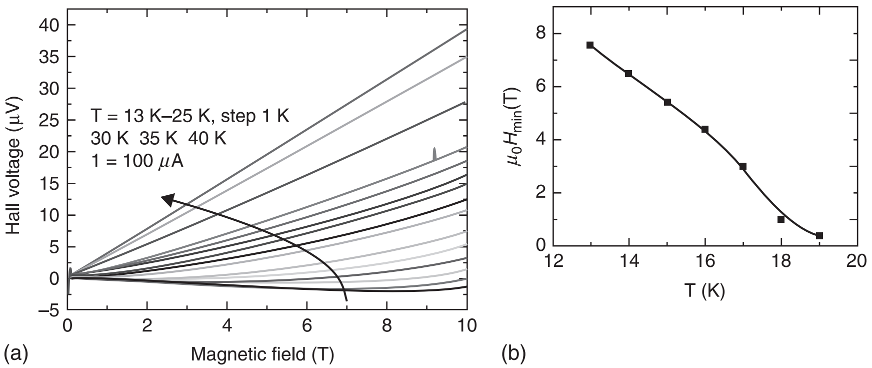

2.25 The Hall voltage sign reversal for the $x = 0.125$ sample. The Hall voltage sign reversal is observed for T = 13 K–19 K (a). The minimum $\mu_0 H_{min}$ of the $V_H(\mu_0 H)$ curves at different temperatures is shown in panel (b).

mixed state of high-T$_c$ cuprates but has been found in some Pb-In (Weijsenfeld 1968), Nb (VanBeelen *et al.* 1967, Noto *et al.* 1976) and V (Usui *et al.* 1969) low-T$_c$ systems as well. Therefore, some authors (Hagen *et al.* 1990, 1991, 1993; Chien *et al.* 1991; Wang *et al.* 1991; Kopnin *et al.* 1993) believe that the effect is rather general and needs an explanation in terms of general properties of vortex dynamics, which are not specific for the mixed state of high-T$_c$ superconductors alone. Conventional models for flux motion (Bardeen and Stephen 1965, Nozières and Vinen 1966) could however not explain the effect as they all predict that the Hall resistivity in the mixed state has the same sign as that in the normal state (Ji and Wong 1999).

Heavy-ion irradiation by a 6 GeV Pb-ion beam ($2 \times 10^{11}/\text{cm}^2$) (performed at the *Grand Accélérateur National d'Ions Lourds* (GANIL), Caen, France) on irradiated $La_{1.75}Sr_{0.25}CuO_4$ shows (Fig. 2.26) a clear sign change of the Hall resistivity. The sign change, observed in the Hall data of the irradiated $La_{1.94}Sr_{0.06}CuO_4$ thin film, is more pronounced than that in the non-irradiated sample. Since overdoped samples usually show a hole-like Hall signal at low temperatures (Nagaoka *et al.* 1998), the negative Hall resistivity, revealed by the irradiated $La_{1.75}Sr_{0.25}CuO_4$ system in the low field range close to T$_c$, is remarkable. Heavy ions amorphize the superconductor and form fine columnar defects of 5–10 nm in diameter, along their trajectory. These defects provide a strong flux-pinning effect in the sample within certain ranges of temperature and field (Gray *et al.* 1996, Trappeniers *et al.* 1999). As a consequence, our observations strongly favor models including flux pinning as an important parameter in the description of the Hall effect (Wang and Ting 1994, Kopnin and Vinokur 1999). According to the theories, pinning affects the backflow current in vortex cores, which may result in a more pronounced sign anomaly as the pinning strength increases.

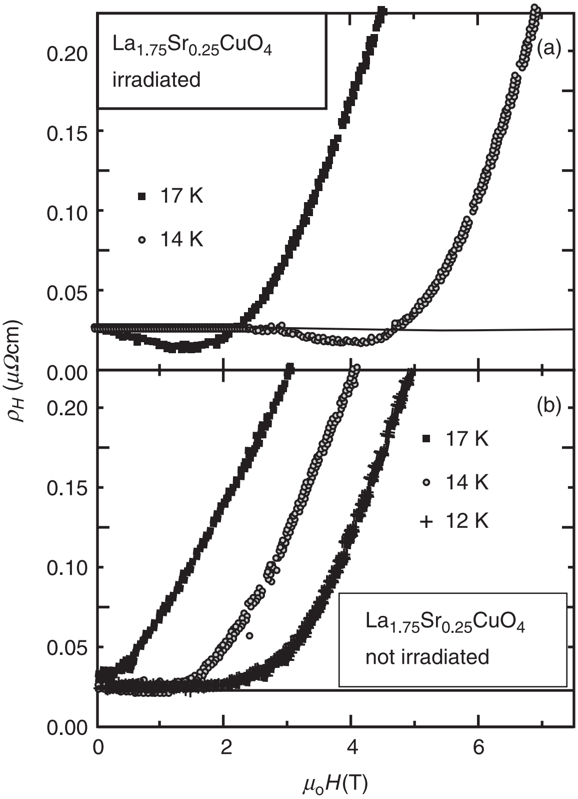

2.26 The transverse Hall resistivity ρ_H versus applied magnetic field for a $La_{1.75}Sr_{0.25}CuO_4$ thin film (T_c = 18.5 K) of thickness 112 nm at 17 K and 14 K. (a) After irradiation with a 6 Ge V Pb ion-beam ($2 \times 10^{11}/cm^2$). (b) Corresponding data for the non-irradiated samples.

Pronounced effects of pinning on the Hall anomaly have been reported earlier by (Kang *et al.* 1999). In any case, our results may imply that the sign reversal is not an intrinsic property of the $La_{2-x}Sr_xCuO_4$ system (or the high-T_c cuprates in general), but rather related to a specific motion of the vortices. It is possible that the stripe formation – constituting intrinsic disorder – influences the flux line motion and pinning (or vice versa). This might explain the differences between the behavior of the Hall resistivity in under- and overdoped systems.

2.4.3 The room temperature Hall coefficient

In Fig. 2.27, the Hall coefficient at 300 K of the different thin film samples as a function of the doping is shown. In this graph a clear exponential law is seen

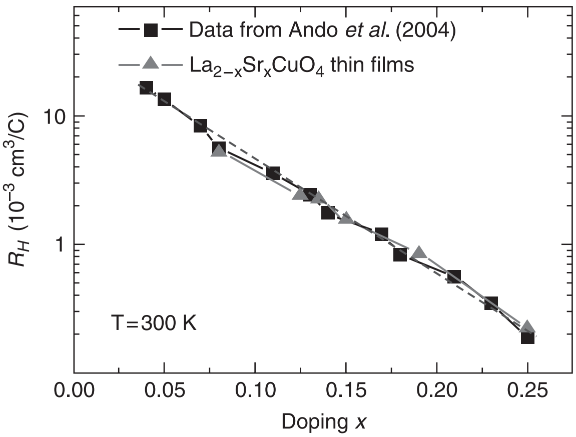

2.27 The Hall coefficient R_H at 10T (logarithmic scale) at 300 K for all the samples used in this study, together with the data reported by Ando *et al.* (2004).

and the data coincide very well with the results obtained by Ando (Ando *et al.* 2004).

$$R_H(x)^{300\,K} = 2.48 \times 10^{-8} \times 10^{-8x}\ \Omega\text{m/T} \qquad [2.40]$$

When using equation [2.40] (see dashed line in the figure), it can be seen that if the chemical doping stays the same, the same amount of carriers is introduced in the sample (*n* is the same) thus the Hall coefficient will stay the same. The temperature can have a large effect on the Hall coefficient.

2.4.4 Temperature dependence of the Hall coefficient

In Fig. 2.28 the Hall coefficient data are presented for the six samples with different Sr-dopings. While this graph only shows data for six samples, many more samples were studied to ensure the reproducibility of the results. We have selected these six samples to focus our discussion. The 10T data points below the critical temperature are removed due to the zero voltage of the superconducting state of the sample. For the high temperatures, T > 100 K, the 50T pulsed fields data and the 10T DC data seem to coincide within the experimental error. For the lower temperatures, a small difference is seen near the superconducting transition while a big difference below the critical temperature is seen due to the superconducting fluctuations. No slope changes or singularities are seen in these data around the critical temperature. The effects are either smeared out over a whole temperature region or no effects are present. For all samples a clear increase in the Hall coefficient from room temperature down to a certain temperature T_{MAX} (see Fig. 2.28) is observed.

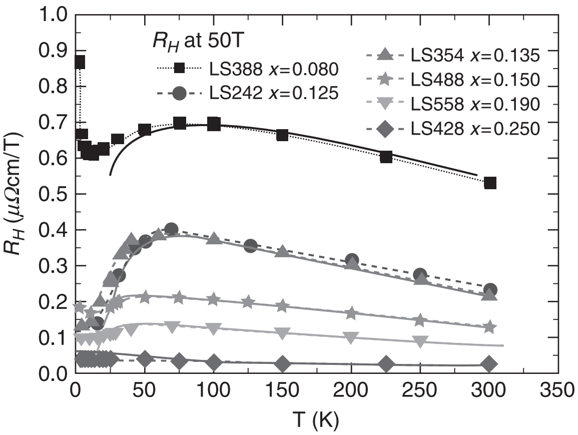

2.28 The 50T Hall coefficient data (symbols) together with the 10T R_H data (solid lines) for the $La_{2-x}Sr_xCuO_4$ samples used in this study.

For the highest doping level the Hall coefficient increases monotonically until the lowest used temperature. In this graph, it is seen that T_{MAX} decreases with increasing doping. When the samples are highly overdoped, the R_H(T) maximum does not exist. This maximum seems to correspond very well to the metal insulator transition which was discussed in section 2.4.2.

The relation between T_{MAX} and T_{MI} was already reported for the $YBa_2Cu_3O_{7-8}$ thin films (Trappeniers 2000). Ando *et al.* (2004) and Dai *et al.* (2004), found that for the highly underdoped non-superconducting samples the maximum in the R_H(T) occurs, but is not seen anymore. A clear maximum is however seen around $x = 0.04$–0.07 which is the doping range at which the superconductor-insulator transition takes place. In the intermediate region the same R_H(T) dependency with maximum is seen. For the samples with doping lower than 0.03 the maximum is not visible anymore, because these samples show almost no temperature dependence of R_H(T). A detailed analysis of the carrier concentration effects on the Hall coefficient will be given in one of the following sections. From Fig. 2.28 it can be noted that the temperature dependence (at temperatures higher than 100 K) of the Hall coefficient becomes less pronounced when the doping is increased. For the lowest doping, as reported by Ando *et al.* (2004), there is also a weak temperature dependence. Thus, when the samples become superconducting, they start showing a clear temperature dependence of R_H, nevertheless superconductivity and all its effects are completely suppressed by the magnetic field. For higher doping, when superconductivity is again disappearing (doping reaches 0.3), the Hall coefficient becomes practically temperature independent, as in normal metals. In Fig. 2.28, a clear difference between $x = 1/8$ and the other Sr concentrations is seen.

2.4.5 Carrier concentration

The carrier concentration can be estimated from the Hall number. The exact theory specifying how to do it for HTSCs is not yet available thus a simplified equation [2.34] is used to calculate the carrier density. In normal metals, according to the Drude model, the Hall coefficient should be temperature independent (Poole *et al.* 1995). This is, however, not the case with Hall data obtained on HTSCs cuprates.

In Fig. 2.29 the carrier concentration is plotted as a function of the temperature in a log-lin graph. Normally one could expect that the lower the temperature, the fewer carriers are mobile. It can indeed be found, at relative high temperatures (70 K < T < 300 K), that the number of carriers decreases with decreasing temperature. For temperatures lower than the critical temperature, however, the Hall number decreases, except for the samples close to the $x = 1/8$ doping range. Fig. 2.29 also shows a mark indicating the concentration exactly at 1 hole per Cu atom. By decreasing the temperature, fewer carriers will participate in the conduction process due to thermal excitation effects. In all the samples, except around $x = 0.125$, the carrier concentration decreases rapidly at temperatures below 30 K. A localization effect takes place. When the carriers start moving in one-dimensional lanes (stripes), the Hall coefficient will decrease if these stripes are aligned parallel to the current. This is expected for $x = 0.125$ (in the analysis of the Hall conductivity we will come back to this). The resistivity will in this case rise due to localization effects. The carrier concentration, determined from the Hall coefficient, will increase. Other electron correlations configurations (checkerboards or crossed stripes, etc. (Kohsaka *et al.* 2007, Howald *et al.* 2003, Hoffman *et al.* 2002, Wise *et al.* 2008)) can also induce similar effects in the Hall coefficient and even in the resistivity measurements (Hanaguri *et al.* 2004).

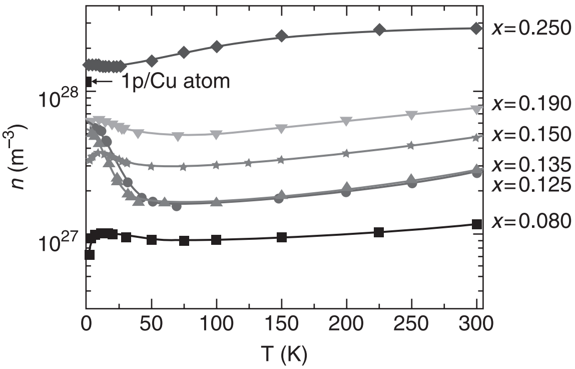

2.29 The hole concentration at 50T determined from equation [2.31]. The six different $La_{2-x}Sr_xCuO_4$-samples are included with Sr-content 0.08 (■), 0.125 (●), 0.135 (▲), 0.15 (★), 0.19 (▼) and 0.25 (◆).

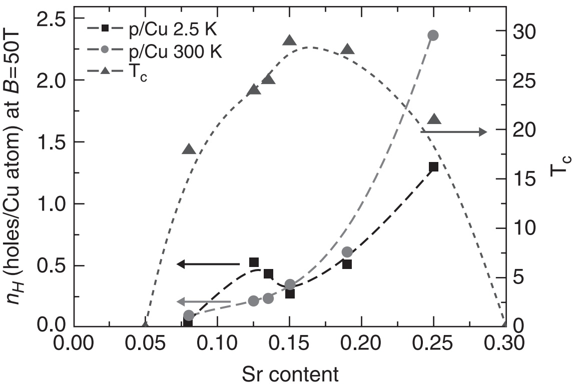

2.30 The hole concentration dependence on Sr doping in $La_{2-x}Sr_xCuO_4$ at T = 2 K (■) and T = 300 K (●) along with the superconducting dome $T_c(x)$ (▲). The lines are guides to the eye.

It is interesting to compare the Hall data at high temperatures with those obtained at low temperatures and to interpret the difference between them (see Fig. 2.30). It can be seen from this figure that at 300 K, the hole concentration increases monotonically with doping, but not linearly. A linear dependence would be expected from the amount of carriers introduced in the system by the La/Sr substitution. The 2.5 K data show an n_H increase with the carrier concentration around $x = 1/8$. This maximum seems to correspond to about 1/2 carrier per Cu-atom.

Balakirev *et al.* measured the Hall coefficient of the $Bi_2Sr_{2-x}La_xCuO_{6+}$ compound down to low temperatures (Balakirev *et al.* 2003). They found that the carrier density calculated by using formula [2.34] increases at low temperature to a saturation level of one carrier per Cu atom around the optimally doped system. This feature possibly favors the existence of a quantum critical point (QCP) (Balakirev *et al.* 2003) in the high-temperature superconductors. In our experiments, this QCP-feature is however not seen at all. This might be discussed as the differences between the thin films and the single crystals where the single crystals could show a larger *c*-axis contribution than the thin films.

2.4.6 Hall mobility

The Hall mobility for six different samples can be seen in Fig. 2.31. The Hall mobility decreases with temperature for all the samples above 50 K while at low temperatures μ_H decreases until at around 50 K a maximum mobility is reached. This maximum is not observed for the highly overdoped sample. The decrease at low temperatures in the Hall mobility comes from the onset of the insulating behavior in the samples. This temperature corresponds well, but not exactly, to the metal-insulator transition temperature T_{MI}. No difference in the slope of $\mu(T)$ around the critical temperature is seen.

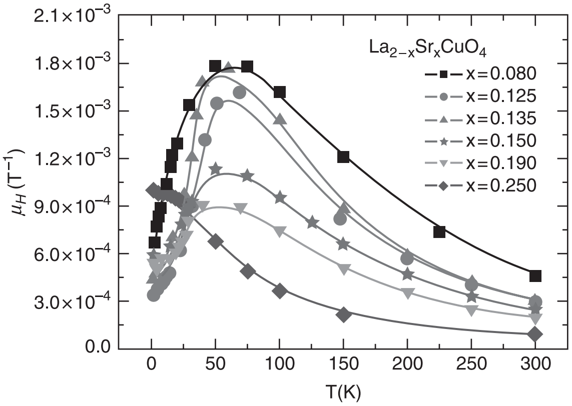

2.31 The Hall mobility at 50T for six different samples as a function of the temperature.

2.4.7 Hall angle

Figure 2.32 shows cot(Θ_H) for the different samples. The cotangent of the angle indicates how easy the conductivity in the *xx* direction occurs, compared to the transverse direction *xy*. When the cotangent of the Hall angle is small, the electrical field along the current will be much lower than the electrical field in the transverse direction. In our samples, it is observed that the higher the doping the higher the cot(Θ_H). An exception holds for temperatures below 50 K where the samples with doping around 1/8 have much higher cot(Θ_H) than the other samples. When the cotangent of the Hall angle is small, the electrical field along the current will be much lower than the electrical field in the transverse direction. In our samples, it is observed that the higher the doping the higher the cot(Θ_H). An exception holds for temperatures below 50 K where the samples with doping around 1/8 have much higher cot(Θ_H) than the other samples. The cotangent of the Hall angle is decreasing with decreasing temperature for the temperatures higher than 50 K. When looking at the lowest doping, the carriers in the sample have difficulties in conducting the current in the *xx* direction and the Hall coefficient becomes much more pronounced, thus a smaller cotangent (or a bigger angle) is observed. In all the samples, it can be seen that the cotangent of the Hall angle stays above 11, which corresponds to a respective angle below 5 degrees.

2.4.8 Hall conductivity

The Hall conductivity can be used to verify that the transport properties have a one-dimensional character. The Hall conductivity in 2D can be calculated via the

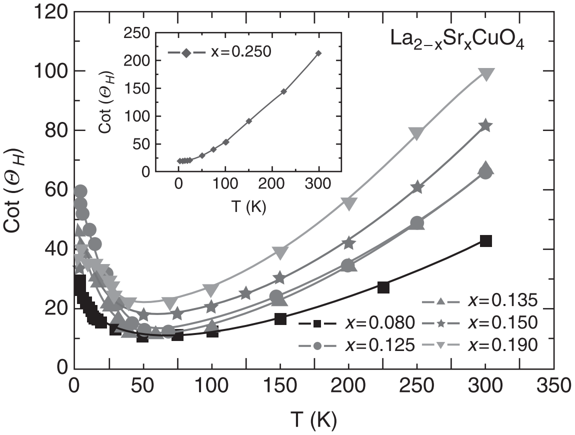

2.32 The cot(Θ_H) vs T for different $La_{2-x}Sr_xCuO_4$ samples at 50T.

conductivity tensor (and Onsager's relations) as $\sigma_{xy} = \rho_{xy}/(\rho_{xx}\ \rho_{yy} - \rho_{xy}\ \rho_{yx})$. In the case where the Hall coefficient is much lower than the ρ_{xx}, this formula can be simplified to $\sigma_{xy} = \rho_{xy}/\rho^2_{xx}$ where $\rho_{xy} = R_{xy}\ d$, with d the thickness of the sample. The Hall coefficient at 50 T is less than 5% of the magnetoresistivity at 50 T, so this satisfies the conditions for this simplification. Since at low temperatures, a high magnetoresistivity is observed, ρ_{xx} and ρ_{xy} will be replaced by their high field data. The Hall conductivity as a function of the temperature is given in Fig. 2.33(a). At high temperatures all the samples show the same characteristic functional behavior. This can be related to the theory $\rho_{xy} = \alpha_C\ \rho^B{}_{xx}/(\Phi_0 B)$ with Φ_0 the flux quantum and $\alpha_C = \eta\tan(\Theta_H)$ with η the friction coefficient (Vinokur *et al.* 1993, Hagen *et al.* 1993), which is a quite general expression, found for all the vortex states. It is valid for our samples at temperatures higher than 150 K.

Noda *et al.* (1999) reported that the Hall conductivity decreased from a certain temperature T_0. T_0, in that paper, denotes a structural transition temperature in the Nd doped $La_{2-x}Sr_xCuO_4$. The authors claim that this reduction shows that the charge order (stripe behavior) causes suppression of the conductivity in the transverse direction. They also plotted the intensities of the charge order peak seen in x-ray-diffraction on the same graph and found an excellent agreement (see Fig. 2.33(b)). To ensure that the samples show this one-dimensional character, the Hall conductivity should completely vanish at the zero temperature. In the theory, much effort is put into the stripe structure to discuss various properties. Many experiments indicate that these stripe structures are surviving in the material up to an optimal doping of 1/8. The maximum in the R_H(T) graphs is also observed around the metal insulator transition temperature T_{MI}. The same functional behavior, as seen in the Noda paper, is presented in Fig. 2.33(a). For the samples with low doping, the Hall conductivity decreases with temperature. These dependencies show the same characteristic functional behavior as the ones reported by Noda *et al.*

T^{-3}-*scaling*

In Fig. 2.33(b), it can be seen that the Hall conductivity σ_{xy} at high temperatures ($T > 50$ K) can be fitted easily with a T^{-3} law. A possible explanation for the T^{-3} fit was proposed by Stoijkovic *et al.* 1997, where the authors start from the nearly antiferromagnetic Fermi Liquid. They calculated the Hall conductivity and found a T^{-3} law, in a certain temperature region between T_0 and $2T_0$, with T_0 a crossover temperature. They also stated that above a temperature $2T_0$ the curves should follow the T^{-2} law. A constant difference with the T^{-3} law ($1/(T^3+C)$) was seen in the $La_{2-x}Sr_xCuO_4$ compounds in their paper. This was claimed to come from a certain amount of disorder in the $La_{2-x}Sr_xCuO_4$ system. The power law was checked with the experiments and a clear fit with the $1/(T^3+T_I^3)$ law has indeed been found.

T_I depends on the sample and changes from 132 K at the lowest doping to 100 K at a 0.19 doping. The dependency of the T_I on doping corresponds very well with the metal insulator transition temperature $T_{MI}(x)$ (see Fig. 2.34). The T^{-3} law can be well fitted between 35 K and 300 K for the $x = 0.19$ sample, while for the $x = 0.08$ sample, the fit works well between 70 K and 300 K. For the highest doping the data is fitted with a T^{-2} law down to the lowest temperatures. This makes it possible that the temperature T_0 is doping dependent and it becomes very low in the highly overdoped samples, varying in these samples from 70 K at the lowest doping, over 35 K for the $x = 0.19$ sample and becoming almost zero in the highly overdoped samples.

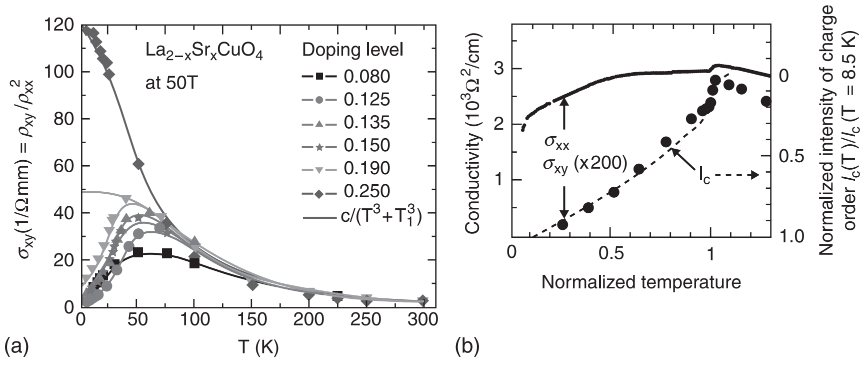

2.33 (a) The Hall conductivity vs. temperature. (b) The Hall conductivity σ_{xy} and the normalized X-ray intensity of the charge order peak in a Nd doped $La_{2-x}Sr_xCuO_4$ (after Noda *et al.* (1999)).

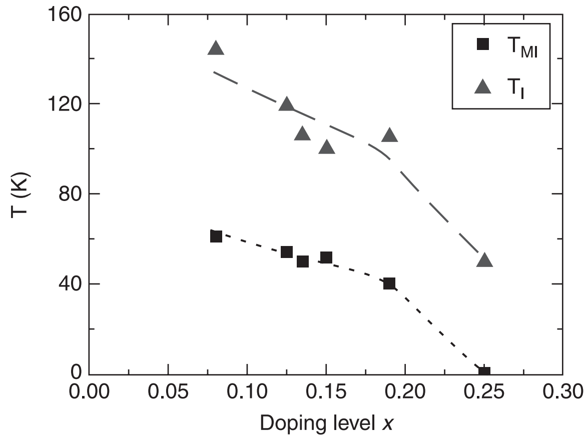

2.34 The temperature T_{MI} and T_I as a function of doping. Two lines are also added as a guide to the eye.

Low temperature behavior

At low temperatures, the best way to distinguish between the different samples is to use the log-log or log-linear plots of the Hall conductivity as a function of the temperature, as noticed from the magnetoresistivity data. For the highest doping, the T^{-2} law fits well down to the lowest temperatures (also see Lange and Kotliar (1999)). The lowest doping samples, however, exhibit a linear σ_{xy} dependence in the log-log plot (see Fig. 2.35(b)). The dependency can be described as $\sigma_{xy} = CT^{3/4}$. For other samples, a linear dependence can be seen in the log-lin graph (see Fig. 2.35(a)). The slope decreases with increasing doping. The equation in this case is given by $\sigma_{xy} = C10^{T/T_{ms}}$ with T_{ms} a temperature increasing with increasing doping. For the samples with the highest doping, no insulating behavior at low temperatures is observed and the Hall conductivity does not decrease. The higher the doping, the higher the saturation point in the conductivity and the more the materials behave like a normal metal. Correlating this with the resistivity data, the following observation can be made: For the lowest doping level ($x = 0.08$), the σ_{xy} data show a linear dependency in a log-log graph, whereas the other samples have linear behavior in a log-lin graph. This analysis is also valid for the resistivity data.

2.4.9 Scaling of the Hall coefficient and Hall mobility

The temperature dependent resistivity data $\rho(T)$ were found to scale (Fig. 2.5) with a characteristic parameter $\Delta(x)$, which turned out later to correspond to the pseudogap. Just as the scaling was performed in section 2.2.2, we can now try to obtain a scaling for the Hall coefficient.

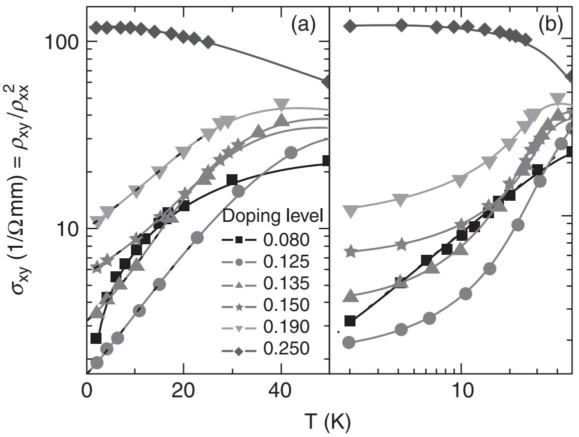

2.35 Two different $\sigma_{xy}(B = 50T)$ graphs as log-linear plot (a) and log-log plot (b). Guides to the eye are also seen as solid lines.

Hall coefficient

In section 2.2 it has already been mentioned that a scaling was possible using the pseudogap $\Delta(x)$. A similar scaling also works for the Hall coefficient data. For the scaling parameters the same temperature dependency is chosen, namely T/Δ with exactly the same pseudogap value $\Delta(x)$ used already in section 2.2.3. The pseudogap values obtained from the zero field resistivity data Δ(T) and from the Hall coefficient R_H(T) are identical. The Hall coefficient scales as $(R_H - R_{H0})/(R_{H2/3\Delta} - R_{H0})$ with R_{H0} an extrapolated Hall coefficient at 0 K and $R_{H2/3\Delta}$ the Hall coefficient at 2/3Δ. Figure 2.36 shows the Hall coefficient scaling for the under and optimally doped samples at 10T and 50T. The full lines correspond to the low DC field data while the separate data points correspond to the high pulsed field data. The 10T and the 50T data coincide very well in the reduced temperature region of 0.4–1.75, as seen in Fig. 2.36. In the graph it can be noticed that all the curves coincide very well in the reduced temperature T/Δ region of 0.5–1.25. This is the same region where a good agreement was found between the resistivity ρ(T) of $La_{2-x}Sr_xCuO_4$ and the $Sr_{2.5}Ca_{11.5}Cu_{24}O_{41+\delta}$ ladder compound.

The spin-ladder compound is not included in the Hall coefficient scaling, because no R_H(T) experimental data is available in the literature. The overdoped regime is not plotted in the same graph, because no relevant scaling can be applied for the Hall coefficient. The temperature dependence of the scaled Hall coefficient looks almost linear, but the exact dependency is not yet known. For the low temperatures, no scaling can be applied to the Hall coefficient as a function of the temperature. In the ρ(T), a big change has been seen when crossing the 10 K temperature in the high field data in the log-log plot. However, in the Hall

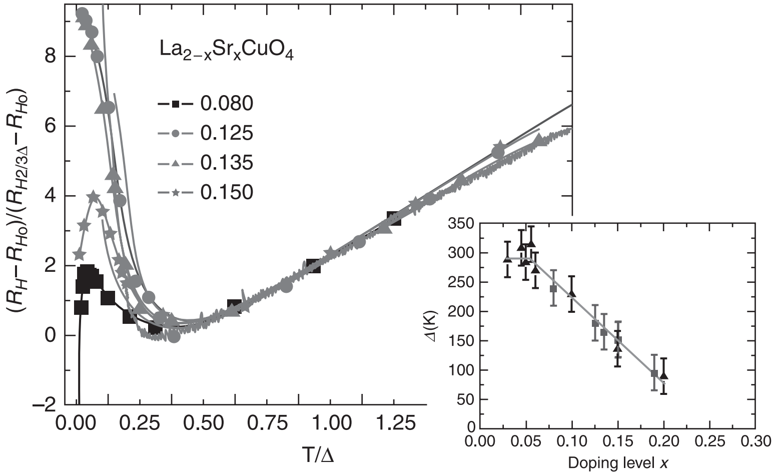

2.36 Scaling of the Hall coefficient at 50T for the under and optimally doped La$_{2-x}$Sr$_x$CuO$_4$ samples. The inset at the right shows the doping dependence of the pseudogap, as obtained from both resistivity and Hall coefficient scaling.

coefficient data, no change is observed in different log-log and log-lin graphs. The R_H(T) dependence for all the samples are smooth curves without a slope change at 10 K. The resistivity is thus more liable to small changes then the Hall coefficient.

Hall mobility, Hall angle and Hall conductivity: pseudogap used for scaling the Hall coefficient data

Just as for the resistivity and the Hall coefficient, a scaling can also be tried for the Hall mobility, the Hall angle and the Hall conductivity. No scaling with the pseudogap can been found for the Hall conductivity, not even at the lowest temperatures. For the cotangent of the Hall angle cot(Θ_H), the scaling is shown in Fig. 2.37. For the temperature, a scaling is used, $(T/\Delta)^2$, where Δ(*x*) is the same scaling parameter which was applied to scale the resistivity and the Hall coefficient. The values of the cotangent of the angle are scaled as cot(Θ_H)/cot$(\Theta_H)_\Delta$ with cot(Θ_H) the value at the temperature. For the optimally doped and overdoped samples, a simple offset is also introduced before dividing the data by cot(Θ_H). The highest doping is not included, because the Δ value is unknown for this sample.

The scaling works very well between $(T/\Delta)^2 = 0.5$ and 3 for all the samples. This temperature region corresponds to the same one for which the scaling of the resistivity and the Hall coefficient worked well. In Fig. 2.37, it can be seen that the cotangent cot(Θ_H) is well fitting with a quadratic reduced temperature. A guide to

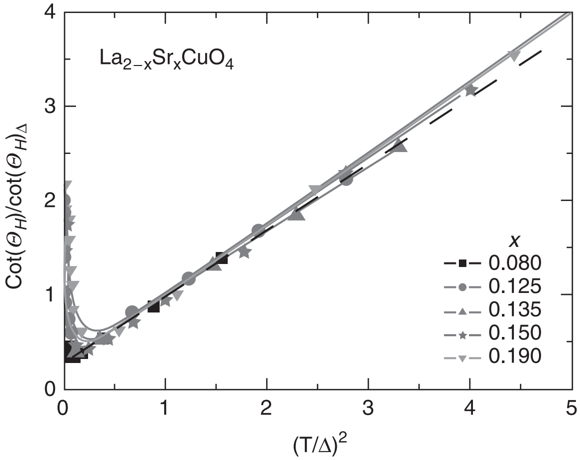

2.37 Scaling of the cotangent of the Hall angle cot (Θ_H) (B = 50T).

the eye line is added in the graph to show the validity of this behavior. Since the scaling is valid for the cotangent of the Hall angle, this will also be valid for the Hall mobility. The mobility is the inverse of the cotangent of Hall angle multiplied by the magnetic field, which is the same for all the samples in Fig. 2.37. The mobility will thus also be scaled with the quadratic reduced temperature. From all the parameters (Hall angle, Hall mobility, Hall conductivity, Hall coefficient and resistivity) it is seen that the only derived quantity which cannot directly be scaled is the Hall conductivity. At high temperatures, the Hall conductivity is the same for all the samples. This might just be a coincidence due to a cancelation of different dependencies or this might have a basic underlying reason, which is not completely clear from these experiments.

2.4.10 Summary of the Hall effect

In this chapter the different characteristics of the Hall effect in LSCO have been discussed. The magnetic field dependencies of the Hall coefficient are also discussed. One of the remarkable features is the Hall voltage sign reversal. A clear temperature dependency is seen for the Hall coefficient as a function of the temperature. The R_H(T) dependency shows different functional behaviors as a function of x. The carrier concentration at 300 K, estimated from the Hall coefficient, increases monotonously with increasing doping. A peak in the carrier concentration is however seen around $x = 0.125$ at the lowest temperatures (2.5 K). The Hall mobility clearly shows the insulating behavior at low temperatures for the under and slightly overdoped samples. The cotangent of the

Hall angle depends quadratically on the temperature in the high-temperature region (T > 50 K). The Hall conductivity, for x around 0.125, shows a similar behavior as reported for the Nd doped $La_{2-x}Sr_xCuO_4$ samples at low temperatures. This made it possible to assume that the stripe behavior is also present in our system. At high temperatures (T > 50 K) a T^{-3} law could be used to fit the $\sigma_{xy}(T)$ up to room temperature. In the last section, the scaling used for the resistivity has also been performed on the Hall coefficient and the Hall angle with the same pseudogap $\Delta(x)$.

2.5 General conclusion

The systematic study of the evolution of the normal state properties (resistivity and Hall effect) of the $La_{2-x}Sr_xCuO_4$ cuprates with doping has revealed the presence of the charge-rich 1D features (stripes), which eventually determine the 1D character of the normal state transport properties at temperatures below the so called 'spin-gap' temperature $T(x)$. Stripe coupling close to T_c recovers the 2D character of the Cu-O planes and is responsible for the 2D Aslamasov–Larkin superconducting fluctuations at $T \sim T_c$ and the superconducting state itself at $T < T_c$. Stripes decoupling, by strong magnetic fields, induces again at low temperature a 1D stripe behavior, which, in the presence of the intra-stripe impurity centers, lead to the formation of the insulating state in underdoped $La_{2-x}Sr_xCuO_4$ at $T \rightarrow 0$. Linking transport properties to stripes which have been recently directly visualized, by using local imaging techniques, is contributing substantially to a consistent explanation of the unusual transport properties of high T_c cuprates.

2.6 References

Abe, Y., Y. Ando, J. Takeya, H. Tanabe, T. Watauchi *et al.* (1999) 'Normal-state magnetotransport in $La_{1.905}Ba_{0.095}CuO_4$ single crystals', *Phys. Rev. B* **59**, 14753.

Abrikosov, A.A. (1988) *Fundamentals of the Theory of Metals*, Elsevier Science Publishers (Amsterdam), ISBN 0444-87095-4.

Almasan, C.C., S.H. Han, K. Yoshiara, M., Buchgeister, B.W. Lee *et al.* (1994) 'Hall effect studies of the mixed and normal states of $Y_{1-x}Pr_XBa_2Cu_3O_{7-\delta}$ single crystals ($0 \leq X \leq 1$)', *Physica B* **199–200**, 288.

Altshuler, B.L., L.B. Ioffe, A.J. Millis (1996) 'Theory of the spin gap in high-temperature superconductors', *Phys. Rev. B* **53**, 415.

Ando, Y., G.S. Boebinger, A. Passner, T. Kimura, K. Kishio (1995) 'Logarithmic divergence of both inplane and out-of-plane normal state resistivities of superconducting $La_{2-x}Sr_xCuO_4$ in the zero-temperature limit', *Phys. Rev. Lett.* **75**, 4662.

Ando, Y., G.S. Boebinger, A. Passner, K. Tamasaku, N. Ichikawa *et al.* (1996) 'Supporting evidence of the unusual insulating behavior in the low-temperature normal-state resistivity of underdoped $La_{2-x}Sr_xCuO_4$', *J. Low Temp. Phys.* **105**, 867.

Ando Y., G.S. Boebinger, A. Passner, N.L. Wang, C. Geibel, F. Steglich (1996) 'Metallic in-plane and divergent out-of-plane resistivity of a high-T-c cuprate in the zero-temperature limit', *Phys. Rev. Lett.* **77**, 2065.

Ando, Y., G.S. Boebinger, A. Passner, N.L. Wang, C. Geibel *et al.* (1997) 'Low-temperature normal-state resistivity of high-T-c cuprates', *Physica C* **282–287**, 240.

Ando, Y., G.S. Boebinger, A. Passner, N.L. Wang, C. Geibel *et al.* (1997) 'Normal-state Hall effect and the insulating resistivity of high-T-c cuprates at low temperatures', *Phys. Rev. B* **56**, R8530.

Ando, Y., G.S. Boebinger, A. Passner, L.F. Schneemeyer, T. Kimura *et al.* (1999) 'Resistive upper critical fields and irreversibility lines of optimally doped high-T-c cuprates', *Phys. Rev. B* **60** 12475.

Ando, Y., Y. Kurita, S. Komiya, S. Ono, K. Segawa (2004) 'Electronic phase diagram of high-T-c cuprate superconductors from a mapping of the in-plane resistivity curvature', *Phys. Rev. Lett.* **93** 267001.

Asai, Y. (1994) 'Reduced-density-matrix analysis of superconducting correlation in two-dimensional and two-chain Hubbard models', *Phys. Rev. B* **50**, 6519.

Ashcroft, N.W. and N.D. Mermin (1976) *Solid State Physics*, Sounders College Publishing, Philadelphia.

Aslamazov, L.G. and A.I. Larkin (1968) 'Effect of fluctuations on properties of a superconductors above critical temperature', *Sov. Phys. Solid State* **10**, 875.

Azuma, M., Z. Hiroi, M. Takano, K. Ishida, Y. Kitaoka (1994) 'Observation of a spin gap in $SrCu_2O_3$ comprising spin- 1/2 quasi-1D 2-leg ladders', *Phys. Rev. Lett.* **73**, 3463.

Balakirev, F.F., I.E. Trofimov, S. Guha, M.Z. Cieplak, P. Lindenfeld (1998) 'Orbital magnetoresistance in the $La_{2-x}Sr_xCuO_4$ system', *Phys. Rev. B* **57**, R8083.

Balakirev, F.F., J.B. Betts, A. Migliori, S. Ono, Y. Ando, G.S. Boebinger (2003) 'Signature of optimal doping in Hall-effect measurements on a high-temperature superconductor', *Nature* **424**, 912.

Bardeen, H. and M.J. Stephen (1965) 'Theory of motion of vortices in superconductors', *Phys. Rev.* **140**, 1197.

Barnes, T., E. Dagotto, J. Riera, E. Swanson (1993) 'Excitation spectrum of Heisenberg spin ladders', *Phys. Rev. B* **47**, 3196.

Batlogg, B., H.Y. Hwang, H. Takagi, R.J. Cava, H.L. Kao, J. Kwo (1994) 'Normal-state phase diagram of $(La,Sr)_2CuO_4$ from charge and spin dynamics, *Physica C* **235–240**, 130.

Bianconi, A., A. Valletta, A. Perali, N.L. Saini (1998) 'Superconductivity of a striped phase at the atomic limit', *Physica C* **296**, 269.

Boebinger, G.S., Y. Ando, A. Passner, T. Kimura, M. Okuya *et al.* (1996) 'Insulator-to-metal crossover in the normal state of $La_{2-x}Sr_xCuO_4$ near optimum doping', *Phys. Rev. Lett.* **77**, 5417.

Bucher, B., P. Steiner, P. Wachter (1994) 'Relation of spin and charge dynamics in HTSCS', *Physica B.* **199–200**, 268.

Bulaevskii, L.N., M.V. Sadovskii, A.A. Varlamov (1986) 'Conductivity and diamagnetic suscetibility fluctuations in dirty semiconductors near the Anderson localization threshold', *Sov. Phys. Solid State* **28**, 997.

Chien, T.R., Z.Z. Wang, N.P. Ong (1991) 'Effect of Zn impurities on the normal-state Hall angle in single crystal YBaCuZnO', *Phys. Rev. Lett.* **67**, 2088.

Dagotto, E., J. Riera, D. Scalapino (1992) 'Superconductivity in ladders and coupled planes', *Phys. Rev. B* **45**, 5744.

Dagotto, E. and T.M. Rice (1996) 'Surprises on the way from one- to two-dimensional quantum magnets: The ladder materials', *Science* **271**, 618.

Dagotto, E. (1999) 'Experiments on ladders reveal a complex interplay between a spin-gapped normal state and superconductivity', *Rep. Prog. Phys.* **62**, 1525.

Dai, Y., W.J. Kossler, K.G. Petzinger, A.J. Greer (2004) ‘Magnetic field distributions in a large single crystal of YBa2Cu3O7-delta with cylindrical non-conducting inclusions’, *Physica C* **403**, 263.

Damianov, D.Ch. and T.M. Mishonov (1997) ‘Fluctuation paraconductivity within the framework of time-dependent Ginzburg-Landau theory’, *Superlattices and Microstructures* **21**, 467.

Emery V.J., S.A. Kivelson, J.M. Tranquada (1999) ‘Stripe phases in high-temperature superconductors’, *Proceedings of the National Academy of Sciences of the United States of America* **96**, 8814–8817.

Fournier, P., P. Mohanty, E. Maiser, S. Darzens, T. Venkatesan *et al.* (1998) ‘Insulator-metal crossover near optimal doping in Pr2-xCexCuO4: Anomalous normal-state low temperature resistivity’, *Phys. Rev. Lett.* **81**, 4720.

Gazza, C., G. Martins, J. Riera, E. Dagotto (1999) ‘Hole pairs in a spin liquid: Influence of electrostatic hole-hole repulsion’, *Phys. Rev. B* **59**, R709.

Ginzburg, V.L. and D.A. Kirzhnit (1967) ‘On high-temperature and surface superconductivity’, *Doklady Akademii Nauk SSSR* **176** 553; V.L. Ginzburg, ‘Problem of high temperature superconductivity’, (1968) *Contemporary Physics* **9**, 355.

Gray, K.E., J.D., Hettinger, D.J. Miller, B.R. Washburn, C. Moreau *et al.* (1996) ‘Interaction of two-dimensional vortices with linear ion tracks in the highly anisotropic layered cuprates’, *Phys. Rev. B* **54**, 3622.

Greven, M., R.J. Birgeneau, U.-J. Wiese (1996) ‘Monte Carlo study of correlations in quantum spin ladders’, *Phys. Rev. Lett.* **77**, 1865.

Hagen, S.J., C.J. Lobb, R.L. Greene, M.G. Forrester, J.H. Kang (1990) ‘Anomalous Hall-effect in superconductors near their critical temperatures’, *Phys. Rev. B* **41**, 11630.

Hagen, S.J., C.J. Lobb, R.L. Greene, M. Eddy (1991) ‘Flux flow Hall-effect in superconducting $Tl_2Ba_2CaCu_2O_8$ films’, *Phys. Rev. B* **43**, 6246.

Hagen, S.J., A.W. Smith, M. Rajeswari, J.L. Peng, Z.Y. Li *et al.* (1993) ‘Anomalous flux-flow Hall-effect in $Nd_{1.85}Ce_{0.15}CuO_{4-y}$ and evidence for vortex lattice dynamics’, *Phys. Rev. B* **47**, 1064.

Hall, E.H. (1879) ‘On a new action of the magnet on electrical current’, *AM. J. Math.* **2**, 287.

Hanaguri, T., C. Lupien, Y. Kohsaka, D.H. Lee, M. Azuma *et al.* (2004) ‘A “checkerboard” electronic crystal state in lightly hole-doped $Ca_{2-x}Na_xCuO_2Cl_2$’, *Nature* **430**, 1001.

Harris, J.M., Y.F. Yan, N.P. Ong (1992) ‘Experimental test of the T^2 law for the Hall angle from Tc to 500-K in oxygen-reduced $YBa_2Cu_3O_{6+x}$ crystals’, *Phys. Rev. B* **46**, 14293.

Harris, J.M., Y.F. Yan, P. Matl, N.P. Ong, P.W. Anderson *et al.* (1995) ‘Violation of Kohlers rule in the normal-state magnetoresistance of $YBa_2Cu_3O_{7-\delta}$ and $La_{2-x}Sr_xCuO_4$’, *Phys. Rev. Lett.* **75**, 1391.

Hasenfratz, P. and F. Niedermayer (1991) ‘The exact correlation length of the antiferromagnetic D = 2 + 1 Heisenberg model at low-temperatures’, *Phys. Lett. B* **268**, 231.

Hayward, C.A., D. Poilblanc, R.M. Noack, D.J. Scalapino, W. Hanke (1995) ‘Evidence for a superfluid density in T-J ladders’, *Phys. Rev. Lett.* **75**, 926.

Hirayama, T., M. Nakagawa, Y. Oda (2000) ‘Hall effect-in electrochemically oxidized $La_2CuO_{4+\delta}$ and $(La_{1-x}Sr_x)_2CuO_{4+\delta}$’, *Physica C* **334**, 289.

Hiroi, Z., S. Amelinckx, G. Van Tendeloo, N. Kobayashi (1996) ‘Microscopic origin of dimerization in the CuO_2 chains in $Sr_{14}Cu_{24}O_{41}$’, *Phys. Rev. B* **54**, 15849.

Hoffman, J.E., K. McElroy, D.-H. Lee, K.M. Lang, H. Eisaki *et al.* (2002) ‘Imaging quasiparticle interference in $Bi_2Sr_2CaCu_2O_{8+\delta}$’, *Science* **297**, 1148.

Howald, C., E. Eisaki, N. Kaneko, A. Kapitulnik (2003) 'Coexistence of periodic modulation of quasiparticle states and superconductivity in $Bi_2Sr_2CaCu_2O_{8+\delta}$', *PNAS* **100**, 9705.

Hwang, H.Y., B. Batlogg, H. Takagi, H.L. Kao, J. Kwo *et al.* (1994) 'Scaling of the temperature-dependent Hall-effect in $La_{2-x}Sr_xCuO_4$', *Phys. Rev. Lett.* **72**, 2636.

Ino, A., Ch. Kim, T. Mizokawa, Z.-X. Shen, A. Fujimori *et al.* (1999) 'Fermi surface and band dispersion in $La_{2-x}Sr_xCuO_4$', *J. Phys. Soc. Jpn.* **68**, 1496.

Ioffe, A.F. and A.R. Regel (1960) 'Non-crystalline, amorphous, and liquid electronic semiconductors', *Prog. Semicond.* **4**, 237.

Ishida, K., Y. Kitaoka, G. Zheng, K. Asayama (1991) '^{17}O and ^{63}Cu NMR investigations of high-TC superconductor $La_{1.85}Sr_{0.15}CuO_4$ with $T_C = 38$ K', *J. Phys. Soc. Jpn.* **60**, 3516.

Isobe, M., T. Ohta, M. Onoda, F. Izumu, S. Nakano *et al.* (1998) 'Structural and electrical properties under high pressure for the superconducting spin-ladder system $Sr_{0.4}Ca_{13.6}Cu_{24}O_{41+\delta}$', *Phys. Rev. B* **57**, 613.

Ito, T., K. Takenaka, S. Uchida (1993) 'Systematic deviation from T-linear behavior in the in-plane resistivity of $YBa_2Cu_3O_{7-y}$ – evidence for dominant spin scattering', *Phys. Rev. Lett.* **70**, 3995.

Iye, Y., S. Nakamura, T. Tamegai (1989) 'Hall-effect in high-temperature superconductors near T_c', *Physica C* **159**, 616.

Ji, H.L. and K.W. Wong (1999) 'Hall resistivity sign reversal in superconductor's mixed state', *Phys. Lett. A* **256**, 66.

Kambe, S., K. Kitazawa, M. Naito, A. Fukuoka, I. Tanaka, H. Kojima (1989) 'Anisotropic resistivity in the two-dimensional metal $(La_{1-x}Sr_x)_2CuO_4$', *Physica C* **160**, 35.

Kang, W.N., B.W. Kang, Q.Y. Chen, J.Z. Wu, S.H. Yun *et al.* (1999) 'Scaling of the Hall resistivity in epitaxial $HgBa_2CaCu_2O_{6+\delta}$ thin films with columnar defects', *Phys. Rev. B* **59**, R9031.

Kimura, T., K. Kishio, T. Kobayashi, Y. Nakayama, N. Motohira *et al.* (1992) 'Compositional dependence of the transport anisotropy in large $(La, Sr)_2CuO_4$ single-crystals and 2nd peak in magnetization curves', *Physica C* **192**, 247.

Kimura, T., S. Miyasaka, H. Takagi, K. Tamasaku, H. Eisaki *et al.* (1996) 'In-plane and out-of-plane magnetoresistance in $La_{2-x}Sr_xCuO_4$ single crystals', *Phys. Rev. B* **53**, 8733.

Kohler, M. (1938) 'Zur magnetischen Widerstandsanderung reiner Metalle', *Ann. Phys.* **32**, 211.

Kohsaka, Y., C. Taylor, K. Fujita, A. Schmidt, C. Lupien *et al.* (2007) 'An intrinsic bond-centered electronic glass with unidirectional domains in underdoped cuprates', *Science* **315**, 1380.

Konstantinovi, Z., Z.Z. Li, H. Raffy (2000) 'Temperature dependence of the Hall effect in single-layer and bilayer $Bi_2Sr_2Ca_{n-1}Cu_nO_y$ thin films at various oxygen contents', *Phys. Rev. B* **62**, R11989; Z. Konstantinovi, Z.Z. Li, H. Raffy (2000) 'Normal state transport properties of single- and double-layered $Bi_2Sr_2Ca_{n-1}Cu_nO_y$ thin films and the pseudogap effect', *Physica C* **341**, 859.

Kopnin N.B., B.I. Ivlev, V.A. Kalatsky (1993) 'The flux-flow Hall-effect in type-II superconductors – an explanation of the sign reversal', *J. Low Temp. Phys.* **90**, 1.

Kopnin, N.B. and V.M. Vinokur (1999) 'Effects of pinning on the flux flow Hall resistivity', *Phys. Rev. Lett.* **83**, 4864.

Kugler, M., Ø, Fischer, Ch. Renner, S. Ono, Y. Ando (2001) 'Scanning tunneling spectroscopy of $Bi_2Sr_2CuO_{6+\delta}$. New evidence for the common origin of the pseudogap and superconductivity', *Phys. Rev. Lett.* **87**, 4911.

Lacerda, A., J.P. Rodriguez, M.F. Hundley, Z. Fisk, P.C. Canfield *et al.* (1994) 'Magnetoresistance in the normal-state of $La_{1.925}Sr_{0.075}CuO_{4+\delta}$', *Phys. Rev. B* **49**, 9097.

Lange, E. and G. Kotliar (1999) 'Magnetotransport in the doped Mott insulator', *Phys. Rev. B* **59**, 1800.

Larkin, A. and A. Varlamov (2005) *Theory of Fluctuations in Superconductors* Oxford University Press, New York, (ISBN: 0198528159/0–19–852815–9), pp. 1–430.

Lawrence, W. and S. Doniach (1971) 'Theory of layer structure superconductors', *Proc. 12th Int. Conf. on Low Temp. Phys.*, p. 361.

Levanyuk, A.P. (1959) 'Contribution to the theory of light scattering near the 2nd order phase-transition points', *Zh. Exp. Teor. Fiz.* **36**, 810; *Sov. Phys. JETP* **36**, 571.

Loeser, A.G., Z.-X. Shen, D.S. Dessau, D.S. Marshall, D.H. Park *et al.* (1996) 'Excitation gap in the normal state of underdoped $Bi_2Sr_2CaCu_2O_{8+\delta}$', *Science* **273**, 325.

Maki, K. (1968) 'Critical fluctuations of the order parameter in a superconductor', *Progr. Theor. Phys.* **40**, 193.

Malinowski, A., M.Z. Cieplak, A.S. van Steenbergen, J.A. Perenboom, K. Karpinska *et al.* (1997) 'Magnetic-field-induced localization in the normal state of superconducting $La_{2-x}Sr_xCuO_4$', *Phys. Rev. Lett.* **79**, 495.

Maly, J., B. Janko, K. Levin (1998) 'Superconductivity from a pseudogapped normal state: A mode-coupling approach to precursor superconductivity', *Phys. Rev. B* **59** (1999) 1354–1357 and cond-mat/9805018.

Matsuda, Y., T. Nagaoka, G. Suzuki, K. Kumagai, M. Suzuki *et al.* (1995) 'Hall anomaly in the vortex state of $La_{2-x}Sr_xCuO_4$', *Phys. Rev. B* **52**, R15749.

Moshchalkov, V.V. (1993) 'High T_C cuprates as 2-dimensional quantum antiferromagnets', *Sol. St. Comm.* **86**, 715.

Moshchalkov, V.V., L. Trappeniers, J. Vanacken (1999) '1D quantum transport in the even-chain spin-ladder compound $Sr_{2.5}Ca_{11.5}Cu_{24}O_{41}$ and $YBa_2Cu_4O_8$', *Europhys. Lett.* **46**, 75.

Moshchalkov, V.V. (1999) 'Crossover from the 2D Heisenberg to the 1D quantum spin ladder regime in underdoped high T-c cuprates', *Physica C* **317**, 361.

Moshchalkov, V.V., J. Vanacken, L. Trappeniers (2001) 'Phase diagram of high-T-c cuprates: Stripes, pseudogap, and effective dimensionality', *Phys. Rev. B.* **64**, 214504.

Nagaoka, T., Y. Matsuda, H. Obara, A. Sawa, T. Terashima *et al.* (1998) 'Hall anomaly in the superconducting state of high-T-c cuprates: Universality in doping dependence', *Phys. Rev. Lett.* **80**, 3594.

Nagata, T., M. Uehara, J. Goto, N. Komiya, J. Akimitsu *et al.* (1997) 'Superconductivity in the ladder compound $Sr_{2.5}Ca_{11.5}Cu_{24}O_{41}$ (single crystal)', *Physica C* **282–287**, 153.

Nakao, K., K. Hayashi, T. Utagawa, Y. Enomoto, N. Koshizuka (1998) 'Double sign reversal of the Hall effect in the mixed state of $YBa_2Cu_3O_x$', *Phys. Rev. B* **57**, 8662.

Narozhny, B.N. (1994) 'Fluctuations in strong-coupling superconductors', *Phys. Rev. B* **49**, 6375.

Noda, T., H. Eisaki, S. Uchida (1999) 'Evidence for one-dimensional charge transport in $La_{2-x-y}Nd_ySr_xCuO_4$', *Science* **286**, 265.

Noto, K., S. Shinzawa, Y. Muto (1976) 'Hall-effect in intrinsic type-II superconductors near lower critical field', *Sol. St. Comm.* **18**, 1081.

Nozières, P. and W.F. Vinen (1966) 'Motion of flux lines in type 2 superconductors', *Philos. Mag.* **14**, 667.

Ono, S., Y. Ando, T. Murayama, F.F. Balakirev, J.B. Betts, G.S. Boebinger (2000) 'Metal-to-insulator crossover in the low-temperature normal state of $Bi_2Sr_{2-x}La_xCuO_{6+\delta}$', *Phys. Rev. Lett.* **85**, 638.

Poole, C.P., H.A. Farach, R.J. Creswick (1995) *Superconductivity*, Academic Press (California), ISBN 0-12-561455-1, pp. 1–620.

Popovic, R.S. (1991) *Hall Effect Devices, Magnetic Sensors and Characterization of Semiconductors*, The Adam Hilger series on sensors (Adam Hilger Publishing, Bristol), ISBN 0-7503-0096-5.

Randeria, M. (1997) *Precursor Pairing Correlations and Pseudogaps*, cond-mat/9710223.

Reefman, D. (1993) PhD Thesis, 'Monte Carlo Study of the Local Pair Superconductor', Rijksuniversiteit Leiden.

Rice, T.M. (1998) 'The rich variety of cuprates', *Physica B* **241–243**, 5.

Riera, J. (1994) 'Phase separation and pairing in coupled chains and planes', *Phys. Rev. B* **49**, 3629.

Sadovskii, M.V. (1997) 'Superconductivity and localization', *Phys. Rep.* **282**, 225.

Semba, K., and A. Matsuda (1997) 'Vanishingly small Maki-Thompson superconducting fluctuation in the magnetoresistance of high-Tc superconductors', *Phys. Rev. B* **55**, 11103.

Sigrist, M., T.M. Rice, F.C. Zhang (1994) 'Superconductivity in a quasi-one-dimensional spin liquid', *Phys. Rev. B* **49**, 12058.

Stojkovic, B.P. and D. Pines (1997) 'Theory of the longitudinal and Hall conductivities of the cuprate superconductors', *Phys. Rev. B* **55**, 8576.

Suzuki, M. and M. Hikita (1991) 'Resistive transition, magnetoresistance, and anisotropy in $La_{2-x}Sr_xCuO_4$ single-crystal thin films', *Phys. Rev. B* **44**, 249.

Takagi, H., B. Batlogg, H.L. Kao, J. Kwo, R.J. Cava *et al.* (1992a) 'Systematic evolution of temperature-dependent resistivity in $La_{2-x}Sr_xCuO_4$', *Phys. Rev. Lett.* **69**, 2975.

Takagi, H., R.J. Cava, M. Marezio, B. Batlogg, J.J. Krajewski *et al.* (1992b) 'Disappearance of superconductivity in overdoped $La_{2-x}Sr_xCuO_4$ at a structural phase boundary', *Phys. Rev. Lett.* **68**, 3777.

Takano, M., M. Azuma, Y. Fujishiro, M. Nohara, H. Takagi *et al.* (1997) 'Impurity effects on a 2-leg spin ladder compound $SrCu_2O_3$', *Physica C* **282–287**, 149.

Tinkham, M. (1996) *Introduction to superconductivity*, McGraw-Hill Book Co. (Singapore), ISBN 0-07-114782-9 , pp. 1–454.

Tranquada, J.M., B.J. Sternlieb, J.D. Axe, Y. Nakamura, S. Uchida (1995) 'Evidence for stripe correlations of spins and holes in copper-oxide superconductors', *Nature* **375**, 561.

Trappeniers, L., J. Vanacken, L. Weckhuysen, K. Rosseel, A. Yu. Didyk *et al.* (1999) 'Critical currents, pinning forces and irreversibility fields in $(Y_xTm_{1-x})Ba_2Cu_3O_7$ single crystals with columnar defects in fields up to 50 T', *Physica C* **313**, 1.

Trappeniers, L. (2000) PhD Thesis, 'Transport Properties of Underdoped Cuprates in High Magnetic Fields', KULeuven.

Troyer, M., H. Tsunetsugu, D. Würtz (1994) 'Thermodynamics and spin gap of the Heisenberg ladder calculated by the look-ahead Lanczos algorithm', *Phys. Rev. B* **50**, 13515.

Tsunetsugu, H., M. Troyer, T.M. Rice (1995) 'Singlet stripe phases in the planar t-J model', *Phys. Rev. B* **51**, 16456 .

Uehara, M., T. Nagata, J. Akimitsu, H. Takahashi, N. Mori, K. Kinoshíta (1996) 'Superconductivity in the ladder material $Sr_{0.4}Ca_{13.6}Cu_{24}O_{41.84}$', *J. Phys. Soc. Jpn.* **65**, 2764.

Usui, N., T. Ogasawara, K. Yasukochi, S. Tomoda (1969) 'Magnetization, flux flow resistance, and Hall effect in superconducting vanadium', *Phys. Soc. Jpn. J.*, **27**, 574.

Van Beelen, H., J.P. Van Braam Houckgeest, H. M. Thomas, C. Stolk, R. De Bruyn Ouboter (1967) ‘Some measurements on effective resistance and Hall angle in type 2 superconductors’, *Physica C* **36**, 241.

Vanacken, J., L. Trappeniers, P. Wagner, L. Weckhuysen, V.V. Moshchalkov, Y. Bruynseraede (2001) ‘Scaling of the transport properties in the $Y_{1-y}Pr_yBa_2Cu_3O_x$ system’, *Phys. Rev. B* **64**, 184425.

Varlamov, A.A., G. Balestrino, E. Milani, D.V. Livanov (1999) ‘The role of density of states fluctuations in the normal state properties of high T-c superconductors’, *Adv. Phys.* **48**, 655.

Vinokur, V.M., V.B. Geshkenbein, M.V. Feigelman and G. Blatter (1993) ‘Scaling of the Hall resistivity in high-Tc superconductors’, *Phys. Rev. Lett.* **71**, 1242.

Wang, Z.Z., T.K. Chien, N.P. Ong, J.M. Tarascon, E. Wang (1991) ‘Positive Hall coefficient observed in single-crystal $Nd_{2-x}Ce_xCuO_{4-\delta}$ at low temperatures’, *Phys. Rev. B* **43**, 3020.

Wang, Z.D., and C.S. Ting (1992) ‘Theory of flux motion with backflow current in high-k superconductors’, *Phys. Rev. B* **46**, 284.

Weijsenfeld, C.H. (1968) ‘A core model explaning Hall effect and resistivity in mixed state of type 2 superconductors’, *Phys. Lett.* **28A**, 362.

White, S.R., and I. Affleck (1996) ‘Dimerization and incommensurate spiral spin correlations in the zigzag spin chain: Analogies to the Kondo lattice’, *Phys. Rev. B* **54**, 9862.

Wise, W.D., K. Chatterjee, M.C. Boyer, T. Kondo, T. Takeuchi *et al.* (2008) ‘Charge-density-wave origin of cuprate checkerboard visualized by scanning tunnelling microscopy’, *Nature Physics* **4**, 696.

Wuyts, B. (1994). PhD Thesis, ‘Normal-state transport properties of metallic oxygen deficient $YBa_2Cu_3O_x$ films’, KULeuven.

Wuyts, B., V.V. Moshchalkov, Y. Bruynseraede (1996) ‘Resistivity and Hall effect of metallic oxygen-deficient $YBa_2Cu_3O_x$ films in the normal state’, *Phys. Rev. B* **53**, 9418.

Xiong, P., G. Xiao, X.D. Wu (1993) ‘Hall angle in $YBa_2Cu_3O_{7-\delta}$ epitaxial films: Comparison between oxygen reduction and Pr doping’, *Phys. Rev. B* **47**, 5516.

Yamada, K., C.H. Lee, Y. Endoh, G. Shirane, R.J. Birgeneau, M.A. Kastner (1997) ‘Low-frequency spin fluctuations in the superconducting $La_{2-x}Sr_xCuO_4$’, *Physica C* **282–287**, 85.

Yamaji, K. and Y. Shimoi (1994) ‘Superconducting transition of the 2-chain hubbard model indicated by diagonalization calculations’, *Physica C* **222**, 349.

Yip, S.K. (1990) ‘Fluctuations in an impure unconventional superconductor’, *Phys. Rev. B* **41**, 2612.

Zaanen, J. (1999) ‘Superconductivity – self-organized one dimensionality’, *Science* **286**, 251.

Zhou, J.S. and J.B. Goodenough (1997) ‘Electron-lattice coupling and stripe formation in $La_{2-x}Ba_xCuO_4$’, *Phys. Rev. B* **56** 6288–6294.

Ziman, J.M. (1964) *Principles of the Theory of Solids*, Cambridge University Press (Cambridge).

3

The optical conductivity of high-temperature superconductors

R. P. S. M. LOBO, ESPCI, UPMC, CNRS, France

Abstract: This chapter discusses some of the current topics in the analysis of the optical conductivity of high-temperature cuprate superconductors. It presents a detailed description of the optical response in conducting media, stressing the points relative to strongly correlated systems. The pseudogap response in the normal state of hole-doped cuprates is extensively discussed in terms of spectral weight and the scattering rate. This chapter also discusses which changes the optical conductivity undergoes when moving, in the normal state, from the underdoped to the overdoped regime. A spectral weight analysis is utilized to understand the normal state gap in electron doped materials. The superconducting state is discussed in terms of the superconducting gap, kinetic energy changes in the transition and the analysis of the $I^2\chi(\omega)$ Eliashberg function characterizing the glue that keeps the pairs together. The chapter closes with a very brief overview of new systems such as MgB_2 and pnictide superconductors.

Key words: optical conductivity, high-temperature superconductors, electronic kinetic energy, *f*-sum rule, pseudogap, strongly correlated fermionic systems.

3.1 Introduction

The optical conductivity is the extension of electrical transport to high (optical) frequencies. It is a contact free quantitative measurement, mostly sensitive to charged responses. Current techniques allow us to cover over three orders of magnitude in energy in a range spanning 1 meV to 6 eV (or, in the lingo of spectroscopists, 10 to 50000 cm^{-1}). It is a most powerful tool in the study of conducting media. The optical conductivity of cuprates has been measured (often several times) in every system we can get single crystals. Still, the complexity of high-temperature superconductors is so high that only now a common picture is emerging. This chapter makes an attempt at describing the developments during the last ten years. Two excellent reviews of the early days of optics in cuprates are Timusk and Tanner (1989) and Tanner and Timusk (1992), while a very complete more recent view of high-temperature superconductivity can be found in Basov and Timusk (2005). My goal in this chapter is not to give a complete picture of high-T_c superconductors. I have mostly tried to develop some topics that are at the forefront of current research (and topics which I personally find attractive). Several questions remain open in the physics of high-temperature superconductors, but many of these questions can be addressed by the optical conductivity.

In the beginning of high-T_cs, a heated debate went on as to whether or not optics could see the superconducting gap in cuprates. This is a valid point and I will discuss it in this chapter. But the gap is not the most important signature in the electrodynamics of these materials. The top of the pile in the optics of the superconducting state is the superfluid stiffness. Much deeper insights on cuprates are obtained from the study of the superfluid condensate. How large is it? Which energies is it being built from? Are there any competing low energy excitations taking over the superfluid weight?

Several descriptions of the cuprates link the formation of the superconducting phase to the normal state pseudogap, either as a competing order or as a cooperating factor. How can we extract information on the pseudogap from the optical conductivity? Can we infer specific energy scales associated to the pseudogap? The pseudogap phase is most definitely not a standard metal. How does the system evolve from this strange conductor towards a Fermi liquid? Actually, does it evolve at all towards a Fermi liquid?

The optical conductivity is a quantitative measurement. How can we link it to energy of charge carriers? Does this energy change at the superconducting transition? And does it tell us anything about the pairing glue and the pairing mechanism?

These are a few questions to which optics can give new insights, so this chapter will try to address some of these points. Section 3.2 discusses the phase diagram of high-temperature superconductors, with an emphasis on the phenomena that can be probed by the optical conductivity. Section 3.3 shows what we should expect to see from the interaction of light with a conducting media stressing superconductivity and strong correlation phenomena. Section 3.4 deals with the properties observed in the normal state of (mostly) hole doped cuprates. It discusses the controversial pseudogap and how the system evolves from a nodal metal to a Fermi liquid upon doping. The end of this section makes a special discussion on the normal state of electron doped cuprates. Section 3.5 looks into three aspects of superconductivity: (i) the superconducting gap; (ii) the kinetic energy changes in the superconducting transition; and (iii) the ‘glue’ that keeps pairs together. This chapter closes on Section 3.6 with a look at new trends in the field, such as the optical response of superconducting pnictides.

A few very interesting phenomena not analyzed in this chapter are stripes (Dumm *et al.*, 2002), disorder (Lobo *et al.*, 2002), magneto-optics (Laforge *et al.*, 2007), inhomogeneities (Kusar *et al.*, 2005), new techniques such as THz (Kaindl *et al.*, 2002) and far-infrared ellipsometry (Bernhard *et al.*, 2000). Although a few points about the c-axis response are present, most of the chapter is dedicated to the spectroscopy in the CuO_2 planes.

3.2 The phase diagram of cuprate superconductors

This section presents a short overview of the phase diagram of cuprate superconductors with an emphasis on the excitations which optical conductivity probes. In this section I will not discuss features in the phase diagram that do not show a clear signature in the optical conductivity – such as the antiferromagnetic phase (Lee *et al.*, 2005), or that will not be treated in this chapter – such as stripes (Homes *et al.*, 2006a).

Conventional band theory shows that the parent compound of cuprates should have a half-filled band and, hence a metallic character. Strong electron–electron correlations split this band into two, the so-called upper and lower Hubbard bands, and a Mott insulator showing an antiferromagnetic order replaces the expected metallic compound. Imada *et al.* (1998) give a very complete description of the Mott-Hubbard transition in strongly correlated systems.

Figure 3.1 depicts the general phase diagram of cuprates. At zero doping we find the Mott-Hubbard insulator with a Néel temperature around $T_N \sim 300$ K. It can be doped with either electrons (left hand diagram) or holes (right hand diagram) creating, in both cases, a conducting material with exotic phases.

The number of hole doped cuprates is considerably larger than electron doped, and so is the literature and body of experimental data. This is therefore the natural place to start the discussion of the phase diagram.

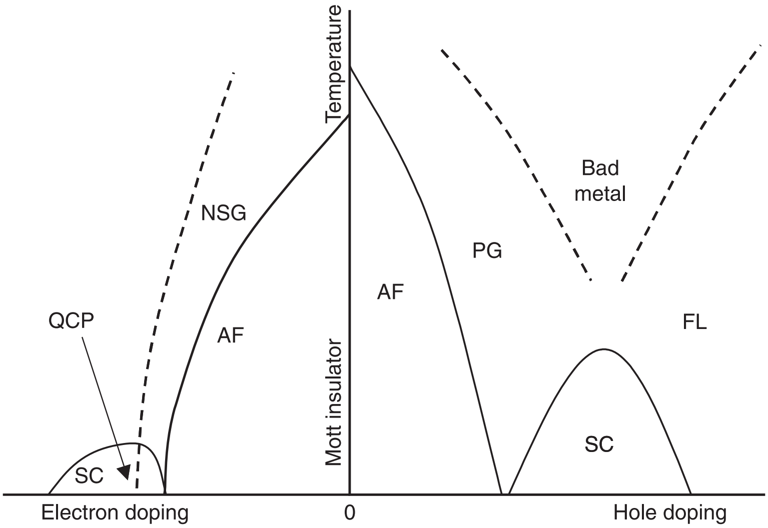

3.1 Phase diagram for electron doped and hole doped cuprate superconductors. AF stands for the antiferromagnetic phase; SC for the superconducting state; PG for the pseudogap region; and FL is representative of a phase tending to approach a Fermi liquid behavior. In the electron doped side, the term normal state gap (NSG) – as opposed to pseudogap – is preferred. The NSG line terminates into a quantum critical point (QCP) inside the superconducting dome.

3.2.1 Hole-doped cuprates

Examples of hole-doped cuprate superconductors are $YBa_2Cu_3O_{7-\delta}$ (YBCO), $Bi_2Sr_2CaCu_2O_{8+\delta}$ (Bi2212) and $La_{2-x}Sr_xCuO_4$ (LSCO). Lightly doping the Mott insulator with holes leads to a decrease of T_N and eventually to a conducting material. A superconducting dome appears upon increasing the doping in this conducting phase. The highest critical superconducting temperature (T_c) on this dome – around 90 K for most systems – defines the optimal doping. By definition, compositions having a smaller charge density, with respect to the optimal doping, are underdoped. Conversely, the material enters the overdoped regime when the carrier concentration is above optimal doping.

The early days of high-temperature superconductivity were filled with a heated debate on the gap symmetry, which was not settled until the mid-1990s. Measurements of flux quantization in YBCO tricrystals (Tsuei *et al.*, 1994) and angle-resolved photoemission spectroscopy (ARPES) on Bi2212 crystals (Ding *et al.*, 1996) made it clear that the gap symmetry is mostly $d_{x^2-y^2}$ ('mostly' means that a small secondary component may or may not exist) with a maximum value at the antinodal (π,0) and (0,π) reciprocal space directions and vanishing at the Brillouin zone (π,π) diagonals. Nevertheless, a myriad of questions remain open. What is the mechanism responsible for superconductivity? What is the glue that keeps the pairs together? What are the energy scales involved in pair formation? Do pair formation and pair condensation happen at the same temperature? Section 3.5 discusses what optical conductivity can say about these issues.

Although superconductivity in cuprates is fascinating, the understanding of the normal state above the superconducting dome is the highest challenge in the field. Indeed, theories for superconductivity in cuprates such as the resonating valence bond (Anderson, 1987) and the quantum critical point (Varma *et al.*, 2002) heavily depend on the normal state properties.

Just above optimal doping we find a metallic phase with strange properties. This regime shows a 'bad metal' character. Opposite to conventional metals, it has an electrical resistivity that increases linearly with temperature over a very large temperature range. And this, from far below the Debye temperature, where the resistivity should follow T^2, to temperatures above which the mean free path (l) of carriers is smaller than the lattice parameter (Emery and Kivelson, 1995). As we will see in Section 3.4, this linear temperature dependence of the resistivity has immediate consequences in the optical response of cuprates. Another clue about the unconventional behavior of carriers in this region comes from ARPES. In the normal state of optimally doped materials the quasiparticle peak, characteristic of carriers with well defined momenta at the Fermi surface, is very smeared out or even absent (Damascelli *et al.*, 2003).

Going towards the overdoped regime, the normal state of cuprates gets closer to a more conventional metallic response. This 'Fermish' liquid response is characterized by a well defined quasiparticle peak in ARPES spectra and by a resistivity that approaches a T^2 behavior. However, it is important to note that even in the overdoped regime cuprates do not represent a perfectly well defined Fermi liquid and Section 3.4 discusses the optical consequences of this.

The pseudogap state dominates the underdoped regime. It was discovered by nuclear magnetic resonance (NMR) in YBCO (Warren *et al.*, 1989; Alloul *et al.*, 1989). In a metal, the NMR lines shift due to electronic screening of nuclear momenta, the so-called Knight shift. When a conventional superconductor forms, electrons pair themselves into a spin zero state and the screening of nuclear momenta disappears. NMR data on YBCO shows that whereas the Knight shift decreases at T_c for optimally doped samples, in underdoped materials this effect happens at a T^* temperature well above the superconducting transition. As the Knight shift does not completely disappear, this represents an incomplete gap, or pseudogap, in the spin density of states. ARPES showed that not only is the spin gap active in the charge channel, but it is also restricted to portions of the Fermi surface (Norman *et al.*, 1998). It opens at higher temperatures along the antinodal $(\pi,0)$ and $(0,\pi)$ directions and spreads towards the nodal (π,π) directions near T_c. Timusk and Statt (1999) stress two important points about the pseudogap: (i) T^* does not fully characterize the pseudogap, one must also consider its $\mathbf{k}$ space dependence; and (ii) the number of excitations in the spin and charge channels are equivalent. Among the theories for the pseudogap, one can find preformed Cooper pairs without phase coherence (Lee, 1999), time-reversal symmetry breaking (Varma, 2000), density wave gaps (Markiewicz *et al.*, 1999), stripes (Fine, 2004) and phase separation (de Mello and Caixeiro, 2004).

A final remark on the hole-doped phase diagram shown in Fig. 3.1 concerns the lines separating the various normal state regimes. One question still unsettled is whether they represent true phase transitions or else are rather just signatures of a behavior crossover. Also, how they evolve at lower temperatures remains a mystery. Do they cross each other and remain outside the superconducting dome? Or do they enter the superconducting dome creating different superconducting properties between under- and overdoped materials?

3.2.2 Electron-doped cuprates

Let us switch to the much less studied electron-doped side of the phase diagram, populated by materials such as $\mathrm{Nd_{2-x}Ce_xCuO_4}$ (NCCO) and $\mathrm{Pr_{2-x}Ce_xCuO_4}$ (PCCO). Is it equivalent to dope a Mott-Hubbard insulator with electrons or holes? A quick glance at Fig. 3.1 would suggest so, but this illusion does not survive a closer inspection. First of all, the antiferromagnetic phase spans a larger doping range and competes closely with the superconducting dome. This competition forms a superconducting dome with a much sharper edge on the underdoped regime. In addition, electron doped systems have a maximum critical temperature of about 25 K which is much lower than that of their hole-doped alter egos. The superconducting gap also has a $d_{x^2-y^2}$ symmetry, but the maximum gap value is shifted from the antinodal directions (Blumberg *et al.*, 2002; Matsui *et al.*, 2005).

The normal state is not as well characterized as the one in hole-doped materials. However a normal state gap is indeed present. I will refrain from using the term pseudogap for this normal state gap to avoid any assumption that the normal state gaps seen in both sides of the phase diagram have the same origin. As far as the current state of measurements indicates, they do not! In electron-doped materials, the crossing of the Fermi surface and the antiferromagnetic Brillouin zone play a very important role and these hot spots dominate the physics of these systems. The normal state gap in electron-doped materials is a consequence of antiferromagnetic fluctuations. This normal state gap line, however, is well defined and goes all the way into the superconducting dome terminating at a quantum critical point (QCP) at $T = 0$. Section 3.4.3 discusses the optical signatures of these properties in detail.

3.3 Optical response of conducting media

Most of the data shown in this chapter is derived from reflectivity measurements near normal incidence. These correspond to elastic scattering of light, largely dominated by the interaction of charges in the material with the electric field of light. The reflectivity only measures the modulus square of the reflected electric field and hence is a real quantity. However it does depend on the complex response function of the material. Writing the reflectivity R in terms of the complex dielectric function ε gives

$$R = \left| \frac{1-\sqrt{\varepsilon}}{1+\sqrt{\varepsilon}} \right|^2 . \qquad [3.1]$$

The fundamental quantity discussed in this chapter is the complex optical conductivity σ. It is the extension to high frequencies of dc transport measurements and is related to the dielectric function by $\sigma = 2\,\pi\, i\,(1 - \varepsilon)\,\omega/Z_0$, where $Z_0 = 377\ \Omega$ is the vacuum impedance.

Knowledge of R at all frequencies from zero to infinity allows one to use Kramers-Kronig causality relations to calculate the complex reflection coefficient and, consequently, any other complex optical function. However, in practice, R is measured over a finite frequency range and the choice of low and high frequency extrapolations becomes a delicate operation. It is therefore dangerous to dwell upon small changes in the complex optical functions close to the measurement boundaries. Nevertheless, techniques that probe directly the complex response (e.g. ellipsometry) as well as conservation laws, such as the *f*-sum rule discussed in Section 3.3.4, create conditions to check that pitfalls in Kramers-Kronig transformations are not introducing extraneous features in the data. For the remainder of this chapter, I will assume that the necessary checks and problems have been dealt with.

3.3.1 The Drude model

In the early 1900s, Paul Drude proposed a simple model based on an electron gas with elastic collisions to describe the conduction phenomena in metals. The frequency dependent complex optical conductivity in the Drude model is

$$\sigma(\omega) = \frac{\sigma_0}{1 - i\omega\tau}, \qquad [3.2]$$

where $\sigma_0 = n\,e^2\,\tau/m$ is the dc conductivity of a metal with carriers of mass m and charge density n; τ represents the average time between collisions. Instead of the collision time, it is more common to refer to the scattering rate τ^{-1}. Figure 3.2 (a) shows the measured reflectivity for Bi2212 (Quijada *et al.*, 1999) and that for metallic silver. The reflectivity of silver is typical of a Drude metal. It is close to unity up to a certain frequency where it drops sharply reaching almost zero reflectivity. This frequency, around 30 000 cm^{-1} for Ag, represents the plasma edge $\Omega_p/\sqrt{\varepsilon_\infty}$ where $\Omega_p^2 = Z_0 ne^2/2\pi m$ is the plasma frequency and ε_∞ is the oscillator strength of optical transitions having an energy above the plasma edge. The contrast between Ag and Bi2212 is striking. In the cuprate, the reflectivity decreases from zero frequency up to 10 000 cm^{-1} almost linearly. The minimum of the reflectivity is smeared out and it is very difficult to define a plasma edge.

Figure 3.2 (b) shows the real part of the optical conductivity (σ_1) calculated from the reflectivity for these two materials (σ_1 for Ag was divided by a factor of 100 to fit in the same scale). Both data sets show a peak centered at the origin. In the case of Ag, this peak decreases extremely rapidly and the high frequency σ_1 is vanishingly

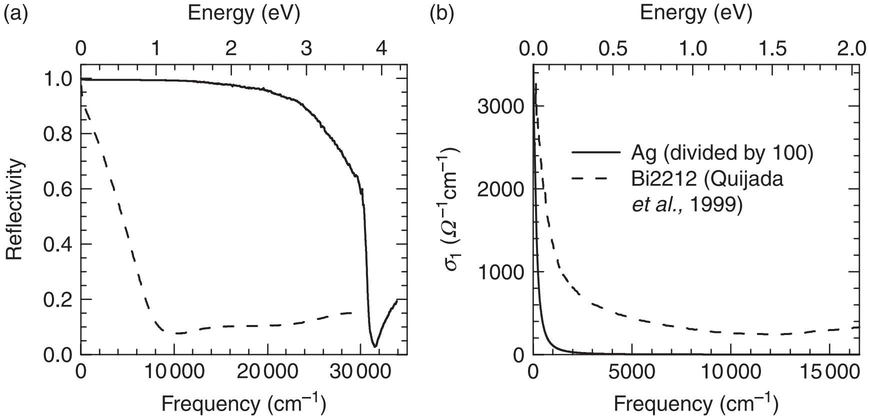

3.2 (a) Reflectivity spectra for Bi2212, adapted from Quijada *et al.* (1999), and for metallic silver. (b) The real part of the optical conductivity (σ_1) for both systems. Note that σ_1 for silver was divided by a factor of 100 to fit in the same scale.

small. In the cuprates, σ_1 remains finite throughout the whole spectral range. A well behaved Drude peak, such as the one in Ag, has a Lorentzian shape and its half width at half maximum gives the value of the scattering rate. In the cuprates the Lorentzian peak is poorly defined and the determination of the scattering rate is a more complex task as described in Sections 3.3.2 and 3.3.3 below.

3.3.2 Two component optical conductivity

A first attempt to reconcile the Drude model with the cuprate superconductors is to adopt an optical conductivity composed of different types of excitations such as

$$\frac{Z_0}{2\pi}\sigma(\omega)=\frac{\Omega_p^2}{\tau^{-1}-i\omega}+\sum_j\frac{S_j^2\omega}{i\left(\Omega_j^2-\omega^2\right)+\gamma_j\omega}. \qquad [3.3]$$

The first term is the Drude component (Eq. 3.2) and the sum represents a series of bound states of resonance frequency Ω_j, intensity S_j and width γ_j. We can look at Eq. 3.3 just as a convenient way of parameterizing the optical conductivity. However, Quijada *et al.* (1999) applied the two-component approach to Bi2212 and showed that the Drude peak extracted from Eq. 3.3 explains perfectly the dc transport properties. The magnitude of the Drude conductivity follows the inverse of the resistivity. Most importantly, they showed that the plasma frequency remains constant and the scattering rate of the Drude term increases linearly with the temperature. The left panel of Fig. 3.3 shows the fit obtained by Quijada *et al.* at 100 K. It is composed of a narrow Drude peak and two mid-infrared bands,

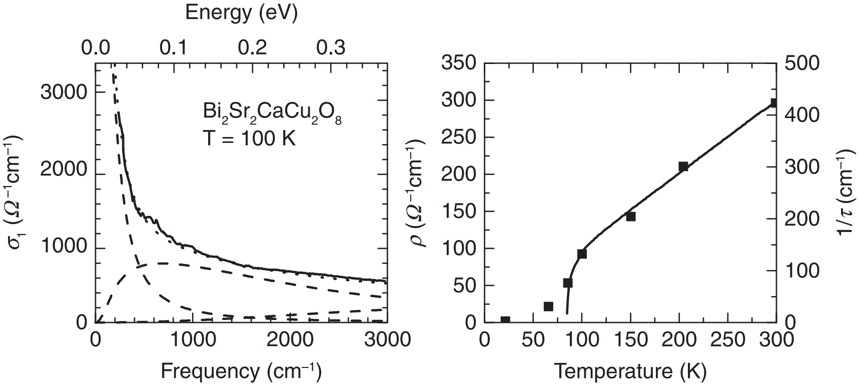

3.3 Adapted from Quijada *et al.* (1999). The left panel shows the measured optical conductivity (continuous line) for Bi2212 at 100 K. The dotted line is a fit using the two component approach given by Eq. 3.3. This fit is the sum of one Drude term and two mid infrared bands shown by the dashed lines. The continuous line in the right panel is the resistivity for the same sample (left hand scale) and the squares are the scattering rate (right hand scale) obtained from the Drude term in the two-component approach.

shown as dashed lines. Figure 3.2 (b) shows the resistivity compared to the Drude scattering rate. The temperature dependencies of these two quantities match wonderfully. Finally, Quijada *et al.* show that the mid infrared bands have no temperature dependence at all.

More recently, Lee *et al.* (2005) showed that the two component approach is a hallmark of the pseudogap state. Looking at 10 different doping levels in YBCO, they showed that in the pseudogap state there is a clear peak centered at zero frequency well separated from a mid-infrared bump. They make a case for a 'nodal metal' where the Drude peak describes well the quasiparticles along the Fermi arcs, which were not destroyed by the pseudogap opening. This data will be discussed in detail in Section 3.4.

If the two-component approach produces a Drude term that correlates very well with transport data, a clear physical meaning for the bound states is missing. Some conjectures for the mid infrared bands include spin (Grüninger *et al.*, 1996) or charge (Degiorgi *et al.*, 1995) density waves, polarons (Calvani *et al.*, 1996; Mertelj *et al.*, 2000), spin-fluctuations (Eom *et al.*, 2004) and bimagnons coupled to charges (Grüninger *et al.*, 1999). All these propositions remain very speculative and at this time there is no clear explanation for the mid-infrared bands of the two-component approach. Actually, there is not even a consensus that the two-component approach has any use beyond being a convenient parameterization of the optical conductivity. However, we should keep in mind that the two-component approach grasps very well the rough behavior of σ_1.

3.3.3 The extended Drude model

Allen (1971) showed that a single component extended Drude model can account for electron-phonon interactions in metals and the formalism used should be valid for the interaction of electrons with any bosonic energy spectrum. This model is a simple extension of Eq. 3.2 with the addition of a frequency dependency for the scattering rate. To respect causality, the effective mass renormalization $(1 + \lambda)$ also becomes frequency dependent. The optical conductivity then becomes (Puchkov *et al.*, 1996):

$$\sigma(\omega) = \frac{2\pi}{Z_0} \frac{\Omega_p^2}{\tau^{-1}(\omega) - i\omega\left[1 + \lambda(\omega)\right]}. \qquad [3.4]$$

A frequency dependent scattering rate is equivalent to a local definition of a Drude peak with the lifetime between collisions varying at each frequency. It does not depend on a particular model and implies that the deviations of a Drude behavior in the optical conductivity are a signature of electronic correlations. The extended Drude model successfully described variegated strongly correlated systems such as heavy fermions (Bonn *et al.*, 1988), manganites (Takenaka *et al.*, 2002), and of course, cuprate superconductors (Puchkov *et al.*, 1996). Although the modeling of τ and λ are important topics in condensed matter theory, the power of Eq. 3.4

relies in the ability to experimentally determine the scattering rate and effective mass from the optical conductivity. The inversion of Eq. 3.4 leads to

$$\frac{1}{\tau} = \frac{2\pi}{Z_0} \Omega_p^2 Re \frac{1}{\sigma} \tag{3.5}$$

and

$$\frac{m^*}{m} = 1 + \lambda = \frac{2\pi}{Z_0} \Omega_p^2 \frac{1}{\omega} Im \frac{1}{\sigma}. \tag{3.6}$$

There are two pitfalls with the above equations. First, one must know the plasma frequency Ω_p to properly determine the absolute values of these quantities. In the absence of a well established Drude peak, Ω_p is poorly defined. Always keep this in mind when looking at absolute values of τ^{-1} and λ. Second, the physical interest of this formulation is to understand the charge carrier behavior. Hence, before the inversion of σ, it is necessary to subtract the response of the excitations that are not related to the carriers spectrum. Examples of such excitations are phonons, interband transitions and deep core electronic excitations. A simple subtraction of a properly chosen constant (ε_∞) from the dielectric function takes care of eliminating the very high energy excitations. The subtraction of low frequency excitations, such as phonons or mid-infrared bound states, is more dangerous as one must know its spectral response.

The extended Drude model is closely connected to the concept of Fermi liquid which predicts that in a metal of weakly interacting carriers the scattering rate should behave as max[ω^2, $(\pi T)^2$]. This chapter deals mostly with the frequency behavior, and the temperature dependence will be ignored in the discussion. Figure 3.4 (a), shows the scattering rate for chromium (Basov *et al.*, 2002) above its Néel temperature. It follows a beautiful ω^2 evolution for almost two orders of magnitude, stating the robustness of the Fermi liquid in this material. The same figure shows the scattering rate calculated for Bi2212 at room temperature. The Fermi liquid breakdown is obvious, with a scattering rate depending linearly on the frequency. Based on the linear behavior of both the resistivity and the optical scattering rate, Varma *et al.* (1989) proposed the marginal Fermi liquid model (MFL). Although the nature of the bad metal normal state is still under intense debate, the MFL provides for a simple and straightforward way to describe the optical conductivity and can be seen as a phenomenological approach. Nevertheless, this linear ω behavior is very robust. Hwang *et al.* (2004b) showed that a two component description of the reflectivity in Bi2212 improves when adding a MFL-like term.

Figure 3.4 (b) shows the mass enhancement over a broad frequency range for optimally doped YBCO at 100 K (Puchkov *et al.*, 1996). The value of the effective mass at zero frequency relates to the strength of electronic correlations. It decreases with frequency and reaches a plateau having $m^*/m = 1$ in the mid-infrared. This means that high enough inside the conduction band, the electron–electron

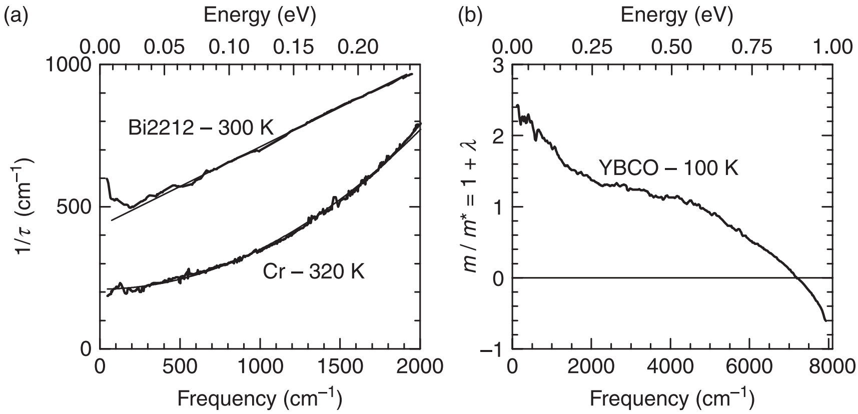

3.4 (a) Graph [adapted from Basov *et al.* (2002)], shows the frequency dependent scattering rate for a Fermi liquid (chromium above its Néel temperature). The thin line is the ω^2 behavior. The same panel also shows the scattering rate for Bi2212 at 300 K. The thin line in this case is the linear ω behavior. (b) Graph [adapted from Puchkov *et al.* (1996)], shows the mass enhancement for YBCO at 100 K over a broad energy range.

interaction is negligible. The sudden decrease of the mass enhancement, which eventually becomes negative, is the signature of interband transitions. These transitions do no represent the behavior of charge carriers and the frequency where this feature appears indicates the upper boundary where the extended Drude model stops giving information about the carriers.

To close this topic, it is important to note that the scattering rate and the mass enhancement are related to the optical self energy $\Sigma^{op} = \Sigma_1^{op} + i\Sigma_2^{op}$ by $1/\tau = -2\Sigma_2^{op}$ and $\omega\lambda = -2\Sigma_1^{op}$. Although the optical self-energy is averaged over the whole Fermi surface, it is a valuable complement to ARPES (Hwang *et al.*, 2004a). If optics lacks the **k** resolution of ARPES, it has a much better signal-to-noise ratio and energy resolution.

3.3.4 The optical conductivity sum rule and gaps in the excitation spectrum

Charge conservation implies that the total area under σ_1 is conserved upon changes of external parameters such as the temperature or pressure. The *f*-sum rule represents this conservation:

$$\int_0^\infty \sigma_1(\omega)d\omega = \frac{\pi}{2}\frac{ne^2}{m} = \frac{\pi^2\Omega_p^2}{Z_0}. \qquad [3.7]$$

When integrated to infinite, n refers to the total number of electrons (including the deep core electrons) and m to the bare electron mass. As σ_1 is a linear response function, the conductivity for different excitations are simply added to produce the total optical conductivity. If these excitations are decoupled, the sum rule is fulfilled separately for each kind of excitation. In particular, for conduction electrons limited to one band, one can replace the upper limit in the integration of Eq. 3.7 by a cut-off frequency representative of the band width. In this case *n* and *m* refer to the conduction electrons density and their effective mass.

Although there is not a straightforward relation between the density of states (DOS) and σ_1, the opening of a gap in the former should produce a depletion of low lying states in the latter. Figure 3.5 (a) shows σ_1 for $P_4W_{14}O_{50}$ (Zhu *et al.*, 2002), which has a charge density wave (CDW) transition at 60 K (incidentally, this material is also superconducting at 0.3 K). At 300 K there is a zero frequency centered Drude-like peak. At 10 K, when the CDW gap (1400 cm^{-1}) is fully open, the low frequency σ_1 is depleted. Simultaneously, σ_1 increases at higher energies. Equation 3.7 requires that the total area under the optical conductivity be conserved. This imposes that the spectral weight lost below the gap exactly matches the spectral weight gained above the gap energy. This is the typical behavior of a density wave gap: transfer of low energy spectral weight to high energies. A brief remark on the gap is that its value is close to the minimum in σ_1 rather than the crossing point between high and low temperature curves.

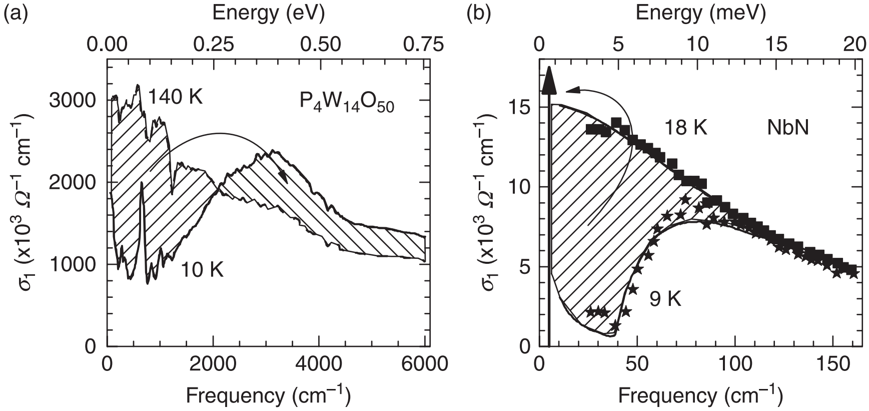

3.5 Panel (a) [adapted from Zhu *et al.* (2002)], shows the real part of the optical conductivity for $P_4W_{14}O_{50}$ above and below its charge density wave transition. Panel (b) [adapted from Somal *et al.* (1996)], shows the real part of the optical conductivity above and below the superconducting transition of NbN. The large vertical arrow is the δ function representing the superfluid condensate. The points are the data and the lines are either Drude or BCS isotropic gap fits. In both panels the thin arrows indicate the spectral weight transfer at the phase transition.

And what about the superconducting gap? Figure 3.5 (b) shows the optical conductivity for the conventional superconductor NbN above and below T_c (Somal *et al.*, 1996). The opening of a superconducting gap is clearly associated with a diminution of the optical conductivity at low frequencies. However, opposite to a density wave gap, there is no sign of spectral weight transfer to higher energies. Yet, Eq. 3.7 must be fulfilled. The zero resistivity state of a superconducting transition is represented by a $\delta(\omega)$ function at the origin of the optical conductivity. It is this δ function that recovers the spectral weight lost at T_c. This is known as the Ferrell-Glover-Tinkham (Ferrell and Glover, 1958; Tinkham and Ferrell, 1959) sum rule.

The ability to see the superconducting gap in cuprates or not is a long standing debate. The consensus is that 'in a clean high-T_c superconductor you do not see the gap' (Kamarás *et al.*, 1990). Figure 3.6 shows the meaning of this statement in its left panel. The definition of clean and dirty superconductivity comes from the comparison of the mean free path l of quasiparticles to the pairs coherence length ξ. In a clean superconductor $l >> \xi$ and the opposite happens in a dirty superconductor. As $l \sim v_F\tau/2\pi$ and $\xi \sim \hbar v_F/\pi\Delta$ (v_F being the Fermi velocity) the conditions for clean and dirty superconductivity from the optics point of view are, respectively, $\tau^{-1} << 2\Delta$ and $\tau^{-1} >> 2\Delta$. The dashed curve shows the calculated normal and superconducting σ_1 for a dirty material (Mattis and Bardeen, 1958; Zimmermann *et al.*, 1991). At 0 K, σ_1 vanishes for frequencies below twice the gap. A photon of energy 2Δ can break a pair and the conductivity above the gap will reach that of a normal metal (the factor 2 is necessary as the highest occupied state is Δ below the Fermi level and the lowest unoccupied state is Δ above the Fermi level). As τ^{-1} is large compared to Δ, the normal state Drude peak is very

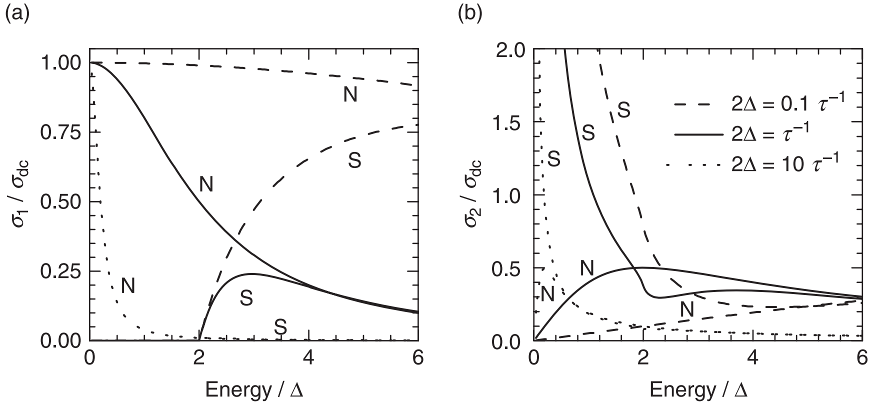

3.6 Real part (a) and imaginary part (b) of the optical conductivity calculated for a BCS isotropic superconductor at $T = 0$ in the clean limit ($2\Delta >> \tau^{-1}$ – dotted lines), the dirty limit ($2\Delta << \tau^{-1}$ – dashed lines) and an intermediate case ($2\Delta \sim \tau^{-1}$ – solid lines). The labels 'S' and 'N' refer to the superconducting and normal states, respectively.

broad and its conductivity is large at 2Δ, almost as large as σ_{dc}. Thus, at the superconducting transition, the collapse of low frequency states to the δ function will produce very marked features at 2Δ as shown by the dashed lines. The dotted lines in this figure show what happens in the clean limit. In this case, the width of the Drude peak is much smaller than the gap and the normal state conductivity at 2Δ is vanishingly small. Upon condensation of the Drude peak into the δ function, almost no changes in σ_1 happen. In the clean case, the superconducting σ_1 is null everywhere but at zero frequency.

The above description leads to the key property of the optical conductivity in superconductors: in the dirty limit σ_1 is dominated by 2Δ whereas in the clean limit it is dominated by $1/\tau$. It is paramount to remark that the signature of the superconducting transition is not the observation of a gap in the optical conductivity. The important feature is the condensation of the Drude peak into the δ function and its consequent suppression of low frequency σ_1.

The condensation of Cooper pairs produces dramatic changes in the imaginary part of the optical conductivity σ_2, as shown in the right panel of Fig. 3.6. In the normal state, σ_2 vanishes at zero frequency and is peaked at $1/\tau$. In the superconducting state, because of causality relations, the δ function in σ_1 produces a $(2\pi/Z_0)\rho_s/\omega$ zero frequency divergence in σ_2. By measuring the coefficient of this ω^{-1} term, one can determine with a high degree of accuracy the superfluid weight ρ_s. This is the important value from optical measurements.

3.3.5 Restricted spectral weight

It is very useful to define a restricted spectral weight (RSW) function based on Eq. 3.7:

$$RSW(\omega_1,\omega_2) = \int_{\omega_1}^{\omega_2} \sigma_1(\omega)d\omega. \qquad (3.8)$$

When a gap opens, the full sum rule does not make a distinction between spectral weight transfer to high or low frequencies. The RSW function eliminates this shortcoming.

Figure 3.7 illustrates the use of Eq. 3.8 in two hypothetical systems. Panel (a) is a Drude metal with a scattering rate decreasing linearly with temperature. Panel (b) starts as the same metal of panel (a) but a density wave gap opens below 150 K. The spectral weight transfer from the Drude term to the gap is taken to increase linearly with decreasing temperature. The sum rule given by Eq. 3.7 states the areas under each curve in panel (a) and each curve in panel (b) are all the same. Panel (c) shows an example of using the restricted sum rule with integration boundaries of $\omega_1 = 0$ and $\omega_2 = \omega_c$ (the cutoff frequency is shown in the figure as a vertical dashed line).

When the metallic system of panel (a) is cooled, the scattering rate diminishes which produces a narrowing of the Drude peak and an increase of the dc conductivity. This induces a spectral weight transfer from high to low frequencies.

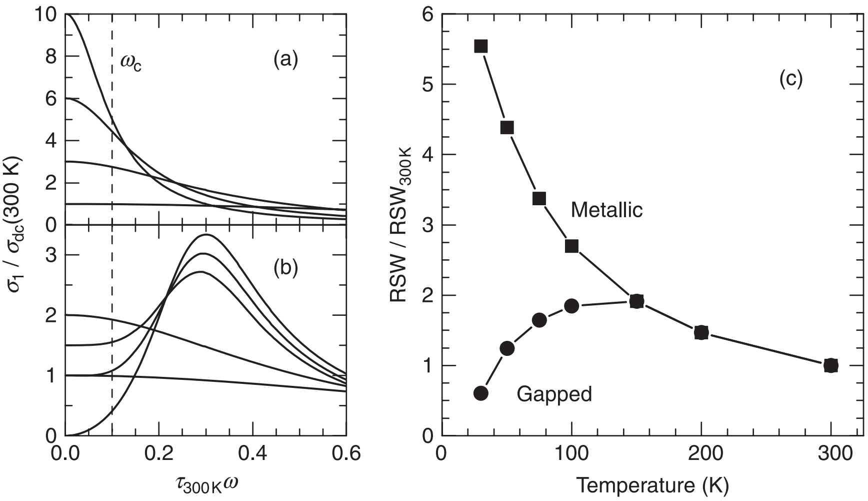

3.7 Panel (a) shows the optical conductivity for a Drude metal where the scattering rate decreases linearly with temperature (temperatures shown: 300, 100, 50 and 30 K). Panel (b) is the case where the Drude metal of panel (a) develops a density wave gap below 150 K (temperatures shown: 300, 150, 75, 50 and 30 K). The spectral weight transfer from the Drude peak to the gap is assumed to increase linearly with decreasing temperature. Panel (c) shows the relative spectral weight integrated from 0 to ω_c for the model materials shown in panels (a) and (b). The vertical dashed line in panels (a) and (b) indicates the value chosen for ω_c.

Integration of the area under the low frequency conductivity produces, instead of a constant value, a number that increases with decreasing temperatures (squares in panel (c)). In the gapped material shown in panel (b), the situation is different. At high temperatures, where by design the system is metallic, we find the same properties of material (a). However, below the gap opening temperature, there is a transfer of spectral weight from low frequencies to high frequencies. Then, if we just look at low frequencies, we see a decrease in the RWS.

An astute combined use of the sum rule and the restricted spectral weight function goes a long way in understanding gap openings and spectral weight transfer in conducting materials. They will come in particularly handy in the analysis of electron doped cuprates (section 3.4.3).

3.4 The normal state

The discussion of the phase diagram (section 3.2) shows that the normal state of cuprate superconductors has a fascinating set of exotic properties. Here I want to discuss some specific issues that have gained a lot of interest in the past few years. The pseudogap is such an important part of the physics of cuprates that its optical behavior is discussed in detail in section 3.4.1. The topic discussed in section 3.4.2 covers the general optical signatures when moving from the pseudogap state towards the overdoped regime. Section 3.4.3 makes a special discussion on the normal state gap in electron-doped materials.

3.4.1 The pseudogap in the optical response

Besides being a spin gap, the pseudogap also represents an equally strong gap in the charge excitation channel. However, the pseudogap is only a partial gap at the Fermi level. By partial gap, one has to understand that there are directions on the Brillouin zone where the Fermi surface survives and other directions that show no states at the Fermi energy. ARPES showed that below T^* the antinodal directions are gapped and the nodal directions are metallic. This observation led to the term ‘nodal metal’ to describe the pseudogap state. The first question to address then is what happens to the optical conductivity.

If states are lost at the Fermi level, the low frequency optical conductivity should decrease. In section 3.3.4 we discussed what happens for a density wave and for a superconducting gap. In both cases, finite low frequency spectral weight is lost. The difference between the two situations is the final destination of this spectral weight (either high frequencies or the $\delta(\omega)$ function). But, again, low frequency spectral weight is lost in the two situations. Therefore, it is natural to look for such an effect in the pseudogap state.

Panel (a) of Fig. 3.8 shows the real part of the optical conductivity for four different dopings in YBCO ranging from slightly overdoped to heavily underdoped (Lee *et al.*, 2005). This data is measured with the electric field of light lying on the CuO_2 planes. The room temperature spectra is shown as dashed lines for all samples. It shows the Drude-like peak observed in the strongly correlated cuprates. The zero frequency limit of these data decreases when going towards the underdoped side, as expected by the higher dc resistivity in this region. The shape of all curves are nevertheless similar. The solid line in these figures show the optical conductivity in the normal state just above T_c. One common characteristic is that for all samples the zero frequency limit of σ_1 increases. This increase follows very well the decrease in the resistivity. The striking difference between the near optimal doped ($x = 7.00$) sample and all the underdoped samples is the dip around 500 cm^{-1}. On first sight, we would say that this is the normal low frequency loss of spectral weight due to the pseudogap. This is not the case! As we discuss below, this conclusion was reached for Bi2212 (Santander-Syro *et al.*, 2002) but the same result is valid for all hole-doped cuprates.

The first hint that we are not facing a spectral weight loss is that we cannot see a gain of spectral weight at higher energies as expected for a density wave gap (Fig. 3.5). Transfer to a zero frequency δ function is most certainly not reasonable as the system is not entering the superconducting state. Panels (b) and (c) of Fig. 3.8 shed some light on what is happening. They show the RSW for an underdoped

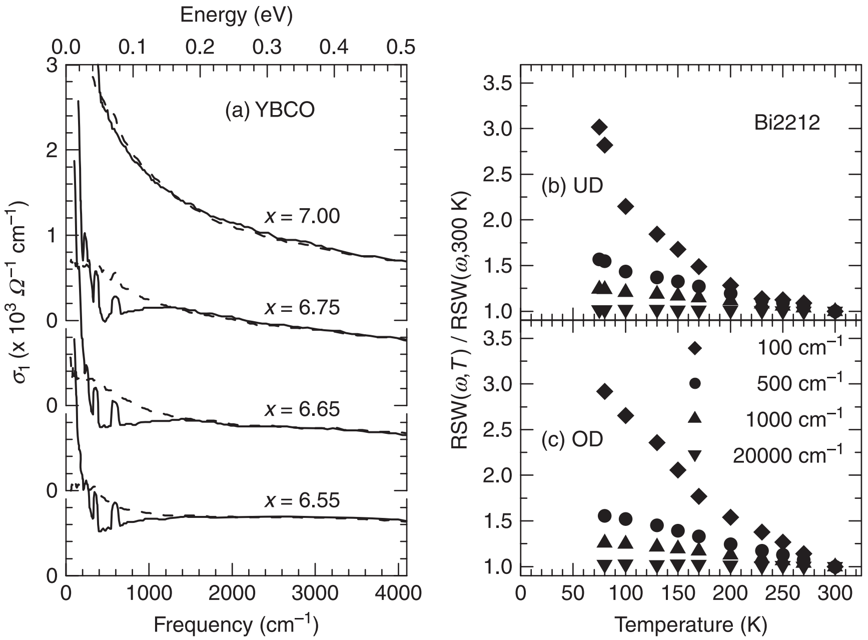

3.8 Panel (a) shows the optical conductivity for YBCO superconducting crystals of several dopings [adapted from Lee *et al.* (2005)]. The dashed line is the room temperature data and the solid line is in the normal state just above T_c for each sample. The right-hand figures show the RSW (integrated from 0 to the several cut-off frequencies shown in the legend) for (b) underdoped (UD) and (c) overdoped (OD) Bi2212 films [adapted from Santander-Syro *et al.* (2002)].

(pseudogap present) and an overdoped (no pseudogap) Bi2212 film. The RSW is calculated from zero to several cut-off frequencies. The first thing to remark is that when the cut-off frequency is chosen at 20 000 cm^{-1} (2.5 eV), the *f*-sum rule is fulfilled, meaning that spectral weight is conserved in this range. When the cut-off frequency decreases, the low temperature spectral weight increases. Always! When the integration starts from zero, there is not any upper cut-off frequency that will lead to a spectral weight decreasing with decreasing temperature. Even more astonishing is the fact that the trend seen in the underdoped sample is similar to the one in the overdoped sample. In the discussion of the RSW (Fig. 3.7) I argued that such an increase of low frequency spectral weight is the hallmark of a metallic behavior. Therefore, what we are seeing in the underdoped state is a Drude peak getting very narrow when the temperature is decreased. There is no gap opening and the spectral weight is conserved. Panel (a) fully supports this picture: we can describe the low temperature σ_1 as a sharp Drude peak and a mid-infrared band. This is probably the region where the two-component approach (Eq. 3.3) finds its best justification. Indeed, Lee *et al.* (2005) argue that the pseudogap line can be described as the crossover from the two-component to the one-component (Eq. 3.4) description of the optical conductivity.

The pseudogap picture also breaks down if one looks at the energy of the dip. Regardless of doping, σ_1 in the pseudogap state always starts decreasing at a similar energy, around 1200 cm^{-1} (150 meV). The pseudogap, however, does increase with decreasing doping. It becomes more and more obvious that this feature is not the pseudogap signature.

A follow up question is why we do not see the pseudogap in the spectral weight or σ_1? Why do we mostly see the nodal metal response? A qualitative answer comes from the semi-classical conductivity formula (Ashcroft and Mermin, 1976)

$$\sigma(\omega) \propto \int \frac{v_{\mathbf{k}}^2}{\tau^{-1}(\varepsilon_{\mathbf{k}}) - i\omega} \left(\frac{\partial f}{\partial \varepsilon} \right)_{\varepsilon = \varepsilon_{\mathbf{k}}} d^2k, \qquad [3.9]$$

where $v_{\mathbf{k}}$ and $\varepsilon_{\mathbf{k}}$ are the bare values calculated from band-structure for the carriers velocity and energy, respectively. $\tau^{-1}(\varepsilon_{\mathbf{k}})$ is the dc scattering rate, and f is the Fermi distribution function. In cuprates, the Fermi velocity is higher along the diagonal (nodal) directions. Moreover, as the pseudogap opening diminishes the number of final states to which carriers can be scattered, the scattering rate along nodal directions also decreases. These two factors show that the integral in Eq. 3.9 has much higher contributions from the nodal directions. Therefore, the in-plane conductivity is looking at the nodal metal, not at the pseudogapped regions. It seems hardly surprising, then, that no loss of spectral weight is seen as the nodal directions are dominated by a narrowing Drude peak. This hand-waving argumentation finds much more rigorous support in the calculations of Devereaux (2003).

So how do we see the gap in the optical response? Look at the c-axis! Panel (d) in Fig. 3.9 shows the optical conductivity (from which phonons were subtracted) for underdoped YBCO along the c-axis (Homes *et al.*, 1993). Note that the absolute values of σ_1 are much smaller in this direction. The high-temperature optical conductivity does not show a Drude-like peak and it is rather dominated by a flat incoherent background. Homes and co-workers noticed that upon cooling the sample, low frequency spectral weight is lost, and this far above $T_c = 63$ K for this sample. Even better, as the inset of this figure shows, the spectral weight lost scales very well with the Knight shift measured for the Cu(2) NMR line (Takigawa *et al.*, 1991). Once again, the calculations of Devereaux (2003) support this picture by showing that the c-axis transport probes the antinodal (hence gapped) regions with a stronger weight. Panels (a) and (b) of Fig. 3.9 compare σ_1 along the c direction and on the CuO$_2$ planes (Lee *et al.*, 2005). The difference in the energies where σ_1 shows a pseudogap feature gives yet another evidence that the in-plane optical conductivity is probing only the Drude response of the nodal metal, not the pseudogap.

Although it will not be discussed here, it is interesting to point out that the pseudogap does represent a transfer of optical spectral weight from low to high frequencies. Hwang *et al.* (2008a) showed that the real part of the self-energy,

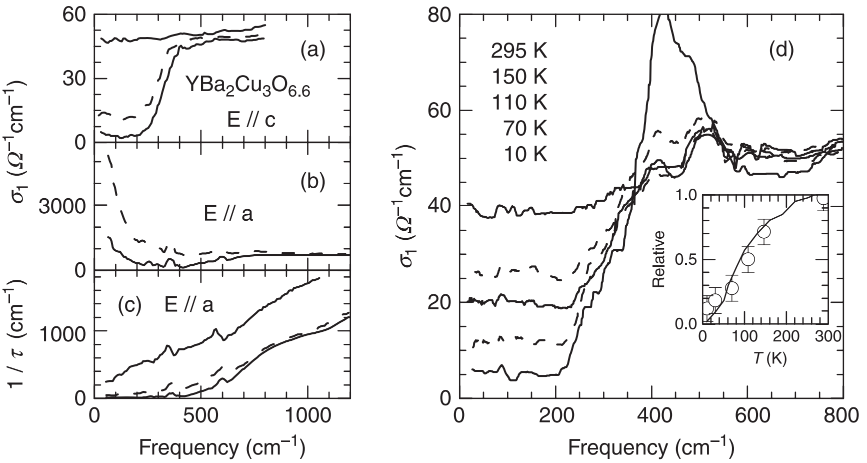

3.9 The panels on the left-hand side show data for underdoped YBCO in the pseudogap regime [adapted from Basov *et al.* (1996)]. The dashed lines represent data in the normal state just above T_c. The higher solid line is the data at room temperature and the lower at 10 K. The room temperature σ_1 for *E* // *a* is not shown. Panel (a) shows σ_1 along the c-axis and panel (b) along the a-axis. Panel (c) depicts the scattering rate along the a-axis. Panel (d) shows σ_1 for YBa$_2$Cu$_3$O$_{6.7}$ (T_c = 63 K) for several temperatures [adapted from Homes *et al.* (1993)]. The inset compares the normalized low frequency spectral weight lost at low temperatures (open circles) to the Knight shift for Cu(2) [from Takigawa *et al.* (1991)].

related to the mass enhancement (Eq. 3.6), has a pile up of states above the gap energy associated to a loss at low energies.

As I mentioned above, the pseudogap state is accompanied by a decrease in the scattering rate. This is the main reason why dc transport is sensitive to the pseudogap. It is only natural, then, to look into the optical scattering rate, but we must take extra care when doing so. Lee *et al.* (2005) argue that the pseudogap is well characterized by the two component model, where carriers and bound states are different excitations. When looking at the scattering rate, we use the extended single component Drude model which assumes that the whole conductivity comes from a single excitation. There is yet no clear solution for this conundrum. In this chapter I will just ignore the contradictions and use whichever model highlights the features of interest best. With this in mind, Fig. 3.10 (a) shows the in-plane scattering rate for underdoped Bi2212. At room temperature it shows the marginal Fermi liquid linear behavior. At 200 K, where the pseudogap is already open, the low frequency scattering rate deviates from the high frequency linear behavior defined by the dashed line. Upon cooling the material, this deviation increases. The low frequency $1/\tau$ contains the definite signature of the pseudogap. It is very tempting to assign the energy at which the deviation from the straight line begins to the pseudogap energy. We should restrain our enthusiasm. The data from

Hwang *et al.* (2004b) shows that this energy is roughly doping independent, contrary to the pseudogap value. In addition, panel (c) in Fig. 3.9 shows that the scattering rate departure from linear behavior follows the energy scale in the in-plane optical conductivity, not the pseudogap signature along the c-axis.

We close the pseudogap discussion comparing systems of the same family having different number of copper oxygen planes per unit cell. Lee *et al.* (2005) had already noticed that the pseudogap seems to be a property of isolated CuO_2 planes, regardless of the host material. Panel (b) in Fig. 3.10 illustrates this very well. This figure shows the superconducting dome (open symbols) for three different Bi-based cuprates, with one, two or three CuO_2 planes per unit cell. Data for Bi2223 (Fujii *et al.*, 2002) and Bi2212 (Watanabe *et al.*, 2000) are from dc transport. Data for Bi2201 (Lobo *et al.*, 2009) comes from the optical scattering rate. T_o values for these materials are radically different and T_c^{max} ranges from 20 K (one plane) to 108 K (three planes). Yet the pseudogap opening temperature

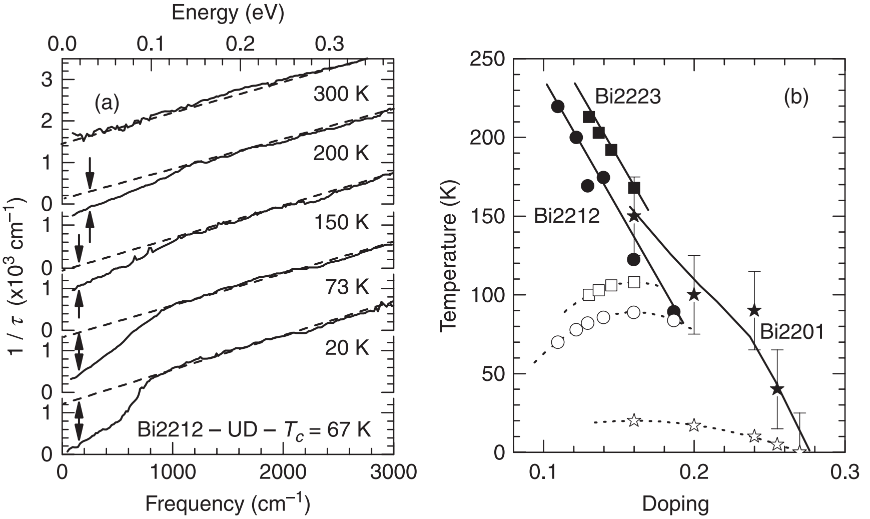

3.10 Panel (a) shows the scattering rate for underdoped Bi2212 [adapted from Hwang *et al.* (2004)] at several temperatures. Note that the curves are shifted by 1500 cm^{-1} and that above 1500 cm^{-1} they are indistinguishable. The dashed lines are straight lines corresponding to their high frequency behavior. The arrows at low frequency indicate the suppressed scattering, with respect to the linear behavior, at each temperature. Panel (b) shows the superconducting dome and the pseudogap opening temperatures for Bi2223 [squares, adapted from Fujii *et al.* (2002)], Bi2212 [circles, adapted from Watanabe *et al.* (2000)] and Bi2201 [stars, adapted from Lobo *et al.* (2009)]. The pseudogap for Bi2223 is obtained from transport measurements whereas it is obtained by several techniques in Bi2212 and by the optical scattering rate in Bi2201.

seems to completely ignore the number of planes. It just follows the same line for all families. There is a caveat here, though. Transport, dc or optical, will probe the most conducting channels. In three-layer Bi2223 the inner plane is notoriously underdoped, hence the above statement is only valid for the outer, more conducting, planes.

3.4.2 From a nodal metal to a bad metal to a Fermi liquid

The optical scattering rate, which gave us a wealth of information on the pseudogap, is also very useful in the analysis of the bad metal and the Fermi liquid regimes. And so is the mass enhancement function. Panel (a) of Fig. 3.11 shows the optical scattering rate for Bi2212 in the underdoped, optimally doped and lightly overdoped regimes (Hwang *et al.*, 2004a). It also shows $1/\tau$ for deeply overdoped Tl2201 (Ma and Wang, 2006). The normal state conductivity increases with doping. Naturally, the absolute value of $1/\tau$ decreases when moving from underdoped to overdoped. A low frequency depletion of the scattering rate characterizes the pseudogap phase, as discussed in the previous section. The lightly overdoped Bi2212 shows the perfectly linear scattering rate typical of the marginal Fermi liquid response. The scattering rate of deeply overdoped Tl2201 shows an upward curvature, reminiscent of a more conventional Fermi liquid. However, it does not follow a ω^2 trend but rather $\omega^{1.78}$. This is an important point, as this is one of the most overdoped

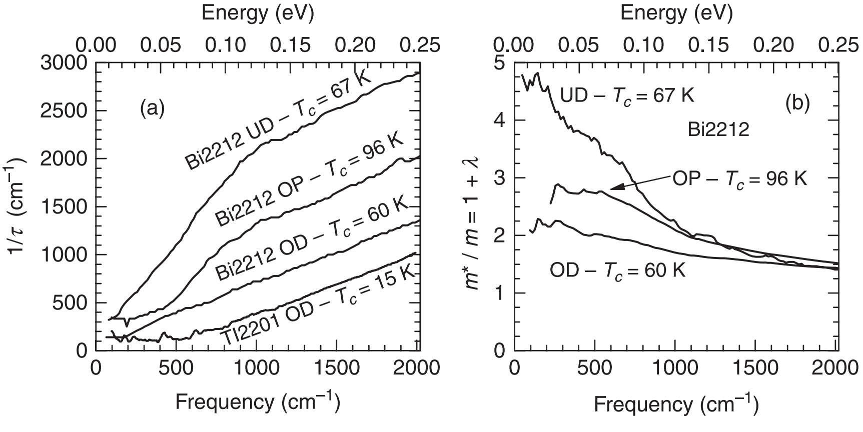

3.11 Panel (a) shows the optical scattering rate for Bi2212 in the underdoped (UD), optimally doped (OP) and overdoped (OD) states, adapted from Hwang *et al.* (2004a). The data are shown at 73 K for the UD sample and 100 K for OP and OD. This panel also shows the scattering rate for heavily overdoped $Tl_2Ba_2CuO_{6+\delta}$ (Tl2201) at 90 K [adapted from Ma and Wang (2006)]. Panel (b) shows the mass enhancement corresponding to the Bi2212 of panel (a) [adapted from Hwang *et al.* (2004a)]. The critical temperatures are indicated in the figure for all samples.

materials we know. One should not take a Fermi liquid behavior for granted at high dopings. We are getting closer but strong electron–electron correlations are still present.

Panel (b) of Fig. 3.11 shows the mass enhancement function for the Bi2212 shown in panel (a). At high frequencies, but below the band edge, all the curves tend to unity, as expected. At low frequencies a clear trend develops: increasing the doping decreases the value of m^*/m. This quantity is expected to relate to the electron–electron correlation strength. Therefore, as increasing the doping leads to a more conventional Fermi liquid, we should find a smaller effective mass enhancement, as shown in panel (b). But once again the one component vs. two component approach brings trouble to the situation. Padilla *et al.* (2005) used the concept that the pseudogap state is intrinsically two-component and calculated the effective mass enhancement for YBCO. The tricky point here is that the absolute value of the effective mass given by Eq. 3.6 depends on the plasma frequency. By taking Ω_p from the Drude weight of a two-component model, Padilla *et al.* showed that the effective mass remains unchanged over the full phase diagram. Such a situation means that underdoping is equivalent to a decrease in charge density and not in charge dressing by mass enhancement. This shows that underdoping does not change the intrinsic properties of charges and, as pointed out by Padilla *et al.*, the changes in the material properties would be due simply to the smaller volume occupied by carriers in **k** space.

The one vs. two component battle is still a hot topic. It has very fundamental implications on the physics of cuprates and the understanding of carrier behavior in strongly correlated systems.

3.4.3 The normal state gap in electron-doped materials

Electron-doped cuprates, like their hole-doped counterparts, are materials built across CuO_2 planes. However they lack the apical oxygen present in most hole-doped materials. In addition, 'electron-doped' is almost a misnomer, as they seem to contain electron and hole pockets in their Fermi surface (Armitage *et al.*, 2001; Dagan *et al.*, 2004). From the optics point of view they are as strongly correlated as hole-doped materials (Millis *et al.*, 2005).

Figure 3.12 summarizes the whole situation about the optics of the normal state gap in electron-doped cuprates. The optical response of these materials was measured by several groups (Onose *et al.*, 1999, 2001, 2004; Singley *et al.*, 2001; Zimmers *et al.*, 2004) and there is an overall agreement on its interpretation. Here we discuss the data from Onose *et al.* and Zimmers *et al.*, Panel (a) shows the raw reflectivity data for several dopings (from underdoped to overdoped) of PCCO at room temperature and 25 K, which is larger than T_c for all samples. When going from overdoped to underdoped, the low temperature spectrum develops a dip around 2000 cm^{-1}. At the 13% and 11% Ce content samples, we can clearly observe a crossing between low-temperature and high-temperature data around 4000 cm^{-1}.

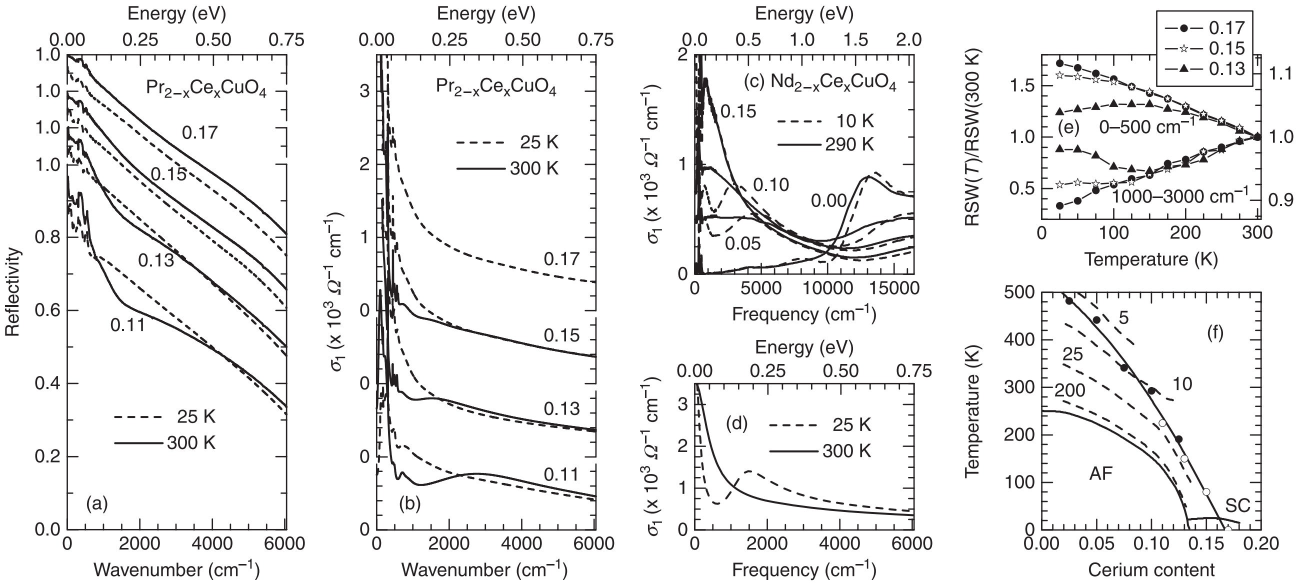

3.12 Panel (a) shows the reflectivity of PCCO as a function of Ce content and temperature. Panel (b) depicts the optical conductivity derived from the data in panel (a). Panels (a) and (b) are adapted from Zimmers *et al.* (2005). Panel (c) contains the real part of the optical conductivity, measured by Onose *et al.* (2004), for several doping levels in NCCO. Panel (d) is a calculation based on a local spin density wave instability for PCCO, from Zimmers and co-workers. Panel (e), also by Zimmers *et al.*, shows the restricted spectral weight at low frequencies and high frequencies for the PCCO samples. Panel (f) [adapted from Motoyama *et al.* (2007)], shows the neutron scattering determined antiferromagnetic phase, and the temperature where the normal state gap opens for the PCCO (open circles) and NCCO (solid circles) data. The dashed lines are spin correlation lengths (ξ) and the numbers are ξ/a_0, where a_0 is the lattice parameter.

Panel (b) shows the consequences of this reflectivity dip in the real part of the optical conductivity. A dip at low frequencies slowly develops when the sample is underdoped. In the overdoped sample the high frequency optical conductivity is almost temperature independent. Upon underdoping, a clear overshoot of the high frequency σ_1 appears at low temperatures. The data for the 11% Ce sample is very close to the density wave example shown in Fig. 3.5. This is in striking contrast to the hole-doped pseudogap where no clear transfer from low to high frequencies is present (see Section 3.4.1 and Fig. 3.8). The normal state gap in PCCO has a very well characterized density wave character.

Panel (c) shows that this phenomenon is not restricted to PCCO. The NCCO data shown has the same features as panel (b). A theoretical explanation for this, proposed by Millis in Zimmers *et al.* (2004), assumed a local spin density wave perturbation in the system. His calculations reproduce the gap opening and the high frequency overshoot as shown in panel (d). ARPES (Armitage *et al.*, 2001) shows that this density wave gap opens only in a portion of the Fermi surface. This is portrayed in the optical data by a remaining zero frequency Drude peak even in the gapped phase. For clarity, this Drude peak is not shown in panels (b) and (c) but the optical dc conductivity reaches values of at least 10 000 Ω^{-1}cm^{-1} at low temperatures for all samples shown.

Panel (e) shows the application of the RSW (Eq. 3.8) on the data in panel (b). In the top three curves, the integration limits are 0 and 500 cm^{-1}. In the lower three curves these limits are 1000 and 3000 cm^{-1}. The RSW for these two different integration limits are opposite, indicating spectral weight transfer between these two ranges. They show a perfect example of a density wave gap opening. In the overdoped sample, we only see the Drude peak growing at low frequencies at the expense of the spectral weight in the mid-infrared. The Drude peak in the 15% Ce sample initially follows the overdoped sample. But at about 100 K this growth slows down and the RSW saturates. Accordingly, the mid-infrared loss of spectral weight slows down. For the heavily underdoped 13% sample we see that the initial increase of low frequency spectral weight due to the Drude narrowing is quickly overwhelmed by the gap opening at around 125 K and the spectral weight decreases. Again, the mid infrared region shows the opposite of this behavior.

Panel (f) shows the phase diagram for electron doped samples indicating the antiferromagnetic phase, the superconducting dome and the spin correlation length measured by neutron scattering (Motoyama *et al.*, 2007). The gap opening temperature for NCCO (Onose *et al.*, 2004) and PCCO (Zimmers *et al.*, 2004) are superimposed on this phase diagram. It shows that the optical gap opens at a spin correlation length of about ten unit cells. This means that the optical conductivity is probing the short range 2D antiferromagnetic fluctuations and it can be interpreted as the formation of a spin density wave phase. The line defining this phase disappears inside the superconducting dome in a quantum critical point.

3.5 The superconducting state

The first optical conductivity forays into the superconducting state were attempts trying to measure the superconducting gap. This is probably one of the few topics settled and I discuss its outcome in section 3.5.1. I will also try to tackle a somewhat bolder question: What is the glue that binds the Cooper pairs? A series of papers starting in the early 2000s raised the issue of kinetic energy driven superconductivity, and this is discussed in section 3.5.2. From another front, radical improvements in data analysis lead to the calculation of the bosonic spectrum of excitations responsible for superconductivity. This is the central topic of section 3.5.3.

3.5.1 Is there a gap in the superconducting optical conductivity?

In section 3.3.4 we discussed the consequences of the superconducting transition in the optical conductivity. The important feature is the lost area at finite frequencies representing the superfluid weight. As a bonus we might be able to determine the gap value. The hole-doped cuprates do not seem to come with this bonus.

Figure 3.13 (a) shows the optical conductivity for underdoped and optimally doped YBCO (Orenstein *et al.*, 1990). As discussed in section 3.3.4, the gap

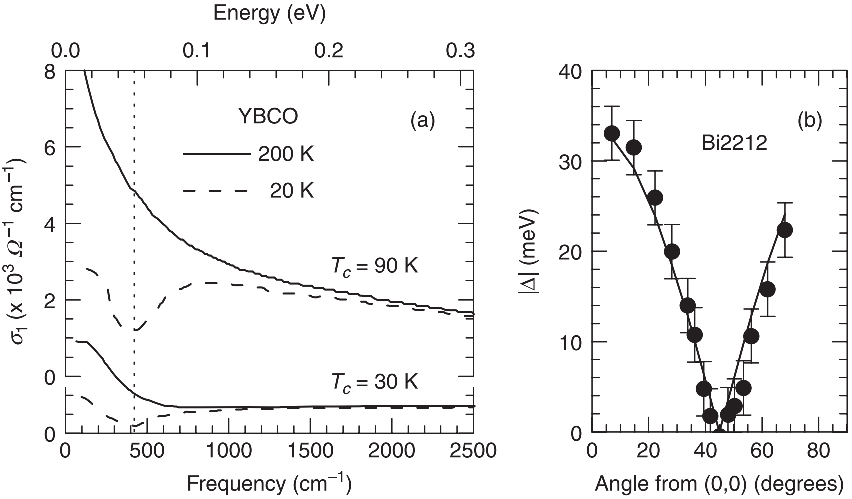

3.13 (a) Optical conductivity for underdoped and optimally doped YBCO [adapted from Orenstein *et al.* (1990)]. The vertical line is a guide to the eyes showing the minimum σ_1 in the superconducting state. (b) Gap value along the Fermi surface for optimally doped Bi2212 [adapted from Ding *et al.* (1996)]. The solid line is the *d*-wave expectation.

value is located close to the minimum in the optical conductivity. The vertical line shows that the minima for both compositions in the superconducting state are at the same location. There is a debate on the value for the gap in the underdoped state. However, this debate jumps between a gap that increases with underdoping or a gap that follows T_c. In fact, Le Tacon *et al.* (2006) showed that both energy scales are present in underdoped cuprates, and the debate is rather which of the two is representative of the superconducting gap. In any case, no measurement shows a constant superconducting gap throughout the phase diagram. Two arguments support this invisibility of the gap in the optical conductivity. The right panel of this figure shows the gap magnitude measured by ARPES (Ding *et al.* 1996) for optimally doped Bi2212 as a function of the angle in the Fermi surface. It is the typical *d*-wave symmetry and the gap vanishes at the Brillouin zone diagonals (π,π). In the discussion of the pseudogap (section 3.4.1) we saw that the optical conductivity mostly probes the nodal directions, and those are the regions where the gap goes to zero. A second factor hampering the gap visibility comes strictly from the electrodynamics of clean limit superconductors. Kamarás *et al.* (1990) showed that optimally doped YBCO (but this is valid for hole doped cuprates in general) is in the clean limit. Its scattering rate is at least 10 times smaller than the gap. Figure 3.6 shows that in the clean limit, almost all the spectral weight in the normal state is already below the gap and that the energetics of the system is controlled by $1/\tau$. So, there is no signature in the optical conductivity at the gap energy.

I said that that the issue was settled, but I should have said *almost* settled. In some cases such as Pr-doped YBCO (Lobo *et al.*, 2001) and the electron-doped cuprates (Zimmers *et al.*, 2004; Homes *et al.*, 2006b), the system might be dirty enough to produce a signature at the gap value.

3.5.2 Sum rules and the kinetic energy

The *f*-sum rule, defined by Eq. 3.7, represents charge conservation and is a constant. However, in the framework of a single band, tight-binding, nearest neighbor hopping model, and when written in terms of a properly chosen cut-off ω_c, it is a measurement of the kinetic energy of carriers:

$$\int_0^{\omega_c} \sigma_1(\omega)d\omega = -\frac{\pi}{2}\frac{e^2a^2}{\hbar^2 V}E_{kin}, \qquad [3.10]$$

where a is the in-plane lattice constant and V the unit cell volume. Equation 3.10 is valid when ω_c is smaller than the charge transfer energy, yet larger than the conduction bandwidth. It is important to note that in the superconducting state, Eq. 3.10 must include the δ function due to the superfluid formation. Also note the minus sign relating the spectral weight and E_{kin}.

In the superconducting state we can separate the optical conductivity into two terms:

$$\sigma_1^s(\omega) = \rho_s \delta(\omega) + \sigma_1^u(\omega), \qquad [3.11]$$

where the first term in the right-hand side represents the superfluid condensation and $\sigma_1^u(\omega)$ is the residual conductivity due to unpaired carriers. Using Eqs. 3.10 and 3.11 we can write the superfluid weight as a function of the variation in the kinetic energy and the differences between the normal and superconducting optical conductivities:

$$\rho_s + E_{kin}^s - E_{kin}^n = \int_{0^+}^{\omega_c} \left[\sigma_1^n(\omega) - \sigma_1^u(\omega)\right] d\omega = \Delta W(\omega_c), \qquad [3.12]$$

where the superscripts *n, s*, and *u* refer to normal, superconducting, and unpaired carriers in the superconducting state, respectively. Note that here the lower integration limit does not include the δ function in the superconducting state. Equation 3.12 also defines the quantity $\Delta W(\omega_c)$ and shows that the comparison of $\Delta W(\omega_c)$ to ρ_s gives information on the magnitude and sign of kinetic energy changes in the superconducting transition. For simplicity in the notation, the energies in Eq. 3.10 are measured in units of spectral weight.

BCS theory indicates that the fractional kinetic energy change at the transition is of the order $(\Delta/E_F)^2$, with Δ being the superconducting gap and E_F the Fermi energy (Deutscher *et al.*, 2005). In conventional superconductors, this estimation produces ΔE_{kin}~10^{-5}–10^{-8}, a value much too small to be detected experimentally. In the cuprates, the larger gap and smaller Fermi energy, leads to ΔE_{kin}~10^{-2}–10^{-3}, a much more manageable order of magnitude.

The first attempts to measure the kinetic energy changes across the superconducting transition were done along the c-axis. Figure 3.14 (a) shows the difference between normal and superconducting state spectral weight as a function of frequency along the c-axis of underdoped Tl2201 and YBCO (Basov *et al.*, 2001). At high enough energies these curves, according to Eq. 3.12, should saturate at $\rho_s + E_{kin}^s - E_{kin}^n$. The dashed line in this figure is the superfluid weight calculated from the imaginary part of the optical conductivity. In both cases it is much higher than the saturation values for ΔW representing a FGT (section 3.3.4) sum rule violation. Therefore, to respect Eq. 3.12, one must have $E_{kin}^s < E_{kin}^n$. The BCS behavior states that the kinetic energy always increases in the superconducting state (Marsiglio *et al.*, 2006). Here, the opposite is happening. The kinetic energy decreases when entering the superconducting state. On a second thought, despite BCS predictions, this is finally not completely unexpected. As the coherence length in cuprates is small, bringing carriers together increases their interaction (potential) energy. As the total energy of the superconducting state must decrease, the kinetic energy takes the bullet. This result, originally seen by Basov *et al.* (1999), gave support for the interlayer tunneling mechanism where the condensation energy comes from interlayer pair delocalization (Wheatley *et al.*, 1988). Unfortunately, the kinetic energy gain measured along the c-axis is two orders of magnitude too small to account for condensation.

Molegraaf *et al.* (2002) and Santander-Syro *et al.* (2003) showed that the FGT is also violated on the in-plane optical conductivity of Bi2212. Figure 3.14 (b)

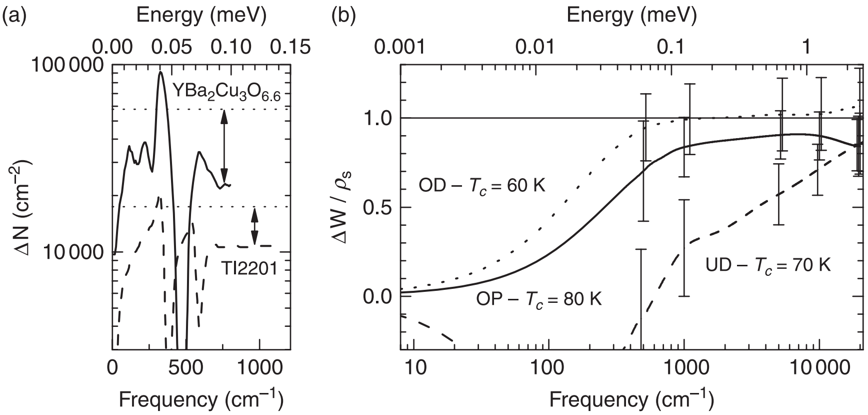

3.14 (a) FGT sum rule violation along the c-axis of optimally doped Tl2201 and underdoped YBCO shown by comparing the difference between the normal and superconducting state charge density (equivalent to the RSW) as a function of the upper cut-off frequency. The dotted lines are the values for the superfluid weight obtained from σ_2 [adapted from Basov *et al.* (2001)]. (b) The difference between the normal and superconducting state RSW as a function of the upper cut-off frequency for Bi2212 films from the underdoped to the overdoped regime. The curves are normalized to the superfluid weight obtained from σ_2 [adapted from Santander-Syro *et al.* (2004)].

Fig. 3.14 shows the difference in the spectral weights of the normal and the superconducting states normalized to the superfluid weight for Bi2212. In optimally and overdoped Bi2212, the FGT sum rule is fulfilled and, at a first glance, variations in the kinetic energy are too small to be detected. The situation is radically different in underdoped Bi2212. In this case, at 1 eV – a value representative of the bandwidth – the FGT sum rule is still not satisfied. The fact that ΔW is smaller than ρ_s implies that the kinetic energy decreases in the superconducting state. However here, on the ab-plane, the gain in kinetic energy is about 1 meV per Cu atom, much larger than the 0.25 meV/Cu condensation energy measured by Loram *et al.* (2001). These results show that an electronic mechanism, such as kinetic energy driven superconductivity (Hirsch, 2000), must be considered.

Another way to look at the kinetic energy change from the spectral weight is shown in Fig. 3.15 (a) (Carbone *et al.*, 2006). These figures show the total spectral weight (including the δ function in the superconducting state) integrated from 0 to 10 000 cm^{-1} for Bi2212 from underdoped to overdoped as a function of the temperature squared. In all cases the spectral weight increases (almost as a T^2 behavior as shown by the straight line) in the normal state. This means that the kinetic energy is decreasing with the temperature. Three different situations

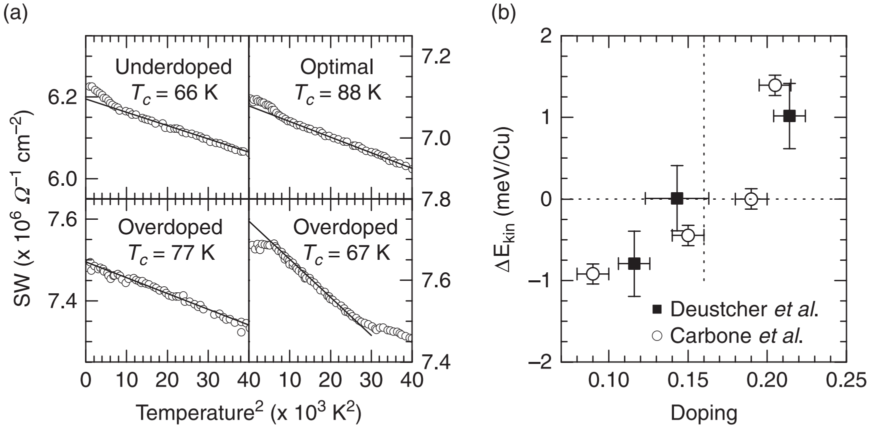

3.15 (a) The four panels show the spectral weight from 0 (including the superfluid weight in the superconducting state) to 10 000 cm^{-1} as a function of T^2 in Bi2212 at several dopings corresponding to the indicated T_c's. The straight lines are guides to the eye and help to visualize the changes in the RSW at T_c [adapted from Carbone *et al.* (2006)]. (b) The variation of the kinetic energy for several cuprates as a function of doping [adapted from Deutscher *et al.* (2005)]. The vertical dotted line indicates the position of optimal doping.
Panel (b) also includes data calculated from panel (a).

appear upon crossing the superconducting transition. In the underdoped (T_c = 66 K) and optimally doped T_c = 88 K the spectral weight increases faster below T_c. This corresponds to an extra decrease of kinetic energy as discussed above. For the overdoped T_c = 77 K sample, no change is seen at T_c, meaning neither gain nor loss of kinetic energy. Finally, the overdoped T_c = 67 K shows a spectral weight decreasing in the superconducting state. This is the 'conventional' BCS behavior of kinetic energy increasing below T_c. This change of regime had been remarked on a little earlier by Deutscher *et al.* (2005) as summarized in Fig. 3.15 (b). Coming from the underdoped to overdoped the kinetic energy gain at T_c becomes a kinetic energy loss. This is an effect that must be taken into account when describing superconductivity in cuprates. Deutscher and co-workers propose a Bose-Einstein condensate to BCS regime crossover near optimal doping, but this is still an open topic.

A brief, but necessary final remark on the sum rule is that much ado was made about the microscopic origins for the temperature T^2 evolution of the optical E_{kin} in the normal state. It turned out to be a non sequitur (Norman *et al.*, 2007). This shape depends more on the choice of the cut-off frequency and is not reproducible from sample to sample. However, the kinetic energy changes calculated from optics in the formation of the superconducting condensate remain valid (Marsiglio *et al.*, 2008).

3.5.3 The bosonic mode

The binding of a Cooper pair happens through the exchange of a boson by two electrons. BCS theory leans on the isotope effect to assign a phonon to this boson. It then uses an average value (e.g. the Debye frequency) for the phonon spectrum to calculate all superconducting properties. Eliashberg theory extended the BCS approach by introducing the full phonon spectrum $\alpha^2F(\omega)$ into the calculations (Carbotte, 1990). This function contains all the information pertinent to superconductivity. Yet the justification for the phonon exchange is based on the isotope effect present in classical superconductors. In principle, any boson and its generic $I^2\chi(\omega)$ spectral response could lead to pairing.

In his review, Carbotte showed that the $\alpha^2F(\omega)$ has been extensively and successfully obtained for BCS superconductors by inverting tunneling data. Farnworth and Timusk (1976) showed that the same function can be extracted from the far-infrared response of superconducting Pb, as in Fig. 3.16 (a). This possibility comes from the relation between the scattering rate and the bosonic function proposed by Shulga *et al.* (1991):

$$\tau_{op}^{-1}(\omega,T) = \tau_{imp}^{-1} + \int_0^\infty d\nu K(\omega,\nu,T) I^2\chi(\nu) \qquad [3.13]$$

where τ_{imp}^{-1} is a dirty limit impurity scattering, and $K(\omega,\nu,T)$ is a kernel that depends on the physics of the system. It can be as simple as $(\omega-\nu)$ for a metal at zero temperature. Kernels for finite temperature, *s*-wave and *d*-wave are also available (Schachinger *et al.*, 2008). The first attempts on solving Eq. 3.13 were carried out by Carbotte *et al.* (1999) on YBCO. Their approach was based on calculating the second derivative of $1/\tau$ (Marsiglio *et al.*, 1988). Dordevic *et al.* (2005) pushed the analysis further using inverse theory and obtained smoother solutions for $I^2\chi$. These solutions however, often contain negative unphysical regions. Schachinger *et al.* (2006) demonstrated that the use of maximum entropy techniques results in a positive defined $I^2\chi$.

Figure 3.16 (b) shows $I^2\chi$ for optimally doped PCCO as well as the scattering rate used in the inversion (Schachinger *et al.*, 2008). This figure illustrates very nicely that peaks in the bosonic spectral function correspond to a change in the slope of the scattering rate. Even subtle changes as the one observed around 125 meV produce marked features in $I^2\chi$. Note that the shoulder in $1/\tau$, around 75 meV, corresponds to a minimum rather than a peak in $I^2\chi$. Remembering that $1/\tau$ is related to the imaginary part of the self-energy, panel (c) shows an interesting property of the real part of the self-energy. The dashed curve is the $I^2\chi$ function calculated for Hg1201 at 29 K (Yang *et al.*, 2009). The solid line is the real part of the optical self-energy in the superconducting state, recalculated from the $I^2\chi$ shown. The dotted line uses the same $I^2\chi$ to calculate the normal state response but, as it is in the normal state, it requires a different kernel in Eq. 3.13. The peak around 100 meV in the superconducting curve disappears above T_c. In the superconducting state, this peak

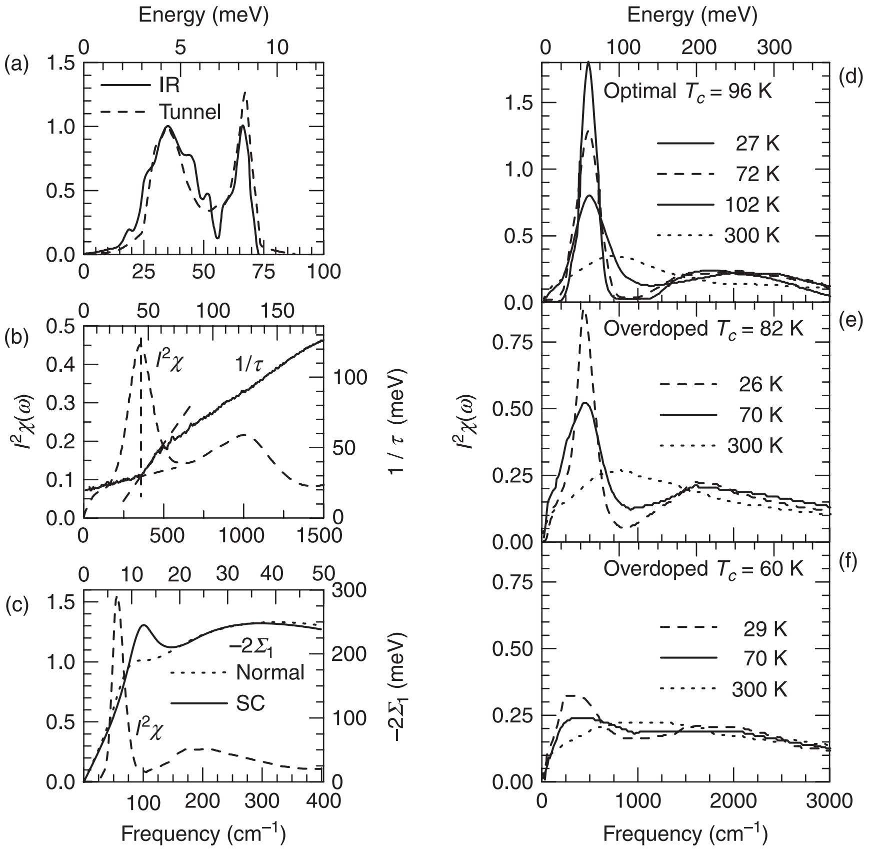

3.16 Panel (a) shows the $\alpha^2F(\omega)$ Eliashberg function obtained for Pb from tunnel and infrared data [adapted from Farnworth and Timusk (1976)]. Panel (b) compares the features observed in the scattering rate of PCCO to the strong signatures in the bosonic function [adapted from Schachinger *et al.* (2008)]. Panel (c) compares the bosonic function to the mass enhancement factor in Hg1201 [adapted from Yang *et al.* (2009)]. Panels (d) to (f) show the evolution of $I^2\chi(\omega)$ in Bi2212 in the optimal and overdoped regimes for different temperatures [adapted from Hwang *et al.* (2007)].

is located at $\Omega + \Delta$, where Ω is the position of the sharp peak in the bosonic spectrum and Δ is the superconducting gap. This is a direct experimental way to determine the presence of low frequency structures in the bosonic spectrum.

Panels (d) to (f) show how the bosonic function evolves with temperature and doping in Bi2212 (Hwang *et al.*, 2007). These figures indicate that the resonance peak is built at the expense of spectral weight lost in the continuum and that it survives in the normal state. The question is then, What are the underlying bosonic excitations producing this spectrum?

Figure 3.17 is a step in the direction of understanding the origins of the bosonic spectrum. Panel (a) shows $I^2\chi$ for optimally doped PCCO at a few temperatures (Schachinger *et al.*, 2008). Panel (b) shows the same function for LSCO (Hwang *et al.*, 2008b). In both cases there is a large peak around 40 meV at all temperatures. But notice that another peak in the vicinity of 10 meV appears at low temperatures in both cases. The inset of panel (b) shows neutron scattering data for LSCO (Vignolle *et al.*, 2007). This neutron spectrum contains the same two peaks observed in optics. Panel (c), from Yang *et al.* (2009), summarizes the position of the resonance peak seen in the optical $I^2\chi$ for several compounds as a function of T_c. The first thing we observe is that the position of the peak scales wonderfully well with $6.3\ k_BT_c$ (dashed line). But we also see that the points are not far from the dotted line. This line is the position of the resonance mode seen in the inelastic neutron scattering data. The correlation between the optical Eliashberg 'glue' function and neutron scattering is striking. It is very important to note that the candidate for the 'glue' is not the resonance peak itself, as in some cases it disappears before T_c (Hwang *et al.*, 2004a). The important part of the bosonic

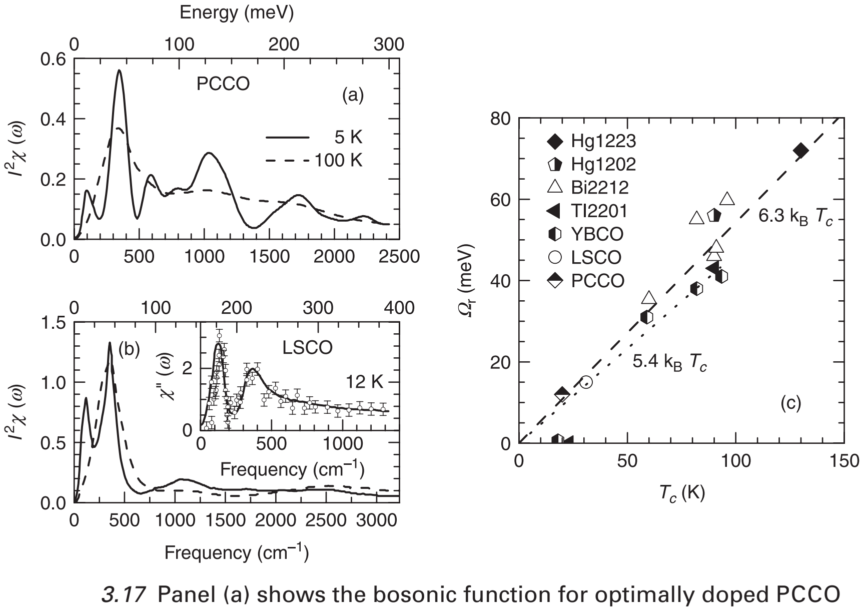

3.17 Panel (a) shows the bosonic function for optimally doped PCCO at different temperatures [adapted from Schachinger *et al.* (2008)]. Panel (b) shows the same function for LSCO [adapted from Hwang *et al.* (2008)] and its inset shows the neutron resonance [adapted from Vignolle *et al.* (2007)]. Panel (c) at the right shows the correlation between the position of the IR bosonic peak and the critical temperature. The dashed line is a best fit through the IR data and the dotted line is the behavior observed from neutron scattering data [adapted from Yang *et al.* (2009)].

spectrum is the continuum background. In fact the resonance peak spectral weight comes from this continuum.

The correlation between the optical $I^2\chi$ function and neutron data leaves no doubt that, in cuprates, carriers are coupled to spin fluctuations.

3.6 Future trends

Two events dominated the aftermath of the discovery of high-temperature superconductivity. They were the discovery of superconductivity in MgB_2 and in iron pnictides. Here I give a brief summary of the main findings in their optical conductivity.

3.6.1 MgB_2: two superconductors for the price of one

In 2001 Nagamatsu *et al.* (2001) blew away the record for T_c in a non copper-oxide when they found superconductivity at 39 K in MgB_2. The physics behind this material turned out be close to a conventional superconductor with optimized parameters (Choi *et al.*, 2002). Nevertheless, MgB_2 opened the door for the understanding of multi-band superconductivity at high temperatures. Indeed, this compound has two bands at the Fermi level and both go superconducting (Giubileo *et al.*, 2001; Liu *et al.*, 2001). The first important result coming out of the optical conductivity in MgB_2 (Tu *et al.*, 2001) was the observation that this material had a reasonably well behaved Drude response and strong correlation effects were not invited to the party. Guritanu *et al.* (2006) beautifully showed the consequences in the reflectivity and optical conductivity of the existence of two bands at the Fermi level. They found a large plasma edge shift depending on whether one probes the 3D character π band or the 2D character, higher electronic density, σ band. Although MgB_2 represented a breath of fresh air in the field, the real shake on superconductivity was yet to come.

3.6.2 Behind the iron curtain

The big turmoil in the field came in 2006. In the pre-high-T_c era, 'common sense' said that superconductivity and magnetism were mutually exclusive. Little did we know that Hosono's group would find superconductivity in another non-copper oxide material based, precisely, on iron (Kamihara *et al.*, 2006) and arsenic (Kamihara *et al.*, 2008). These so-called pnictides have already reached critical temperatures over 50 K (Liu *et al.*, 2008) and have a phase diagram which seems to be strongly driven by magnetism. A global picture of these materials is still not achieved. They are definitely more complex than conventional superconductors, but many successful theoretical predictions were made based on electronic structure calculations (Mazin, 2010). A generic phase diagram of iron pnictides is shown in Fig. 3.18 (a).

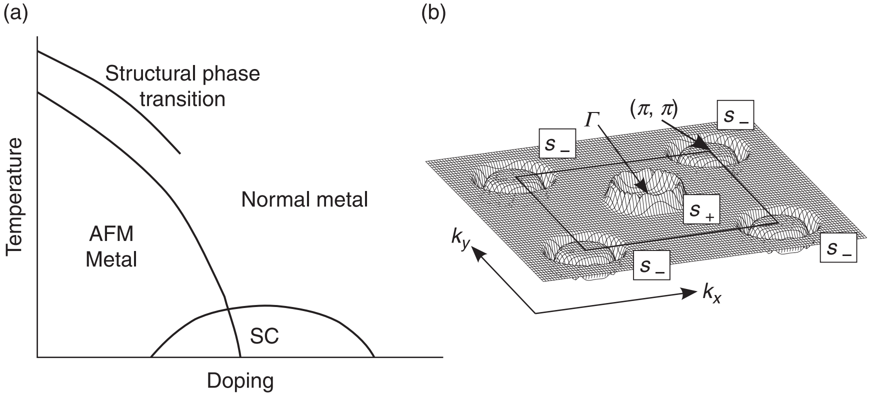

3.18 (a) Generic phase diagram for iron pnictide superconductors. One should not be fooled by its similar appearance to the cuprates phase diagram (Fig. 3.1). Here the parent compound is not a Mott insulator but rather an antiferromagnetic (AFM) metal. Just above, but close, to the AFM transition there is a structural phase transition from a high-temperature tetragonal symmetry to a low-temperature orthorhombic state. Also notice the overlap between the AFM state and the superconducting dome. Panel (b) depicts the main band positions in the Brillouin zone with the probable $s_{\pm}$ gap symmetry.

At first sight it is similar to the cuprates phase diagram (Fig. 3.1), but do not be fooled! The only real similarity is the existence of a superconducting dome when one varies the doping. Otherwise, the parent compound of pnictide superconductors is an antiferromagnetic metal (as opposed to a Mott insulator). In the normal state we find a structural tetragonal–orthorhombic phase transition happening at temperatures very close to the magnetic transition. The metallic state shows several bands crossing the Fermi level. This multi-band metal, already seen in MgB_2, leads to an interesting property in the superconducting state. The right-hand panel of Fig. 3.18 depicts schematically the location of the main bands in the Brillouin zone and the expected $s_{\pm}$ gap symmetry – the band at the Γ point has an s gap with a sign opposite to the s gap of the bands at (π,π). This gap phase change has not been proved, yet. However, many experimental hints, some from the optical conductivity as I will discuss below, indicate that this is the case.

These materials also show signs of electron–electron correlations as well as phase competition and coexistence. When a new superconductor is discovered, the first question to pop in the optical conductivity community is 'Can we see the gap?' The iron pnictides were not an exception. One of the obvious possibilities is to expect that, in a multi-band system, one can observe several gaps. The measured optical conductivity, however, do not show any clear multigap signature. Nevertheless, a single gap theoretical description does not fit the data either. There are propositions to describe the data using one (Li *et al.*, 2008), two (van Heuman *et al.*, 2009), or three gaps (Kim *et al.*, 2010) having values compatible with other techniques. Although no clear-cut picture emerges from this multigap fitting analysis, the $s_{\pm}$ symmetry allows for an interesting property. Chubukov *et al.* (2009) showed that (non-magnetic) impurity scattering can create nodes in the gap. The idea is that if carriers are scattered from a band having an s_+ gap to another having an s_- gap, they will annihilate each other. Impurity scattering can be pair-breaking. Panel (a) of Fig. 3.19 reproduces data from Gorshunov *et al.* (2010). The

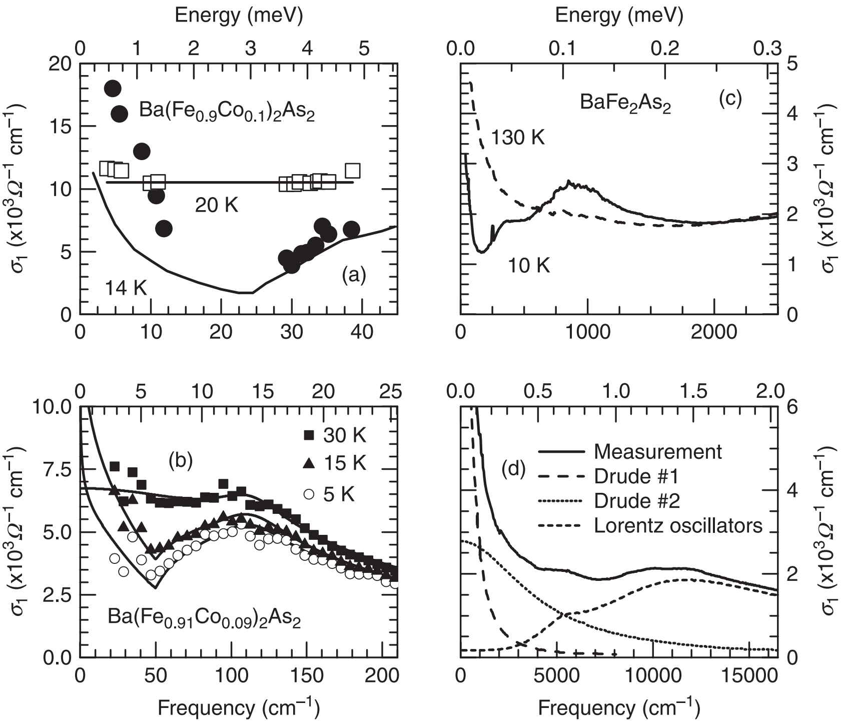

3.19 The left-hand panels show the far-infrared optical conductivity in the normal and superconducting states for Ba(Fe,Co)$_2$As$_2$. In panel (a) [adapted from Gorshunov *et al.* (2010)], the open squares are the normal state and the solid circles the superconducting response. The lines are fits to Drude and Mattis-Bardeen behaviors. Gorshunov *et al.* showed that a Mattis-Bardeen fit fails at low frequencies, the measured optical conductivity being larger. In panel (b) [from Lobo *et al.* (2010)], the low frequency discrepancy is resolved by adding an extra Drude peak in the superconducting state. This Drude response is the signature of pair-breaking due to impurity scattering. Panel (c) [adapted from Hu *et al.* (2008)], shows the density-wave-like gap corresponding to the magnetic transition in BaFe$_2$As$_2$. Panel (d) [from Chen *et al.* (2009)], shows that the description of the normal state optical conductivity of BaNi$_2$As$_2$ needs at least two Drude components. This seems to be a generic property of pnictides.

open squares represent the normal state optical conductivity and the solid circles the superconducting response. The lines are fits to Drude (normal state) and Mattis-Bardeen (superconducting) behaviors. Gorshunov and co-workers point out that although a gap seems to be present in the optical conductivity, the Mattis-Bardeen response fails at low frequencies. The data shows a residual conductivity that is much higher than that produced by thermally broken pairs. A possible solution for this problem is to admit that impurity scattering breaks pairs giving origin to an extra Drude peak in the superconducting state. The data by Lobo *et al.* (2010) shows that this approach describes the data perfectly. The presence of this Drude peak is only possible because of the $s_\pm$ gap symmetry.

The magnetic transition observed in the pnictides also has a marked optical conductivity signature as shown in panel (c) of Fig. 3.19. It behaves like a density-wave gap in the sense that there is a transfer of spectral from energies below the gap to energies above the gap (Hu *et al.*, 2008). This response is very similar to the one observed in electron-doped cuprates (panel (b) of Fig. 3.12) and is indicative of a Fermi surface reconstruction due to magnetic interactions.

Panel (d) of Fig. 3.19 illustrates the multi-band character of pnictides in a large energy scale. Chen *et al.* (2009) showed that the optical conductivity of $BaNi_2As_2$ can be described by a few Lorentz oscillators and two different Drude peaks, allegedly due to carriers from different bands. As shown by Wu *et al.* (2010), the presence of two Drude peaks is a generic feature observed in several families of pnictides.

Although magnetism plays an important role in pnictides, phonons cannot be ignored as they also have an unconventional behavior. Akrap *et al.* (2009) showed that upon crossing the structural phase transition a sharp drop in the 260 cm^{-1} (32 meV) phonon frequency is accompanied by an increase in its intensity. Akrap and co-workers argue that this behavior is a signature of Fe-As orbital ordering. Another intriguing phonon behavior was observed by Dong *et al.* (2010) who show that substituting La by heavier atoms Nd and Sm in LaFeAsO leads to phonon hardening instead of a conventional softening. This is indicative of a lattice renormalization. Dong and co-workers argue that as T_c is higher for the materials with the heavier atoms, electron–phonon coupling cannot be dismissed out of hand.

A final remark on the pnictides concerns the degree of correlation. These systems are expected to be in a moderate correlation region as Coulomb repulsion is neither negligible nor strong enough to localize carriers. In a single band superconductor, Millis *et al.* (2005) proposed a way to measure correlations comparing the spectral weight of the real part of the optical conductivity to values expected from band structure calculations. Although, strictly speaking, this method is only valid for a single band system, it is worth looking into the multiband pnictides. Qazilbash *et al.* (2009) compared and estimated the degree of electron–electron correlations in LaFePO and found a moderate, yet significant, level of correlations. After this promising result, it remains to be seen how this method to measure correlations can be adapted to multi-band superconductors.

3.6.3 Concluding remarks

During the past 20 years a full set of measurements on virtually any known superconducting material has been carried out. Yet the comprehension we have of superconductivity in cuprates is far from complete. In the past few years we have seen an increasing interest in probing the properties spanning the phase diagram working on the very same sample. This is a very difficult and time consuming task but it will surely enlighten our understanding on the physics of cuprates. The availability of very low-energy-probing techniques such as THz and direct measurement of far-infrared complex optical functions by ellipsometry are very promising. We are facing a time where cross-spectroscopy approaches involving optical conductivity, Raman, neutrons, STM and ARPES are unveiling the microscopic excitations pertinent to high-temperature superconductivity. The recent appearance of the new non-copper-based high-temperature pnictide superconductors is a very welcome boost to the field. Understanding this wealth of information from optical conductivity will represent a lot of our future work.

3.7 References

Akrap A, Tu J J, Li L J, Cao G H, Xu Z A, and Homes C C (2009). 'Infrared phonon anomaly in $BaFe_2As_2$.' *Phys Rev B*, **80**, 180502. doi:10.1103/PhysRevB.80.180502

Allen P B (1971). 'Electron–phonon effects in the infrared properties of metals.' *Phys Rev B*, **3**, 305–320. doi:10.1103/PhysRevB.3.305

Alloul H, Ohno T, and Mendels P (1989). 'Y^{89} NMR evidence for a Fermi-liquid behavior in $YBa_2Cu_3O_{6+x}$.' *Phys Rev Lett*, **63**, 1700–1703. doi:10.1103/PhysRevLett.63.1700

Anderson P W (1987). 'The resonating valence bond state in La_2CuO_4 and superconductivity.' *Science*, **235**, 1196–1198. doi:10.1126/science.235.4793.1196

Armitage N P, Lu D H, Kim C, Damascelli A, Shen K M, *et al.* (2001). 'Anomalous electronic structure and pseudogap effects in $Nd_{1:85}Ce_{0:15}CuO_4$.' *Phys Rev Lett*, **87**, 147003. doi:10.1103/PhysRevLett.87.147003

Ashcroft N W and Mermin N D (1976). *Solid State Physics*. Thomson Learning (College Edition), p. 252. ISBN 0–03–083993–3.

Basov D N, Homes C C, Singley E J, Strongin M, Timusk T, *et al.* (2001). 'Unconventional energetics of the pseudogap state and superconducting state in high-T_c cuprates.' *Phys Rev B*, **63**, 134514. doi:10.1103/PhysRevB.63.134514

Basov D N, Liang R, Dabrowski B, Bonn D A, Hardy W N, and Timusk T (1996). 'Pseudogap and charge dynamics in CuO_2 planes in YBCO.' *Phys Rev Lett*, **77**, 4090–4093. doi:10.1103/PhysRevLett.77.4090

Basov D N, Singley E J, and Dordevic S V (2002). 'Sum rules and electrodynamics of high-T_c cuprates in the pseudogap state.' *Phys Rev B*, **65**, 054516. doi:10.1103/PhysRevB.65.054516

Basov D N and Timusk T (2005). 'Electrodynamics of high-T_c superconductors.' *Rev Mod Phys*, **77**, 721–59. doi:10.1103/RevModPhys.77.721

Basov D N, Woods S I, Katz A S, Singley E J, Dynes R C, *et al.* (1999). 'Sum rules and interlayer conductivity of high-T_c cuprates.' *Science*, **283**, 49–52. doi:10.1126/science.283.5398.49

Bernhard C, Holden T, Golnik A, Lin C T, and Cardona M (2000). 'Far-infrared c-axis conductivity of flux-grown $Y_{1-x}Pr_xBa_2Cu_3O_7$ single crystals studied by spectral ellipsometry.' *Phys Rev B*, **62**, 9138–9142. doi:10.1103/PhysRevB.62.9138

Blumberg G, Koitzsch A, Gozar A, Dennis B S, Kendziora C A, *et al.* (2002). 'Nonmonotonic $d_{x^2-y^2}$ superconducting order parameter in $Nd_{2-x}Ce_xCuO_4$.' *Phys Rev Lett*, **88**, 107002. doi:10.1103/PhysRevLett.88.107002

Bonn D A, Garrett J D, and Timusk T (1988). 'Far-infrared properties of URu_2Si_2.' *Phys Rev Lett*, **61**, 1305–1308. doi:10.1103/PhysRevLett.61.1305

Calvani P, Capizzi M, Lupi S, Maselli P, Paolone A, and Roy P (1996). 'Polaronic optical absorption in electron-doped and hole-doped cuprates.' *Phys Rev B*, **53**, 2756–2766. doi:10.1103/PhysRevB.53.2756

Carbone F, Kuzmenko A B, Molegraaf H J A, van Heumen E, Lukovac V, *et al.* (2006). 'Doping dependence of the redistribution of optical spectral weight in $Bi_2Sr_2CaCu_2O_{8+\delta}$.' *Phys Rev B*, **74**, 064510. doi:10.1103/PhysRevB.74.064510

Carbotte J P (1990). 'Properties of boson-exchange superconductors.' *Rev Mod Phys*, **62**, 1027–1157. doi:10.1103/RevModPhys.62.1027

Carbotte J P, Schachinger E, and Basov D N (1999). 'Coupling strength of charge carriers to spin fluctuations in high-temperature superconductors.' *Nature*, **401**, 354–356. doi:10.1038/43843

Chen Z G, Xu G, Hu W Z, Zhang X D, Zheng P, *et al.* (2009). 'Origin of the structural phase transition in $BaNi_2As_2$ at 130 K: A combined study of optical spectroscopy and band structure calculations.' *Phys Rev B*, **80**, 094506. doi: 10.1103/PhysRevB.80.094506

Choi H J, Roundy D, Sun H, Cohen M L, and Louie S G (2002). 'The origin of the anomalous superconducting properties of MgB_2.' *Nature*, **418**, 758–760. doi:10.1038/nature00898

Chubukov A V, Vavilov M G, and Vorontsov A B (2009). 'Momentum dependence and nodes of the superconducting gap in the iron pnictides.' *Phys Rev B*, **80**, 140515. doi: 10.1103/PhysRevB.80.140515

Dagan Y, Qazilbash M M, Hill C P, Kulkarni V N, and Greene R L (2004). 'Evidence for a quantum phasetransition in $Pr_{2-x}Ce_xCuO_{4-\delta}$ from transport measurements.' *Phys Rev Lett*, **92**, 167001. doi:10.1103/PhysRevLett.92.167001

Damascelli A, Hussain Z, and Shen Z X (2003). 'Angle-resolved photoemission studies of the cuprate superconductors.' *Rev Mod Phys*, **75**, 473–541. doi:10.1103/RevModPhys.75.473

de Mello E V L and Caixeiro E S (2004). 'Effects of phase separation in the cuprate superconductors.' *Phys Rev B*, **70**, 224517. doi:10.1103/PhysRevB.70.224517

Degiorgi L, Thieme S, Alavi B, Grner G, McKenzie R H, *et al.* (1995). 'Fluctuation effects in quasi-one-dimensional conductors: Optical probing of thermal lattice fluctuations.' *Phys Rev B*, **52**, 5603–5610. doi:10.1103/PhysRevB.52.5603

Deutscher G, Santander-Syro A F, and Bontemps N (2005). 'Kinetic energy change with doping upon superfluid condensation in high-temperature superconductors.' *Phys Rev B*, **72**, 092504. doi:10.1103/PhysRevB.72.092504

Devereaux T P (2003). 'Optical symmetries and anisotropic transport in high-T_c superconductors.' *Phys Rev B*, **68**, 094503. doi:10.1103/PhysRevB.68.094503

Ding H, Norman M R, Campuzano J C, Randeria M, Bellman A F, *et al.* (1996). 'Angle-resolved photoemission spectroscopy study of the superconducting gap anisotropy in $Bi_2Sr_2CaCu_2O_{8+x}$.' *Phys Rev B*, **54**, R9678–R9681. doi:10.1103/PhysRevB.54.R9678

Dong T, Chen Z G, Yuan R H, Hu B F, Cheng B, and Wang N L (2010). 'Formation of partial gap below the structural phase transition and strong electron-phonon coupling effect in RFeAsO (R = La, Nd, and Sm).' arxiv:10050780v1

Dordevic S V, Homes C C, Tu J J, Valla T, Strongin M, *et al.* (2005). 'Extracting the electron-boson spectral function $\alpha^2 F(\omega)$ from infrared and photoemission data using inverse theory.' *Phys Rev B*, **71**, 104529. doi:10.1103/PhysRevB.71.104529

Dumm M, Basov D N, Komiya S, Abe Y, and Ando Y (2002). 'Electromagnetic response of static and fluctuating stripes in cuprate superconductors.' *Phys Rev Lett*, **88**, 147003. doi:10.1103/PhysRevLett.88.147003

Emery V J and Kivelson S A (1995). 'Superconductivity in bad metals.' *Phys Rev Lett*, **74**, 3253–3256. doi:10.1103/PhysRevLett.74.3253

Eom J H, Lee S S, Kim K S, and Salk S H S (2004). 'Origin of the hump structure in the in-plane optical conductivity of high-T_c cuprates based on a SU(2) slave-boson theory.' *Phys Rev B*, **70**, 024522. doi:10.1103/PhysRevB.70.024522

Farnworth B and Timusk T (1976). 'Phonon density of states of superconducting lead.' *Phys Rev B*, **14**, 5119–5120. doi:10.1103/PhysRevB.14.5119

Ferrell R A and Glover R E (1958). 'Conductivity of superconducting films: A sum rule.' *Phys Rev*, **109**, 1398–1399. doi:10.1103/PhysRev.109.1398

Fine B V (2004). 'Hypothesis of two-dimensional stripe arrangement and its implications for the superconductivity in high-T_c cuprates.' *Phys Rev B*, **70**, 224508. doi:10.1103/PhysRevB.70.224508

Fujii T, Terasaki I, Watanabe T, and Matsuda A (2002). 'Doping dependence of anisotropic resistivities in the trilayered superconductor $Bi_2Sr_2Ca_2Cu_3O_{10+\delta}$.' *Phys Rev B*, **66**, 024507. doi:10.1103/PhysRevB.66.024507

Giubileo F, Roditchev D, Sacks W, Lamy R, Thanh D X, *et al.* (2001). 'Two-gap state density in MgB_2: A true bulk property or a proximity effect?' *Phys Rev Lett*, **87**, 177008. doi:10.1103/PhysRevLett.87.177008

Gorshunov B, Wu D, Voronkov A A, Kallina P, Iida K, *et al.* (2010). 'Direct observation of the superconducting energy gap in the optical conductivity of the iron pnictide superconductor $Ba(Fe_{0.9}Co_{0.1})_2As_2$.' *Phys Rev B*, **81**. doi: 10.1103/PhysRevB.81.060509

Grüninger M, Münzel J, Gaymann A, Zibold A, Geserich H P, and Kopp T (1996). 'Spin-waves in the mid-infrared spectrum of antiferromagnetic $YBa_2Cu_3O_{6:0}$.' *Europhys Lett*, **35**, 55–60. doi:10.1209/epl/i1996–00530–3

Grüninger M, van der Marel D, Damascelli A, Zibold A, Geserich H P, *et al.* (1999). 'Charged magnons and magneto-elastic polarons in the mid-infrared spectrum of $YBa_2Cu_3O_6$.' *Physica C*, **317–318**, 286–291. doi:10.1016/S0921–4534(99)00070–2

Guritanu V, Kuzmenko A B, van der Marel D, Kazakov S M, Zhigadlo N D, and Karpinski J (2006). 'Anisotropic optical conductivity and two colors of MgB_2.' *Phys Rev B*, **73**, 104509. doi:10.1103/PhysRevB.73.104509

Hirsch J E (2000). 'Superconductivity from undressing.' *Phys Rev B*, **62**, 14487–14497. doi:10.1103/PhysRevB.62.14487

Homes C C, Dordevic S V, Gu G D, Li Q, Valla T, and Tranquada J M (2006a). 'Charge order, metallic behavior, and superconductivity in $La_{2-x}Ba_xCuO_4$ with $x = 1/8$.' *Phys Rev Lett*, **96**, 257002. doi:10.1103/PhysRevLett.96.257002

Homes C C, Lobo R P S M, Fournier P, Zimmers A, and Greene R L (2006b). 'Optical determination of the superconducting energy gap in electron-doped $Pr_{1:85}Ce_{0:15}CuO_4$.' *Phys Rev B*, **74**, 214515. doi:10.1103/PhysRevB.74.214515

Homes C C, Timusk T, Liang R, Bonn D A, and Hardy W N (1993). 'Optical conductivity of c axis oriented $YBa_2Cu_3O_{6.70}$: Evidence for a pseudogap.' *Phys Rev Lett*, **71**, 1645–1648. doi:10.1103/PhysRevLett.71.1645

Hu W Z, Dong J, Li G, Li Z, Zheng P, *et al.* (2008). 'Origin of the spin density wave instability in AFe_2As_2 (A = Ba,Sr) as revealed by optical spectroscopy.' *Phys Rev Lett*, **101**, 257005. doi:10.1103/PhysRevLett.101.257005

Hwang J, Carbotte J P, and Timusk T (2008a). 'Evidence for a pseudogap in underdoped $Bi_2Sr_2CaCu_2O_{8+d}$ and $YBa_2Cu_3O_{6.50}$ from in-plane optical conductivity measurements.' *Phys Rev Lett*, **100**, 177005. doi:10.1103/PhysRevLett.100.177005

Hwang J, Schachinger E, Carbotte J P, Gao F, Tanner D B, and Timusk T (2008b). 'Bosonic spectral density of epitaxial thin-film $La_{1:83}Sr_{0.17}CuO_4$ superconductors from infrared conductivity measurements.' *Phys Rev Lett*, **100**, 137005. doi:10.1103/PhysRevLett.100.137005

Hwang J, Timusk T, and Gu G D (2004a). 'High-transition-temperature superconductivity in the absence of the magnetic-resonance mode.' *Nature*, **427**, 714–717. doi:10.1038/nature02347

Hwang J, Timusk T, Puchkov A V, Wang N L, Gu G D, *et al.* (2004b). 'Marginal fermi liquid analysis of 300 k reflectance of $Bi_2Sr_2CaCu_2O_{8+\delta}$.' *Phys Rev B*, **69**, 094520. doi:10.1103/PhysRevB.69.094520

Hwang J, Timusk T, Schachinger E, and Carbotte J P (2007). 'Evolution of the bosonic spectral density of the high-temperature superconductor $Bi_2Sr_2CaCu_2O_{8+\delta}$.' *Phys Rev B*, **75**, 144508. doi:10.1103/PhysRevB.75.144508

Imada M, Fujimori A, and Tokura Y (1998). 'Metal-insulator transitions.' *Rev Mod Phys*, **70**, 1039–1263. doi:10.1103/RevModPhys.70.1039

Kaindl R A, Carnahan M A, Orenstein J, Chemla D S, Christen H M, *et al.* (2002). 'Far-infrared optical conductivity gap in superconducting MgB_2 films.' *Phys Rev Lett*, **88**, 027003. doi:10.1103/PhysRevLett.88.027003

Kamarás K, Herr S L, Porter C D, Tache N, Tanner D B, *et al.* (1990). 'In a clean high-T_c superconductor you do not see the gap.' *Phys Rev Lett*, **64**, 84–87. doi:10.1103/PhysRevLett.64.84

Kamihara Y, Hiramatsu H, Hirano M, Kawamura R, Yanagi H, *et al.* (2006). 'Iron-based layered superconductor: LaOFeP.' *J Am Chem Soc*, **128**, 10012–10013. doi:10.1021/ja063355c

Kamihara Y, Watanabe T, Hirano M, and Hosono H (2008). 'Iron-based layered superconductor $La[O_{1-x}F_x]FeAs$ (x = 0:05 – 0:12) with $T_c = 26$ K.' *J Am Chem Soc*, **130**, 3296–3297. doi:10.1021/ja800073m

Kim K W, Rössle M, Dubroka A, Malik V K, Wolf T, and Bernhard C (2010). 'Evidence for multiple superconducting gaps in optimally doped $BaFe_{1.87}Co_{0.13}As_2$ from infrared spectroscopy.' *Phys Rev B*, **81**, 214508. doi:10.1103/PhysRevB.81.214508

Kusar P, Demsar J, Mihailovic D, and Sugai S (2005). 'A systematic study of femtosecond quasiparticle relaxation processes in $La_{2-x}Sr_xCuO_4$.' *Phys Rev B*, **72**, 014544. doi:10.1103/PhysRevB.72.014544

LaForge A D, Padilla W J, Burch K S, Li Z Q, Dordevic S V, *et al.* (2007). 'Interlayer electrodynamics and unconventional vortex state in $YBa_2Cu_3O_y$.' *Phys Rev B*, **76**, 054524. doi:10.1103/PhysRevB.76.054524

Le Tacon M, Sacuto A, Georges A, Kotliar G, Gallais Y, *et al.* (2006). 'Two energy scales and two distinct quasiparticle dynamics in the superconducting state of underdoped cuprates.' *Nat Phys*, **2**, 537–543. doi:10.1038/nphys362

Lee P A (1999). 'Pseudogaps in underdoped cuprates.' *Physica C*, **317–318**, 194–204. doi:10.1016/S0921–4534(99)00059–3

Lee Y S, Segawa K, Li Z Q, Padilla W J, Dumm M, *et al.* (2005). 'Electrodynamics of the nodal metal state in weakly doped high-T_c cuprates.' *Phys Rev B*, **72**, 054529. doi:10.1103/PhysRevB.72.054529

Li G, Hu W Z, Dong J, Li Z, Zheng P, *et al.* (2008). 'Probing the superconducting energy gap from infrared spectroscopy on a $Ba_{0.6}K_{0.4}Fe_2As_2$ single crystal with $T_c = 37$ K.' *Phys Rev Lett*, **101**, 107004. doi:10.1103/PhysRevLett.101.107004

Liu A Y, Mazin I I, and Kortus J (2001). 'Beyond eliashberg superconductivity in MgB_2: Anharmonicity, two-phonon scattering, and multiple gaps.' *Phys Rev Lett*, **87**, 087005. doi:10.1103/PhysRevLett.87.087005

Liu R H, Wu G, Wu T, Fang D F, Chen H, *et al.* (2008). 'Anomalous transport properties and phase diagram of the FeAs-based $SmFeAsO_{1-x}F_x$ superconductors.' *Phys Rev Lett*, **101**, 087001. doi:10.1103/PhysRevLett.101.087001

Lobo R P S M, Bontemps N, Racah D, Dagan Y, and Deutscher G (2001). 'Pseudogap and superconducting condensate energies in the infrared spectra of Pr-doped $YBa_2Cu_3O_7$.' *Europhys Lett*, **55**, 854–860. doi:10.1209/epl/i2001–00360–9

Lobo R P S M, Dai Y M, Nagel U, Rõõm T, Carbotte J P, Timusk T, Forget A, and Colson D (2010). 'Optical signature of subgap absorption in the superconducting state of Ba (Fel-xCox) 2As2, *Phys Rev B*, **82**, 100506 (R) (2010). doi: 10.1103/PhysRevB.82.100506

Lobo R P S M, Li Z Z, and Raffy H (2009). 'The pseudogap energy and the number of CuO_2 planes.' Unpublished

Lobo R P S M, Sherman E Y, Racah D, Dagan Y, and Bontemps N (2002). 'Localization by disorder in the infrared conductivity of $Y_{1-x}Pr_xBa_2Cu_3O_7$ films.' *Phys Rev B*, **65**, 104509. doi:10.1103/PhysRevB.65.104509

Loram J W, Luo J, Cooper J R, Liang W Y, and Tallon J L (2001). 'Evidence on the pseudogap and condensate from the electronic specific heat.' *J Phys Chem Solids*, **62**, 59–64. doi:10.1016/S0022–3697(00)00101–3

Ma Y C and Wang N L (2006). 'Infrared scattering rate of overdoped $Tl_2Ba_2CuO_{6+\delta}$.' *Phys Rev B*, **73**, 144503. doi:10.1103/PhysRevB.73.144503

Markiewicz R S, Kusko C, and Kidambi V (1999). 'Pinned Balseiro-Falicov model of tunnelling and photoemission in the cuprates.' *Phys Rev B*, **60**, 627–644. doi:10.1103/PhysRevB.60.627

Marsiglio F, Carbone F, Kuzmenko A B, and Dvan der Marel A B (2006). 'Intraband optical spectral weight in the presence of a van Hove singularity: Application to $Bi_2Sr_2CaCu_2O_{8+\delta}$.' *Phys Rev B*, **74**, 174516. doi:10.1103/PhysRevB.74.174516

Marsiglio F, Schossmann M, and Carbotte J P (1988). 'Iterative analytic continuation of the electron self-energy to the real axis.' *Phys Rev B*, **37**, 4965. doi:10.1103/PhysRevB.37.4965

Marsiglio F, van Heumen E, and Kuzmenko A B (2008). 'Impact of a finite cut-off for the optical sum rule in the superconducting state.' *Phys Rev B*, **77**, 144510. doi:10.1103/PhysRevB.77.144510

Matsui H, Terashima K, Sato T, Takahashi T, Fujita M, and Yamada K (2005). 'Direct observation of a nonmonotonic $d_{x^2-y^2}$-wave superconducting gap in the electron-doped high-T_c superconductor $Pr_{0:89}LaCe_{0:11}CuO_4$.' *Phys Rev Lett*, **95**, 017003. doi:10.1103/PhysRevLett.95.017003

Mattis D C and Bardeen J (1958). 'Theory of the anomalous skin effect in normal and superconducting metals.' *Phys Rev*, **111**, 412–417. doi:10.1103/PhysRev.111.412

Mazin I I (2010). 'Superconductivity gets an iron boost.' *Nature*, **464**, 183–186. doi: 10.1038/nature08914

Mertelj T, Kuscer D, Kosec M, and Mihailovic D (2000). 'Photoinduced infrared absorption in $(La_{1-x}Sr_xMn)_{1-\delta}O_3$: Changes of the small polaron binding energy with doping.' *Phys Rev B*, **61**, 15102–15107. doi:10.1103/PhysRevB.61.15102

Millis A J, Zimmers A, Lobo R P S M, Bontemps N, and Homes C C (2005). 'Mott physics and the optical conductivity of electron-doped cuprates.' *Phys Rev B*, **72**, 224517. doi:10.1103/PhysRevB.72.224517

Molegraaf H J A, Presura C, van der Marel D, Kes P H, and Li M (2002). 'Superconductivity-induced transfer of in-plane spectral weight in $Bi_2Sr_2CaCu_2O_{8+\delta}$.' *Science*, **295**, 2239–2241. doi:10.1126/science.1069947

Motoyama E M, Yu G, Vishik I M, Vajk O P, Mang P K, and Greven M (2007). 'Spin correlations in the electron-doped high-transition-temperature superconductor $Nd_{2-x}Ce_xCuO_4$.' *Nature*, **445**, 186–189. doi:10.1038/nature05437

Nagamatsu J, Nakagawa N, Muranaka T, Zenitani Y, and Akimitsu J (2001). 'Superconductivity at 39 K in magnesium diboride.' *Nature*, **410**, 63–64. doi:10.1038/33105

Norman M R, Chubukov A V, van Heumen E, Kuzmenko A B, and van der Marel D (2007). 'Optical integral in the cuprates and the question of sum-rule violation.' *Phys Rev B*, **76**, 220509. doi:10.1103/PhysRevB.76.220509

Norman M R, Ding H, Randeria M, Campuzano J C, Yokoya T, *et al.* (1998). 'Destruction of the Fermi surface in underdoped high-T_c superconductors.' *Nature*, **392**, 157–160. doi:10.1038/32366

Onose Y, Taguchi Y, Ishikawa T, Shinomori S, Ishizaka K, and Tokura Y (1999). 'Anomalous pseudogap formation in a nonsuperconducting crystal of $Nd_{1:85}Ce_{0.15}CuO_{4+y}$: Implication of charge ordering.' *Phys Rev Lett*, **82**, 5120–5123. doi:10.1103/PhysRevLett.82.5120

Onose Y, Taguchi Y, Ishizaka K, and Tokura Y (2001). 'Doping dependence of pseudogap and related charge dynamics in $Nd_{2-x}Ce_xCuO_4$.' *Phys Rev Lett*, **87**, 217001. doi:10.1103/PhysRevLett.87.217001

Onose Y, Taguchi Y, Ishizaka K, and Tokura Y (2004). 'Charge dynamics in underdoped $Nd_{2-x}Ce_xCuO_4$: Pseudogap and related phenomena.' *Phys Rev B*, **69**, 024504. doi:10.1103/PhysRevB.69.024504

Orenstein J, Thomas G A, Millis A J, Cooper A S, Rapkine D H, *et al.* (1990). 'Frequency- and temperature-dependent conductivity in $YBa_2Cu_3O_{6+x}$ crystals.' *Phys Rev B*, **42**, 6342–6362. doi:10.1103/PhysRevB.42.6342

Padilla W J, Lee Y S, Dumm M, Blumberg G, Ono S, *et al.* (2005). 'Constant effective mass across the phase diagram of high-T_c cuprates.' *Phys Rev B*, **72**, 060511. doi:10.1103/PhysRevB.72.060511

Puchkov A V, Basov D N, and Timusk T (1996). 'The pseudogap state in high-T_c superconductors: an infrared study.' *J Phys: Condens Matter*, **8**, 10049–10082. doi:10.1088/0953–8984/8/48/023

Qazilbash M M, Hamlin J J, Baumbach R E, Zhang L, Singh D J, *et al.* (2009). 'Electronic correlations in the iron pnictides.' *Nature Phys*, **5**, 647–650. doi: 10.1038/nphys1180

Quijada M A, Tanner D B, Kelley R J, Onellion M, Berger H, and Margaritondo G (1999). 'Anisotropy in the ab-plane optical properties of $Bi_2Sr_2CaCu_2O_8$ single-domain crystals.' *Phys Rev B*, **60**, 14917–14934. doi:10.1103/PhysRevB.60.14917

Santander-Syro A F, Lobo R P S M, Bontemps N, Konstantinovic Z, Li Z, and Raffy H (2002). 'Absence of a loss of in-plane infrared spectral weight in the pseudogap regime of $Bi_2Sr_2CaCu_2O_{8+\delta}$.' *Phys Rev Lett*, **88**, 097005. doi:10.1103/PhysRevLett.88.097005

Santander-Syro A F, Lobo R P S M, Bontemps N, Konstantinovic Z, Li Z Z, and Raffy H (2003). 'Pairing in cuprates from high-energy electronic states.' *Europhys Lett*, **62**, 568–574. doi:10.1209/epl/i2003–00388–9

Santander-Syro A F, Lobo R P S M, Bontemps N, Lopera W, Giratá D, *et al.* (2004). 'In-plane electrodynamics of the superconductivity in $Bi_2Sr_2CaCu_2O_{8+\delta}$: Energy scales and spectral weight distribution.' *Phys Rev B*, **70**, 134504. doi:10.1103/PhysRevB.70.134504

Schachinger E, Homes C C, Lobo R P S M, and Carbotte J P (2008). 'Multiple bosonic mode coupling in the charge dynamics of the electron-doped superconductor $Pr_{2-x}Ce_xCuO_4$.' *Phys Rev B*, **78**, 134522. doi:10.1103/PhysRevB.78.134522

Schachinger E, Neuber D, and Carbotte J P (2006). 'Inversion techniques for optical conductivity data.' *Phys Rev B*, **73**, 184507. doi:10.1103/PhysRevB.73.184507

Shulga S V, Dolgov O V, and Maksimov E G (1991). 'Electronic states and optical spectra of HTSC with electron-phonon coupling.' *Physica C*, **178**, 266. doi:10.1016/0921–4534(91)90073–8

Singley E J, Basov D N, Kurahashi K, Uefuji T, and Yamada K (2001). 'Electron dynamics in $Nd_{1:85}Ce_{0.15}CuO_{4+\delta}$: Evidence for the pseudogap state and unconventional c-axis response.' *Phys Rev B*, **64**, 224503. doi:10.1103/PhysRevB.64.224503

Somal H S, Feenstra B J, Schützmann J, Hoon Kim J, Barber Z H, *et al.* (1996). 'Grazing incidence infrared reflectivity of $La_{1.85}Sr_{0.15}CuO_4$ and NbN.' *Phys Rev Lett*, **76**, 1525–1528. doi:10.1103/PhysRevLett.76.1525

Takenaka K, Shiozaki R, and Sugai S (2002). 'Charge dynamics of a double-exchange ferromagnet $La_{1-x}Sr_xMnO_3$.' *Phys Rev B*, **65**, 184436. doi:10.1103/PhysRevB.65.184436

Takigawa M, Reyes A P, Hammel P C, Thompson J D, Heffner R H, *et al.* (1991). 'Cu and O NMR studies of the magnetic properties of $YBa_2Cu_3O_{6.63}$ (T_c = 62 K).' *Phys Rev B*, **43**, 247–257. doi:10.1103/PhysRevB.43.247

Tanner D B and Timusk T (1992). *Physical Properties of High Temperature Superconductors III*. World Scientific, Singapore, pp. 363–469.

Timusk T and Statt B (1999). 'The pseudogap in high-temperature superconductors: an experimental survey.' *Rep Prog Phys*, **62**, 61–122. doi:10.1088/0034–4885/62/1/002

Timusk T and Tanner D B (1989). *Physical Properties of High Temperature Superconductors I*. World Scientific, Singapore, pp. 339–407.

Tinkham M and Ferrell R A (1959). 'Determination of the superconducting skin depth from the energy gap and sum rule.' *Phys Rev Lett*, **2**, 331–333. doi:10.1103/PhysRevLett.2.331

Tsuei C C, Kirtley J R, Chi C C, Yu-Jahnes L S, Gupta A, *et al.* (1994). 'Pairing symmetry and flux quantization in a tricrystal superconducting ring of $YBa_2Cu_3O_{7-\delta}$.' *Phys Rev Lett*, **73**, 593–596. doi:10.1103/PhysRevLett.73.593

Tu J J, Carr G L, Perebeinos V, Homes C C, Strongin M, *et al.* (2001). 'Optical properties of c-axis oriented superconducting MgB_2 films.' *Phys Rev Lett*, **87**, 277001. doi:10.1103/PhysRevLett.87.277001

van Heuman E, Huang Y, de Jong S, Kuzmenko A B, Golden M S, and van der Marel D (2009). 'Optical properties of $BaFe_{2-x}Co_xAs_2$.' arxiv:09120636v1

Varma C M (2000). 'Proposal for an experiment to test a theory of high-temperature superconductors.' *Phys Rev B*, **61**, R3804–R3807. doi:10.1103/PhysRevB.61.R3804

Varma C M, Littlewood P B, Schmitt-Rink S, Abrahams E, and Ruckenstein A E (1989). 'Phenomenology of the normal state of cu-o high-temperature superconductors.' *Phys Rev Lett*, **63**, 1996–1999. doi:10.1103/PhysRevLett.63.1996

Varma C M, Nussinov Z, and van Saarloos W (2002). 'Singular or non-Fermi liquids.' *Phys Rep*, **361**, 267–417. doi:10.1016/S0370–1573(01)00060–6

Vignolle B, Hayden S M, McMorrow D F, Ronnow H M, Lake B, *et al.* (2007). 'Two energy scales in the spin excitations of the high-temperature superconductor $La_{2-x}Sr_xCuO_4$.' *Nat Phys*, **3**, 163–167. doi:10.1038/nphys546

Warren W W, Walstedt R E, Brennert G F, Cava R J, Tycko R, *et al.* (1989). 'Cu spin dynamics and superconducting precursor effects in planes above T_c in $YBa_2Cu_3O_{6.7}$.' *Phys Rev Lett*, **62**, 1193–1196. doi:10.1103/PhysRevLett.62.1193

Watanabe T, Fujii T, and Matsuda A (2000). 'Pseudogap in $Bi_2Sr_2CaCu_2O_{8+\delta}$ studied by measuring anisotropic susceptibilities and out-of-plane transport.' *Phys Rev Lett*, **84**, 5848–5851. doi:10.1103/PhysRevLett.84.5848

Wheatley J M, Hsu T C, and Anderson P W (1988). 'Interlayer pair hopping: Superconductivity from the resonating-valence-bond state.' *Phys Rev B*, **37**, 5897–5900. doi:10.1103/PhysRevB.37.5897

Wu D, Barišić N, Kallina P, Faridian A, Gorshunov B, *et al.* (2010). 'Optical investigations of the normal and superconducting states reveal two electronic subsystems in iron pnictides.' *Phys Rev B*, **81**, 100512. doi: 10.1103/PhysRevB.81.100512

Yang J, Hwang J, Schachinger E, Carbotte J P, Lobo R P S M, *et al.* (2009). 'Exchange boson dynamics in cuprates: Optical conductivity of $HgBa_2CuO_{4+\delta}$.' *Phys Rev Lett*, **102**, 027003. doi:10.1103/PhysRevLett.102.027003

Zhu Z T, Musfeldt J L, Teweldemedhin Z S, and Greenblatt M (2002). 'Anisotropic ab-plane optical response of the charge-density-wave superconductor $P_4W_{14}O_{50}$.' *Phys Rev B*, **65**, 214519. doi:10.1103/PhysRevB.65.214519

Zimmermann W, Brandt E, Bauer M, Seiderc E, and Genzel L (1991). 'Optical conductivity of BCS superconductors with arbitrary purity.' *Physica C*, **183**, 99–104. doi:10.1016/0921–4534(91)90771-P

Zimmers A, Lobo R P S M, Bontemps N, Homes C C, Barr M C, *et al.* (2004). 'Infrared signature of the superconducting state in $Pr_{2-x}Ce_xCuO_4$.' *Phys Rev B*, **70**, 132502. doi:10.1103/PhysRevB.70.132502

Zimmers A, Tomczak J M, Lobo R P S M, Bontemps N, Hill C P, *et al.* (2005). 'Infrared properties of electron-doped cuprates: Tracking normal-state gaps and quantum critical behavior in $Pr_{2-x}Ce_xCuO_4$.' *Europhys Lett*, **70**, 225–231. doi:10.1209/epl/i2004–10480–2

4

Sputter deposition of large-area double-sided YBCO superconducting films

J. XIONG, B. TAO, and Y. LI, University of Electronic
Science and Technology of China, China

Abstract: Research in the field of high-temperature superconducting films has progressed from the study of their basic chemistry and structure, to a point where an enormous range of desirable properties are being explored for device applications. This review focuses on the synthesis and properties of large-area double-sided $YBa_2Cu_3O_{7-\delta}$ (YBCO) films and thickness-dependent superconductivity.

Double-sided YBCO thin films were prepared by sputter deposition. In order to achieve good performance and lateral homogeneity of large-area (up to 3-inch) films for multi-pole devices or low frequency application, we developed a special modulated biaxial rotation by designing a special substrate clamp, combining the out-of-plane rotation with an automatic interval in-plane rotation, and simultaneously changing the rotation speed periodically in every out-of-plane revolution (namely, modulated biaxial rotation). The biaxial rotation and its development was also used to partially avoid the negative oxygen ion bombardment that resulted from the plate target geometry. The high-quality YBCO thin films were deposited on the various single-crystal substrates such as $LaAlO_3$, $SrTiO_3$, MgO with typical electronic properties: superconducting transition temperature (T_c) 90 K, critical current density (J_c) 2–4 MA/cm^2 at 77 K in self-field and microwave surface resistance (R_s) 0.5 $\mu\Omega$ for 10 GHz at 77 K, which were successfully applied to prepare high performance microwave devices including resonators, oscillators, and filters.

In this chapter, the thickness dependence on residual stress and superconducting properties in YBCO films was also investigated. The results demonstrated that the values of T_c and J_c were strongly dependent on the film thickness. This chapter outlines the reasons underlying the calculation of residual stress in films and demonstrates the levels of control that are now possible.

Key words: double-sided $YBa_2Cu_3O_{7-\delta}$ (YBCO) films, sputtering, large-area, uniformity, thickness dependence.

4.1 Introduction

The discovery of the cuprates high-temperature superconductor (HTS) of $YBa_2Cu_3O_{7-\delta}$ (YBCO) in 1986, marked the beginning of a new era in the theoretical value of solid state physics in general, sparked great interest in the use of HTS materials in practical applications (such as microwave devices, transmission lines, motors, and generators),[1–4] raised an unprecedented scientific euphoria and challenged research in a class of complicated compounds, which otherwise would only have been encountered on the classical research route of systematic investigation with gradual increase of materials complexity far in the future. With the exception of semiconductors, no other class of materials has been so thoroughly investigated by thousands of researchers worldwide.

Since their discovery, cuprate HTS samples have greatly improved in terms of material quality, and can in fact nowadays be prepared in a remarkably reproducible way. The extent of the enormous worldwide effort that has contributed to this achievement can be understood simply from the more than 150 000 articles that have been published on cuprate high-T_c superconductivity in this period.

The development of technically applicable HTS materials has progressed along several routes. Almost all the thin film deposition methods, including evaporation,[5,6] sputtering,[7–10] pulsed laser deposition (PLD),[11–13] molecular beam epitaxy (MBE),[14,15] metal-organic chemical vapor deposition (MOCVD),[16,17] chemical solution deposition (CSD),[18,19] and so on, have been used for preparing YBCO thin films in the last 20 years. Most of these methods can be used to produce high quality epitaxial YBCO thin films with excellent superconducting properties (transition temperature $T_c > 90$ K; critical current density J_c (77 K, 0 T) $> 10^6$ A/cm^2; microwave surface resistance R_s (77 K, 10 GHz) $< 500\ \mu\Omega$) that are well suited to superconductive electronics.

Of all the deposition methods, we know that the co-evaporation technique, developed by a group in the Technical University of Munich, has been commercialized by THEVA and their YBCO thin films have been sold worldwide.[6] This method has a very high deposition rate and can easily be scaled up. It can deposit film on as large as ∅200 mm substrate or several small substrates in one run. The oxygen pocket technique[20] is also impressive. Pulsed laser deposition (PLD) is another fast method, and often used in laboratories.[11–13] With source scan or substrate rotation,[11,15,20,21] uniform films of up to three inches can be deposited. Sputtering is an old method in YBCO thin film preparation when compared with the co-evaporation and PLD. Though the deposition rate is relatively low due to the low sputtering yield on oxide targets, this method can easily be scaled up to industrial level, simply by installing a large size target or multi-targets in the system, or by enlarging the substrate-to-target distance.

YBCO HTS thin films on low dielectric loss substrates are suitable candidates for applications in commercial and military microwave filter systems. There are a huge number of projects, across many countries, to develop microwave devices using HTS thin films, and some HTS subsystems have already been applied in this field real market.[22–25] In devices such as microwave stripline filters, a superconducting ground could reduce as much as 30% insertion loss compared with a metal ground.[26] Therefore, double-sided film is better than single-sided. With every method, the double-sided film can be deposited side by side, in other words, the substrate is turned off and coated again after the first side is finished.[5,11–13] And in this case, a simple planar heater with uniform temperature distribution is good enough. But the overheating of the first side during the second side deposition may cause the quality of the film to deteriorate, so simultaneous deposition is preferable in order to maintain side-to-side equality. Geerk *et al.*[27] developed simultaneous sputtering deposition systems with opposite cylindrical targets and a box-like heater for large-area films. They have prepared 2–3 inch films with good lateral uniformity and side-to-side equality by using off-axis in-plane substrate rotation. A highly reproducible sputter process for large-area 3-inch diameter and double-sided YBCO films on various single crystal substrates such as $LaAlO_3$, sapphire and MgO for microwave applications has also been developed and is continuously being improved at the University of Electronic Science and Technology of China.[28–30] The electrical and microwave performance of these sputtered YBCO films is comparable to high-quality films deposited by other techniques such as thermal coevaporation[31] and PLD.[32]

However, it is relatively difficult to obtain a uniform thickness distribution for large-area YBCO thin films using the sputtering method. Due to the variation of source-to-sink distance and the different angular distribution of atom emissions, the deposition rate on different places of a substrate cannot be a constant. Generally, in order to meet the requirements of microwave application, the deviation should be less than 10% on a 3-inch wafer. An enormous amount of theoretical and experimental results about how to deposit uniform large-area thin films has been obtained.[33–37]

At the same time, microwave applications require film thickness to be a few times greater than the London penetration depth λ_L, otherwise the microwave signal losses increase. The λ_L is roughly 140–180 nm[38] for a perfect crystal along the c axis of the unit cell, and is considerably greater in real films because of their structural imperfections, i.e., point defects, grain boundaries, etc. This means that films with satisfactory quality must be obtained with thickness over 0.5 μm.[39] Furthermore, the second-generation HTS YBCO wires under development using the ‘coated conductor’ approach are epitaxially deposited on metal tapes.[40–42] The deposition of YBCO films greater than 1 μm in thickness for achieving high critical current (I_c) while maintaining adequate J_c has been an elusive goal in producing commercially viable superconducting films. However, it has been reported that the J_c decreases rapidly as the thickness of epitaxial YBCO films increases.[43–49] There seems to be a universal trend towards an exponential drop in J_c with YBCO thickness, regardless of the deposition technique employed. For these reasons, the thickness dependence of the critical current density of YBCO films is complicated, and the optimum thickness of the superconducting layer will be different for different conditions of temperature, magnetic field and electric field, depending on the kind of application. Possible causes for the drop in J_c that have been reported in the literature include a transition to a-axis orientation,[43–45] a loss of in-plane and/or out-of-plane texture,[46,47] a decrease in the number of pinning sites,[48] and a change in the microstructure.[50]

Since the HTS deposition takes place at 650–900 °C, the thermal expansion coefficients of the substrates and the HTS films have to match, or else the different contraction of HTS film and substrate on cooling to room or even cryogenic temperature will lead to mechanical stress, which can only be tolerated by the film up to a certain maximum thickness without crack formation.[51] Many research results[52] have shown that the residual compressive stress may cause the film to delaminate from the substrate. The residual tensile stress may result in microcracks in the film, which perhaps is the reason for the drop in J_c. Hence, it is important to study residual stress in YBCO superconducting thin films, and also necessary to clarify all the mechanisms which influence the critical current properties and to find a method for estimating J_c for the optimum design of superconducting layer thickness in the case of each application.

This chapter has two main components. Section 4.4 introduces sputtering technique with a modulated biaxial rotation mode and describes the epitaxial growth of large area double-sided YBCO films. In section 4.5, the thickness dependence of YBCO films is studied in the range of 0.2–2 μm. The influence of thickness-induced residual stress on surface morphology and electrical properties is also investigated.

4.2 Sputter deposition technique

Sputtering is the process of removing atoms from the surface of a target by kinetic energy transferred from an incoming flux of highly energetic particles. This technique, in particular geometries or with specific deposition parameters, is able to stoichiometrically transfer the composition of the target to the growing film,[53,54] and this characteristic makes it highly suited to the growth of multi-element compounds such as complex oxides, with relative ease, compared to thermal processes such as evaporation and PLD.

A schematic of the electrode configuration for basic sputtering process is shown in Fig. 4.1. The source material or target is attached to the cathode. An electric field of sufficient strength is applied between the anode and cathode, causing the ionization of the gas between the electrodes. The gas is typically Ar, which is ionized to Ar^+. The Ar^+ ions are accelerated by the electric field towards the target, while electrons are attracted to the anode. The heavy Ar^+ ions bombard the target, transferring their kinetic energy to the target, and causing the atoms at or near the surface of the target to be ejected. The ejected target atoms are then collected onto a heated substrate.

The synthesis of HTS thin films generally involves problems such as multi-component control and negative-ion bombardment effect. In the case of oxide targets, it is found that when the cathode is a planar disc and the substrates are facing the cathode, the film composition deviates significantly from that of the target, the film thickness is unexpectedly small and, even for very low sputtering pressures, no film is deposited, although the substrate surface shows signs of sputter etching. These effects are due to the bombardment of the substrates with

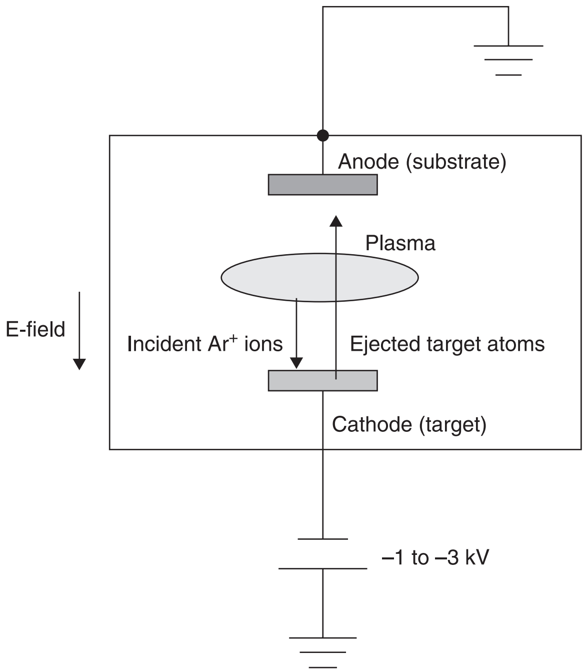

4.1 Schematic diagram of a basic sputtering system. The target is attached to the cathode, which is negatively biased compared to the rest of the system.

the negatively charged particles emerging from the cathode during deposition. Such particles (e.g., O^-, O~, BaO^-) are generated at the surface of the cathode, simply due to the fact that many of the sputtered species containing oxygen leave the cathode surface in a negatively charged state due to their strong electronegativity. The negatively charged species then are accelerated away from the cathode by the voltage gap of the cathode dark space in the sputtering discharge. In other words, the negative ions bombard the film surface with the same energy as the argon ions bombard the target surface.

There are, in principle, two technical possibilities of reducing these bombardment effects at the substrate position. The first possibility is to work with the sputtering gas at very high pressure (e.g., 400–600 Pa) in order to thermalize the fast particles before they reach the substrates. Unfortunately, this method will result in a significant reduction of the sputtering rate. The second possibility, which has been the most widely used since the discovery of the HTS, is to work in the commonly used gas pressure region (10–20 Pa) and to avoid substrate bombardment by proper choice of the position of the substrates. More strictly speaking, the substrate position is optimum at locations where the ratio of bombardment rate and deposition is minimized. For the planar magnetron, many experimenters found these positions to be in the center of the plasma ring with the substrates facing the target plane. Another possibility is to place the substrates outside of the plasma ring, at a suitable angle, in order to maximize the deposition rate, which is known as 'off-axis' geometry. In order to improve the uniformity of the film thickness distribution and deposition rate for off-axis geometry, it is possible to sputter from two opposing planar targets. In this case, the negative particles from one target sputter the opposite one and thus are easily neutralized by stripping, and proceed as neutral particles which are no longer influenced by electric or magnetic fields. This may serve to increase the deposition rate, at least at very low pressures. To further increase deposition rate, many opposing targets can be placed in a circle. The result is a tubelike target, called an 'inverted cylindrical target', as shown in Fig. 4.2.

Therefore, a single inverted cylindrical (IC) sputter gun is employed in our sputtering systems (shown schematically in Fig. 4.2) to simultaneously deposit YBCO thin films on both sides of the substrate. The substrate rotates in an out-of-plane mode in all of the deposition processes, which is driven by a speed adjustable motor through a magnet-coupled feed through. The rotation speed is controlled by the signal of position sensors. In fact, the biaxial rotation is also helpful in terms of partially avoiding negative oxygen ion bombardment.

In the beginning, we always isolated the substrate from the targets with shielding. In this way we could pre-sputter the YBCO target until it has a stable

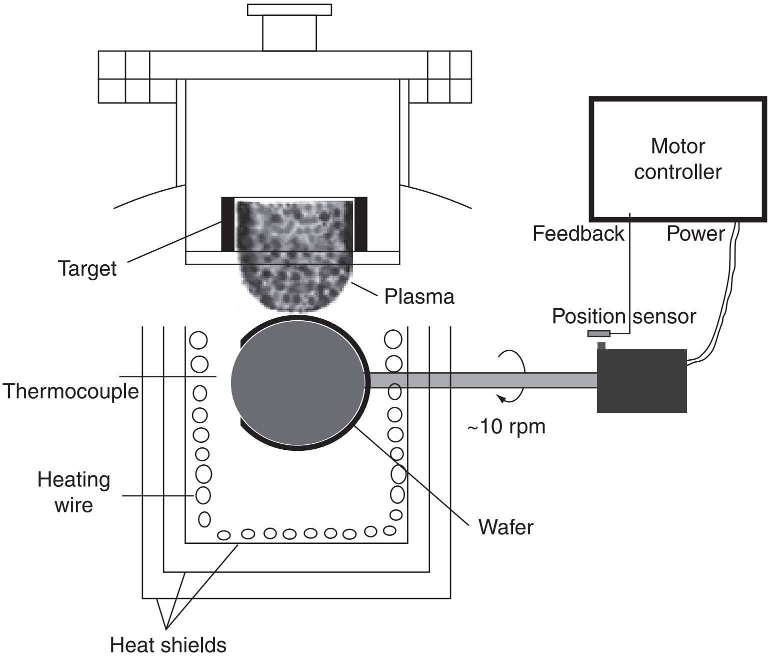

4.2 Schematics of IC sputtering systems for simultaneous deposition of large-area double-sided YBCO thin films.

Table 4.1 Deposition parameters for YBCO thin films

Sputtering power	100 W
Deposition rate	0.24 nm/min
Total pressure	45 Pa
O_2:Ar	1:2
Substrate temperature	800 °C
Substrate	≤76 mm
Target–substrate distance	50 mm
Dimension of the cylindrical target (inner surface)	∅50 mm × 40 mm
In-plane rotation speed	0.5 r/min
Average out-of-plane rotation speed	30 r/min
Modulation ratio	1–3

voltage and current. After the substrate was loaded, the heater was set to a fixed temperature. Then argon and oxygen were mixed and inlet into the chamber. The gas flow rates were adjusted with mass flow controllers. After pre-sputtering, we shifted the shielding away from the target and deposited for 36 hours with an inverted cylindrical target to achieve a 500 nm thin film. The deposition parameters are shown in Table 4.1. After the deposition, the sample was cooled down and kept at 400 °C in 1 atm oxygen for 30 minutes in order to fully transform the non-superconducting tetragonal phase into the superconducting orthogonal phase.

4.3 Epitaxial YBCO thin films

The growth of HTS thin films involves a specific optimization of the synthesis process in order to achieve optimum superconducting properties. Since HTS materials are multi-cation oxides with rather complex crystal structures, the general requirements for the formation of HTS films with little or no impurity phase include stringent control of the composition during the deposition process. Even with the correct cation composition, the formation of a specific HTS oxide phase requires an optimization of both the temperature and the oxygen partial pressure, consistent with the phase stability.

The epitaxial growth and characterization of YBCO thin films has received significantly more attention than any other HTS compound. Compared with other HTS materials, epitaxial YBCO films are the easiest to synthesize and to achieve a T_c for the film that is near the bulk value. This is partly due to the relative stability of the $YBa_2Cu_3O_7$ phase. The structure of $YBa_2Cu_3O_{7-\delta}$, shown schematically in Fig. 4.3, can be derived by stacking three oxygen-deficient perovskite unit cells ($ACuO_y$) in the layered sequence, BaO–CuO_2–$YCuO_2$–BaO–CuO. $YBa_2Cu_3O_7$ contains two CuO_2 planes per unit cell, separated by a Y atom. CuO chains lie between the BaO layers. The oxygen content can be varied from $\delta = 0$ to $\delta = 1$ through the removal of oxygen from the CuO chain layer.

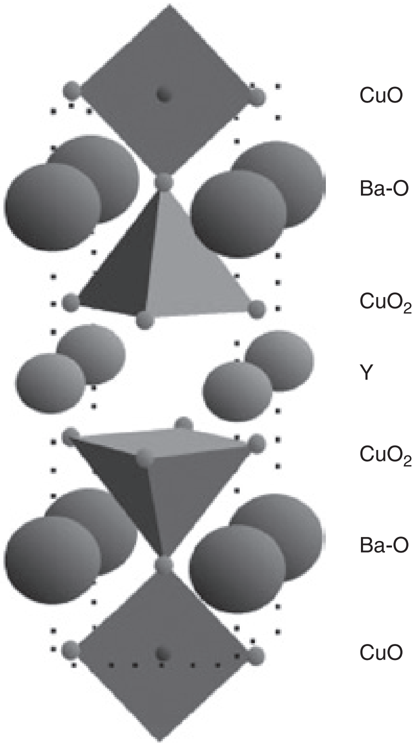

4.3 Unit cell of $YBa_2Cu_3O_7$.

Fully oxygenated $YBa_2Cu_3O_7$ is a hole-doped superconductor with $T_c = 92$ K. The crystal structure is orthorhombic with $a = 3.82$ Å, $b = 3.88$ Å, and $c = 11.68$ Å.[55] When the oxygen content decreases, namely δ is from 0 to 1, YBCO changes from an orthorhombic type to a tetragonal type with deteriorated superconducting properties.

Epitaxial YBCO thin films were successfully grown on different single-crystal substrates, such as $LaAlO_3$, MgO, $SrTiO_3$, and sapphire, with excellent crystal perfection using our sputter system. J_c of 2–4 MA/cm^2 at 77 K in self-filed and R_s lower than 200 $\mu\Omega$ for 10 GHz at 77 K is typical for high quality films. YBCO is less anisotropic than other hole-doped HTS materials. These collective properties make YBCO films quite attractive for many applications.

4.4 Issues related to scale-up

4.4.1 Large-area deposition

With simple out-of-plane rotation, uniform double-sided YBCO films could be realized only on a very small area, usually less than one inch with a reasonable substrate-to-target distance, $D_{s\text{-}t}$. Or else, a larger uniform area must be traded with a lower deposition rate with a longer $D_{s\text{-}t}$ or with an in-plane rotation or linear scan.

We designed a special biaxial rotation,[56] which combined the out-of-plane rotation and an automatic interval in-plane rotation (rolling might be better, driven by substrate weight) together, shown in Fig. 4.4. With this rotation, we could produce uniform double-sided films on 2-inch wafer without extending $D_{s\text{-}t}$ (kept at about 50 mm) so the deposition rate could be maintained. Taking into account the clamp shadowing effect, uniform 3-inch films were also prepared with a modulated biaxial rotation, in which the rotation speed was adjusted according to different substrate postures in every out-of-plane revolution. The schematics of speed-modulated biaxial rotation and the corresponding speed modulation regions are shown in Fig. 4.5. When the substrate faces the target, we promote its speed

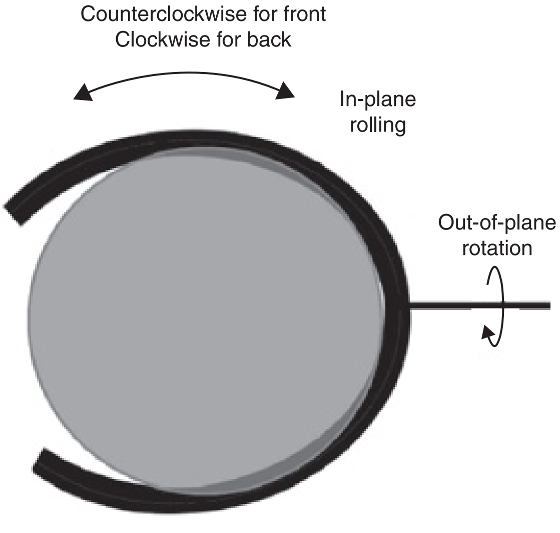
Counterclockwise for front
Clockwise for back
In-plane rolling
Out-of-plane rotation

4.4 Special clamp design for in-plane wafer rotation.

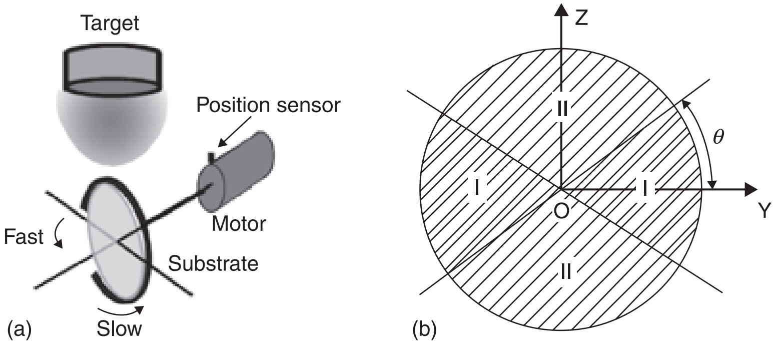
Target
Position sensor
Motor
Fast
Substrate
Slow
(a)
Z
II
θ
I
I
O
Y
II
(b)

4.5 (a) Schematic showing configuration with speed-modulated biaxial rotation; (b) regions for out-of-plane speed modulation.

and slow it down as its edge goes near to the target. By adjusting the speed ratio in the two regions, shown in Fig. 4.5(b), we can modulate the lateral thickness distribution and still keep the equality of both sides.

The film crystallization temperature is critical for high quality YBCO films, especially for large-area deposition. Many groups have designed different heaters for YBCO film growth. In our single-target system, a one-end-open tube-like heater was made with rounded Thermocoax heating wire, the dimensions of which were 100 mm in diameter and 75 mm in height, as shown in Fig. 4.6(a). The substrate was loaded near to the opening and facing the target. Its temperature distribution is shown in Fig. 4.6(b). From the profile that can be seen in Fig. 4.6(b), we know that the temperature is uniform in the radius direction, but changes considerably in the axial direction – by more than 10 °C/mm. In fact, the plasma can compensate for the heat loss caused by the heater opening. Within the region that the 3-inch wafer passes through, the temperature deviation is about 20 °C when plasma is off, and is reduced to 5 °C when the plasma is on. With a 10 to 60 rpm rotation, the substrate temperature distribution must be more uniform because of the cyclic compensation and the heat conduction inside the substrate itself.

4.4.2 Film homogeneity

In sputtering, there are three possible reasons for multicomponent oxide films not to be homogeneous:

1 Different angular distribution of atom emission. The atoms will be emitted from the target surface with determinate distribution for a given condition,

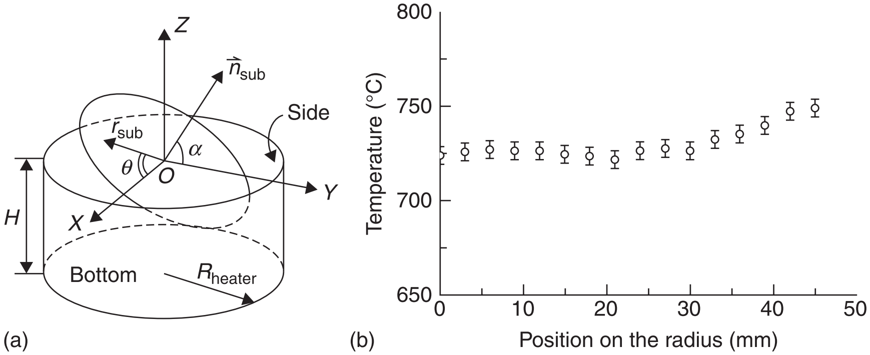

4.6 (a) Geometrical relation of substrate and cylindrical target for biaxial rotation (X, Y, Z = three dimensional coordinates, H = heater height, r_{sub} = substrate radius, R_{heater} = heater radius, $\vec{n}_{sub}$ = substrate normal, α = included angle between the substrate normal and Y-coordinate, θ = included angle between substrate horizontal and X-coordinate); (b) measured temperature distribution along the radius of the upper opening of the cylindrical heater.

and become thermalized and transfer diffusively due to colliding with atoms in a high pressure environment. Therefore, atoms with different masses have different angular concentration distributions.

2 Negative ion bombardment originating from the cathode. Negative ions are accelerated by the electrical field and can strike the substrate with high energy. The bombardment will selectively re-sputter the film according to different sputtering yields.
3 Possible difference of deposition parameters. For instance, if the deposition temperature is not uniform across the entire substrate, different sticking coefficients will result in inhomogeneity.

So, both the substrate-to-target distance ($D_{s\text{-}t}$) and the angle ($\theta_{s\text{-}t}$) are continuously varying rather than fixed, as in an off-axis mode. Therefore, the negative ion bombardment was also partially eliminated by the substrate tilting in the process. In our experiment, we deposited large-area $NdBa_2Cu_3O_{7-\delta}$ (NBCO) films on aluminum sheets at room temperature (without the heater) for composition and thickness distribution analysis.

Figure 4.7(a) shows the RBS spectra of NBCO film deposited on a static aluminum sheet for 5 hours with a 50 mm $D_{t\text{-}s}$. From the peak intensities of Cu, it is obvious that the central film is Cu-rich, and that the barium and neodymium concentrations at the edge are much higher than those in the center. Because the atom numbers of barium and neodymium are very close and difficult to distinguish,

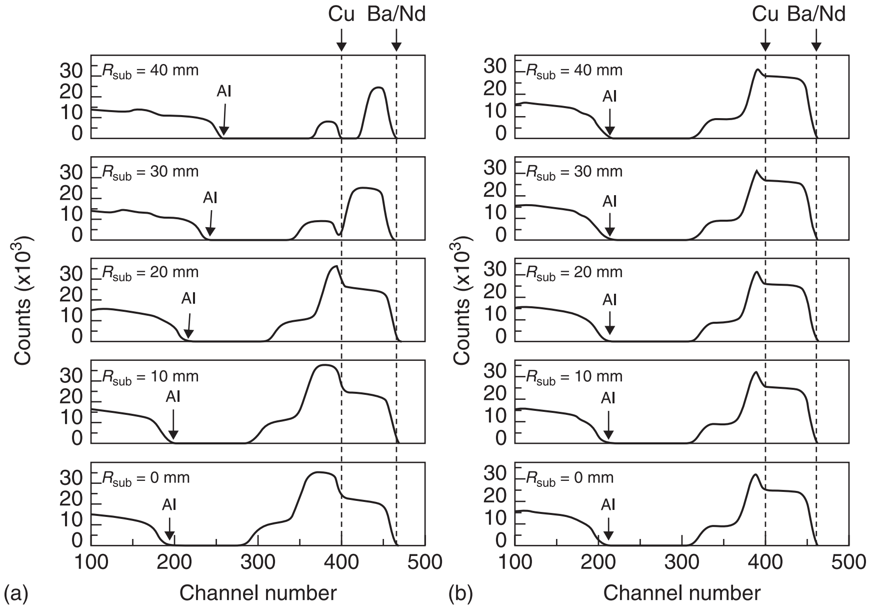

4.7 RBS results along the radius of the samples: (a) sample with static substrate; (b) sample with speed modulated bi-axial rotation.

(Ba + Nd) was taken together for concentration distribution. Besides Cu and (Ba + Nd) concentrations, the concentration ratio of Cu/(Ba + Nd) was taken as a comparable parameter for the extent of stoichiometry. The ratio is equal to 1 for stoichiometric NBCO film. The maximum difference, (max – min)/mean, of Cu concentrations is 28%, the maximum difference of (Ba + Nd) concentrations is 21%, and the ratios of Cu/(Ba + Nd) range from 1.3 to 2.2 within ∅86 mm (solid squares in Fig. 4.8(a)). The relative thickness distribution was determined by RBS (solid squares in Fig. 4.8(b)) and is consistent with that measured by the profiler. Further, we measured the aluminum peak shift for valuating the thickness distribution – it was also valid. The maximum film thickness deviation from center to edge is as much as 75% within ∅86 mm.

Biaxial rotation is designed specially for the simultaneous deposition of double-sided large-area thin films. In this case, the substrate edge can go very near to the target and catch more atoms in the high particle density region. With speed modulation, the distribution could be further improved and uniform film thickness could be obtained.

Figure 4.7(b) shows RBS spectra of film deposited with 60 mm target-to-substrate distance for 10 hours in single-target system with speed modulated biaxial rotation. Within ∅84 mm, the maximum difference of Cu concentrations is only 6%, while the maximum difference of (Ba + Nd) concentrations is only 8%. The homogeneity of Cu concentration is much improved by biaxial rotation (open circles, as shown in Fig. 4.8(a)). The thickness distribution of biaxial rotation (open circles, shown in Fig. 4.8(b)) is much better than that of a static substrate. Within the ∅80 mm range, the maximum thickness deviation is limited to 10%.

With the speed modulation technique, high quality double-sided YBCO films have been deposited on 3-inch $LaA1O_3$ substrates with very good side-to-side uniformities and lateral homogeneities. The deposition of 500 nm films can be finished in 36 hours with about 14 nm/h deposition rate for both sides.

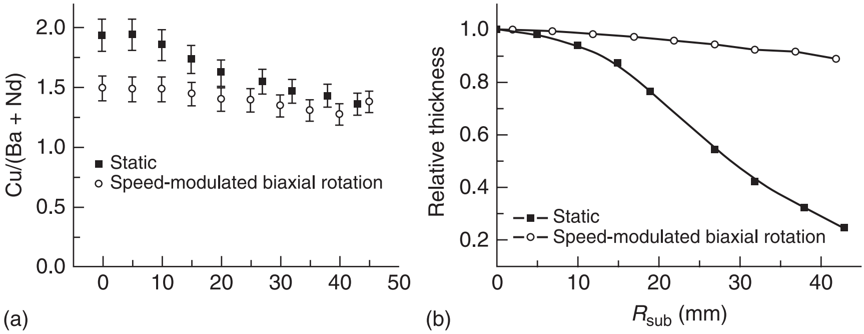

4.8 Stoichiometric (a) and thickness (b) distribution for static sample (solid squares) and speed modulated biaxial rotating sample (open circles).

The samples were pure c-axis oriented and with good out-of-plane and in-plane epitaxy, as shown in Fig. 4.9. The typical properties of a 3-inch sample are T_c 90 K, ΔT_c about 0.5 K, J_c 2–4 MA/cm^2, and R_s less than 0.5 $\mu\Omega$. The T_c, J_c, and thickness distributions are shown in Plate II in the colour section between pages 244 and 245.

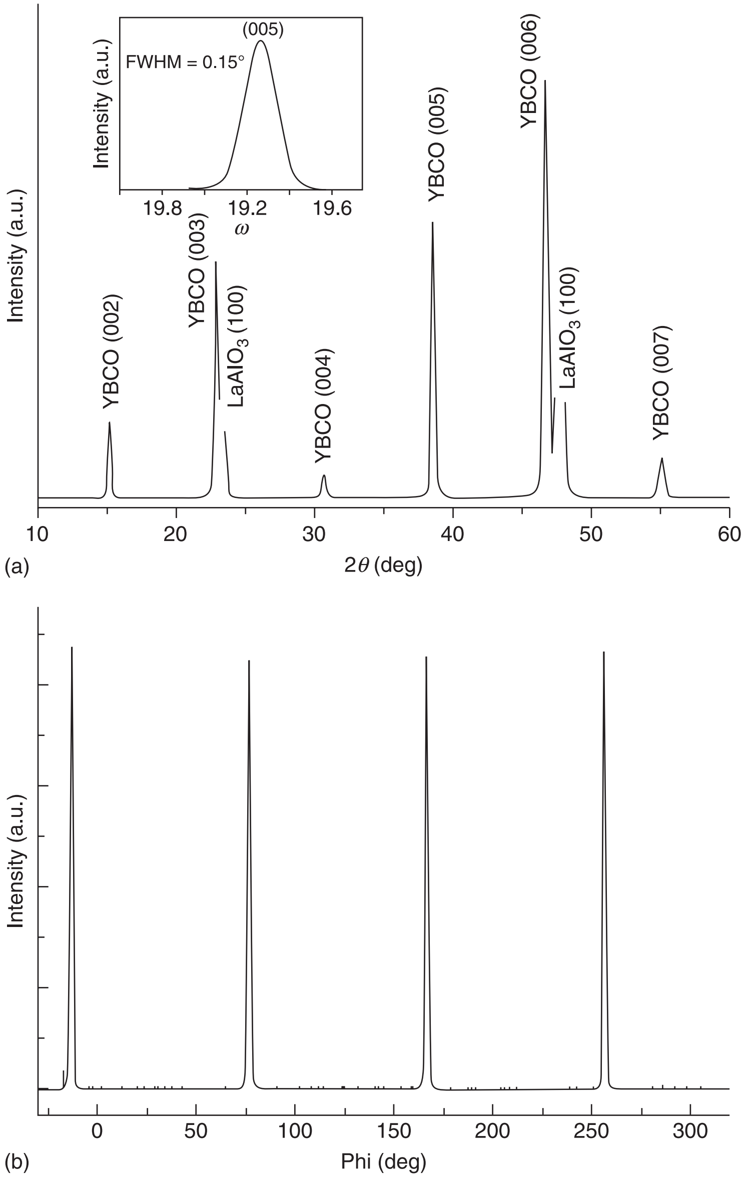

4.9 (a) Typical XRD θ–2θ pattern of YBCO thin film on LAO substrates. The inset is the corresponding rocking curve on YBCO (005) peaks; (b) XRD ∅-scan of the same YBCO thin film.

4.5 Thickness-dependent superconductivity behavior

4.5.1 Residual stress in thickness-modulated YBCO films

In order to study the effect of thickness on film quality, YBCO epitaxial films were prepared with various thicknesses from 0.2 to 2 μm. The XRD θ–2θ scan is shown in Fig. 4.10. All films are single phased and grow with (00*l*) orientation normal to the substrate surface, and no other orientation of YBCO has been detected, indicating good quality film with full c-axis orientation. Figure 4.11 shows the dependence of the full width at half maximum (FWHM) of the (006)

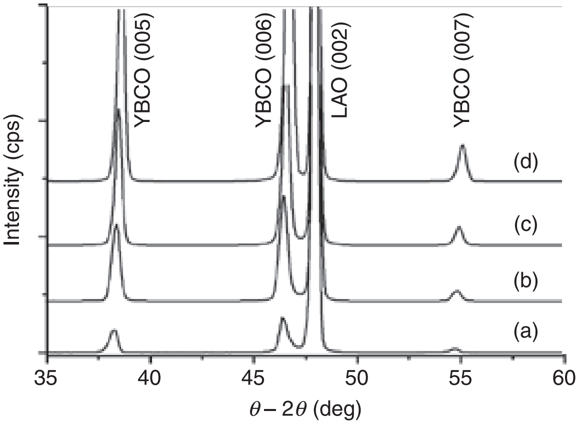

4.10 X-ray diffraction spectra of YBCO films with different thickness (a) 0.2 μm, (b) 0.5 μm, (c) 1 μm, (d) 2 μm YBCO films.

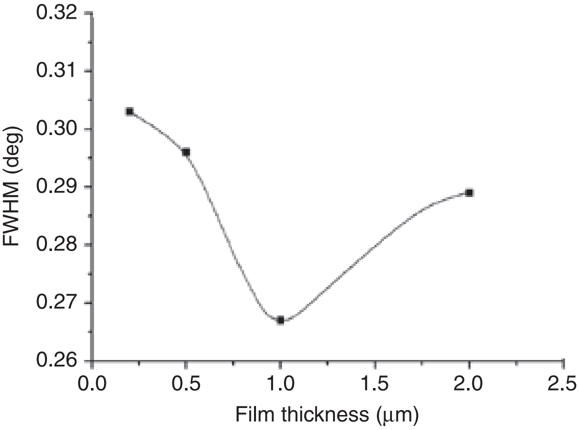

4.11 The FWHM of the (006) YBCO peak in the rocking curve as a function of film thickness.

YBCO peak as a function of film thickness, obtained by ω-scan. It was found that the FWHM was first decreased and then increased with the increasing film thickness, revealing that structural perfection for thicker films was deteriorating as a result of defects and dislocations.[57]

To get more structural information and calculate out-of-plane and in-plane lattice parameters, high-resolution reciprocal space mappings (HR-RSMs) were recorded. Figure 4.12(a) is an RSM obtained from the symmetric reflection near LAO (002) for a sample with a thickness of 1 μm. The highest point from the reflection of the LAO (002) was defined as the origin. From the figure, we can conclude that these two reflection spots are coming from the (006) YBCO and (002) LAO. There is no signal from the YBCO (200) reflection. Out-of-plane lattice parameters can be easily calculated from the peak positions in Figure 4.12(a). To obtain the in-plane lattice parameters of the films, RSMs near the asymmetric reflection were acquired using glancing exit scans. Figure 4.12(b) shows the RSM around the asymmetric reflection of LAO (103). We defined $\phi = 0°$ for this case. Figure 4.12(c) shows the RSM around the asymmetric

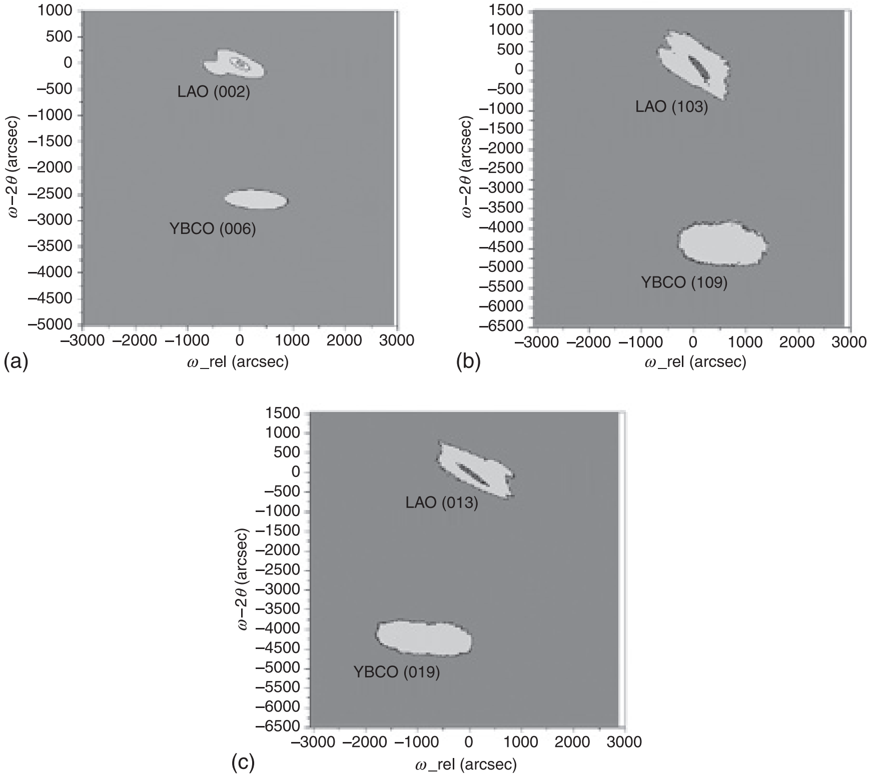

4.12 Reciprocal space mapping near (a) LAO (002), (b) LAO (103), (c) LAO (013) with YBCO film thickness of 1 μm.

reflections of LAO (013) obtained with the same measurement setting, but ϕ rotated 90°. It is worth noting that the reflection spots except for the substrate, which can be identified as YBCO (109) and YBCO (019), are observed in both $\phi = 0°$ and $\phi = 90°$ (Fig. 4.12(b) and (c)). For YBCO films with thickness of 0.2, 0.5 and 2 μm, the same experiments were performed but are not shown here. Table 4.2 lists the lattice parameters calculated from the RSMs using Bragg's law and the relationship between the measured planes.[58]

Using the calculated lattice parameters, the strain in directions *a*, *b*, and *c* was evaluated from Eqs. [4.1], [4.2] and [4.3].[59–61]

$$\varepsilon_a = (a - a_o)/a_o \tag{4.1}$$

$$\varepsilon_b = (b - b_o)/b_o \tag{4.2}$$

$$\varepsilon_c = (c - c_o)/c_o \tag{4.3}$$

where ε_a, ε_b, ε_c are the misfit strains in directions a, b, and c, respectively; *a*, *b*, *c*, are the lattice constants of the strained thin film on the substrate; and a_o, b_o, c_o are the bulk (unstressed) values ($a_o = 3.82$, $b_o = 3.884$, $c_o = 11.67$ Å from JCPDS card No. 85–1877).

Applying Hooke's law to an isotropic triaxial system, the residual stress can be estimated using the following relations:

$$\varepsilon_a = \frac{1}{E}\left[\sigma_a - v\left(\sigma_b + \sigma_c\right)\right] \tag{4.4}$$

$$\varepsilon_b = \frac{1}{E}\left[\sigma_b - v\left(\sigma_a + \sigma_c\right)\right] \tag{4.5}$$

$$\varepsilon_c = \frac{1}{E}\left[\sigma_c - v\left(\sigma_a + \sigma_b\right)\right] \tag{4.6}$$

Due to the thickness of film materials being negligible compared with the substrate, on the assumption that $\sigma_c = 0$, the biaxial residual stress of in-plane of YBCO films can be calculated using Eqs. [4.7] and [4.8] deduced from [4.4], [4.5] and [4.6]:

$$\sigma_a = -\frac{E}{1+v}(\varepsilon_c - \varepsilon_a) \tag{4.7}$$

$$\sigma_b = -\frac{E}{1+v}(\varepsilon_c - \varepsilon_b) \tag{4.8}$$

where E and v are the elastic modulus and the Poisson ratio, respectively (for YBCO $E = 157$ GPa, and $v = 0.3$).[62]

Due to the assumption that YBCO film was in the isotropic system, residual stress in YBCO film can be determined as:

$$\sigma = \frac{\sigma_a + \sigma_b}{2} \tag{4.9}$$

According to the *a, b, c* lattice parameters in Table 4.2, residual stress in YBCO films can be calculated using Eqs. [4.1]–[4.9] and the deposition parameters listed in Table 4.1. Figure 4.13 shows the relationship between film thickness and residual stress. Compressive residual stress is expressed with a negative sign. For the films thinner than 0.5 μm, YBCO film is under a compressive stress. A compression of the ab-plane is likely to result in an elongation along the c-axis because of lattice mismatch relaxation between YBCO and the LAO substrate. This shows a tendency toward a reduction in compressive stress with increasing thickness. For films with thicknesses of 0.5–1 μm, YBCO films have the lowest residual stress of nearly all free-standing films. As the film thickness was increased beyond 1 μm, tensile stress increased, which resulted in cracks appearing in YBCO films. Furthermore, the effect of residual stress on the surface morphology and electric properties of YBCO film will be tackled in section 4.5.2.

In the case of all films with a thickness greater than 1 μm, deposited at the same temperature, with the same elastic modulus and coefficient of thermal expansion, the difference in their thermal stress is negligible. Therefore, there must be some other reasons responsible for the changes in the residual stress. One hypothesis,[63] which could explain the increasing tensile stress with increasing film thickness, may be the formation of oxygen vacancies. Oxygen is known to play a key role in

Table 4.2 Lattice parameters, strain, and residual stress calculated from RSMs

Thickness (μm)	*a* (Å)	*b* (Å)	*c* (Å)	ε_a (%)	ε_b (%)	ε_c (%)	σ_a (MPa)	σ_b (MPa)	σ (MPa)
0.2	3.795	3.841	11.854	–0.654	–1.107	1.5766	–2695	–3241	–2968
0.5	3.818	3.854	11.732	–0.0523	–0.772	0.531	–704	–1514	–1109
1	3.826	3.892	11.687	0.157	0.206	0.146	14	73	44
2	3.829	3.893	11.67	0.21	0.258	0	254	311	283

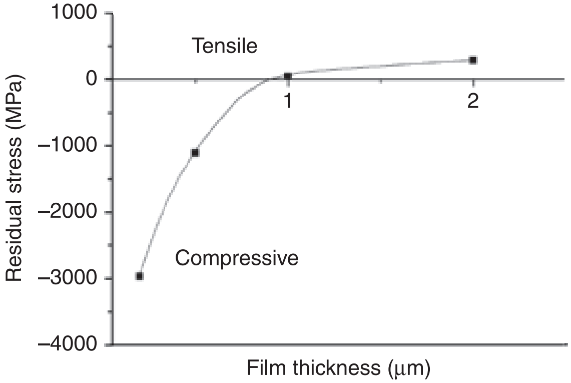

4.13 The residual stress in YBCO films as a function of film thickness.

the development of compressive stress in thin films deposited by sputtering and evaporation. Consequently, excess oxygen vacancies in the lattice sites may facilitate the development of tensile stress. Since oxygen diffusion is known to be much faster along the ab-plane of YBCO than in the c-axis direction.[64,65] It could suppress oxygen diffusion into an internal layer as film thickness increases, resulting in the as-grown state becoming oxygen-deficient and hence increasing tensile stress in the films. To further substantiate this hypothesis, it is expected that this film will benefit from post-deposition annealing due to oxygen deficiency. Therefore, this simple analysis shows that oxygen vacancy may cause tensile stress in thin films when a remarkable improvement is observed via annealing treatment.

4.5.2 Effect of residual stress on surface morphology and electrical properties of YBCO films

SEM was used to investigate the surface morphology of the films. As shown in Fig. 4.14, the characteristic morphology consists of islands of varied height and with deep pores in between, leading to a relatively porous surface. There were

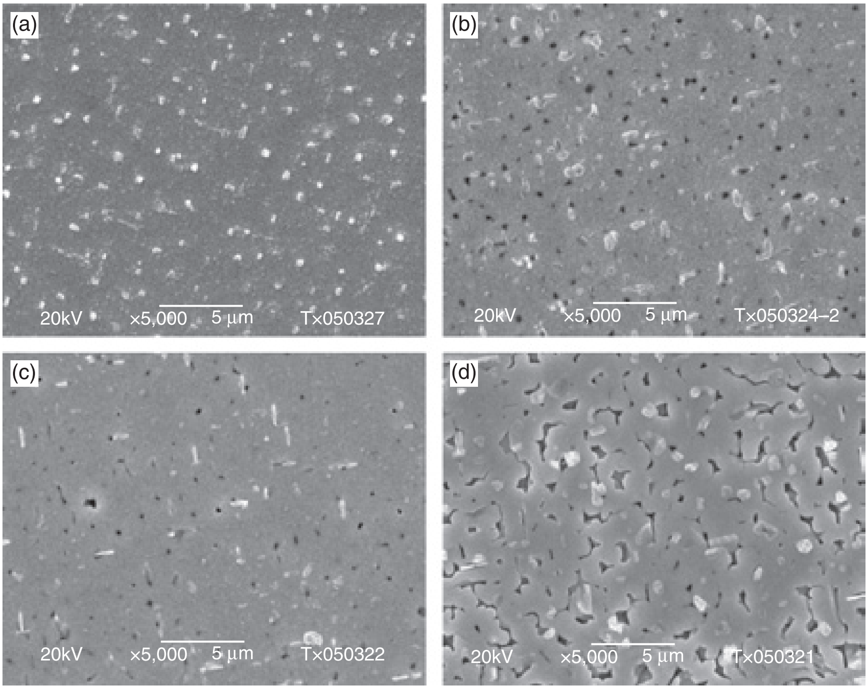
(a)
20kV ×5,000 5 μm Tx050327
(b)
20kV ×5,000 5 μm Tx050324–2
(c)
20kV ×5,000 5 μm Tx050322
(d)
20kV ×5,000 5 μm Tx050321

4.14 SEM figures showing the surface morphology of (a) 0.2 μm, (b) 0.5 μm, (c) 1 μm, (d) 2 μm YBCO films.

more pores on the surface of the thicker samples, while more outgrowths on the surface of the thinner samples. The microstructural imperfection of the film (i.e., the presence of pores) appears to be beneficial in relieving the strain induced in the films, as evidenced by the large thickness value. The porosity of the film is corrected with the yttrium-rich composition, which results in an yttrium-rich secondary phase occlusion, identified as BaY_2O_4.[66–68] When film thickness is further increased to over 1 μm, short microcracks were observed. In many cases, the causes of these crack formations[69,70] are tensile stresses rather than compressive ones, consistent with the results of Fig. 4.13.

Figure 4.15 shows the thickness dependence of T_c values for YBCO films. T_c tends to increase with film thickness, while ΔT_c remains almost unchanged. The suppression of T_c values for YBCO at a thickness below 0.5 μm can be explained as follows. As mentioned above, films within 0.5 μm suffered from compressive stress. Considering the effect of this stress on the hetero-epitaxial growth, the YBCO crystals include much greater amounts of misoriented nuclei. As these misoriented nuclei form misoriented islands, and then coalesce with each other during the early stage of the film growth, extra stress is generated in the films due to differences in the in-plain orientation,[71] which would suppress the T_c values for the YBCO films.

The measurements of J_c are performed on samples with thickness $d = 0.2$, 0.5, 1, 2 μm by the J_c-scan Leipzig system. Fig. 4.16 shows the thickness dependence of J_c values for YBCO. The J_c values increased with the increasing thickness of relatively thin films, which corresponds to the thickness dependence of T_c.

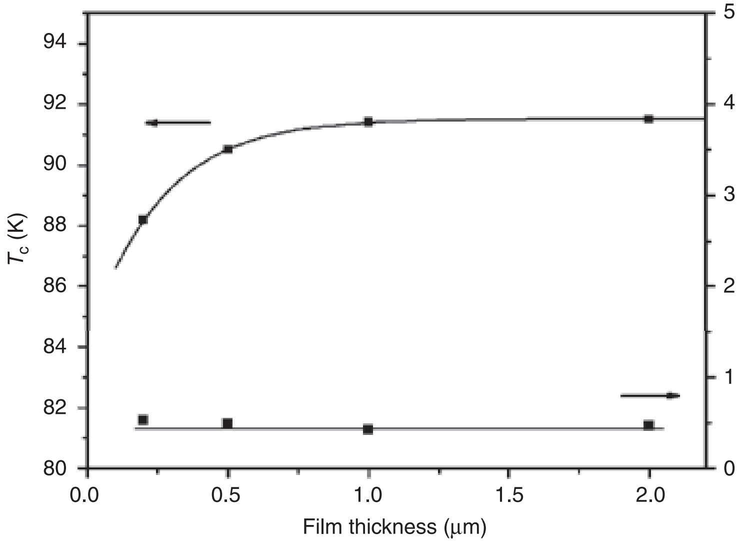

4.15 Film thickness dependence of T_c and ΔT_c of YBCO films.

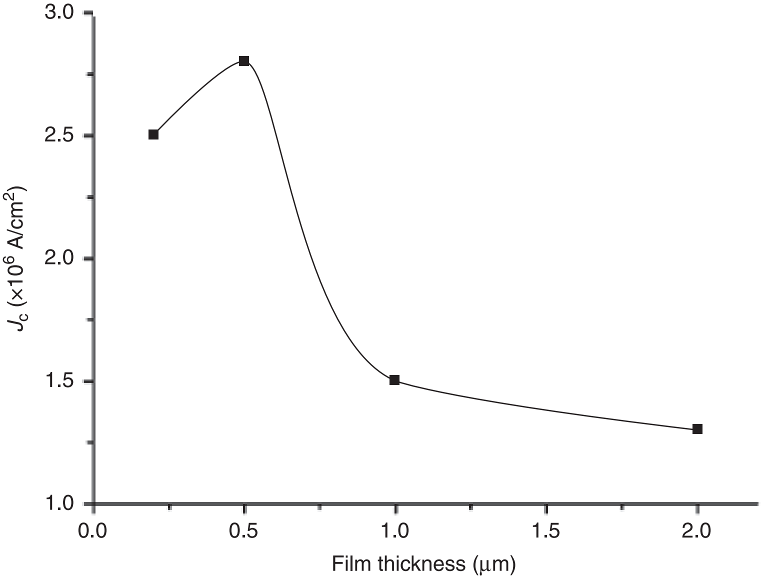

4.16 Critical current density J_c (77 K, 0 T) as a function of YBCO film thickness.

Although the J_c value decreases for films with thicknesses above 0.5 μm, YBCO films keep their high values, more than 1×10^6 A/cm.^{2} Several possible explanations for this behavior have been proposed: the presence of a-axis oriented YBCO grains, changes of film surface morphology (i.e. pores and microcracks) and a decrease in the number of pinning sites.[72–74]

4.6 Challenges

Comparing the 23 years since HTS discovery with the time frame of about 50 years that classical superconductors and semiconductors have taken to become established as reliable high-tech materials, these achievements of HTS applications are truly amazing. Large area YBCO films are applied in many microelectronic device applications, such as microwave components/systems and Josephson junctions, and the long length YBCO tapes in the range of several kilometers are used for power transmission cables, superconducting magnets, motors/generators, etc. Nevertheless, there is still no 'killer application' where HTS could prove its ability to provide a unique technical solution required in order to realize its potential as a broad-impact technology, as has been the case with MRI magnets for classical superconductors. The lesson from this example is that this breakthrough will probably happen in an application field which no one has even thought of today. Until then, again in analogy with classical superconductors, HTS materials will probably find their main use in some niche applications, in particular in scientific research, where they have the chance to finally reach the status of a readily available mature technology.

4.7 Conclusions

In this chapter, sputter deposition with a special modulated biaxial rotation has been shown to be a powerful method for the fabrication of large-area double-sided YBCO thin films. Three-inch YBCO samples exhibit excellent material characteristics (epitaxy, composition, and microstructure) and electrical properties on different single crystal substrates with T_c 90 K, ΔT_c about 0.5 K, J_c (77 K, 0 T) 2–4 MA/cm^2, and R_s (77 K, 10 GHz) less than 0.5 $\mu\Omega$ with good lateral uniformity and side-to-side equality. The dependencies of the residual stress, surface morphology and electrical properties on the thickness of the superconducting layer were also investigated, and the explanations for these phenomena were elucidated.

4.8 References

1 K.A. Muller and J.G. Bednorz, 1987, 'The discovery of a class of high-temperature superconductors', *Science* **237**, 1133.

2 M.K. Wu, J.R. Ashburn, C.J. Torng, P.H. Hor, R.L. Meng, *et al.*, 1987, 'Superconductivity at 93-K in a new mixed-phase Y-BA-CU-O compound system at ambient pressure', *Phys. Rev. Lett.* **58**, 908.

3 D. Larbalestier, A. Gurevich, D.M. Feldmann, A. Polyanskii, 2001, 'High-T-c superconducting materials for electric power applications', *Nature* **414**, 368.

4 R.M. Scanlan, A.P. Malozemoff, D.C. Larbalestier, 2004, 'Superconducting materials for large scale applications', *Proc. IEEE* **92**, 1639.

5 H. Kinder, P. Berberich, W. Prusseit, S. Rieder-Zecha, R. Semerad, *et al.*, 1997, 'YBCO film deposition on very large areas up to 20 × 20 cm^2', *Physica C* **282–287**, 107.

6 R. Wördenweber, 1999, 'Growth of high-T-c thin films', *Supercond. Sci. Technol.* **12**, R86.

7 J. Geerk, G. Linker, O. Meyer, 1992, 'HTSC thin-film growth by inverted cylindrical magnetron sputtering', *J. Supercond.* **5**, 345.

8 T. Puzzer, Z.T. Zheng, S. Bosi, G.J. Russell, K.N.R. Taylor, 1989, 'Thin-films of 123 on silicon substrates', *Physica C* **162–164**, 603.

9 G. Koren, 1993, 'DC sputter deposition of $YBa_2Cu_3O_7$ thin-films for 2 sided coating', *Physica C* **209**, 369.

10 M. Hong, S.H. Liou, J. Kwo, B.A. Davidson, 1987, 'Superconducting Y-Ba-Cu-O oxide-films by sputtering', *Appl. Phys. Lett.* **51**, 694.

11 M. Lorenz, H. Hochmuth, H. Natusch, T. Thrigen, D.G. Patrikarakos, *et al.*, 1997, 'Large-area and double-sided pulsed laser deposition of Y-Ba-Cu-O thin films applied to HTSC microwave devices', *IEEE Trans. Appl. Supercond.* **7**, 1240.

12 M. Schieber, S.C. Han, Y. Ariel, S. Chokron, T. Tsach, *et al.*, 1991, 'Comparison of thin-films of $YBa_2Cu_3O_{7-x}$ deposited by physical (laser ablation) and chemical (omcvd) methods for device applications', *J. Crystal Growth* **115**, 31.

13 H.U. Habermeier, G. Beddies, B. Leibold, G. Lu, G. Wagner, 1991, 'Y-Ba-Cu-O high-temperature superconductor thin-film preparation by pulsed laser deposition and rf-sputtering – a comparative-study', *Physica C* **180**, 17.

14 M. Naito, S. Karimoto, H. Yamamoto, H. Nakada, K. Suzuki, 2001, 'Production of double-sided large-area high-T-c wafers by molecular beam epitaxy', *IEEE Trans. Appl. Supercond.* **11**, 3848.

15 A. Sawa, H. Obara, S. Kosaka, 1994, 'Effect of using pure ozone on in-situ molecular-beam epitaxy of $YBa_2Cu_3O_{7-x}$ thin-films at low-pressure', *Appl. Phys. Lett.* **64**, 649.

16 R. Singh, S. Sinha, N.J. Hsu, P. Chou, P.K. Singh, *et al.*, 1990, 'Superconducting thin-films of Y-Ba-Cu-O prepared by metalorganic chemical vapor-deposition', *J. Appl. Phys.* **67**, 1562.

17 C.S. Chern, J. Zhao, P.E. Norris, S.M. Garrison, K. Yau, *et al.*, 1992, 'Oxidizer partial-pressure window for $YBa_2Cu_3O_{7-x}$ thin-film formation by metalorganic chemical vapor-deposition', *Appl. Phys. Lett.* **61**, 1983.

18 J.A. Smith and N. Sonnenberg, 1999, 'High critical current density thick MOD-derived YBCO films', *IEEE Trans. Appl. Supercond.* **9**, 1531.

19 T. Manabe, J.H. Ahn, I. Yamaguchi, M. Sohma, W. Kondo, *et al.*, 2006, 'Preparation of double-sided YBCO films on $LaAlO_3$ by MOD using commercially available coating solution', *IEICE Trans. Electron.* **E89-C**, 186.

20 W. Prusseit, S. Furtner, R. Nemetschek, 2000, 'Series production of large area $YBa_2CU_3O_7$ films for microwave and electrical power applications', *Supercond. Sci. Technol.* **1**, 519.

21 H.U. Müller, J.P. Müller, F. Ludwig, G.J. Ehlers, 1993, 'Large-area deposition of YBaCuO thin-films by means of hollow-cathode sputtering', *J. Alloy. Comp.* **195**, 267.

22 W. Randy, B. Robert, J. Stuart, A. Balam, 2004 'Superconducting Microwave Filter Systems for Cellular Telephone Base Stations', *Proc. IEEE* **92**, 1585.

23 S.K. Remillard and S. Cordone, 2006, 'A review of HTS thick-film microwave filter technology', *J. Supercond.* **19**, 523.

24 A. Kedar and N.D. Kataria, 2005, 'Efficient analysis for nonlinear microwave characteristics of high-power HTS thin film microstrip resonators', *Supercond. Sci. Technol.* **18**, 1129.

25 L.B. Shi, Y.F. Wang, Y.Y. Ke, G.H. Zhang, L. Sheng, *et al.*, 2007, 'A study on the microwave responses of YBCO and TBCCO thin films by coplanar resonator technique', *Chin. Phys.* **16**, 3036.

26 D.G. Smith and V.K. Jain, 1999, 'Superconducting filters for wireless communications: A reappraisal', *IEEE Trans. Appl. Supercond.* **9**, 4010.

27 J. Geerk, H. Rietschel, G. Linker, R. Heidinger, R. Schwab, 1999, 'Simultaneous double-sided deposition of HTS films on 3-inch wafers by ICM-sputtering', *IEEE Trans. Appl. Supercond.* **9**, 1543.

28 B.W. Tao, Y.R. Li, X.Z. Liu, S.M. He, J. Geerk, 2002, 'A biaxial rotation for depositing homogeneous large-area double-sided $YBa_2Cu_3O_{7-x}$ thin films', *J. Vac. Sci. Technol. A* **20**, 1898.

29 B.W. Tao, J.J. Chen, X.Z. Liu, Y. Zhang, X.W. Deng, *et al.*, 2005, 'Speed modulation technique to achieve simultaneous deposition of 3-in. double-sided Y-Ba-Cu-O thin films', *Physica C* **433**, 87.

30 B.W. Tao, X.W. Deng, Y. Zhang, Y.R. Li, 2004, 'Thickness uniformity of large-area double-sided thin films simultaneously deposited with biaxial substrate rotation', *J. Vac. Sci. Technol. A* **22**, 1134.

31 W. Prusseit, S. Furtner, R. Nemetschek, 2000, 'Series production of large area $YBa_2Cu_3O_7$ films for electronic-, microwave-, and electrical power applications', *Advances in Superconductivity* **XII**, 876.

32 A. Lauder, K.E. Myers, D.W. Face, 1998, 'Thin-film high-temperature superconductors for advanced communications and electronics', *Adv. Matter.* **10**, 1249.

33 L. Philippe, M. Bernard, M. Hugues, 1995, 'Influence of angular distribution on the deposition rate of species sputtered from a multicomponent target in different configurations: Applications to mixed valence copper oxides', *J. Vac. Sci. Technol. A* **13**, 2221.

34 Q.H. Fan, 1992, 'Uniformity of targets erosion and magnetic-film thickness distribution in the target-facing-type sputtering method', *J. Vac. Sci. Technol. A* **10**, 3371.

35 R.S. Upadhye and E.J. Hsieh, 1990, 'A unified integrated model for sputter coating uniformity', *J. Vac. Sci. Technol. A* **8**, 1348.

36 T. Serikawa and A. Okamoto, 1985, 'Sputter depositions of silicon film by a planar magnetron cathode equipped with 3 targets', *J. Vac. Sci. Technol. A* **3**, 1784.

37 S. Swann, S.A. Collett, I.R. Scarlett, 1990, 'Film thickness distribution control with off-axis circular magnetron sources onto rotating substrate holders – comparison of computer-simulation with practical results', *J. Vac. Sci. Technol. A* **8**, 1299.

38 F. Vassenden, G. Linker, J. Geerk, 1991, 'Growth direction control in YBCO thin-films', *Physica C* **175**, 566.

39 E.K. Hollmann, D.A. Plotkin, S.V. Razumov, A.V. Tumarkin, 1999, 'Production of thick $YBa_2Cu_3O_{7-\delta}$ films on sapphire with a cerium oxide sublayer', *Tech. Phys.* **44**, 1119.

40 Y. Iijima, N. Tanabe, O. Kohno, Y. Ikeno, 1992, 'Inplane aligned $YBa_2Cu_3O_{7-x}$ thin-films deposited on polycrystalline metallic substrates', *Appl. Phys. Lett.* **60**, 769.

41 X.D. Wu, S.R. Foltyn, P. Arendt, J. Townsend, C. Adams, *et al.*, 1994, 'High-current $YBa_2Cu_3O_{7-\delta}$ thick-films on flexible nickel substrates with textured buffer layers', *Appl. Phys. Lett.* **65**, 1961.

42 D.P. Norton, A. Goyal, J.D. Budai, D.K. Christen, D.M. Kroeger, *et al.*, 1996, 'Epitaxial $YBa_2Cu_3O_7$ on biaxially textured nickel (001): An approach to superconducting tapes with high critical current density', *Science* **274**, 755.

43 A. Mogro-Campero, L.G. Turner, E.L. Hall, N. Lewis, 1990, 'Critical current density and microstructure of $YBa_2Cu_3O_{7-x}$ films as a function of film thickness', *Mater. Res. Soc. Symp. Proc.* **169**, 703.

44 F.E. Luborsky, R.F. Kwasnick, K. Borst, M.F. Garbauskas, E.L. Hall, *et al.*, 1988, 'Reproducible sputtering and properties of Y-Ba-Cu-O films of various thicknesses', *J. Appl. Phys.*, **64**, 6388.

45 S. Sievers, F. Mattieis, H.U. Krebs, H.C. Freyhardt, 1995 'Grain-orientation in thick laser-deposited $Y_1Ba_2Cu_3O_{7-\delta}$ films – adjustment of c-axis orientation', *J. Appl. Phys.* **78**, 5545.

46 S.R. Foltyn, P. Tiwari, R.C. Dye, M.Q. Le, X.D. Wu, 1993, 'Pulsed-laser deposition of thick $YBa_2Cu_3O_{7-\delta}$ films with J_c-greater-than-1 ma/cm^2', *Appl. Phys. Lett.* **63**, 1848.

47 S. Miura, K. Hashimoto, F. Wang, Y. Enomoto, T. Morishita, 1997, 'Structural and electrical properties of liquid phase epitaxially grown $Y_1Ba_2Cu_3O_x$ films', *Physica C* **278**, 201.

48 A. Ignatiev, Q. Zhong, P.C. Chou, X. Zhang, J.R. Liu, *et al.*, 1997, 'Large J(C) enhancement by ion irradiation for thick $YBa_2Cu_3O_{7-\delta}$ films prepared by photoassisted metalorganic chemical vapor deposition', *Appl. Phys. Lett.* **70**, 1474.

49 V.F. Solovyov, H.J. Weisemann, L.J. Wu, M. Suenaga, R. Feenstra, 1999, 'High rate deposition of 5 μm thick $YBa_2Cu_3O_7$ films using the BaF_2 ex-situ post annealing process', *IEEE Trans. Appl. Supercond.* **4**, 429.

50 S.R. Foltyn, Q.X. Jia, P.N. Arendt, L. Kinder, Y. Fan, *et al.*, 1999, ‘Relationship between film thickness and the critical current of $YBa_2Cu_3O_{7-\delta}$-coated conductors’, *Appl. Phys. Lett.* **75**, 3692.

51 Y. Yamada, J. Kawashima, J.G. Wen, Y. Niiori, I. Hirabayashi, 2000, ‘Evaluation of thermal expansion coefficient of twinned $YBa_2Cu_3O_{7-\delta}$ film for prediction of crack formation on various substrates’, *Jpn. J. Appl. Phys.* **39**, 1111.

52 X.J. Zheng, Z.Y. Yang, Y.C. Zhou, 2003, ‘Residual stresses in $Pb(Zr_{0.52}Ti_{0.48})O_3$ thin films deposited by metal organic decomposition’, *Scripta Mater.* **49**, 71.

53 P.R. Willmott, 2004, ‘Deposition of complex multielemental thin films’, *Prog. Surf. Sci.* **76**, 163.

54 G. Betz and G.K. Wehner, 1983, ‘Sputtering of multicomponent materials’, *Top. Appl. Phys.* **52**, 11.

55 D.P. Norton, 1998, ‘Science and technology of high-temperature superconducting films’, *Annu. Rev. Mater. Sci.* **28**, 299.

56 B.W. Tao, X.Z. Liu, J.J. Chen, Y.R. Li, R. Fromknecht, *et al.*, 2003, ‘Some calculations for the thickness distribution of large-area high-temperature superconducting film deposited by inverted cylindrical sputtering’, *Vac. Sci. Technol. A*, **21**, 431

57 K. Senapati, L.K. Sahoo, N.K. Pandey, R.C. Budhani, 2002, ‘Irreversibility field and superconducting screening currents in $EuBa_2Cu_3O_7$ films’, *Appl. Phys. Lett.*, **80**, 619.

58 Y. Lin, H. Wang, M.E. Hawley, Q.X. Jia, 2005, ‘The effect of growth rates on the microstructures of $EuBa_2Cu_3O_{7-x}$ films on $SrTiO_3$ substrates’, *Appl. Phys. Lett.*, **86**, 192508.

59 K.N. Tu, J.W. May, L.C. Feldman, *Electronic Thin Film Science*, MacMillan, New York, 1992.

60 Y. Chen, D.A. Gulino, R. Higgins, 1999, ‘Residual stress in GaN films grown by metalorganic chemical vapor deposition’, *J. Vac. Sci. Techno. A*, **17**, 3029.

61 P.K. Petrov, K. Sarma, N.M. Alford, 2004, ‘Evaluation of residual stress in thin ferroelectric films using grazing incident X-ray diffraction’, *Integr. Ferroelectr.* **63**, 183.

62 J. Xiong, W.F. Qin, X.M. Cui, B.W. Tao, J.L. Tang, *et al.*, 2006, ‘Effect of processing conditions and methods on residual stress in CeO_2 buffer layers and YBCO superconducting films’, *Physica C*, **442**, 124.

63 R.W. Hoffmann, 1966, ‘Thermal strains in thin metallic films’, *Phys. Thin Films* **3**, 211.

64 S.J. Rothman, J.L. Routbort, J.E. Baker, 1989, ‘Tracer diffusion of oxygen in $YBa_2Cu_3O_{7-\delta}$, *Phys. Rev. B* **40**, 8852.

65 S.J. Rothman, J.L. Routbort, U. Welp, J.E. Baker, 1991, ‘Anisotropy of oxygen tracer diffusion in single-crystal $YBa_2Cu_3O_{7-\delta}$, *Phys. Rev. B* **44**, 2326.

66 K. Develos-Bagarinao, H. Yamasaki, Y. Nakagawa, K. Endo, 2004, ‘Pore formation in YBCO films deposited by a large-area pulsed laser deposition system’, *Supercond. Sci. Technol.*, **17**, 1253.

67 K. Develos-Bagarinao, H. Yamasaki, Y. Nakagawa, K. Endo, 2004, ‘Relationship between composition and surface morphology in YBCO films deposited by large-area PLD’, *Physica C*, **412–414**, 286.

68 K.D. Bagarinao, H. Yamasaki, J.C. Nie, M. Murugesan, H. Obara, Y. Nakagawa, 2005, ‘Control of porosity and composition in large-area YBCO films to achieve micrometer thickness and high J(c) on sapphire substrates’, *IEEE T. Appl. Supercond.*, **15**, 2962.

69 J.A. Thorton and D.W. Hoffman, 1989, ‘Stress-related effects in thin-films’, *Thin Solid Films*, **171**, 5.

70 K.H. Muller, 1987, ‘Stress and microstructure of sputter-deposited thin-films – molecular-dynamics investigations’, *J. Appl. Phys.* **62**, 1796.

71 K. Hasegawa, J. Shibata, T. Zumi, Y. Shiohara, Y. Sugawara, 2003, ‘Improvement of superconducting properties of $SmBa_2Cu_3O_y$ films on MgO substrate by using $BaZrO_3$ buffer layer’, *Physica C*, **392–396**, 835.

72 S. Siever, F. Mattieis, H.U. Krebs, H.C. Freyhardt, 1994, ‘Grain orientation in thick laser-deposited $Y_1Ba_2Cu_3O_{7-\delta}$ films: Adjustment of c-axis orientation’, *J. Appl. Phys.*, **78**, 5545.

73 A. Ignatiev, Q. Zhong, P.C. Chou, X. Zhang, J.R. Liu, *et al.*, 1997, ‘Large Jc enhancement by ion irradiation for thick $YBa_2Cu_3O_{7-\delta}$ films prepared by photoassisted metalorganic chemical vapor deposition’, *Appl. Phys. Lett.* **70**, 1474.

74 S.R. Foltyn, Q.X. Jia, P.N. Areudt, L. Kinder, Y. Fan, *et al.*, 1999, ‘Relationship between film thickness and the critical current of $YBa_2Cu_3O_{7-\delta}$-coated conductors’, *Appl. Phys. Lett.*, **75**, 3692.

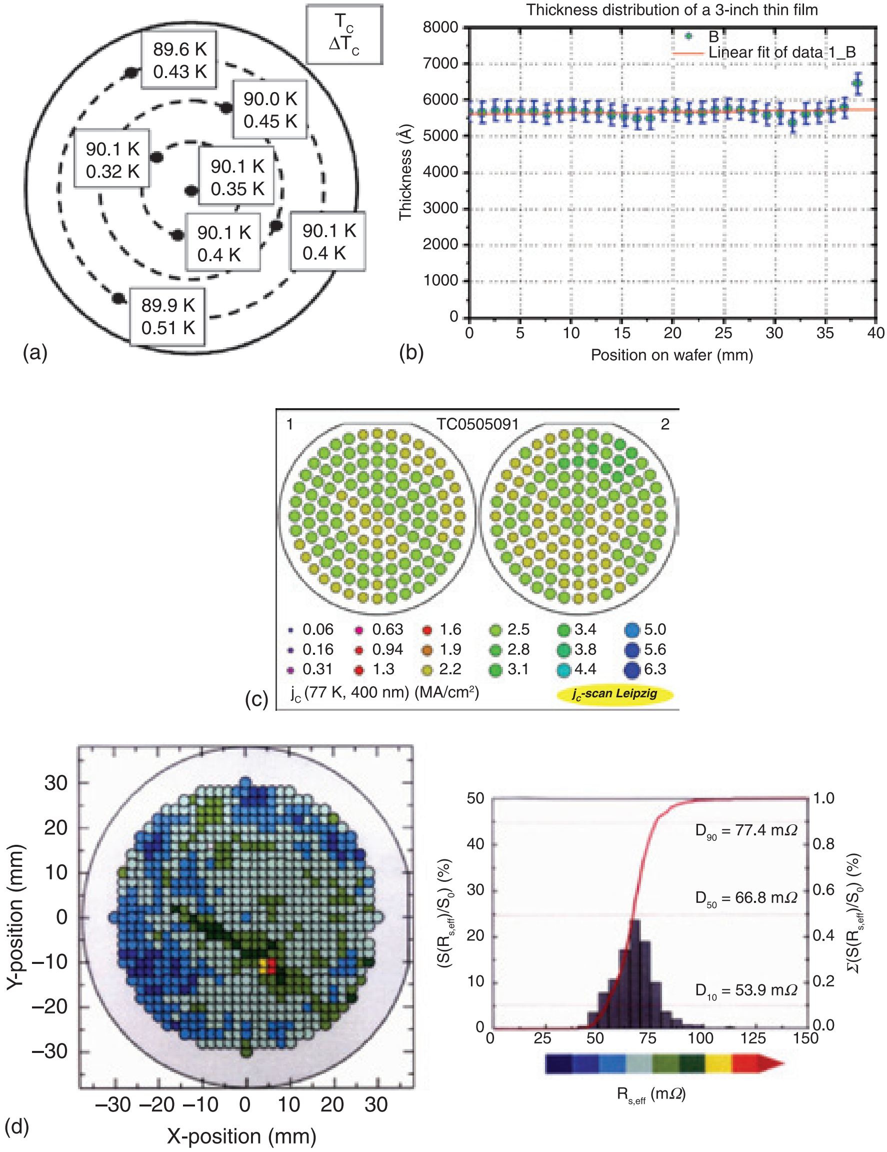

Plate II Analyses of homogeneity of large area YBCO thin films on LAO. (a) Distribution of critical temperatures; (b) thickness distribution; (c) distribution of critical current at 77 K; (d) distribution of microwave resistance at 77 K, 10 GHz.

5

BSCCO high-T_c superconducting films

H. RAFFY, South Paris University, France

Abstract: Since its discovery in 1986, the BiSrCaCuO cuprate family has given rise to an impressive number of studies both in fundamental and applied research. This chapter relates some fundamental studies carried out in BiSrCaCuO thin films and multilayers. In section 5.1, the main techniques of synthesis are described. Section 5.2 focuses on physical properties specifically studied in thin films. In the first part of this section, the role of anisotropy on the mixed state transport properties of thin films and multilayers is emphasized. In the second part, the influence of hole doping in the normal state is demonstrated by describing the temperature dependence of the resistance and Hall effect and comparing with angular photoemission spectroscopy (ARPES) results conducted in parallel on similar $Bi_2Sr_2CaCu_2O_{8+x}$ thin films.

Key words: cuprate thin films and multilayers, superconductivity, magnetoresistance, critical currents, Hall effect, doping.

5.1 Growth techniques of BSCCO thin films

5.1.1 Generalities

The $Bi_2Sr_2Ca_{n-1}Cu_nO_{2n+4}$ (in abbreviated form BSCCO) family of cuprates presents three stable superconducting phases: n = 1, 2 and 3, usually labelled from their cationic composition as 2201, 2212, and 2223 phases, with a critical temperature T_c increasing with n (20 K, 90 K, 110 K for n = 1, 2, 3, respectively). These compounds have a layer structure consisting schematically of charge reservoir blocks, the BiO double planes, alternating with conducting slabs made of one, two or three CuO_2 planes separated by Ca atoms, while SrO planes provide the stability of the structure (Fig. 5.1). One major difficulty for preparing thin films of such compounds is therefore to obtain single phase samples. Nevertheless, the major interest in studying this family is the possibility to grow artificial multilayers (ML) made by stacking one to a few unit cells of different phases.

The main techniques used to grow BSCCO thin films are vacuum based, with also a few techniques coming from chemistry science such as liquid phase epitaxy (LPE) or metal organic chemical vapour deposition (MOCVD). Whatever the technique, a number of parameters (pressure, oxygen, temperature of deposition) have to be carefully established in order to obtain deposits with good morphologies and transport properties. The first deposits of BSCCO were grown at room temperature and the amorphous deposits were annealed *ex situ* at high temperature (800–850 °C) in a furnace under an Ar/O_2 flow. The first 2212 and 2223 thin films

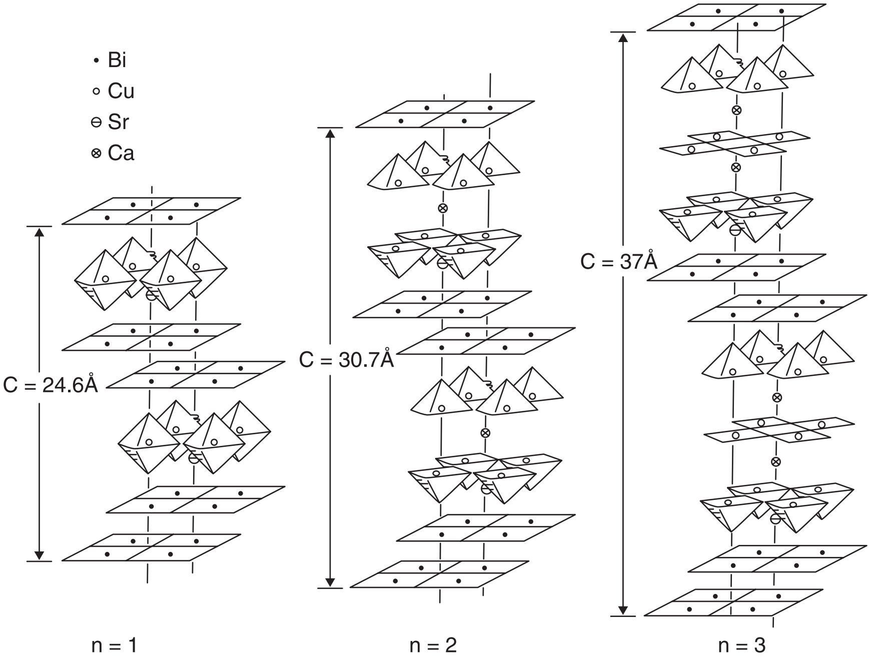

5.1 Crystallographic structure of $Bi_2Sr_2Ca_{n-1}Cu_nO_{4+2n}$ for n = 1, 2, 3.

with high T_c values around 90 K for 2212 (see for instance Raffy *et al.*, 1989) and 108 K for 2223 deposits (generally these films were multiphased) were obtained in this way (Labdi *et al.*, 1990). Although T_c was high, the critical current densities J_c of these films were rather low and rapidly decreased under magnetic fields over 100 Oe (Raffy *et al.*, 1991a). This was related to their structural characteristics. There was in general no preferential in-plane orientation: the films were c-axis oriented with a disorientation of the c-axis of the order of one degree. However, taking advantage of the presence of weak link grain boundaries, the first *dc* superconducting quantum interference devices (SQUID) operating at 77 K were patterned in 2223 thin films with T_c of 108 K (Müller *et al.*, 1992).

Soon after, a great improvement of the quality of the films (structure, critical currents, etc.) was accomplished by preparing *in situ* epitaxial superconducting thin films deposited on heated substrates. In this process, the crystallisation of the deposit occurs from the vapour phase at lower temperature than in the *ex situ* process: the films are smoother and there is no grain boundary, leading to a large increase of J_c. Another unique advantage was the possibility to prepare heterostructures and ML such as 2212/2201 ML, where epitaxy is easily preserved from one phase to the other, as they have nearly the same *a*, *b* lattice parameters. Synthesizing *in situ* superconducting BSCCO thin films requires appropriate substrates for epitaxy, and deposition at high temperature in the presence of oxygen. The oxygen content and the doping state of the film are tuned during the cooling phase of the preparation of the sample by adjusting the cooling rate and the oxygen partial pressure.

5.1.2 Techniques of deposition

The following sub-sections describe the techniques mostly employed for *in situ* preparation of BSCCO thin films.

Molecular beam epitaxy (MBE)

This technique was first developed for the synthesis of semiconductors. It is an ideal technique for growing layered compounds such as BSCCO. However, growing an oxide layer requires the presence of oxygen, which is a difficulty with the high vacuum environment necessary in MBE systems. It is certainly the best technique for growing artificial metastable high-temperature superconductor (HTS) cuprates and it has been used for this purpose by several groups in Japan, in the United States and in Europe. The most impressive MBE installation devoted to the growth of oxides is the one developed by I. Bozovic, at Brookhaven National Laboratory (see fig. 2 in Logvenov and Bozovic 2008), which includes a large number of *in situ* control facilities.

To grow BSCCO thin films, the metallic elements are thermally evaporated either from thermal effusion cells (Bi, Sr, Ca, etc.) or eventually with an e-gun for refractory elements. The atomic flux from each source can be monitored to a high accuracy using atomic absorption spectroscopy (Klausmeier-Brown *et al.*, 1992). It can also be measured prior to deposition by an ionization gauge at the substrate position. For atomic layer by layer deposition (ALL-MBE), computer controlled shutters allow one to open or close sequentially the sources of the different component elements (Eckstein *et al.*, 1991). Generally, the formation of the deposit is observed by reflection high energy electron diffraction (RHEED). It gives information, in real time, on the growing film surface, that is the epitaxy of the deposit (presence of the superstructure modulation, twinning) or the roughness of the surface (Bozovic and Eckstein, 1995). To provide oxygen during the growth, a source of atomic oxygen or of ozone is installed near the substrate and the substrate is heated at high temperature (600–760 °C). The values given in the different reports are generally that of the substrate holder, and they depend on the partial pressure of oxygen. During the cooling process, oxygen can be added to the deposit in the same way.

Films of the different phases have been grown by this technique: 2201 thin films (Schlom *et al.*, 1990; Tsukada *et al.*, 1991; Eckstein *et al.*, 1992; Salvato *et al.*, 1999a); 2212 thin films (Eckstein *et al.*, 1991; Brazdeikis *et al.*, 1995); 2223 films (Eckstein *et al.*, 1990a, b, 1991). More specifically, the ALL-MBE technique allowed one to prepare metastable $Bi_2Sr_2Ca_{n-1}Cu_nO_{2n+4}$ phases (n > 3) (Tsukada *et al.*, 1991a; Bozovic *et al.*, 1992, 1994; Nakayama *et al.*, 1991); particle-free superconducting $Bi_2Sr_2CaCu_2O_x$ ultrathin films deposited on a $Bi_2Sr_2CuO_y$ buffer layer (Ota *et al.*, 1999); and also ML with different stacking periodicities (Bozovic *et al.*, 1992; Nakao *et al.*, 1991). Also Di Luccio *et al.* (2003) were able to grow, by ALL-MBE technique, superconducting 2301 thin films ($T_c = 55$ K) by replacing Ca by Sr. This metastable compound cannot be obtained by equilibrium techniques.

Pulsed laser deposition (PLD)

This method has been largely developed with the advent of cuprates and since then it is the most used technique for preparing thin films of various oxides (manganites, cobaltites, pnictides, etc.). It ablates a ceramic target of the material with laser pulses, the ablated material depositing itself on a substrate fixed on a substrate holder maintained at high temperature. The earlier drawbacks encountered with this technique, which have been overcome now, were the formation of droplets and macro-particles of the material. This was detrimental in view of the synthesis of ML and junctions. To take advantage of the photoablation mechanism, the wavelength of the laser has to be in the UV range. So the laser is either an excimer laser or a Nd-YAG laser with doubling, tripling or quadrupling of the frequency. The laser ablation can take place in an UHV environment and, as in MBE systems it is possible to control the growth with a RHEED. The system can work as a Laser MBE system. An important advantage of this PLD technique is the possibility to work with a single target of one compound, as there is a good transfer of the composition of the target into the deposit. This is particularly important for the BSCCO compounds with many different elements. Besides, several targets can be used for artificial structure growth. As for MBE, the adjunction of oxygen is necessary to grow oxides. The following have been prepared by this technique: mainly Bi-2212 thin films (Ranno *et al.*, 1992; Kerboeuf *et al.*, 1993), Bi-2201 (Perrrière *et al.*, 1999) or Bi(La)-2201 (Cancellieri *et al.*, 2007a, b) thin films and metastable phases with up to four or five CuO_2 layers by multitarget PLD with an N_2O oxidizing source (Kanai *et al.*, 1989) and 2212/2201 ML (Horiuchi *et al.*, 1991). However one may notice that the reported T_c's of laser ablated BSCCO films had in general lower T_c values than those prepared with the MBE and the sputtering techniques.

The sputtering technique

The cathodic sputtering technique was largely used to grow a variety of films before the development of PLD. Also it has appeared that BSCCO deposits can grow half-unit cell by half-unit cell, rendering less sophisticated techniques, like the sputtering technique, competitive. The process gas is a mixture of Ar and O_2, or even pure O_2 (Hakuraku *et al.*, 1991). One major advantage for growing oxide films by cathodic sputtering is the presence of a reactive plasma, which has a powerful oxidant capability. Before the advent of cuprates, sputtering was used for growing ferroelectric perovskite-type oxide thin films. Therefore, it has been easy to apply the same technique to cuprates.

Different configurations of sputtering have been used: single or multiple targets to adjust more precisely the stoichiometry of the deposits (Ohbayashi *et al.*, 1994), planar or cylindrical targets, *dc* or *rf* sputtering, magnetron diode, etc. In many cases, one uses diode sputtering with one planar or cylindrical ceramic target of the compound. ML can be produced with the use of one target for each layer and a rotating sample holder (Fig. 5.2). Stoichiometric deposits are obtained with a good choice of the parameters: total pressure, partial pressure of O_2 (up to 100% (Hakuraku *et al.*, 1991)), power applied on the target, sample–target distance, temperature of the substrate (750–800 °C, being higher for higher oxygen pressure). In single target sputtering systems, the composition of the target is in general close to the nominal composition of the compound with eventually some deviation to compensate Bi losses or Cu excess in the deposit. In order to avoid the ion resputtering phenomena due to oxygen ions, it is necessary to work at relatively high pressure (0.3–3 torr) (Prieto *et al.*, 1991), with a small distance between target and substrate. It is also

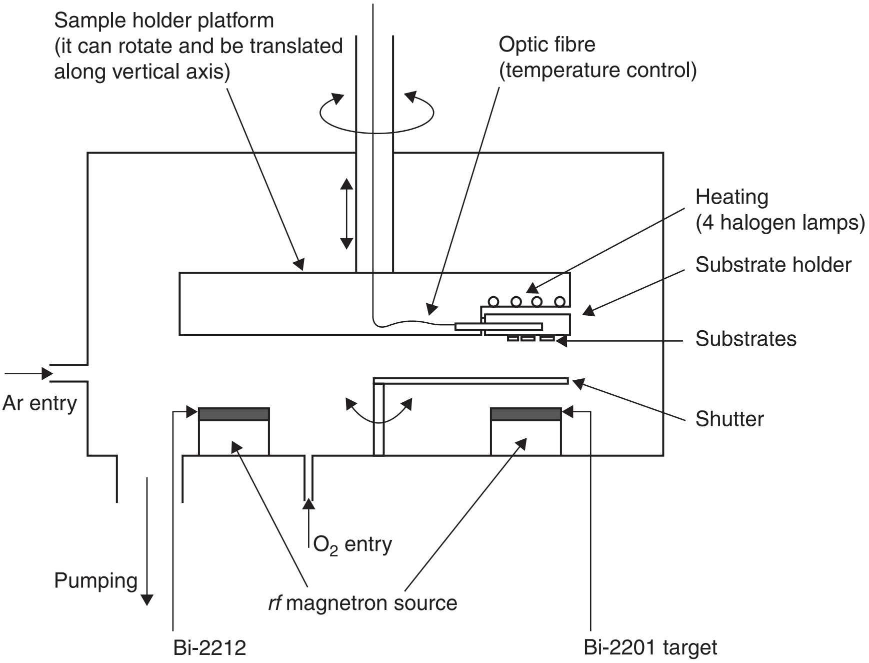
Sample holder platform
(it can rotate and be translated
along vertical axis)
Optic fibre
(temperature control)
Heating
(4 halogen lamps)
Substrate holder
Substrates
Ar entry
Shutter
O_2 entry
Pumping
rf magnetron source
Bi-2212
Bi-2201 target

5.2 Scheme of a sputtering system we used for preparing Bi-2212, Bi-2201 and 2212/2201 multilayers.

possible to use a hollow cylindrical target, the substrate holder being perpendicular to the axis of the target (Geerk *et al.*, 1991; Ohkubo *et al.*, 1995; Ye *et al.*, 2000). The first (*rf*) sputtered 2212 thin films and 2212/2201 ML were prepared by K. Wasa's group in Japan (Adachi *et al.*, 1988; Matsushima *et al.*, 1989, 1990; Wasa *et al.*, 1992). Also BSCCO films with 2223, 2234, 2245 structures were prepared by multitarget sputtering by Nakamura *et al.* (1990). Professor Adrian's group prepared by *de* diode sputtering both 2212 and 2223 thin films (Wagner *et al.*, 1992, 1993; Holiastou *et al.*, 1997a). We have prepared by *rf* magnetron sputtering 2212, 2201, La-2201 thin films and 2212/2201 ML (Li *et al.*, 1992, 1993, 1994, 2005).

The main drawback of the sputtering technique is the absence of *in situ* control of the growth, the deposit control being made *ex situ*. The advantages are the simplicity and versatility of the sputtering installation and the reproducibility of sputtering conditions.

Two 'chemical' techniques

One technique derived from semiconductor film technology is the metalorganic chemical vapour deposition process (MOCVD). It requires the good choice of metalorganic precursors, for instance $Bi(C_6H_5)_3$, $Sr(DPM)_2$, $Ca(DPM)_2$ and $Cu(DPM)_2$, used by Endo *et al.* (1991, 1992) for preparing 2223 films (see also Leskelä *et al*, 1993 for a review). The precursors are loaded in individual vaporizers, heated to appropriate temperatures and carried into a quartz reactor by a flow of Ar. The reactor must also be fed with oxygen gas. The substrate is placed on a susceptor heated at high temperature (800 °C). The total pressure in the case of Endo *et al.* (1991–1992) was 50 torr while p_{O2} was equal to 23 torr. Films of 2223 phase with $T_c = 97$ K (Endo *et al.*, 1991, 1992), and also (119) oriented films of mixed 2212 and 2223 phases deposited on (110) $SrTiO_3$ substrates with T_c in the 70 K range (Sugimoto *et al.*, 1992) have been obtained by this technique.

Another 'non vacuum technique' is liquid phase epitaxy (LPE) which was used for garnets. It has been performed by some groups, in particular by Balestrino *et al.* (1991) to prepare 2212 films. It consists of dipping a substrate ($SrTiO_3$, $LaGaO_3$, $NdGaO_3$) in a KCL solution of the material, maintained at high temperature (800 °C or more). Epitaxial films have been obtained with good structural and electronic properties. The thickness of the films prepared by this technique ranges from one to a few microns.

5.1.3 Nature of the substrates

The substrates mostly used for epitaxial growth of c-axis oriented BiSrCaCuO thin films are oxide single crystal with parameters close enough to the *a*, *b* lattice parameters of BSCCO: (100) $SrTiO_3$ ($a = 3.905$ Å), (100) MgO ($a = 4.212$ Å), (100) $LaAlO_3$ ($a = 3.821$ Å). For optical or high frequency measurements MgO is preferred to $SrTiO_3$ which has a high dielectric constant. However MgO has a significant mismatch with the compound, possibly leading to several crystalline orientations in the deposit. $LaAlO_3$ substrates are twinned, which induces twinning in the deposit. Some other less used substrates are $NdGaO_3$ ($a = 5.43$ Å, $b = 5.50$ Å); $SrLaGaO_4$ (3.84 Å; $c = 12.68$ Å), $SrLaAlO_4$ ($a = 3.75$ Å; $c = 12.63$ Å). Let us indicate also that (110) $SrTiO_3$ substrates have been used to grow BSCCO deposits with a tilted c-axis (Sugimoto *et al.*, 1992).

Some other types of substrates are required for particular purposes: vicinal substrates for transport studies both along the c-axis and ab plane (Ye *et al.*, 2000; Raffy *et al.*, 2007), or for obtaining deposits without twinning (Tsukada *et al.*, 1991b); bicrystal or tricrystal $SrTiO_3$ substrates to grow grain boundary junctions.

5.1.4 Main techniques of characterization

Films and multilayers are characterized by recording various X-ray diffraction spectra (Holiastou *et al.*, 1997a, b). θ–2θ X-ray spectra allow one to demonstrate that films are single-phase and c-axis oriented. It should be noted that, contrary to YBaCuO thin films, it is very difficult to grow 2212 films which are not c-axis oriented and only a few attempts have been reported (Sugimoto *et al.*, 1992; Tanimura *et al.*, 1993).

Even if the films appear to be single phase, the main defect encountered in BSCCO films is the presence of intergrowth. An analysis of the position of the reflection peaks (especially of the (002) reflection) allows one to determine their presence, nature and proportion (Ranno *et al.*, 1993; Brazdeikis *et al.*, 1995). Even 2201 films are not exempt of such defects, as intergrowths of one BiO layer 1201 compound (indicative of a lack of Bi) have been detected in $Bi_2Sr_{2-x}La_xCuO_6$ thin films grown by laser ablation (Cancellieri *et al.*, 2007a). Phi-scan spectra allow one to check that films are epitaxially grown, while ω scan spectra characterize their mosaicity. The compositions are checked by Rutherford backscattering spectroscopy (RBS) (Ranno *et al.*, 1992), energy dispersive X analysis (EDX) or inductive coupled plasma emission spectroscopy (ICP).

Transmission electron microscopy (TEM) studies require the preparation of ultrathin samples, for planar or transverse examinations, which is delicate (large difference in hardness between the substrate and the deposit) and destructive. High-resolution transmission electron microscopy (HR-TEM) has been used to characterize the microstructure of BSCCO films (Vailonis *et al.*, 1996). It allows observation of the quality of film/substrate interface (Fig. 5.3) and of the stacking faults and to detect defects present in the film (secondary phase, intergrowth, etc.).

Currently used techniques for scanning the surface of the deposits are atomic force microscopy (AFM) (Yang *et al.*, 1997; Ye *et al.*, 2000), scanning electron microscopy (SEM) and scanning tunnelling microscopy (STM) (Wagner *et al.*, 1993). Other techniques such as Raman spectroscopy (Holiastou *et al.*, 1997b) or photoemission are also used in some studies. It is interesting to mention the development of direct angle resolved spectroscopy systems (DARPES) in

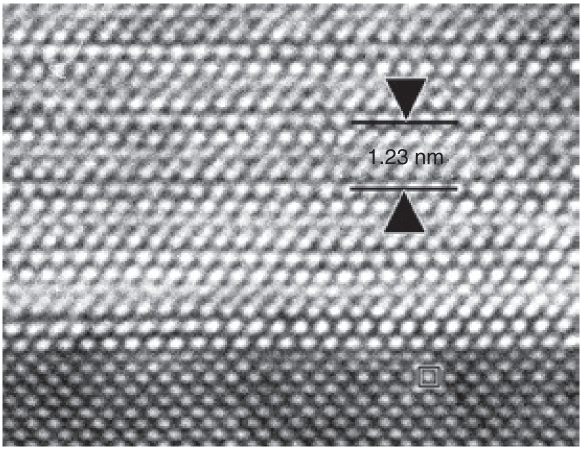

5.3 (110) HR-TEM image of a 2201 thin film deposited on a $SrTiO_3$ substrate. The cations are imaged as bright dots in the present conditions (adapted from Li *et al.*, 2005).

synchrotron facilities, such as the one installed at EPFL where the films grown by PLD are directly transferred to the Scienta chamber for advanced DARPES studies (see fig. 3 in Pavuna *et al.*, 2008). Finally the electronic properties are checked by transport or magnetic measurements.

5.1.5 Results overview for *in situ* grown BSCCO thin films

The growth of superconducting Bi-2201 thin films has been reported by relatively few groups, using different techniques. Thin films with a T_c of 15 K–20 K have been prepared by MBE (Eckstein *et al.*, 1991). Most Bi-2201 films have been prepared by sputtering with a planar single ceramic target. The maximum T_c attainable depends strongly on the ratio Sr/Bi. Pure 2201 thin films with a T_c of 20 K–22 K have been epitaxially deposited by single target *rf* magnetron sputtering on $SrTiO_3$ or MgO single crystal substrates (Li *et al.*, 1993). The FWHM was of the order of 0.1°. Films with higher T_c are obtained by using the cationic substitution Sr^{2+}/La^{3+}: this substitution reduces the hole content in the CuO_2 planes and it also decreases the amplitude of the structural modulation (Li *et al.*, 2005). Films with a $T_c(R = 0)$ of 30 K have been obtained with $x = 0.3–0.4$. Higher La content ($x = 0.9$) allows preparation of insulating films (Li *et al.*, 2005).

Films of the phase n = 2 are the most frequently studied. They have been *in situ* grown by all the different vacuum techniques described above. Films with T_c in the range 80 K–90 K have been obtained by MBE (Eckstein *et al.*, 1991) and sputtering (Wagner *et al.*, 1992, 1993; Li *et al.*, 1992), as indicated previously. Films prepared by laser ablation usually show a lower value of $T_{c\,max}$.

The films of the n = 3 phase are the most difficult to elaborate. The main problem is to obtain a pure phase and avoid the presence of intergrowth (mainly 2201, 2212 phases), and to obtain a high T_c value. This may be related to the difficulty of sufficiently doping the internal CuO_2 layer in the CuO_2 trilayer. Thin films of Bi-2223 with T_{c0} = 85 K have been prepared by MBE (Eckstein *et al.*, 1991) on $SrTiO_3$ subtrates in a sequential way: Bi-Bi-Sr-Cu-Ca-Cu-Ca-Cu-Sr-. The oxidation was insured by an O_3/O_2 beam near the substrate.

One of the best results concerning T_c was reported by Endo *et al.* (1991, 1992) who prepared 2223 films by MOCVD on $LaAlO_3$ (100) single crystal substrates. The reason for their success may be found in an extremely slow growth rate (1.2 nm h^{-1}) and a high oxygen pressure: P_{total} = 50 torrs, P_{O2} = 23 torrs during film growth. The maximum T_c (R = 0) of their films was equal to 94 K–97 K. The films were almost single phase and highly c-axis oriented. The good quality of the film was also shown by the critical current density value, J_c at 77 K, equal to approximately 10^5 A/cm^2.

Several groups reported some interesting results on the preparation of Bi-2223 films by sputtering. Professor Adrian's group obtained films with a T_c of 85 K–90 K (Wagner *et al.* 1995; Holiastou *et al.*, 1997a, b). By on-axis *dc* diode, high pressure sputtering, with a cylindrical target, they prepared *in situ* thin films on MgO subtrates by employing a range of sputtering parameters (Ptotal = 0.6–0.9 mbar, O_2/Ar = 0.8–1, T_{sub} = 730 °C–760 °C, as close as possible to the melting temperature T_m). Although their T_c onset was equal to 110 K, the T_c (R = 0) value was only 75 K. The T_c record for *in situ* prepared Bi-2223 thin films was obtained by Ohbayashi *et al.* (1994) using a multitarget sputtering technique for a subtle control of the Bi content. In their experiment, the substrate holder rotates at 20 rpm over three targets: Bi_2O_3, $Bi_2Sr_2CuO_x$, and $CaCuO_x$. They synthesized deposits with T_{c0} equal to 102.5 K and J_c(77 K) = 5 × 10^5 A/cm^2.

5.2 Physical properties of BSCCO thin films and multilayers

5.2.1 Introduction

This section describes a selected choice of typical experiments carried out on BSSCO thin films and multilayers, performed to investigate some particular properties of these cuprates. Although the mechanism of superconductivity is not yet established, original experiments based on thin films have been designed to look for the symmetry of the order parameter in these cuprates. HTS cuprates being layered compounds, anisotropy is therefore an important parameter which drives the properties of these compounds. Many experiments have been performed, based on multilayers, to study the role of anisotropy and coupling between CuO_2 bilayers on T_c. Consequences of the anisotropy of BSCCO have been widely demonstrated in transport experiments carried under magnetic field in the superconducting state.

Another way to investigate the mechanism of superconductivity in the cuprates is to study their normal state properties. They strongly depend on the doping state of the compound, ranging from a Mott insulator to a metallic and a superconducting state. The possibility to easily modify the oxygen doping level of a film allowed the exploration of the phase diagram by transport measurements carried on a single film. In addition, spectroscopic techniques like ARPES have shown fundamental information on the same systems.

5.2.2 The symmetry of the order parameter in 2212 thin films

Although the mechanism of superconductivity in cuprates is still under debate, one important and well-established result is the d-wave symmetry of the order parameter. In their phase sensitive tricrystal experiments, C.C. Tsuei and J.R. Kirtley have demonstrated the d-wave symmetry of the order parameter. Using a scanning SQUID microscope, they recorded the low temperature magnetic state of a superconducting deposit epitaxially grown on a tricrystal substrate, with three grain boundary junctions (Tsuei and Kirtley, 2000). Such experiment, first realized on a YBaCuO thin film, has been performed on epitaxial 2212 thin films at optimal doping (Kirtley *et al.*, 1996) and at various doping states showing a d-wave symmetry whatever the doping level (Tsuei *et al.*, 2004). The observation at the tricrystal point of the half-flux quantum vortex, the generation of which requires phase change by π, provides strong evidence for a dominating d x_2-y_2 wave component (Fig. 5.4).

Another independent set of phase-sensitive measurements has been performed by looking at the field dependence of the critical current, I_c, of faceted asymmetric 45° [100]/[110] bicrystal junctions (Schneider *et al.*, 2003). The experiment was carried on two types of c-axis oriented epitaxial 2212 thin films, one grown by MBE, the other by *rf* sputtering. In both cases, the anomalous recorded $I_c(H)$ characteristics lead to the conclusion that the pairing symmetry is dominated by a d-wave component.

Although angular photoemission spectroscopy (ARPES) is not phase sensitive, the spectra put evidence for a d-wave symmetry in 2212 at various doping levels.

5.2.3 Anisotropy and critical temperature in BSCCO multilayers

BSCCO compounds are natural superlattices, where metallic CuO_2 layers alternate with charge reservoir layers. In order to understand the mechanism of superconductivity (role of anisotropy and coupling between CuO_2 layers, proximity effect, etc.) in these systems, it became rapidly clear that an interesting method was to grow artificial superlattices or ML with different sequences of stacking. This was particularly important in the BSCCO family which presents several phases

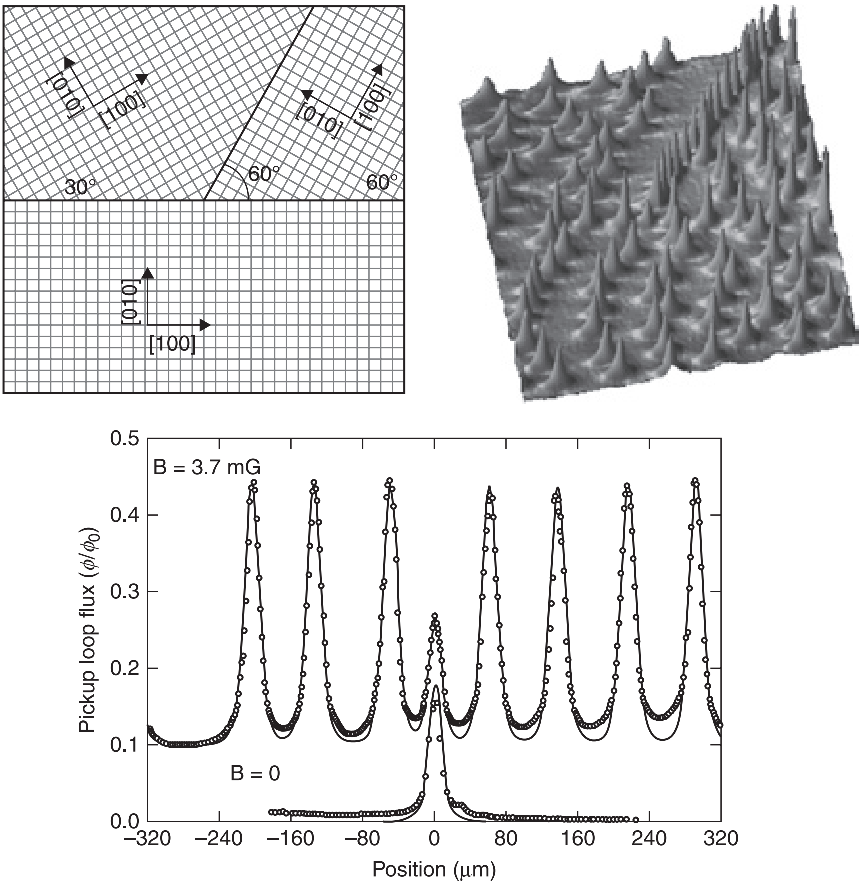

5.4 Scanning SQUID microscope picture (upper right figure) of the magnetic state (B = 3.7 mG, T = 4.2K) of a 2212 film epitaxially grown on a tricrystal $SrTiO_3$ substrate (upper left figure). Note the half flux quantum vortex at the tricrystal point, which is the only vortex left after degaussing (see graph) (adapted from C. C. Tsuei; Kirtley *et al.*, 1996).

with different T_c and similar in plane lattice parameters. Therefore, a number of groups started the elaboration of 2212/2201 ML. The first results showed that T_c was either decreased (Matsushima *et al.*, 1990) or not changed by layering (Kanai *et al.*, 1989; Nakao *et al.*, 1991). However these films and ML had rather low T_c and their 2201 layers were insulating (the importance of this fact will be shown later on). High quality ML were grown by MBE, with a spatial superlattice period composed of one half-unit cell of 2212 (15 Å thick) and a number n (1, 2 or 5) of 2201 half-unit cell (12 Å). Such ML are called $(2212)_1(2201)_n$ ML. It was found that T_c of these ML was essentially nearly independent of n and equal to that of a single phase 2212 thick film (T_c = 75 K) and it was not decreasing with the number of spacer cells (2201). This led the authors to conclude that HTS is a 2D phenomenon (Bozovic *et al.*, 1992). Interestingly, the synthesis of very high T_c $(2212)_1(2201)_n$ multilayers was also realized by two target sputtering (Li *et al.*, 1994). We showed the new result that the critical temperature of such ML ($T_c(R = 0) = 94$ K for $n = 2, 3$) was in fact *enhanced* compared to that of single phase 2212 films prepared in the same conditions ($T_c(R = 0) = 75$ K–80 K) (Fig. 5.5). This fact was attributed by us to the metallic nature of the 2201 layer (overdoped, with $T_c = 5$ K). In accordance with this scenario, we found that T_c of

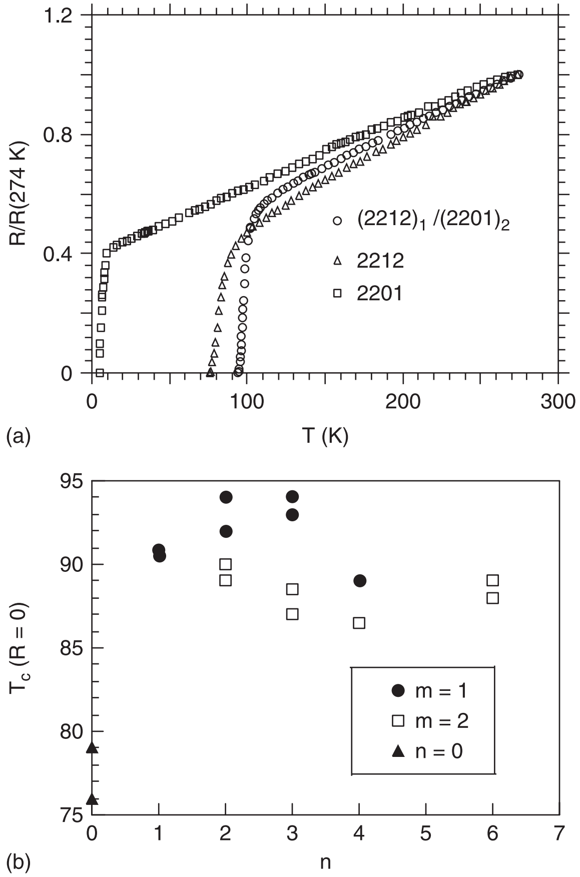

5.5 (a) Normalized resistive transition of a $(2212)_1(2201)_2$ multilayer (the superlattice period is composed of a half unit cell of 2212 and two half-unit cells of 2201 respectively), compared to the resistive transition of a 2212 and a 2201 film grown in the same conditions as the multilayer. (b) $T_c(R = 0)$ for two series of $(2212)_m(2201)_n$ multilayers with $m = 1$ and 2 respectively, as a function of n (the number of half unit cells in the 2201 separating layer), compared to the T_c values of 2212 films ($n = 0$) grown in the same conditions (adapted from Li *et al.*, 1994).

the ML to be decreased when the 2201 layer was insulating. It was concluded, in view of these results, that charge transfer was the most probable mechanism to explain this T_c increase. It is interesting to note that the observed 'proximity effect' is opposite to that expected for conventional superconductors in proximity with either a metallic layer or an insulating layer. Following these results, in another work reported some time later, a T_c enhancement in a $(2245)_1(2201)_1$ ML was also grown by multi-target sputtering, with $T_c = 40$ K, while a 2245 layer alone had $T_c = 10$ K and 2201 layer T_c less than 2 K (Hatano *et al*, 1997).

5.2.4 Mixed state transport properties and anisotropy of BSCCO thin films

Resistive transition under magnetic field and upper critical fields

It is known from the beginning of research on this cuprate family that the resistive transition of BSCCO submitted to a perpendicular magnetic field is strongly broadened, while in a parallel magnetic field the transition is much less affected. Earlier measurements of the resistive transition of 2212 thin films prepared by different techniques (MBE, sputtering) and with different morphologies (*ex situ* or *in situ* grown films), measured in magnetic fields up to 15 T have demonstrated that this broadening is not caused by inhomogeneities (Kucera *et al.*, 1992). It was also shown that the R(T) curves are well described by an Arrhenius law: $R = R_0 \exp\text{-}U(H)/T$, demonstrating the existence of an activated behaviour, with the activation energy, U, varying as $1/\sqrt{H}$. This property is explained by the anisotropy of the compound due to its layered structure. In the following years, a number of reports appeared analysing these enlarged transitions under perpendicular magnetic fields (for instance, Wagner *et al.*, 1993; Miu *et al.*, 1998).

The onset of the resistive transition, $\rho(T,H)$, provides, in principle, a way to determine the upper critical magnetic fields, or the fields which completely suppress superconductivity. For 2212 and 2223 phases, these fields are too high to be accessible with laboratory fields, except close to T_c. In contrast, their study has been possible in the case of the low T_c 2201 phase in a perpendicular field. By performing measurements of the resistive transition up to 35 T and down to 35 mK, Osovsky *et al.* (1994) have shown the anomalous temperature dependence of the upper perpendicular critical field $H_{c2}(T)$ of an optimally doped 2201 thin film, grown by MBE, with $T_c = 15$ K. Similar results have been reported by Rifi *et al.* (1994) on 2201 thin films made by sputtering, measured under 20 T. The origin of the anomalous T dependence of $H_{c2}(T)$, which is characterized by the presence of an upward positive curvature and the absence of saturation at low T, is still under debate. Among discussed arguments, there is the validity of the resistive determination of H_{c2}, the role of anisotropy and the presence of fluctuations above T_c. It is to be noted that similar $H_{c2}(T)$ variations were obtained either below T_c from the onset of the resistive transition or above T_c from the analysis of the orbital magnetoresistance in the framework of the Aslamazov–Larkin theory, for pure 2201 thin films at various doping (Bouquet *et al.*, 2006). This result points towards the existence of a similar correlation length above and below T_c.

It was also shown that, in a perpendicular magnetic field, the resistive transition of pure 2201 films is not broadened as in the 2212 case, but rather shifted to lower T. This fact (together with the absence of 2D angular scaling of the magnetoresistance indicated in the following sub-section) points towards a lower anisotropy of this phase compared to that of the 2212 phase. This point will be discussed further below.

From the foot of the resistive transition under a magnetic field, one can extract the magnetic field where the dissipation occurs, which is also called the irreversibility field, H_{irr}. For the higher fields, or not too close to T_c, its T variation is found to be of the form exp-T/T_0 where the temperature T_0 (~$0.1T_c$) is lower for lower T_c (Raffy *et al.*, 1991b, c). In the (H,T) phase diagram, the curve representing $H_{irr}(T)$ separates a lower field region where there is a vortex solid phase from a higher field region where there is a vortex liquid phase, its upper limit being $H_{c2}(T)$. As just described, this region is particularly wide for 2212, compared to less anisotropic cuprates like YBaCuO.

Anisotropy of the dissipation in the liquid vortex phase: angular and temperature scaling laws

In the vortex liquid region, the dissipation has been studied as a function of the magnetic field orientation with respect to the ab plane. Measurements of the mixed state magnetoresistance (MR) performed on 2212 thin films below T_c and under magnetic fields up to 20 T (Raffy *et al.*, 1991b) at different orientations of the magnetic field have shown that the MR depends only on the component of the field along the c-axis (Fig. 5.6), as suggested by Kes *et al.* (1990). This scaling breaks down very close to the parallel field situation (within 1°), reflecting the finite anisotropy of the compound. On the other hand, by recording, close to the ab plane ($-1° < \Theta < 1°$) and near T_c, the angular dependence of the magnetic field for which the dissipation appears in 2212 thin films, Fastampa *et al.* (1991) have demonstrated the existence of a crossover from a 2D to a 3D behaviour close to T_c.

While for La doped-2201 ($La \geq 0.2$) the same behaviour as that of 2212 films is observed, the 2D angular scaling property is not satisfied by the MR in pure 2201 thin films when the angle Θ between the ab plane and the magnetic field H becomes less than 30° and there is a rather large MR in parallel field (Rifi *et al.*, 1994). In contrast, the 2D scaling is perfectly satisfied in $(2212)_1(2201)_2$ ML at any angle. In the latter case, the resistance remains equal to zero in parallel magnetic fields up to 20 T and close to T_c. This system appears to be completely transparent to a parallel magnetic field, without Josephson coupling between the CuO_2 bilayers. It behaves as an ideal 2D system (Raffy *et al.*, 1994; Labdi *et al.* 1997).

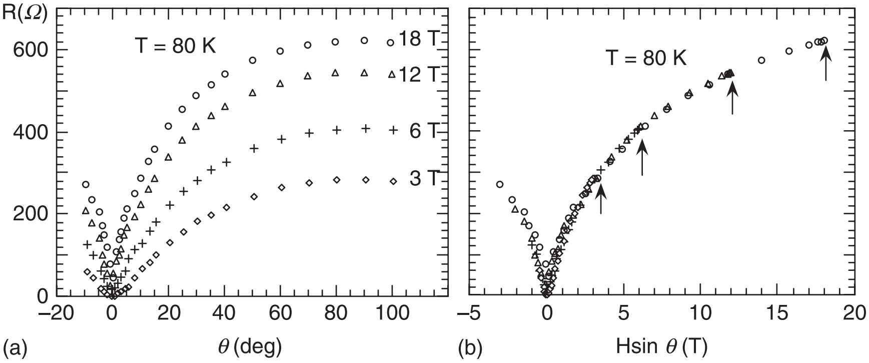

5.6 (a) Angular variation of the mixed state magnetoresistance of a $Bi_2Sr_2CaCuO_2$ thin film (T_c = 88 K) measured at T = 80 K, for various field intensities, when the applied magnetic field is rotated from parallel ($\theta = 0$) to perpendicular ($\theta = 90$ deg) to CuO_2 planes respectively. (b) Resistance data of (a) as a function of Hsin θ, the transverse component of the field. The arrows indicate the maximum resistance reached at $\theta = 90$ deg. for each given field intensity (adapted from Raffy *et al.*, 1991).

From the MR data close to T_c, the anisotropy under a magnetic field of BSCCO films can be estimated from the ratio of the parallel and perpendicular fields giving the same dissipation. So an anisotropy of 200–400 is found for 2212 (*in situ* deposited) and La-2201 films. A smaller value of the anisotropy, 8–20, depending on the doping level, was found for pure 2201 thin films. In contrast, a huge anisotropy, larger than 2000, was found for $(2212)_1/(2201)_2$ multilayers with T_c = 94 K (Raffy *et al.*, 1994).

From the MR measured in a perpendicular field, the 2D angular scaling law, described above, allows one to derive the MR behaviour for any field direction. Nevertheless it is important to consider the field dependence of the MR in a perpendicular magnetic field for 2212 films. It is observed that its behaviour is quite unusual, as compared to a conventional superconductor, with a quadratic variation at low fields, and a logarithmic one at high fields. It was shown that, for not too low resistance or sufficiently high fields, it can be described by the same expression, established by Larkin (1980) in order to describe the MR in the fluctuating regime of a 2D superconducting film above T_c. It indicates a decoherence effect between superconducting CuO_2 sheets above a phase breaking field, called $H_\Phi(T)$, which varies similarly to the irreversibility field: $H = H_0 \exp\text{-}T/T_0$. So the MR data measured at various temperatures can be described by a law of the form A(T).F(H/H(T)) and they lie on a single curve when plotted in the form: $R/A(T) = F(H/H_\Phi(T))$ (Raffy *et al.*, 1991c). Afterwards several other groups confirmed this observation in various 2D cuprate samples: 2212 single crystals (Fu *et al.*, 1992; Supple *et al.*, 1995; Babic *et al.*, 1997), 2D $(YBaCuO)_1/(PrBaCuO)_3$ or $(YBaCuO)_1/(PrBaCuO)_5$ ML (Fu *et al.*, 1993), which indicates that this result is not sample dependent and is a common property of CuO_2 bilayers. This mirror effect between the MR below T_c and the MR due to 2D SC fluctuations above T_c is still an intriguing result.

Another scaling law has been reported for the low resistance data tails, R(T,H), for 2D La-2201 thin films (Zhang *et al.*, 2000). Using a modified Coulomb gas scaling law, the low resistance data for various perpendicular magnetic fields ($0 \leq H \leq 5T$) fell on a single curve and a relationship between the activation energy and the scaling parameters was obtained.

Anisotropy of the critical currents

In the vortex solid phase, the critical current of BSCCO thin films measured in a constant magnetic field as a function of its orientation with respect to the ab planes presents a pronounced peak in a parallel field (Fig. 5.7). The sharper the peak, the higher the field or the temperature. Earlier angular measurements of J_c under high magnetic fields ($H \leq 20$ T) were made on *ex situ* c-axis oriented 2212 thin films at different temperatures and demonstrated that J_c essentially depends on the component of the field along the c-axis (Raffy *et al.*, 1991a). In a perpendicular field $H\perp$, at 4.2 K, $J_c(H\perp)$ varies like $1/\sqrt{H}$ above some field value, while $J_c(\theta)$ varies like $1/\sqrt{\cos\theta}$. This angular dependence was in agreement with theoretical results of Tachiki and Takahashi (1989), which emphasized the role of the intrinsic pinning of vortices by the crystallographic structure in a parallel field, while in a perpendicular field pinning centres are extrinsic defects. Similar 2D angular scaling was reported by Schmitt *et al.* (1991) from measurements on *in situ* grown (by PLD) 2212 thin films, which also demonstrates that this 2D scaling is not dependent on the presence of grain boundary weak links found in textured thin films. Only the amplitude of the critical current is different by a factor 10–100 going from *ex situ* to *in situ* grown thin films. 2D angular scaling was also reported by Jakob *et al.* (1993) both in 2212 thin films prepared by sputtering and in YBCO/PBCO ML. As for R(H), one may notice that when this 2D scaling is valid, by measuring the field dependence of $J_c(H\perp)$, one can establish the angular dependence $J_c(\theta)$ and reciprocally.

Considering now the variation of J_c $(H\perp,T)$ in a perpendicular field at different T, temperature scaling laws were also observed for the macroscopic pinning force: $F_P = J_c.H$. All the curves representing the pinning force, F_P/F_{Pmax}, normalized to its maximum value $F_{Pmax,}$ *vs* H/H_{irr}, collapse onto a single curve (Labdi *et al.*, 1992). Similarly, a scaling is also observed for the hysteresis loops measured at different T in epitaxial 2212 films (Kim *et al.*, 1995).

In parallel field, as already pointed out, the vortices are pinned by the intrinsic modulation of the superconducting parameter along the c-axis, reducing the rate of decrease of $J_c(H \parallel)$ in increasing field. So, at 4.2 K, in 2212 thin films, it is found that $J_c(H \parallel)$ is almost constant. At high T, $J_c(H \parallel)$ presents a decreasing behaviour like $J_c(H\perp)$, but occurring at much higher field (Labdi *et al.*, 1992).

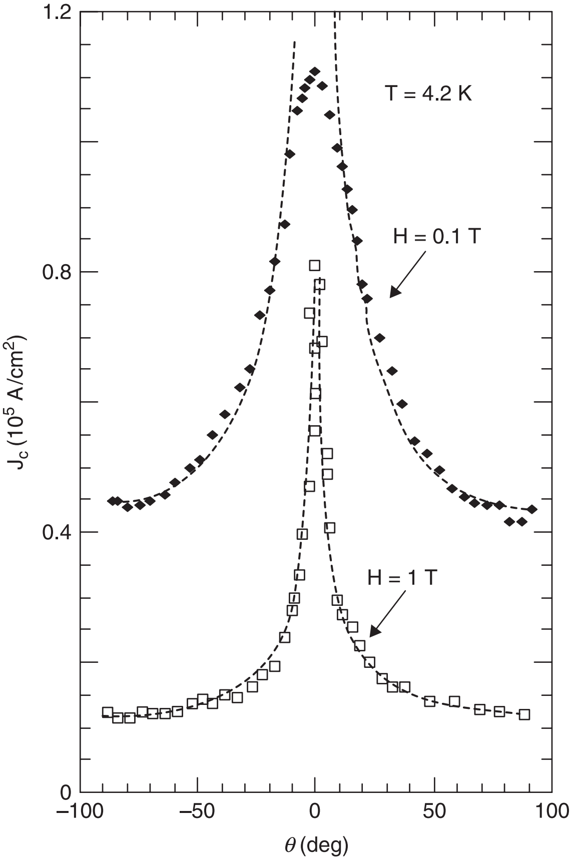

5.7 Angular dependence at 4.2 K of the critical current density J_c of a 2212 film (*ex-situ* prepared), as a function of magnetic field orientation (H parallel to the CuO_2 planes at $\theta = 0$. The dotted lines represent the function $J_c(H\perp)/\sqrt{\sin\theta}$ (adapted from Raffy *et al.*, 1991).

When the spacing between the superconducting CuO_2 bilayers (15 Å spacing) is increased by multilayering, as is the case in $(2212)_1(2201)_2$ ML (40 Å spacing), the critical current measured in strictly parallel field is found constant up to 20 T and at high T (80 K) (Fig. 5.8). The system appears to be transparent to a parallel magnetic field (no Josephson vortices). In contrast, a small decrease of $J_c(H \parallel)$ reappears above 60 K in $(2212)_2(2201)_2$ ML attributed to the possible formation of Josephson vortices inside the $(2212)_2$ double layer. Then the observed dissipation has been explained by activated hopping of Josephson segments to neighbouring layers and to the subsequent motion along the layers of vortex kinks (Labdi *et al.*, 1997). The same mechanism occurs in 2212 thin films in parallel fields at higher temperature (35–40 K).

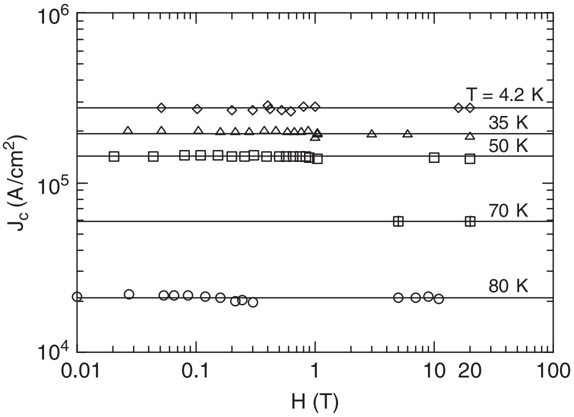

5.8 Field dependence of the critical current density of a $(2212)_1(2201)_2$ multilayer (T_c = 92 K) in a magnetic field parallel to the layers and at constant temperatures going from 4.2 K to 81 K.

In the case of 2201 thin films, although $J_c(\theta)$ is maximum in a parallel field, the 2D angular scaling is no longer valid, as there is a noticeable decrease of $J_c(H \parallel)$ in increasing field even at 4.2 K. This is related to the weaker anisotropy of this phase.

Probing the anisotropy by columnar pinning centres

The value of anisotropy in cuprates has a strong influence on the vortex behaviour. In a perpendicular magnetic field, one has pancake vortices in 2D systems (Crisan *et al.*, 2005) while one has line vortices in 3D systems. This can be evidenced by introducing linear pinning centres such as columnar defects (CD) created by heavy ion irradiation (Gerhaüser *et al.*, 1992; Hillmer *et al.*; 1999, Martel *et al.*, 2000). So, by measuring the angular dependence of the mixed state MR and of $J_c(\theta)$ at given field and temperature, the vortex pinning behaviour by the same concentration of CDs perpendicular to the CuO_2 planes has been compared in the different systems: 2201 and La-2201 thin films ($0 < La \leq 0.4$), 2212 thin films and $(2212)_1(2201)_2$ ML. A minimum of the MR or a maximum of J_c (Fig. 5.9) occurs when the field is parallel to the direction of the CDs in pure 2201 films or La-doped 2201 films with La < 0.2 (Pomar *et al.*, 2001a; Raffy *et al.*, 2004, 2006). There is no selective pinning effect of the vortices in 2201 (La = 0.3–0.4) and 2212 films, and in $(2212)_1$ $(2201)_2$ ML the 2D scaling laws are still valid. Therefore it was confirmed that pure Bi-2201 films are weakly anisotropic under magnetic field while in La^{3+}/Sr^{2+} substituted films, the high anisotropy is recovered and they behave as 2212 thin films (Raffy *et al.*, 2004, 2005, 2006). The reason for the increase of the anisotropy in La-2201 thin films is attributed to a decrease of the amplitude of the structural modulation as

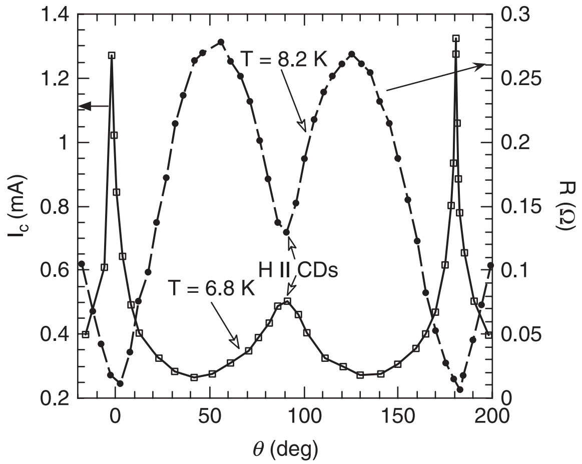

5.9 Directional pinning effect observed in the angular dependence of the MR and I_c of a $Bi_2Sr_{0.9}La_0.1CuO_x$ thin film with columnar defects parallel to the c-axis (irradiation dose: $n = 10^{15}$ ions/m^2 or $B_\Phi = n\Phi_0 = 2$ T) and measured in a field H = 1 T (adapted from Raffy *et al.*, 2004)

shown in an X-ray study (Li *et al.*, 2005) and to the consecutive decrease of the Josephson coupling between the CuO_2 planes.

A surprising result obtained in the study of the mixed state MR of irradiated 2212 thin films and $(2212)_1(2201)_2$ ML is the observation, in the liquid vortex phase, of a re-entrant pinning effect of the pancake vortices by CDs, while the 2D scaling remains valid. This was attributed to a confinement of 2D pancake vortices on the CDs, due to a balance between entropy, the energy gain obtained by vortex localization on the CDs and vortex repulsion (Pomar *et al.*, 2001).

5.2.5 Normal state properties of BSCCO films

How to modify the doping level in BSCCO thin films

It is well known that the electronic properties of BSCCO, like other cuprates, are essentially a function of their doping level. Superconductivity emerges from a Mott insulating state by introducing holes into the CuO_2 planes. This can be made in several ways. One way is heterovalent cationic substitution which is realized during the synthesis: for instance 2201 films with electronic properties going from superconducting to insulating states have been prepared by adjusting the Bi^{3+}/Sr^{2+} ratio (Inoue *et al.*, 1995), or by La^{3+}/Sr^{2+} substitution (Zhang *et al.*, 1998; Li *et al.*, 2005). A reversible way consists of modifying the oxygen content of a deposit, either *in situ* or *ex situ*. In the *in situ* case, it has in general been consistent to find the best conditions to approach the highest T_c of the compound. For instance, the critical temperature, T_c, of 2212 thin films deposited on $SrTiO_3$ substrates by high pressure sputtering ($P_{O2} = 3.5$ mbar, $T_{substrate} = 860$ °C) was maximized ($T_c \sim 90$ K) either by optimizing the oxygen flow during the deposition (Auge *et al.*, 1994) or by an *in situ* annealing stage during the cooling down process (Wagner *et al.*, 1992). The *ex situ* process consists of annealing treatments under a controlled partial pressure of oxygen, at low temperatures ($T \leq 420$ °C), for which there is no modification of the crystallographic structure. This procedure is particularly easy in thin films (large surface/volume ratio), giving the interesting possibility of following the evolution of the electronic properties of a unique sample throughout the complete phase diagram (see the following sub-section).

Other less conventional processes have been reported, able to modify the oxygen content of cuprate deposits. One of them is heavy ion irradiation, used to create amorphous columnar tracks in 2212 or 2201 thin films. It appeared that it also produces a self-oxygenation of the sample, the oxygen liberated in the amorphous tracks diffusing into the CuO_2 planes (Pomar *et al.*, 2000). As the irradiation was generally made on optimally doped samples, the decrease of T_c was attributed to disorder and this effect was ignored for a long time. It was well evidenced by irradiating underdoped non superconducting thin films, as they turned superconducting after irradiation (Fig. 5.10). Subsequently, this effect was also reported in irradiated 2212 single crystals (Li *et al.*, 2002).

Also, the illumination of an underdoped cuprate can produce a photodoping effect (Gilabert *et al.*, 1999, 2000). One explanation is that under illumination there is the creation of hole–electron pairs, and the electrons are pinned by oxygen vacancies while holes are transferred to CuO_2 planes. This technique was conveniently used for adjusting the doping level of grain boundary junctions.

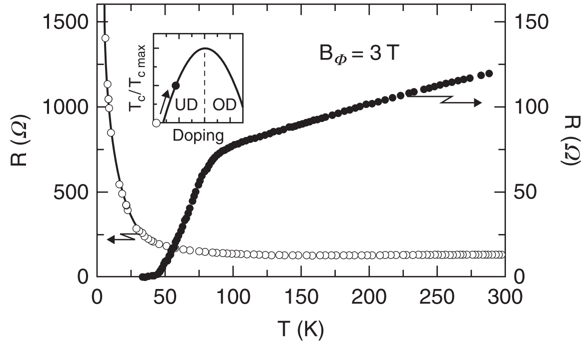

5.10 (○) R(T) of one underdoped semiconducting 2212 thin film. After 1 GeV Pb ion irradiation along the c-axis (dose: $n = 1.5 \times 10^{15}$ ions/m^2, or equivalent induction $B_\Phi = n\Phi_o = 3$ T, if all the columns were occupied by a vortex), a resistive transition is restored (●). In insert, a schematic phase diagram indicates the increase of doping due to irradiation.

Another technique, which potentially allows the changing of the carrier density without affecting the chemical composition, thus avoiding introducing disorder, is the electrostatic field effect. An electric field effect is applied across a gate dielectric (generally the $SrTiO_3$ substrate) and the cuprate film, changing the density of carriers at the interface of the dielectric and of the oxide, and so the electronic properties of the oxide channel. It has been successfully operated for changing the critical temperature (T_c modulation of 10 K, corresponding to induced charge densities of 0.7×10^{14} charges/cm^2) of an underdoped $NdBa_2Cu_3O_y$ thin film (3–4 unit cell thick) (Matthey *et al.*, 2007) and is now routinely used for changing the doping level of superconducting oxide interfaces (Caviglia *et al.*, 2008). However it has not been able to induce superconductivity in a nearly insulating $Bi_2Sr_{1.5}La_{0.5}CaCu_2O_{8+\delta}$ thin film on a $SrTiO_3$ substrate, although, conversely, it has been able to produce a considerable carrier depletion (Oh *et al.*, 2004). The reason given by the authors is a localization of the induced carriers confined to the top single CuO_2 layer.

Finally, another possible doping technique would be chemical electrolysis, which has been applied to YBaCuO thin films. The difficulty is to find an electrolyte which does not attack BiSrCaCuO cuprates.

Evolution of the resistivity vs doping and phase diagram

The evolution of the T dependence of the resistivity of a *same* film, 2212 or 2201, has been reported as a function of its doping level, varied from very overdoped to insulating states by removing a small quantity of oxygen in successive thermal annealing treatments (Konstantinovic *et al.*, 1999a, b, 2000a, b). It is interesting to describe these results in parallel with the results of ARPES experiments conducted on similar 2212 thin films, which followed the evolution of normal state electronic excitations with temperature and carrier concentration.

It should be remarked that the oxygen content cannot be measured in a thin film, due to its small mass. The doping state can be characterized by a parameter which varies monotonically with the doping level, such as the conductivity at 300 K or the Hall number, or even the c-axis lattice parameter. It is also possible to calculate the value of the doping level from the universal phenomenological relation: $T_c/T_{cmax} = 1\text{-}82.6\ (p\text{-}0.16)^2$, T_{cmax} being the maximum value of T_c obtained for $p = 0.16$, where p is the number of holes per Cu in a CuO_2 plane. However this relation may fail in the case of the underdoped 2201 phase (Konstantinovic *et al.*, 2003).

In a large temperature interval from room temperature to the onset of superconducting fluctuations, the in-plane resistivity, $\rho_{ab}(T)$, can be described by an empirical law of the form: $\rho_{ab}(T) = \rho_0 + bT^\nu$. The value of ν allows one to conveniently locate the doping level. In the overdoped region, the exponent ν decreases linearly from 1.3 to 1 with decreasing doping p (Konstantinovic *et al.*, 2000a). In the most overdoped state ($\nu = 1.3$), one can reach a pure metallic state only in the 2201 phase. The value $\nu = 1$ corresponds to the doping state for which there is the largest T interval where there is a linear variation of R(T) and is obtained for a doping level (p = 0.19) close to optimal doping (p = 0.16), but in the overdoped side (Oh *et al.*, 2005). For $p < 0.19$ and in the underdoped side, the value of ν of the law: $\rho_{ab}(T) = \rho_0 + bT^{\nu}$ becomes less than one.

Let us analyse more precisely the evolution of the resistivity through the phase diagram (T, p). In the overdoped side, it appeared that one can determine a temperature T** above which $\rho_{ab}(T)$ is linear and below which R(T) becomes superlinear (positive curvature). Conjugated transport and ARPES experiments on similar 2212 thin films at various doping states have shown that this crossover temperature T**, which increases with increasing doping, separates a coherent region, below T**, where a bilayer splitting is observed in the ARPES spectra, from an incoherent one above T**, without bilayer splitting (Kaminski *et al.*, 2003, and fig. 5 of this reference).

In the underdoped side, a $\rho_{ab}(T)$ curve comprises a high T linear part above a temperature T* while below T* the decrease of $\rho_{ab}(T)$ becomes more rapid and sublinear (negative curvature), the signature of a rapid reduction of the inelastic scattering rate of the electrons. The temperature, T*, higher for lower doping levels, is considered as the temperature below which the pseudogap opens (Ito *et al.*, 1993). In this region, ARPES spectroscopy shows a partial destruction of the Fermi surface near the nodal regions (Norman *et al.*, 1998). Low energy-excitations occupy disconnected segments called Fermi arcs. By ARPES studies on underdoped 2212, it was reported that the Fermi arc length decreases linearly *vs* T/T*(p), where p is the hole content, and extrapolates to zero as T goes to zero, suggesting that the state at T = 0 is a nodal liquid (Kanigel *et al.*, 2006). When the superconducting transition occurs, there is an abrupt collapse from a finite arc length which lies on the scaling line to a point node below T_c, (Kanigel *et al.*, 2007, see Fig. 5.4). The collapse of the Fermi arc has the same width as the resistive transition. Considering the resistive transition at various doping, a scaling law of the temperature dependent part of the resistivity, $(\rho_{ab}(T) - \rho_0)/b$ as function of T/T* has also been reported (Fig. 5.11 and Konstantinovic *et al.*, 2000a). This demonstrates that the important energy scale in this region is T*, while in the superconducting fluctuative region, close to T_c, the corresponding decrease of the resistivity scales with T/T_c. However, important pending questions concern the origin of the pseudogap and the nature of the temperature T*: is it a crossover or a transition temperature? By the use of circularly polarized photons and 2212 thin films in different doping states, underdoped and overdoped, it was shown by ARPES that, below T*, left-circularly polarized photons give a different photocurrent than right circularly polarized ones (Kaminski *et al.*, 2002). This observation, which demonstrates that time reversal symmetry is spontaneously broken below T*, appears to indicate a phase transition at T*. This result has been highly discussed since 2002. The variation with doping of the characteristic temperatures T_c, T*, T** allows us to establish the phase diagram (T, doping) (Fig. 5.12). Except for the region to the right below the T**line,

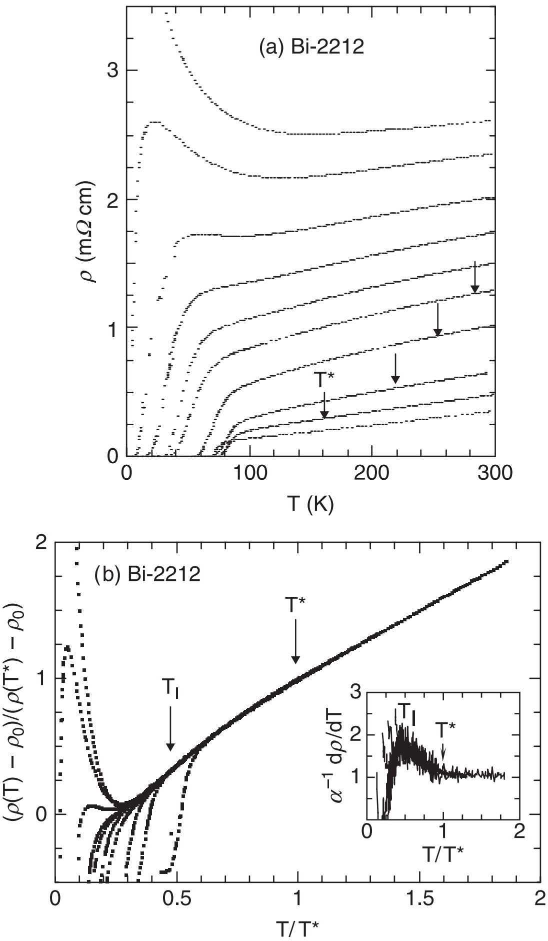

5.11 (a) Temperature dependence of the resistivity of a 2212 thin film, examined at decreasing oxygen content, going from overdoped (lower resistances) to underdoped insulating states. The arrows indicate the temperature T* below which the resistivity decreases more rapidly than linear. (b) Scaling of the temperature dependent part of the resistivity normalized by its value at T*, as a function of T/T* (at T > T*, $\rho = \rho_0 + \alpha T$). The temperatures T* and T_1, indicated by arrows in the main figure, correspond to the temperature where the derivative $\alpha^{-1}d\rho/dT$ starts to increase from 1 (T*) and is maximum (T_1), respectively (adapted from Konstantinovic *et al.*, 2000).

where properties are getting close to that of a Fermi liquid for strong doping, the electronic properties of cuprates are anormal. The two lines representing T* and T** *vs* doping delimit a wedge region called strange metal where the temperature dependence of the resistivity is linear. The region below T* is the pseudogap region which is not yet understood.

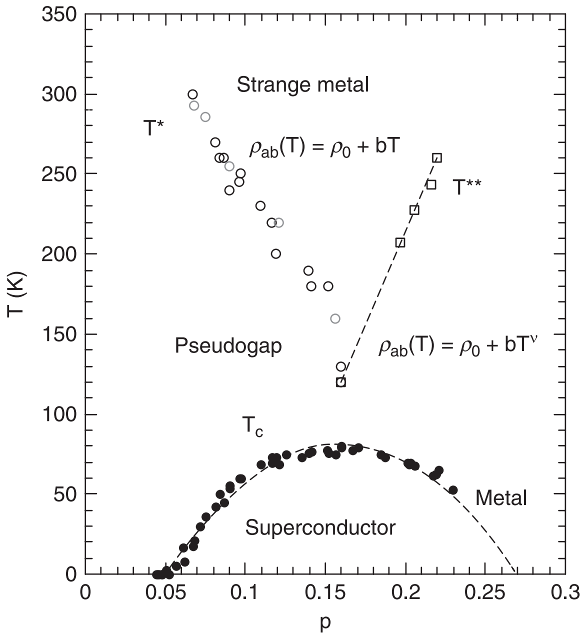

5.12 Experimental phase diagram and characteristic temperatures T_c, T*, T** obtained by studying the evolution of the temperature dependence of the resistivity of 2212 films as a function of their carrier concentration varied by progressively decreasing their oxygen content (adapted from Konstantinovic *et al.*, 2000a).

By comparing the evolution of R(T) curves of 2212 and 2201 thin films *vs* doping, it was found that T* has comparable values in both phases despite a factor four difference in their optimal critical temperature, suggesting that superconductivity and pseudogap are independent phenomena (Konstantinovic *et al.*, 2000a). This result on T* was confirmed later on by Yurgens *et al.* (2003) by a tunnelling experiment on La-2201 single crystals.

By further decreasing the oxygen content, the superconducting-insulating transition (SIT) is approached. So adjusting the oxygen content offers a convenient way to drive the SIT in cuprates. This has been studied both in 2212 and 2201 thin films (Konstantinovic *et al.*, 2000a, 2001; Oh *et al.*, 2006; Matei *et al.*, 2009). In all cuprates, near the SIT, R(T) exhibits a high T metallic behaviour, a minimum at a temperature T_{min} followed by a non metallic behaviour ($dR/dT< 0$) and a maximum at T_p caused by the onset of the superconducting transition at T_c. This re-entrant metallic behaviour was attributed to a phase segregation in the sample due to strong electronic correlations and/or inhomogeneous oxygen distribution (Oh *et al.*, 2006; Matei *et al.*, 2009). Here again, a scaling of the resistance divided by its value at T_p *vs* the reduced temperature T/T_p is observed both for 2212 and

2201 films (Fig. 5.13). By further deoxidation, superconductivity disappears and an insulating behaviour is only shown with successively logarithmic, activated and variable range hopping behaviours of R(T), with increasing deoxidation. Oh *et al.* (2006) claimed that the SIT transition occurs without an intermediate metallic state. Recently, ARPES experiments on underdoped non-superconducting

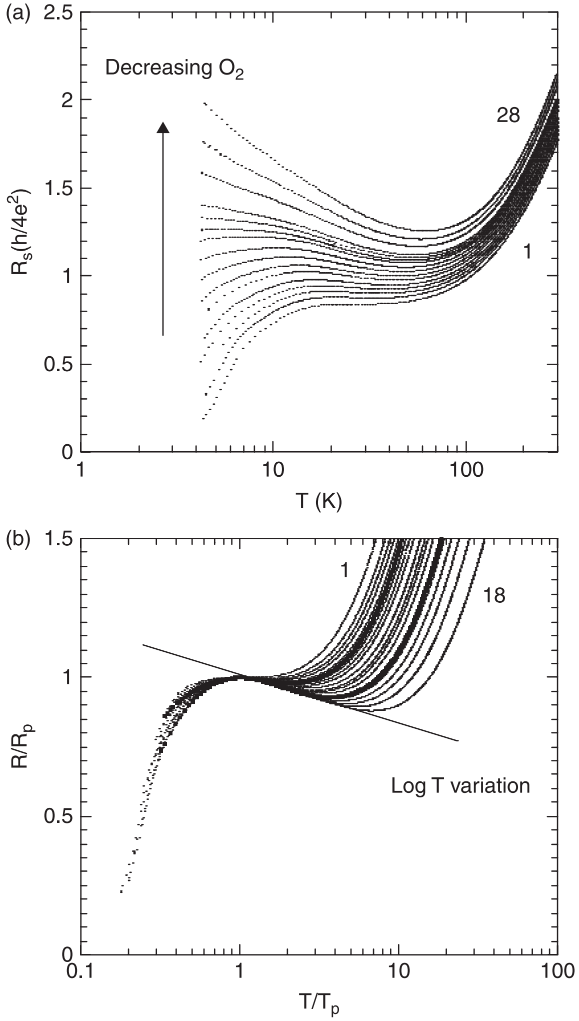

5.13 Superconducting–insulating transition of a La-2201 (La = 0.6) thin film monitored by oxygen doping: (a) resistance per square as a function of log T for decreasing oxygen contents for the states going from 1 to 28 (not all the curves are represented for clarity); (b) scaling for the states 1 to 18 of the low T part of R renormalized by its value R_p *vs* T/T_p, where R_p and T_p are the coordinates of the maximum of R(T) (adapted from Matei *et al.*, 2009).

films have shown the existence of a d-wave-like gap that persists through the insulator to superconductor transition (fig. 2d in Chatterjee *et al.*, 2010). This led the authors to conclude that the nodal liquid appears as a phase-incoherent version of the d-wave superconductor (Chatterjee *et al.*, 2010). How superconductivity emerges from the Mott insulating state is a fundamental question to be solved in the route towards the comprehension of cuprate properties.

Interestingly, it was thought possible to follow the evolution of the resistivity along the c-axis, ρ_c(T), as a function of the oxygen content of a Bi-2212 film deposited on a vicinal substrate. The resistivity curves, ρ_c(T), along the c-axis, metallic at high T, exhibit a minimum at T_{min} followed by an insulating low T increase. A remarkable scaling was observed on the resistivity normalized by its value at T_{min}, $\rho_c(T)/\rho_c(T_{min})$, *vs* T/T_{min}. Here, T_{min} was considered as the temperature of the opening of the pseudogap, easier to detect on ρ_c(T) (Raffy *et al.*, 2007).

Temperature dependence of the Hall effect at various doping

Another anormal property of the normal state of cuprates is the fact that the Hall effect is T dependent. It has been measured on 2212 and La-2201 (La = 0.4) thin films at various doping levels (Konstantinovic *et al.*, 2000b). All the R_H(T) curves exhibit a broad maximum (around 130 K in the underdoped region). A quantity studied theoretically (Anderson, 1991), the cotangent of the Hall angle, θ_H, defined as $\rho/R_H H$, displays a simpler behaviour which can be described by a phenomenological expression of the form $b + cT^{\alpha}$ above a temperature T_0. The exponent α is equal to two only in the strongly underdoped region and decreases with increasing doping to the value 1.65 in the overdoped region. No evidence of the opening of a pseudogap is seen in the T variation of cot θ_H. The behaviour of the two phases (2212 and La-2201 with La = 0.4) is very similar. Interestingly the Hall number n_H measured at 300 K appears to be proportional to the number of holes per Cu. Also it varies linearly as a function of the conductivity at 300 K, $\sigma_{300\,K}$.

The T dependence of the Hall effect has been revisited in a pure 2201 film with a maximum T_c of 10 K. The pure 2201 phase is more disordered due to the larger amplitude of the incommensurate modulation (Li *et al.*, 2005). The T dependence of the Hall effect has been found weakly dependent on doping (Fruchter *et al.*, 2007). It is proposed that the maximum in R_H(T) arises from a combination of a large T-independent scattering rate and an anisotropic T dependent one in this compound.

5.3 Concluding remarks and future trends

The synthesis of epitaxial BSCCO thin films and multilayers, described in the first part of the chapter, has stimulated a lot of work leading to improvements and advances in the techniques of thin film synthesis. Techniques previously used for semiconductor preparation, like MBE, have been adapted to grow oxides. A new technique, PLD, has known an impressive development and is now the most frequently used technique to grow various kinds of oxide thin films. Sputtering appears to be well suited to grow BSCCO thin films and it allows one to reach very high doping levels with an oxygen-rich plasma.

In the second part, the description of physical properties was focused on a few important aspects of BSCCO properties, as obtained from the study of BSCCO thin films. Although there is a consensus on the d-wave character of the order parameter, there is still no answer concerning the mechanism of HTC superconductivity which remains an open question. The research on BSCCO ML with ultrathin layers has shown that HTC superconductivity exists in CuO_2 bilayers, provided they are in proximity with metallic layers. Such a result, which is inverse of usual proximity effect, is an important fact to take into account in the search for the mechanism of superconductivity. The works on cuprate multilayers have been pioneering, leading to a wider range of study of oxide heterostructures. This is now a field in active development.

In the mixed state, strong anisotropy ($n = 2$ phase and $(2212)_1(2201)_2$ML) leads to interesting scaling laws of the MR and J_c, as a function both of angle and temperature. However the $n = 1$ phase, which has a much lower T_c than other cuprates, also has a lower anisotropy under magnetic field, probably related to the presence of a structural modulation leading to an increase of the interlayer coupling. Interestingly, the temperature T* of the pseudogap opening, the puzzling phenomenon of the normal state, is unchanged in contrast to T_c. The study of the normal state (temperature, doping) phase diagram of BSCCO thin films with various doping has been performed using resistivity and spectroscopic experiments. In the underdoped region, various scaling laws have been shown to be a function of T/T*, pointing out the fact that, in this region, the important energy scale is T*. Such experiments will no doubt contribute to resolving the mystery of HTC.

Although only fundamental aspects were considered in this chapter, some properties are of interest for applied research. One of them is the possibility to easily tune the doping in BSCCO thin films, and modulate it spatially by appropriate masking during oxygenation or deoxidation, to produce insulating zones in contact with SC areas. Finally, an interesting property of BSCCO is the fact that its structure realizes a natural nanometric, 1D, Josephson lattice. Studies are being carried out, mainly on single crystals, to see if such a system may be used to produce or detect signals in the THz range. If this turns out to be the case, BSCCO thin films and multilayers could know a new development.

5.4 Acknowledgements

I am indebted to my colleague C. Pasquier for critical reading of this chapter.

5.5 References

Adachi H, Ichikawa Y, Hirochi K, Matsushima T, Setsune K and Wasa K (1988), 'Preparation and properties of superconducting Bi-Sr-Ca-Cu-O thin films', *Jpn J Appl Phys,* **27**, L643–L645.

Anderson P W (1991), 'Hall effect in the two-dimensional Luttinger liquid', *Phys Rev Lett*, **67**, 2092–2094.

Auge J, Rüdiger U, Frank H, Roskos H G, Güntherodt G and Kurz H (1994), 'Oxygen control of dc-sputtered $Bi_2Sr_2CaCu_20_{8+\delta}$ films', *Appl Phys Lett*, **64**, 15448–15455.

Babic D, Ivkov J and Leontic B (1997), 'Two-dimensinal decoherence effects in superconducting sheets of single crystal $Bi_2Sr_2CaCu_2O_{8+x}$', *Physica C*, **277**, 203–212.

Balestrino G, Marinelli M, Milani E, Paoletti A and Paroli P (1991), 'Compositional dependence of properties of $Bi_{2-y}Pb_ySr_{3-x}Ca_xCu_2O_{8+z}$ films grown by liquid phase epitaxy', *J Appl Phys*, **70**, 6939–6944.

Bouquet F, Fruchter L, Sfar I, Li Z Z and Raffy H (2006), 'Upper critical field from normal state fluctuations in $Bi_2Sr_2CuO_{6+d}$', *Phys. Rev. B*, **74**, 064513–064520.

Bozovic I, Eckstein J N, Klausmeier-Brown M E and Virshup G (1992), 'Superconductivity in epitaxial $Bi_2Sr_2CuO_6$/$Bi_2Sr_2CaCu_2O_8$ superlattices: The superconducting behavior of ultrathin cuprate slabs', *Journal of Superconductivity*, **5**, 19–23.

Bozovic I, Eckstein J N, Virshup G F, Chaiken A, Wall M *et al.* (1994), 'Atomic-layer engineering of cuprate superconductors', *Journal of Superconductivity*, **7**, 187–195.

Bozovic I and Eckstein J N (1995), 'Analysis of growing films of complex oxides by RHEED', *MRS Bull*, May, 32–38.

Brazdeikis A, Vailionis A, Flodström A S and Traeholt C (1995), 'Molecular beam epitaxy growth and microstructure of thin superconducting $Bi_2Sr_2CaCu_2O_x$ films', *Physica C*, **253**, 383–390.

Cancellieri C, Lin P H, Ariosa D and Pavuna D (2007a), 'Embedded polytypes in $Bi_2Sr_{2-x}La_xCuO_6$ thin films grown by laser ablation', *Phys. Rev. B*, **76**, 174520–174527.

Cancellieri C, Lin P H, Ariosa D and Pavuna D (2007b), 'Dopant rearrangement and superconductivity in $Bi_2Sr_{2-x}La_xCuO_6$ thin films under annealing', *Journal of Physics: Cond Mat*, **19**, 246214–246221.

Caviglia A D, Gariglio S, Reyren N, Jaccard D, Schneider T *et al.* (2008), 'Electric field effect control of the $LaAlO_3$/$SrTiO_3$ interface ground state', *Nature (London)*, **456**, 624–627.

Chatterjee U, Shi M, Ai D, Zhao J, Kanigel A *et al.* (2010), 'Observation of a d-wave nodal liquid in highly underdoped $Bi_2Sr_2CaCu_2O_{8+d}$', *Nature Physics*, **6**, 99–103.

Crisan A, Bending S J, Popa S, Li Z Z and Raffy H (2005), 'Observation of interacting crossing vortex lattices in $Bi_2Sr_2CaCu_2O_{8+d}$', *Phys Rev B*, **72**, 214509–214513.

Di Luccio T, Lukic V, Oh S, Maritato L and Eckstein J N (2003), 'Complete substitution of Sr for Ca in $Bi_2Sr_{2+x}Ca_{1-x}Cu_2O_{8+d}$', *Phys Rev B*, **67**, 092504–092507.

Eckstein J N, Bozovic I, von Desonneck K E, Schlom D G, Harris J S and Baumann S M (1990a), 'Atomically layered heteroepitaxial growth of single-crystal films of superconducting $Bi_2Sr_2Ca_2Cu_3O_x$', *Appl Phys Lett*, **57**, 931–933.

Eckstein J N, Bozovic I, Schlom D G and Harris J S (1990b), 'Growth of untwinned $Bi_2Sr_2Ca_2Cu_3O_x$ thin films by atomically layered epitaxy', *Appl Phys Lett*, **57**, 1049–1051.

Eckstein J N, Bozovic I, Schlom D G and Harris J S (1990b), 'Growth of superconducting $Bi_2Sr_2Ca_{n-1}Cu_nO_x$ thin films by atomically layered epitaxy', *Journal of Crystal Growth*, **111**, 973–977.

Endo K, Yamasaki H, Misawa S, Yoshida S and Kajimura K (1991), 'High-Tc and high-Jc superconducting BSCCO thin films grown by MOCVD', *Physica C*, **185–189**, 1949–1950.

Endo K, Yamasaki H, Misawa S, Yoshida S and Kajimura K (1992), 'High quality superconducting thin films of $Bi_2Sr_2Ca_2Cu_3O_x$ grown by metalorganic CVD' *Nature (London)* **355**, 327–328.

Fastampa R, Giura M, Marcon R and Silva E (1991), '2D to 3D Crossover in Bi-Sr-Ca-Cu-O: Comparison with synthetic multilayered superconductors', *Phys Rev Lett*, **67**, 1795–1798.

Fu C M, Boon W, Wang Y S, Moshchalkov V V and Bruynseraede Y (1992), 'Magnetoresistance and conductivity fluctuations in single crystalline $Bi_{1.7}Pb_{0.3}Sr_{1.9}CaCu_{1.9}O_{8+x}$', *Physica C*, **200**, 17–22.

Fu C M, Moshschalkov V V, Rossel E, Baert M, Boon W *et al.* (1993), 'Effect of dimensional crossover on the magnetoresistance of $YBa_2Cu_3O_7/PrBa_2Cu_3O_7$ superlattices', *Physica* C, **206**, 110–118.

Fruchter L, Raffy H, Bouquet F and Li Z Z (2007), 'Contribution of disorder to the Hall effect in $Bi_2Sr_2CuO_{6+d}$', *Phys Rev B*, **75**, 092502–092505.

Geerk J, Linker G, Meyer O, Ratzel F, Reiner J *et al.* (1991), 'Systematic studies of HTSC thin film growth by ion-sputtering', *Physica C*, **180**, 11–16.

Gerhaüser W, Ries G, Neumüller H W, Schmidt W, Eibl O *et al.* (1992), 'Flux-line pinning in $Bi_2Sr_2CaCu_2O_x$ crystals: Interplay of intrinsic 2D behaviour and irradiation-induced columnar defects', *Phys Rev Lett*, **68**, 879–882.

Gilabert A, Hoffmann A, Medici M G and Schüller I K (2000), 'Photodoping effects in high critical temperature superconducting films and Josephson junctions', *Journal of Superconductivity*, **13**, 1–19.

Gilabert A, Plecenik A, Medici M G, Grajcar M, Karlovsky K and Dittman R (1999), 'Influence of illumination on the properties of $Bi_2Sr_2CaCu_2O_{8+y}$ bicrystal grain-boundary junction', *Appl Phys Lett*, **74**, 3869–3871.

Hakuraku Y, Nagayama K and Ogushi T (1991), 'Effect of pure oxygen sputtering gas pressure on the *in situ* growth of BiSrCaCuO superconducting thin films', *Supercond Sci Technol*, **4**, 717–720.

Hatano T, Ishii A and Nakamura K (1997), 'Synthesis and superconductivity of a $(Bi_2Sr_2Ca_4Cu_5O_{14})_1(Bi_2Sr_2CuO_6)_1$ superlattice film', *Physica C*, **273**, 342–348.

Hillmer F, Jacob G, Haibach P, Frey U, Kluge Th *et al.* (1999), 'Absence of correlated flux pinning by columnar defects in irradiated epitaxial $Bi_2Sr_2CaCu_2O_8$ thin films', *Physica C*, **311**, 11–18.

Holiastou M, Psyharis V, Niarchos D, Haibach P, Frey U and Adrian H (1997a), 'Preparation and X-ray pole-figure, characterization of DC-sputtered Bi-2201, Bi-2212 and Bi-2223 thin films', *Supercond Sci Technol*, **10**, 712–716.

Holiastou M, Poulakis N, Palles D, Liarokapis E, Niarchos D *et al.* (1997b), 'XRD and micro Raman characterization of epitaxial Bi-2201, Bi-2212 and Bi-2223 thin films', *Physica C*, **282–287**, 583–584.

Horiuchi K, Kawai T, Kanai M and Kawai S (1991), '$Bi_2Sr_2CaCu_2O_8/Bi_2Sr_2CuO_6$ superconducting superlattices: modulation of the number of CuO_2 plane between Bi_2O_2 layers', *Jpn J Appl Phys*, **30**, L1381–1383.

Inoue M, Matsushita H, Hayakawa H and Ohbayashi K (1995), 'Critical sheet resistance and two-dimensional properties of $Bi_2Sr_2CuO_x$ thin films', *Phys Rev B*, **51**, 15448–15455.

Ito T, Takenaka K and Uchida S (1993), 'Systematic deviation from T-linear behaviour in the in-plane resistivity of $YBa_2Cu_3O_{7-y}$: evidence for dominant spin scattering', *Phys Rev Lett*, **70**, 3995–3998.

Jakob G, Schmitt M, Kluge Th, Tomé-Rosa C, Wagner P *et al.* H (1993), 'Scaling of the angular dependence of the critical current density in high-T_c superconductors', *Phys Rev B*, **47**, 12099–12103.

Kaminski A, Rosenkranz S, Fretwell H M, Campuzano J C, Li Z Z *et al.* (2002), 'Spontaneous breaking of time-reversal symmetry in the pseudogap state of a high-T_c superconductor' *Nature (London)* **416**, 610–613.

Kaminski A, Rosenkranz S, Fretwell H M, Li Z Z, Raffy H *et al.* (2003), 'Crossover from coherent to incoherent electronic excitations in the normal state of high temperature superconductors', *Phys Rev Lett*, **90**, 207003–207006.

Kanai M, Kawai T and Kawai S (1989), 'Low-temperature formation of multilayered Bi(Pb)-Sr-Ca-Cu-O thin films by successive deposition using laser ablation', *Appl Phys Lett*, **54**, 1802–1804.

Kanigel A, Norman M R, Randeria M, Chatterjee U, Souma S *et al.* (2006), 'Evolution of the pseudogap from Fermi arcs to the nodal liquid', *Nature Physics*, **2**, 447–451.

Kanigel A, Chatterjee U, Randeria M, Norman M R, Souma S *et al.* (2007), 'Protected nodes and the collapse of Fermi arcs in high-*Tc* cuprate superconductors', *Phys Rev Lett*, **99**, 157001–157004.

Kerboeuf S, Toledano J C, Barnole V, Savaru H, Litzler A *et al.* (1993), 'Insulating materials for BiSrCaCuO-multilayers', *Applied Superconductivity*, **1**, 761–768.

Kes P H, Aarts J, Vinokur V M and van der Beek C J (1990), 'Dissipation in highly anisotropic superconductors', *Phys Rev Lett*, **64**, 1063–1066.

Kim S F, Li Z Z and Raffy H (1995), 'Scaling behaviour of the irreversible magnetization in epitaxial $Bi_2Sr_2CaCu_2O_y$ thin films', *Physica C*, **244**, 78–82.

Kirtley J R, Tsuei C C, Raffy H, Li Z Z, Gupta A *et al.* (1996), 'Half-integer flux quantum effect in tricrystal $Bi_2Sr_2CaCu_2O_{8+d}$', *Europhysics Lett*, **36**, 707–712.

Klausmeier-Brown M E, Eckstein J N, Bozovic I and Virshup G F (1992), 'Accurate measurements of atomic beam flux by pseudo-double-beam atomic absorption spectroscopy for growth of thin-film oxide superconductors', *Appl Phys Lett*, **60** 657–659.

Konstantinovic Z, Li Z Z and Raffy H (1999a) 'Temperature dependence of the resistivity of oxygen-controlled $Bi_2Sr_2CaCu_2O_{8+d}$ thin films: pseudogap effect', *Physica C*, **259–261**, 567–568.

Konstantinovic Z, Laborde O, Monceau P, Li Z Z and Raffy H (1999b), 'Normal state magnetoresistance in $Bi_2Sr_2CaCu_2O_{8+d}$ thin films with different oxygen contents', *Physica C*, **259–261**, 569–570.

Konstantinovic Z, Li Z Z and Raffy H (2000a), 'Temperature dependence of the Hall effect in single-layer and bilayer $Bi_2Sr_2Ca_{n-1}Cu_nO_n$ thin films at various oxygen contents', *Phys Rev B*, **62**, R11989–R11992.

Konstantinovic Z, Li Z Z and Raffy H (2000b), 'Normal state transport properties of single- and double-layered $Bi_2Sr_2Ca_{n-1}Cu_nO_y$ thin films and pseudogap effect', *Physica C*, **341–348**, 859–862.

Konstantinovic Z, Li Z Z and Raffy H (2001), 'Evolution of the resistivity of single-layer $Bi_2Sr_{1.6}La_{0.4}CuO_y$ thin fims with doping and phase diagram', *Physica C*, **351**, 163–168.

Kucera J T, Orlando T P, Virshup G and Eckstein J N (1992), 'Magnetic-field and temperature dependence of the thermally activated dissipation in thin films of $Bi_2Sr_2CaCu_2O_{8+\delta}$', *Phys Rev B*, **46**, 11004–11013.

Labdi S, Raffy H, Megtert S, Vaures A and Tremblay P (1990), 'Growth of the 110 K superconducting phase and characterization of Pb-doped Bi-Sr-Ca-Cu-O thin films prepared by sputtering', *Journal of the Less Common Metals*, **164–165**, 687–694.

Labdi S, Raffy H, Laborde O and Monceau P (1992), 'Angular dependence of critical currents in $Bi_2Sr_2CaCu_2O_8$ thin films predominant role of the transverse magnetic field component', *Physica C*, **197**, 274–282.

Labdi S, Kim S F, Li Z Z, Raffy H, Laborde O and Monceau P (1997), 'Magnetic field dependence of the critical currents of $Bi_2Sr_2CaCu_2Oy/Bi_2Sr_2CuO_z$ multilayers: an approach to the ideal two dimensional situation', *Phys Rev Lett*, **79**, 1381–1385.

Larkin A I, 'Reluctance of two-dimensional systems' (1980), *JETP Lett*, **31**, 219–224.

Leskelä M, Mölsä H and Niinistö L (1993), 'Chemical vapour deposition of high-Tc superconducting thin films', *Supercond Sci Technol*, **6**, 627–656.

Li M, van der Beek C J, Konczykowski M, Zandbergen H W and Kes P H (2002), 'Self-doping caused by oxygen displacements in heavy-ion-irradiated $Bi_2Sr_2CaCu_2O_{8+x}$ crystals', *Phys Rev B*, **66**, 014535–014540.

Li Z Z, Labdi S, Vaurès A, Megtert S and Raffy H (1992), 'In situ growth of superconducting Bi-Sr-CaCu-O thin films by RF magnetron sputtering', in Correra L, *High Tc Superconductor Thin Films*, Amsterdam, Elsevier Science Publishing Company, pp. 487–492.

Li Z Z, Rifi H, Vaures A, Megtert S and Raffy H (1993), 'Oxygen induced superconducting, metallic or insulating behaviour in as-grown epitaxial $Bi_2Sr_2CuO_X$ thin films,' *Physica C*, **206**, 367–372.

Li Z Z, Rifi H, Vaurès A, Megtert S and Raffy H (1994), 'Synthesis of $Bi_2Sr_2CaCu_2O_8/Bi_2Sr_2CuO_6$ superlattices with a T_c enhancement effect', *Phys Rev Letters*, **72**, 4033–4036.

Li Z Z, Raffy H, Bals S, van Tendeloo G and Megtert S (2005), 'Interplay of doping and structural modulation in superconducting $Bi_2Sr_{2-x}La_xCuO_y$ thin films', *Phys Rev B*, **71**, 174503–174509.

Logvenov G and Bozovic I (2008), 'Artificial superlattices grown by MBE: could we design novel superconductors?', *Physica C*, **468**, 100–104.

Martel L, Pomar A, Li Z Z and Raffy H (2000), 'Pinning effect of columnar defects as a probe of anisotropy of $Bi_2Sr_2Ca_{n-1}Cu_nO_{2n+1}$ thin films', *Physica C*, **341–348**, 1297–1298.

Matei I, Li Z Z and Raffy H (2009), 'Observation of the superconducting-insulating transition in a BiSr(La)CuO thin film tuned by varying the oxygen content', *Journal of Physics: Conference series*, **150**, 052154–052157.

Matsushima T, Ichikawa Y, Adachi H, Setsune K and Wasa K (1990), 'Superconducting properties of $Bi_2Sr_2CaCu_2O_y/Bi_2Sr_2CuO_x$ multilayer thin films', *Solid State Commun*, **76**, 1201–1204.

Matsushima T, Hirochi K, Adachi H, Setsune K and Wasa K (1989), 'Structure and superconducting properties of Bi-Sr-Ca-Cu-O thin films annealed at low temperatures', *Jpn J Appl Phys*, **28**, L97–L99.

Matthey D, Reyren N, Triscone J M and Schneider T (2007), 'Electric-field-effect modulation of the transition temperature, mobile carrier density, and in-plane penetration depth of $NdBa_2Cu_3O_{7-d}$ thin films', *Phys Rev Lett*, **98**, 057002–057005.

Miu L, Jakob G, Haibach P, Hillmer F, Adrian H and Almasan C C (1998), 'Vortex-liquid entanglement in $Bi_2Sr_2CaCu_2O_{8+d}$ films in the presence of quenched disorder', *Phys Rev B*, **57**, 3151–3155.

Müller F J, Gallop J C, Caplin A D, Labdi S and Raffy H (1992), 'A DC SQUID using natural grain boundaries in BSCCO', *Physica C*, **202**, 268–270.

Nakayama Y, Tsukada I and Uchinokura K (1991), 'Superconductivity of $Bi_2Sr_2Ca_{n-1}Cu_nO_y$ (n = 2, 3, 4, and 5) thin films prepared in situ by molecular-beam epitaxy technique', *Appl Phys Lett*, **70**, 4371–4377.

Nakamura K, Sato J and Ogawa K (1990), 'Formation of thermally stable multilayered BSCCO films with 2223, 2234 and 2245 structures', *Jpn J Appl Phys*,' **29**, L77–L80.

Nakao M, Furukawa H, Yuasa R and Fujiwara S (1991), 'Superconductivity in BiSrCaCuO superlattices: two-dimensional properties of CuO planes', *Jpn J Appl Phys*, **30**, L3929–L3932.

Norman M R, Ding H, Randeria M, Campuzano J C, Yokoya T *et al.* (1998), 'Destruction of the Fermi surface in underdoped high-T_c superconductors', *Nature (London)*, **392**, 157–160.

Oh Seongshik, Warusawithana M and Eckstein J N (2004), 'Electric field effect on insulating cuprate planes', *Phys Rev B*, **70**, 064509–064513.

Oh Seongshik, Di Luccio Tiziana and Eckstein J N (2005), 'T linearity of in-plane resistivity in $Bi_2Sr_2CaCu_2O_{8+d}$ thin films', *Phys Rev B*, **71**, 052504–052506.

Oh Seongshik, Crane Trevis A, Van Harlingen D J and Eckstein J N (2006), 'Doping controlled superconductor-insulator transition in $Bi_2Sr_{2-x}La_xCaCu_2O_{8+\delta}$', *Phys Rev Lett*, **96**, 107003–107006.

Ohbayashi K, Ohtsuki T, Matsushita H, Nishiwaki H, Takai Y and Hayakawa H (1994), 'As grown superconducting $Bi_2Sr_2Ca_2Cu_3O_x$ thin films with T_{c0} of 102 K prepared by rf magnetron sputtering', *Appl Phys Lett*, **64**, 369–371.

Ohkubo M, Geerk J, Linker G and Meyer O (1995),'Phase intergrowth in $Bi_2Sr_2Ca_2Cu_3O_x$ superconducting thin films prepared by single cylindrical-sputtering gun', *Appl Phys Lett*, **67**, 2403–2406.

Osovsky M S, Soulen R J, Wolf S A, Broto J M, Rakoto H *et al.* (1994), 'Measurements of Hc_2(T) in Bi-Sr-Cu-O', *Journal of Superconductivity*, **7**, 279–282.

Ota H, Migita S, Kasai Y, Matsuhata H and Sakai S (1999), 'Particle-free superconducting $Bi_2Sr_2CaCu_2O_x$ ultrathin films prepared by atomic-layer-controlled molecular beam epitaxy', *Physica C*, **311**, 42–48.

Pavuna D, Ariosa D, Cancellieri C, Cloetta D and Abrecht M (2008), 'Direct angle resolved photoelectron spectroscopy (DARPES) on high-T_c films: doping, strains, Fermi surface topology and superconductivity', *Journal of Physics: Conference Series*, **108**, 012040–012047.

Perrière J, Defourneau R M, Laurent A, Mocrette M and Seiler W (1999), 'Growth of $Bi_2Sr_2CuO_x$ films by laser ablation', *Physica C*, **311**, 231–238.

Pomar A, Martel L, Li Z Z, Laborde O and Raffy H (2001), 'Reentrant pinning effect in the vortex liquid phase of a quasi-two-dimensional $Bi_2Sr_2CaCu_2O_8$/$Bi_2Sr_2CuO_6$multilayer with columnar defects', *Phys Rev B*, **63**, R020504–R020507.

Pomar A, Konstantinovic Z, Martel L, Li Z Z and Raffy H (2000), 'Interplay of self-doping and disorder in epitaxial $Bi_2Sr_2Ca_{n-1}Cu_nO_{2n+4+x}$ (n = 1, 2) thin films under heavy-ion irradiation', *Phys Rev Lett*, **85**, 2809–2812.

Presland M R, Tallon J L, Buckley R G, Liu R S and Flower N E (1991), 'General trends in oxygen stoichiometry effects on T_c in Bi and Tl superconductors', *Physica C*, **176**, 95–105.

Prieto P, Gomez M E, Castro L F, Soltner H, Poppe U *et al.* (1991), 'In situ growth of superconducting Bi-Sr-Ca-Cu-0 thin films by a high pressure sputtering process', *Surface Science*, **251–252**, 712–716.

Raffy H, Labdi S, Vaures A, Arabski J, Megtert S and Perriere J (1989) 'Elaboration and characterization of superconducting Bi-Sr-Ca-Cu-O and Bi(Pb)-Sr-Ca-Cu-O thin films made by single target sputtering', *Physica C*, **162–164**, 613–614.

Raffy H, Labdi S, Laborde O and Monceau P (1991a), 'Critical current anisotropy of BiSrCaCuO thin films under magnetic fields', *Supercond Sci Technol*, **4**, S100–102.

Raffy H, Labdi S, Laborde O and Monceau P (1991b), 'Scaling properties of the anisotropic magnetoresistivity of $Bi_2Sr_2CaCu_2O_8$ thin films below T_c', *Phys Rev Lett*, **66**, 2515–2518.

Raffy H, Labdi S, Laborde O and Monceau P (1991c) 'Scaling of the mixed state magnetoresistance of high T_c superconductors in terms of two dimensional fluctuations', *Physica C*, **184**, 159–164.

Raffy H, Labdi S, Li Z Z, Rifi H, Kim S F *et al.* (1994), 'Superconducting properties and anisotropy of $Bi_2Sr_2CaCu_2O_y$ films and $Bi_2Sr_2CaCu_2O_y/Bi_2Sr_2CuO_y$ superlattices grown by sputtering', *Physica C*, **235–240**, 182–185.

Raffy H, Murrills C, Pomar A and Li Z Z (2004), 'Novel effects observed in heavy ion irradiated $Bi_2Sr_{2-x}La_xCuO_y$ thin films', *Ann Phys,* **13**, 97–98.

Raffy H, Murrills C D, Pomar A, Stiufiuc G, Stiufiuc R and Li Z Z (2006), 'Anisotropy and vortex behaviour in BiSrCaCuO thin films and multilayers probed by columnar pinning centers', *Physica Status Solidi (a)*, **203**, 2938–2943.

Raffy H, Toma V, Murrills C and Li Z Z (2007), 'c-Axis resistivity of $Bi_2Sr_2CaCu_2O_y$ thin films at various oxygen doping: phase diagram and scaling law', *Physica C*, **460–462**, part 2, 851–853.

Ranno L, Perrière J, Enard J P, Kerhervé F, Laurent A and Perez-Casero R (1992), 'RBS study of *in situ* grown BiSrCaCuO films', *Solid State Commun*, **83**, 67–71.

Ranno L, Martinez-Garcia D and Perrière J (1993), 'Phase intergrowth in $Bi_2Sr_2Ca_{n-1}Cu_nO_y$ thin films', *Phys Rev B*, **48**, 13945–13948.

Rifi H, Li ZZ, Megtert S, Raffy H, Laborde O and Monceau P (1994), 'Angular dependence of the magnetoresistance below T_c of epitaxial $Bi_2Sr_2CuO_y$ thin films', *Physica* C, **235–240**, 1433–1434.

Salvato M, Salluzzo M, Di Luccio T, Attanasio C, Prischepa S L and Maritato L (1999a), 'Properties of $Bi_{2+x}Sr_{2-x}CuO_{6+\delta}$ thin films obtained by MBE', *Thin Solid Films*, **353**, 227–232.

Salvato M, Attanasio C, Carbone G, Di Luccio T, Prischepa SL *et al.* (1999b), '$Bi_2Sr_2CuO_{6+\delta}/ACuO_2$ (A = Ca,Sr) superconducting multilayers obtained by molecular epitaxy', *Physica C*, **316**, 215–223.

Schlom D G, Marshall A F, Sizemore J T, Chen Z J, Eckstein J N et al. (1990), 'Molecular beam epitaxial growth of layered Bi-Sr-Ca-Cu-O compounds', *Journal of Crystal Growth*, **102**, 361–375.

Schneider C W, Neils W K, Bielefeldt H, Hammerl G, Schmehl A *et al.* (2003) 'Pairing symmetry in $Bi_2Sr_2CaCu_2O_y$', *Europhys Lett*, **64** (4), 489–495.

Sugimoto T, Kubota N, Shiora Y and Tanaka S (1992), 'Electrical anisotropy in Bi-Sr-Ca-Cu-O thin films prepared on (110) SrTiO3 by metalorganic chemical vapour deposition', *Appl Phys Lett*, **60**, 1387–1389

Supple F, Campbell A M and Cooper J R (1995), 'An investigation of the irreversibility line in $Bi_2Sr_2CaCuO_2$ single crystals', *Physica C*, **206**, 233–245.

Tachiki M and Takahashi S (1989), 'Anisotropy of critical current in layered oxide superconductors', *Solid State Commun*, **72**, 1083–1096.

Tanimura J, Kuroda K, Kataoka M, Wada O, Takami T *et al.* (1993), '(01n)-Oriented BiSrCaCuO thin films formed on CeO_2 buffer layers', *Jpn J Appl Phys*, **32**, L254–L256.

Tsuei C C and Kirtley J R (2000), 'Pairing symmetry in cuprates', *Rev Modern Phys*, **72**, 969–1016.

Tsuei C C, Kirtley J R, Hammerl G, Mannhart J, Raffy H and Li Z Z (2004), 'Robust $d_{x^2-y^2}$ pairing symmetry in hole-doped cuprate superconductors', *Phys Rev Lett*, **93**, 187004–187007.

Tsukada I and Uchinokura K (1991a), 'In situ preparation of superconducting $Bi_2Sr_2Ca_{n-1}Cu_nO_y$ (n = 1~5) thin films by molecular beam epitaxy technique', *Jpn J Appl Phys*, **30**, L1114–1117.

Tsukada I and Uchinokura K (1991b), 'Nearly untwinned $Bi_2Sr_2CuO_y$ thin films grown on (Y, Nd)AlO_3 (001) substrate' *Jpn J Appl Phys*, **30**, L1468–1470.

Vailionis A, Brazdeikis A and Flodström A S (1996), 'Microstructural properties of $Bi_2Sr_2Ca_{n-1}Cu_n O_y$ multilayers grown by molecular beam epitaxy', *Phys Rev B*, **54**, 15457–15462.

Wagner P, Adrian H and Tomé–Rosa C (1992), 'In situ-preparation of $Bi_2Sr_2CaCu_2O_y$-thin films by DC-sputtering', *Physica C*, **195**, 258–262.

Wagner P, Hillmer F, Frey U, Adrian H, Steiborn T *et al.* (1993), 'Preparation and structural characterization of thin epitaxial $Bi_2Sr_2CaCu_2O_{8+d}$ films with T_c in the 90 K range', *Physica C*, **215**, 123–131.

Wagner P, Frey U, Hillmer F and Adrian H (1995), 'Evidence for a vortex-liquid-vortex-glass transition in epitaxial $Bi_2Sr_2Ca_2Cu_3O_{10+d}$', *Phys Rev B*, **51**, 1206–1212.

Wasa K, Matsushima T and Setsune K (1992), 'Layer-by-layer deposition of multilayer Bi-Sr-Ca-Cu-O/Bi-Sr-Cu-O', *Vacuum*, **43**, 1027–1029.

Yang H, Tao H, Zhang Y, Yang D, Li L and Zhao Z (1997), 'AFM study of growth of $Bi_2Sr_{2-x}La_xCuO_6$ thin films', *Supercond Sci Technol*, **10**, 782–785.

Ye M, Zhang Y Z, de Marneffe J F, Delplancke-Ogletree M P and Deltour R (2000), 'Structural characterization of epitaxial $Bi_2Sr_2CuO_6$ thin films deposited on $SrTiO_3$ substrates using inverted cyclindrical magnetron sputtering', *Thin Solid Films* **377–378**, 597–601.

Yurgens A, Winkler D, Claeson T, Ono S and Ando K (2003), 'Intrinsic tunneling spectra of $Bi_2(Sr_{2-x}La_x)CuO_{6+\delta}$', *Phys Rev Lett*, **90**, 147005–147008.

Zhang Y Z, Li L, Yang D G, Zhao B R, Chen H *et al.* (1998), 'Epitaxial growth of $Bi_2Sr_{2-x}La_xCuO_{6+x}$ by RF-magnetron sputtering', *Physica C*, **295**, 75–79.

Zhang Y Z, Deltour R and Zhao Z X (2000), 'Coulomb-gas scaling law for a superconducting $Bi_2Sr_{2-x}La_xCuO_{6+d}$ thin films in magnetic fields' (2000), *Phys Rev Lett*, **85**, 3492–3495.

6

Electron-doped cuprates as high-temperature superconductors

M. NAITO, Tokyo University of Agriculture and Technology, Japan

Abstract: The divalent copper ion in high-T_c copper oxides takes three different oxygen coordinations: 6-fold octahedral, 5-fold pyramidal, and 4-fold square-planar coordinations, which is different from other 3*d* transition-metal ions taking only the 6-fold octahedral coordination in most cases. Copper oxides with the 4-fold square-planar coordination may be the least familiar but the most distinguished compounds. Only two families are known at present: 'Nd_2CuO_4' compounds and 'infinite-layer' compounds. The two families have been categorized as 'electron-doped' superconductors since superconductivity appears only by electron doping. However, one long-standing puzzle is why superconductivity in these compounds appears only after oxygen reduction. With regard to this puzzle, it has now been well established that impurity oxygen atoms at the apical site in the square-planar coordination are quite harmful to high-T_c superconductivity, and hence have to be cleaned up. In this chapter, copper oxides with the Nd_2CuO_4 structure are reviewed from both the material and physical points of view, especially regarding how to clean up impurity oxygen atoms more completely and what to see in these compounds free of impurity oxygen atoms.

Key words: square-planar cuprates, electron-doped cuprates, rare earth cuprates, tolerance factor, electronic phase diagram, electron-hole symmetry, doped Mott-insulator scenario, pairing symmetry.

6.1 Introduction

The divalent copper ion in high-T_c copper oxides takes three different oxygen coordinations as shown in Fig. 6.1: 6-fold octahedral, 5-fold pyramidal, and 4-fold square-planar coordinations. Historically, the first copper oxide superconductor, La-Ba-Cu-O, discovered by Bednorz and Müller (1986), has the K_2NiF_4 structure, in which Cu^{2+} is coordinated octahedrally by six O^{2-}. The octahedron in $(La,Ba)_2CuO_4$ is notably elongated in the *c*-axis direction, which is in contrast to basically regular octahedron observed in other transition-metal oxides. In *RE*-123 discovered in 1987 (Wu *et al.*, 1987) and in Bi-2212 discovered in 1988 (Maeda *et al.*, 1988), Cu^{2+} is coordinated pyramidally by five O^{2-}. In Bi-2223, Tl-2223, (Tl,Pb)-1223 with T_c of 120–130 K discovered in 1988 (Maeda *et al.*, 1988; Sheng and Hermann, 1988; Parkin *et al.*, 1988; Subramanian *et al.*, 1988) and also in Hg-1223 discovered in 1993 (Schilling *et al.*, 1993), the 5-fold pyramidal and 4-fold square-planar coordinations coexist. Finally, in 1989, the copper oxide superconductors composed only of the 4-fold square-planar coordination came onstage as an 'electron-doped superconductor' or '*n*-type superconductor' (Tokura

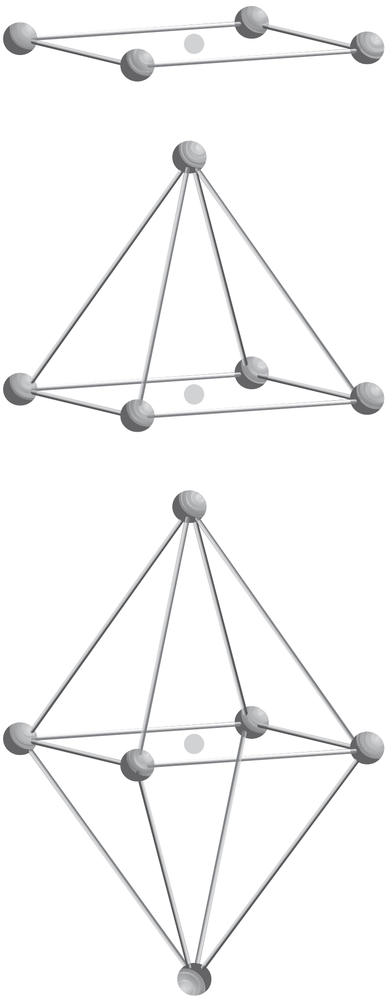

6.1 Three different coordinations of O^{2-} ions around a Cu^{2+} ion in high-T_c cuprates: 4-fold square-planar coordination (upper), 5-fold pyramidal coordination (middle), 6-fold octahedral coordination (lower).

et al., 1989; Takagi *et al.*, 1989). This historical order together, with the fact that the 6-fold coordination is more familiar in other 3*d* transition-metal perovskite-type oxides, have lead many researchers to regard the 6-fold octahedral coordination as the most basic crystal structure in copper oxides. However, the strong Jahn-Teller effect of Cu^{2+} should favor the 4-fold square-planar coordination for Cu^{2+} oxides. In fact, the simple copper oxide, CuO, also takes the 4-fold coordination although the crystal structure, called the 'tenorite' structure, is complex (Fig. 6.2). In contrast, the oxide (NiO) of Ni, which is located on one left of Cu in the periodic

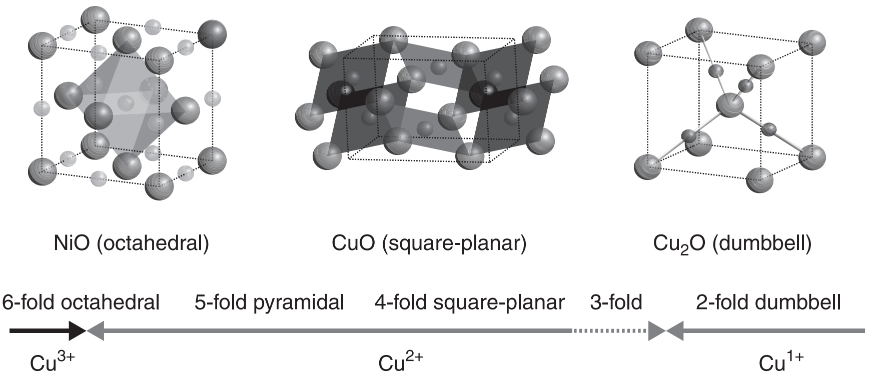

6.2 Crystal structures of NiO, CuO, and Cu_2O. Schematic below shows relation between the Cu valence and oxygen coordination in copper oxides.

table, takes the simple NaCl structure, indicating predominantly ionic character of the Ni-O bond. The unusual coordination in oxides of Cu^{2+} reflects, at least partly, the strong covalent character of the Cu-O bond. The author takes the view that the square-planar coordination is the most natural appearance of Cu^{2+} oxides and that the 5-fold or 6-fold coordination has one or two extra oxygen atoms added at the apical site to this fundamental structure.

The critical temperature of square-planar copper oxides is not very high, 43 K at the highest (Smith *et al.*, 1991). This is because no hole doping has yet been achieved. However, their potential T_c should be high. If one speculates optimal T_c for three different coordinations from one homologous series, for example, Hg-12(n – 1)n, one can reach the conclusion 'T_c(octahedral) < T_c(pyramidal) < T_c(square-planar)'. In tri-layer compounds, empirically, the inner square-planar plane is supposed to have a higher T_c than the outer pyramidal plane. Square-planar copper oxides are important from the following two viewpoints: the distinguished character of a Cu^{2+} ion and the potential of higher T_c (perhaps, both are related). However, only two families are known at present: 'Nd_2CuO_4' compounds (Müller-Buschbaum and Wollsglager, 1975) and 'infinite-layer' compounds (Siegrist *et al.*, 1988). The two families have the following features in common:

- Superconductivity appears only by electron doping. No clear success of hole doping has been reported.
- Removal of impurity oxygen atoms at the apical site is indispensable to achieve superconductivity.

Since it is difficult to prepare high-quality samples of both families, reliable experimental data are quite limited, in spite of many articles reported in ~20 years since their discovery. In this situation, the author tried to collect the data that he judged as most reliable. In this chapter, only 'Nd_2CuO_4' compounds are reviewed because of the space limitation.

6.2 Structure

6.2.1 214 cuprates: RE_2CuO_4

The rare earth copper oxides of the general chemical formula RE_2CuO_4 possess a richness of structural and physical properties because of the wide range of the ion size of RE^{3+}. There are two closely related structures as shown in Fig. 6.3(a) and 6.3(c): the K_2NiF_4 (abbreviated as T) and Nd_2CuO_4 (abbreviated as T′) structures. The structural difference between T and T′ can be viewed as the difference in the *RE*-O arrangements: rock-salt-like versus fluorite-like; or alternatively as the difference in the Cu-O coordination: octahedral CuO_6 versus square-planar CuO_4. The key parameter determining which of these structures is formed is the ionic radius of the RE^{3+} ion. The T structure is formed with large La^{3+} whereas the T′ structure is formed with smaller RE^{3+} ions such as *RE* = Pr, Nd, Sm, Eu, and Gd. By employing high-pressure synthesis, the T′ structure is also formed with Dy to Tm as well as Y (Okada *et al.*, 1990; Bordet *et al.*, 1992). The T–T′ boundary lies between La^{3+} and Pr^{3+}. In a mixed-lanthanide system $(La,RE)_2CuO_4$, a third structure (denoted T*, Fig. 6.3(b)), which consists of alternating stacking of T- and T′-slabs, is observed (Sawa *et al.*, 1988). The stabilization of this structure requires

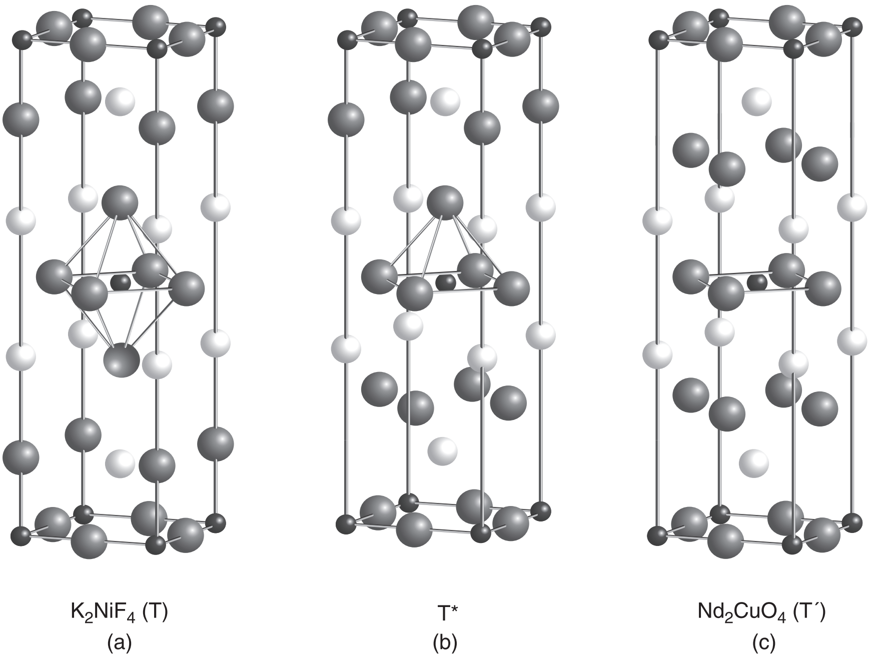
K_2NiF_4 (T)
(a)

T*
(b)

Nd_2CuO_4 (T′)
(c)

6.3 Three crystal structures of rare-earth copper oxides: (a) K_2NiF_4 (abbreviated as T) structure, (b) T* structure, and (c) Nd_2CuO_4 (abbreviated as T′) structure.

Table 6.1 Superconducting transition temperatures (T_c) of rare earth copper oxides (RE_2CuO_4)

	Material	T_c (K)	Ref.
T	$La_{1.85}Ba_{0.15}CuO_4$	30	Bednorz and Müller, 1986
	$La_{1.85}Sr_{0.15}CuO_4$	37	Kishio *et al.*, 1987
T*	$Nd_{1.32}Sr_{0.41}Ce_{0.27}CuO_4$	28	Sawa *et al.*, 1989
	$La_{0.82}SmSr_{0.18}CuO_4$	37	Fisk *et al.*, 1989
T′	$Nd_{1.85}Ce_{0.15}CuO_4$	24	Tokura *et al.*, 1989
	$La_{1.9}Ce_{0.1}CuO_4$	30	Naito and Hepp, 2000

two *RE* ions with significantly different ionic sizes: one large La^{3+} and the other smaller RE^{3+}. All of the three types of 214 cuprates show superconductivity with T_c of 30–40 K as shown in Table 6.1. It has been empirically claimed that T and T* cuprates accept only hole doping whereas T′ cuprates accept only electron doping.

6.2.2 Tolerance factor

The crystal chemistry, mentioned above, on the structure versus the ionic radius in the rare earth copper oxides has been explained by Bringley *et al.* (1990) and Manthiram *et al.* (1990) in terms of the crystallographic tolerance factor (t), which is defined as

$$t = [r_i^{IX}(RE^{3+}) + r_i^{VI}(O^{2-})]/[\sqrt{2}^* [r_i^{VI}(Cu^{2+}) + r_i^{VI}(O^{2-})], \qquad [6.1]$$

where $r_i^{IX}(RE^{3+})$, $r_i^{VI}(Cu^{2+})$, and $r_i^{VI}(O^{2-})$ are the empirical *room-temperature* ionic radii by Shannon and Prewitt (1969) for RE^{3+}, Cu^{2+}, and O^{2-} ions with the coordination indicated by superscript Roman numerals. The tolerance factor (t) was initially proposed to argue the stability of the perovskite structure (ABO_3) by Goldshimidt (1926). It represents the bond length matching between AO layers and BO_2 layers. Ideal matching corresponds to $t = 1$, and the perovskite structure is stable for ~ $0.8 < t < 1.0$. This factor can also be used to argue the stability of the T and T′ structure. The calculated values for t are listed in Table 6.2. Figure 6.4(a) gives a schematic illustration for the bond length mismatch between Cu-O and La-O in the case of T-La_2CuO_4. The cell size of the CuO_2 layer (4.26 Å) is apparently larger than that of the LaO layer (3.70 Å).

Bringley *et al.* (1990) obtained the following empirical trend on the basis of the systematic investigation on the mixed lanthanide systems $La_{2-x}RE_xCuO_4$, in which 'average' t can be varied continuously,

- For $0.87 \leq t \leq 0.99$, the T structure is stable.
- For $0.83 \leq t \leq 0.86$, the T′ structure is stable. The critical value for the T to T′ transition is $t_c^R = 0.865$, where the superscript, R, denotes the *room-temperature* value. See below for the temperature effect.

Table 6.2 Room-temperature ionic radius of RE^{3+} for 9- and 8-fold coordinations and corresponding tolerance factors for T and T′ stability calculated from eq. [6.1] and [6.2]

RE^{3+}	$r_i^{IX}(RE^{3+})$ (Å)	$r_i^{VIII}(RE^{3+})$ (Å)	Tolerance factor for T stability t	Tolerance factor for T′ stability t'
La^{3+}	1.216	1.160	0.8685	1.0392
Ce^{3+}	1.196	1.143	0.8618	1.0322
Pr^{3+}	1.179	1.126	0.8562	1.0252
Nd^{3+}	1.163	1.109	0.8509	1.0182
Pm^{3+}	1.144	1.093	0.8445	1.0116
Sm^{3+}	1.132	1.079	0.8406	1.0058
Eu^{3+}	1.120	1.066	0.8366	1.0005
Gd^{3+}	1.107	1.053	0.8323	0.9951
Tb^{3+}	1.095	1.040	0.8283	0.9897
Dy^{3+}	1.083	1.027	0.8243	0.9844
Ho^{3+}	1.072	1.015	0.8206	0.9794
Er^{3+}	1.062	1.004	0.8173	0.9749
Tm^{3+}	1.052	0.9940	0.8140	0.9708
Yb^{3+}	1.042	0.9850	0.8107	0.9671
Lu^{3+}	1.032	0.9770	0.8074	0.9638
Y^{3+}	1.075	1.019	0.8216	0.9811

In calculating the tolerance factor, one should use $r_i^{IX}(RE^{3+})$ corresponding to the T structure for eq. [6.1] and $r_i^{VIII}(RE^{3+})$ corresponding to the T′ structure for eq. [6.2]. For Cu^{2+} and O^{2-}, the following ionic radii are used: $r_i^{IV}(Cu^{2+}) = 0.57$ Å, $r_i^{V}(Cu^{2+}) = 0.65$ Å, $r_i^{VI}(Cu^{2+}) = 0.73$ Å and $r_i^{IV}(O^{2-}) = 1.36$ Å, $r_i^{VI}(O^{2-}) = 1.40$ Å.

- For $t < 0.83$, neither of the T nor T′ forms. Instead the complicated, so-called, '$Ho_2Cu_2O_5$' structure forms (Freund and Müller-Buschbaum, 1977).

Similar geometrical considerations can be made for the T′ stability. In this case, the cell size of the CuO_2 layer is given by $2\sqrt{2}*r_i^{VI}(O^{2-}) = 3.96$ Å. This is because Cu^{2+} for the square-planar 4-fold Cu-O coordination has $r_i = 0.57$ Å, which is substantially smaller than 0.73 Å for the 6-fold coordination, and fits in the space surrounded by four oxygen ions, tangential to one another (see Fig. 6.4 (right)). The evaluation of the cell size of the RE_2O_2 layer is made by assuming the ideal fluorite structure, namely oxygen ion is surrounded by four *RE* ions with regular tetrahedron (the bond angle of *RE*-O-*RE* is arccos(–1/3) = 109.5°). Then the cell size of the RE_2O_2 layer is given by $2\sqrt{6}*[r_i^{VIII}(RE^{3+}) + r_i^{IV}(O^{2-})]/3$, and varies from 4.15 Å (La) to 3.88 Å (Tm), which should be compared with the cell size of the CuO_2 layer of 3.96 Å. It should be noted that O^{2-} in the RE_2O_2 layer is surrounded only by four RE^{3+} whereas O^{2-} in the CuO_2 layer is surrounded by four RE^{3+} and two Cu^{2+}, namely the coordination number is different for two O^{2-}. The resultant tolerance factor for the T′ stability is given by

$$t' = [r_i^{VIII}(RE^{3+}) + r_i^{IV}(O^{2-})]/[\sqrt{3}*\, r_i^{VI}(O^{2-})], \qquad [6.2]$$

and is also listed in Table 6.2.

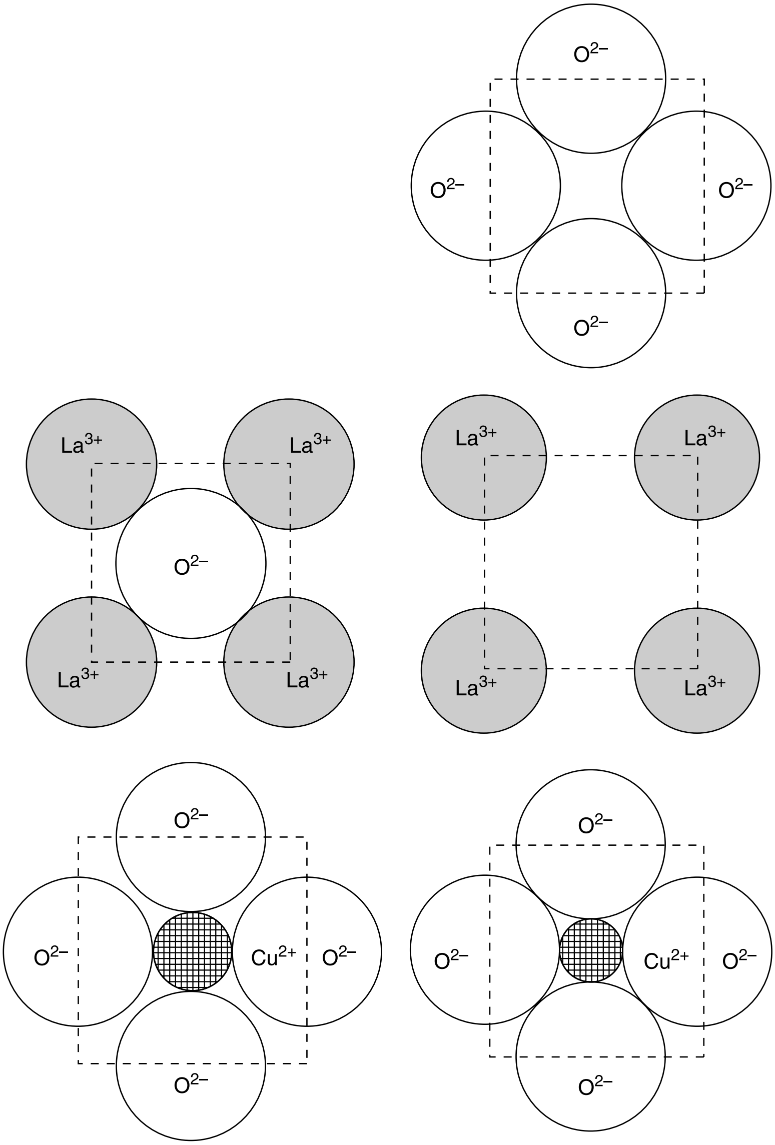
O2–
O2–
O2–
O2–
La3+
La3+
O2–
La3+
La3+
La3+
La3+
La3+
La3+
O2–
O2–
Cu2+
O2–
O2–
O2–
O2–
Cu2+
O2–
O2–

6.4 Sliced view of CuO_2 and La_2O_2 layers in T-La_2CuO_4 (left) and T′-La_2CuO_4 (right).

6.2.3 Thermal expansion of bond length

The above discussion neglects the temperature effect on the bond length, as the bond length expands with temperature. The room-temperature ionic radii are used above in calculation of the tolerance factor although the values at synthesis temperatures (~1000 °C) should be used in discussion of the phase stability. As pointed out by Manthiram and Goodenough (1991), the 'ionic' *RE*-O bond has a larger thermal expansion coefficient than the 'covalent' Cu-O bond. The different thermal expansion coefficients ('thermal-expansion mismatch') of the *RE*-O and Cu-O bond length leads to the increase of t with temperature ($t = t_0 + \alpha T$, $\alpha \sim 2\text{–}3 \times 10^{-5}$ by rough estimate), where t_0 is the tolerance factor at 0 °C (≈ room temperature) and T is measured in °C, and thereby plays an important role in the T versus T′ stability. Then the actual threshold for the T to T′ transition will be $t_c = 0.875\text{–}0.880$ instead of the above room-temperature value, $t_c^R = 0.865$. Therefore, if one *could* synthesize La_2CuO_4 at room temperatures, one *would* get T′-La_2CuO_4 since $t = 0.8685$ of $La_2CuO_4$is smaller than $t_c = 0.875\text{–}0.880$.

Manthiram and Goodenough (1991) succeeded in the selective stabilization of T versus T′ in the $La_{2-y}Nd_yCuO_4$ system by changing the synthesis temperature (T_s). $La_{1.5}Nd_{0.5}CuO_4$ ($t = 0.8641$ at room temperature) is stabilized as single-phased T′ below T_s = 625 °C or single-phased T above T_s = 775°. A two-phase mixture of T and T′ is obtained in between 625 °C and 775 °C. In their experiments, coprecipitation powders were employed to promote chemical reaction at firing temperatures as low as 500 °C. At T_s = 500 °C, even La_2CuO_4 becomes not single-phased T but a two-phase mixture of T and T′. By extrapolation of the T/T′ phase boundary in the $La_{2-y}Nd_yCuO_4$ system to $y = 0$, it is predicted that La_2CuO_4 can be stabilized as the T′ structure below T_s = 425 °C, which is too low for bulk synthesis. By means of thin-film synthesis, however, the reaction temperature can be lowered significantly, since reactants are much smaller in size and also more reactive than in bulk synthesis. Success in synthesizing the T′ phase of pure La_2CuO_4 by reactive coevaporation technique was achieved by Tsukada *et al.* (2002).

6.2.4 Structural parameters and interstitial oxygen

As mentioned above, T-La_2CuO_4 is located at the borderline of the K_2NiF_4 stability, and hence it distorts to the orthorhombic structure (LTO: low-temperature orthorhombic phase) at temperatures below 550 K so as to accommodate the large bond length mismatch by tilting of CuO_6 octahedra. On the other hand, T′-RE_2CuO_4 shows no distortion and keeps the original tetragonal (*I*4/*mmm*) structure except for T′-Gd_2CuO_4, which is located at the borderline of the Nd_2CuO_4 stability. Table 6.3 shows the structural parameters obtained from the powder neutron diffraction experiments on oxygenated and reduced $Nd_{1.9}Ce_{0.1}CuO_4$ by Petrov *et al.* (1999). There are two regular oxygen sites in the T′ structure: the planar site (O1) and the out-of-plane site (O2). In addition, T′ cuprates have a strong tendency to have excess oxygen atoms at the interstitial apical site (O_{ap}). As mentioned in section 6.1, 'reduction' is required to achieve superconductivity in T′ cuprates. The reduction is not intended for further electron

Table 6.3 Structural parameters (atomic position (z) and occupancy (n)) determined by the powder neutron diffraction on oxygenated and reduced $Nd_{1.9}Ce_{0.1}CuO_{4+\delta}$

Atom	z/n	Oxygenated ($\delta = 0.03$)	Reduced ($\delta = 0.00$)
Nd/Ce	z	0.3519	0.3520
	n	2	2
Cu	n	1	1
O1	n	1.95	1.96
O2	n	2.00	2.00
O_{ap}	z	0.1904	0.1905
	n	0.08	0.04

The atomic positions are: Nd 4*e*[0,0,*z*]; Cu 2*a*[0,0,0]; O1 4*c*[1/2,0,0]; O2 4*d*[0/1/2,1/4]; O_{ap} 4*e*[0,0,*z*]. After Petrov *et al.* (1999).

doping by oxygen deficiencies, but for removal of impurity oxygen atoms at O_{ap}, which is very harmful to high-T_c superconductivity. As seen from Table 6.3, in the oxygenated sample (annealed in air at 950 °C, and then quenched to room temperature), a significant amount of oxygen (~0.08 atoms/formula unit) is present at O_{ap}. On the other hand, in the reduced sample (annealed in $p_{O2} = 4.57 \times 10^{-2}$ atm at 1200 °C, and then quenched to room temperature), the occupancy of O_{ap} is reduced to ~0.04 atoms/formula unit. With regard to the regular oxygen sites, the occupancy of O2 is essentially full (2.00) and unchanged by reduction whereas the occupancy of O1 is slightly less than 2.00 even in the oxygenated sample. In the experimental results by Petrov *et al.* (Table 6.3), there appears to be essentially no change by reduction in the O1 occupancy, but many results indicate that oxygen vacancies at O1 increase by reduction, especially in samples with no or low Ce doping (Radaelli *et al.*, 1994). The results can be summarized as follows: oxygen vacancies at O1 and interstitial oxygen atoms at O_{ap} coexist with their occupancies in thermal equilibrium. This makes quite complex the oxygen chemistry of T′ cuprates, resulting in the defect structure dependent on the temperature, oxygen partial pressure, and even cerium content.

6.2.5 Lattice parameters

First, we take a look at the *RE* dependence of the lattice parameters of the parent compounds, T′-RE_2CuO_4. Since the ionic radius of RE^{3+} changes from 1.160 Å (La) to 0.977 Å (Lu), the lattice parameters of T′-RE_2CuO_4 change accordingly. One can investigate a systematic variation in both physical and chemical properties with the lattice parameters, which is one benefit to the research of T′ cuprates. Figure 6.5 and Table 6.4 summarize the *RE* dependence of the *a*-axis and *c*-axis lattice parameters (a_0 and c_0). The a_0 changes by ~5 %

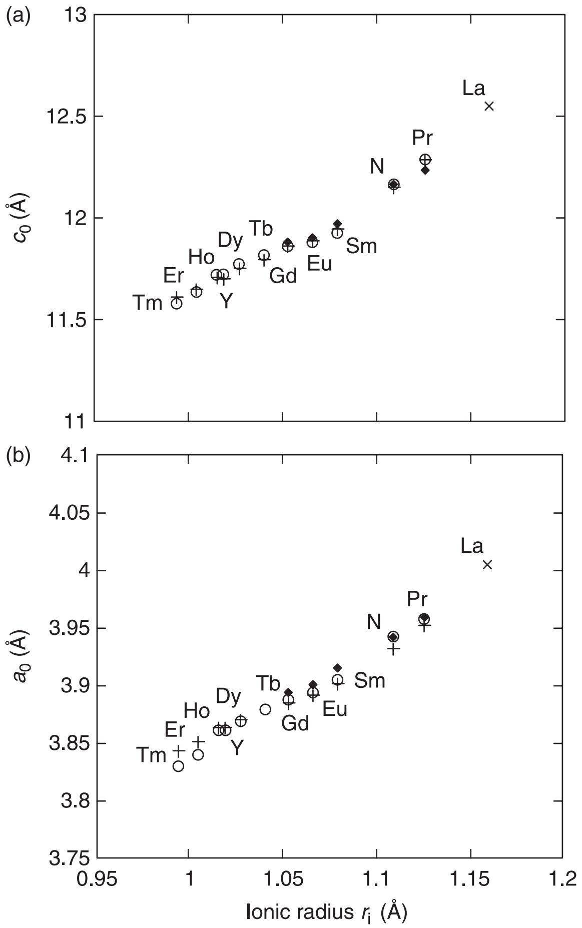

6.5 RE dependence of the *c*-axis (a) and *a*-axis (b) lattice parameters of T′-RE_2CuO_4. The data are collected from Okada *et al.* (1990) (+), Bordet *et al.* (1992) (○), Uzumaki *et al.* (1992) (♦), and Chou *et al.* (1990) (×).

from 4.025 Å (La) to 3.830 Å (Tm) and the c_0 changes by ~8 % from 12.55 Å (La) to 11.58 Å (Tm). Both of the a_0 and c_0 do not show a linear dependence on the ionic radius, but show a weaker dependence from Sm to Tm. This behavior may be due to interstitial O_{ap} impurities, which are contained more in heavier RE^{3+}.

Next, we take a look at the Ce doping dependence of the lattice constants. In general, Ce can be trivalent as well as tetravalent. Which valence Ce takes depends on the environment around Ce ions in lattice and also on the synthesis condition. The early chemical analysis (iodometry titration) by Idemoto *et al.*

Table 6.4 Lattice parameters (a_0 and c_0) of T′-RE_2CuO_4 with different *RE*

RE	a_0 (Å)	c_0 (Å)
La	4.005	12.550
Pr	3.958	12.288
Nd	3.943	12.163
Sm	3.905	11.929
Eu	3.894	11.882
Gd	3.888	11.859
Tb	3.880	11.815
Dy	3.869	11.771
Ho	3.861	11.721
Er	3.840	11.637
Tm	3.830	11.578
Y	3.861	11.721

The values for La are taken from Chou *et al.* (1990) whereas those for other *RE* are from Bordet *et al.* (1992).

(1990) gave the Ce valence of +3.84 in T′-$Nd_{1.85}Ce_{0.15}CuO_4$, which is close to +4. The ionic radius of tetravalent Ce, $r_i^{VIII}(Ce^{4+})$, is 0.97 Å, which is smaller than $r_i^{VIII}(RE^{3+})$ of trivalent *RE* ions. Therefore the lattice constants of T′ cuprates should decrease with substitution of Ce for *RE*. Figure 6.6 summarizes the a_0 and c_0 for T′-$RE_{2-x}Ce_xCuO_4$ for different *RE* as a function of the Ce content, *x*. The filled symbols are the data for reduced samples, and the empty symbols for oxygenated samples. They are essentially the same within the experimental accuracy. The c_0 decreases with *x* in accordance with the above expectation whereas the a_0 increase slightly with *x*, which is opposite to the expectation. The increase of a_0 with electron doping is due to the stretching of the Cu-O bond by filling electrons into the antibonding (σ^*) orbitals, which makes the Cu-O covalent bond less stable.

In Fig. 6.6, both a_0 and c_0 change linearly with *x* in low Ce doping, but they show no change for *x* above a certain value, which is the solubility limit (x_c) of Ce (Vegard's law). Figure 6.7 summarizes the *RE* dependence of x_c in bulk synthesis and molecular beam epitaxy (MBE) growth. With any *RE*, the x_c in MBE growth is larger than x_c in bulk synthesis. As shown in Fig. 6.7, the x_c increases with the ionic radius of RE^{3+}, and is ~ 0.3 for La and ~ 0.1 for Gd. This *RE* dependence of x_c can be understood from the geometrical considerations as mentioned in section 6.2.2. As shown in Table 6.2, the tolerance factor (t') for the T′ structure is less than 1.00 for small RE^{3+}, namely the cell size of the fluorite RE_2O_2 layer is smaller than that of the CuO_2 layer. The Ce substitution decreases the average ionic radius of $RE^{3+}_{2-x}Ce^{4+}_x$ and at the same time stretches the Cu-O bond, which reduces t' to a further smaller value and makes the T′ phase less stable.

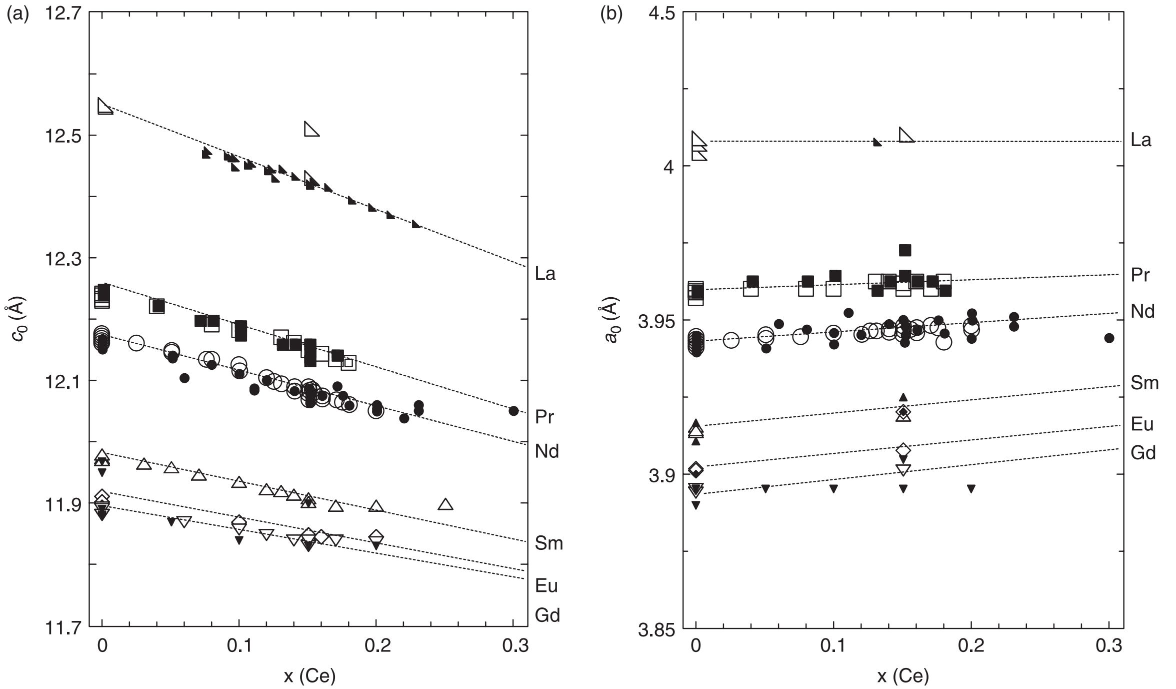

6.6 Ce doping dependence of the c_0 (a) and a_0 (b) lattice parameters of T′-$RE_{2-x}Ce_xCuO_4$ with different *RE*. The data are collected from:

La: Takayama-Muromachi *et al.* (1990), Chou *et al.* (1990), Yamada *et al.* (1994), Naito and Hepp (2001);
Pr: Markert *et al.* (1990), Matsuda *et al.* (1991), Uzumaki *et al.* (1992), Zhou *et al.* (1993), Kawashima *et al.* (1994);
Nd: Takagi *et al.* (1989), Huang *et al.* (1989a, 1989b), Hidaka and Suzuki (1989), Markert *et al.* (1990), Uzumaki *et al.* (1992), Zhou *et al.* (1993), Kawashima *et al.* (1994);
Sm: Markert *et al.* (1990), Uzumaki *et al.* (1992), Zhou *et al.* (1993), Ishii *et al.* (1993), Kawashima *et al.* (1994);
Eu: Markert *et al.* (1990), Uzumaki *et al.* (1992), Ishii *et al.* (1993), Kawashima *et al.* (1994);
Gd: Markert *et al.* (1990), Uzumaki *et al.* (1992), Zhou *et al.* (1993), Ishii *et al.* (1993), Kawashima *et al.* (1994).

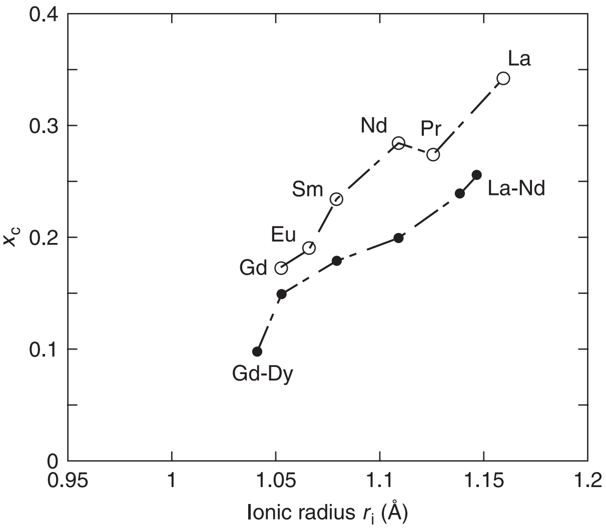

6.7 Solubility limit (x_c) of Ce in T′-$RE_{2-x}Ce_xCuO_4$ with different *RE*. The filled circles are from bulk synthesis (Zhu and Manthiram, 1994a) and the open circles from our MBE growth. In both cases, the x_c increases with $r_i^{VIII}(RE^{3+})$.

6.3 Solid-state chemistry

6.3.1 Phase stability

Copper is an element with weak chemical bonding (affinity) to oxygen. Hence copper oxides inevitably decompose at high temperature or in low oxygen partial pressure. Roughly speaking, the decomposition line (phase stability limit) of all high-T_c cuprates is close to the decomposition line of the divalent simple oxide, CuO, since Cu is essentially divalent in high-T_c cuprates. Figure 6.8 shows a closer comparison between the decomposition lines of 214 and simple copper oxides (CuO and Cu_2O). It also includes a similar comparison for Ni and Co oxides. The decomposition lines of T-La_2CuO_4, T′-Pr_2CuO_4, and T′-Nd_2CuO_4 are all located in between those of CuO and Cu_2O. In fact, the decomposition lines of 214 cuprates are located substantially below that of CuO. One can imagine the reason as follows. The oxygen desorption of the CuO_2 layer triggering the decomposition in 214 cuprates is partially blocked by the RE_2O_2 layers sandwiching above and below. The decomposition lines of La_2NiO_4 and La_2CoO_4 are located at much lower p_{O2} than those of 214 cuprates, but they almost coincide with the decomposition lines of the simple oxides, NiO and CoO. The large difference of the decomposition line between cuprates and Ni, Co oxides reflects much stronger oxygen affinity of Ni or Co than of Cu. These observations indicate

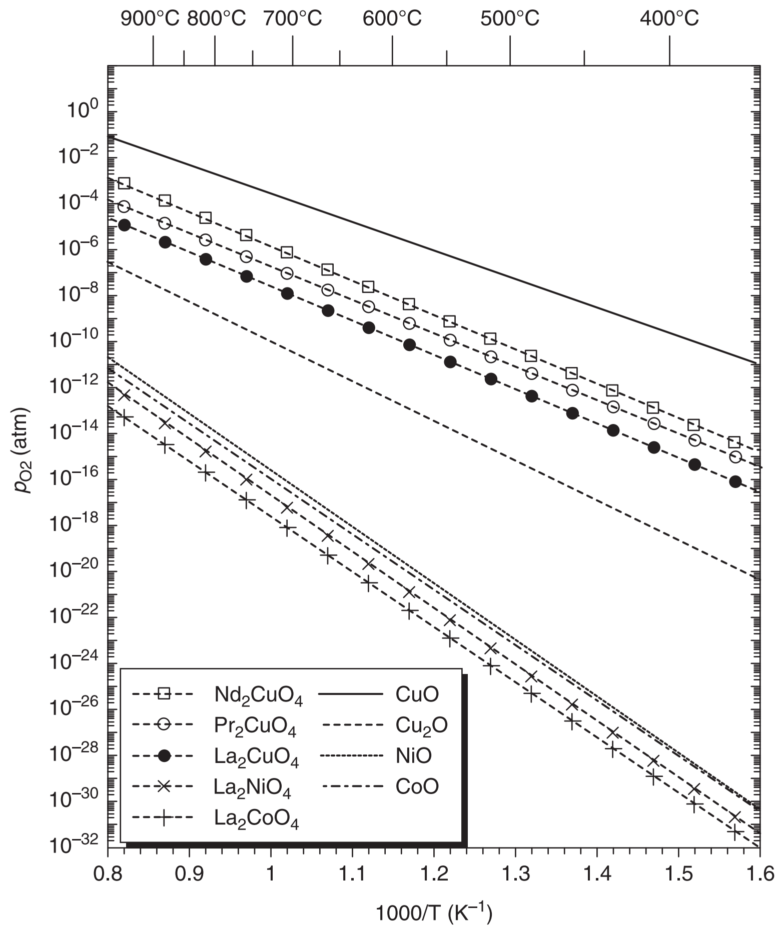

6.8 Comparison of the decomposition lines for cuprates with those for nickelates and cobaltates. The decomposition lines for both simple oxides and 214 oxides are included. The decomposition lines of 214 cuprates are located at much higher p_{O2} than those of La_2NiO_4 and La_2CoO_4.

that the decomposition in 214 transition-metal (M) oxides is triggered by the break of the M-O bond with much stronger La-O or *RE*-O bond intact.

Next we take a look at the *RE* dependence of the decomposition lines. T cuprates decompose by the following reaction,

$$4RE_2CuO_4 \rightarrow 4RE_2O_3 + 2Cu_2O + O_2 \quad [6.3]$$

or

$$4RE_2CuO_4 \rightarrow 4RECuO_2 + 2RE_2O_3 + O_2. \quad [6.4]$$

In either case, the Cu valence changes from +2 to +1 whereas the *RE* valence is unchanged. The thermodynamic data (standard Gibbs energy change, standard enthalpy change, standard entropy change) in decomposition [6.3] or [6.4] were obtained by electrochemical measurements using galvanic cells by Tretyakov *et al.* (1976), Petrov *et al.* (1989a, 1989b), and Idemoto *et al.* (1992). Table 6.5 summarizes the standard Gibbs energy change, standard enthalpy change, and standard entropy change in decomposition [6.3] for T′-RE_2CuO_4 with different *RE*. The data for CuO and T-La_2CuO_4 are also included in the table for a comparison. All the data are normalized so as to desorb 1 mol of O_2 gas by decomposition. The thermodynamic data in Table 6.5 can be converted to the decomposition lines by the following equation (van't Hoff equation),

$$\ln p = -\frac{\Delta G^\circ}{RT} = -\frac{\Delta H^\circ - T\Delta S^\circ}{RT}, \qquad [6.5]$$

which are also included in Table 6.5 and illustrated in Fig. 6.9(a). As seen in Table 6.5, the standard enthalpy change in decomposition of T′-RE_2CuO_4 is close to the value (292 kJ/mol) for CuO. Furthermore ΔH° does not change by a subtle difference in structure between the T and T′ structure. This universal behavior reconfirms that the decomposition in 214 cuprates is governed by the strength of the Cu-O bond.

Taking a closer look at Table 6.5 and Fig. 6.9(a), one can notice the following trend for the phase stability of T′-RE_2CuO_4, 'the larger RE^{3+}, the more stable'. This trend

Table 6.5 Thermodynamic data for decomposition reaction [6.3] in T′-RE_2CuO_4 with different *RE*

Material	ΔH° (kJ/mol)	ΔS° (kJ/mol/K)	ΔG° (kJ/mol)	$\log p_{O2}$ (atm)	Ref.
CuO	292.0	0.2050	292–0.205*T*	10.637–15153/*T*	
T-La_2CuO_4	303.0	0.1548	303–0.155*T*	8.086–15828/*T*	Kanai *et al.*, 1997
T′-Pr_2CuO_4	329.0	0.1828	329–0.183*T*	9.549–17186/*T*	Petrov *et al.*, 1988b
T′-Nd_2CuO_4	298.3	0.1806	298–0.181*T*	9.434–15582/*T*	Tretyakov *et al.*, 1976
T′-Sm_2CuO_4	300.1	0.1961	300–0.196*T*	10.243–15676/*T*	Tretyakov *et al.*, 1976
T′-Eu_2CuO_4	240.6	0.1613	241–0.161*T*	8.426–12568/*T*	Tretyakov *et al.*, 1976
T′-Gd_2CuO_4	234.4	0.1613	234–0.161*T*	8.426–12244/*T*	Tretyakov *et al.*, 1976

The data for the decomposition of CuO and T-La_2CuO_4 are also included for comparison. All the values are normalized so as to desorb 1 mol of O_2 gas by decomposition.

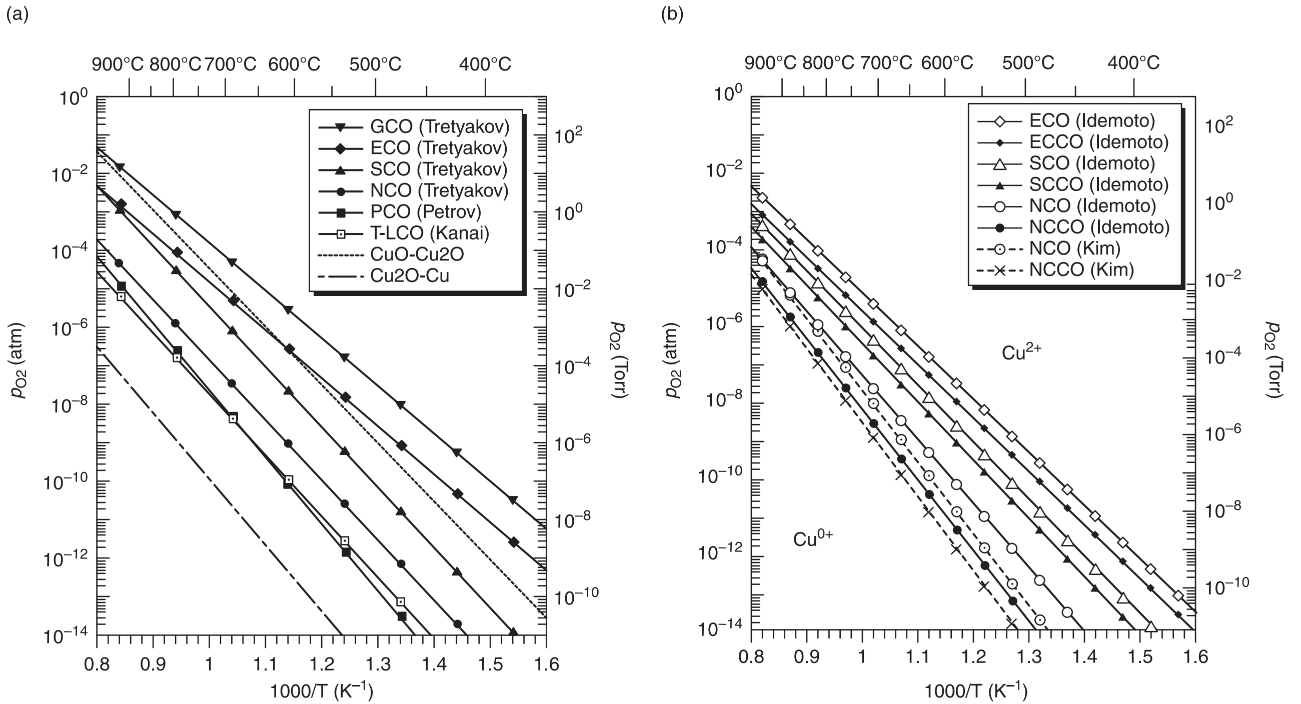

6.9 (a) *RE* dependence of the decomposition lines for T′-*RE*$_2$CuO$_4$. The trend 'the larger *RE*$^{3+}$, the more stable' can be noticed. (b) Comparison of the decomposition lines between T′-*RE*$_2$CuO$_4$ and T′-*RE*$_{1.85}$Ce$_{0.15}$CuO$_4$ with different *RE*. In any *RE*, the phase stability field of T′ cuprates is enlarged by Ce substitution of $x = 0.15$. Both of the figures are constructed based on the results of the electrochemical measurements by Tretyakov *et al.* (1976), Petrov *et al.* (1988a, 1988b), and Idemoto *et al.* (1992). The results of thermogravimetric measurements on T-La$_2$CuO$_4$ by Kanai *et al.* (1997), and on T′-Nd$_2$CuO$_4$ and T′-Nd$_{1.85}$Ce$_{0.15}$CuO$_4$ by Kim and Gaskell (1993) are also included.

may be explained partly from the stronger oxygen affinity of larger RE^{3+}. RE^{3+} is coordinated (surrounded) by eight oxygen atoms, four of which are in the CuO_2 layer. Hence larger RE^{3+} takes a firmer grip on weakly bound oxygen atoms in the CuO_2 layer.

Next we see how the phase stability changes with Ce doping. Figure 6.9(b) compares the decomposition lines of T′-RE_2CuO_4 and T′-$RE_{1.85}Ce_{0.15}CuO_4$ for RE = Nd, Sm, and Eu. In any RE, the phase stability field of T′ cuprates is enlarged by Ce substitution of $x = 0.15$. The enhanced phase stability by Ce substitution can be explained similarly to the above RE dependence of the phase stability. Ce is nearly tetravalent in T′ cuprates, and takes a firmer grip on surrounding O^{2-} ions by stronger electrostatic force than trivalent RE.

6.3.2 Oxygen nonstoichiometry

Oxygen nonstoichiometry is a phenomenon common to cuprates, which is due to the weak nature of a Cu-O bond and to the multivalent character of Cu (Cu^0, Cu^{1+}, Cu^{2+}, Cu^{3+}, etc.). Oxygen loss in the CuO_2 layer starts to occur in low p_{O2} prior to decomposition, and this loss, in general, degrades and eventually kills high-T_c superconductivity. In high p_{O2}, excess oxygen atoms occupy the interstitial site in the RE_2O_2 layer in 214 cuprates: the tetrahedral site in T (the position close to O2 in T′) and the apical site (O_{ap}) in T′. It is well known that interstitial excess oxygen atoms in T-La_2CuO_4 provide the CuO_2 layer with holes, achieving high-T_c superconductivity without Sr substitution. In contrast, interstitial oxygen atoms in T′ cuprates are strong pair breakers, and harmful to high-T_c superconductivity. Therefore accurate data on oxygen nonstoichiometry in T′ cuprates are required, but not available. Although there are dozens of articles, the results do not concur (Takayam-Muromachi *et al.*, 1989; Kawashima *et al.*, 1994; Moran *et al.*, 1989; Wang *et al.*, 1990; Idemoto *et al.*, 1990, 1991; Suzuki *et al.*, 1990; Yamaguchi *et al.*, 1991; Kim and Gaskell, 1993; Klamut, 1993; Zhu *et al.*, 1994a, 1994b, 1995; Radaelli *et al.*, 1994; Schultz *et al.*, 1996; Prado *et al.*, 1995, 1999; Petrov *et al.*, 1999; Kang *et al.*, 2007; Tanaka *et al.*, 2008).

Even the presence of excess oxygen atoms is not supported by some articles. Early iodometry titration experiments, employed for evaluation of the absolute value (y) of oxygen in T′-$(RE,Ce)_2CuOy$, often concluded $y < 4.0$. The behavior of conductivity of T′ cuprates, increasing monotonically with lowering p_{O2}, is also typical of n-type oxides with oxygen deficiencies. However, the presence of excess oxygen atoms at the apical site (O_{ap}) is in no doubt, as systematic photoemission spectroscopy from Yamamoto *et al.* (1997) shows. The contradiction between the conclusions by this study and others can be traced to the unique feature of interstitial oxygen in T′ cuprates. In fact, there is no space sufficient for a large free O^{2-} to reside at O_{ap}, which may indicate the formation of a peroxide ion (O_2^{2-}) with neighboring regular oxygen atoms. In this case, interstitial excess oxygen atoms will neither provide holes to the CuO_2 layer nor change the

Cu valence. Since iodometry titration is, in principle, not to determine the oxygen content but to determine the Cu valence, it will give a misleading conclusion on the oxygen content in the case that a peroxide O_2^{2-} ion exists. There has been no experiment performed to take account of such a complicated situation. Hence, based on several well researched articles, the author gives his understanding for the oxygen nonstoichiometry in T′ cuprates, specifically T′-$Nd_{2-x}Ce_xCuO_y$, as follows.

- Oxygen deficiency and excess oxygen coexist in T′ cuprates. Even with $y = 4.00$, the oxygen sublattice is not perfect. It is very difficult (almost impossible) to remove O_{ap} impurities without introducing oxygen deficiencies in the CuO_2 layer.
- The maximum occupancy at O_{ap} is ~0.10 at $x = 0.00$ and decreases to ~0.05 at $x = 0.15$. Impurity oxygen atoms of 0.02–0.04 at O_{ap} remain, even after reduction.
- The maximum amount of oxygen deficiency in the CuO_2 layer is ~0.05 at $x = 0.00$ decreasing to ~0.02–0.03 at $x = 0.15$. Oxygen deficiencies may not be filled up completely even after annealing in 1 atm of oxygen.

Oxygen loss in the CuO_2 layer is a precursor of the decomposition. This is illustrated in Fig. 6.10, which plots the iso-composition lines (a line connecting

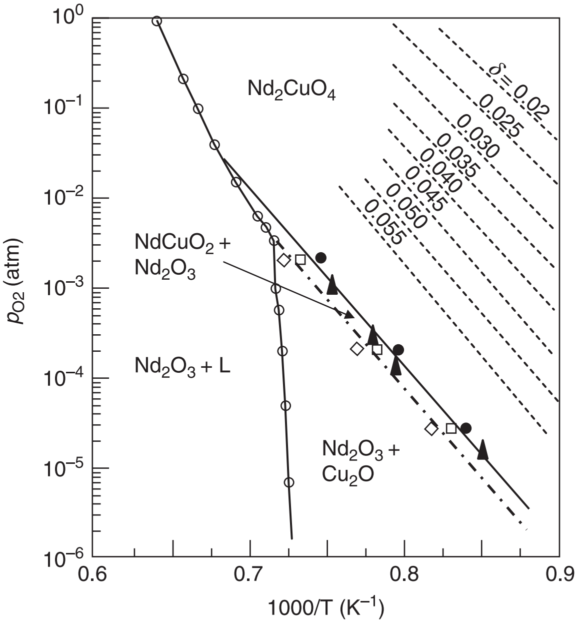

6.10 Phase diagram for T′-$Nd_2CuO_{4-\delta}$. The iso-composition lines connecting the same oxygen loss (δ) are also plotted, and they are essentially parallel to the decomposition line. (Adapted from Kim and Gaskel, 1993.)

the same oxygen loss, δ) in the p_{O2}-vs-1/T plane. These lines were obtained by the thermogravimetric analysis for T′-Nd_2CuO_4 by Kim and Gaskel (1993) (excess oxygen is not taken into account in their study, therefore the absolute value of the oxygen deficiency may not be reliable). All the iso-composition lines with different values of δ are essentially parallel to the decomposition line. The slope of the iso-composition lines gives the standard enthalpy change, $\Delta H°$, to desorb 1 mol of O_2 gas by the following process,

$$2RE_2CuO_4 \text{->} 2\, RE_2CuO_{4-\delta} + \delta O_{2.} \qquad [6.6]$$

$\Delta H°$ is 300–400 kJ/mole regardless of δ, which is essentially the same as $\Delta H°$ for the decomposition, indicating that the oxygen loss and the decomposition are governed by the same mechanism, namely the break of the Cu-O bond.

Finally, I point out two empirical trends about the *RE* dependence of the oxygen chemistry:

1 The binding energy of O1 in the CuO_2 layer is larger for larger RE^{3+}, which is explained in section 6.3.1.
2 The binding energy of O_{ap} in the RE_2O_2 layer is smaller for larger RE^{3+} (Zhu and Manthiram, 1994b, 1995).

Both of the trends suggest that more perfect oxygen sublattice can be obtained with larger RE^{3+} such as Pr^{3+}, Nd^{3+}, which agrees with the trend to have better superconductivity in T′ cuprates. Ce substitution also affects the oxygen chemistry and increases the binding energy of O1, thereby allowing stronger reduction than for pristine compounds. Oxygen diffusion is also an important factor in low-temperature reduction. The reduction time required for homogeneous oxygen is a function of the sample size/thickness, grain size, etc. Thin films with small grain size may be best to achieve homogeneous oxygen distribution in a short time.

6.4 Sample preparation

6.4.1 Bulk single crystal versus epitaxial thin films

Early sintered pellets of T′ cuprates showed high resistivity (10–100 mΩcm), semiconducting behavior, and a broad superconducting transition in most cases. The reasons for such poor properties are high-resistance impurity phases at grain boundaries and residual O_{ap} impurities. At present, bulk single crystals of T′ cuprates can be grown by the flux method (Hidaka and Suzuki, 1989) or the traveling-solvent floating zone (TSFZ) method (Tanaka *et al.*, 1991) and epitaxial thin films can be prepared by various methods such as molecular beam epitaxy (MBE), pulsed laser deposition (PLD), sputtering, metal organic decomposition (MOD), etc. However, good superconducting properties are still difficult to obtain for T′ cuprates. The problem is the removal of O_{ap} impurities without introducing oxygen deficiencies into the CuO_2 layer. The amount of residual O_{ap} impurities significantly affects the experimental results, even entirely changing the most fundamental properties such as the electronic phase diagram, which will be discussed in the next section.

Bulk single crystals eliminate grain boundaries but make O_{ap} removal more difficult due to limited paths of oxygen diffusion. Better superconducting properties can be obtained with epitaxial thin films. In general, epitaxial films of cuprates are not single-crystalline in a rigorous sense since they consist of submicron grains aligned in and out of plane. Such microstructure, however, is favorable in obtaining good properties for T′ cuprates since oxygen diffusion is prompt and grain boundaries with a small misorientation angle do not generate resistance. So far the best quality samples have been obtained in films grown by MBE and MOD, which are briefly described below.

6.4.2 Molecular beam epitaxy growth of T′ cuprates

Molecular beam epitaxy (MBE) is the primary tool used for the deposition of III–V semiconductors, such as GaAs and InP, employed in a variety of optoelectronic devices. The volatility of the group V elements (e.g., As and P) has been a key for the stoichiometric growth of these compounds, which has resulted in retarding the development of composition control techniques. Oxide MBE is a field emerging after the discovery of high-temperature superconductors. The growth of multi-component oxides by MBE poses many challenges, the primary one being the precise composition control of the constituent elements in an oxidizing environment. The demands of oxide MBE have led to the development of real-time *in situ* composition control techniques such as atomic absorption spectroscopy (AAS), electron impact emission spectroscopy (EIES), etc.

MBE growth of $RE_{2-x}Ce_xCuO_4$ films were performed by electron beam coevaporation from metal sources in a customer designed UHV chamber as shown in Fig. 6.11 (Naito *et al.*, 1997). The main feature of this MBE system is the precise control of evaporation flux based on EIES. The EIES sensors are calibrated against the quartz crystal microbalance, which can be inserted at the substrate holder position with the substrate holder swung up. The accuracy of control is ~ 10^{-3} Å/s for Cu and 10^{-1} to 10^{-2} Å/s for *RE* other than Ce. The flux of Ce is controlled by a quartz crystal microbalance (not the same one for calibration, but one located near the Ce source) since Ce has no sharp and strong atomic emission line. The actual composition of films was confirmed by inductively coupled plasma spectroscopy (ICP).

The oxidation during growth is performed by either O_3 gas (nondistilled, ~ 10% concentration) from a commercial ozone generator or O* generated from a commercial RF-activated source (HD25, Oxford Applied Research) operated at 250–300 W. In either case, the gas flow is typically 1–2 c.c./min, and the resultant chamber pressure during growth is, at highest, $1\text{–}2 \times 10^{-5}$ Torr, which enables stable rate control. The growth temperature is 650 °C to 750 °C, growth rate is

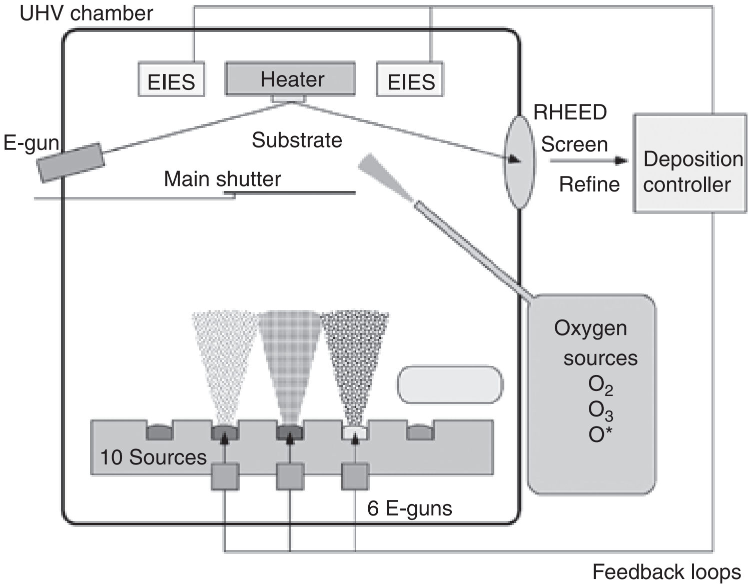

6.11 Schematic picture of the oxide MBE system (Naito *et al.*, 1997). The main feature is the precise control of evaporation flux based on electron impact emission spectrometry (EIES) sensors, which are located very close to the substrate holder.

~1.5 Å/s, and the total thickness is typically 1000 Å. The substrates used are $SrTiO_3$(001) in most cases and *RE*ScO_3(110) in some cases (*RE*ScO_3 has the $GdFeO_3$ structure, distorted perovskite structure, and the (110) face of the $GdFeO_3$ structure is equivalent to the (001) face of the perovskite structure). Real-time *in situ* RHEED observations show streaky diffraction patterns, which are evidence of the growth of smooth epitaxial films.

The reduction of O_{ap} impurities is a crucial step to optimizing the superconducting properties of films. After growth, by cutting oxygen, the films were held in vacuum ($p_{O2} \sim 1 \times 10^{-8}$ Torr) for 10 min at the optimum reduction temperature (T_r) of 600 °C to 650 °C. The optimization for T_r is performed using RHEED observations. The films were slowly heated in vacuum with observation of the film surface by RHEED. The appearance of diffraction spots due to impurity phases shows the decomposition. The optimum T_r is about 20 to 30 °C lower than the decomposition temperature.

6.4.3 Metal organic decomposition growth of T′ cuprates

Metal organic decomposition (MOD) is a rather inexpensive and easy-to-implement thin film process, which is in contrast to MBE. The MOD process to synthesize T′ cuprate films is summarized in Table 6.6 (Matsumoto *et al.*, 2008).

Table 6.6 (Matsumoto *et al.*, 2008) MOD process to synthesize T′ cuprate films

MO	*RE* and Cu naphthenates
Substrates	$DyScO_3(110)$ for *RE* = Pr, Nd $SrTiO_3(001)$ for *RE* = Nd, Sm, Eu, Gd
Calcination	400°C/30 min/in air
Firing	850–900°C/60 min/in N_2/O_2 mixture ($p_{O2} = 10^{-4} \sim 10^{-2}$ atm)
Reduction	400–450°C/10 min/in vacuum

The stoichiometric mixture of naphthenate solutions was spin-coated on substrates. The coated films were first calcined at 400 °C in air to obtain precursors, then fired at 850–900 °C in a tubular furnace under a mixture of O_2 and N_2, controlling the oxygen partial pressure (p_{O2}) from 4×10^{-5} atm to 10^{-2} atm. Finally the films were 'reduced' in vacuum ($< 10^{-4}$ Torr $\approx 10^{-7}$ atm) at various temperatures for O_{ap} removal. As compared with the MBE growth conditions, the synthesis temperature is higher, and the reduction temperature is lower. A comparison of the morphologies of MBE and MOD films observed by AFM indicated that the MBE films consist of 2D grains with the size of 2000–3000 Å whereas the MOD films consist of 3D grains with the size of less than 1000 Å. The smaller grain size in MOD films facilitates O_{ap} removal at lower temperatures than in MBE films.

6.5 Electronic phase diagram

6.5.1 Early results

The first article reporting the discovery of 'electron-doped' superconductors (Takagi *et al.*, 1989) demonstrated the following results on T_c as a function of Ce doping (x) in $Nd_{2-x}Ce_xCuO_4$. Superconductivity of $T_c > 20$ K suddenly appears at $x = 0.14$, and the highest T_c is achieved at $x = 0.15$. Further Ce doping lowers T_c until superconductivity disappears at $x = 0.18$. The superconducting window in $Nd_{2-x}Ce_xCuO_4$ was quite narrow. It was revealed by later μSR experiments (Luke *et al.*, 1990) that the antiferromagnetic order develops in $x < 0.14$, which competes with the superconducting order. This first report employed polycrystalline specimens annealed in an Ar + O_2 mixture of $p_{O2} \sim 10^{-4}$ atm at 950–1000 °C for 10 hours, and then quenched to room temperature (it was reported that additional low-temperature annealing in $p_{O2} \sim 10^{-4} - 1$ atm at 550 °C improves the width of a superconducting transition). The reduction field (950–1000 °C in $p_{O2} \sim 10^{-4}$ atm) is located almost on the phase stability line.

Specimens used in most of the early experiments were similar polycrystalline pellets with a small superconducting volume fraction (~10%), a broad superconducting transition, and high resistivity. Subsequent developments in single-crystal growth techniques enabled production of single-crystalline specimens with a full superconducting volume fraction and metallic low resistivity (0.5 – 1 mΩcm at room temperature). However, the initial T_c-vs-x as described above has been believed to be 'typical' of T′ cuprates over 20 years. The superconducting window ($x = 0.14$ to 0.18) of T′-$Nd_{2-x}Ce_xCuO_4$ is much narrower than $0.05 < x < 0.30$ of the hole-doped analog, T-$La_{2-x}Sr_xCuO_4$, but electron-hole symmetry appears to hold roughly in that the T_c-vs-x shows a dome shape with the optimum doping of $x = 0.15$. Based on this 'apparent' electron-hole symmetry, the currently accepted 'doped Mott insulator' scenario for high-T_c superconductors has been developed.

6.5.2 Electronic phase diagram modified by more complete removal of O_{ap} impurities

As mentioned in section 6.4.1, O_{ap} impurities entirely change the most fundamental properties such as the electronic phase diagram. There have been some efforts performed toward more complete removal of O_{ap} impurities, which changed the electronic phase diagram dramatically. In general, it takes longer to remove O_{ap} impurities from single crystals due to limited paths of oxygen diffusion, than it does for polycrystalline specimens. Raising the reduction temperature to shorten the reduction time often results in partial decomposition at the surface of single crystals but with a fair amount of O_{ap} impurities remaining inside. For the purpose of more homogeneous reduction, Brinkmann *et al.* (1995) proposed the following reduction. They sandwiched $Pr_{2-x}Ce_xCuO_4$ single crystals with polycrystalline pellets of the same composition, and reduced them together in a mixture of Ar + O_2 at much higher temperatures (up to 1080 °C) for a much longer time (3 days) than in the standard reduction. The result is shown in Fig. 6.12, which compares the T_c-vs-x by the improved (solid line) and standard (broken line) reduction. With the improved reduction, the superconducting window expands down to $x = 0.04$ and there is a clear tendency of an increasing T_c with decreasing x.

Brinkmann *et al.* (1996) also pointed out the following correlation between T_c and residual resistivity (ρ_R) 'the larger ρ_R, the lower T_c', which is demonstrated in Fig. 6.13. Empirically, specimens containing a larger amount of residual O_{ap} impurities show a more prominent upturn in low-temperature resistivity. Hence the above correlation expresses that O_{ap} impurities are a strong scatterer to increase ρ_R as well as a strong pair-breaker to lower T_c. It appears that O_{ap} impurities in T′ cuprates behave like magnetic impurities in conventional superconductors.

Another way for more complete removal of O_{ap} impurities is to employ thin films as oxygen diffusion is prompt in thin films due to a large surface-to-volume ratio and small grain size. Figure 6.14 summarizes the T_c-vs-x curves for MBE-grown $RE_{2-x}Ce_xCuO_4$ thin films with different *RE* (Krockenberger *et al.*, 2008). Table 6.7 is a summary of the optimum doping level (x_{opt}) and highest T_c (T_c^{max}) for each *RE*. T′-$La_{2-x}Ce_xCuO_4$ shows superconductivity in $0.04 < x < 0.22$ with $x_{opt} = 0.08$ and $T_c^{max} =$ 31.0 K (Naito and Hepp, 2000b, 2001). In general, the superconducting

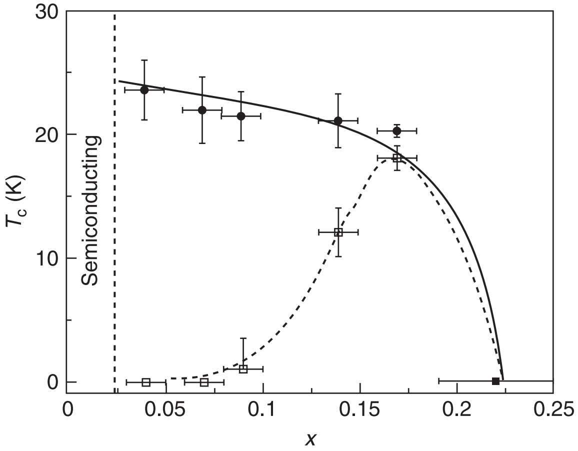

6.12 Ce doping dependence of T_c in T′-$Pr_{2-x}Ce_xCuO_4$. The T_c-vs-x by the improved (solid line) and standard (dashed line) reduction are compared. With the improved reduction, the superconducting window expands down to $x = 0.04$ and there is a clear tendency of an increasing T_c with decreasing x. (Reprinted with permission from Brinkmann *et al.* (1997), *Physica C*, **292**, 104. © 1997 Elsevier.)

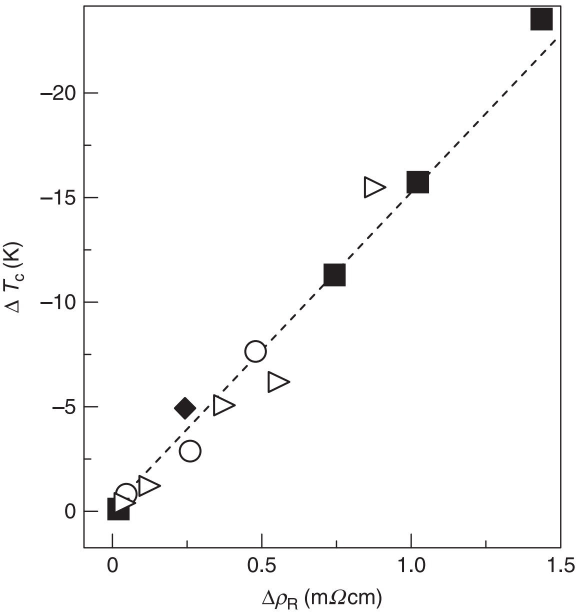

6.13 Correlation between residual resistivity and T_c reduction, 'the larger ρ_R, the lower T_c'. Different symbols represent different specimens: filled squares and open circles are the data for two specimens with $x = 0.15$ whereas filled diamonds and open triangles are the data for two specimens with $x = 0.07$. (Adapted from Brinkmann *et al.*, 1996.)

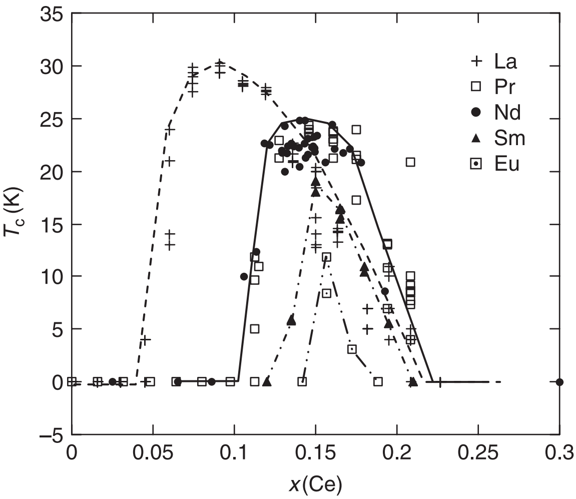

6.14 T_c-vs-x for MBE-grown T′-$RE_{2-x}Ce_xCuO_4$ films with different *RE* (La, Pr, Nd, Sm, and Eu). The superconducting window expands with larger RE^{3+}.

Table 6.7 *RE* dependence of the optimum doping level (x_{opt}) and the highest T_c (T_c^{max}) for MBE-grown T′-$RE_{2-x}Ce_xCuO_4$

RE	x_{opt}	T_c^{max} (K)
La	0.08	31.0
Pr	0.135	27.0
Nd	0.140	25.5
Sm	0.150	19.0
Eu	0.155	12.0
Gd	–	0.0

window expands with lower x_{opt} and higher T_c^{max} for larger RE^{3+}, and consequently the T_c-vs-x curve is not universal. This trend is not explained by the chemical pressure effect since T_c has almost no dependence on pressure in square-planar cuprates. The trend seems to be related to the empirical trend of solid state chemistry in T′ cuprates that O_{ap} removal is easier for larger RE^{3+} (section 6.3.2).

6.5.3 Superconductivity in T′ parent compounds

The parent compounds of high-temperature superconductors have long been believed to be universally a Mott Hubbard insulator. T-La_2CuO_4 is a Mott insulator without doubt. T′-RE_2CuO_4 has also been believed a Mott insulator since the discovery of 'electron-doped' superconductors in 1989. In fact, not only early polycrystalline pellets but also single crystals of Nd_2CuO_4 and Pr_2CuO_4 showed semiconducting behavior with high resistivity. However, it should be noted that T′ parent compounds were not given 'reduction' for O_{ap} removal in most cases. This is because the parent compounds are much easier to decompose than Ce-containing compounds (section 6.3.1). In fact, MBE-grown T′-RE_2CuO_4 films of RE = La, Pr, Nd are not highly insulating after careful 'reduction' but have ρ(300 K) of 2–10 mΩcm and metallic behavior ($d\rho/dT > 0$) down to 150–200 K (Tsukada *et al.*, 2002). However, they showed an upturn of resistivity at lower temperatures and no superconductivity.

The first compounds Tsukada *et al.*, (2005a) made superconducting without electron doping were T′-$(La,RE)_2CuO_4$, grown by MBE. In these compounds, La^{3+} is substituted not by Ce^{4+} but by isovalent RE^{3+} (RE = Sm, Eu, Gd, Tb, Lu, Y), and there is no effective dopant. Since then, further exploration on synthetic routes for more complete O_{ap} removal has taken place. Finally, superconductivity in the parent compounds, T′-RE_2CuO_4 (RE = Pr, Nd, Sm, Eu, Gd), by MOD was achieved by Matsumoto *et al.* (2008, 2009a). Figure 6.15 shows a superconducting transition of a Nd_2CuO_4 film as one example. T_c^{on} is as high as 33 K, which is ~10 K higher than T_c ~ 24 K of 'electron-doped' $Nd_{1.85}Ce_{0.15}CuO_4$. Figure 6.16 compares the T_c with and without Ce doping for each *RE*. It should be noted that undoped T_c is substantially higher than electron-doped T_c for all *RE*. The most remarkable is Gd_2CuO_4: there has been no report that electron-doped $Gd_{2-x}Ce_xCuO_4$ becomes superconducting whereas undoped Gd_2CuO_4 has T_c^{on} as high as 20 K (Manthiram and Zhu, 1994).

The key step for superconductivity is to fire MOD films in a low-p_{O2} atmosphere, the aim of which is to minimize the amount of O_{ap} impurities prior to the post-reduction process. Figure 6.17 shows the effect of p_{O2} during firing, which

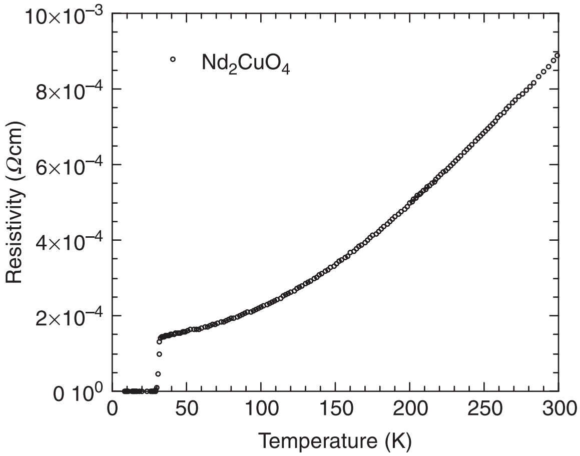

6.15 Superconductivity in Nd_2CuO_4 films prepared by MOD. The T_c^{onset} is as high as 33 K.

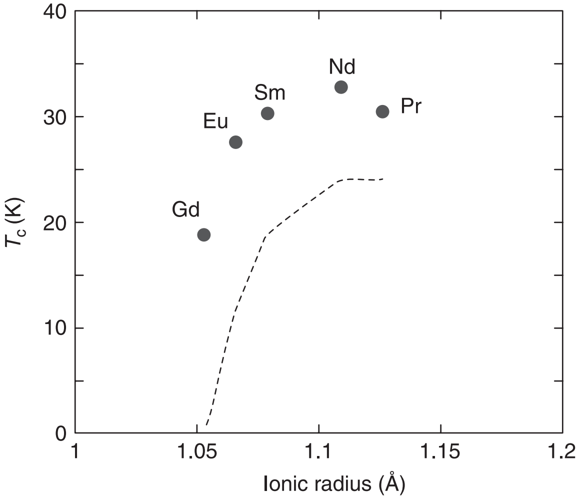

6.16 Comparison of T_c between undoped T′-RE_2CuO_4 (solid circles) and electron-doped T′-$RE_{1.85}Ce_{0.15}CuO_4$ (dashed line). Undoped T′-RE_2CuO_4 has substantially higher T_c than electron-doped T′-$RE_{1.85}Ce_{0.15}CuO_4$.

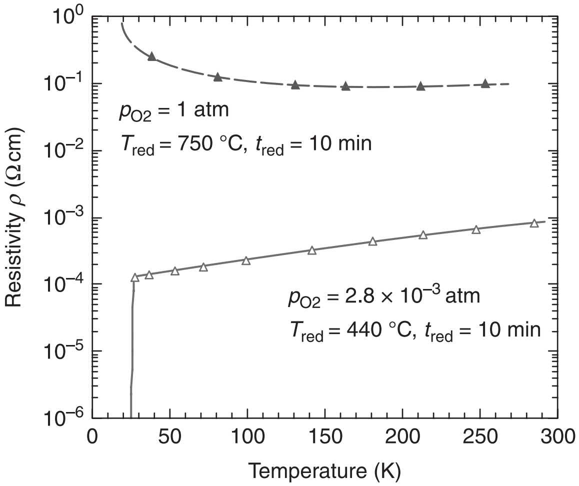

6.17 Superconducting versus nonsuperconducting Sm_2CuO_4 films. The film fired in p_{O2} = 2.8 × 10^{-3} atm at 850 °C became superconducting after reduction whereas the film fired in p_{O2} = 1 atm at 900°C never became superconducting even after stronger reduction.

compares the resistivity of two Sm_2CuO_4 films (A and B): film A fired at 900 °C for 1 h in p_{O2} = 1 atm, followed by vacuum reduction at 750 °C for 10 min, and film B fired at 850 °C for 1 h in $p_{O2} = 2.8 \times 10^{-3}$ atm, followed by vacuum reduction at 440 °C for 10 min. Film A is metallic down to 180 K with

ρ(300 K) ~ 100 mΩcm, but shows resistivity upturn at lower temperatures. In contrast, film B is all metallic with ρ(300 K) ~ 900 μΩcm, and shows superconductivity at $T_c^{on} = 28$ K.

After low-p_{O2} firing, films were 'reduced' in vacuum (< 10^{-4} Torr) at different temperatures (400 °C to 500 °C) for 5 to 60 min. The reduction is optimized based on the *c*-axis lattice constant (c_0) since the c_0 monotonically shrinks with reduction until films decompose (Matsumoto *et al.*, 2009c). Figure 6.18 plots the ρ(300 K)

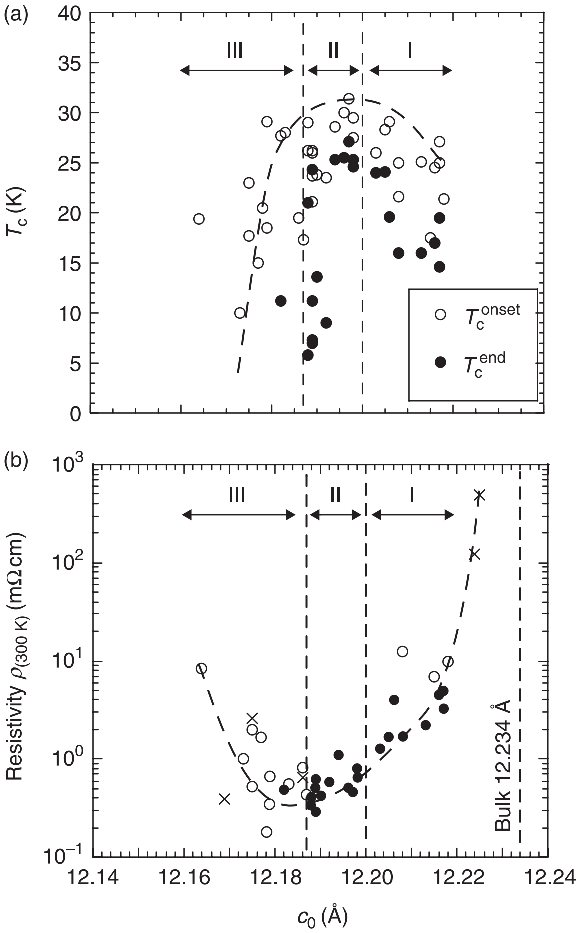

6.18 T_c and ρ(300 K) versus c_0 for Pr_2CuO_4 films on $DyScO_3$(110) substrates prepared by MOD. (a) (T_c-vs-c_0): open and filled circles stand for T_c^{onset} and T_c^{end}. (b) ($\rho_{(300\ K)}$-vs-c_0): crosses stand for films not showing superconductivity, filled and open circles stand for films showing superconductivity with and without zero resistance, respectively. (Reprinted with permission from Matsumoto *et al.* (2009a), *Phys Rev B*, **79**, 100508(R). © 2009 by the American Physical Society.)

(lower) and T_c (upper) as a function of c_0 for MOD-grown Pr_2CuO_4 films. One can divide the range of c_0 into the following three regions.

I *Insufficient* reduction (12.23 Å ≥ c_0 ≥ 12.20 Å): superconductivity improves with reduction.
II *Optimal* reduction (12.20 Å ≥ c_0 ≥ 12.19 Å): superconductivity is optimal.
III *Excessive* reduction (12.19 Å ≥ c_0 ≥ 12.16 Å): superconductivity degrades with reduction.

Figure 6.18 can be understood by assuming that the two effects, namely O_{ap} removal and O1 loss, are involved in the reduction process. The predominant effect in region I is O_{ap} removal, which improves the film properties. In contrast, the predominant in region III is O1 loss, which degrades the film properties although O_{ap} may be removed further as judged from the shrinkage of c_0. The O_{ap} removal is slightly quicker than the O1 loss, which realizes the situation with O_{ap} atoms mostly cleaned up but with O1 atoms mostly preserved, and provides a stage potential for high-T_c superconductivity.

6.5.4 Generic phase diagram of T′ cuprates

The same optimization in 'reduction' has been performed for Ce-containing compounds (Matsumoto *et al.*, 2009b). Figure 6.19 is a plot of T_c-vs-x of resultant T′-$Nd_{2-x}Ce_xCuO_4$ films, which is compared with the one derived from past bulk works and another from previous MBE works. The highest T_c of the MOD films

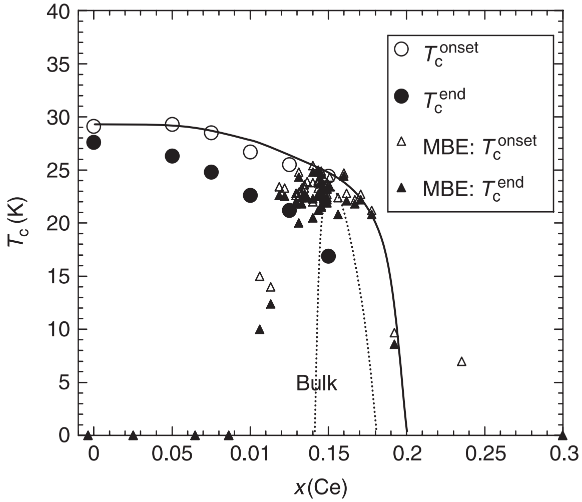

6.19 T_c-versus-x of $Nd_{2-x}Ce_xCuO_4$ films prepared by MOD. For a comparison, the data of bulk samples (dotted line) and MBE films (triangles) are also plotted. Open and filled symbols represent T_c^{onset} and T_c^{end}. The solid line is a guide for the eye.

is 29 K at $x = 0.00$, and T_c monotonically decreases from 29 K to 24 K with increasing x from 0.00 to 0.15. The T_c of 24 K at $x = 0.15$ agrees with the established bulk T_c of $Nd_{1.85}Ce_{0.15}CuO_4$. T_c for $x > 0.15$ could not be determined because of the solubility limit of Ce in the MOD process. In this region, however, the data from MBE growth are complementary. The phase diagram derived from MBE films shows a dome shape extending from $x = 0.10$ to 0.20. Although the T_c of MBE films is always higher than the bulk T_c, it is lower than the T_c of MOD films for $x < 0.15$. With the MOD and MBE data together, the T_c of NCCO films monotonically decreases from 29 K at $x = 0.00$ and disappears around $x = 0.20$. This T_c-vs-x, although it is quite different from the early bulk one, represents the generic phase diagram for NCCO with O_{ap} impurities removed.

6.6 Physical properties (1) – normal-state properties

6.6.1 Magnetism

The normal-state properties of T′ cuprates are reviewed in this section, starting with magnetism as it is the most closely related to the superconductivity in T′ cuprates. The presence of O_{ap} impurities greatly affects the magnetism in the CuO_2 layer as well as the superconductivity (T_c-vs-x) in the previous section. One has to pay attention to how carefully O_{ap} impurities are removed in each article. The first magnetic measurement on T′-$RE_{2-x}Ce_xCuO_4$ was muon spin relaxation (μSR) performed just after the discovery of ‘electron-doped’ superconductors. Since then, magnetic studies on T′ cuprates have been continuing, but experimental results are sometimes contradictory and none of them are definitive, which is somewhat similar to the situation for oxygen nonstoichiometry. The reason is, at least in part, inhomogeneity of oxygen distribution in specimens. Neutron diffraction experiments, especially, require large single crystals, in which homogeneous oxygen distribution is hard to achieve.

The essence of the first result of μSR by Luke *et al.* (1990) is illustrated in Fig. 6.20, and can be summarized as follows.

- The parent compounds show static magnetic order, which was later confirmed by neutron diffraction to be antiferromagnetic order. The Néel temperature (T_N) for 3D static AF order is about 250 K, which is comparable to T_N = 250–300 K in T-La_2CuO_4.
- The initial decrease of T_N with x is more gradual than in T-LSCO. There is an abrupt drop of T_N from ~80 K at $x = 0.14$ to <5 K at $x = 0.15$. Superconductivity appears after long-range AF order disappears.
- In specimens not reduced, the AF order remains and no superconductivity appears even at $x = 0.15$.

The electronic phase diagrams (T_c-vs-x, T_N-vs-x) of T′-$Nd_{2-x}Ce_xCuO_4$ and T-$La_{2-x}Sr_xCuO_4$ in Fig. 6.20 appear to be roughly symmetric. One large difference

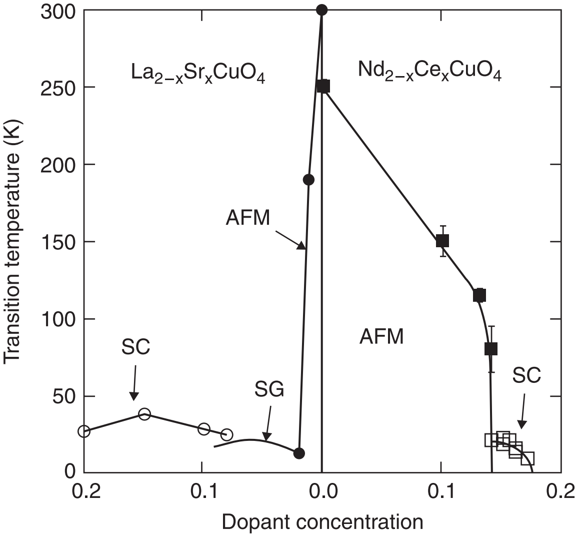

6.20 Electronic phase diagram of hole-doped T-$La_{2-x}Sr_xCuO_4$ and electron-doped T′-$Nd_{2-x}Ce_xCuO_4$ based on the μSR experiments. The electron-hole symmetry appears to hold roughly. However, note that the structure is different in the hole- and electron-doped sides. Since the T_N of T′-$Nd_{2-x}Ce_xCuO_4$ depends crucially on the amount of O_{ap} impurities, the phase diagram in the electron-doped side will change dramatically after complete removal of O_{ap} impurities. (Adapted from Luke *et al.*, 1990.)

is that electron-doped T′-$Nd_{2-x}Ce_xCuO_4$ shows a much wider AF region and a much narrower SC (superconducting) region than hole-doped T-$La_{2-x}Sr_xCuO_4$. Luke *et al.* explained this difference by dilution versus frustration of Cu spins by electron versus hole doping. A doped electron resides at the Cu site and compensates a Cu spin, leading to the dilution of the Cu spin density, whereas a doped hole resides at the oxygen site and forces the neighboring two Cu spins to align, introducing frustration in the AF order. The influence of doping on the AF order is weaker in electron doping than in hole doping, hence the AF phase remains until higher x in electron doping, and touches the SC phase. According to Fig. 6.20, the superconductivity in T′ cuprates suddenly appears at the SC–AF boundary with maximum T_c, which points toward the competition between the SC and AF orders.

The first experiments by Luke *et al.* were performed on $Nd_{2-x}Ce_xCuO_4$ samples that were not well-characterized, especially in oxygen homogeneity, but the results were basically supported by later μSR experiments (Kadono *et al.*, 2003; Fujita *et al.*, 2003a). There are a few reports claiming that the SC and AF orders coexist in $Nd_{2-x}Ce_xCuO_4$ with $x = 0.14 - 0.15$ (Watanabe *et al.*, 2001), but the inhomogeneity of samples is suspected.

The results of μSR were also supported by neutron diffraction. The early neutron diffraction experiment by Matsuda *et al.* (1990, 1992) on single crystals of

$Nd_{2-x}Ce_xCuO_4$ and Pr_2CuO_4 is one of the most extensive works on the magnetism of T′ cuprates. In the parent compounds, Nd_2CuO_4 and Pr_2CuO_4, the Cu^{2+} spin has a magnetic moment of ~ 0.4 μ_B, and the AF order develops below $T_N = 255$ K. The Cu^{2+} spin structure in Nd_2CuO_4 shows complex behavior at low temperatures due to the interaction with Nd^{3+}. moments whereas the spin structure in Pr_2CuO_4 is unchanged with temperature owing to the singlet ground state of Pr^{3+}. In the parent compounds, no significant change in the magnetic behavior was observed by heat treatment in Ar or in O_2. In Ce-doped compounds, however, a large change was observed by heat treatment. In as-grown samples with Ce doping of $x = 0.15$, the AF order remains with T_N varying from 125 K to 160 K. After reduction (950 °C/Ar/20 hr followed by 500 °C/O_2/20 hr), the SC phase was predominant at $x = 0.15$ but with the AF order remaining in 10% or more volume of a specimen, which corresponds to the region in which O_{ap} impurities remain.

From the viewpoint of the mechanism of high-temperature superconductivity, the crucial issue is whether dynamic AF fluctuations exist in superconducting samples or not. In fact, in T-$La_{2-x}Sr_xCuO_4$, it has been claimed that dynamic AF fluctuations are observed in superconducting samples. On clarifying this issue in T′ cuprates, however, high background magnetic scattering by Nd^{3+} moments is one obstacle in obtaining the detailed information on the dynamics of Cu spins in $Nd_{2-x}Ce_xCuO_4$. In the above work by Matsuda *et al.*, no inelastic magnetic peak clearly above the background was observed in the superconducting samples. Later, the improved statistics enabled Yamada and co-workers to observe inelastic magnetic signal at (1/2 1/2 0) in superconducting $Nd_{1.85}Ce_{0.15}CuO_4$ samples, indicating the presence of commensurate AF fluctuations. More recently, further efforts have been performed employing $Pr_{1-x}LaCe_xCuO_4$ single crystals in order to reduce the background magnetic scattering. However, the role of dynamic AF fluctuations to superconductivity has not been settled.

As mentioned above, at $x = 0.15$, T_N is 125 K – 160 K in the as-grown state whereas T_N is 0 K in the reduced state. Hence the T_N of the AF order in T′ cuprates depends not only on the Ce doping level but also (or more crucially) on the amount of O_{ap} impurities. This statement may also be true for lightly doped or parent compounds, and the AF order is expected to be substantially suppressed or even disappear when O_{ap} impurities are fully removed. Taking account of the competition between the SC and AF orders, the expansion of the superconducting window down to $x = 0.0$, as mentioned in sections 6.5.3 and 6.5.4., seems to indicate that the AF order may not be intrinsic at any of x but extrinsic, namely induced by O_{ap} impurities.

6.6.2 Resistivity

The best transport properties can be obtained with epitaxial thin films as mentioned in section 6.4.1. MOD growth provides better results than MBE growth in $x < 0.15$ whereas the opposite is true in $x \geq 0.15$. Figure 6.21 shows the ρ-T curves of MBE-grown $RE_{2-x}Ce_xCuO_4$ films with different *RE* (Naito *et al.,* 2002). The

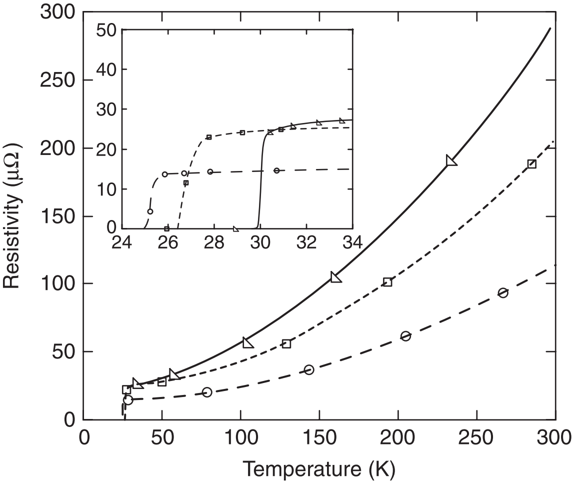

6.21 ρ-T curves of MBE-grown $RE_{2-x}Ce_xCuO_4$ films with different *RE*. The triangles, squares, and circles represent *RE* = La with $x = 0.09$, *RE* = Pr with $x = 0.135$, *RE* = Nd with $x = 0.140$, respectively.

room-temperature resistivity, ρ(300 K), of best $Nd_{1.85}Ce_{0.15}CuO_4$ films is as low as 100 μΩcm, which is 1/3 to 1/4 of the lowest value reported for single crystals. The resistivity becomes the most metallic at around $x = 0.175$, slightly ‘overdoped’: ρ(300 K) ~ 100 μΩcm, ρ(30 K) ~ 10 μΩcm, and *RRR* (≡ ρ(300 K)/ρ(30 K)) ~10. The anisotropy (ρ_c/ρ_{ab}) of resistivity is reported to be ~10^4 from the data of $Nd_{1.85}Ce_{0.15}CuO_4$ single crystals (Hidaka and Suzuki, 1989).

The resistivity is nearly proportional to temperature in most hole-doped cuprates, whereas the resistivity appears to follow a T^2 dependence in T′-$(RE,Ce)_2CuO_4$. Tsuei *et al.* (1989) ascribed the T^2 dependence to electron–electron scattering. However, the coefficient of the T^2 dependence is 2–3 orders of magnitude larger and the temperature range is much wider than electron-electronic scattering observed in conventional metals. Brinkmann *et al.* (1997) reported resistivity up to 700 K, as shown in Fig. 6.22, which is not greatly different from the temperature dependence of conventional metals, but with a substantially higher Debye temperature (~ 500 K). The T^2 dependence in T′-$(RE,Ce)_2CuO_4$ appears to be a conclusion derived from the data in a limited temperature range below room temperature.

The behavior of the low-temperature resistivity should be commented on. T′ cuprates often show a resistivity upturn at low temperatures (Fournier *et al.*, 1997; Sekitani *et al.*, 2002). Figure 6.23 shows two examples: nonsuperconducting $Pr_{2-x}Ce_xCuO_4$ film with x ~ 0.10 and superconducting $Nd_{2-x}Ce_xCuO_4$ with x ~ 0.15, both grown by MBE. In the latter film, the normal-state behavior is revealed by suppressing superconductivity in magnetic fields. The upturn has a log T dependence below the resistivity minimum but saturates to a finite value toward lowest temperatures. In addition, the upturn is suppressed in magnetic fields

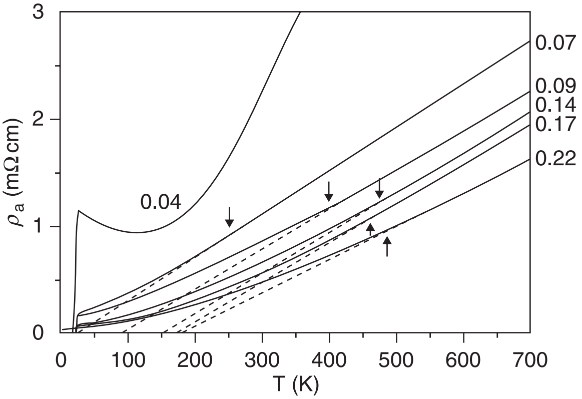

6.22 ρ-T curves of $Pr_{2-x}Ce_xCuO_4$ single crystals up to 700 K. The specimens were given special reduction described in section 6.5.2. The arrows indicate the crossover from a low-temperature T^2 to high-temperature T-linear dependence. (Reprinted with permission from Brinkmann *et al.* (1997), *Physica C*, **292**, 104. © 1997 Elsevier.)

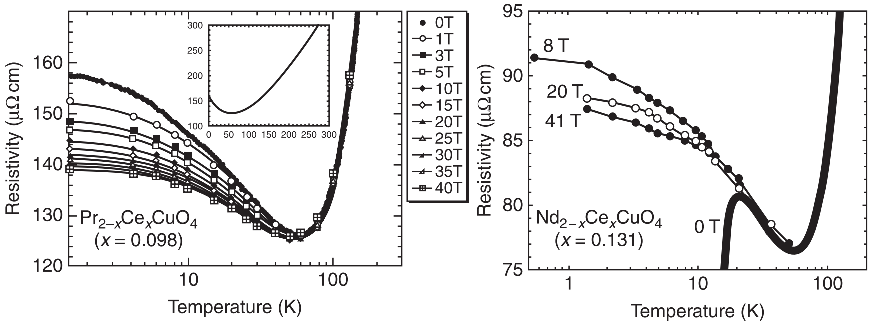

(a)

(b)

6.23 Behavior of the low-temperature resistivity under magnetic fields in underdoped T′ cuprates (nonsuperconducting $Pr_{1.902}Ce_{0.098}CuO_4$ (a) and superconducting $Nd_{1.869}Ce_{0.131}CuO_4$ (b) grown by MBE). The resistivity upturn at low temperatures has a log T dependence but saturates to a finite value toward lowest temperatures. In addition, the upturn is suppressed in magnetic fields (negative magnetoresistance). (Panel (a) is reprinted with permission from Sekitani *et al.* (2003), *Phys Rev B*, **67**, 174503. © 2003 by the American Physical Society.)

(negative magnetoresistance, Sekitani *et al.*, 2003). These features are reminiscent of the Kondo effect. The origin of the low-temperature upturn in T′ cuprates can be understood as follows. As speculated in section 6.6.1., Cu^{2+} seems to be nonmagnetic in the ideal T′ structure with no O_{ap} impurity. However, an O_{ap} impurity atom changes Cu^{2+} just beneath to be magnetic, thereby giving rise to the Kondo effect. The Kondo effect causes strong carrier scattering as well as pair breaking.

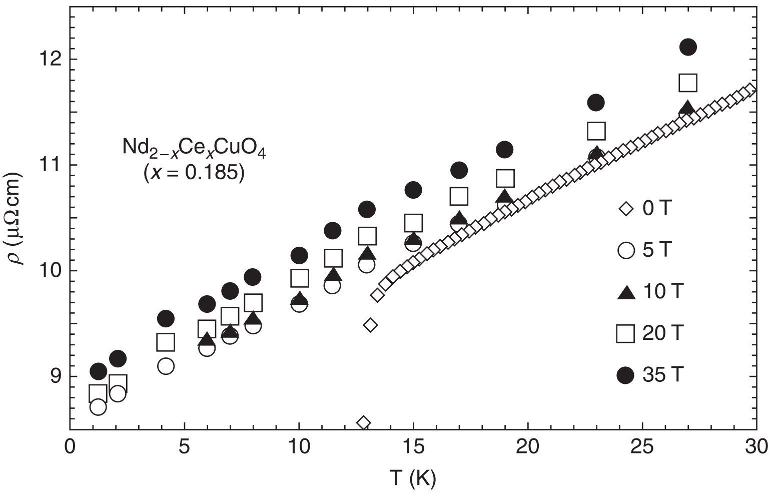

6.24 Behavior of the low-temperature resistivity under magnetic fields in overdoped T′ cuprates ($Nd_{1.815}Ce_{0.185}CuO_4$ grown by MBE). The resistivity with superconductivity suppressed in magnetic fields continues to decrease almost linearly down to the lowest temperature measured.

Strange behavior in resistivity is also seen in the overdoped region (Fournier *et al.*, 1997; Sekitani *et al.*, 2002). In conventional metals, resistivity comes down to a finite value (residual resistivity) at lowest temperatures. However, the resistivity of a $Nd_{2-x}Ce_xCuO_4$ film of $x \sim 0.185$, with superconductivity suppressed in magnetic fields, continues to decrease almost linearly down to the lowest temperature measured (Fig. 6.24). The absence of low-temperature saturation in resistivity is not understood although similar behavior is seen in overdoped $Tl_2Ba_2CuO_6$ (Mackenzie *et al.*, 1996).

6.6.3 Hall coefficient and Seebeck coefficient

Next the Hall coefficient (R_H) and Seebeck coefficient (S) are discussed. Both of the coefficients represent the character of conduction careers, and are supposed to be negative in electron conduction and positive in hole conduction. However, such a simple view applies only to one-band semiconductors, and R_H and S in metals are a very complex function of the $\boldsymbol{k}$ dependent energy and relaxation time of quasi-particles (Hurd, 1972). With such circumstances in mind, we take a look at the Hall coefficient first. Figure 6.25 shows the early result on the Ce doping dependence of R_H for T′-$Nd_{2-x}Ce_xCuO_4$, which is compared with the result for hole-doped T-$La_{2-x}Sr_xCuO_4$ (Uchida *et al.*, 1989). The R_H of $Nd_{2-x}Ce_xCuO_4$ is negative at $x < 0.15$ and becomes positive at $x > 0.175$. The R_H of $La_{2-x}Sr_xCuO_4$ shows an opposite change, namely positive to negative. In this early report, the R_H follows nearly a $1/x$ dependence $x < 0.10$ in both of the compounds. The data

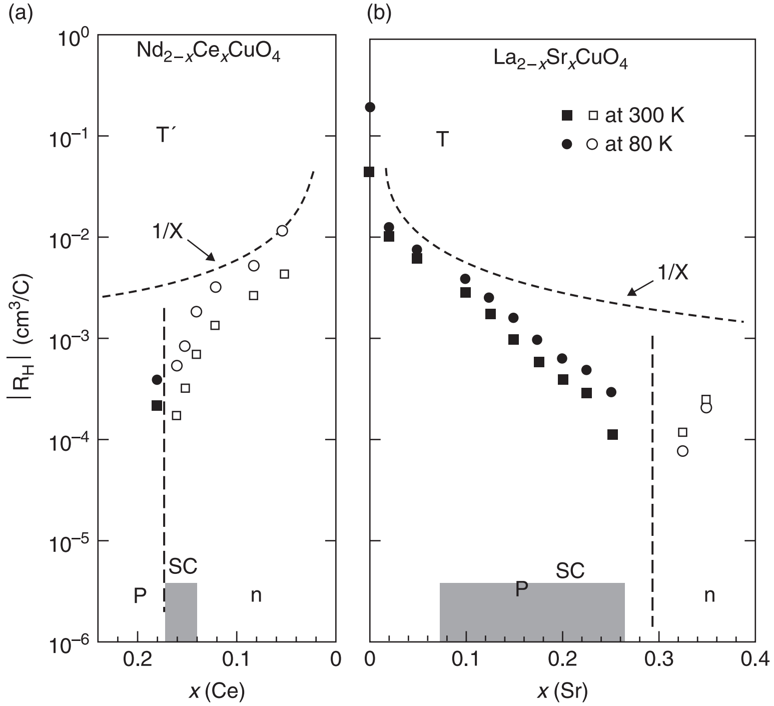

6.25 Doping dependence of R_H in electron-doped T′-$Nd_{2-x}Ce_xCuO_4$ (a) and hole-doped T-$La_{2-x}Sr_xCuO_4$ (b). The R_H of $Nd_{2-x}Ce_xCuO_4$ is negative at $x < 0.15$ and becomes positive at $x > 0.175$. The R_H of $La_{2-x}Sr_xCuO_4$ shows an opposite change, namely positive to negative. (Reprinted with permission from Uchida *et al.* (1989), *Physica C*, **162–164**, 1677. © 1989 Elsevier.)

seem to suggest that $RE_{2-x}Ce_xCuO_4$ is an 'electron-doped' superconductor, distinguished from the holed-doped superconductor, $La_{2-x}Sr_xCuO_4$. Even in early reports, however, positive R_H or positive S was sometimes reported in optimum doped NCCO and PCCO (Wang *et al.*, 1991; Lee *et al.*, 1990). Furthermore it was pointed out that R_H of T′-$Nd_{1.85}Ce_{0.15}CuO_4$ shows not only a large temperature dependence but also a large sample dependence. Later studies on transport properties of T′ cuprates suggested that there exist two types of careers: one electron-like, and the other hole-like, and this led to controversy over which type of career is crucial for superconductivity in T′ cuprates.

The origin of the sample dependence of R_H in T′ cuprates was clarified from the systematic studies varying the reduction condition to remove O_{ap} impurities. It turned out that R_H shifts toward a more positive value with reduction. Figure 6.26 shows the data by Brinkmann *et al.* (1996) for $Pr_{2-x}Ce_xCuO_4$ single crystals, which underwent 'improved' reduction as described in section 6.5.2. When decreasing p_{O2} during reduction, R_H shifts towards positive. Simultaneously

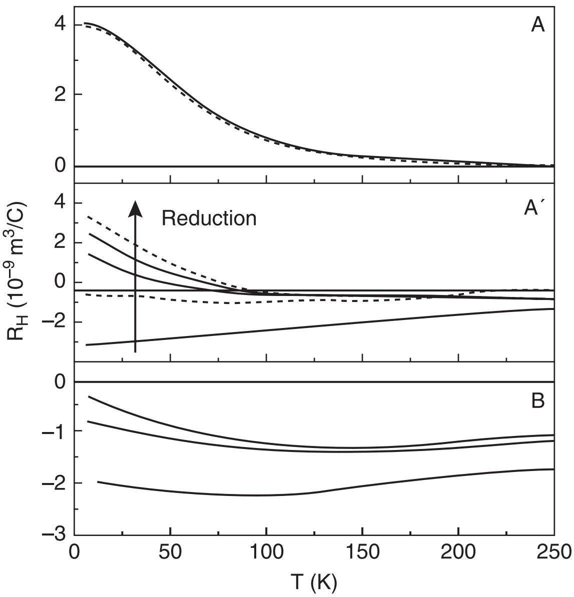

6.26 Reduction dependence of R_H in $Pr_{2-x}Ce_xCuO_4$ single crystals, which underwent 'improved' reduction as described in section 6.5.2. R_H shifts towards positive with stronger reduction. Samples A and A′ are $x = 0.15$ whereas sample B is $x = 0.10$. The p_{O2} during reduction is 0.05 mbar (solid line), 0.46 mbar (dashed line) in A, 0.05, 0.68, 1.00, 2.00, 4.00 mbar from the top in A′, and 0.17, 0.30, 0.45 mbar from the top in B. (Reprinted with permission from Brinkmann *et al.* (1996), *Physica C*, **269**, 76. © 1996 Elsevier.)

the resistivity lowers and T_c increases. Jiang *et al.* (1994) and Suzuki *et al.* (1994) obtained similar results using $Nd_{1.85}Ce_{0.15}CuO_4$ epitaxial thin films. Moreover, Jiang *et al.* (1994) reported the state of excessive reduction with superconductivity rapidly degraded by further reduction, which was not reached in the bulk work by Brinkmann *et al.* (1996). This state is identical to the one observed in superconducting parent compounds as described in section 6.5.3. Excessive reduction eventually makes thin films transparent and insulating while the T′ structure is preserved. The Seebeck coefficient shows behavior similar to the Hall coefficient, and shifts towards a more positive value with reduction (Xu *et al.*, 1996).

6.7 Physical properties (2) – superconducting properties

6.7.1 Tunneling

Next, the superconducting properties of T′ cuprates are reviewed. We start by tunneling. In most high-T_c cuprates, no quasiparticle spectrum showing a clear superconducting gap structure is seen in tunneling experiments. The reason is that

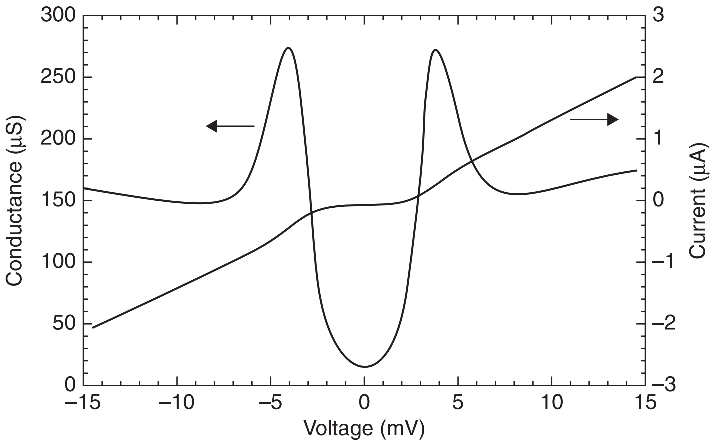

6.27 Point-contact spectrum for a $Nd_{1.85}Ce_{0.15}CuO_4$ sintered pellet (T_c = 22 K). The spectrum shows a clear superconducting gap structure with reasonably low zero-bias conductance. The superconducting gap (Δ) is 3.7 meV, amounting to $2\Delta/k_BT_c = 3.9$. (Reprinted with permission from Zasadzinski *et al.* (1992), *J Phys Chem Solids*, **53**, 1635. © 1992 Elsevier.)

the CuO_2 networks consisting of weak Cu-O bonds in high-T_c cuprates become disordered at the interface, leading to severely deteriorated superconductivity. However, a reasonably good quasiparticle spectrum has been observed in T′ cuprates using point-contact junctions or sandwich junctions. Figure 6.27 shows a point-contact spectrum for a $Nd_{1.85}Ce_{0.15}CuO_4$ sintered pellet (T_c = 22 K) obtained by Zasadzinski *et al.* (1992) (see also Huang *et al.*, 1990). The spectrum shows a clear superconducting gap structure with reasonably low zero-bias conductance. The spectrum suggests $Nd_{1.85}Ce_{0.15}CuO_4$ to be an '*s*' wave superconductor. The superconducting gap (Δ) is 3.7 meV, amounting to $2\Delta/k_BT_c = 3.9$, indicating intermediate coupling like Nb. Zasadzinski *et al.* (1992) also derived the Eliashberg function, $\alpha^2F(\omega)$, by the McMillan-Rowell method (1969), which represents the frequency-dependent interaction between electrons and bosons that play the role of glue in Cooper pairing. Here $F(\omega)$ is the density of states of bosons with a frequency of ω and α the interaction strength. The results are shown in Fig. 6.28. One can see a good correspondence between the ω dependence of $\alpha^2F(\omega)$ and the phonon density of states obtained from neutron inelastic scattering. Then Zasadzinski *et al.* (1992) concluded that bosons relevant to superconductivity in NCCO are phonons, namely NCCO is a phonon-mediated BCS superconductor. The dimensionless electron–phonon coupling constant, λ ($\equiv 2 \int d\omega\alpha^2F(\omega)/\omega$) is evaluated to be ~1.0, again indicating intermediate-coupling. The T_c as high as ~22 K in spite of $\lambda \sim 1.0$ can be attributed to high-frequency phonons originating from oxygen vibrations ranging up to ~100 meV.

A reasonably good quasi-particle spectrum was also obtained using sandwich junctions, Pb/native/$Nd_{1.85}Ce_{0.15}CuO_4$, as shown in Fig. 6.29 (Naito *et al.*, 2000a).

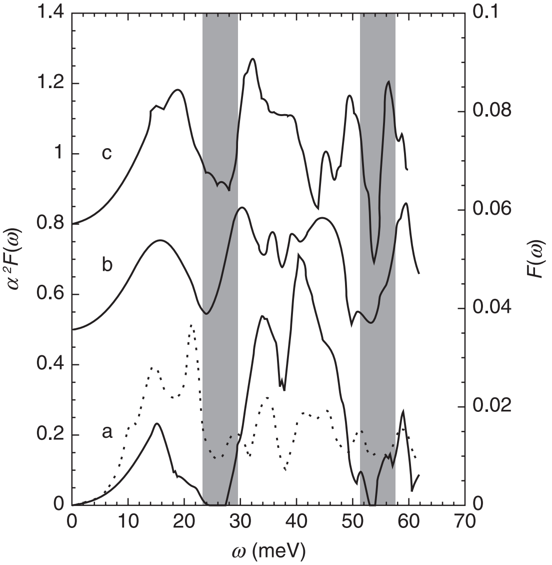

6.28 Eliashberg function, $\alpha^2F(\omega)$, derived from the point contact spectra in Fig. 6.27 using the McMillan-Rowell method (a, b, and c are from three different point contact spectra). A good correspondence is seen between the ω dependence of $\alpha^2F(\omega)$ (solid line) and the phonon density of states (dotted lines) obtained from neutron inelastic scattering. The shades indicate the pronounced minima in $\alpha^2F(\omega)$. (Reprinted with permission from Zasadzinski *et al.* (1992), *J Phys Chem Solids*, **53**, 1635. © 1992 Elsevier.)

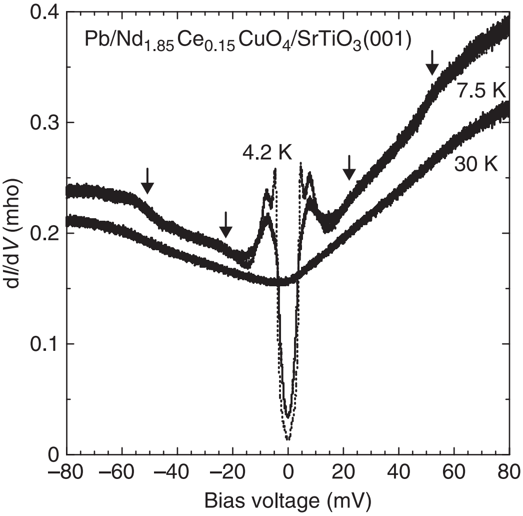

6.29 Tunneling spectrum of Pb/PbO_x/$Nd_{1.85}Ce_{0.15}CuO_4$/$SrTiO_3$(001). The fine structures in the d*I*/d*V* curve indicated by the arrows correspond to the pronounced minima in $\alpha^2F(\omega)$ (Naito *et al.*, 2000a).

In this figure, the fine structures in the d*I*/d*V* curve indicated by the arrows corresponds to the pronounced minima of $\alpha^2F(\omega)$ in Fig. 6.28. The junctions were fabricated simply by depositing Pb on an $Nd_{1.85}Ce_{0.15}CuO_4$ film. The reason why such a simple process works was pursued by photoemission spectroscopy (Yamamoto *et al.*, 1997). Once NCCO films are exposed to air after growth, oxygen atoms are adsorbed at O_{ap}. Pb deposited subsequently on this surface extracts most of the adsorbed oxygen atoms with a thin interfacial Pb layer oxidized at the same time, resulting in a $Pb/PbO_x/NCCO$ junction. In this junction, NCCO at interface is nearly free from O_{ap} impurities and O1 deficiencies, hence superconductivity is preserved at the interface. In contrast, when Pb is deposited directly on NCCO films without air exposure, junctions show no trace of superconductivity. This is because Pb extracts oxygen atoms at O1 instead of those at O_{ap}, making NCCO at the interface nonsuperconducting (Naito *et al.*, 2000a).

6.7.2 Magnetic penetration depth

Magnetic penetration depth (λ_L) is a fundamental length scale that characterizes superconductors as well as coherence length (ξ). In addition, the temperature dependence of λ_L provides important information on the pairing symmetry in superconductors. The $\lambda_L(T)$ is related to the superfluid density, $n_s(T)$, by the following equation,

$$\lambda_L(T)^{-2} = \frac{\mu_0 n_s(T) e^2}{m}. \qquad [6.7]$$

The BCS theory for *s*-wave superconductors gives the following exponential formula in the low temperature limit (Halbritter, 1971),

$$\frac{\delta\lambda(T)}{\lambda_L(0)} = \frac{\lambda_L(T) - \lambda_L(0)}{\lambda_L(0)} = \sqrt{\frac{\pi\Delta(0)}{2k_BT}}\exp(-\frac{\Delta(0)}{k_BT}) \qquad [6.8]$$

In *d*-wave superconductors, however, the superconducting gap $\Delta(k)$ depends on *k* with $\Delta(k) = 0$ in a certain direction. In the case of Cooper pairing via antiferromagnetic fluctuations, the gap vanishes in $\Delta(k)$ // [110] (so called 'line node'), leading to $\delta\lambda(T)$ proportional to *T* at low temperatures. Therefore the pairing symmetry can be judged by the temperature dependence of $\lambda_L(T)$ at low temperatures.

The first precise measurements of $\lambda_L(T)$ were performed by a Maryland University group in 1993 by the cavity method (resonant frequency ~9.6 GHz) using both high-quality single crystals and epitaxial thin films of $Nd_{1.85}Ce_{0.15}CuO_4$ (Wu *et al.*, 1993; Anlage *et al.*, 1994). They observed an exponential temperature dependence for in-plane $\delta\lambda_{ab}(T)$ at low temperatures, and hence concluded that $Nd_{1.85}Ce_{0.15}CuO_4$ is an *s*-wave superconductor. Moreover, they evaluated the superconducting gap from the exponential dependence and obtained $\Delta(0) = 3.7$ meV and $2\Delta/k_BT_c = 4.1$ (assuming $T_c = 21$ K). The values agree well with the values from the tunnel experiments in section 6.7.1. A similar conclusion was also reached by Schneider *et al.* (1994) and Andreone *et al.* (1994) almost at the same time.

In 1996, however, Cooper (1996) made one caution to the interpretation of the experimental results of $\lambda_L(T)$ of NCCO. He suggested that raw data need to be corrected by the increasing susceptibility $\chi \sim 1/(T + \Theta)$ at low temperatures due to Nd^{3+} moments (Θ is 1.2 K in NCCO). The correction is simply to divide the raw data for $\lambda_{ab}(T)$ by a factor $\sqrt{\mu_r}$, where $\mu_r = (1 + \chi)$ is a magnetic permeability, in the case that the sample thickness, d, is substantially larger than $2\lambda_{ab}$. Applying the correction to the above results from the Maryland University group, Cooper claimed that the temperature dependence of $\delta\lambda_{ab}(T)$ becomes T linear or T^2 at low temperatures, indicating a *d*-wave superconductor. A more detailed study was performed after Cooper's paper when Alff *et al.* (1999) compared $\lambda_L(T)$ between $Pr_{1.85}Ce_{0.15}CuO_4$ with nonmagnetic Pr^{3+} and $Nd_{1.85}Ce_{0.15}CuO_4$ with magnetic Nd^{3+}. The results are shown in Fig. 6.30. The $\lambda_L(T)$ of NCCO is in fact anomalous and increases below 4 K, which can be attributed to Nd^{3+} moments whereas the $\delta\lambda_L(T)$ of PCCO follows a simple exponential dependence. Alff *et al.* (1999) concluded that both NCCO and PCCO are an *s*-wave superconductor with $\Delta(0) = 3.0$ meV, $2\Delta/k_BT_c = 2.9$. Experimental results appeared to converge to the conclusion that electron-doped T′ cuprates are an *s*-wave superconductor before the results of phase-sensitive experiments were reported by Tsuei *et al.* (2000a).

In 2000, Tsuei *et al.* (2000a) claimed on the basis of their phase-sensitive experiments (see section 6.7.3) that electron-doped cuprates as well as hole-doped cuprates are a *d*-wave superconductor. This work stimulated the re-examination of $\lambda_L(T)$. Then there emerged many experimental reports supporting *d* wave for T′ cuprates. Kokales *et al.* (2000) repeated microwave cavity measurements and

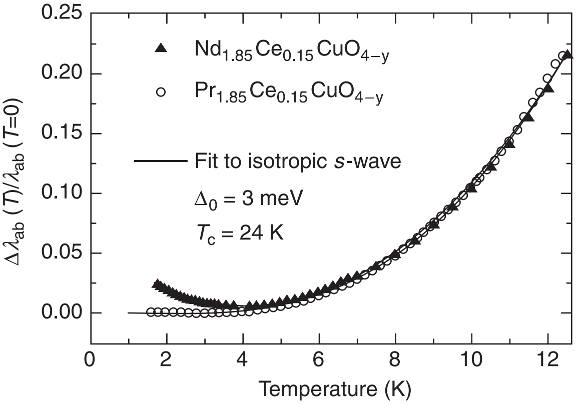

6.30 Comparison of the temperature dependence of magnetic penetration depth, $\lambda_L(T)$, between $Pr_{1.85}Ce_{0.15}CuO_4$ with nonmagnetic Pr^{3+} and $Nd_{1.85}Ce_{0.15}CuO_4$ with magnetic Nd^{3+}. The $\lambda_L(T)$ of NCCO is anomalous and increases below 4 K, which can be ascribed to Nd^{3+} moments whereas the $\delta\lambda_L(T)$ of PCCO follows a simple exponential dependence. (Reprinted with permission from Alff *et al.* (1999), *Phys Rev Lett*, **83**, 2644. © 1999 by the American Physical Society.)

Prozorov *et al.* (2000) employed a tunnel-diode driven *LC* resonator method (resonance frequency 11 MHz), both using single crystals and thin films of PCCO and NCCO prepared by the Maryland University group. A T^2 dependence was observed at low temperatures in both of the experiments, which was regarded as evidence of a dirty *d*-wave superconductor. However, more careful experiments performed by Kim *et al.* (2003) using high-quality MBE-grown films reached a different conclusion. In penetration depth experiments using thin films, an interfacial deteriorated layer (typically a few hundred Å) between a substrate and a film gives an undesired contribution. In order to eliminate such contributions, Kim and co-workers deposited a thin buffer layer (250 Å) of nonsuperconducting Pr_2CuO_4 before the deposition of $Pr_{2-x}Ce_xCuO_4$. Then the $\delta\lambda_L(T)$ measured by a mutual inductance method (~ 50 kHz) clearly showed an exponential dependence for all films of $x = 0.115 \sim 0.152$. In the case of T′ films, not only an interfacial deteriorated layer but also a surface dead layer due to O_{ap} adsorption should cause an undesired effect on $\lambda_L(T)$. Without paying careful attention to such material issues, one cannot reach an intrinsic temperature dependence of $\lambda_L(T)$ of T′ cuprates, even if a very precise measurement is performed. The author believes that the results by Kim *et al.* may be the closest to the intrinsic behavior of T′ cuprates. Table 6.8 is a summary of penetration depth experiments on T′ cuprates to date.

Table 6.8 Summary of the experimental results on the magnetic penetration depth experiments for T′-$RE_{2-x}Ce_xCuO_4$

Ref.	Materials	Doping level	Technique	*s* or *d*
Wu *et al.*, 1993	NCCO epi-films by PLD	Optimum	Cavity	*s*
Anlage *et al.*, 1994	NCCO single crystals			
Schenider *et al.*, 1994	NCCO epi-films by PLD	Optimum	Mutual inductance	*s*
Andreone *et al.*, 1994	NCCO epi-films by PLD	Optimum	Ring resonator	*s*
Alff *et al.*, 1999	NCCO/PCCO epi-films by MBE	Optimum	Josephson current	*s*
Kokales *et al.*, 2000	PCCO epi-films by PLD NCCO/PCCO single crystals	Optimum	LC resonator	*d*
Prozorov *et al.*, 2000	NCCO/PCCO single crystals	Optimum	Cavity	*d*
Skinta *et al.*, 2002a	PCCO epi-films by MBE	Optimum	Mutual inductance	*s*
Skinta *et al.*, 2002b	LCCO/PCCO epi-films by MBE	Underdope to overdope	Mutual inductance	*d* (underdope) → *s* (optimum to overdope)
Kim *et al.*, 2003	Buffered PCCO epi-films by MBE	Underdope to overdope	Mutual inductance	*s*

6.7.3 Phase-sensitive experiments

The first phase-sensitive experiments on high-T_c cuprates were performed in 1993 on YBCO by Wollman *et al.* (1993). They employed the configuration of corner superconducting quantum interference devices (SQUIDs) (or later corner Josephson junctions in Wollmann *et al.* (1995)) consisting of YBCO single crystals and Pb, and concluded from a π phase shift in the magnetic field modulation of I_c that YBCO is a *d*-wave superconductor (see Fig. 6.31). Tsuei and Kirtley (1994) employed the ring configuration containing weak-link junctions made of YBCO films (1200 Å) deposited on tricrystal $SrTiO_3$ substrates (rings are 48 μm in inner diameter, 10 μm in width). Using a scanning SQUID microscope, they observed spontaneous magnetization of a half magnetic flux quantum, $\Phi_0/2 = h/4e$, in the 3-junction ring, but not in the 2-junction ring, which is consistent with the behavior predicted for a $d_{x^2-y^2}$ superconductor. Since then, Tsuei and Kirtley (2000b) performed similar experiments for other hole-doped systems such as Tl cuprates and Bi cuprates, etc., and they claimed the universality of $d_{x^2-y^2}$ superconductivity for hole-doped cuprates.

No phase sensitive experiment had been performed on electron-doped systems until 2000. The grain-boundary Josephson current is much smaller in electron-doped cuprates than in hole-doped cuprates, which impeded tricrystal experiments.

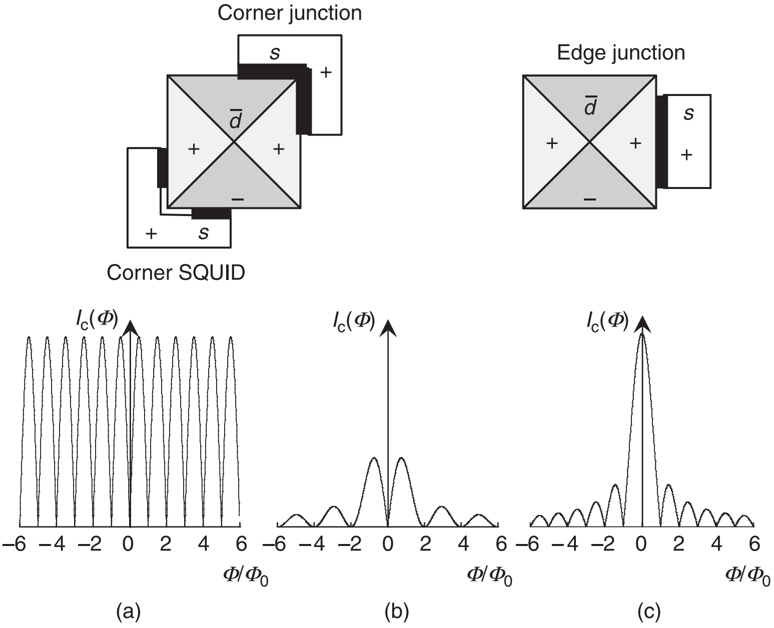

6.31 Top: Josephson junctions and SQUID composed of *s*-wave and *d*-wave superconductors. Bottom: I_c modulation in magnetic field in a corner SQUID (a), in a corner junction (b), and in an edge junction (c).

Tsuei and Kirtley (2000a), however, managed to overcome this problem. They obtained the Josephson current by omitting the patterning to rings and also employing 1 μm thick $Nd_{1.85}Ce_{0.15}CuO_4$ and $Pr_{1.85}Ce_{0.15}CuO_4$ films, which are eight times thicker than YBCO films used in tricrystal rings. The resultant scanning SQUID images showed a Josephson vortex centered at the tricrystal point. As compared with hole-doped cuprates, the Josephson vortex was much more diffusive and extended along the grain boundaries up to about 100 μm. After a complicated numerical fitting procedure to the magnetic field profile from the Josephson vortex, the flux was evaluated to be $0.33 \sim 0.65\Phi_0$. In spite of a large error bar, Tsuei and Kirtley claimed that their experimental results present evidence that electron-doped NCCO and PCCO are a $d_{x^2-y^2}$ superconductor and that the pairing symmetry of $d_{x^2-y^2}$ hold universally for high-T_c cuprates.

The manufacture of tricrystal substrates, which were performed in the early 1990s by Shinkosha Co., a Japanese substrate supplier, requires state-of-the-art perovskite substrate technology including growth of high-quality crystals, welding, polishing, etc. At present it is hard to obtain tricrystal substrates and to repeat the same experiments as Tsuei and Kirtley did. In 2002, a Twente University group proposed a new phase sensitive experiment with no tricrystal substrate (Smilde *et al.*, 2002). The junctions proposed are called 'zigzag' junctions, and are schematically illustrated in Fig. 6.32. The zigzag junction, in which [100] and [010] junctions alternate, is basically a series of corner junctions. The Twente University group fabricated the zigzag junctions using NCCO by the ramp-edge junction process: NCCO as a bottom electrode, Au a normal layer as well as serving a diffusion barrier of oxygen, and Nb a counter electrode (Ariando *et al.*, 2005). They compared the magnetic field dependence, of I_c in standard straight junctions ([100] junctions) and zigzag junctions. The I_c of straight junctions showed normal behavior with a maximum at zero field whereas the I_c of zigzag junctions is small below a threshold field and suddenly goes up. These observations were claimed to be consistent with $d_{x^2-y^2}$ pairing. The two phase sensitive experiments support electron-doped $RE_{2-x}Ce_xCuO_4$ to be a $d_{x^2-y^2}$ superconductor. On the other hand, some of the tunneling and penetration experiments point toward an *s*-wave superconductor. Hence further efforts are required to reconcile all of the experimental results and to establish the pairing symmetry in $RE_{2-x}Ce_xCuO_4$.

6.7.4 Critical fields

All high-T_c cuprates are extreme type-II superconductors (GL parameter $\kappa = \lambda/\xi >> 1$) with large anisotropy reflecting the layered structure. Many articles were reported on the anisotropic superconducting parameters such as upper/lower critical fields, λ, ξ, etc., just after the discovery of electron-doped T′ cuprates. In most of the early measurements, however, a rough estimate for the upper critical fields was made using non-qualified specimens from broad superconducting transitions in magnetic fields. Since then, the quality of single crystals and

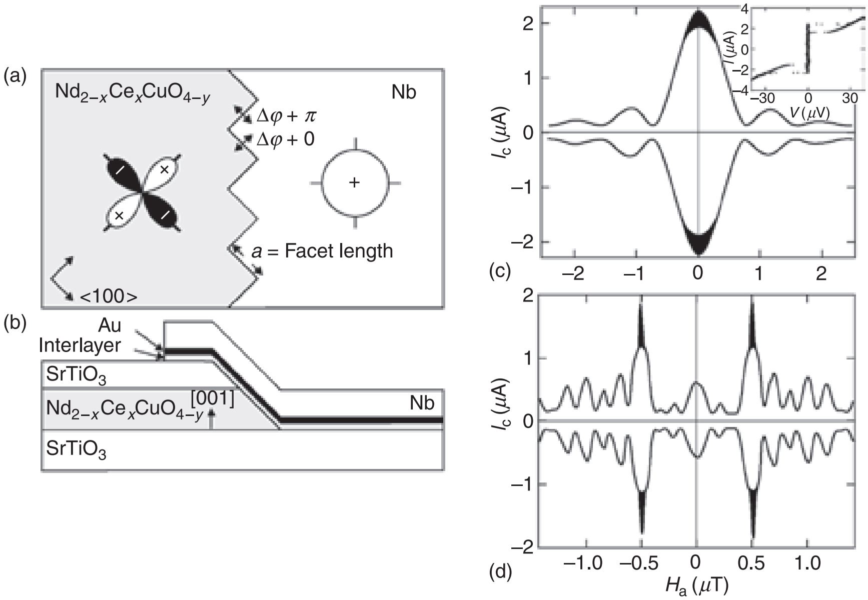

6.32 Left: schematic illustrations ((a) top view and (b) side view) for a 'zigzag' junction fabricated by the Twente University group. The zigzag junction is basically a series of corner junctions. In (a), $\Delta\varphi + 0$ and $\Delta\varphi + \pi$ are the differences of the phase of the superconducting order parameter between $Nd_{2-x}Ce_xCuO_{4-y}$ and Nb along [100] and [010], respectively. Right: comparison of the magnetic field dependence of I_c between standard straight junctions ([100] junctions) (c) and zigzag junctions (d). (Reprinted with permission from Ariando *et al.* (2005), *Phys Rev Lett*, **94**, 167001. © 2005 by the American Physical Society.)

epitaxial thin films has gradually improved with time. In a fast stream of high-T_c research, however, not many groups repeated the measurements on improved-quality of specimens. Therefore there are only a few data using high-quality specimens with the doping level varied systematically. In such circumstances, the author collected some reliable data of H_{c2} and H_{c1} in Table 6.9. The coherence length ξ calculated from H_{c2} and magnetic penetration depth λ directly measured as mentioned in section 6.7.2 are also included. As typical values of NCCO and PCCO with $x = 0.15$, $H_{c2}{}^{c} \sim 8$ T, $H_{c2}{}^{ab} \sim 50$–60 T, $H_{c1}{}^{c} \sim 20$–30 mT, $H_{c1}{}^{ab} \sim 5$ mT, $\xi_{ab} \sim 70$ Å, $\xi_c \sim 10$ Å, $\lambda_{ab} \sim 1500$ Å have been obtained. The anisotropy parameter γ is 8–10, which is defined as $\gamma = \sqrt{m^*_c / m^*_{ab}}$, where m^*_c and m^*_{ab} are the effective masses in the c and ab direction.

6.7.5 Impurity effect

The impurity effect in high-T_c cuprates has been claimed to be anomalous, which has been discussed in relation to the pairing symmetry. In isotropic s-wave

Table 6.9 Superconducting parameters of T′ cuprates

Material	x	T_c (K)	$H_{c2}{}^{c}(0)$ (T)	$H_{c2}{}^{ab}(0)$ (T)	$H_{c1}{}^{c}(0)$ (mT)	$H_{c1}{}^{ab}(0)$ (mT)	ξ_{ab} (Å)	ξ_c (Å)	λ_{ab} (Å)	λ_c (Å)	Ref.
LCCO	0.087	28.7							3200		Skinta *et al.*, 2002b
	0.112	29.3							2500		″
	0.135	21.7							2200		″
PCCO	0.115	13.0							3900		Kim *et al.*, 2003
	0.124	21.3							2300		″
	0.127	23.1							2000		″
	0.131	23.6							1900		″
	0.133	23.3							1600		″
	0.137	23.2							1550		″
	0.144	21.2							1600		″
	0.152	19.8							1700		″
	0.13	10	6.5				70				Fournier and Greene, 2003
	0.14	21	10				56				″
	0.15	23	9				60				″
	0.17	13	7				67				″
	0.20	6	2.5				113				″
NCCO	0.16	21	6.7	137			70	3.4			Hidaka and Suzuki, 1989
	0.131	13.4	1.86	51			139	5			Nakagawa, 1999
	0.137	17.0	4.35	55			87	7			″
	0.146	22.9	6.26	52			73	9			″
	0.166	20.2	4.46	56			86	7			″
SCCO	0.15	11.4	5.2	28.2			79	15			Dalichaouch *et al.*, 1990
	0.15	19	9.8				48				Han *et al.*, 1992

superconductors, T_c does not change by nonmagnetic impurities whereas T_c decreases rapidly by magnetic impurities. This is because magnetic impurities break Cooper pair singlets (pair breaking). The quantitative expression for the T_c depression by magnetic impurities is given by the well-known Abrikosov-Gorkov (AG) theory (de Gennes, 1969). For anisotropic pairing superconductors including *d*-wave superconductors, in general, nonmagnetic impurities also reduce T_c by the following equation,

$$\log\frac{T_c^0}{T_c} = \chi\{\psi\left(\frac{1}{2}+\frac{\hbar}{4\pi\tau k_B T_c}\right)-\psi(\frac{1}{2})\}, \qquad [6.9]$$

where χ is the anisotropy parameter and τ the impurity potential scattering time (Tolpygo *et al.*, 1996). In *d*-wave superconductors, $\chi = 1$, then nonmagnetic impurities reduce T_c as rapidly as magnetic impurities reduce T_c in isotropic *s*-wave superconductors. Hole-doped cuprates show a large T_c depression by nonmagnetic impurities. In LSCO, the rate ($-\mathrm{d}T_c/\mathrm{d}x$) of T_c depression by nonmagnetic Zn is as large as that by magnetic Ni and Co. In YBCO, $-\mathrm{d}T_c/\mathrm{d}x$ by Zn is larger than that by Ni and Co. These results have been regarded as evidence of *d*-wave superconductivity. In $Nd_{1.85}Ce_{0.15}CuO_4$, however, magnetic Co and Ni decrease T_c more effectively than nonmagnetic Zn, as shown in Fig. 6.33, which appears to be not consistent with *d*-wave superconductivity. The detailed comparison of the impurity effect between T-LSCO and T′-NCCO indicate that $-\mathrm{d}T_c/\mathrm{d}x$ by Zn is not much different in NCCO and LSCO, whereas $-\mathrm{d}T_c/\mathrm{d}x$ by Ni and Co in NCCO is significantly greater than in LSCO. Therefore simple arguments seem not to work, and it may not be appropriate to discuss the pairing symmetry from the impurity effect alone.

6.8 Electronic structure and spectroscopy

6.8.1 Ionic model

High-T_c superconductivity evolves in the two-dimensional CuO_2 layers and there are two approaches to describe the electronic state of the CuO_2 layers. One approach is based on the ionic model (strong correlation model) and the other is based on the band model. The ionic model is grounded on the fact that T-La_2CuO_4 with odd-number electrons is not a metal but an insulator. The electronic configuration in $(La^{3+})_2Cu^{2+}(O^{2-})_4$ is basically Cu3d^9 since La^{3+} and O^{2-} have a closed shell. The band theory predicts La_2CuO_4 to be a metal, but La_2CuO_4 is in fact an insulator. The contradiction can be eliminated if the *d* orbitals of Cu^{2+} in La_2CuO_4 are localized as in an isolated Cu^{2+} ion. In this case, electron transfer to the neighboring *d* orbitals requires Coulomb energy, leading to the insulating conduction. According to Torrance *et al.* (1991), the Coulomb energy for transition-metal ions (M^{v+}) can be approximated by the energy difference between

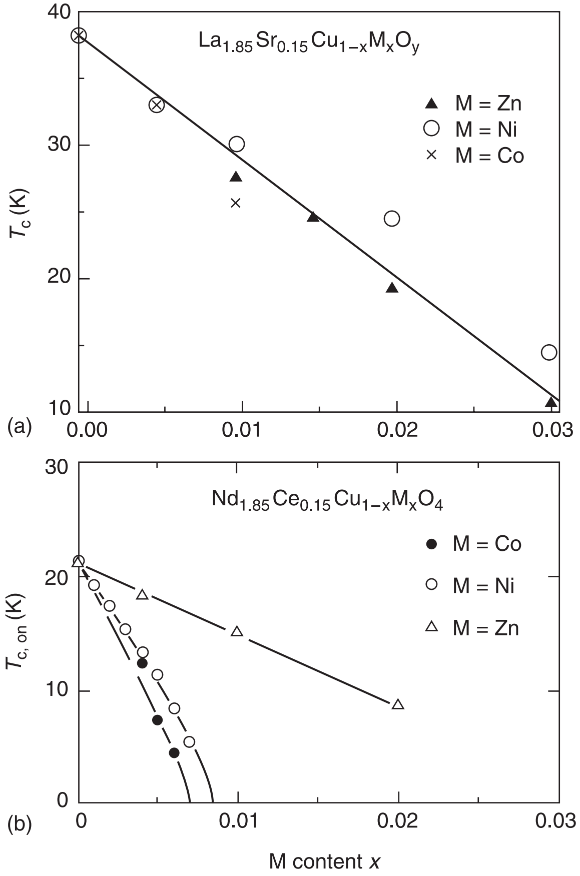

6.33 Comparison of the impurity effect on T_c in T-$La_{1.85}Sr_{0.15}CuO_4$ (a) and T′-$Nd_{1.85}Ce_{0.15}CuO_4$ (b). In T-$La_{1.85}Sr_{0.15}CuO_4$, $-dT_c/dx$ is almost the same for nonmagnetic Zn and magnetic Ni, Co impurities whereas in T′-$Nd_{1.85}Ce_{0.15}CuO_4$, $-dT_c/dx$ is larger for Ni, Co than for Zn. (Reprinted with permission from Tarascon *et al.* (1990), *Phys Rev B*, **42**, 218 and Sugiyama *et al.* (1991), *Phys Rev B*, **43**, 10489. © 1990, 1991 by the American Physical Society.)

the ionization potential I_{v+1} of M^{v+} and the electron affinity A (=I_v) of M^{v+} in the following equation,

$$U_0{}' = I_{v+1}(\mathrm{Cu}) - I_v(\mathrm{Cu}) - \frac{e^2}{d_{\mathrm{M-M}}}. \qquad [6.10]$$

The last term $e^2/d_{\mathrm{M-M}}$ is the attraction energy between the excited electron and hole left behind (*excitonic* effect). For Cu^{2+}, $U_0{}'$ is ~ 12.8 eV, assuming $d_{\mathrm{M-M}} = 3.80$ Å. In solids, however, this bare $U_0{}'$ in an isolated Cu ion is substantially reduced by the effect of the overlap between ions (covalency/hybridization, screening, electronic polarizability, etc.).

Next the presence of an O^{2-} ion has to be taken into account. The Cu 3*d* orbitals are deep in energy due to a large nuclear charge and approach the O2*p* orbitals. The charge transfer energy (Δ_0) of an electron from O^{2-} to $M^{\nu+}$ can also be approximated in a similar way,

$$\Delta_0 = e\Delta V_{\mathrm{M}} + A(\mathrm{O}^-) - I_\nu(\mathrm{M}) - \frac{e^2}{d_{\mathrm{M-O}}}, \qquad [6.11]$$

where $A(O^-)$ ($= -7.70$ eV) is the electron affinity of O^-, equivalent to the ionization energy of O^{2-}. The negative sign means that 7.70 eV is released by removing an electron from O^{2-}. The Δ_0 includes the difference ($\Delta V_M = V_M(O) - V_M(Cu)$) of the electrostatic potentials (called the Madelung potential) between the oxygen site and the copper site, which can be calculated numerically. In solids, the bare Δ_0 is also substantially reduced by overlap. We write U' and Δ to represent the Coulomb and charge transfer energy *in solids*.

A simple but powerful framework to classify oxides was proposed by Zaanen-Sawatzky-Allen (ZSA, 1985). The ZSA scheme distinguishes two different types of insulators. One is Mott-Hubbard insulators for $U' < \Delta$, in which the energy gap is given by U'. The other is charge transfer insulators for $U' > \Delta$, in which the energy gap is given by Δ. In both cases, if the band width W is sufficiently large, the energy gap collapses, resulting in conducting oxides. Based on the ZSA scheme, Torrance *et al.* (1991) reached an empirical criterion to predict whether an oxide is insulating or conducting, using bare U_0' and Δ_0. They pointed out that oxides, either simple or perovskite-type oxides, satisfying $U_0' \leq 11$ eV or $\Delta_0 \leq 10$ eV, are conducting. This criterion applied to copper oxides correctly predicts that perovskite $LaCuO_3$ ($\Delta_0 = 8.59$ eV, $U_0' = 14.64$ eV) and T-$LaSrCuO_4$ ($\Delta_0 = 8.17$ eV, $U_0' = 14.55$ eV) with Cu^{3+} are predicted to be conducting whereas T-La_2CuO_4 ($\Delta_0 = 13.69$ eV, $U_0' = 12.76$ eV) with Cu^{2+} is insulating. However, Cu^{2+} oxides are not always predicted to be insulating since Δ_0, which includes ΔV_M, is material dependent. Figure 6.34 summarizes Δ_0 for T′-RE_2CuO_4 and T-La_2CuO_4. The Δ_0 of T′-La_2CuO_4 is 9.90 eV, smaller by 3.79 eV than Δ_0 of T-La_2CuO_4, predicting T′-La_2CuO_4 to be conducting. The difference in Δ_0 between T-and T′-La_2CuO_4 mostly comes from the difference in $V_M(Cu)$, which is ascribed primarily to the absence of apical oxygen and subsidiarily to the substantially longer Cu-O1 distance in T′-La_2CuO_4.

In the ionic model (strong correlation model), the energy levels of the three electronic states, $Cu3d^9$, $Cu3d^{10}$, O2*p*, are semi-quantitatively estimated. Then the levels broaden by overlap, but are still quasi-localized (as opposed to itinerant) with each level capable of accommodating one electron (not two). The schematic energy diagram based on the ionic model for insulating parent compounds of high-T_c cuprates is shown in Fig. 6.35(a).

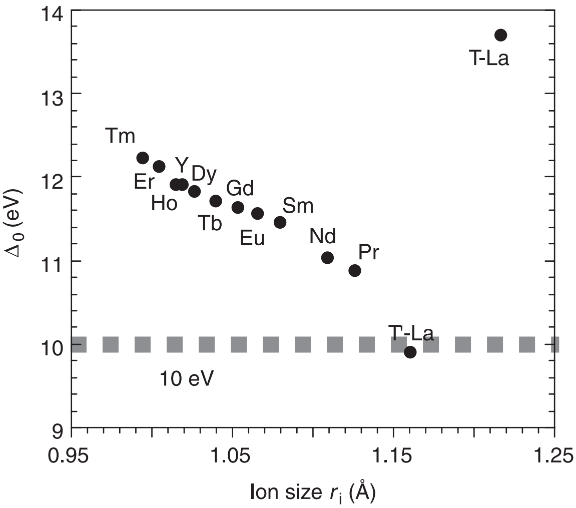

6.34 Charge transfer energy, Δ_0, for T′-RE_2CuO_4 and T-La_2CuO_4.

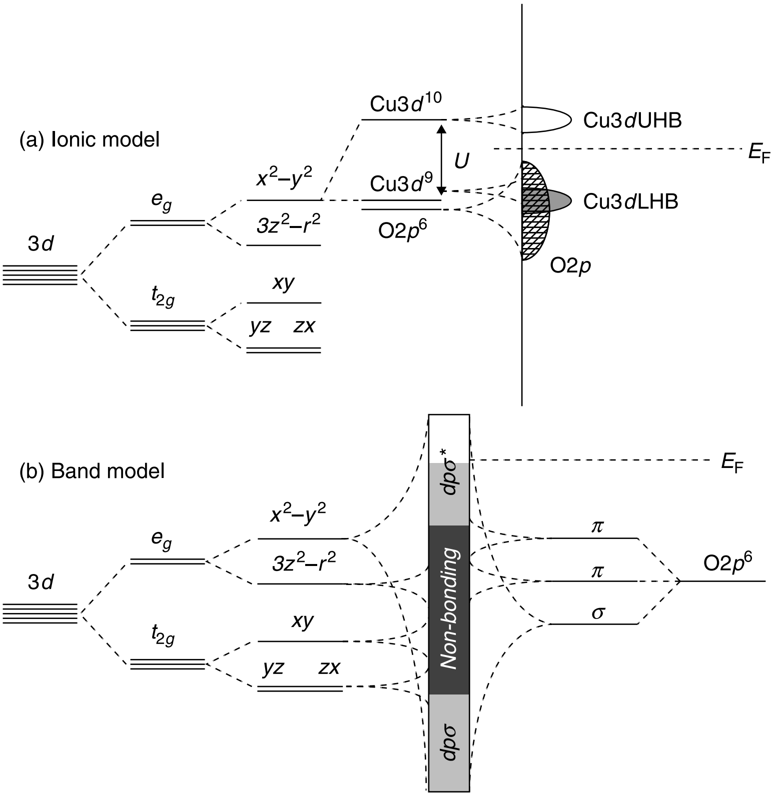
(a) Ionic model
3d
e_g
t_{2g}
$x^2–y^2$
$3z^2–r^2$
xy
yz zx
Cu3d^{10}
Cu3d^9
O2p^6
U
Cu3dUHB
E_F
Cu3dLHB
O2p
(b) Band model
3d
e_g
t_{2g}
$x^2–y^2$
$3z^2–r^2$
xy
yz zx
$dp\sigma^*$
Non-bonding
$dp\sigma$
E_F
π
π
σ
O2p^6

6.35 Comparison of the schematic energy diagrams based on the ionic model (a) and the band model (b).

6.8.2 Band model

Figure 6.36 illustrates the energy level, in oxides, of 3*d* orbitals of transition-metal ions relative to the energy levels of oxygen 2*p* and metal 4*s* orbitals (Goodenough *et al.*, 1990). As seen in this figure, the energy levels of O2*p* and $3d_{x^2-y^2}$ of Cu^{2+} are close, hence one has to take account of hybridization between them. Figure 6.37(a) is a schematic illustration for the hybridization of $3d_{x^2-y^2}$, $O2p_x$, and $O2p_y$ orbitals in a simple 2D square lattice (Andersen *et al.*, 1995). The resultant energy bands for $\varepsilon_d - \varepsilon_p = 0.9$ eV and $t_{pd} = 1.6$ eV is also shown in Fig. 6.37(b). The two bands having large *k* dispersion are strongly hybridized $Cu3d_{x^2-y^2} - O2p_{x,y}$ bonding (σ) and antibonding (σ^*) bands whereas the triply-degenerate bands with no dispersion are non-bonding bands. In the parent compounds with Cu^{2+}, the Fermi level is located at the middle of the anitbonding band. The energy diagrams based on the band model and the ionic model are compared in Fig. 6.35. Strong hybridization with the O2*p* orbitals may substantially spread the $Cu3d_{x^2-y^2}$ orbitals, thereby weaken Coulomb repulsion (U'). In this case the band model is more appropriate to describe the electronic states of cuprates than the ionic model.

Band calculations for T′ cuprates were performed immediately after the discovery of superconductivity in the compounds in 1989. Figure 6.38 shows one example (APW calculation) for T′-Nd_2CuO_4 calculated by Massidda and Freeman (1989). The energy bands are highly two-dimensional, and the correspondence between their results and the schematic cartoon in Fig. 6.37 is apparent. Two highly *k*-dispersive bands are the bonding and antibonding bands, which are truncated by many non-bonding or π-bonding bands derived from Cu3*d* and O2*p* orbitals. Near the Fermi level, the band structure is very simple. The Fermi level crosses the antibonding band at the middle, namely half-filled position. The resultant Fermi surface is hole-like and has a rounded square shape centered

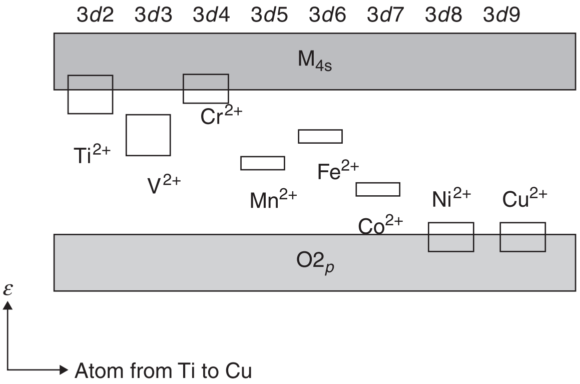

6.36 Semiempirical variation of M^{2+} energy levels relative to the *M*4s conduction and $O2_p$ valence bands for the first-row transition atoms *M* in an octahedral site of an oxide. (Adapted from Goodenough and Zhou (1990).)

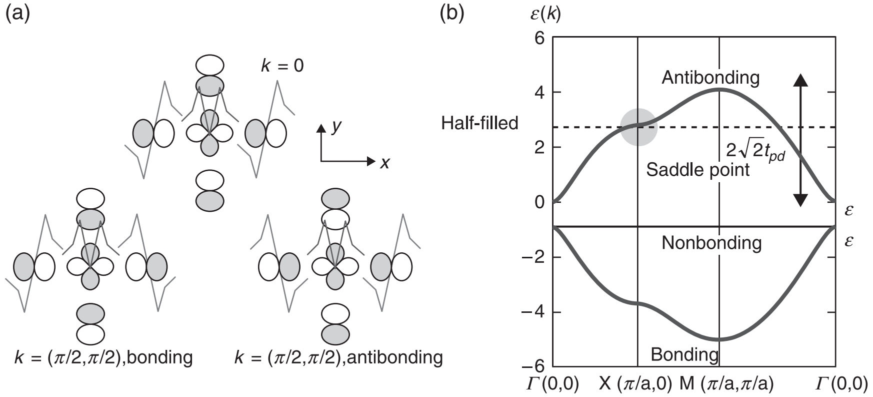
(a)
k = 0
y
x
k = (π/2,π/2),bonding
k = (π/2,π/2),antibonding
(b)
ε(k)
6
4
2
0
−2
−4
−6
Antibonding
Half-filled
2√2t_pd
Saddle point
Nonbonding
Bonding
ε
ε
Γ(0,0)
X (π/a,0)
M (π/a,π/a)
Γ(0,0)

6.37 (a) Schematic illustration for the hybridization of Cu3$d_{x^2-y^2}$, O2p_x, and O2p_y orbitals in a simple 2D square lattice. (b) Resultant energy bands with $\varepsilon_d - \varepsilon_p = 0.9$ eV and $t_{pd} = 1.6$ eV. The two bands having large k dispersion are strongly hybridized Cu3$d_{x^2-y^2}$-O2$p_{x,y}$ bonding (σ) and antibonding (σ^*) bands whereas the triply-degenerate bands with no dispersion are non-bonding or π-bonding bands.

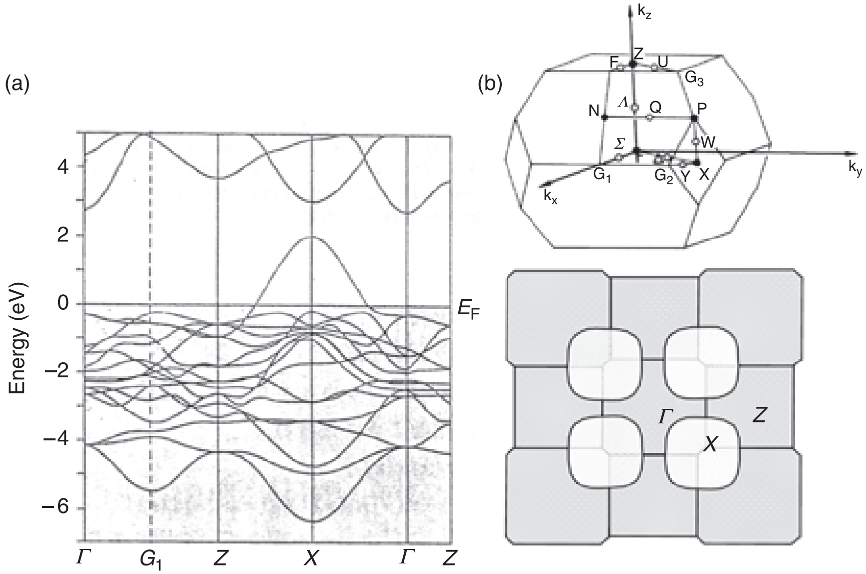

6.38 (a) Energy bands for T′-Nd_2CuO_4 calculated using APW. The energy bands are highly two-dimensional, and the correspondence to the schematic picture in Fig. 6.37 is obvious. (b) Resultant Fermi surface. The Fermi surface is hole-like and has a rounded square shape centered around the X point (see the notation of the symmetry points of the Brillouin zone of the body-centered tetragonal lattice in the upper panel). (Reprinted with permission from Massidda *et al.* (1989), *Physica C*, **157**, 571. © 1989 Elsevier.)

around the X point. The Fermi level is raised by ~ 0.2 eV for a doping of Ce by $x = 0.15$.

Early band calculations failed to explain that T-La_2CuO_4 is an antiferromagnetic insulator. The above band calculation again predicts a metallic nature for T′ parent compounds, which for a long time have been believed to also be antiferromagnetic insulators. These failures at the beginning of high-T_c research resulted in great skepticism in the reliability of band calculations for cuprates. As shown in section 6.5.3., however, the apparent insulating behavior of T′ parent compounds may be an artifact derived from early experiments on non-qualified specimens, and the generic behavior may be quite different (metallic and superconducting). Hence the band calculations deserve to be revisited.

6.8.3 Angle-resolved photoemission spectroscopy

It has been established that the band calculations make correct predictions for the optimum doped to overdoped region. The predicted Fermi surface in Fig. 6.38 can be tested directly by angule-resolved photoemission spectroscopy (ARPES). Plate III(a) in colour section between pages 244 and 245 shows the results of ARPES by a Stanford University group in 1993 on bulk single crystals of $Nd_{2-x}Ce_xCuO_4$ with $x = 0.15$ and $x = 0.22$ (King *et al.*, 1993). The experiments were carried out on cleaved surface of single crystals grown by the flux method using synchrotron radiation beam of Stanford Synchrotron Radiation Laboratory. The experimental Fermi surface is in good agreement with the calculated one. Moreover the hole-like Fermi surface shrinks in the rigid-band manner as the doping proceeds from $x = 0.15$ to $x = 0.22$. Overall, the band calculations give a correct description of the electronic states of optimum doped and overdoped $Nd_{2-x}Ce_xCuO_4$ although there is a small disagreement in the k dispersion of the energy bands.

Next we take a look at the results for the underdoped region. Colour plate III(b) shows the result of ARPES on $Nd_{2-x}Ce_xCuO_4$ single crystals with $x = 0.04$, 0.10, and 0.15 performed again by the Stanford University group in 2002. The energy resolution is significantly improved: 140 meV in 1993 to 10–20 meV in 2002 (Armitage *et al.*, 2002). The improved resolution did not change the shape of the Fermi surface for $x = 0.15$, but revealed a new feature, namely, substantial modulation of the spectral weight (integrated intensity of photoelectrons in a 60 meV window near E_F) along the Fermi surface. As the doping is reduced, the spectral weight in the [0,0] to $[\pi,\pi]$ direction diminishes at $x = 0.10$ and is eventually lost at $x = 0.04$. In effect, a part of the Fermi surface disappears. The behavior is now understood to be related to the development of the AF order in the underdoped region. As the AF order changes the lattice periodicity, while the magnetic Bragg reflection creates new energy gaps and truncates the Fermi surface. Then the Fermi surface partially disappears at the magnetic Brillouin zone boundaries. As seen in colour plate III(b), the spectral weight is lost exactly at the intersection between the Fermi surface and the magnetic Brillouin zone. The energy gap is called a spin-density wave (SDW) gap or a high-energy ‘pseudo gap’, whose magnitude is roughly given by the exchange energy (J_K) between conduction electrons and Cu spins. The energy gap decreases with doping, and 0.4 eV at $x = 0.04$ and 0.2 eV at $x = 0.10$. The author suggested in section 6.6.1 that the AF order in T′ cuprates may be not be intrinsic, but induced by O_{ap} impurities. From this point of view, it is interesting to see how the ARPES of T′-$RE_{2-x}Ce_xCuO_4$ with no O_{ap} impurity evolves with the doping level, x.

ARPES can also determine the anisotropy of the superconducting gap, $\Delta(\boldsymbol{k})$, in T′ cuprates. In hole-doped Bi cuprates, it was demonstrated (Shen *et al.*, 1993) that $\Delta(\boldsymbol{k})$ is anisotropic and follows $\Delta_0\{\cos(k_x a) - \cos(k_y a)\}$, which is regarded as evidence of *d*-wave superconductivity. In electron-doped systems, however, there was no ARPES measurement to determine the gap anisotropy until 2001 (Armitage *et al.*, 2001). The energy gap of T′ cuprates is comparable to the energy resolution of ARPES, which was a large problem in detecting the gap anisotropy. The first attempt was made in 2001 again by the Stanford University group. An indication of the gap anisotropy could only be obtained by carefully comparing the spectra between $T = 30$ K and $T = 10$ K. The superconducting gap is maximal in the $[\pi,0]$ direction, and minimal or zero in the $[\pi,\pi]$ direction, consistent with *d*-wave superconductivity. More recently, Matsui *et al.* (2005) showed clearer evidence for the gap anisotropy from measurements on $Pr_{0.89}LaCe_{0.11}CuO_4$ single crystals with an improved signal-to-noise ratio. Their results indicated the anisotropy deviated from $\cos(k_x a) - \cos(k_y a)$ expected for simple *d*-wave superconductivity.

6.8.4 Optics

The optical spectra of T-LSCO reported by Uchida *et al.* (1991) have been considered to be representative of the optical response of high-T_c cuprates. The charge transfer (CT) gap of 2.0 eV is clearly observed in the optical conductivity of parent T-La_2CuO_4. The doping of Sr collapses the CT gap, and grows optical conductivity in the gap (called in-gap states) and a Drude component around $\omega = 0$. The early optical spectra of PCCO single crystals reported by Arima *et al.* (1993) showed many similarities to those of T-LSCO. The CT gap of the parent Pr_2CuO_4 is 1.5 eV, slightly smaller than the value of T-La_2CuO_4. The doping of Ce collapses the CT gap but with the trace of the CT gap remaining even at $x = 0.10$. The doping also grows in-gap conductivity but much more gradually than in LSCO. Other than such small differences, the essential features in T-LSCO and T′-PCCO are almost identical.

The effect of reduction on the optical spectra was also examined. In the parent compound, reduction broadens the shoulder of the CT gap and grows optical conductivity, which is similar to the effect of Ce doping. Then Arima *et al.* claimed that one effect of reduction might be electron doping by oxygen vacancies ($\delta \sim$ 0.02–0.03). They suggested that reduction also creates oxygen vacancies in the CuO_2 layer, which destroys the AF order.

The essence of the above results was not altered by recent experiments. Figure 6.39 shows the optical conductivity of $Nd_{2-x}Ce_xCuO_4$ single crystals with

$x = 0.00 \sim 0.15$ obtained by Onose *et al.* (2004). The specimens except for $x = 0.00$ were reduced in an $Ar + O_2$ mixture at 1000° C for 100 hours, and p_{O2} during reduction is optimized so as to minimize resistivity. The specimen of $x = 0.00$ was not reduced by the reason mentioned in section 6.5.3 (the parent compound is more subject to decomposition than the Ce doped compounds), and it showed a clear CT gap of 1.5 eV. The doping of Ce ($x \geq 0.05$) together with reduction collapses the CT gap and grows optical conductivity in the gap, which agrees well with the early result by Arima *et al.* (1993). A new feature observed is a pseudo gap. In the spectra for $x = 0.05 \sim 0.125$ shown in Fig. 6.39(a), the low-energy optical conductivity is suppressed as the temperature is lowered, which is assigned as a pseudo gap. The size of the pseudo gap is doping dependent, 0.43 eV at $x = 0.05$ and 0.17 eV at $x = 0.125$ (Fig. 6.39(b)). Both the size and the doping dependence of the pseudo gap in optics and ARPES quantitatively agree with each other. The pseudo gap opening temperature, T^*, is about twice the Néel temperature (T_N) for

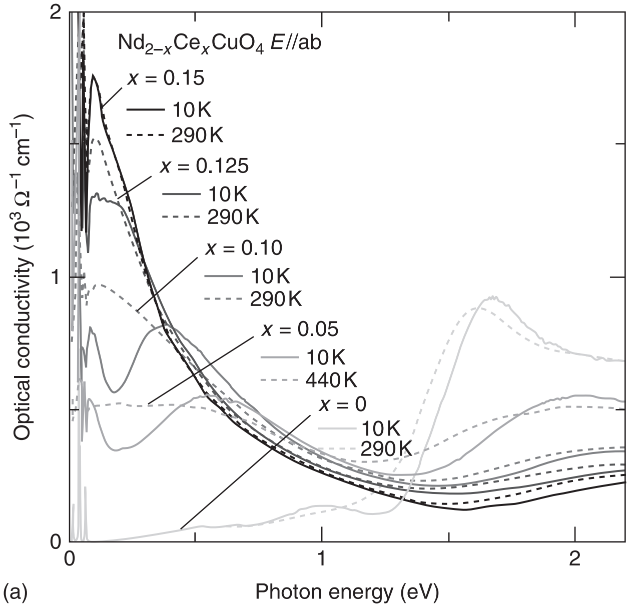

6.39 (a) Optical conductivity of $Nd_{2-x}Ce_xCuO_4$ single crystals with $x = 0.00 \sim 0.15$ obtained by Onose *et al.* (2004). The specimen of $x = 0.00$ (not reduced) showed a clear CT gap of 1.5 eV. The doping of Ce ($x \geq 0.05$) together with reduction collapses the CT gap. In the spectra for $x = 0.05 \sim 0.125$, the low-energy optical conductivity is suppressed as the temperature is lowered, which is assigned as the pseudo gap. On next page: size of the pseudo gap (b) and pseudo-gap opening temperature (T^*) (c). The T^* is about twice the Néel temperature (T_N) for 3D AF order. (Reprinted with permission from Onose *et al.* (2004), *Phys Rev B*, **69**, 024504. © 2004 by the American Physical Society.)

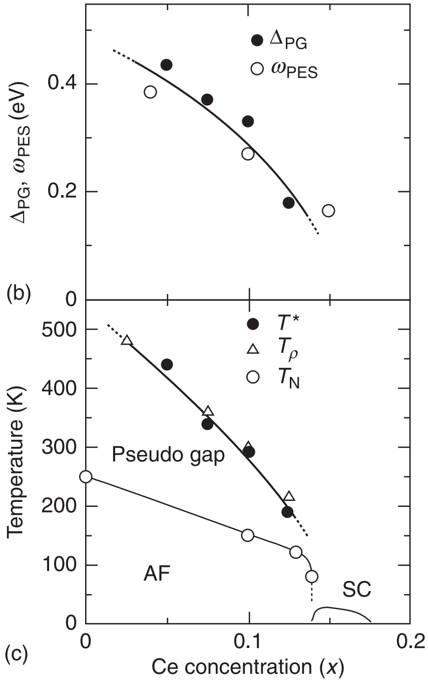

6.39 Continued.

the 3D AF order (Fig. 6.39(c)). It is because the 2D short-range order is sufficient to give rise to Bragg reflection for conduction electrons. Furthermore, below T^*, the Drude response becomes sharper. This behavior can be interpreted as the development of the AF order increases the spin correlation length, thereby reducing the spin disorder scattering of conduction electrons. The development of the AF order is also reflected in the DC resistivity, which shows a kink at T^*.

6.9 Summary

6.9.1 Materials science

T′ phase stability

The T′ structure is stabilized with *RE* = Pr, Nd, Sm, Eu, and Gd by ambient-pressure synthesis, with *RE* = Tb to Tm and Y by high-pressure synthesis, and with *RE* = La by low-temperature thin-film synthesis.

Tolerance factor

The T-versus-T′ stability can be explained by the geometrical tolerance factor. The matching between the NaCl and $Cu^{(VI)}O_2$ layers stabilizes the T structure whereas the matching between the fluorite and $Cu^{(IV)}O_2$ layers stabilizes the T structure.

Structure

The CuO_2 layer is flat in the T′ structure, which is in contrast to the undulated CuO_2 layer in T-La_2CuO_4. The T′ structure contains three oxygen sites: regular O1 in the CuO_2 layer, regular O2 in the fluorite layer, and interstitial O_{ap}.

Lattice parameters

The a_0 changes from 4.025 Å (La) to 3.830 Å (Tm), and the c_0 changes from 12.55 Å (La) to 11.58 Å (Tm). With Ce doping, the c_0 decreases whereas the a_0 increases slightly.

Decomposition

The decomposition lines of the T′ cuprates are located in between those of CuO and Cu_2O. The phase stability field of T′-RE_2CuO_4 is expanded with larger RE^{3+} (except for La^{3+}) and also with the doping of Ce with $x = 0.15$.

Oxygen nonstoichiometry

Oxygen deficiencies at regular O1 and excess oxygen atoms at O_{ap} coexist on approaching the decomposition lines. Even if $y = 4.00$ in $(RE,Ce)_2CuO_y$, the oxygen sublattice is not perfect. It is very difficult (or almost impossible) to remove impurity O_{ap} atoms without losing O1 atoms. With larger RE^{3+}, the binding energy of O1 increases and the binding energy of O_{ap} decreases. Therefore Pr is the best *RE* to obtain a better oxygen sublattice.

6.9.2 Physical science

Pair breaking due to O_{ap} impurities

O_{ap} impurities in T′ cuprates cause strong scattering as well as strong pair breaking. Therefore, in principle, the generic properties of T′ cuprates cannot be reached without complete removal of O_{ap} impurities.

Electronic phase diagram

According to the early reports, the superconducting window of $Nd_{2-x}Ce_xCuO_4$ was $0.14 \leq x \leq 0.18$ with the optimum doping of $x = 0.15$, which suggested that electron-hole symmetry roughly holds in high-T_c superconductivity. This symmetry leads to the picture to regard high-T_c superconductors as 'doped Mott insulators'. The improved reduction to bulk $Pr_{2-x}Ce_xCuO_4$ single crystals, however, expands the superconducting window down to $x = 0.04$. Furthermore, superconductivity is achieved in the parent compounds, T′-RE_2CuO_4, by metal organic decomposition. The T_c-vs-x obtained for $Nd_{2-x}Ce_xCuO_4$ films shows that T_c is a monotonic decreasing function of x, which, the author believes, is the generic phase diagram of T′ cuprates.

Magnetism

The early studies demonstrated that the parent compounds show long-range AF order with $T_N \sim 250$ K and that the T_N decreases with x to below 5 K at $x = 0.15$. However, the magnetism in T′ cuprates is more greatly affected by the presence of O_{ap} impurities than by x. Therefore the intrinsic behavior of magnetism in T′ cuprates has not been established.

Transport

There is a strong correlation between T_c and residual resistivity (ρ_0): higher T_c for lower ρ_0. A low-temperature upturn in resistivity is observed in specimens containing a fair amount of O_{ap} impurities with its temperature dependence and magnetic field dependence in accord with the Kondo effect. The early data showed that the Hall coefficient (R_H) and Seebeck coefficient (S) were negative for $x \leq 0.15$ and positive for $x > 0.15$. However, the later works showed that the removal of O_{ap} impurities shift both of R_H and S shift to a more positive value. The sign change from negative to positive is seen at $x = 0.15$ with stronger reduction.

Pairing symmetry

The point-contact spectra for $Nd_{1.85}Ce_{0.15}CuO_4$ showed a well defined superconducting gap structure, which concluded that NCCO is an s-wave superconductor. The size of the superconducting gap (Δ) is 3.7 meV and $2\Delta/k_BT_c = 3.9$. The Eliashberg function $\alpha^2F(\omega)$, derived from the tunnel spectra, indicated that Cooper pairing is mediated by phonons. The early experiments on the magnetic penetration depth, $\lambda_L(T)$, also supported s-wave superconductivity. But later (after 2000), the situation has become more confused: some support s-wave and the others support d-wave. The phase-sensitive experiments support that NCCO and PCCO are a $d_{x^2-y^2}$ superconductor.

Impurity effect

Magnetic Co and Ni impurities decrease T_c much more rapidly than nonmagnetic Zn. The behavior is in sharp contrast to that observed in hole-doped cuprates such as T-LSCO or YBCO, and argues against d-wave superconductivity.

6.9.3 Electronic structure

There are two approaches to describe the electron state of the CuO_2 layer: the ionic model and the band model.

Ionic model

According to the ionic model, the charge transfer energy is substantially smaller in T′ cuprates than in T′ cuprates. The Torrance's criterion predicts that T′-La_2CuO_4 should be metallic whereas T-La_2CuO_4 should be insulating.

Band model

The nuclear charge is the largest for Cu among 3*d* transition elements, hence the energy levels of 3*d* orbitals are the deepest. The resultant crossing of Cu3*d* and O2*p* orbitals in energy causes strong hybridization between them, which is a feature specific to copper oxides, not seen in other 3*d* transition metal oxides. The results of band calculations represent this feature, yielding the broad bands (~ 8 eV wide): $\mathrm{Cu}3d_{x^2-y^2} - \mathrm{O}2p_{x,y}\sigma$ bonding and $\mathrm{Cu}3d_x{}^2 - y^2 - \mathrm{O}2p_{x,y}\sigma^*$ antibonding bands. The Fermi level crosses the antibonding band at the middle, namely half-filled position.

Spectroscopy

The Fermi surfaces obtained from ARPES on optimum doped and overdoped $Nd_{2-x}Ce_xCuO_4$ single crystals showed a good agreement with those obtained by the band calculations. The ARPES on underdoped specimens showed modulation of the spectral weight along the Fermi surface. This complex feature is explained by the energy gap created by the magnetic Bragg reflection. This energy gap has been detected in the recent optical spectra of NCCO single crystals.

6.10 Acknowledgements

The author would like to thank his collaborators on this subject including H. Yamamoto, A. Tsukada, H. Sato, T. Sekitani, H. Oyanagi, M. Hepp, T. Greibe, Y. Krockenberger, A. V. Pronin, A. Pimenov, O. Matsumoto, A. Ustuki, A. Ikeda, S. Ueda, and T. Manabe. He would also like to thank R. P. Huebener, J. B. Goodenough, B. Raveau, R. Gross, L. Alff, D. Manske, N. Miura, and T. Lemberger for various helpful conversations on these topics.

6.11 References

Alff L., Meyer S., Kleefisch S., Schoop U., Marx A. *et al.* (1999), 'Anomalous low temperature behavior of superconducting $Nd_{1.85}Ce_{0.15}CuO_{4-y}$', *Phys Rev Lett*, **83**, 2644–2647.

Andersen O. K., Liechtenstein A. I., Jepsen O. and Paulsen F. (1995), 'LDA energy bands, low-energy Hamiltonians, t', t'', $t_{\perp}(\boldsymbol{k})$, and $J_{\perp}$', *J Phys Chem Solids*, **56**, 1573–1591.

Andreone A., Cassinese A., Chiara A. D. and Vaglio R. (1994), 'Temperature dependence of the penetration depth in $Nd_{1.85}Ce_{0.15}CuO_{4-\delta}$ superconducting thin films', *Phys Rev B*, **49**, 6392–6394.

Anlage S. M., Wu D.-H., Mao J., Mao S. N., Xi X. X. *et al.* (1994), 'Electrodynamics of $Nd_{1.85}Ce_{0.15}CuO_4$: Comparison with Nb and $YBa_2Cu_3O_{7-\delta}$', *Phys Rev B*, **50**, 523–535.

Ariando, Darminto D., Smilde H.-J. H., Leca V., Blank D. H. *et al.* (2005), 'Phase-sensitive order parameter symmetry test experiments utilizing $Nd_{2-x}Ce_xCuO_{4-y}$/Nb zigzag junctions', *Phys Rev Lett*, **94**, 167001 [4 pages].

Arima T., Tokura Y. and Uchida S. (1993), 'Optical spectra of $Pr_{2-x}Ce_xCuO_{4-\delta}$ crystals: Evolution of in-gap states with electron doping', *Phys Rev B*, **48**, 6597–6603.

Armitage N. P., Lu D. H., Feng D. L., Kim C., Damascelli A. *et al.* (2001), 'Superconducting gap anisotropy in $Nd_{1.85}Ce_{0.15}CuO_4$: Results from photoemission', *Phys Rev Lett*, **86**, 1126–1129.

Armitage N. P., Ronning F., Lu D. H., Kim C., Damascelli A. *et al.* (2002), 'Doping dependence of an *n*-type cuprate superconductor investigated by angle-resolved photoemission spectroscopy', *Phys Rev Lett*, **88**, 257001 [4 pages].

Bednorz J. G. and Müller K. A. (1986), 'Possible high T_c superconductivity in the Ba-La-Cu-O system', *Z Phys B*, **64**, 189–193.

Bordet P., Capponi J. J., Chaillout C., Chateigner D., Chenavas J. *et al.* (1992), 'High pressure synthesis and structural study of R_2CuO_4 compounds with R = Y, Tb, Dy, Ho, Er, Tm', *Physica C*, **193**, 178–188.

Bringley J., Trail S. S. and Scott B. A. (1990), 'An ionic model of the crystal chemistry in the superconducting copper oxides of stoichiometry $(RE)_2CuO_4$', *J Solid State Chem*, **86**, 310–322.

Brinkmann M., Rex T., Bach H. and Westerholt K. (1995), 'Extended superconducting concentration range observed in $Pr_{2-x}Ce_xCuO_{4-\delta}$', *Phys Rev Lett*, **74**, 4927–4930.

Brinkmann M., Rex T., Stief M., Bach H. and Westerholt K. (1996), 'Residual resistivity and oxygen stoichiometry in $Pr_{2-x}Ce_xCuO_{4+\delta}$ single crystals', *Physica C*, **269**, 76–82.

Brinkmann M., Bach H. and Westerholt K. (1997), 'Electrical resistivity study of metallic $Pr_{2-x}Ce_xCuO_{4+\delta}$-single crystals over a broad concentration and temperature range', *Physica C*, **292**, 104–116.

Chou F. C., Cho J. H., Miller L. L. and Johnston D. C. (1990), 'New phases induced by hydrogen reduction and by subsequent oxidation of L_2CuO_4 (L = La,Pr,Nd,Sm,Eu,Gd)', *Phys Rev B*, **42**, 6172–6180.

Cooper J. R. (1996), 'Power-law dependence of the *ab*-plane penetration depth in $Nd_{1.85}Ce_{0.15}CuO_{4-y}$', *Phys Rev B*, **54**, R3753–R3755.

Dalichaouch Y., Lee B. W., Seaman C. L., Markert J. T. and Maple M. B. (1990), 'Upper critical field of a $Sm_{1.85}Ce_{0.15}CuO_{4-y}$ single crystal: Interaction between superconductivity and antiferromagnetic order in copper oxides', *Phys Rev Lett*, **64**, 599–602.

de Gennes P. G. (1966), *Superconductivity of Metals and Alloys*, New York, Benjamin, chapter 8.

Fisk Z., Cheong S-W., Thompson J. D., Hundley M. F., Schwarz R. B. *et al.* (1989), 'T*-phase superconductivity', *Physica C*, **162–164**, 1681–1686.

Fournier P., Mohanty P., Maiser E., Darzens S., Venkatesan T. *et al.* (1998), 'Insulator-metal crossover near optimal doping in $Pr_{2-x}Ce_xCuO_4$: Anomalous normal-state low temperature resistivity', *Phys Rev Lett*, **81**, 4720–4723.

Fournier P. and Greene R. L. (2003), 'Doping dependence of the upper critical field of electron-doped $Pr_{2-x}Ce_xCuO_4$ thin films', *Phys Rev B*, **68**, 094507 [9 pages].

Freund H.-R. and Müller-Buschbaum Hk. (1977), 'Über oxocuprate. XXIII. zur Kenntnis von $Ho_2Cu_2O_5$', *Z Naturforsch B*, **32**, 609–611.

Fujita M., Kubo T., Kuroshima S., Uefuji T., Kawashima K. (2003a), 'Magnetic and superconducting phase diagram of electron-doped $Pr_{1-x}LaCe_xCuO_4$', *Phys Rev B*, **67**, 014514 [5 pages].

Fujita M., Kuroshima S., Matsuda M. and Yamada K. (2003b), 'Neutron-scattering study of spin correlations in electron-doped $Pr_{0.89}LaCe_{0.11}CuO_4$ single crystals', *Physica C*, **392–396**, 130–134.

Goldschmidt V. M. (1926), 'Die Gesetze der Krystallochemie', Naturwissenschaften, **14**, 477–485.

Goodenough J. B. and Zhou J. (1990), 'Correlation bag and high-T_c superconductivity', *Phys Rev B*, **42**, 4276–4287.

Halbritter J. (1971), 'On the penetration of the magnetic field into a superconductor', *Z Physik*, **243**, 201–219.

Han S. H., Almasan C. C., de Andrale M. C., Dalichaouch Y. and Maple M. B. (1992), 'Determination of the upper critical field of the electron-doped superconductor $Sm_{1.85}Ce_{0.15}CuO_{4-y}$ from resistive fluctuations', *Phys Rev B*, **46**, 14290–14292.

Harrison W. A. (1979), *Electronic Structure and the Properties of Solids*, San Francisco, W. H. Freeman and Company, chapter 19.

Hidaka Y. and Suzuki M. (1989), 'Growth and anisotropic superconducting properties of $Nd_{2-x}Ce_xCuO_{4-y}$ single crystals', *Nature*, **338**, 635–637.

Huang T. C., Moran E., Nazzal A. I. and Torrance J. B. (1989a), 'Synthesis and x-ray characterization of superconducting and related $Ln_{2-x}Ce_xCuO_{4-y}$ (Ln = Nd and Gd)', *Physica C*, **158**, 148–152.

Huang T. C., Moran E., Nazzal A. I., Torrance J. B. and Wang P. W. (1989b), 'Determination of the average ionic radius and effective valence of Ce in the $Nd_{2-x}Ce_xCuO_4$ electron superconductor system by X-ray diffraction', *Physica C*, **159**, 625–628.

Huang Q., Zasadzinski J. F., Tralshawala N., Grey K. E., Hinks D. G. *et al.* (1990), 'Tunnelling evidence for predominantly electron–phonon coupling in superconducting $Ba_{1-x}K_xBiO_3$ and $Nd_{2-x}Ce_xCuO_{4-y}$', *Nature*, **347**, 369–372.

Hurd C. M. 1972, *The Hall Effect in Metals and Alloys*, New York, Plenum.

Idemoto Y., Fueki K. and Shinbo T. (1990), 'T-log P_{O2} diagram and copper valence of $Nd_{1.85}Ce_{0.15}CuO_{4-\delta}$', *Physica C*, **166**, 513–517.

Idemoto Y. and Fueki K. (1991), 'Defect thermodynamics of $Nd_{2-x}Ce_xCuO_{4-\delta}$', *Jpn J Appl Phys*, **30**, 2471–2476.

Idemoto Y., Oyagi I. and Fueki K. (1992), 'Determination of thermodynamic data of $Ln_{1.85}Ce_{0.15}CuO_4$ and Ln_2CuO_4 (Ln = Nd,Sm,Eu) by the EMF method', *Physica C*, **195**, 269–276.

Ishii H., Koshizawa T., Hanyu T. and Yamaguchi S. (1993), 'Effects of Ce doping on electronic structures of $Ln_{2-x}Ce_xCuO_4$ (Ln = Nd, Sm, Eu, Gd) studied by core-Level photoemission spectroscopy', *Jpn J Appl Phys*, **32**, 1070–1076.

Jiang W., Mao S. N., Xi X. X., Jiang X., Peng J. L. *et al.* (1994), 'Anomalous transport properties in superconducting $Nd_{1.85}Ce_{0.15}CuO_{4\pm\delta}$', *Phys Rev Lett*, **73**, 1291–1294.

Kadono R., Ohishi K., Koda A., Higemoto W., Kojima K. M. *et al.* (2003), 'Magnetic ground state of $Pr_{0.89}LaCe_{0.11}CuO_{4+\alpha-\delta}$ with varied oxygen depletion probed by muon spin relaxation', *J Phys Soc Jpn*, **72**, 2955–2958.

Kanai H., Mizusaki J., Tagawa H., Hoshiyama S., Hirano K. *et al.* (1997), 'Defect chemistry of $La_{2-x}Sr_xCuO_{4-\delta}$: Oxygen nonstoichiometry and thermodynamic stability', *J Solid State Chem*, **131**, 150–159.

Kang H. J., Dai P., Campbell B. J., Chupas P. J., Rosenkrantz R. *et al.* (2007), 'Microscopic annealing process and its impact on superconductivity in T′-structure electron-doped copper oxides', *Nature Materials*, **6**, 224–229.

Kawashima T. and Takayama-Muromachi E. (1994), 'Oxygen deficiency and superconductivity in $Nd_{2-x}Ce_xCuO_4$', *Physica C*, **219**, 389–394.

Kim J. S. and Gaskell D. R. (1993), 'The phase stability diagrams for the systems $Nd_2CuO_{4-\delta}$ and $Nd_{1.85}Ce_{0.15}CuO_{4-\delta}$', *Physica C*, **209**, 381–388.

Kim M-S., Skinta J. A., Lemberger T. R., Tsukada A. and Naito M. (2003), 'Magnetic penetration depth measurements of $Pr_{2-x}Ce_xCuO_{4-\delta}$ films on buffered substrates: Evidence for a nodeless gap', *Phys Rev Lett*, 91, 087001 [4 pages].

King D. M., Shen Z.-X., Dessau D. S., Wells B. O., Spicer W. E. *et al.* (1993), 'Fermi surface and electronic structure of $Nd_{2-x}Ce_xCuO_{4-\delta}$', *Phys Rev Lett*, **70**, 3159–3162.

Kishio K., Kitazawa K., Kanbe S., Yasuda I., Sugii N. (1987), 'New high temperature superconducting oxides. $(La_{1-x}Sr_x)_2CuO_{4-\delta}$ and $(La_{1-x}Ca_x)_2CuO_{4-\delta}$', *Chem Lett*, **16**, 429–432.

Klamut P. W. (1993), 'Evidence for interstitial oxygen and possible role of reduction in $Nd_{2-x}Ce_xCuO_{4+y}$', *J Alloy and Compounds*, **194**, L5–L7.

Kokales J. D., Fournier P., Mercaldo L., Talanov V. V., Greene R. L. and Anlage S. M. (2000), 'Microwave electrodynamics of electron-doped cuprate superconductors', *Phys Rev Lett*, *85*, 3696.

Krockenberger Y., Kurian J., Winkler A., Tsukada A., Naito M. and Alff L. (2008), 'Superconductivity phase diagrams for the electron-doped cuprates $R_{2-x}Ce_xCuO_4$ (R = La, Pr, Nd, Sm, and Eu)', *Phys Rev B*, **77**, 060505(R) [4 pages].

Lee S-I., Jeong Y. H., Han K. H., Lim Z. S., Song Y. S. and Park Y. W. (1990), 'Superconductivity and thermoelectric power of $Pr_{1.85}Ce_{0.15}CuO_{4-y}$', *Phys Rev B*, **41**, 2623–2626.

Luke G. M., Le L. P., Sternlieb B. J., Uemura Y. J., Brewer J. H. *et al.* (1990), 'Magnetic order and electronic phase diagrams of electron-doped copper oxide materials', *Phys Rev B*, **42**, 7981–7988.

Mackenzie A. P., Julian S. R., Sinclair D. C. and Lin C. T. (1996), 'Normal-state magnetotransport in superconducting $Tl_2Ba_2CuO_{6+\delta}$ to millikelvin temperatures', *Phys Rev B*, **53**, 5848–5855.

Maeda H., Tanaka Y., Fukutomi M. and Asano T. (1988), 'A new high T_c oxide superconductor without a rare earth element', *Jpn J Appl Phys*, **27**, L209–L210.

Manthiram A. and Goodenough J. B. (1990), 'Crystal chemistry of the $La_{2-y}Ln_yCuO_4$, (Ln = Pr, Nd) systems', *J Solid State Chem*, **87**, 402–407.

Manthiram A. and Goodenough J. B. (1991), 'Thermal-expansion mismatch and intergrowth types in the system $La_{2-y}Nd_yCuO_4$', *J Solid State Chem*, **92**, 231–236.

Manthiram A. and Zhu Y. T. (1994), 'On the absence of superconductivity in Gd2-xCexCuO4', *Physica C*, **226**, 165–169.

Markert J. T., Beille J., Neumeier J. J., Early E. A., Seaman C. L. (1990), 'Pressure dependence of T_c in $L_{2-x}M_xCuO_{4-y}$ (L = Pr,Nd,Sm,Eu; M = Ce,Th): Antisymmetric behavior of electron- versus hole-doped copper-oxide superconductors', *Phys Rev Lett*, **64**, 80–83.

Massidda S., Hamada N., Yu J. and Freeman A. J. (1989), 'Electronic structure of Nd-Ce-Cu-O, a Fermi liquid superconductor', *Physica C*, **157**, 571–574.

Matsuda M., Yamada K., Kakurai K., Kadowaki H., Thurston T. R. *et al.* (1990), 'Three-dimensional magnetic structures and rare-earth magnetic ordering in Nd_2CuO_4 and Pr_2CuO_4', *Phys Rev B*, **42**, 10098–10107.

Matsuda M., Endoh Y. and Hidaka Y. (1991), 'Crystal growth and characterization of $Pr_{2-x}Ce_xCuO_4$', *Physica C*, **179**, 347–352.

Matsuda M., Endoh Y., Yamada K., Kojima H., Tanaka I., *et al.* (1992), 'Magnetic order, spin correlations, and superconductivity in single-crystal $Nd_{1.85}Ce_{0.15}CuO_{4+\delta}$', *Phys Rev B*, **45**, 12548–12555.

Matsui H., Terashima K., Sato T., Takahashi T., Fujita M. and Yamada K. (2005), 'Direct observation of a nonmonotonic $d_x{}^2-y^2$-wave superconducting gap in the electron-doped high-T_c superconductor $Pr_{0.89}LaCe_{0.11}CuO_4$', *Phys Rev Lett*, **95**, 017003 [4 pages].

Matsumoto O., Utsuki A., Tsukada A., Yamamoto H., Manabe T. and Naito M. (2008), 'Superconductivity in undoped T′-RE_2CuO_4 with T_c over 30 K', *Physica C*, **468**, 1148–1151.

Matsumoto O., Utsuki A., Tsukada A., Yamamoto H., Manabe T. and Naito M. (2009a), 'Synthesis and properties of superconducting T′-R_2CuO_4 (R = Pr, Nd, Sm, Eu, Gd)', *Phys Rev B*, **79**, 100508(R) [4 pages].

Matsumoto O., Utsuki A., Tsukada A., Yamamoto H., Manabe T. and Naito M. (2009b), 'Generic phase diagram of "electron-doped" T′ cuprates', *Physica C*, **469**, 924–927.

Matsumoto O., Utsuki A., Tsukada A., Yamamoto H., Manabe T. and Naito M. (2009c), 'Reduction dependence of superconductivity in the end-member T′ cuprates', *Physica C*, **469**, 940–943.

McMillan W. L. and Rowell J. M. (1969), *Superconductivity vol. 1*, ed. R. D. Parks, New York, Marcel Dekker, chapter. 11.

Moran E., Nazzal A. I., Huang T. C. and Torrance J. B. (1989), 'Extra oxygen in electron superconductors: Ce and Th doped $Nd_2CuO_{4+\delta}$ and $Gd_2CuO_{4+\delta}$', *Physica C*, **160**, 30–34.

Müller-Buschbaum Hk. and Wollsglager M. W. (1975), 'Über ternäre oxocuprate. VII. zur kristallstruktur von Nd_2CuO_4', *Z Anorg Allg Chem*, **414**, 76–80.

Naito M., Sato H. and Yamamoto H. (1997), 'MBE growth of $(La,Sr)_2CuO_4$ and $(Nd,Ce)_2CuO_4$ thin films', *Physica C*, **293**, 36–43.

Naito M., Sato H. and Yamamoto H. (1998), 'Oxygen nonstoichiometry of MBE-grown cuprate films to lose or give high-T_c superconductivity', *Proceeding of SPIE*, **3481**, 214–225.

Naito M., Yamamoto H. and Sato H. (2000a), 'Intrinsic problem of cuprate surface and interface: why good tunnel junctions are difficult to fabricate', *Physica C*, **335**, 201–206.

Naito M. and Hepp M. (2000b), 'Superconducting T′-$La_{2-x}Ce_xCuO_4$ films grown by molecular beam epitaxy', *Jpn J Appl Phys*, **39**, L485–L487.

Naito M. and Hepp M. (2001), 'Superconducting T′-$La_{2-x}Ce_xCuO_4$ films grown by molecular beam epitaxy', *Physica C*, **357–360**, 333–336.

Naito M., Karimoto S. and Tsukada A. (2002), 'Epitaxy-stabilized n-type superconducting cuprates', *Supercond Sci Technol*, **15**, 1663–1668.

Naito M., Matsumoto O., Utsuki A., Tsukada A., Yamamoto H. and Manabe T. (2008), 'Undoped cuprate superconductors – band superconductors or oxygen-doped Mott-Hubbard superconductors?', *J Phys Conf Ser*, **108**, 012037 [6 pages].

Nakagawa H. (1999), 'Transport properties of high-T_c oxide superconductors in ultra-high magnetic fields', PhD thesis, University of Tokyo.

Noda M., Tsukada A., Yamamoto H. and Naito M. (2005), 'Origin of superconducting carriers in "non-doped" T′-(La,*RE*)$_2$CuO$_4$ (*RE* = Sm, Eu, Gd, Tb, Lu, and Y) prepared by molecular beam epitaxy', *Physica C*, **426–431**, 220–224.

Okada H., Takano M. and Takeda Y. (1990), 'Synthesis of Nd$_2$CuO$_4$-type R_2CuO$_4$ (*R* = Y, Dy, Ho, Er, Tm) under high pressure', *Physica C*, **166**, 111–114.

Onose Y., Taguchi Y., Ishizaka K. and Tokura Y. (2004), 'Charge dynamics in underdoped Nd$_{2-x}$Ce$_x$CuO$_4$: Pseudogap and related phenomena', *Phys Rev B*, **69**, 024504 [13 pages].

Parkin S. S. P., Lee V. Y., Nazzal A. I., Savoy R., Beyers R. and La Placa S. J. (1988), 'Tl$_1$Ca$_{n-1}$Ba$_2$Cu$_n$O$_{2n+3}$ (n = 1,2,3): A new class of crystal structures exhibiting volume superconductivity at up to ≈ 110 K', *Phys Rev Lett*, **61**, 750–753.

Peng J. L., Li Z. Y., Greene R. L. (1991), 'Growth and characterization of high-quality single crystals of R_{2-x}Ce$_x$CuO$_{4-y}$ (*R* = Nd, Sm)', *Physica C*, **177**, 79–85.

Petrov A. N., Cherepanov V. A., Zuev A. Yu. and Zhukovsky V. M. (1988a), 'Thermodynamic stability of ternary oxides in *Ln*-*M*-O (*Ln* = La, Pr, Nd; *M* = Co, Ni, Cu) systems', *J Solid State Chem*, **77**, 1–14.

Petrov A. N., Zuev A. Yu. and Cherepanov V. A. (1988b), 'Thermodynamic stability of the lanthanide cuprites Ln_2CuO$_4$ and *Ln*CuO$_2$, where *Ln* = La, Pr, Nd, Sm, Eu or Gd', *Russian J Phys Chem*, **62**, 1613–1615.

Petrov A. N., Zuev A. Yu. and Rodionova T. P. (1999), 'Crystal and defect structure of Nd$_{1.9}$Ce$_{0.1}$CuO$_{4\pm y}$', *J Am Ceram Soc*, **82**, 1037–1044.

Prado F., Caneiro A. and Serquis A. (1995), 'Thermogravimetric study of the reduction step in Nd$_{1.85}$Ce$_{0.15}$Cu$_{1.01}$O$_y$ as a function of the oxygen partial pressure', *Solid State Commun*, **94**, 75–80.

Prozorov R., Giannetta R. W., Fournier P. and Greene R. L. (2000), 'Evidence for nodal quasiparticles in electron-doped cuprates from penetration depth measurements', *Phys Rev Lett*, **85**, 3700–3703.

Radaelli P. G.., Jorgensen J. D., Schultz A. J., Peng J. L. and Greene R. L. (1994), 'Evidence of apical oxygen in Nd$_2$CuO$_y$ determined by single-crystal neutron diffraction', *Phys Rev B*, **49**, 15322–15326.

Sawa H., Suzuki S., Watanabe M., Akimitsu J., Matsubara H. *et al.* (1989), 'Unusually simple crystal structure of an Nd-Ce-Sr-Cu-O superconductor', *Nature*, **337**, 347–348.

Schilling A., Cantoni M., Guo J. D. and Ott H. R. (1993), 'Superconductivity above 130 K in the Hg-Ba-Ca-Cu-O system', *Nature*, **363**, 56–58.

Schneider C. W., Barber Z. H., Evetts J. E., Mao S. N., Xi X. X. and Venkatesan T. (1994), 'Penetration depth measurements for Nd$_{1.85}$Ce$_{0.15}$CuO$_4$ and NbCN thin films using a kinetic inductance technique', *Physica C*, **233**, 77–84.

Schultz A. J., Jorgensen J. D., Peng J. L. and Greene R. L. (1996), 'Single-crystal neutron-diffraction structures of reduced and oxygenated Nd$_{2-x}$Ce$_x$CuO$_y$', *Phys Rev B*, **53**, 5157–5159.

Sekitani T., Naito M., Miura N. and Uchida K. (2002), 'Kondo effect in the normal state of T′-Ln_{2-x}Ce$_x$CuO$_4$ (*Ln* = La, Pr, Nd)', *J Phys Chem Solids*, **63**, 1089–1092.

Sekitani T., Naito M. and Miura N. (2003), 'Kondo effect in underdoped *n*-type superconductors', *Phys. Rev. B*, **67**, 174503 [5 pages].

Serquis A., Prado F. and Caneiro A. (1999), 'On the role of the reduction step in Nd$_{1.85}$Ce$_{0.15}$Cu$_{1\pm\delta}$O$_y$: a study of thermodynamic properties and electrical resistivity at high temperature', *Physica C*, **313**, 271–280.

Shannon R. D. and Prewitt C. T. (1969), 'Effective ionic radii in oxides and fluorides', *Acta Cryst B*, **25**, 925–946.

Shen Z.-X., Dessau D. S., Wells B. O., King D. M., Spicer W. E. *et al.* (1993), 'Anomalously large gap anisotropy in the *a-b* plane of $Bi_2Sr_2CaCu_2O_{8+\delta}$', *Phys Rev Lett*, **70**, 1553–1556.

Sheng Z. Z. and Hermann A. M. (1988), 'Superconductivity in the rare-earth-free Tl-Ba-Cu-O system above liquid-nitrogen temperature', *Nature*, **332**, 55–58.

Siegrist T., Zahurak S. M., Murphy D. W. and Roth R. S. (1988), 'The parent structure of the layered high-temperature superconductors', *Nature*, **334**, 231–232.

Skinta J. A., Lemberger T. R., Greibe T. and Naito M. (2002a), 'Evidence for a nodeless gap from the superfluid density of optimally doped $Pr_{1.855}Ce_{0.145}CuO_{4-y}$ films', *Phys Rev Lett*, **88**, 207003 [4 pages].

Skinta J. A., Kim M-S., Lemberger T. R., Greibe T. and Naito M. (2002b), 'Evidence for a transition in the pairing symmetry of the electron-doped cuprates $La_{2-x}Ce_xCuO_{4-y}$ and $Pr_{2-x}Ce_xCuO_{4-y}$', *Phys Rev Lett*, **88**, 207005 [4 pages].

Smilde H.-J. H., Ariando, Blank D. H., Gerritsma G. J., Hilgenkamp H. and Rogalla H. (2002), '*d*-wave–induced Josephson current counterflow in $YBa_2Cu_3O_7$/Nb zigzag junctions', *Phys Rev Lett*, **88**, 057004 [4 pages].

Smith M. G., Manthiram A., Zhou J., Goodenough J. B. and Markert J. T. (1991), 'Electron-doped superconductivity at 40 K in the infinite-layer compound $Sr_{1-y}Nd_yCuO_2$', *Nature*, **351**, 549–551.

Subramanian M. A., Torardi C. C., Gopalakrishnan J., Gai P. L., Calabrese J. C. *et al.* (1988), 'Bulk superconductivity up to 122 K in the Tl-Pb-Sr-Ca-Cu-O system', *Science*, **242**, 249–252.

Sugiyama J., Tokuono S., Koriyama S., Yamauchi H. and Tanaka S. (1991), 'Comparison of paramagnetic- and nonmagnetic-impurity effects on superconductivity in $Nd_{1.85}Ce_{0.15}CuO_4$', *Phys Rev B*, **43**, 10489–10495.

Suzuki K., Kishio K., Hasegawa T. and Kitazawa K. (1990), 'Oxygen nonstoichiometry of the $(Nd, Ce)_2CuO_{4-\delta}$ system', *Physica C*, **166**, 357–360.

Suzuki M., Kubo S., Ishiguro K. And Haruna K. (1994), 'Hall coefficient for oxygen-reduced $Nd_{2-x}Ce_xCuO_{4-\delta}$', *Phys Rev B*, **50**, 9434–9438.

Takagi H., Uchida S. and Tokura Y. (1989), 'Superconductivity produced by electron doping in CuO_2-layered compounds', *Phys Rev Lett*, **62**, 1197–1200.

Takayam-Muromachi E., Izumi F., Uchida Y., Kato K. and Asano H. (1989), 'Oxygen deficiency in the electron-doped superconductor $Nd_{2-x}Ce_xCuO_{4-y}$', *Physica C*, **159**, 634–638.

Takayama-Muromachi E., Uchida Y. and Kato K. (1990), 'Electron-doped system $(La, Nd, Ce)_2CuO_4$ and preparation of T′-type (La, *Ln*)CuO_4 (*Ln = Ce, Y*)', *Physica C*, **165** 147–151.

Tanaka I., Watanabe T., Komai N. and Kojima H. (1991), 'Growth and superconductivity of $Nd_{2-x}Ce_2CuO_4$ single crystals', *Physica C*, **185–189**, 437–438.

Tanaka Y., Motohashi T., Karpinnen M. and Yamauchi H. (2008), 'Conditions for superconductivity in the electron-doped copper-oxide system, $(Nd_{1-x}Ce_x)_2CuO_{4+\delta}$', *J Solid State Chem*, **181**, 365–372.

Tarascon J. M., Wang E., Kivelson S., Bagley B. G., Hull G. W. and Ramesh R. (1990), 'Magnetic versus nonmagnetic ion substitution effects on T_c in the La-Sr-Cu-O and Nd-Ce-Cu-O systems', *Phys Rev B*, **42**, 218–222.

Tokura Y., Takagi H. and Uchida S. (1989), 'A superconducting copper oxide compounds with electrons as the charge carriers', *Nature*, **337**, 345–347.

Tolpygo S. K., Lin J.-Y., Gurvitch M., Hou S. Y. and Phillips J. M. (1996), 'Universal T_c suppression by in-plane defects in high-temperature superconductors: Implications for pairing symmetry', *Phys Rev B*, **53**, 12454–12461.

Torrance J. B., Lacorre P., Asavaroengchai C. and Metzger R. M. (1991), 'Why are some oxides metallic, while most are insulating?', *Physica C*, **182**, 351–364.

Tretyakov Yu. D., Kaul A. R. and Makukhin N. V. (1976), 'An electrochemical study of high-temperature stability of compounds between the rare earths and copper oxide', *J Solid State Chem*, **17**, 183–189.

Tsuei C. C., Gupta A. and Koren G. (1989) 'Quadratic temperature dependence of the in-plane resistivity in superconducting $Nd_{1.85}Ce_{0.15}CuO_4$ – Evidence for Fermi-liquid normal state', *Physica C*, **161** 415.

Tsuei C. C., Kirtley J. R., Chi C. C., Yu-Jahnes L. S., Gupta A. *et al.* (1994), 'Pairing symmetry and flux quantization in a tricrystal superconducting ring of $YBa_2Cu_3O_{7-\delta}$', *Phys Rev Lett*, **73**, 593–596.

Tsuei C. C. and Kirtley J. R. (2000a), 'Phase-sensitive evidence for *d*-wave pairing symmetry in electron-doped cuprate superconductors', *Phys Rev Lett*, **85**, 182–185.

Tsuei C. C. and Kirtley J. R. (2000b), 'Pairing symmetry in cuprate superconductors', *Rev Mod Phys*, **72**, 969–1016.

Tsukada A., Greibe T. and Naito M. (2002), 'Phase control of La_2CuO_4 in thin film synthesis', *Phys Rev B*, **66**, 184515 [5 pages].

Tsukada A., Krockenberger Y., Noda M., Yamamoto H., Manske D. *et al.* (2005a), 'New class of T′-structure cuprate superconductors', *Solid State Commun*, **133**, 427–431.

Tsukada A., Noda M., Yamamoto H. and Naito M. (2005b), 'Role of impurity oxygen in superconductivity of "non-doped" T′-$(La,RE)_2CuO_4$', *Physica C*, **426–431**, 459–463.

Tsukada A., Shibata H., Noda M., Yamamoto H. and Naito M. (2006), 'Charge transfer gap for T′-RE_2CuO_4 and T-La_2CuO_4 as estimated from Madelung potential calculations', *Physica C*, **445–448**, 94–96.

Uchida S., Takagi H. and Tokura Y. (1989), 'Doping effect on the transport and optical properties of P-type and N-type cuprate superconductors', *Physica C*, **162–164**, 1677–1680.

Uchida S., Ido T., Takagi H., Arima T., Tokura Y. and Tajima S. (1991), 'Optical spectra of $La_{2-x}Sr_xCuO_4$: Effect of carrier doping on the electronic structure of the CuO_2 plane', *Phys Rev B*, **43**, 7942–7954.

Uzumaki T., Hashimoto K. and Kamehara N. (1992), 'Raman scattering and X-ray diffraction study in layered cuprates', *Physica C*, **202**, 175–187.

Wang E., Tarascon J.-M., Greene L. H., Hull G. W. and McKinnon W. R. (1990), 'Cationic substitution and role of oxygen in the *n*-type superconducting T′ system $Nd_{2-y}Ce_yCuO_z$', *Phys Rev B*, **41**, 6582–6590.

Watanabe I., Uefuji T., Kurahashi K., Fujita M., Yamada K. and Nagamine K. (2001), 'Muon spin relaxation study on magnetic properties of $Nd_{2-x}Ce_xCuO_4$ around a boundary between the magnetically ordered and superconducting states', *Physica C*, **357–360**, 212–215.

Wollman D. A., Van Harlingen D. J., Giapintzakis J. and Ginsberg D. N. (1995), 'Evidence for $d_{x^2-y^2}$ pairing from the magnetic field modulation of $YBa_2Cu_3O_7$-Pb Josephson junctions', *Phys Rev Lett*, **74**, 797–800.

Wu M. K., Ashburn J. R., Torng C. J., Hor P. H., Meng R. L. *et al.* (1987), 'Superconductivity at 93 K in a new mixed-phase Y-Ba-Cu-O compound system at ambient pressure', *Phys Rev Lett*, **58**, 908–910.

Wu D. H., Mao J., Mao S. N., Peng J. L., Xi X. X. *et al.* (1993), 'Temperature dependence of penetration depth and surface resistance of $Nd_{1.85}Ce_{0.15}CuO_4$', *Phys Rev Lett*, 70, 85–88.

Xu X. Q., Mao S. N., Jiang W., Peng J. L. and Greene R. L. (1996), 'Oxygen dependence of the transport properties of $Nd_{1.78}Ce_{0.22}CuO_{4 \pm \delta}$', *Phys Rev B*, **53**, 871–875.

Yamada T., Kinoshita K. and Shibata H. (1994), 'Synthesis of superconducting T′-$(La_{1-x}Ce_x)_2CuO_4$', *Jpn J Appl Phys*, **33**, L168–L169.

Yamada K., Kurahashi K., Endoh Y., Birgeneau R. J. and Sirane G. (1999), 'Neutron scattering study on electron–hole doping symmetry of high-T_c superconductivity', *J Phys Chem Solids*, **60**, 1025–1030.

Yamaguchi S., Yasui K., Matsumoto F., Terabe K., Sukigara T. and Iguchi Y. (1991), 'Defect chemical study of $Nd_{2-x}Ce_xCuO_{4-\delta}$', *Solid State Ionics*, **49**, 63–70.

Yamamoto H., Naito M. and Sato H. (1997), 'Surface and interface study on MBE-grown $Nd_{1.85}Ce_{0.15}CuO_4$ thin films by photoemission spectroscopy and tunnel spectroscopy', *Phys Rev B*, **56**, 2852–2859.

Zhou J.-S., Chan J. and Goodenough J. B. (1993), 'Copper-oxygen bond length and self-doping in R_2CuO_4 (R = Pr, Nd, Sm, Eu, Gd)', *Phys Rev B*, **47**, 5477–5480.

Zhu Y. T. and Manthiram A. (1994a), 'Role of bond-length mismatch in $L_{2-x}Ce_xCuO_4$ (L = lanthanide)', *Phys Rev B*, **49**, 6293–6298.

Zhu Y. T. and Manthiram A. (1994b), 'Role of oxygen in $Ln_{2-x}Ce_xCuO_4$ superconductors', *Physica C*, **224**, 256–262.

Zhu Y. T. and Manthiram A. (1995), 'A thermogravimetric study of the influence of internal stresses on oxygen variations in $Ln_{2-x}Ce_xCuO_4$', *J Solid State Chem*, **114**, 491–498.

Zaanen J., Sawatzky G. A. and Allen J. W. (1985), 'Band gaps and electronic structure of transition-metal compounds', *Phys Rev Lett*, **55**, 418–421.

Zasadzinski J. F., Tralshawala N., Romano P., Huang Q., Chen J. and Grey K. E. (1992), 'Tunneling density of states in cuprate and bismuthate superconductors', *J Phys Chem Solids*, **53**, 1635–1642.

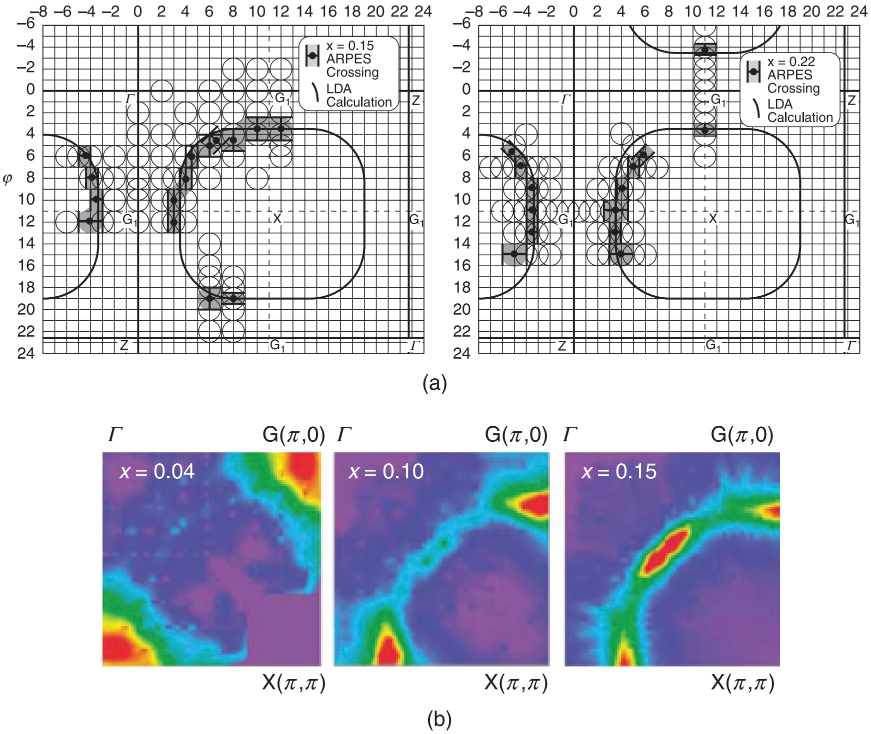

Plate III (a) Early ARPES results by a Stanford University group on $Nd_{2-x}Ce_xCuO_4$ single crystals with $x = 0.15$ and $x = 0.22$. The hole-like Fermi surface shrinks in a rigid-band manner as the doping proceeds from $x = 0.15$ to $x = 0.22$. (b) Latest ARPES results by the same group on $Nd_{2-x}Ce_xCuO_4$ single crystals with $x = 0.04$, 0.10, and 0.15. As the doping is reduced, the spectral weight in the [0,0] to [π,π] direction diminishes at $x = 0.10$ and is eventually lost at $x = 0.04$. (Reprinted with permission from King *et al.* (1993), *Phys. Rev. Lett.*, **70**, 3159 and Armitage *et al.* (2002), *Phys. Rev. Lett.*, **70**, 257001. © 1993, 2002 by the American Physical Society.)

7

Liquid phase epitaxy (LPE) growth of high-temperature superconducting films

X. YAO and Y. CHEN, Shanghai Jiao Tong University, China

Abstract: This chapter mainly discusses the growth of REBCO high-temperature superconducting thick films by liquid phase epitaxy, including physical and chemical reaction among substrate/seed-film/liquid phase epitaxy film, oriented film control, fundamental study on growth mechanism, phase equilibria and epitaxial stabilization.

Key words: liquid phase epitaxy, REBCO film, oriented growth, high thermal stability, hetero seed.

7.1 Introduction

Epitaxy is an important technique in preparing a crystalline film on a single-crystalline substrate as a kind of crystal growth. In accordance with the contribution of source atoms, it can be divided into two typical epitaxial processes: the vapor phase epitaxy (VPE) – a film deposition method from a gas phase; and the liquid phase epitaxy (LPE) – a film deposition method from a liquid phase. The main attention in this chapter will be focused on liquid phase epitaxy. The LPE process as represented in Fig. 7.1 is based on the concept of Czochralski growth, namely, top-seeded solution-growth (TSSG). A lattice-matched film epitaxially grows on the substrate when a single-crystalline one contacts a supersaturated solution. The thickness of the grown film can be controlled (although not precisely) by the processing temperature and the contacting time of the substrate and solution. There are several advantages of the LPE process over the VPE technique listed as follows:

- the LPE process can produce high-quality crystals because the crystal growth occurs near thermal equilibrium;
- LPE features a high growth rate (one or two times higher than that of VPE), which allows the highly efficient growth of thick epitaxial-films:
- as a cost-saving method, no vacuumed-system is required in the LPE process whereas a high vacuum is highly desired in VPE.

In addition, an important distinction between them is that LPE can grow a quasi-single-crystalline film, a micron-order size in thickness, while VPE is suitable for the growth of a polycrystalline and nanometer-order film.

What is more, the LPE technique has several merits compared with the crystal pulling method for the wafer application. First, large LPE thick films can be easily

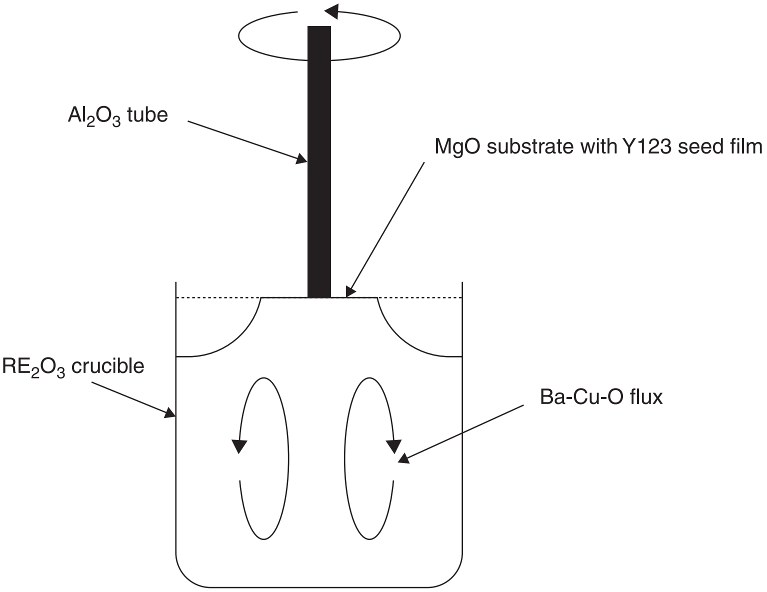

7.1 LPE method.

obtained (simply depending on the substrate size), while a large single crystal needs a long growth period. Secondly, LPE thick films with structural and compositional homogeneity can also be easily obtained due to a nearly-unchanged growth condition within a short LPE growth time, which is difficult for the crystal pulling method. Thirdly, the LPE thick film can directly be used as a wafer while a bulk single crystal via crystal pulling needs cutting. Due to the above mentioned features, LPE is widespread in the production process of the semiconductor industry, e.g., in the manufacturing of garnet films for optical and magneto-optical devices.

With the discovery of the high-temperature superconductor (HTS) $YBa_2Cu_3O_{7-\delta}$ (YBCO or Y123) in 1987, the LPE technique was also used for the growth of superconducting thick films.[1–8] The REBCO films obtained by LPE have high qualities:

- high critical superconductive temperature (T_c) which is over 90 K,
- high critical current density (J_c), reaching 10^6 A/cm^2,
- a quasi-atomically flat surface after being polished.

The potential applications of LPE films can be grouped into two developments:

1 Development of a superconducting electronic device. Inducing a homoepitaxial growth for the HTS vapor deposition, $REBa_2Cu_3O_{7-\delta}$ (REBCO or RE123, RE = rare earth element) LPE thick films acting as contamination-free substrates have a minimal thermal expansion difference and minimal lattice

misfit with thin films, which lead to improvement in characteristics of the multiple-layer structure for superconducting devices.

2 Development of RE123 coated conductor. The LPE-grown thick film with a thickness over 5 mm can be readily achieved with a rate of 1–10 mm/min.

7.2 Fundamental study on LPE growth

The growth mode and the initial growth stage of the epitaxial films are regulated by interface thermodynamics and several parameters. Substrate, seed layer, solution and crucible are the four important parameters that have influence on the LPE growth.

7.2.1 Mode of LPE growth

In epitaxy, the growth mechanisms are classified into three modes:

1 roughing or continuous growth;
2 growth by two-dimensional nucleation or Volmer-Weber (VW) growth mode;
3 growth by screw dislocations or the Frank-Van der Merwe (FVM) layer-by-layer growth.

The mechanism called lateral growth was first introduced by Kossel as illustrated in Fig. 7.2. First of all, an atom is absorbed on the surface by bulk diffusion. Then, by surface diffusion, the atom migrates to a kink site and the kink keeps on moving forward laterally across the interface. After the surface has been completely covered, a new step has been formed. This process is repeatedly going on during the growth period.

In PVD-grown HTSC films, Spiral-Island (SI) growth mode is observed. This epitaxial growth mode occurs during the agglomeration phase of the film which first started with the VW mode. During coalescence, dislocations can easily be

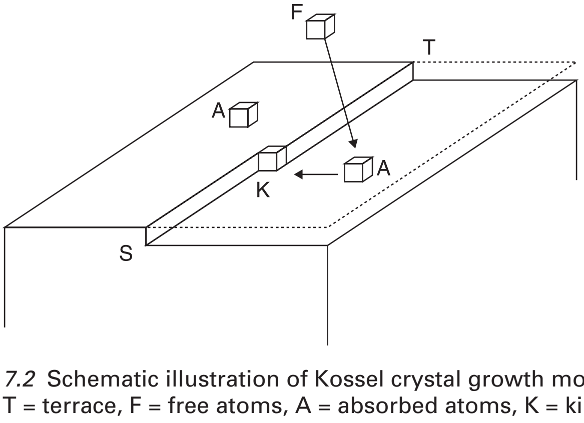

7.2 Schematic illustration of Kossel crystal growth mode. S = step, T = terrace, F = free atoms, A = absorbed atoms, K = kink atoms.

generated by accommodation of translational and rotational displacements between agglomerating islands. The resulting step-growth mode (which is different from the FVM growth mode) permits the achievement of relatively flat surfaces, but at the cost of high step densities. The interstep distance will be similar to the step distances observed in the VW and SI modes and will depend on the supersaturation. Frank suggested that the process of forming the new step does not appear in the FVM growth mode[9] owing to the fact that the screw dislocations can provide a source of steps (Fig. 7.3).

Basically, the growth process of LPE can be divided into three steps.[10] First, stable crystalline nuclei form by the birth and growth of small clusters of atoms on the surface of the substrate. Secondly, the attached solute atoms diffuse over the surface and become part of the growth steps. Finally, the solute atoms transport into the adjacent substrate. At the growth interface, the solute and solvent are separated, leading to boundary diffusion through a thin layer between the solution and the surface of the substrate. In addition, in LPE of YBCO, FVM or layer-by-layer growth over macroscopic distances, a new layer is nucleated after completion of the layer below, and should result in extremely flat layers if substrate and growth parameters are sufficiently met.[11] At high supersaturation, towards growth instability, step bunching occurs. On the *c*-axis, YBCO LPE layers grown on (110) $NdGaO_3$, growth spirals, with bunched steps and large interstep distances, were observed. The step bunching is usually caused by impurity particles, the supersaturation difference, and the difference in the step-advancing rates.

As the most important step, the initial stage of the LPE growth has a great influence on the whole process. Because of the direct growth on the substrate, the defects of the interface may affect the quality of the film at the initial stage, so studies on that stage are really necessary. Now we will take the liquid phase homoepitaxial growth of YBCO and discuss this initial stage. It was reported that the slope angle of YBCO grain augments in accordance with increased growing time,[12] which can be considered

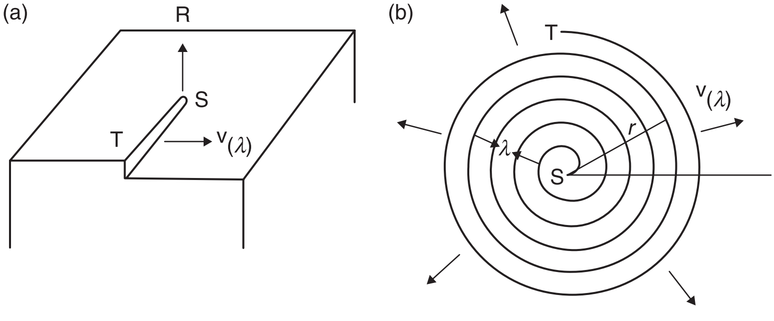

7.3 A schematic Frank-Van der Merwe (FVM) layer-by-layer growth mode: (a) the screw dislocation on interface: R = step advancing direction, (b) the spiral structure: λ = step width of the spiral dislocation, *r* = radius of the spiral dislocation, S = screw dislocation, T = terrace, $v_{(\lambda)}$ = velocity of movement of the step.

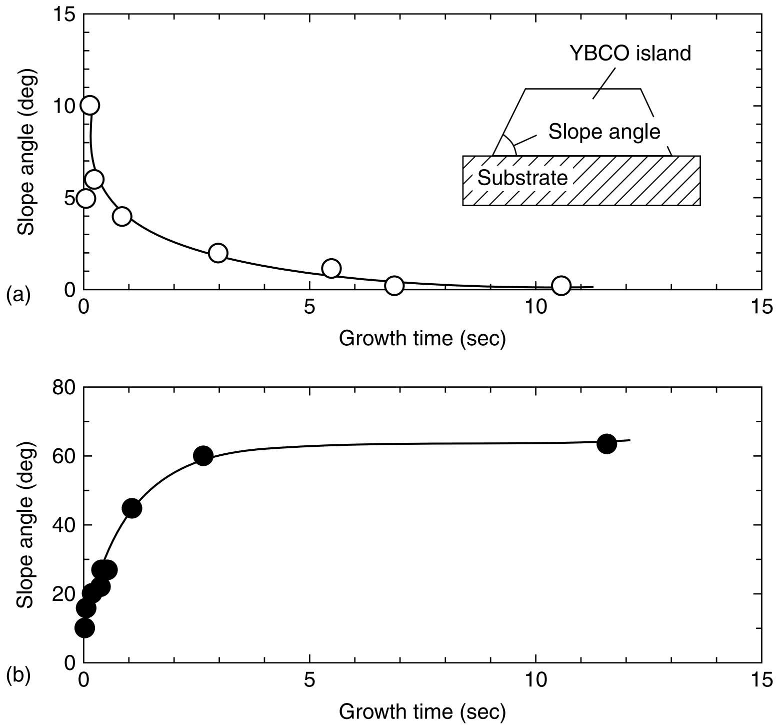

7.4 Slope angle of LPE-grown islands as a function of growth time: (a) homoepitaxial growth, and (b) heteroepitaxial growth. Definition of slope angle is shown in inset.

as a step bunching growth mode (Fig. 7.4). Nomura and co-workers[46] summarized the main reasons for the change of slope angle, the foremost one being the bonding energy difference between the seed layer and the substrate. Another reason for this phenomenon could be that the substrate surface temporarily suffers a high supersaturation caused by both the dissolution of substrate material into the solvent and the formation process of the solute diffusion boundary layer.

In the case of REBCO LPE growth, there are lots of studies on the initial stage of LPE growth, such as the coarsening mechanism to explain the preferential in-plane alignment and the *a*–*c* oriented transition mechanism to explain the competition between inter-growth and out-of-growth, which will be discussed in the following section.

7.2.2 Substrate and its chemical reaction on LPE films

In order to obtain a high-quality LPE thick film, the following should be as small as possible: the lattice mismatch between substrate/thick film; the thermal expansion mismatch between substrate/thick film; the reactivity among substrate/

thick film/flux; and flux wettability to substrate. The main properties of some conventional substrates are listed in Table 7.1, and these conventional substrates can be divided into two groups. The first group has similar lattice constants to REBCO, such as $NdGaO_3$, $LaGaO_3$, $LaSrGaO_4$(the so-called gallate substrate). Epitaxial REBCO thick films can be directly grown on this kind of substrate. The second group has a large lattice misfit with REBCO, such as MgO, $SrTiO_3$, $LaAlO_3$, NiO, Ag and yttrium stabilized ZrO_2(YSZ), for which REBCO LPE growth essentially needs the thin-film-seed layer or even buffer material.[5–8,13–14]

It was reported that the height of the surface-wetting front (h) is approximately linearly related to the square root of the dipping time (t) as follows:[15]

$$h = \alpha\sqrt{t} + C \qquad [7.1]$$

where α is the coefficient of the wettability of solution to the substrate materials. From Table 7.1, we can see that the MgO material has the lowest α value, and the Ba-Cu-O (BCO) liquid allows a low Mg solubility (about 0.4 at %).[16] That is to say, the BCO melt has a low wettability and reactivity with MgO in comparison with the other substrates.

Besides, MgO is the only material acting as a substrate to form a crack-free RE123 LPE thick film due to its larger thermal coefficient than that of REBCO. Cracks were found to occur frequently and develop during the cooling process using other substrates.[7,8] In general, researchers considered that the lattice matching between the growth crystal and the substrate is one of the most important factors for epitaxial growth. Although the MgO substrate has a large lattice mismatch (≈9.4%, in the case of the YBCO) on the *a*-axis lattice constants between the REBCO and the MgO, it is still an excellent substrate material applicable in the HTS LPE process due to its advantages mentioned above.

But one problem is that REBCO film cannot be grown directly on MgO substrate by reason of its large misfit with REBCO, so there must be a seed layer as we mentioned before. In order to obtain high-quality LPE film, the minimum lattice mismatch between substrate and film material is highly desired. As a consequence, a REBCO-film-seed layer on the MgO substrate is the best choice, since it has the same lattice constant with the material that we want. More details about liquid phase epitaxy growth using REBCO/MgO as a seed will be discussed in sections 7.3.3 and 7.3.4.

7.2.3 The crucible and its chemical stability in the solvent

The Ba-Cu-O solvent is generally used for the LPE growth. Therefore, when crucibles are chosen, three points relative to the chemical stability in the melt at a high processing temperature should be taken into consideration. First, the lowest rate of chemical reaction between crucible material and the solvent is required. Otherwise, the high reactivity will lead to a rapid corrosion of the crucible. Moreover, the reacting products will change the liquid properties, e.g., an

Table 7.1 Properties and lattice constants of the substrates

Substrate	Crystal structure	Crystal system	Lattice constant (nm)	Permittivity	Linear thermal expansion coefficient (K^{-1})	Melting point (ºC)	α ($\times 10^{-5}$ m/s)
MgO	NaCl	Cubic	0.4123	10	13.5×10^{-6}	2800	0
YSZ	Fluorite	Cubic	0.5139	27	10.3×10^{-6}	2700	2.5
$LaAlO_3$	Perovskite	Hexagonal	a = 0.5319 c = 1.311	10	12.6×10^{-6}	2100	4.78
$SrTiO_3$	Perovskite	Cubic	0.3905	310	11.1×10^{-6}	1920	15.3
$YAlO_3$	Perovskite	Orthorhombic	a = 0.517 b = 0.5329 c = 0.737	16	7.9×10^{-6}	1875	
$LaGaO_3$	Perovskite	Orthorhombic	a = 0.519 b = 0.594 c = 0.777	25	12×10^{-6}	1750	
$NdGaO_3$	Perovskite	Orthorhombic	a = 0.543 b = 0.550 c = 0.771	25	10×10^{-6}	1750	

α – time constants of the wetted height for substrates in Ba-Cu-O liquid.

enhancement of its viscosity. Secondly, the ratio of wettability of solvent to crucible materials should be low, as a high ratio may result in a severe liquid-creeping problem. Thirdly, the less crucible material dissolved in the Ba-Cu-O liquid the better, as dissolution causes elemental contamination and affects the physical properties of RE123 superconductors.

There are several kinds of crucibles, such as Al_2O_3, MgO, YSZ, $BaZrO_3$ and RE_2O_3, which were successfully employed to grow RE123 single crystals and thick films. The comparison of characteristics of these crucibles is listed in Table 7.2. The Al_2O_3 crucible was widely used at the earlier stage of crystal growth because it could be easily obtained due to the mature crucible-making technology. Both liquid-creeping and crucible-dissolving phenomena are not so appreciative. Additionally, the Al incorporation only slightly affects the superconducting properties. The main advantage of using the MgO crucible is its low solubility in the Ba-Cu-O solvent. Furthermore, the Ba-Cu-O solvent does not wet the MgO material. But there is a relatively high effect to the superconducting property owing to the substitution of Mg at Cu sites. Furthermore, the YSZ crucible is also widely used. Although the crystal grown by the YSZ crucible has a high T_c value, due to the continuous reaction, the $BaZrO_3$ powders may form in the liquid, which raises the liquid viscosity very high. In this case, the crucible cannot be maintained for a long crystal growth run (less than one week from our experience). Moreover, the contamination from Al_2O_3 and YSZ crucible materials often causes a broad superconducting transition width (ΔT) and a low T_c value, indicating compositional inhomogeneity.

The $BaZrO_3$ crucible was reported to be inert to the REBCO liquid solution,[17,18] thus there is no creeping and dissolving phenomena during the crystal growth. T_c was reported to be in the range 91–93 K with a small transition width of 0.1 K. Therefore, it was supposed to be suitable for the growth of REBCO LPE thick films. RE_2O_3 crucibles were mostly used by a so-called solute-rich–liquid crystal-pulling (SRL-CP) method,[17] due to minimal contamination from the crucible materials. In the case of growing Y123 crystals, Y_2BaCuO_5 (Y211) powders were placed at the bottom of the crucible for supplying yttrium solutes so that the Y_2O_3 crucible becomes almost insoluble even at a high growth temperature. Despite the

Table 7.2 The comparison of characteristics of the crucibles listed: Al_2O_3, MgO, YSZ, $BaZrO_3$ and RE_2O_3

Crucible material	Solubility	Wettability	Contamination/ΔT (K)	T_c of YBCO (K)
Al_2O_3	Low	Low	Board	88–93
MgO	Low	None	Board	40–60
YSZ	Low	Low	< 0.25	93.2
$BaZrO_3$	None	None	0.1	91–93
RE_2O_3	None	None	Narrow	> 90

fact that there is a creeping problem, crystal growth runs can be held for about one-month long. The T_c value of the Y_2O_3-crucible-grown film is over 90 K with a sharp transition. But there is also some disadvantage of using the RE_2O_3 crucible. The wall of the crucible may act as nucleation sites at the processing temperature, leading to an unclean liquid (floating particles on the surface). To solve this problem, a horizontal temperature gradient can be applied from the wall to the center in the liquid. That is to say the wall has a higher temperature than the center, which repels the RE123 nucleation from the wall.

7.3 LPE growth mechanism of REBCO films

7.3.1 Transition between *a*-axis and *c*-axis growth of REBCO films

Because of the complicated atomic structure and the anisotropy of the REBCO films, the orientation-control is very important for application. For instance, *c*-axis films deposited on the metal substrates with buffer layers can be employed as current transport approach, while *a*-axis films are appropriate in making Josephson junction devices.[19] So far, there have been many studies associated with the mechanism of the transition between *a*-axis and *c*-axis REBCO films.

YBCO

Ba/Cu ratio in the solvent, supersaturation and atmosphere are three main parameters related to the *a–c* transition. The influence of the liquid composition and the growth temperature on the YBCO film has been systematically studied. Kitamura *et al.*[20] reported that in the case of copper-rich flux composition (Ba/Cu = 3/6.5), both *c*-axis and *a*-axis oriented films were obtained, while only *c*-axis oriented growth was observed using the melts of copper-poor compositions (Ba/Cu = 3/5). They also suggested a relationship between the growth temperature and the film orientation in the LPE growth. When using a Cu-rich flux composition, the *a*-axis oriented growth was observed under lower ΔT (undercooling), whereas the films showed *c*-axis orientation under higher ΔT. Endo *et al.*[21] summed up the influence of growth parameters on the *a–c* oriented growth of YBCO thin films by ion beam sputtering (IBS). In contrast to Kitamura's results, the high-quality *a*-axis films can be achieved at a lower substrate temperature. Meanwhile, the higher oxygen partial pressure is favorable to *a*-axis growth owing to the contraction of the *c*-axis. On the other hand, the *c*-phase growth dominates at higher substrate temperature as well as lower oxygen partial pressure (P_o). The previous studies of this steep *a–c* phase transition are not satisfactorily understood, and the dispersive experimental data are not enough to draw a definitive conclusion.

The mechanism of *a–c* transitions was well interpreted in YBCO thick films as discussed below. It was reported that an inclusive description of the competition between *a* and *c* growth under various growth environments was given, which further revealed the origin of the *a*–*c* transition in YBCO thick films, based on the ‘nucleation and growth’ mode.

By virtue of controlling both processing temperature and the Ba/Cu ratio in liquid, YBCO films with different orientations on (110) NGO substrate were grown. A vertical dipping method was used to exhibit the evolution of YBCO growth on the first several seconds of the entire LPE process to investigate the initial stage of the LPE growth. Both flux of Ba:Cu = 3:5 and Ba:Cu = 3:6.5 compositions were used in the experiment. *c*-Axis growth-dominated YBCO film was obtained by using a melt of 3:5 Ba/Cu ratio, which corresponds with the results of Kitamura. Whereas drastic transformation of orientation appeared under various Ts by using a flux of Ba: Cu = 3:6.5 composition. The mixed films appear instead of pure *c*-axis or pure *a*-axis films, in which the *c* or *a* phase dominated, different from the result of Kitamura.[20] In order to give a semiquantitative description of the coexistence of *a*- and *c*-phase YBCO grains, the phase ratio γ is introduced, which is defined in the sense of equation [7.1]:[21]

$$\gamma = \frac{\sum \text{Peaks of each YBCO phase } (a \text{ or } c)}{\sum \text{Peaks of all phases}} \times 100 \qquad [7.2]$$

The values of *a*-phase ratio (γ_a) of YBCO films grown under the two different flux were calculated and listed in Table 7.3, which describe the approximate tendency of the orientation change. Obviously, in the case of Ba:Cu = 3:5 composition, the *c*-phase dominates the orientation and the proportion of *a*-phase descends gradually as the undercooling increases. On the other side, the value of γ_a presents a transition from 95.9% at T_s = 993 °C to 2.3% at T_s = 985 °C in a drastic manner when using a Ba:Cu = 3:6.5 melt. After that, it is likely to remain approximately constant. It is notable that the width of the transition region is very narrow, even less than 8 K. Notice that the orientation of the YBCO layer is strongly dependent on the Cu content in flux at the growth temperature above 993 °C. What is more, the lower supersaturation has a preference for *a*-axis film, especially in a Cu-rich melt.

Table 7.3 The values of *a*-phase ratio (γ_a) under various growth conditions

T_s	γ_a, Ba:Cu = 3:5	γ_a, Ba:Cu = 3:6.5
993 °C	18.2	95.9
985 °C	↓	2.3
980 °C		5.2
960 °C	3.1	×

The initial stage of the YBCO growth was investigated in order to understand the mechanism. Therefore, as shown in Fig. 7.5(c), in accordance with the dipping time that the area undergoes, the dipping region is partitioned into three sections: (A) the boundary area between YBCO grains and the bare NGO substrate, which approximately corresponds to undergoing a 0 s dipping time; (B) the intermediary

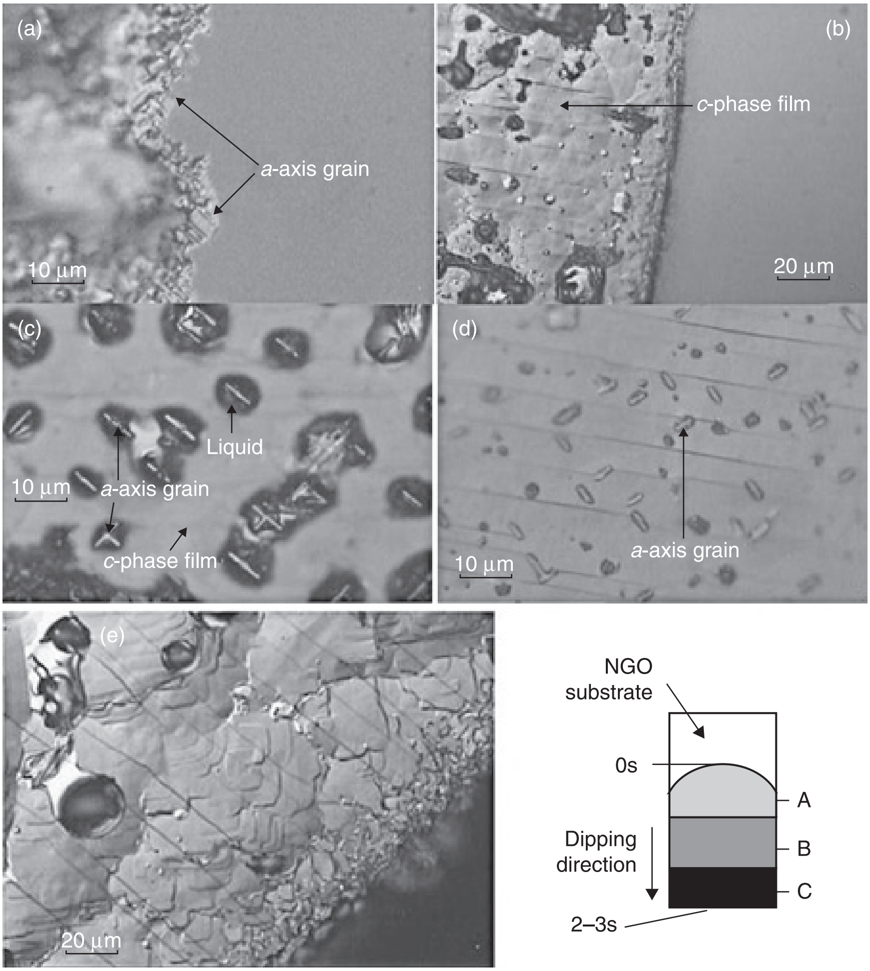
(a)
a-axis grain
10 μm
(b)
c-phase film
20 μm
(c)
Liquid
10 μm
a-axis grain
c-phase film
(d)
a-axis grain
10 μm
(e)
20 μm
NGO substrate
0s
A
B
C
Dipping direction
2–3s

7.5 Optical micrographs of the dipping region of YBCO with peculiar morphology. The region is divided into (A) boundary area between YBCO and NGO, (B) intermediary area, and (C) bottom area. Panels (a) and (b) correspond to region A of the *c*-phase dominated film grown by using a Ba:Cu = 3:6.5 melt and 3:5 melt, respectively. Panels (c) and (d) correspond to region B of the *c*-phase dominated film grown by using a Ba:Cu = 3:6.5 melt and 3:5 melt, respectively. Panel (e) corresponds to region C of the *c*-phase dominated film grown by using a Ba:Cu = 3:6.5 melt, which the case of using a Ba:Cu = 3:5 melt is quite similar to.

area of the dipping part; (C) the bottom of the entire area which is considered to have grown for 2–3 s. As shown in Fig. 7.5, dissimilar morphologies were obtained in different dipping regions. Protruding *a*-axis grains, similar to the *a*-axis grains found in the YBCO[22] thin film, disperse consistently with length of about 5~15 μm in the case of Cu-rich melt, which are seldom found in YBCO thick films deposited by the LPE method. Possibly, this out-growth reflects an incomplete cover by *c*-axis growth due to the very short growth time, less than 1s. By using the *in situ* observation on *c*-dominated film, it was found that the long-axis grains still maintained their original orientation, while Ba-Cu-O liquids had completely melted after holding at 1000 °C (Fig. 7.6). It follows from the above results that the *a*-axis grains were grown epitaxially from the NGO substrate, which were confirmed to be Y123 phase by EDX. More significantly, the *a*-axis oriented grains appearing on the boundary line were observed by using SEM. On the other hand, typical *c*-axis YBCO grains with square-like shape were not found in the surrounding area of the boundary line.

The mechanism of *a*–*c* phase transition in the VPE system seems not to be suitable in the LPE growth. According to the above results it was implied that at the initial period of LPE growth of the *c*-dominated film, *a*-axis YBCO grains nucleated prior to *c*-axis grains, which is similar to the *a*-axis oriented preference in VPE growth of thin films.[23,24] But subsequently, *c*-phase growth occupied most volume and promptly exceeded, which led to a complete covering of *a*-phase growth after only several seconds, with the absence of protruding *a*-axis grains.

Moreover, it was reported that the lattice of *c*-axis grains match much better than *a*-axis grains. Nevertheless, the chemical bonding factor is assumed to be responsible for facilitating the *a*-phase nucleation to overwhelm *c*-phase

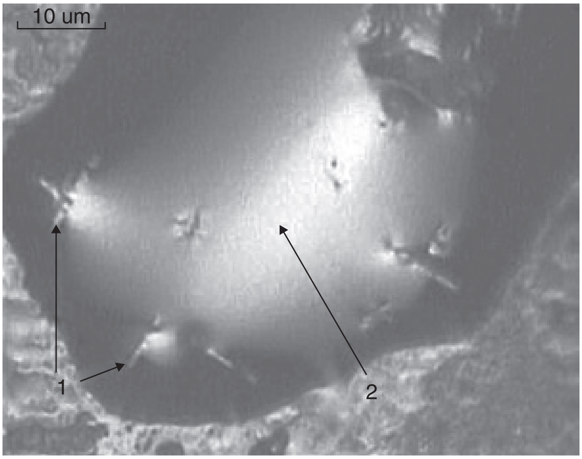

7.6 Optical micrograph of *c*-dominated film after holding at 1000 °C for 5 min. The arrows in the image, respectively, indicate (1) the long-axis grains which still maintained original orientation and (2) the melting liquid.

nucleation. A comprehensive illustration in Fig. 7.7 exhibits *a*–*c* phase transition in LPE films, from which it can be implied that *a*-phase growth is really sensitive to the growth parameters. As demonstrated in Fig. 7.8, under the situation of Ba/Cu = 3/6.5 and T_s = 993 °C, the relations are $\sigma_{993°C} > \sigma_C > \sigma_a$ and $R_a > R_c$, which lead to a *a*-axis dominated YBCO film, where σ_a and σ_c are represented for the critical supersaturation for *a*- and *c*-phase nucleation, respectively. Below 980 °C, the supersaturation is accordingly situated in the region of *c*-dominated growth. Additionally, the role of the oxygen content can be active when using the melt of Ba:Cu = 3:5 composition. The *c*-axis growth of YBCO thin film is enhanced at low oxygen pressure.[25] In analogy with the above case, melt with Ba/Cu = 3:5 composition can be considered as a low oxygen content environment when compared with Ba/Cu = 3/6.5 composition. The *a*-axis film is seldom obtained in the Ba/Cu = 3/5 flux, due to the decline of oxygen content. What is more, the supersaturation at 993 °C has transferred to the *c*-dominated region, which is responsible for another longitudinal *a*–*c* transition. Distinctly, further increase of the supersaturation gives rise to a gradual drop in the *a*-phase ratio. In short, the analysis based on 'nucleation and growth' mode has theoretically interpreted the *a*–*c* phase transition in YBCO-LPE films.

As mentioned before, the optimal growth 'window' for *a*-axis films is usually narrow (less than 10 K in the Cu-rich melt), and no *a*-axis YBCO-LPE film was obtained by using Ba/Cu = 3.0/5.0 fluxes. However, the progress was made by change growth atmosphere. It was reported that in pure oxygen high quality *a*-axis oriented films readily grew from the flux with Ba/Cu ratio = 3.0/5.0. Figure 7.9 presents the surface morphology of the *a*-axis film, with the inset showing a

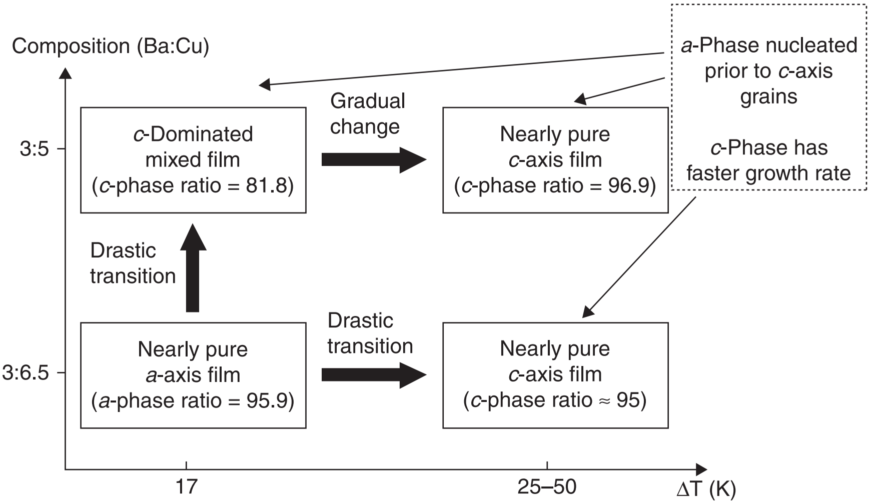
Composition (Ba:Cu)
3:5
3:6.5
17
25–50
ΔT (K)
c-Dominated mixed film (c-phase ratio = 81.8)
Gradual change
Nearly pure c-axis film (c-phase ratio = 96.9)
Drastic transition
Nearly pure a-axis film (a-phase ratio = 95.9)
Drastic transition
Nearly pure c-axis film (c-phase ratio ≈ 95)
a-Phase nucleated prior to c-axis grains
c-Phase has faster growth rate

7.7 An integrated illustration showing the *a*–*c* phase crossover occurring along the shift of undercooling and composition.

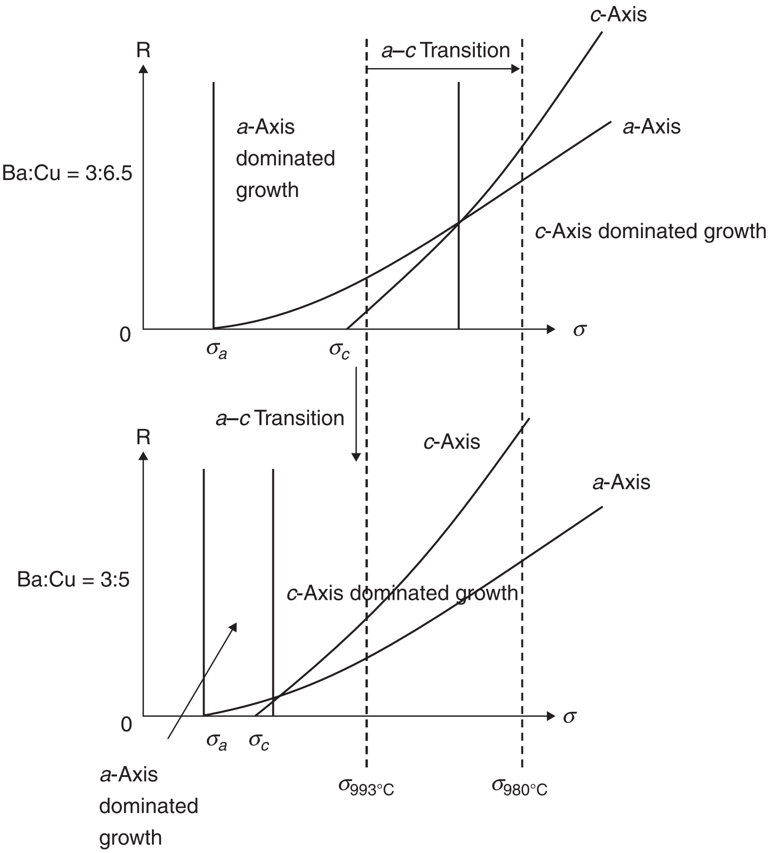
c-Axis
R
a–c Transition
a-Axis
a-Axis dominated growth
Ba:Cu = 3:6.5
c-Axis dominated growth
0
σ
σ_a
σ_c
a–c Transition
R
c-Axis
a-Axis
Ba:Cu = 3:5
c-Axis dominated growth
0
σ
σ_a
σ_c
a-Axis dominated growth
$\sigma_{993°C}$
$\sigma_{980°C}$

7.8 A schematic illustration presenting the mechanism of the *a–c* transition under different environments (*y*-axis represents growth rate, while *x*-axis represents supersaturation; two curves represent growth rate of *a* and *c* phases, respectively).

typical spiral island with concentric ellipse pattern. Besides, extensive preferential twinning was present in the films which did not appear in the LPE films grown in the air. The illustration in Fig. 7.10 shows the tendency of crystalline orientation under different growth conditions which is divided into three parts as A, B, C. The *a*-axis film appears when condition A turns to condition B, which brings a slight oxygen enhancement in the flux. But the growth window was small and sensitive to supersaturation while the growth condition turned to C, that is to say, there was an intensive oxygen enhancement in the atmosphere. The *a*-axis growth 'window' was evidently broadened up to and over 20 K.

The diagram in Fig. 7.11 simply explains the different surface migration lengths during *a*- and *c*-axis growth. Due to all the atomic sites being located at the topmost surface of the growing film,[21] the species of incoming flux need much

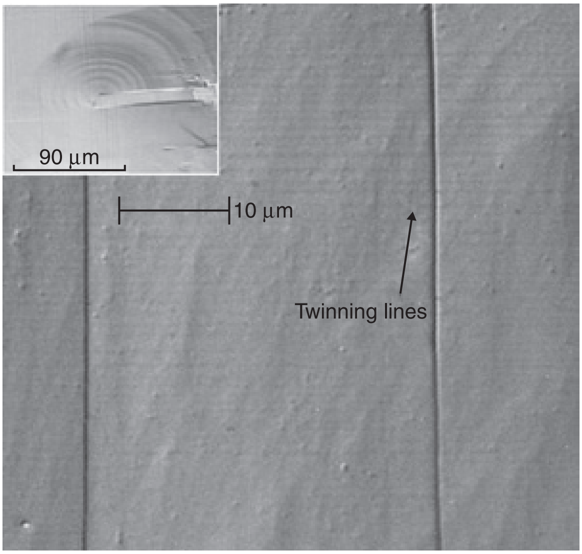

7.9 The surface morphology of the *a*-axis film, with inset showing a typical spiral island with concentric ellipse pattern.

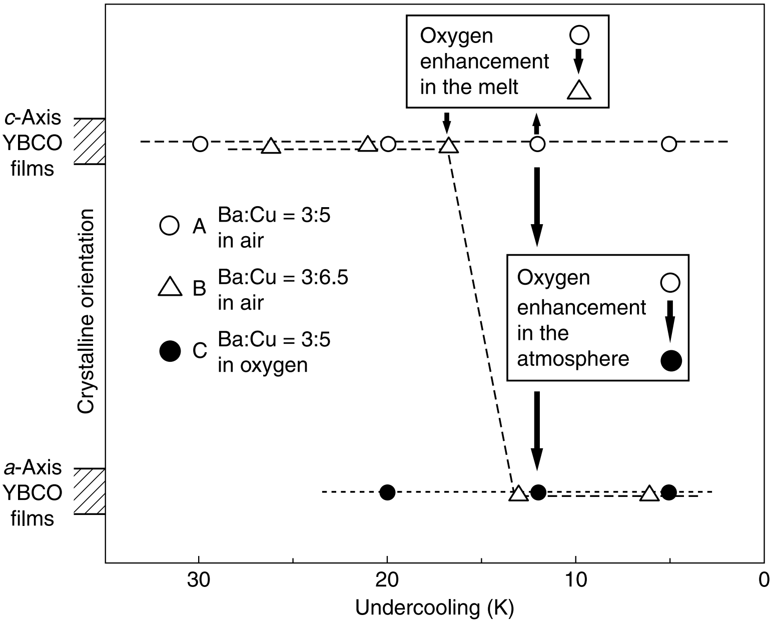

7.10 Schematic illustration showing the orientation transition of YBCO films dependent on the undercooling, the Ba:Cu melt ratio, and the oxygen partial pressure.

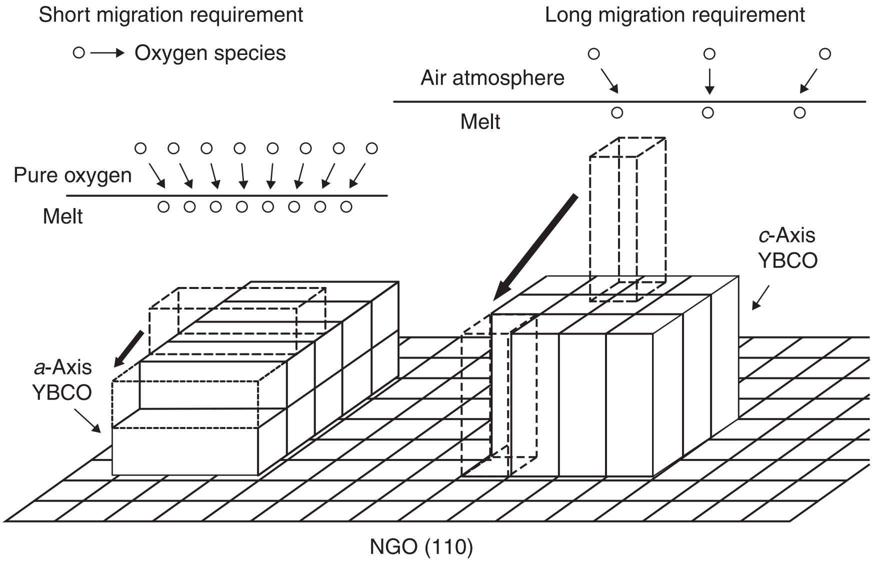

7.11 Surface migration model of the *a*- and *c*-axis YBCO films when different oxygen partial pressures are applied.

shorter migration to occupy the appropriate crystal growth site in *a*-axis growth mode compared with the growth of *c*-axis film. It is well known that under inadequate oxygen supply, vacancies in oxygen sublattice induce transformation of entire lattice units, thus facilitating cation migration.[25] On the other hand, the pure oxygen atmosphere increases the chemical potential of oxygen in the melt, which should get into equilibrium with that in the surrounding oxygen gas. The saturated oxygen state is thought to reduce the cation mobility, up to a 'frozen' state. Consequently, *a*-axis oriented growth was considerably enhanced.

In short, the oxygen factor manifested itself by promoting *a*-axis growth in the YBCO system, and gradually became dominant in comparison with supersaturation, which had played the most important role in promoting the *a*-axis growth so far.

SmBCO

The mechanism between *a*- and *c*-axis transition was consummated by Tang and co-workers in the SmBCO system, who first reported that pure *a*-axis orientated SmBCO films were grown by combination of Cu-rich flux and 1 atm oxygen atmosphere. Compared to YBCO, it is more difficult to grow SmBCO *a*-axis film. Several possible reasons were considered, especially the reversible substitution between Sm^{3+} and Ba^{2+}, which may favor the *c*-axis growth. As mentioned above, the *c*-axis growth needs a longer distance for the atoms to move to a suitable site based on the migration theory. In the SmBCO system, due to that substitution, the travel distance can be divided into several short jumps, with some possible migration paths of Sm^{3+} shown in Fig. 7.12. Importantly, it was reported that with the increase of x in the $Sm_{1+x}Ba_{2-x}Cu_3O_{7-\delta}$ solid solution, the lattice parameter of *c*-axis rapidly reduced, while that of *a*-axis showed only a little change,[26] which led to a decrease of jump length of *c*-axis growth. Notice that the Cu-rich melt will enhance that substitution, which is the reason why the melt of Ba/Cu = 3:7 does not evidently support the *a*-axis growth in SmBCO, but in YBCO.

On the other hand, from the growth kinetics point of view, the interfacial energy between SmBCO crystal and the melt is about 20% lower than that of YBCO.[27] In other words, nucleation of SmBCO might occur at a small supersaturation, which means, the '*a*-axis dominated growth region' of SmBCO should move towards a lower supersaturation area compared to YBCO. Furthermore, it is well known that the liquid slope of samarium solubility in the solution is considerably smaller than that of yttrium.[28] A small undercooling in the SmBCO system can produce a large supersaturation, which can easily exceed the *a*-axis growth limits and lead to a high growth rate of SmBCO. The high growth rate can cause both *a*-phase and *c*-phase nuclei to grow into large grains in a short period of time. This makes it difficult to isolate pure *a*-phase growth from the *a*/*c* mixed one.

Until now, discussions explaining the transition between *a* and *c* growth were limited to the migration theory which is mainly associated with the thermal factors such as temperature and supersaturation. However, besides those thermal factors, the kinetic factors play a critical role. In vapor phase deposition (VPD), the growth temperature is several hundred degrees below T_p of REBCO. At such a low temperature, the growth of both *a*- and *c*-axis grains is thermodynamically allowed. In such a case, kinetic energy of the migrating atoms or ions is the dominant factor determining the film orientation. The temperature range of the *a*–*c* transition is usually around 100 degrees wide,[29,30] and in LPE, the growth

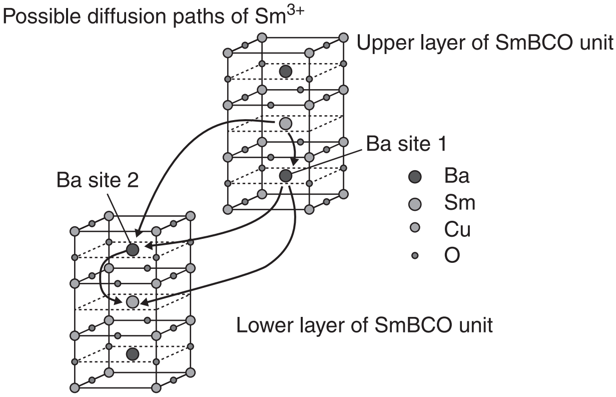
Possible diffusion paths of Sm3+
Upper layer of SmBCO unit
Ba site 1
Ba site 2
Ba
Sm
Cu
O
Lower layer of SmBCO unit

7.12 Schematic diagram of the influence of Sm^{3+} and Ba^{2+} substitution on the diffusion path of Sm^{3+} ions.

condition is close to the thermodynamic equilibrium.[2] The kinetic energy of the migrating atoms is no longer a limiting factor and the *a–c* transition happens dramatically, within 10 degrees.[20,31–33] This does not allow for enough kinetic energy difference necessary for the *a–c* transition.

Hence, other factors have to stand behind the kinetic limit of *a–c* transition in LPE films. The time during which atoms can diffuse along the grain/flux interface plays a critical role in the difference between LPE and VPD. Thus a more general LPE mechanism on the growth kinetic was suggested. As shown in Fig. 7.13, the situation is composed of four steps:

1 an atom from the environment attaches to the grain/flux interface;
2 the atom does not reach a suitable site on the growth edge and goes back to the environment;
3 the atom reaches an appropriate site and becomes a part of the crystal matrix;
4 the atom diffuses on the interface.

Different from VPD, the atoms can effectively go back to the environment in LPE, so both the diffusion time and the diffusion length are finite and important. Suppose that t is the mean time that atoms can stay on the interface, t_c is the average time during which an atom reaches a growth site in *c*-axis growth and t_a is the same in *a*-axis growth, where t_c is longer than t_a according to the surface migration theory. Consequently, if $t > t_c$, LPE would produce a *c*-axis oriented film; if $t_c > t > t_a$, the LPE would result in an *a*-axis oriented film. In this case, the diffusion time becomes a controlling factor of the kinetic limit. Combining the diffusion time with the thermodynamic factors, we can obtain results as a higher growth temperature can provide more migration energy. Therefore the atoms can more easily escape from the interface. On the other hand, a low supersaturation in the melt corresponds to a low slope of the RE element concentration curve (the solute concentration profile

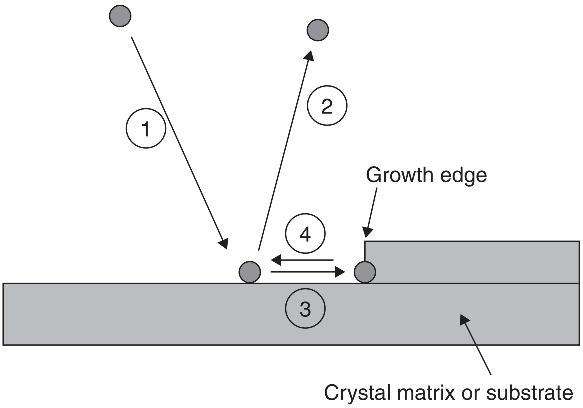

7.13 A schematic kinetic model of the surface migration in LPE.

in the flux near the growth frontier of the crystal), which makes it easier for atoms to return to the liquid and leads to an interfacial controlled growth mode.[34] These two factors reduce the mean holding time *t* for atoms on the interface as temperature increase. Therefore, *a*-axis growth can be obtained when under the conditions of high growth temperature and small supersaturation. However, in an extreme case, if the growth temperature is very close to T_p *a*-axis grains may not appear because of the weak thermal stability of *a*-axis film. Accordingly, on the other hand, the kinetics play a key role when there is supercooling (ΔT) of more than 10 K.

In conclusion, combining the effect of both thermodynamic and kinetic factors, this model offers a new way in understanding the mechanisms of *a*–*c* growth transition in REBCO.

7.3.2 Pinning structure and growth mechanism of *a/c* axes REBCO films

We have discussed the *a* and *c* growth of the REBCO-LPE films due to their considerable anisotropy. Besides, an *a*/*c* mixed structure is also very attractive. The *a*/*c* grain boundary may possibly serve as a connection instead of the conventional SIS structure or as a source of flux pinning.[35]

Tang presented some different *a*/*c* mixed LPE films both in pure SmBCO and mixed Y-Sm systems by controlling growth conditions. For the reasons that the *c*-axis films are not usually flat and clean due to the high growth rate of SmBCO and *a*-oriented grains are too small to observe in the YBCO system, we focus on the Y-Sm mixed system. Figure 7.14 demonstrates the morphology of different kinds of *a*/*c* grain boundaries on (Y, Sm) BCO-LPE film. Figure 7.14(b) and (c) shows different details of the same image taken on the film grown from the 3:5 flux in a pure oxygen atmosphere. Figure 7.14(b) focuses on rod-like *a*-axis grains, while (c) is focused on platelet-like *c*-axis grains. Obviously, the distance between the levels of *a*- and *c*-grain tops is larger than the microscope's depth of field, so the microscope could not focus on both grain types at the same time. Figure 7.14(a) shows *a*-oriented grains isolated in the *c*-axis film, while the rectangular growth spiral and the typical *c*-axis twinning demonstrate the film orientation. The *a*-axis grains seem to be trapped by the *c*-oriented film. Grains marked as 1, 2, and 3 are partially covered, while grains 4, 5 and 6 are almost buried in the film. It directly proves that the *c*-oriented grains grow faster and cover the *a*-oriented grains. As Shingai *et al.* mentioned,[34] this kind of *a*/*c* boundary might be a potential source of flux pinning. Figure 7.14(d) shows an edge of the film, from which we can see that the *c*-axis oriented film has the tendency to cover the *a*-axis growth and the *a*-axis elliptical spiral cores lie on the *a*/*c* boundary. Maybe the reason is that the core of a growth spiral always has the highest growth rate and stands on the top, which prevents the *c*-oriented film from growing over.

With analogy to the growth mode of the *a*–*c* transition, we suppose that supersaturation plays an important role in the growth of *a*/*c* grain boundaries in

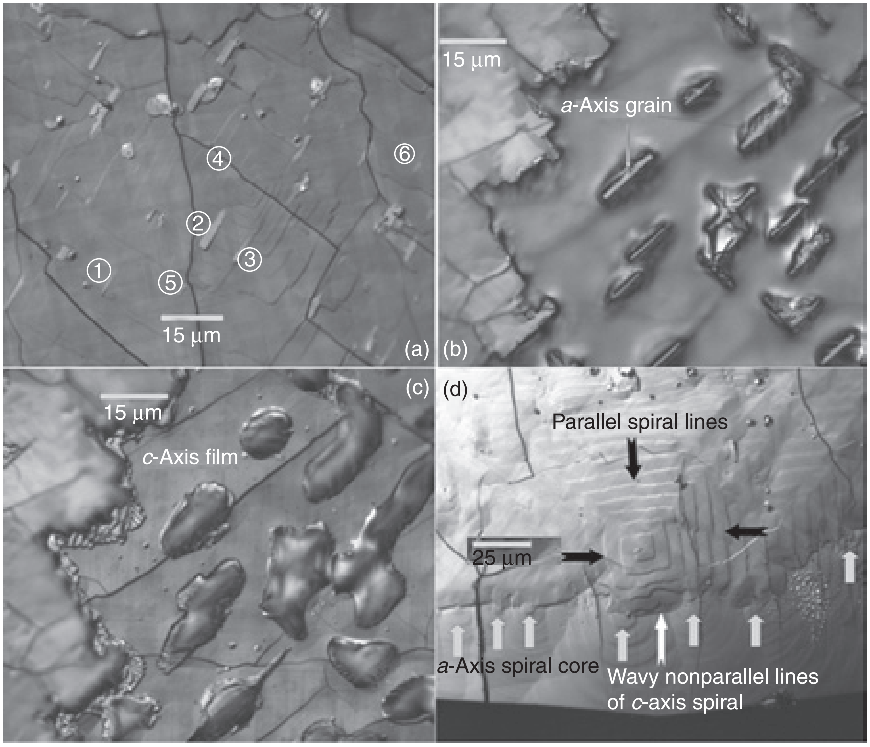

7.14 Morphology of different kinds of *a–c* grain boundaries on the (Y, Sm) BCO-LPE film. The growth parameters (temperature, Ba:Cu ratio, atmosphere) were: (a) 1037 °C, 3:5, O_2; (b, c) 1043 °C, 3:5, O_2; (d) 1020 °C, 3:5, air. The scale bar in (d) is different from the other three, because the picture was taken under a different magnification level.

the Y-Sm system. It may be helpful to understand the scenario according to the schematic illustration shown in Fig 7.15. Since the supersaturation is related to supercooling, the tendency of $\delta_A > \delta_B > \delta_C > \delta_D$ is clear, although we did not know the exact supersaturation. Thus, when supersaturation lies in region A or D, pure *a* or *c* growth can be obtained. While in region B, the *a*-axis grains grow over the *c*-axis ones because the growth rate of *a*-oriented grains is higher than that of *c*-oriented ones. Henceforward, this kind of growth mode is defined as the α-mode. On the other hand, the β-mode was denoted when supersaturation was set into region C, in other words, the *a*- and *c*-oriented grains had similar growth rates. The differences between the two modes are demonstrated in Fig 7.16. When films grow in the α-mode because of the high growth rate of *a*-axis grains, the standing ones disturb the solvent convection, leaving the space filled with a trapped flux instead of forming an *a*/*c* boundary. In contrast, the nutrient flow can easily reach

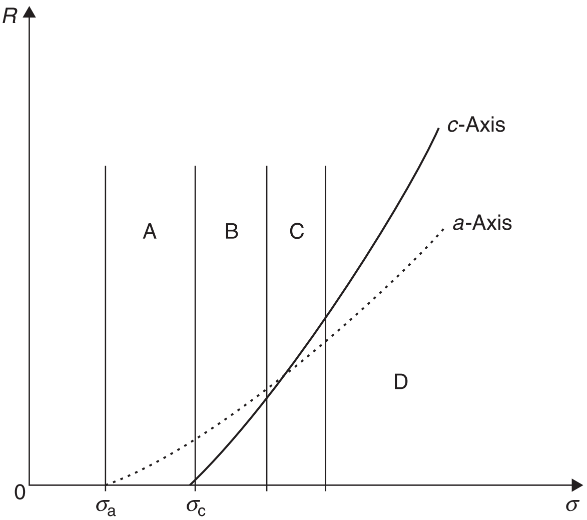

7.15 A schematic grain growth rate diagram, *R* vs supersaturation. The *y*-axis represents the growth rate (*R*), the *x*-axis represents the supersaturation (σ).

the growth frontier when growing in the β-mode. As a result, a fine *a*/*c* mixed structure can be obtained as presented in Fig 7.14(a) and (d). Note that the grains orientation is very sensitive to growth conditions, which lead to an extraordinarily narrow growth window for a fine *a*/*c* mixed structure.

What is important is that the combination between the *a*/*c* axis boundaries is believed to be very tight. Additionally, the *a*-axis grains are coherently oriented due to the differences of lattice constant between the *a*-axis grain and the substrate,[36] which will not prevent the flow of current since the current may flow along the long axes of *a*-oriented grains. These make the *a*/*c* mixed structure an effective pinning centre which can improve the properties of a superconductor in the field.

7.3.3 The thermal stability of REBCO films

Recently, the superheating phenomenon has been of great concern. If heterogeneous nucleation at free interfaces or grain boundaries is suppressed, crystals could be superheated above their equilibrium melting points, which was the so-called superheating.[28,37–39]

In 1986, the superheating phenomenon was first reported by Daeges *et al.*[28] in the Ag system, and in 2000, superheating in trapped Pb two-dimensional film was found by Zhang *et al.*[34] and a new superheating mode was established. But the research above were limited to the metal or its alloy materials until the discovery

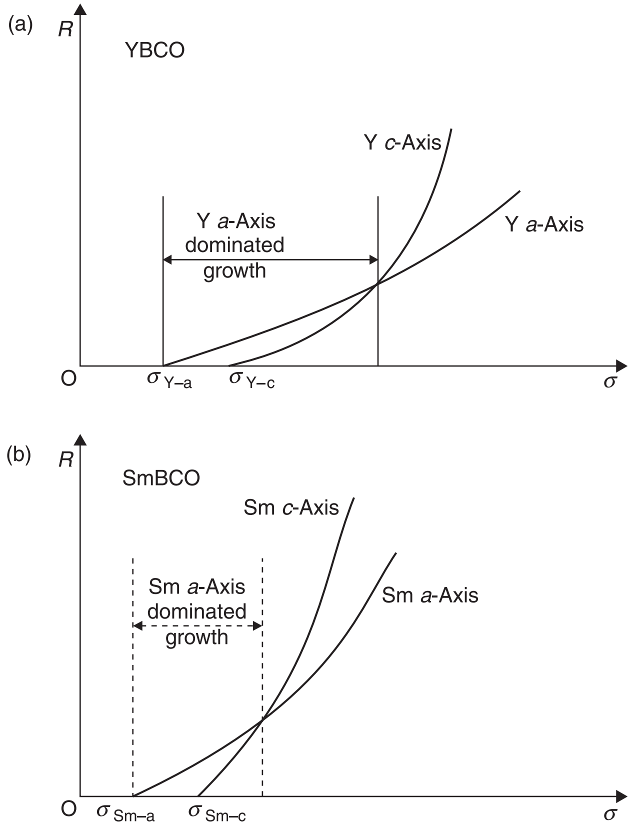

7.16 Schematic illustration of the differences in the LPE process in (a) YBCO and (b) SmBCO. The *y*-axis represents the growth rate (*R*), the *x*-axis represents the supersaturation (σ).

of the superheating phenomenon in YBCO/MgO thin film in the YSNG (YBCO seeded NdBCO growth by LPE).[35,40] The most important criterion of the hetero-seed growth is that the seed material should have a higher melting temperature than the processing one. While in this instance the behavior is plainly opposite to the general conception, this so-called hetero-seeded growth can be extended to a wider application, not only suitable for all REBCO and mixed REBCO systems, but also for other seed-required HTS processes. The application of superheating in acquiring superconductor materials attracts much interest.

The mechanism of hetero-seed LPE growth using YBCO-thin-film as a seed

In order to study the mechanism of YSNG, a vertically-dipping experiment[35,41] was conducted with a continuous traveling mode. Figure 7.17 shows an optical micrograph of a vertically-dipped LPE specimen in the undipped region with an

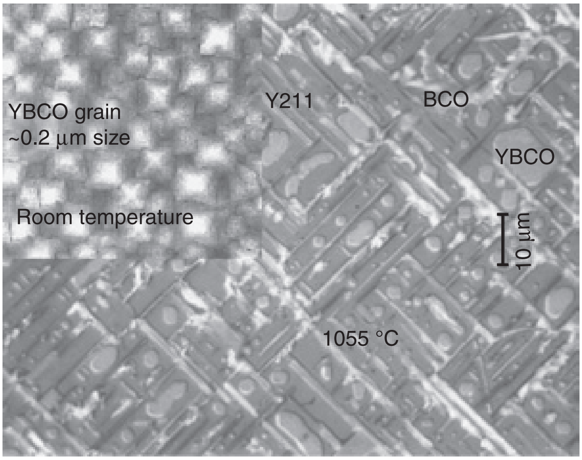

7.17 An optical micrograph showing microstructures of a vertically-dipped specimen in the undipped region with an AFM image showing YBCO seed-film structure on the upper left side.

AFM image of the vapor-deposited YBCO-seed on the upper left side. When the specimen was put into the liquid, the YBCO grains underwent heating from room temperature to 1055 °C, which is higher than the peritectic temperature (~1010 °C) of YBCO, and became thermodynamically unstable. Consequently, Y211 grains and solidified Ba-Cu-O (BCO) melts can be observed, which are the products of the YBCO decomposition. Needle-shaped Y211 grains with the *c*-axis in a long length direction[42] are well aligned on the MgO substrate due to a good lattice matching. On the other hand, the undecomposed YBCO particles are clearly visible, implying a superheating phenomenon since they endured a higher processing temperature than the T_p of YBCO. The epitaxial relation between YBCO and NdBCO grains can be confirmed. First, NdBCO grains morphologically exhibit a squared shape, indicating the 0°-oriented NdBCO grain on the MgO substrate, which behaves the same as the YBCO seed-grain on MgO. Secondly, the EPMA mapping analysis was used to determine the Y and Nd distribution near the dipping boundary. It was found that there are Yttrium-segregated regions close to the boundary in the dipped side. These concentrated-Y regions are visible only and exactly underneath the initially grown NdBCO grains as displayed in Fig. 7.18. All information suggests that these Y-segregated regions are previous YBCO grains, which act as hetero-seeds for the growth of NdBCO grains. This confirmed existence of the Y element from the initially grown NdBCO grains provides direct evidence that NdBCO-LPE films could grow from YBCO film-seeds at a higher processing temperature than the T_p of YBCO.

Additionally, the YBCO-thin-film seeded LPE thick-film growth also succeeded in other systems, including: SmBCO (T_g: 1020~1057 °C); and mixed

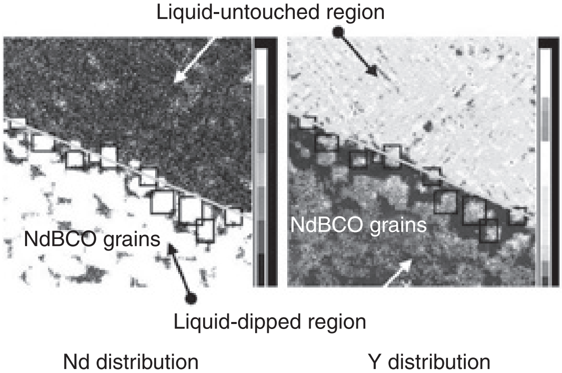

7.18 EPMA mapping images showing Y and Nd distributions at the boundary between the undipped region on the top and the dipped region on the bottom.

RE123 systems of Ni-NdBCO (T_g: ~1057 °C), Sr-NdBCO (T_g: ~1057 °C), Nd-YBCO (T_g: 1000~1030 °C), Yb-YBCO (T_g: 970~980 °C), Ca-YBCO (T_g: 957~980 °C) and Zn-YBCO (T_g: 966~984 °C). In those REBCO LPE processes, YBCO film became universal seeds. It should be pointed out that a severe dissolution of YBCO seed grains may take place when a high processing temperature and a non-Y liquid were used. In contrast, the YBCO hetero-seed produces insignificant seed dissolution when a low processing temperature (lower than the T_p of YBCO) and a Y-saturated liquid were employed.

The mechanism of the high stability of YBCO thin film

To understand the superheating mechanism of YBCO thin films, the melting process of the films was observed by high-temperature optical microscopy (HTOM), which offered a direct proof of the high thermal stability of YBCO thin films. It was found that the YBCO/MgO thin film can be substantially superheated above the peritectic temperature of YBCO (at least 50 °C) for 3 min at a heating rate of 5 °C/min to 1060 °C,[40] as shown in Fig. 7.19. Three factors have been mainly considered to explain this superheating phenomenon. First, the film was *c*-oriented. It is well known that due to the anisotropy of the YBCO crystals, the lowest-energy (001) free surface plays an important role in the superheating phenomenon of YBCO film. Secondly, the semi-coherent bonding suppresses the heterogeneous melting nucleation at the interface, leading to a low-energy interface between them. Thirdly, the Ba-Cu-O liquid wets neither the parent phase of Y123 nor the MgO substrate, which causes a liquid migration from the melting front. A continuous driving force for nucleation of melting is required after the Ba-Cu-O liquid migrates away. Moreover, a locally low temperature region was

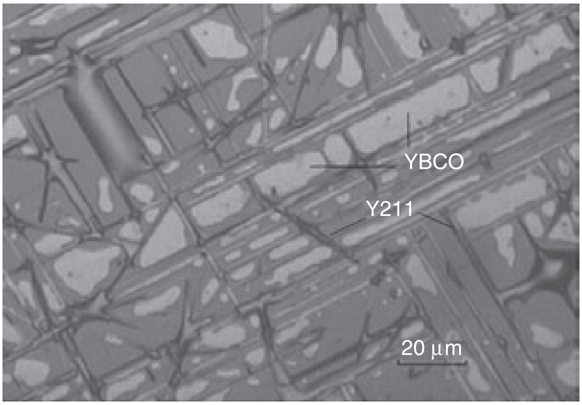

7.19 An optical microscope showing microstructure of a sample at 1060 °C for 3 minutes.

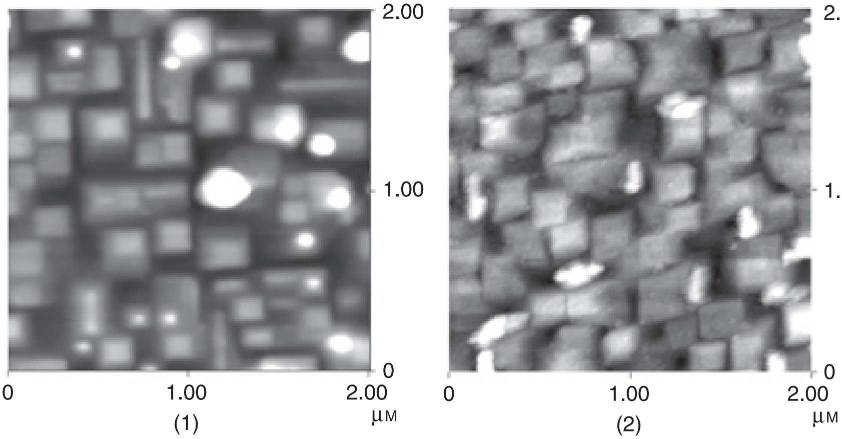

(1) (2)

7.20 AFM images presenting the microstructures of YBCO thin films: (1) sample A; (2) sample B.

induced owing to the endothermic reaction of Y123 melting. In brief, all the above-mentioned three points may cause a delay to melting.

Besides, further studies of *in situ* observation of the melting process of YBCO thin films with different microstructures and crystallinity were taken to have more insights into the high thermal stability of YBCO. The *c*-axis films were denoted as A and B according to their degree of crystallinity. As illustrated in Fig. 7.20, the YBCO grains in film A have a relatively regular square shape, while the shape of the grains in film B are twisted. Besides, the *a*-axis oriented YBCO grains are only visible in film A. As can be seen in Fig. 7.21, the two films exhibited different evolutions in their melting progresses. Furthermore, film A can be superheated up

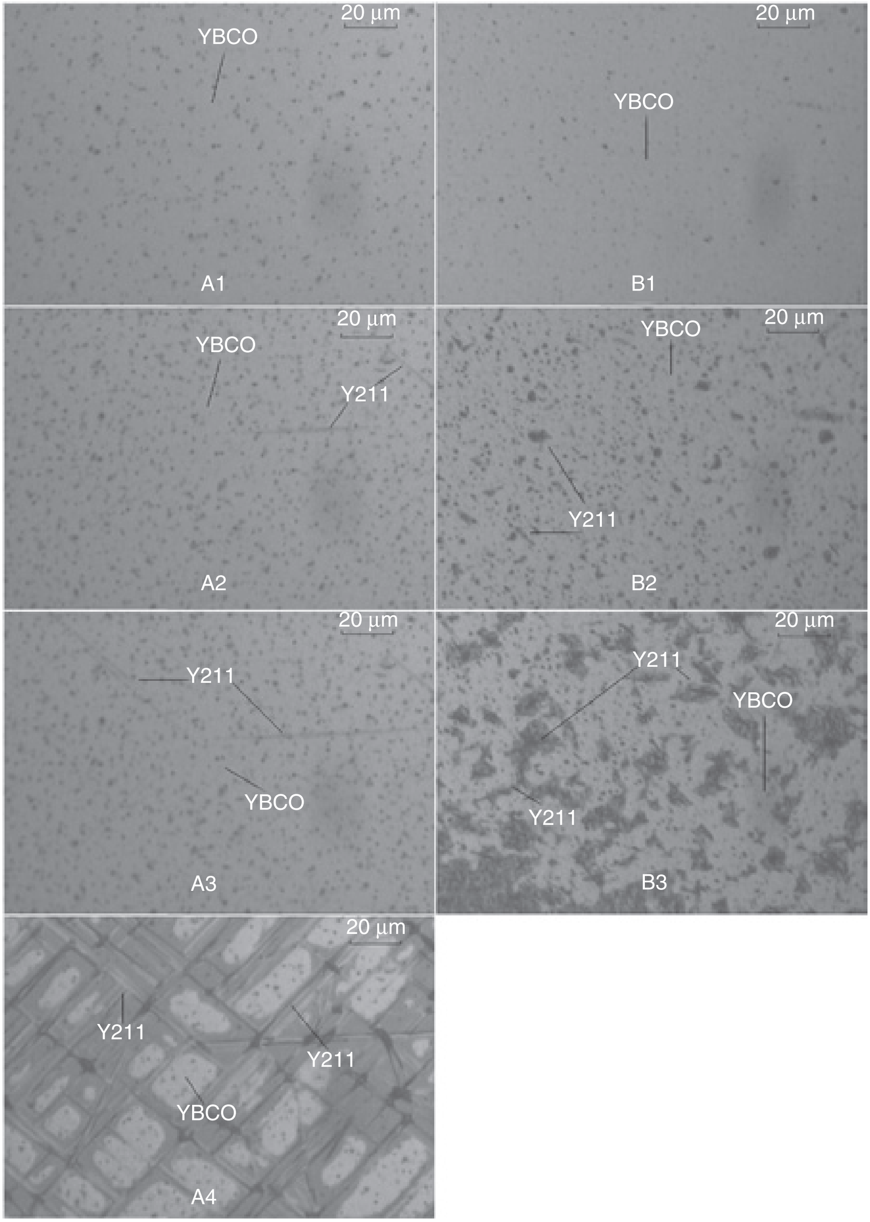
20 μm
YBCO
A1
20 μm
YBCO
B1
20 μm
YBCO
Y211
A2
YBCO
20 μm
Y211
B2
20 μm
Y211
YBCO
A3
20 μm
Y211
YBCO
Y211
B3
20 μm
Y211
Y211
YBCO
A4

7.21 A comparison of the surface microstructures between two samples, A and B, at the consistent temperatures shown in two groups of optical micrographs. (1) 1010 °C for 3 min; (2) 1050 °C for 3 min; (3) 1060 °C for 0 min; (4) 1060 °C for 3 min (there is no Y123 left in sample B when reaching 1060 °C; thus, the image is absent).

to a higher temperature than that of film B. These experimental results can be explained as below. First, the *a*-axis oriented YBCO grain has smaller misfit than the *c*-axis oriented one. Therefore, the existence of *a*-axis oriented YBCO grains may relieve most of the stress energy, and also make the total system energy descend, which indicates that film A has a lower energy film/substrate interface than that in film B. Additionally, in terms of the semi-coherent interface energy theory, the semi-coherent interface is divided into coherent regions and defect regions. The total interface energy is proportional to the area fraction of the interfacial defects.[43] As a consequence, the semi-coherent interface in sample A is more stable, leading to the higher superheating level of the YBCO grains on film A from a thermodynamic perspective. In brief, the thermal stability and melting behaviors rely highly on microstructures and crystallinity of YBCO thin films.

The correlation between thermal stability and in-plane alignments of films

In order to study the relationship of the thermal stability of REBCO films with in-plane alignments, the melting behaviors of YBCO thin films denoted as C and D with different in-plane orientations were compared and discussed on the grounds of interface energy. The XRD results represent that both 0° and 45° Y123 grains exist in film C, which means a weak epitaxial interface. On the other hand, a fourfold symmetry indicates that only 0° oriented YBCO grains exist in film D, which exhibits a semi-coherent interface at the film/substrate interface. By means of HTOM, great differences were found between the melting behaviors of two films. First of all, the melting of film C began at a temperature 40 °C lower than the T_p of Y123, which is 60 °C lower compared with that of film D. Secondly, the amount of Y211 appeared in film D is much smaller than that of film C at the very beginning of melting. However, a clear growth of Y211 was evident when the heating temperature increased, while film C stayed uniform. What is more, a similar enlarging process was observed in the size of Y211. Besides, the grains with 0° (Y211 < 001 > // MgO < 100 >) and 45° (Y211 < 001 > // MgO < 110 >) orientation appeared simultaneously on film C whereas on sample D most Y211 grains had 45° orientation, which is known as the preferential growth orientation of Y211 on the MgO substrate.[40]

From the viewpoint of interface energy, the different melting mode of the two films can be elucidated. For film C, the weak epitaxial interface implies the existence of additional defects and grain boundaries, which stores a large excess energy and constitutes an extra driving force for the melting, leading to a decrease of the initial melting temperature. Besides, the nucleation and growth of Y211 grains were also encouraged due to the high-energy interface. As for film D, a semi-coherent interface plays an important role in understanding the melting behavior. It is well known that the energy of coherent and semi-coherent interfaces is significantly lower than that of non-coherent ones.[44] Meanwhile, the nucleation of melting requires a sufficiently large driving force. These two points result in the decomposition of Y123 at a temperature higher than the T_p. Moreover, the semi-coherent interface forms barriers against the growth of melt as well. Additionally, and different from film C, 45° grains occupied the majority of the Y211 population at the outset of melting in film D, which gives one more evidence of the suppression of melt growth on the grounds that the 45° orientation growth requests the minimum energy supply. Zhang *et al.* [34] suggested that the nucleation of melting could not be prevented and the superheating was due to the suppression of melting growth. As explained above, a sketch map of the melting process of the two films can be given, as represented in Fig. 7.22.

As a result, it can be inferred that a fine epitaxial confinement restrains both the melting nucleation and growth, while a partly epitaxial interface only delays the melting growth. In short, a fine in-plane alignment, with lowered interface energy, could be an obstacle against melting/decomposion.

7.3.4 The in-plane alignment transformation on REBCO-LPE films

In addition to the control of out-of-plane crystalline orientation, perfect in-plane texture of REBCO films is also important for obtaining superior superconducting performance. Taking YBCO for instance, there are two main in-plane alignments: 0° (Y123 < 100 > // MgO < 100 >) and 45° (Y123 < 100 > // MgO < 110 >) (Fig. 7.23). It was reported that a YBCO film on MgO substrate with 5% of its grains rotated 45° with respect to the prevailing alignment, had critical current density (J_c) reduced by 75% compared to the one with no 45° grain boundaries.[45] Actually, it was difficult to achieve some specific in-plane alignments of the transporting layer, especially the in-plane alignment of 45°. Consequently, the investigation on the stability among the grains with different in-plane orientations is essential. Up to the present, there have been many studies regarding the preferential growth mechanism of YBCO crystals on the MgO substrates in the LPE growth under various oxygen partial pressures (PO_2).

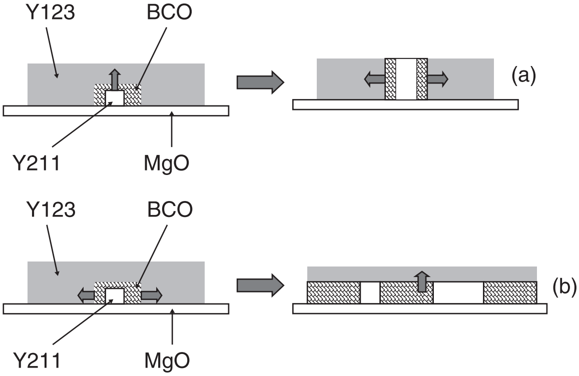

7.22 A sketch map of the melting process of films (a) and (b).

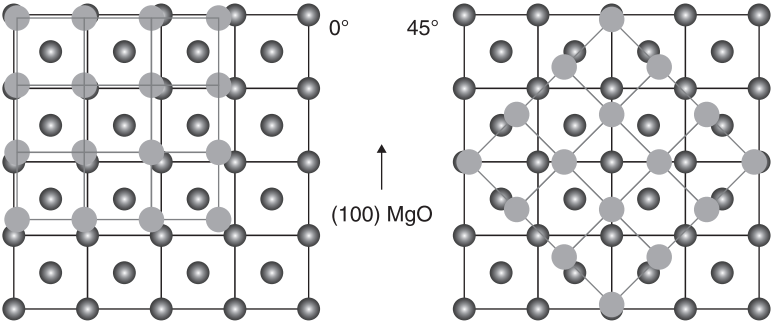

7.23 The two kinds of prevailing in-plane orientation of YBCO grains in (100) MgO substrates: 0° and 45°.

The preferential growth of 0° grain

As a rule, a polycrystalline seed YBCO film with an eightfold symmetry resulted in a LPE film with a fourfold symmetry of 0° in the air atmosphere condition, which was called the preferential growth of 0° grains. The grains orientation of in-plane texture was improved in the LPE process, which should be attributed to the preferential dissolution of the so-called 45° YBCO grains. The coarsening model was proposed to interpret this in terms of lattice matching and bonding energy at the interface between YBCO and MgO substrate.[46]

Y solute will dissolve from the unstable grain to the stable one, leading to the disappearance of the unstable grains and the growing of the stable ones. It was supposed that the sizes of 45° and 0° grain are almost the same, in other words, the curvature effect can be ignored. Therefore, the difference in the interface energy should be taken into consideration, which can be regarded as the enthalpy difference. The undercooling of the Y123 grains on the MgO substrate can be expressed by the following equation:

$$\Delta T = \left(\frac{\Delta H'_m - \Delta H_m}{\Delta H_m}\right) T_m \qquad [7.3]$$

In this equation, ΔH_m, $\Delta H'_m$ and T_m are the change of the enthalpy for the melting of Y123 grains without the MgO substrate, the change of the enthalpy for the melting of Y123 with the MgO substrate and the melting point of Y123 grain without the MgO substrate, respectively. Because of the bonding energy difference with the MgO substrate, $\Delta H'_m$ of the 0° grain is different from that of the 45° grain, resulting in a difference in undercooling between the two kinds of grains, which can be regarded as another driving force. Consequently, the interfacial structure of YBCO/MgO is focused when studying the phenomenon of preferential growth, since the bonding energy between the REBCO grains and the MgO substrate strongly depends on their crystallographic relationship (lattice matching). The coincidence of reciprocal lattice points (CRLPs)[47] and the near coincidence site lattice theory (NCSL)[48] was adopted to evaluate the lattice matching of the REBCO and MgO at the growth temperature. It indicated that 0° in-plane alignment has the highest stability, followed by 45° in-plane texture. Normura *et al.*[8,49] introduced the Coulomb force as another factor for the bonding energy. In the case of YBCO, the attraction exists at both 0° and 45° orientations and the magnitude of the attraction at 0° orientation is larger than that at 45° orientation.

In short, both the lattice matching and the Coulomb force between the REBCO and the MgO crystal are consistent with the preferential growth of 0° in-plane alignment under the air atmosphere.

The preferential growth of 45° grain

The preferential growth we have discussed before is in the air condition, but the in-plane orientation on LPE film was completely different when the environment was changed to a pure oxygen atmosphere. In that case, it was reported that the 45° oriented LPE film was obtained when using the eightfold symmetry YBCO thin film as the seed film.

As shown in Fig. 7.24, a typical surface morphology of the as-grown LPE film can be observed. Moreover, the [100] axis of MgO substrate is parallel to the

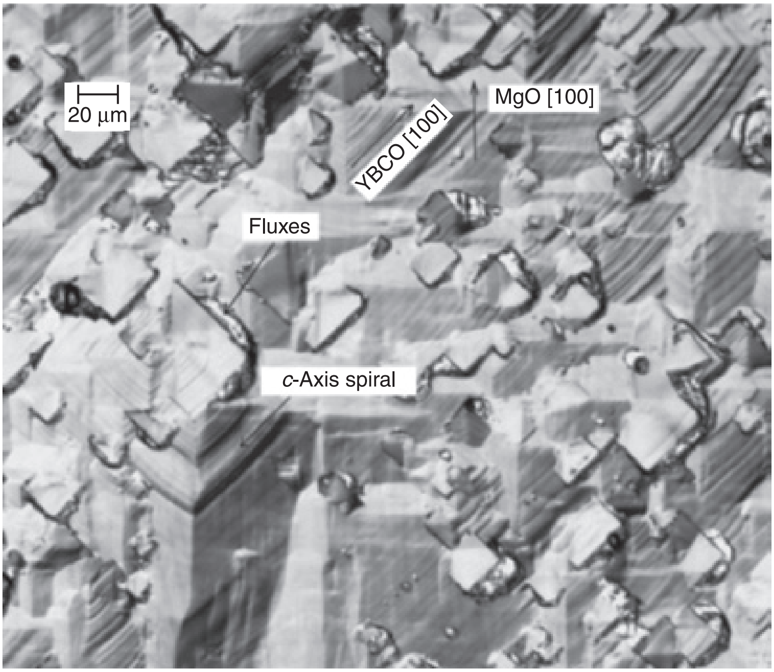

7.24 The optical micrograph of as-grown 45°-oriented YBCO-LPE film, in which the 45°-oriented growth hillocks are distinct.

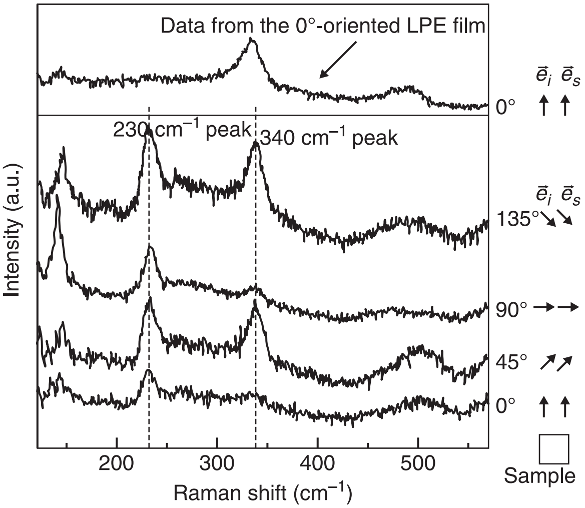

7.25 The Raman spectrum of the 45°-oriented YBCO-LPE film. The angle between the polarization orientation (e_i,e_s) and the (100) axis of the MgO substrate is 0°, 45°, 90°, and 135°, respectively. In the upper inset, the Raman spectrum of typical 0°-oriented LPE film is presented to make a comparison, when the polarization orientation ($\vec{e}_i$, $\vec{e}_s$) was chosen to be parallel to the (100) axis of the MgO substrate.

[110] axis of YBCO crystal. It is obvious that a 45° in-plane alignment is favorable under a pure oxygen atmosphere. On the second affirmance, Raman scattering was employed to detect the in-plane texture of the grown LPE sample. As presented in Fig. 7.25, the peaks around 340 cm^{-1} almost vanish when the polarization orientation $\vec{e}_i$, $\vec{e}_s$ were parallel to the [100] axis of MgO substrate, but reach maximum value when $\vec{e}_i$, $\vec{e}_s$ were parallel to the MgO [110] orientation. The appearance of a group of strong peaks around 230 cm^{-1} was of note, which implies that during the LPE process, the YBCO layer may undergo specific transformation in microstructure. One possibility is an indication of 'chain fragments'. It was reported that the strong peak at 230 cm^{-1} was attributed to vibrations at the end of Cu-O chain fragments,[22,50] which is a probe of the discontinuous degree of the Cu-O chain. In other words, it is a representation of broken Cu-O chain structures on either a macroscopic or microscopic scale, which can be the evidence of poor grain connectivity. Obviously, 0° and 45° seed grains suffered different evolutions during LPE: 45° grains kept growing and coalesced into the film while 0° grains dissolved into the liquid phase.

Similar to section 7.3.1, the initial evolution of the YBCO LPE growth was investigated. In Fig. 7.26, the optical and SEM micrograph of the area around the boundary line is shown, which is considered to nearly undergo a 3s dipping time. At the very beginning, small 45° grains formed and partly joined to form a smooth

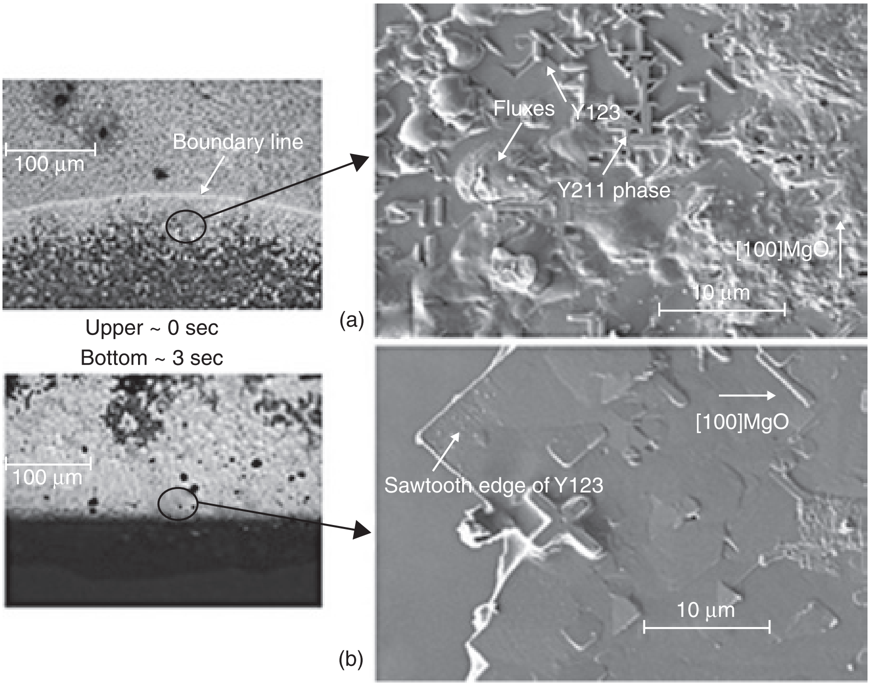

7.26 The optical and SEM images of the vertical dipping region of the YBCO-LPE film under a pure oxygen atmosphere. In the left inset, the upper optical micrograph shows a general view around the dipping boundary line; (a) shows the corresponding SEM image. The lower optical micrograph shows the bottom dipping region which underwent a growth time of 3 s; (b) shows the amplified SEM image.

region. Nevertheless, the existence of entrapped fluxes and the Y211 phase holds back the coalescence of these 45° islands. On the other hand, the superior grain connectivity appeared in the initial stage of 0° oriented YBCO thick films.

The preferential growth phenomenon shows a great difference in the solid solution REBCO systems, since NdBCOs and SmBCOs always exhibit dissimilar properties with YBCO in many aspects due to the divergent atomic radius and being a solid solution. Taking NdBCO for instance, the result of in-plane orientation measurement of the NdBCO thick film obtained by using a polycrystalline NdBCO/MgO seed film in air is consistent with that of YBCO-LPE film grown in pure oxygen condition.[44] The initial growth of 45° NdBCO-LPE film is investigated as well. In addition, the poor grain connectivity was also found at the very beginning of the LPE process. These similarities might indicate some common features. As mentioned above, CRLP calculation was adopted to evaluate the geometrical coherency for the RE123/MgO system, which indicated that 45° in-plane texture has lower stability in terms of the geometrical lattice matching, not only in the YBCO system but also in the NdBCO system, which is in opposition to the results of LPE. Therefore, there must be other factors to account for these abnormalities.

Both surface and interface energy should be taken into consideration to evaluate the stability of epitaxial grains.[51] It is well known that the change of in-plane alignment shows no difference in the surface energy, and the terminal layer of atoms between the epitaxial film and the substrate is important to estimate the energy at the whole interface. The results reported by Matsuda *et al.*[47] indicate that YBCO films are terminated by BaO layers and NdBCO films by CuO chain layers. The detailed atomic arrangements are illustrated in Fig. 7.27, from which we can see that the formation of the BaO bottom layer in (a) corresponds to an equivalent cut on the *c*-axis YBCO block between BaO and CuO_2 layers, while the condition of the CuO bottom layer in (b) means a cut between the CuO and BaO layers. It is well known that the formation of a more stable interface corresponds to a lower energy cut. In this regard, Granozio *et al.*[52] pointed out that the minimum energy cut of YBCO along the *c*-axis orientation corresponds to the interface between the BaO and the CuO_2 layers under an oxygen deficient status, while the minimum energy cut is between the CuO layer and the BaO layer when oxygen is saturated. Consequently, it can be deduced that in the air growth condition, 0° YBCO films are in the oxygen deficient status, while 45° NdBCO

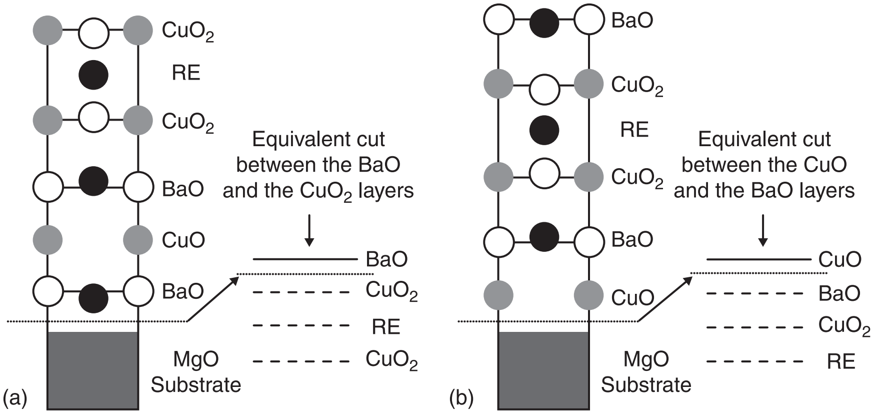

7.27 A schematic illustration of the atomic configuration around the REBCO/MgO interface and corresponding equivalent cut. (a) The YBCO film grown under the air condition. (b) The NdBCO film grown under the air condition or the YBCO film grown under the pure oxygen atmosphere. In our experiments, the LPE growth of NdBCO film was carried out in the air and the terminal plane in the interface of NdBCO film was thought to be similar to that of YBCO film grown in pure oxygen.

films correspond to the oxygen saturated status. Besides that, the 45°-oriented YBCO seed grains should have the same terminal plane with 45° NdBCO films, owing to those properties they exhibited in common. In addition, a series of comparisons among these three cases is listed in Table 7.4.

Moreover, Fig. 7.28 presents another kind of interface feature in the 45° YBCO film. Figure 7.28(b) identifies two unexpected rows of atoms between MgO and the BaO-CuO-BaO blocks of Y123, which do not belong to Cu-O chain. Afrosimov *et al.*[53] pointed out the possibility of occurrence of additional protoxide composition Cu_2O at the YBCO/MgO interface and that the atoms are not located right above the Mg atoms but are shifted by about 0.21 nm along [100] MgO, which is in good agreement with the crystal structure of Cu_2O.[54] From this we deduce that these arrays are comprised of Cu_2O. The existence of the Cu_2O intermediate layer is a new kind of interfacial structure in 45° grains, which belongs neither to Y123 lattice nor to the MgO substrate. Therefore, the influence of this middle layer on the preferential growth of 45° grains should be considered. Foremost, its decomposition temperature may directly influence the thermal stability of seed grains. From the chemical phase diagram it follows that the melting point of Cu_2O increases with the rise of oxygen partial pressure.[55] So the possible situation is: in air the T_c of the incomplete Cu_2O lattice is lower than of Y123, so it negatively affects stability of the 45° YBCO seed grains; while in oxygen, the situation runs in the opposite direction. The different interfacial

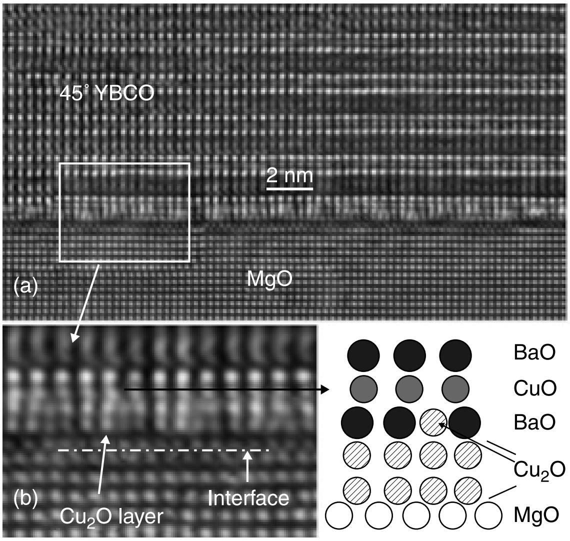

7.28 (a) HRTEM image taken near the interface between 45° YBCO film and MgO substrate. (b) The blow-up indicates the detailed structure including an inserted Cu_2O layer and an interstitial Cu atom.

Table 7.4 A comprehensive comparison among three experimental systems: YBCO film grown in the air, NdBCO film grown in the air, and YBCO film grown in pure oxygen

Polycrystalline seed film on MgO	Environment	In-plane orientation	Geometry coherency	Raman peak at 230 cm^{-1}	Islands grown at initial stage	Terminal plane	Oxygen content	Minimum energy cut along the ⟨001⟩ axis
$YBa_2Cu_3O_x$	Air	0°	Better	No	Coalesced	Ba-O	Deficient	Between BaO/CuO_2
$Nd_{1+x}Ba_{2-x}Cu_3O_Z$	Air	45°	Worse		Isolated	Cu-O	Saturated[a]	Between CuO/BaO
$YBa_2Cu_3O_y$	Pure oxygen	45°	Worse	Yes	Isolated	Cu-O[b]	Saturated	Between CuO/BaO

[a] Here the evaluation of oxygen content status is relatively saturated when compared with the case of YBCO grown in air.

[b] This hypothetical interface condition is deduced from the NdBCO case due to many similar properties they have shown.

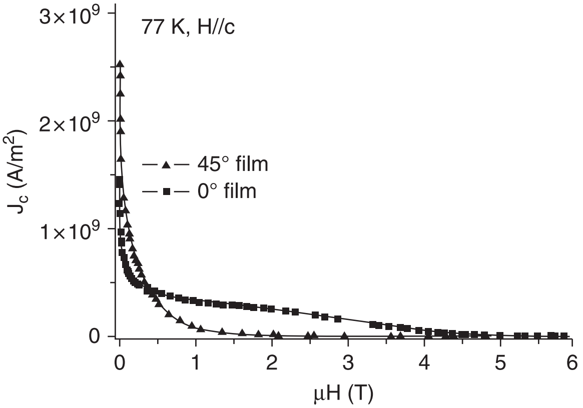

7.29 Field dependence of J_c at 77 K of YBCO-LPE films with pure 45° and 0° in-plane orientation.

configuration in 0° and 45° oriented YBCO films is thus considered to be responsible for their different stability.

Furthermore, the special interfacial configuration of 45° oriented YBCO films may draw into the pinning centre and lead to an increase in the value of J_c. Field dependence of critical current density of the LPE YBCO films with pure 0° and 45° in-plane orientation was deduced from the inductively measured M-H curves. As shown in Fig. 7.29, the remnant J_c (J_{c0}) of the 45° film was approximately 2.5×10^9 A/m^2, nearly 2 times higher than in the 0° film, 1.45×10^9 A/m^2. It resembles a similar J_{c0} data difference in the 0° and 45° YBCO-pulsed laser deposition thin films. It may be caused by the different structures of the interfacial atoms.

To sum up, the transformation and its mechanism of the in-plane alignment of REBCO-LPE film in different growth atmosphere have been presented, which are strongly related to the microstructure of the interface.

7.4 Conclusion

The field of REBCO-HTS films grown by the liquid phase epitaxy is introduced in this chapter, which are most promising for electronic device and coated conductor applications. Recent progresses achieved and the problems to be solved have been briefly described. Several points are focused on and discussed:

1 The chemical reactions between both the substrate and the LPE films and the crucible and solvent.
2 The oriented growth control of both out-of-plane and in-plane alignment, as well as their transition mechanism related to thermodynamic and kinetic factors.
3 Some new results such as broadening the growth window for gaining *a*-axis REBCO films by raising oxygen partial pressure; gaining well-distributed *a*/*c*

boundaries in a *c*-oriented film with highly-aligned *a*-oriented grains for potential pinning.

4 Superheating effect of YBCO thin films and its role in REBCO LPE growth as a universal seed; the correlation between the thermal stability and the YBCO films quality: including microstructure, crystallinity and orientation.

7.5 References

1 Klemenz, C., Scheel, H.J. (1993). Liquid phase epitaxy of high-Tc superconductors. *J. Cryst. Growth,* **129**(3–4), 421–428.

2 Scheel, H.J., Klemenz, C., Reinhart, F.K., Lang, H.P., Guntherodt, H.J. (1994). Monosteps on extremely flat $YBa_2Cu_3O_{7-x}$ surfaces grown by liquid-phase epitaxy. *Appl. Phys. Lett*, **65**(7), 901–903.

3 Yoshida, M., Nakamoto, T., Kitamura, T., Hyun, O.B., Hirabayashi I., *et al.* (1994). Critical currents of $YBa_2Cu_3O_y$ thick films prepared by liquid phase epitaxial growth. *Appl. Phys. Lett*, **65**(13), 1714–1716.

4 Scheel, H.J. (1994), *Mater. Res. Bull.,* **19**, 26.

5 Miura, S., Hashimoto, K., Wang, F., Enomoto, Y., Morishita, T. (1997). Structural and electrical properties of liquid phase epitaxially grown $Y_1Ba_2Cu_3O_x$ films. *Physica C*, **278**(3–4), 201–206.

6 Takagi, A., Wen, J.-G., Hirabayashi, I., Mizutani, U. (1998). Growth mode dependence of microstructures and superconducting properties of $Nd_{1+x}Ba_{2-X}Cu_3O_y$ thick films prepared by liquid-phase epitaxy. *J. Cryst. Growth*, **193**(1–2), 71–79.

7 Yamada, Y. (2000). Liquid-phase epitaxy processing of $RBa_2Cu_3O_{7-\delta}$. *Supercond. Sci. Technol*, **13**(1), 82–87.

8 Nomura, K., Hoshi, S., Yao, X., Nakamura, Y., Izumi, T., *et al*. (2001). Preferential growth mechanism of $REBa_2Cu_3O_y$ (RE = Y, Nd) crystal on MgO substrate by liquid phase epitaxy. *J. Mater. Res.*, **16**(4), 979–989.

9 Frank, F.C. (1949). The influence of dislocations on crystal growth. *Discuss. Faraday Soc.,* **5**, 48.

10 Elwell, D., Scheel, H.J. (1975). *Crystal Growth from High-Temperature Solutions*. Academic Press, London, p.146 ch.6.

11 Grabow, M.H., Gilmer, G.H. (1988). Thin film growth modes, wetting and cluster nucleation. *Surf. Sci.*, **194**(3), 333–346.

12 Yao, X., Nomura, K., Yoshizumi, M., Kuznetsov, M., Nakamura, Y., *et al.* (2001). Superconducting transition temperature of NdBCO liquid phase epitaxy film on MgO substrate and effect of Mg diffusion. *Physica C*, **357–360**(Suppl. 1), 1059–1062.

13 Kakimoto, K., Sugawara, Y., Izumi, T., Shiohara, Y. (2000). Initial growth mechanism of YBCO films in liquid phase epitaxy process. *Physica C: Superconductivity and its Applications*, **334**(3), 249–258.

14 Gornert, P. (1997). Crystal growth and crystalline layers of high temperature superconductors: Characterization and application. *Cryst. Res. Technol.*, **32**(1), 7–33.

15 Krauns, Ch., Tagami, M., Yamada, Y., Nakamura, M., Shiohara, Y. (1994). Wetting between prospective crucible materials and the Ba-Cu-O melt. *J. Mater. Res.*, **9**(6), 1513–1518.

16 Kanamori, Y., Shiohara, Y. (1996). Effect of temperature gradient in the solution on spiral growth of $YBa_2Cu_3O_{7-x}$ bulk single crystals. *J. Mater. Res.*, **11**(11), 2693–2697.

17 Erb, A., Biermath, T., MullerVogt, G. (1993). $YBa_2Cu_3O_{7-\delta}$-$BaCuO_2$-CuO: investigations on the phase diagram and growth of single crystals I. The system $BaCuO_2$-CuO_x. *J. Cryst. Growth.*, **132**(3–4), 389–395.

18 Erb, A., Walker, E., Flukiger, R. (1995). BaZrO3: the solution for the crucible corrosion problem during the single crystal growth of high-Tc superconductors $REBa_2Cu_3O_{7-\delta}$; RE = Y, Pr. *Physica C*, **245**(3–4), 245–251.

19 Tsuchiya, R., Kawasaki, M., Kubota, H., Nishino, J., Sato, H., *et al.* (1997). $YBa_2Cu_3O_{7-\delta}$ trilayer junction with nm thick $PrGaO_3$ barrier. *Appl. Phys. Lett.*, **71**(11), 1570–1572.

20 Kitamura, T., Yoshida, M., Yamada, Y., Shiohara, Y., Hirabayashi, I., *et al.* (1995). Crystalline orientation of $YBa_2Cu_3O_y$ film prepared by liquid-phase epitaxial growth on $NdGaO_3$ substrate. *Appl. Phys. Lett.*, **66**(11), 1421–1423.

21 Endo, T., Yoshii, K., Iwasaki, S., Kohmoto, H., Saratani, H. *et al.* (2003). Oxygen partial pressure dependences of a–c phase ratio, crystallinity, surface roughness and in-plane orientation in YBCO thin film depositions by IBS. *Supercond. Sci. Tech.*, **16**(1), 110–119.

22 Jee, Y.A., Li, M., Ma, B., Maroni, V.A., Fisher, B.L., *et al.* (2001). Comparison of texture development and superconducting properties of YBCO thin films prepared by TFA and PLD processes. *Physica C*, **356**(4), 297–303.

23 Mukaida, M., Miyazawa, S. (1993). Nature of preferred orientation of $YBa_2Cu_3O_x$ thin films. *Jpn. J. Appl. Phys.*, Part 1: Regular Papers and Short Notes and Review Papers, **32**(10), 4521–4528.

24 Homma, N., Okayama, S., Takahashi, H., Yoshida, I., Morishita, T., *et al.* (1991). Crystallinity of a-axis oriented $YBa_2Cu_3O_{7-\delta}$ thin film epitaxially grown on $NdGaO_3$ (110) by 95 MHz magnetron sputtering. *Appl. Phys. Lett.*, **59**(11), 1383–1385.

25 Feenstra, R., Lindemer, T.B., Budai, J.D., Galloway, M.D. (1991). Effect of oxygen pressure on the synthesis of $YBa_2Cu_3O_{7-x}$ thin films by post-deposition annealing. *J. Appl. Phys.*, **69**(9), 6569–6585.

26 Zhang, D.L., Cantor, B. (1991). elting behaviour of In and Pb particles embedded in an Al matrix. *Acta Metall. Mater.*, **39**(7), 1595–1602.

27 Qi, X., MacManus-Driscoll, J.L. (2001). Liquid phase epitaxy processing for high temperature superconductor tapes. *Current Opinion in Solid State and Materials Science,* **5**(4), 291–300.

28 Daeges, J., Gleiter, H., Perepezko, J.H. (1986). Superheating of metal crystals. *Phys. Lett. A*, **119**(2), 79–82.

29 Sudoh, K., Yoshida, Y., Takai, Y. (2003). Effect of deposition conditions and solid solution on the $Sm_{1+x}Ba_{2-x}Cu_3O_{6+\delta}$ thin films prepared by pulsed laser deposition. *Physica C*, **384**(1–2), 178–184.

30 Ramesh, R., Schlom, D.G. (2002). Orienting ferroelectric films. *Science*, **296**(5575), 1975–1976.

31 Kitamura, T., Yamada, Y., Shiohara, Y., Hirabayashi, I., Tanaka, S., *et al.* (1996). Growth mechanism and crystalline orientation of liquid-phase epitaxially grown $YBa_2Cu_3O_{7-y}$ films. *Appl. Phys. Lett.*, **68**(14), 2002–2004.

32 Aichele, T., Bornmann, S., Dubs, C., Gornert, P. (1997). Liquid Phase Epitaxy (LPE) of $YB_2Cu_3O_{7-\delta}$ high Tc superconductors. *Cryst. Res. Technol.*, **32**(8), 1145–1154.

33 Klemenz, C., Scheel, H.J. (1996). Flat $YBa_2Cu_3O_{7-x}$ layers for planar tunnel-device technology. *Physica C*, **265**(1–2), 126–134.

34 Zhang, L., Jin, Z.H., Zhang, L.H., Sui, M.L., Lu, K. (2000). Superheating of confined Pb thin films. *Phys. Rev. Lett.*, **85**(7), 1484.

35 Yao, X., Nomura, K., Huang, D.X., Izumi, T., Hobara, N., *et al*. (2002). $YBa_2Cu_3O_{7-\delta}$ thin-film-seeded $Nd_{1+x}Ba_{2-x}Cu_3O_{7-\delta}$ thick-film grown by liquid phase epitaxy. *Physica C*, **378–381**(Part 2), 1209–1212.

36 Utke, I., Klemenz, C., Scheel, H.J., Sasaura, M., Miyazawa, S. (1997). Misfit problems in epitaxy of high-Tc superconductors. *J. Cryst. Growth*, **174**(1–4), 806–812.

37 Cahn, R.W. (1986). Materials science: Melting and the surface. *Nature*, **323**(6090), 668–669.

38 Zhang D. L., Cantor B., *Acta Metall. Mater.* (1991), **39**, 1595.

39 Sheng, H.W., Ren, G., Peng, L.M., Hu, Z.Q., Lu, K. (1996). Superheating and melting-point depression of Pb nanoparticles embedded in Al matrices. *Phil. Mag. Lett.*, **73**(4), 179–186.

40 Huang, D.X., Yao, X., Nomura, K., Wu, Y., Nakamura, Y., *et al*. (2002). Mechanism of NdBCO film growth on YBCO-seeded MgO substrate using liquid phase epitaxy. *Physica C*: Superconductivity and its Applications, **378–381**(Part 2), 980–983.

41 Huang, D.X., Yao, X., Nomura, K., Wu, Y., Nakamura, Y., *et al*. (2002). Mechanism of liquid-phase epitaxy growth of $NdBa_2Cu_3O_{7-x}$ film from low-peritectic-temperature $YBa_2Cu_3O_{7-x}$ seed film. *J. Mater. Res.*, **17**(4), 747–754.

42 Yao, X., Nomura, K., Nakamura, Y., Izumi, T., Shiohara, Y. (2002). Growth mechanism of high peritectic temperature $Nd_{1+x}Ba_{2-x}Cu_3O_{7-\delta}$ thick film on low peritectic temperature $YBa_2Cu_3O_{7-\delta}$ seed film by liquid phase epitaxy. *J. Cryst. Growth*, **234**(4), 611–615.

43 Hu, J., Yao, X., Rao, Q.L. (2003). Real-time observation of the melting process of YBCO thin film on MgO substrate. *J. Phys.: Condens. Matter*, **15**(43), 7149–7154.

44 Gorbenko, O.Y., Samoilenkov, S.V., Graboy, I.E., Kaul, A.R. (2002). Epitaxial stabilization of oxides in thin films. *Chem. Mater.*, **14**(10), 4026–4043.

45 Kromann, R., *et al.* (1992). Relation between critical current densities and epitaxy of $YBa_2Cu_3O_7$ thin films on MgO(100) and $SrTiO_3$(100). *J. Appl. Phys.*, **71**(7), 3419–3426.

46 Izumi, T., Kakimoto, K., Nomura, K., Shiohara, Y. (2000). Preferential growth mechanism of YBCO film on MgO substrate in initial stage of LPE growth. *J. Cryst. Growth*, **219**(3), 228–236.

47 Matsuda, J.S., *et al.* (2004). Interfacial structures of Y123 and Nd123 films formed on MgO(001) substrates by liquid phase epitaxy. *J. Mater. Res.*, **19**(9), 2674–2682.

48 Hwang, D.M., *et al.* (1990). Application of a near coincidence site lattice theory to the orientations of $YBa_2Cu_3O_{7-x}$ grains on (001) MgO substrates. *Appl. Phys. Lett.*, **57**(16), 1690–1692.

49 Nomura, K., Hoshi, S., Yao, X., Kakimoto, K., Izumi, T., *et al.* (2001). Preferential growth of RE-Ba-Cu-O crystal by liquid phase epitaxy process. *J. Cryst. Growth*, **229**(1), 384–390.

50 Fainstein, A., Maiorov, B., Guimpel, J., Nieva, G., Osquiguil, E. (2000). Annealing disorder and photoinduced order of oxygen chains in detwinned $YBa_2Cu_3O_{6.65}$ single crystals probed by Raman scattering. *Phys. Rev. B*, **61**(6), 4298–4304.

51 Eom, C.B., Marshall, A.F., Laderman, S.S., Jacowitz, R.D., Geballe, T.H. (1990). Epitaxial and smooth films of a-axis $YBa_2Cu_3O_7$. *Science*, **249**(4976), 1549–1552.

52 Granozio, F.M., di Uccio U.S. (1997). Gibbs energy and growth habits of YBCO. *J. Alloy. Compd.*, **251**(1–2), 56–64.

53 Afrosimov, V.V., Il'in, R.N., Karmanenko, S.F., Melkov, A.A., Sakharov, V.I., *et al.* (2005). Evidence of multiphase nucleation in perovskite film growth on MgO substrate from medium energy ion scattering analysis: Example of YBaCuO and (Ba,Sr)TiO_3. *Thin Solid Films*, **492**(1–2), 146–152.
54 Wyckoff, R.W.G. (1988) *Crystal Structures,* 2nd ed., New York: Wiley Interscience Publishers, 1963. Reprinted by Krieger Publishing Company, Melbourne, FL, 1986.
55 Li, W.C. *et al.* (2001). *In Metallurgy and Material Physical Chemistry*, Metallurgical Industry: Beijing, China, Vol. 4, Chapter 3, pp. 51–53.

8

High-T_c Josephson junctions

P. SEIDEL, Friedrich-Schiller University Jena, Germany

Abstract: The Josephson effects describe the transfer of Cooper pairs and the coupling of the macroscopic wave functions between two superconductors via a weak link. Some of the dependencies of such junctions are strongly related to the fundamental flux quantum. This gives excellent possibilities for application in measurement science and electronics. Within this chapter the general properties of Josephson junctions are summarized with respect to the nature of the high-T_c superconductors. Preparation technologies and performance of different types of thin film Josephson are discussed in detail and selected examples of applications of such junctions are given.

Key words: Josephson effects, Josephson junctions, weak links, superconductor electronics, grain boundaries.

8.1 Introduction

8.1.1 Josephson effects

Many applications of superconducting materials are based on the Josephson effects which occur when two superconductors are weakly coupled. The Cooper pair systems of each of these superconductors are characterized by their wave function with an amplitude corresponding to the Cooper pair density and the quantum mechanical phase. If the coupling is strong both superconductors will have the same wave function, but if there is a weak interaction the two Cooper pair systems will only exchange phase information. One mechanism of such a coupling is realized if the two superconductors are coupled via a very thin insulating barrier (Fig. 8.1a). The quantum mechanical tunnelling effect leads to a tunnelling transfer of Cooper pairs which was theoretically predicted by Josephson (1962). He showed that there is a supracurrent I_s across the insulating barrier without a voltage difference between the superconducting electrodes (d.c. Josephson effect). This supracurrent (Josephson current) has a maximum value I_c which is called the critical current of the Josephson junction. The supracurrent depends on the phase difference φ between the Cooper pair wave functions of both superconducting electrodes. For tunnelling junctions with a small transmission coefficient of the insulating barrier there is a sinusoidal phase dependence resulting in the first Josephson equation

$$I_s = I_c \cdot \sin \varphi, \qquad [8.1]$$

with $\varphi = \varphi_1 - \varphi_2$.

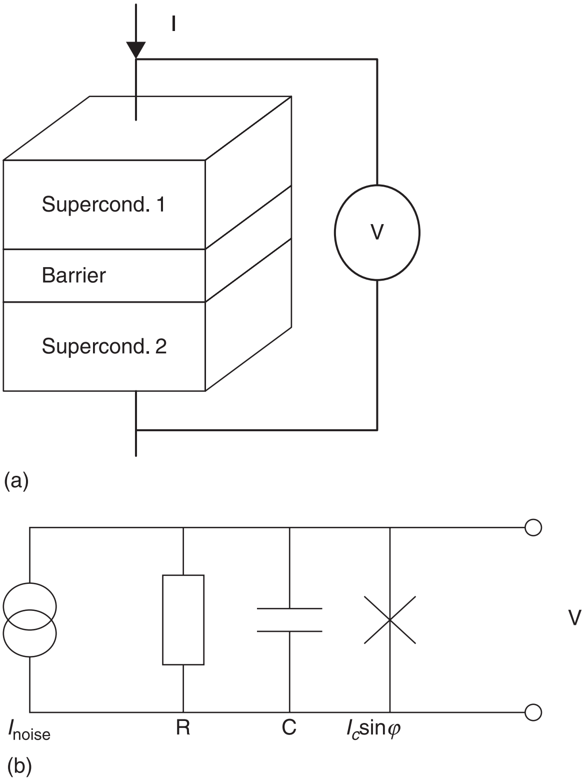

8.1 (a) Schematic circuit of a Superconductor–Insulator–Superconductor (SIS) Josephson junction with voltage measurement and current supply; (b) equivalent circuit of a Josephson junction within the resistively shunted junction (RSJ) model.

Similar effects occur for other kinds of coupling like the direct ballistic transport or Andreev reflections depending on the physics of the coupling mechanism, see e.g. Tafuri and Kirtley (2005). Besides the tunnelling junctions there is a wide variety of devices called ‘weak links’ showing more or less such Josephson behaviour. For example, for some cases the sin-function in Eq. [8.1] has to be replaced by other periodic functions or higher order terms have to be added (non-sinusoidal current-phase relations), see Likharev (1986). It can be shown that the critical current I_c depends on the external magnetic field. For an homogeneous critical current density within the junction the flux Φ through the junction leads to the dependence

$$I_c(\Phi) = I_c(0) \left| \frac{\sin(\pi\Phi/\Phi_0)}{\pi\Phi/\Phi_0} \right| \qquad [8.2]$$

which is called the Fraunhofer pattern in analogy to optics (light scattering at a single slit). Here $\Phi_0 = h/2e = 2.0678 \times 10^{-15}\,Tm^2$ is the elementary flux quantum.

The dependence on flux changes for inhomogeneous current density distributions as well as for ‘long’ junctions (dimension perpendicular to the current as well as to the magnetic field), see Barone and Paterno (1982). This can be used to investigate these properties with respect to junction quality or spread.

If an external voltage is applied between the electrodes or if the bias current is higher than the critical one (thus a finite voltage occurs across the junction) the phase difference will change in time. For a d.c. voltage U_s, this leads to the second Josephson equation

$$\frac{d\varphi}{dt} = \frac{2e}{\hbar} U_s . \qquad [8.3]$$

Equations [8.1] and [8.3] result in this case in an alternating current within the junction (a.c. Josephson effect) with the frequency given by

$$\upsilon = \left(\frac{2e}{h}\right) U_s . \qquad [8.4]$$

Thus the frequency and the voltage are related only via natural constants by $\upsilon / U_s = 483.59767$ *GHz/mV*. This r.f. current will also leave the junction as microwave radiation, thus a Josephson junction is a voltage-tuned oscillator for microwave radiation, too.

The power of this radiation of a single junction is very small but the direct experimental detection of the Josephson radiation was made by Langenberg, *et al.* (1965) and Dmitrenko, *et al.* (1965), respectively. Higher power can be obtained by arrays of many junctions, see e.g. Ruggerio and Rudman (1990). In the case that an external microwave signal is applied to the junction (as r.f. voltage or a.c. current from irradiated microwaves) there will be an interaction of the intrinsic Josephson oscillations, Eq. [8.4], with the external signal with frequency f. One result is the synchronization of the intrinsic oscillation by the external radiation leading to the so-called Shapiro steps in the current-voltage characteristics at constant voltages

$$U_n = n \cdot \left(\frac{h}{2e}\right) f, \quad \mathrm{n} = 0, 1, 2, \ \ldots \qquad [8.5]$$

in analogy to Eq. [8.4]. For an external frequency which is measured with a very high precision, the voltage of the Shapiro step can be given with the same precision. This is the basis of the voltage standard. If there is no additional d.c. biasing this effect often is called the ‘inverse Josephson effect’ because irradiation of microwaves leads to quantisized voltage values across the junction.

8.1.2 Modelling and junction parameters

Many applications of Josephson devices are based on their non-linear current-voltage (IV) characteristics, see e.g. van Duzer and Turner (1999) or Kadin

(1999). A good approximation for many types of weak links can be given by the Stewart-McCumber model of the resistively shunted junction (RSJ) (Stewart, 1968; McCumber, 1968). Within this model the junction is described by an equivalent circuit with a Josephson junction with I_s following Eq. [8.1], a normal resistance R_N and a junction capacitance C in parallel, see Fig. 8.1b.

From the resulting differential equation the time-dependence of the phase difference can be calculated. The current-voltage characteristics results from averaging in time the phase changes corresponding to Eq. [8.3]. Figure 8.2 shows the general shape of the IV-characteristics of a weak link Josephson device for an

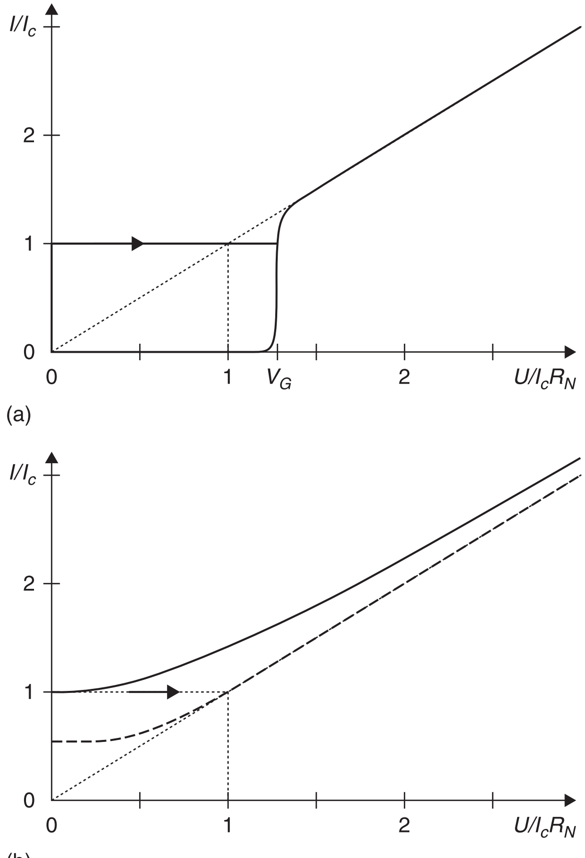

8.2 Current-voltage characteristic of a Josephson junction (shown schematically): (a) highly hysteretic tunnelling junction with $V_G = (\Delta_1 + \Delta_2)/e$; (b) RSJ-like junctions with two different McCumber parameters $ßc = 0$ (non-hysteretic; solid line) and $ßc = 4$ (hysteretic; broken line).

RSJ-like junction and a tunnelling junction, respectively. The non-linearity of this characteristic, the characteristic voltage

$$V_c = I_c R_N \tag{8.6}$$

respectively, the characteristic frequency

$$\omega_c = \frac{2e}{\hbar} I_c R_N \tag{8.7}$$

are important parameters to describe the junction performance. The signal frequency and the switching time (from zero-resistance to voltage state) were determined by the I_cR_N product. At the working temperature the I_cR_N product had to fit the conditions of the experimental application that results in the importance of the temperature dependence of the critical current and normal resistance. For a classical tunnelling junction (superconductor–insulator–superconductor, SIS) the I_cR_N product is connected to the superconducting energy gap Δ and temperature dependence is given by the Ambegaokar-Baratoff relation (Ambegaokar and Baratoff, 1963). Below $T = T_c/2$ the influence of temperature on I_c is quite small, thus the device should work below or near this temperature. At higher working temperatures the change of the I_cR_N product with temperature fluctuations has to be taken into account. Near the critical temperature of the junction the fluctuations lead to a noise-rounding of the IV-characteristics near I_c, which influences the performance of the devices. Thus in general the thermal noise current

$$I_{tn} = \frac{2\pi}{\phi_0} k_B T \tag{8.8}$$

should be smaller than the critical current I_c. This results in restrictions for many applications and additional demands on the cooling of the devices.

The finite junction capacitance in the RSJ model (often called the RCSJ model) is described by the McCumber parameter

$$\beta_c = \frac{2\pi}{\phi_0} I_c R_N^2 C \tag{8.9}$$

and results in hysteretic behaviour for $\beta_c \geq 0.8$ (van Duzer and Turner, 1999). Highly hysteric IV-characteristics, as for tunnelling junctions, can be used for digital applications in the sense of a bistable switching logic, but also result in stability problems especially for currents near to I_c and high working temperatures. For more complex (SIS tunnelling junctions with realistic densities of states for quasiparticles and Cooper pairs) or other transport types (SNS junctions with normal barrier N, ScS junctions with a constriction c, etc.) the RSJ model has to be replaced by other models described in the literature, see e.g. Likharev (1986), van Duzer and Turner (1999), Barone and Paterno (1982), Tafuri and Kirtley (2005). All of these models provide device parameters and dependencies important for applications.

For the high-T_c superconductors (HTS) these models can be adapted, leading to device parameters scaling with the higher T_c. This results in promising properties in comparison to conventional low-T_c (LTS) superconductors (Beasley, 1995). For example the frequency range is now extended to several THz. On the other hand, the nature of the high-T_c materials results in new aspects like anisotropy of the parameters with crystal orientation, pairing symmetry (d-wave instead of conventional s-wave), high penetration depth and small coherence length. An excellent review on weak links in high critical temperature superconductors is given by Tafuri and Kirtley (2005). Another physics is related to high-T_c cuprate superconductors because they have an atomically layered structure of superconducting sheets S and S′ separated by insulating or normal conducting layers with different coupling strengths t and t′, respectively (see Fig. 8.3). In this way the weak coupling is realized in a periodic stack of Josephson junctions with atomic dimensions along the crystallographic c-axis. These intrinsic Josephson junctions can be described by the Josephson or more general weak link

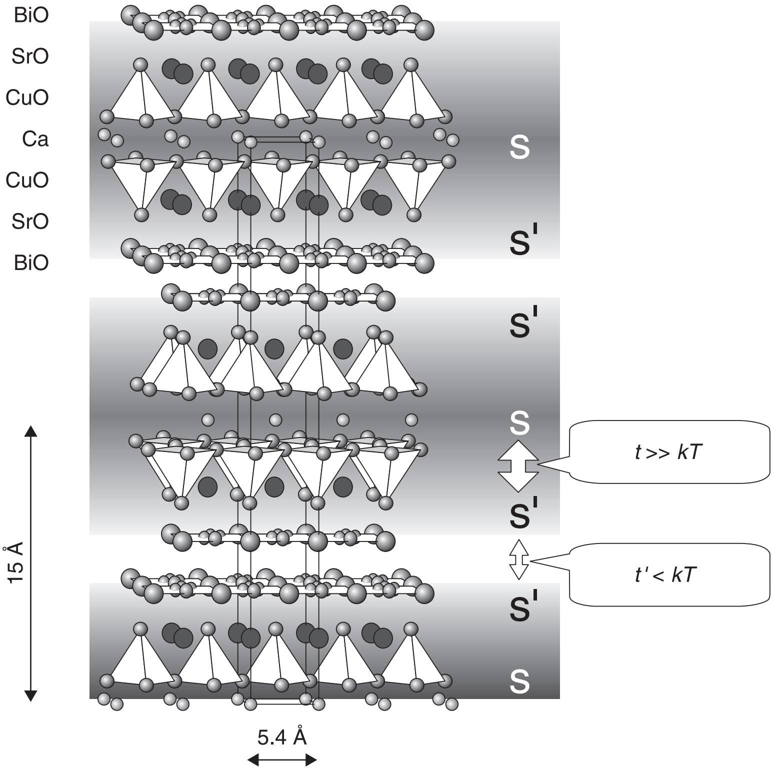

8.3 Intrinsic Josephson junctions within the unit cell of the high-T_c superconductor $Bi_2Sr_2CaCu_2O_8$ (Yurgens, 2000, Fig.1, Copyright (2000) by IOP Publishing Ltd). Reprinted with permission from Yurgens A (2000) ‘Intrinsic Josephson junctions: recent developments’, *Supercond. Sci. Technol.* **13**, R85–R100, Fig.1. Copyright (2000) by IOP Publishing Ltd.

physics but the small dimensions as well as the series connection of many junctions gives rise to some special behaviour and parameters (so-called intrinsic Josephson effects). Modelling of high-T_c Josephson junctions has to take into account these special properties. Thus within the last years many improved, adapted or new models have been introduced to describe the physics of high-T_c Josephson junctions. $I_c(T)$ or $I_cR_N(T)$ have been calculated for d-wave superconductors and different kinds of coupling barriers, see e.g. Tanaka and Kashiwaya (1997), Golubov and Tafuri (2000), Yokoyama *et al.* (2007), and references therein. As one example of the unusual behaviour, it should be pointed out that the magnetic field pattern in the case of a hybrid junction with one electrode with d-wave symmetry (S_sIS_d junction) drastically changes, resulting in a zero critical current without field (so called 'π-junction'), see Fig. 8.4.

8.1.3 Possibilities of applications

There are many applications of Josephson junctions or related weak link devices in superconducting electronics and measurement science. The superconducting quantum interference device (SQUID), as the most prominent application, will be treated in the next chapter. Thus single junction and junction array applications

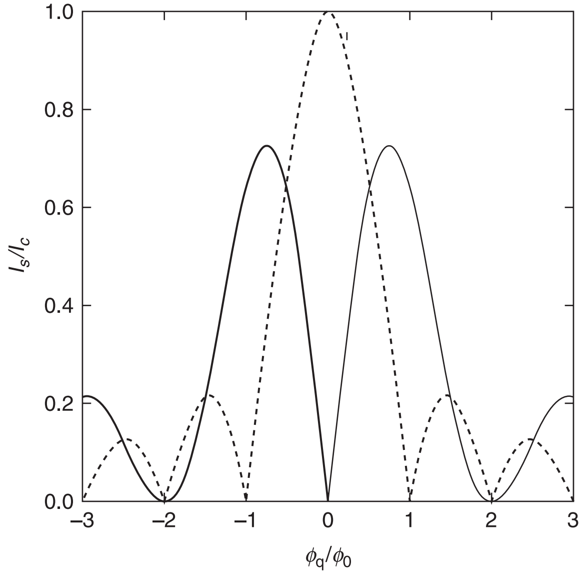

8.4 Magnetic field pattern of a conventional Josephson junction, eq. [8.2] (dashed line), and a hybrid π-junction of a d-wave high-T_c superconductor and an s-wave low-T_c superconductor (Tafuri and Kirtley, 2005, Fig. 19b. Copyright (2005) by IOP Publishing Ltd). Reprinted with permission from Tafuri F and Kitley JR (2005), 'Weak links in high critical temperature superconductors', *Rep. Prog. Phys.* **68**, 2573–2663, Fig. 19b. Copyright (2005) by IOP Publishing Ltd.

in other fields will be discussed here.

The unique properties of Josephson devices offer interesting new systems. The IV-characteristics (Fig. 8.2) are highly non-linear thus amplification and mixing is possible. In the case of hysteretic junctions, there are two branches of the characteristic which allow switching between the two states. This can be used for latching logic and digital circuits. The modulation of the IV-characteristics in an external magnetic field (Fig. 8.4) can be used as magnetic sensor devices similar to SQUIDs. Photons produce characteristic changes of the IV-characteristics, too – a broadband video detection results from changes in the characteristics connected to the adsorbed energy of the radiation. Photon-assisted tunnelling leads to additional structures in the IV-characteristics and Josephson junctions can be used for photon detection down to the single-photon limit. If the frequency of the radiation is in the range of the internal Josephson oscillations (depending on the voltage from MHz over GHz up to the THz range) there are synchronization effects like Shapiro steps which can be used for detection, too. Because of the fundamental relation of Eq. [8.4], a voltage standard can be realized using the direct relation between external frequency and voltage across the junction. The use of large junction arrays allows exact voltages, up to 10 V as well as digital standards and a.c. voltage standards, see Hamilton (2000). Because the Josephson oscillations are strongly connected to the applied voltage, a tuneable frequency source can be realized. Especially in the THz range, this offers new ways of compact radiation sources in contrast to extended laser systems. To enhance the power of radiation instead of single junctions, synchronized arrays of many junctions have to be used.

The dynamics of Josephson junctions can be used for many digital electronics applications. Rapid single flux quantum (RSFQ) logic is based on the equivalence of a voltage pulse and a single flux quantum. In contrast to the latched logic, the switching times are very small and the dissipated power is very low. Thus SFQ or RSFQ circuits will bring out many applications in superconducting electronics, see ter Brake *et al.* (2006).

For each application, the main important parameters of the junctions have to be realized in adapted technologies within small margins. For large junction arrays this requires a small spread of single junction parameters like I_c and R_N. Stability of the parameters on temperature during operation and on long time scales (ageing) have to be realized. In the case of the high-T_c Josephson junction, this situation is even more complex and has to include a lot of additional requirements. For example, the high-T_c materials often use adapted single crystalline substrates with high dielectric constants resulting in decreased r.f. properties and parasitic capacitances. The small coherence lengths result in problems of weak link dimensions and possible junction types, including multilayer systems. On the other hand, the intrinsic nature of the high-T_c materials offers new ways like the intrinsic Josephson junctions and phase-sensitive junctions with new properties. For example, with the π-junctions a new digital logic family can be installed, e.g. Ortlepp *et al.* (2007) and references therein.

8.2 Types of high-T_c Josephson junctions

8.2.1 Overview

The general verification of the Josephson effects for high-T_c superconductors was first realized by point contracts and break junctions. It was shown that even if there are some differences to conventional superconductors, Josephson effects can be observed which can be qualitatively described by the usual models, especially with the same flux quantum. Meanwhile there are many types of thin film Josephson junctions using different coupling mechanisms:

- grain boundary junctions,
- artificial barrier junctions,
- modified microbridges,
- intrinsic Josephson junctions,
- hybrid junctions.

8.2.2 Grain boundary junctions

The first group of junctions uses the special property of the high-T_c cuprates that, because of the very small coherence length of a grain boundary in the thin film, acts as a weak link or Josephson junction. This strong spatially reduction of superconductivity can be artificially induced in an epitaxial thin film. Thus a junction can be placed in a superconducting line by induction of a grain boundary. This can be done by modification of the substrate or an additional thin film layer of a non-superconducting material. Most popular but quite expensive is the use of bicrystal substrates where a single crystal substrate is cut and after some polishing coupled again with a fixed disorder of the crystal orientation of both parts. There are different possibilities of disorientation depending on the tilt direction and grain boundary angle. The standard bicrystal substrate uses a well installed angle between the a- or b-axis, while c-axis of both parts is parallel. The resulting junction is determined by this grain boundary angle. An asymmetric or a symmetric case can be realized (Fig. 8.5). It was shown that the dependence of the critical current density on that angle covers a wide range (Fig. 8.6), and can be reproduced with good accurancy, see Gross *et al.* (1990), Hilgenkamp and Mannhart (2002), Gross (2005), and Mannhart (2006). This leads to commercial standards of symmetric and asymmetric bicrystal substrates with, e.g., 24 and 36 degrees for a lot of materials like $SrTiO_3$, $LaAlO_3$, $NdGaO_3$, sapphire (Al_2O_3), MgO, Si, etc. Other kinds of bicrystal junctions can be realized if there is a tilt with respect to the ab-planes or c-axis of both parts of the crystal. Because of the anisotropy and the d-wave symmetry in the high-T_c materials, such substrates can be used to realize junctions with different superconducting phase coupling.

Another way of inducing a well-defined grain boundary in the growing high-T_c film is a step-edge in the substrate. It was shown that for angles larger than

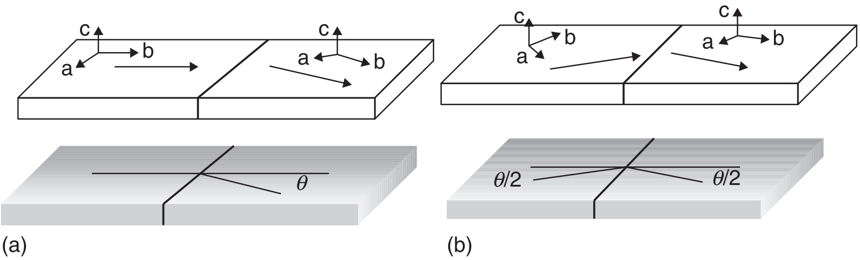

8.5 Two types of bicrystal junctions with (a) asymmetric and (b) symmetric grain boundaries (Tafuri and Kirtley, 2005, Fig. 23, Copyright (2005) by IOP Publishing Ltd.). Reprinted with permission from Tafuri F and Kitley JR (2005), 'Weak links in high critical temperature superconductors', *Rep. Prog. Phys.* **68**, 2573–2663, Fig. 23. Copyright (2005) by IOP Publishing Ltd.

60 degrees there are well-pronounced grain boundaries at both ends of the substrate step induced in the high-T_c film during deposition (Fig. 8.7). Depending on step angle and substrate material as well as technology, one or two junctions will be established. There was some discussion and investigation of the crystal structure concerning the question of whether the lower or upper step-edge determines the junction with the lower critical current dominating the IV-characteristics of the whole contact. In general the existence of two junctions in series causes problems in the dynamics and the stability of the system, see Seidel *et al.* (1995). Thus one tries to make both junctions very different in their critical current. Another way is to avoid a second junction, as is done for MgO step-edges by Foley *et al.* (1999) where only the upper junction exists, while at the lower end of the step-edge there is a smooth growth of the film.

A general advantage of the step-edge junctions in comparison to bicrystal junctions is that they can be placed anywhere on a flat, quite cheap substrate. By etching the step into a thin film of an insulating material with crystallographic parameters allowing growth of the high-T_c material in the top layer, the junctions can be placed in higher levels of multi-layered devices, too.

The third possibility, to produce an artificial grain boundary in the high-T_c film, is the so-called biepitaxial junction (Fig. 8.8). A seed layer partially covers the substrate and the material of the seed layer induces another orientation of the film growth in comparison to the uncovered regions of the substrate. The disadvantage of this type of junction is that often there is only a fixed angle between the two film parts of 45 degrees, which is not optimal with respect to critical current (see Fig. 8.6). A placement of the junction anywhere on the substrate is an advantage, including multi-layer technology. Thus a junction can be realized very easily in the upper layers of a thin film system.

The grain boundary junctions offer an excellent standard technology for many applications. Even if the nature of the barrier and the coupling mechanism is still

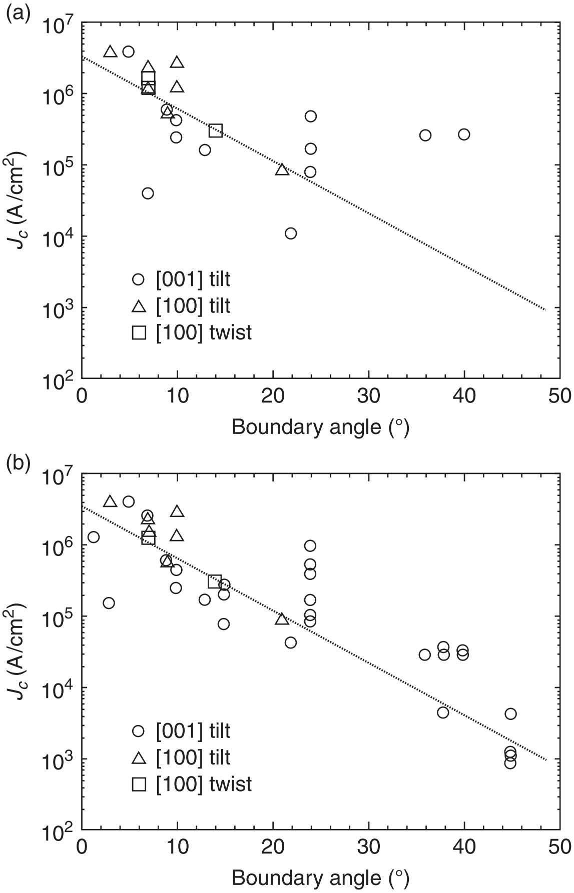

8.6 Critical Josephson current density on grain boundary angle at 4.2 K of different bicrystal junctions, reproduced from Mannhart, 2006, Fig. 4 a and b; for details see comments therein. Reprinted with permission from Mannhart J (2006), 'Properties of grain boundaries in high-T_c superconductors – Notes on a recent presentation', *Physica C* **450**, 152–155, Fig. 4 a and b, Copyright (2006) by Elsevier Science Ltd.

under discussion, see for example Hilgenkamp and Mannhart (2002) and references therein, they give a high reproducibility and good performance like a high I_cR_N product.

8.2.3 Artificial barrier junctions

This kind of Josephson junction uses an artificial barrier layer between the superconductors and various geometries (Fig. 8.9). Depending on the nature of the barrier material (insulating, semiconducting, normal conducting, superconducting

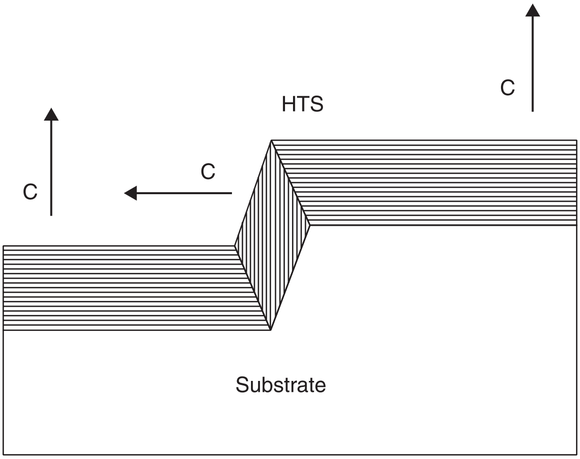
C
HTS
C
C
Substrate

8.7 Step-edge junction with two grain boundaries induced in the HTS film (shown schematically). C = c-axis direction of the crystals.

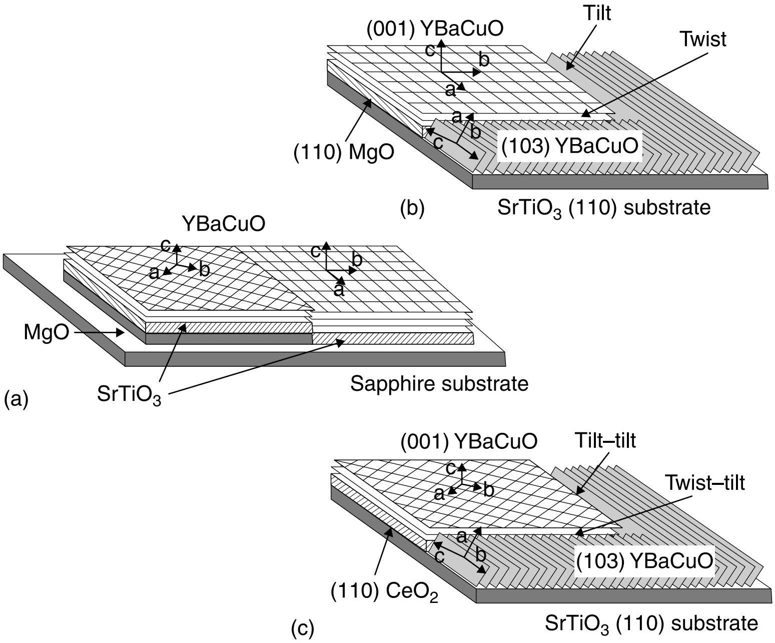
(001) YBaCuO
Tilt
Twist
c
b
a
a
b
c
(103) YBaCuO
(110) MgO
(b)
SrTiO$_3$ (110) substrate
YBaCuO
c
a
b
c
b
a
MgO
SrTiO$_3$
Sapphire substrate
(a)
(001) YBaCuO
Tilt–tilt
Twist–tilt
c
a
b
a
c
b
(103) YBaCuO
(110) CeO$_2$
(c)
SrTiO$_3$ (110) substrate

8.8 Biepitaxial junction types (shown schematically): (a) classically, (b) MgO-based and (c) CeO-based out-of-plane type (Tafuri and Kirtley, 2005, Fig. 24, Copyright (2005) by IOP Publishing Ltd). Reprinted with permission from Tafuri F and Kitley JR (2005), 'Weak links in high critical temperature superconductors', *Rep. Prog. Phys.* **68**, 2573–2663, Fig. 24. Copyright 2005 by IOP Publishing Ltd.

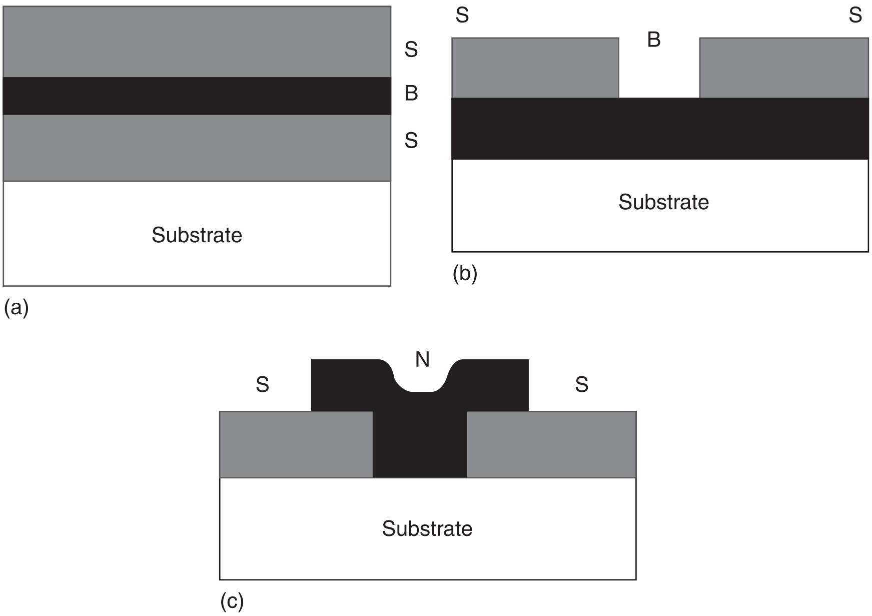

8.9 Some types of planar artificial barrier junctions (shown schematically): (a) sandwich, (b) trench in bilayer, (c) SNS trench-bridge type. B = barrier, S = superconductor, N = normal conductor.

with depressed T_c, geometrical constriction, etc.) the thickness and the transport mechanism can vary in a wide range. Insulating barriers have to be in the order of 0.1 nm because of the very low quantum mechanical tunnelling probability. While this SIS type in planar geometry (sandwich, Fig. 8.9a), with insulating metal oxides is the standard junction in LTS circuits (e.g. Nb-NbO_x-Pb or Nb-Al-AlO_x-Nb), the requirements of HTS technology lead to additional problems. The insulating barrier has to grow epitaxially in layered SIS junctions in sandwich or ramp-edge geometry, and even for a very thin barrier shorts have to be avoided. The tunnelling probability can be drastically enhanced using semiconducting or normal conducting barriers. But in this case the direct conductivity, Andreev reflexion or hopping mechanisms dominate the transport through the barrier and determine the Josephson coupling. For epitaxial growth in multilayer systems, perovskite-like materials such as doped YBaCuO, PrBaCuO and NdCeCuO are used. Even for such materials the problems with homogeneity, multi-layer epitaxy, barrier thickness control and reproducibility are hard to solve, so the interfaces play an important role.

An interesting way to reduce the problems leads to trench bilayer junctions where the coupling barrier is deposited first, (Fig. 8.9b). The epitaxially grown superconductor film on top of this barrier layer has to be cut by electron lithography.

The resulting trench has to be in the order of 100 nm to realize a proximity effect-based coupling via the base layer. To avoid the problems with multilayer epitaxy, a trench in a single HTS layer can be filled with normal metal (Au or Ag) resulting in an SNS bridge junction (Fig. 8.9c). But the trench width below 200 nm, as well as the interface problems between the HTS and the normal metal, lead to problems, too. The first problem can be avoided with a step in the substrate, the buffer layer or the insulating interface layer. One version is shown in Fig. 8.10a, the so-called SNS step-edge junction (Dilorio *et al.*, 1993, 1995).

The deposition of the normal metal and the HTS layer is realized with different angles of incidence. These junctions show reduced I_cR_N-products because of the normal shunt between large parts of the superconducting film and the normal metal. The I_cR_N-product can be enhanced up to 10 mV by etching away these shunts (Rosenthal *et al.*, 1993), see Fig. 8.10b. Another version uses additional insulating layers on top of the superconductor before etching the trench that leads to capacitive shunts, (Fig. 8.10c). A widely used type with a good reproducibility is the so-called ramp-type or ramp-edge junction, see Fig. 8.11. Here the barrier is placed at the etched ramp of a superconductor/insulator double layer. As barrier materials, normal metals, semiconductors or insulators can be used if they grow epitaxially or do not strongly disturb the growth of the superconducting counter-electrode. An interesting version uses no artificially deposited material as barrier,

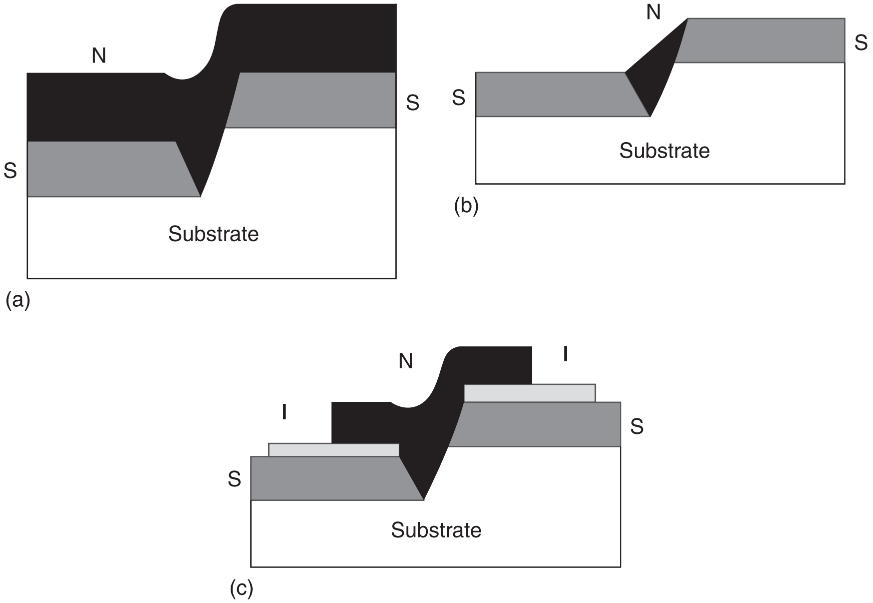

8.10 Different SNS step-edge junctions (shown schematically): (a) shunted, (b) without shunt (after etching), (c) capacitively shunted.

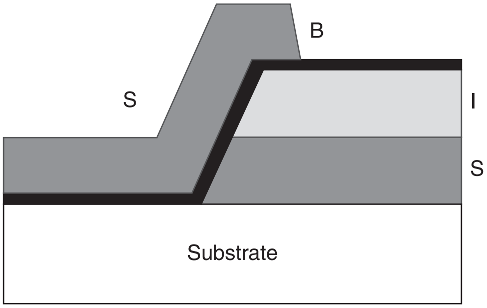

8.11 Ramp-type junction (shown schematically). There exist different variations where the barrier layer is restricted to parts like the edge only.

but uses the disturbed interface at the etched ramp. This ‘natural’ barrier depends on the etching process but is easy to realize and offers a high reproducibility (‘interface-engineered barriers’).

Problems in barrier junction technology result from shorts and inhomogeneities as well as from the strong influence of the intrinsic transport mechanism of the barrier materials on the noise properties of these junctions, e.g. Sarnelli and Testa (2002).

8.2.4 Modified microbridges

This kind of junction uses artificially induced weak links in superconducting microbridges. The modification of the superconducting material can be done by electron, ion or proton beams if the diameter of the beam is clearly below 100 nm (Fig. 8.12). Directly written focussed e-beam (FEBI) junctions show an excellent Josephson behaviour but often have a low stability over time because the modification is self-annealing at room temperature. By additional annealing processes these problems can be solved (Pauza *et al.*, 1997). The modification with ions as a focussed beam as well as through masks with slit width below 150 nm are very stable over time. But besides complex dependencies on preparation parameters, there are often problems with a very restricted range of working temperature or with flux-flow coupling instead of Josephson behaviour. Modified microbridges can also be obtained if in the bridge region a scratch or a small etch trench is induced in the substrate before superconducting film is deposited. Another type uses diffusion of material into the bridge region in a small part of the bridge. If it is technologically possible to prepare the active part of the bridge with geometrical dimensions in the order of the coherence length of the superconductor, the traditional concept of nanobridges works (Fig. 8.13a). For high-T_c materials, the very small coherence length results in additional requirements on the technology. If the nanobridges do not show typical flux-flow behaviour it can be assumed that besides the geometrical dimensions (Fig. 8.13b

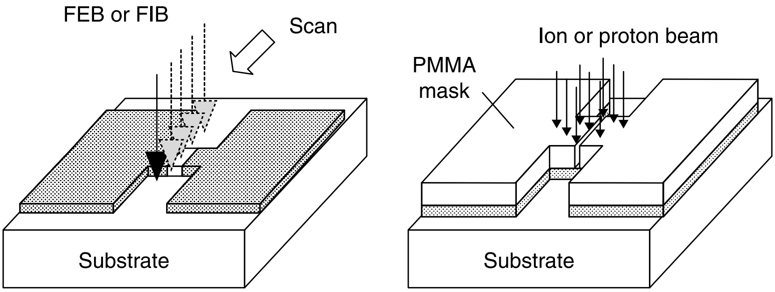
FEB or FIB
Scan
Substrate
Ion or proton beam
PMMA mask
Substrate

(a) (b)

8.12 Different types of modified microbridges (shown schematically): (a) focussed beam written junctions, (b) modified bridge using mask technology. PMMA (polymethylmethacrylate) is a negative photo resist with high resolution.

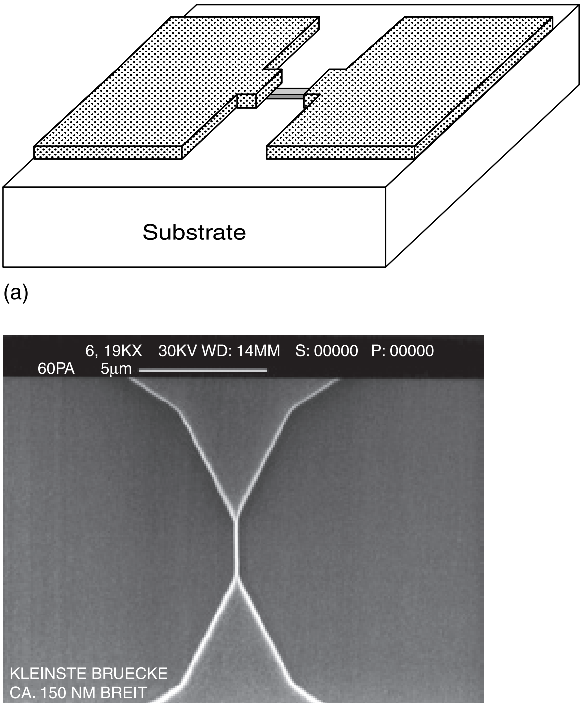
Substrate
6, 19KX 30KV WD: 14MM S: 00000 P: 00000
60PA 5µm
KLEINSTE BRUECKE
CA. 150 NM BREIT

(a)

(b)

8.13 High-T_c nanobridge: (a) schematically, (b) SEM picture of a 150 nm nanobridge (Schneidewind, 1995, Fig. 6.17, Copyright (1995) by Shaker, Aachen). Reprinted with permission from Schneidewind H (1995), *Beiträge zum Ionenstrahlätzen von kryoelektronischen Bauelementen auf der Basis von Kupratsupraleitern*, Thesis at Friedrich-Schiller-Universität Jena, Fig. 6.17, Copyright (1995) by Shaker.

shows an example of a 150 nm bridge of YBCO by Schneidewind, 1995) an additional modification of the material during the preparation process occurs and leads to improvement of junction performance.

8.2.5 Intrinsic Josephson junctions

The intrinsic Josephson effects in the cuprates, where the superconducting CuO_2-planes are coupled via non-superconducting barrier layers within the unit cell of the materials, can be used to produce series junction arrays. The number of junctions depends on the thickness of the high-T_c material between the electrodes. Optimization of technology and a complex control of the preparation process allows the reduction of the number of junctions to a few or even to one. There are different technologies using mesa geometry of vertical stacks, stacks grown at steps in the substrate, focussed ion beam cut single crystal or film structures and planar 'horizontal stacks' grown on vicinal cut substrates, some examples of which are shown in Fig. 8.14. Additional doping or external shunting of the intrinsic arrays can be used to adjust the junction parameters or to enhance the synchronization of the junctions within the array.

8.2.6 Hybrid junctions

Within the past few years hybrid junctions were developed where one electrode is realized by a conventional LTS superconductor, but the other by a high-T_c superconductor. Originally such junctions were used to demonstrate the d-wave symmetry of HTS in contrast to conventional s-wave superconductors. This offers new kinds of coupling of the two superconductors and results in junction behaviour different from the conventional Josephson junctions. Such a hybrid junction in Nb-Au-YBCO technology by Smilde *et al.* (2002b) is shown in Fig. 8.15. Their behaviour can be used for different kinds of electronic devices in logic circuits as well as for better understanding the physics of high-T_c Josephson junctions, e.g. the meandering effect in grain boundary junctions. The hybrid junctions have, in general, the disadvantage that their working temperature is determined by the conventional low-temperature superconductor.

8.3 Grain boundary junctions

8.3.1 Physics of grain boundary junctions

There is an excellent review on grain boundaries in high-T_c superconductors by Hilgenkamp and Mannhart (2002). Thus only the main features will be summarized here. The different types of grain boundaries are usually classified according to the displacement and the rotation of both crystalline parts. For rotational grain boundaries there exist tilt and twist components of the misorientation which often

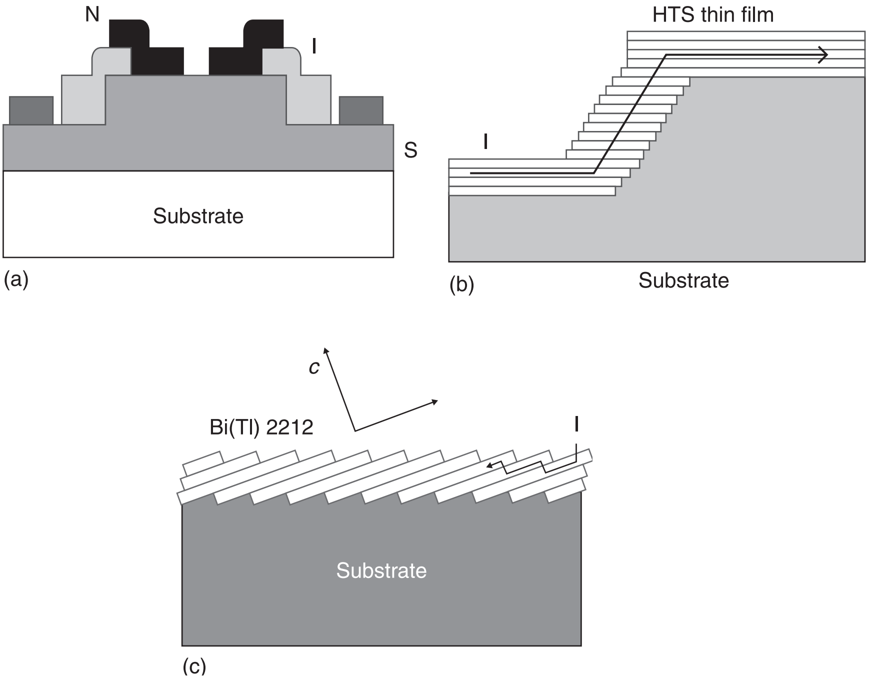

8.14 Different types of intrinsic Josephson junction arrays (schematically): (a) mesa; (b) step-stack array, reproduced from Yurgens, 2000, Fig. 4, Copyright (2000) by IOP Publishing Ltd. (reprinted with permission from Yurgens A (2000) 'Intrinsic Josephson junctions: recent developments', *Supercond. Sci. Technol.* **13**, R85–R100, Fig. 4, Copyright 2000 by IOP Publishing Ltd); (c) bridge on vicinal substrate, reproduced from Yurgens (2000), Fig. 5, Copyright 2000 by IOP Publishing Ltd. (reprinted with permission from Yurgens A (2000) 'Intrinsic Josephson junctions: recent developments', *Supercond. Sci. Technol.* **13**, R85-R100, Fig. 5, Copyright 2000 by IOP Publishing Ltd).

appears in a combination, leading to so-called mixed boundaries. The tilt grain boundary shows a rotation around one axis in the plane of the grain boundary while the twist type is caused by a rotation around the axis perpendicular to this plane. Symmetric grain boundaries have identical misorientation of both grains with respect to the interface; otherwise they are asymmetric (see Fig. 8.5). Figure 8.16 shows three examples of 90 degree grain boundaries: a 90° [010]-twist boundary, a 90° [010]-basal-plane-faced tilt boundary and a symmetrical 90° [010]-tilt boundary. The latter two are frequently found in step-edge Josephson junctions. An example is given in Fig. 8.17 for YBaCuO on an ion-milled 78° step in a $LaAlO_3$ substrate where two 90° grain boundaries are formed at the upper and lower ends of the step (Jia *et al.*, 1992). This results in a series connection of two

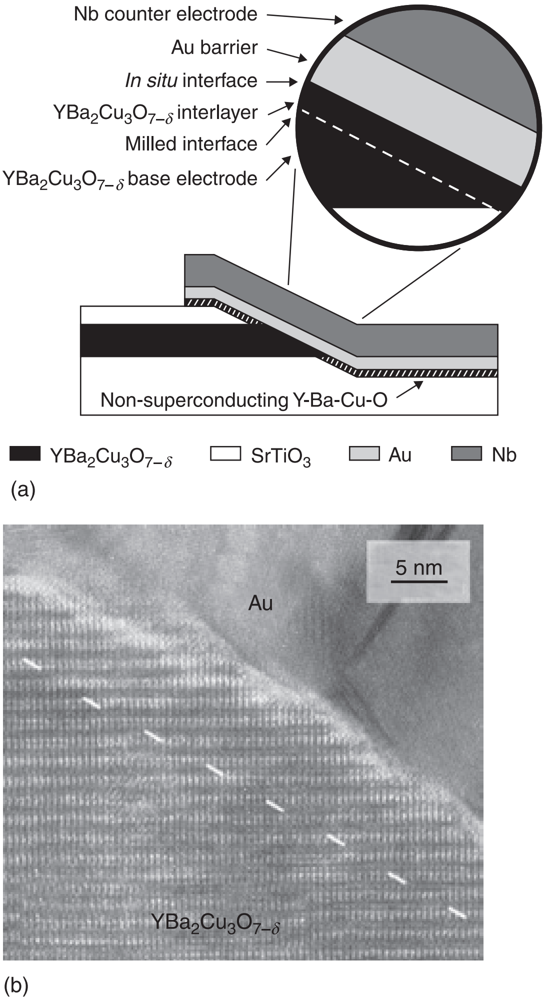
Nb counter electrode
Au barrier
In situ interface
$YBa_2Cu_3O_{7-\delta}$ interlayer
Milled interface
$YBa_2Cu_3O_{7-\delta}$ base electrode
Non-superconducting Y-Ba-Cu-O
$YBa_2Cu_3O_{7-\delta}$
$SrTiO_3$
Au
Nb
(a)
5 nm
Au
$YBa_2Cu_3O_{7-\delta}$
(b)

8.15 YBCO/Au/Nb hybrid junction: (a) schematically, (b) TEM image (Smilde, 2002b, Figs 1 and 2, Copyright (2002) by the American Institute of Physics). Reprinted with permission from Smilde HJH, Hilgenkamp H, Rijnders G, Rogalla H, and Blank DHA (2002), 'Enhanced transparency ramp-type Josephson contacts through interlayer deposition', *Appl. Phys. Lett.* **80**, 4579–4581, Figs 1 and 2, Copyright (2002) by the American Institute of Physics.

Josephson junctions instead of a single junction which can lead to problems in the junction performance and noise (Seidel *et al.*, 1995). To avoid the influence of one of these junctions the angle of the step can be changed, resulting in different values of the critical Josephson currents of both junctions. For MgO substrates there is a technology by Du and Foley (2003) to avoid the grain boundary junction

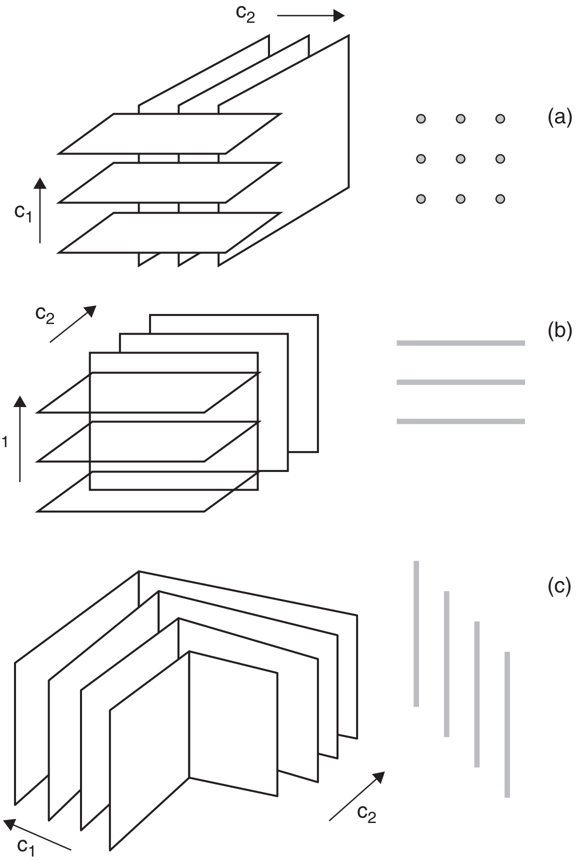

8.16 Schematic diagrams of three types of 90° grain boundaries: (a) [010]-twist, (b) [010]-basal-plane-face tilt, (c) symmetrical [010]-tilt. The c-axis directions of the crystalline two parts of the bicrystal c_1 and c_2 are given by arrows (Tafuri and Kirtley, 2005, Fig. 22, Copyright (2005) by IOP Publishing Ltd). Reprinted with permission from Tafuri F and Kitley JR (2005), 'Weak links in high critical temperature superconductors', *Rep. Prog. Phys.* **68**, 2573–2663, Fig. 22, Copyright (2005) by IOP Publishing Ltd.

at the lower edge of the step resulting in a single junction behaviour, Fig. 8.18. Another important effect, the faceting or meandering, occurs along the grain boundary interface, see e.g. Miller *et al.* (1995), Hilgenkamp *et al.* (1996), Carmody *et al.* (2002). Facets with typical lengths of less than 100 nm are clearly visible in the TEM images or AFM pictures. Their orientation and dimensions depend on the high-T_c material, the substrate material and its grain-boundary configuration as well as on film deposition process. The three dimensional growth of different oriented grains along the grain boundary results in a meandering path

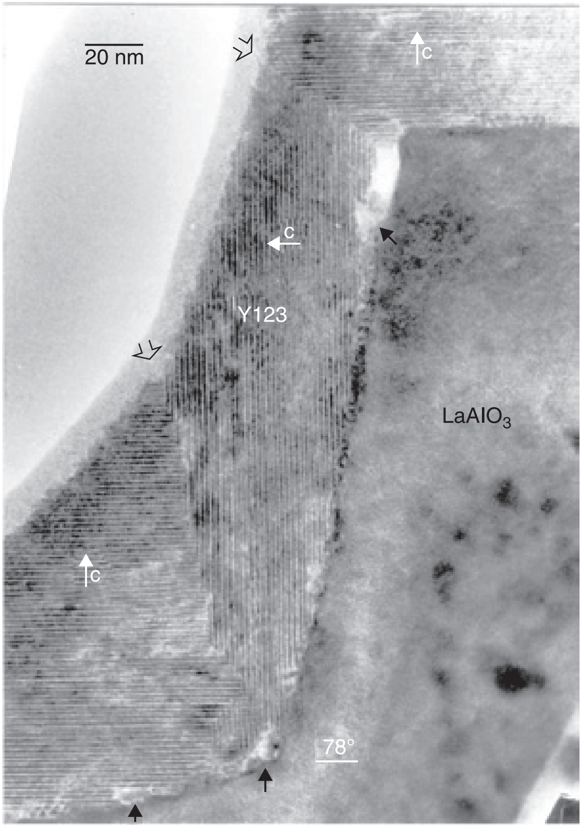

8.17 TEM image of a YBaCuO step-edge junction on a LaAlO$_3$ substrate; open arrows indicate the two 90° grain boundary junctions (Jia *et al.*, 1992, Fig. 4, Copyright (1992) by Elsevier Science Ltd.). Reprinted with permission from Jia CJ *et al.* (1992), 'The microstructure of epitaxial YBaCuO films on steep steps in LaAlO substrates', *Physica C* **196**, 211–226, Fig. 4, Copyright (1992) by Elsevier Science Ltd.

with changes in the phases of the superconducting wave function corresponding to the different crystal directions. Thus the Josephson current flows across some facets in the direction opposite to the bias current. The order parameter orientations can result in a π-phase shift across the junction and the faceting leads to an inhomogeneous distribution of the Josephson current density including regions with 'negative' critical current. This inhomogeneity causes anomalous magnetic field dependencies of the critical current and leads to spontaneously generated magnetic fluxes along the grain boundary, Fig. 8.19.

At the interfaces of the grain boundary the bending of the electronic band structure causes space charge layers depressing the order parameter and the

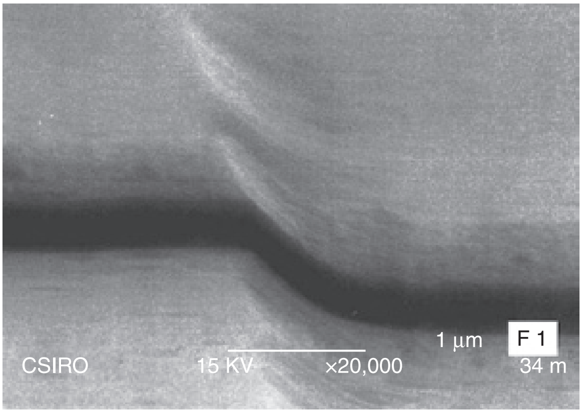

8.18 SEM image of a YBaCuO step-edge junction on a MgO substrate where there is no grain boundary junction at the lower end of the step (Du and Foley, 2003, Fig. 1, Copyright (2003) by Elsevier Science Ltd). Reprinted with permission from Du J and Foley CP (2003), 'Trimming, stability and passivation of YBCO step-edge junctions', *Physica C* **391**, 31–41, Fig. 1, Copyright (2003) by Elsevier Science Ltd.

I_cR_N-product. Additional doping of the grain boundary thus gives new possibilities to improve the junction parameters, see Hilgenkamp and Mannhart (2002) and references therein.

8.3.2 Preparation and performance of grain boundary junctions

Depending on the junction type, the preparation technology has to be optimized to produce time stable junctions with adjusted parameters in a reproducible way. The critical Josephson current I_c, the I_cR_N product at the expected working temperature and also noise properties are of main interest. The selection of the junction type is influenced by the whole device and circuit concept as well as the high-T_c materials for the films. There are a lot of commercial bicrystal substrates of high quality. The good and reproducible quality of the junctions on such substrates is used if the high cost of the substrates plays no role and the circuits can be designed in such a way that the 'parasitic' junctions, which appear everywhere when superconducting lines cross the grain boundary, have high critical currents without an influence on the 'wanted' junctions. The step-edge technology has the advantage to place the junction free on the whole substrate and to avoid such 'parasitic' junctions. The step preparation by ion beam etching requires additional processes in technology but is in general possible for all substrates, even within buffer layers in multi-layer systems.

The biepitaxial junctions have similar advantages for a multi-layer technology and with respect to their free placement on the substrate, but depending on the

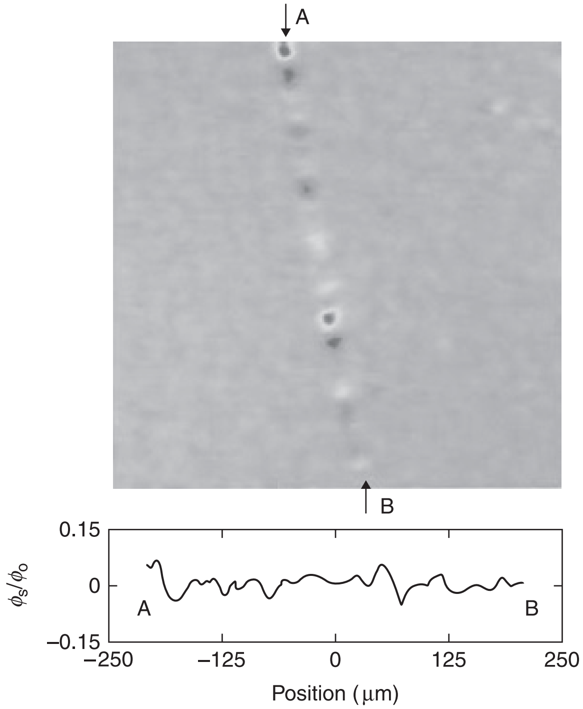

8.19 Scanning SQUID microscope image of an asymmetric 45° [001]-tilt YBaCuO bicrystal grain boundary (marked by arrows A and B). Self generated magnetic flux is apparent along the grain boundary (Hilgenkamp and Mannhart, 2002, Fig. 58, Copyright (2002) by the American Physical Society). Reprinted with permission from Hilgenkamp H and Mannhart J (2002), 'Grain boundaries in high-T_c superconductors', *Rev. Mod. Phys.* **74**, 485–549, Fig. 58, Copyright (2002) by the American Physical Society.

materials only fixed angles of the grain boundary misfit are possible. In the standard case this is the 45° tilt leading to very small critical currents corresponding to the scaling law given in Fig. 8.6. Lombardi *et al.* (2002) demonstrated the influence of the intrinsic d-wave effects on the angular dependence of the critical current for different biepitaxial junctions. As an additional advantage the meandering effect can be avoided resulting in homogeneous current distribution and improved noise properties (see Carillo *et al.*, 2000).

8.3.3 Selected applications of grain boundary junctions

As already mentioned, the bicrystal junctions are the most widely used type of high-T_c Josephson junctions. There is a wide range of applications, from single junctions up to many arrays with over 100 junctions. Because the bicrystal

SQUIDs will be discussed in the next chapter, some selected applications will be given here which use the special performance of bicrystal junctions. The I_cR_N-product of bicrystal junctions is in the order of 2 mV at 4.2 K (Hilgenkamp and Mannhart, 2002). Values up to 8 mV have been reported by Poppe *et al.* (2001) for [100]-tilt grain boundary junctions. This allows the detection of radiation in the THz range by observation of Shapiro steps (Miyadera *et al.*, 2005; Kawayama, 2006) or by the Hilbert spectroscopy (Divin *et al.*, 2001, 2002; Shirotov *et al.*, 2002).

A meandering superconducting line across the grain boundary gives an easy way to realize a series array of junctions with quite similar parameters. Such arrays can be used as voltage standards. In contrast to the usual standards, where a zero-crossing Shapiro step of highest order (and thus of largest voltage) is used, such digital standards work with the first Shapiro step in nonhysteretic IV-characteristics. The necessary shunt resistor for the reduction of the McCumber parameter can be realized with a gold layer on top of the grain boundary. An example of a high-T_c shunted bicrystal Josephson junctions array with 365 junctions was given by Klushin *et al.* (1996). Klushin and co-workers (2002) demonstrated that accurate measurements of quantum voltage steps with such arrays can be realized with an uncertainty of two parts in 10^8 suitable for meteorological purposes. In comparison to usual electronic standards based on Zener diodes, the HTS arrays permit one to ignore the influence of pressure, temperature and humidity on the output voltage of the standard. Moreover, such arrays are promising for development of an arbitrary voltage waveform synthesizer with quantum-mechanical accuracy (Hamilton, 2000 and references therein). To further improve the performance of HTS arrays, the Josephson junctions were coupled to a Fabry-Perot resonator to enhance the effectiveness of interaction with the electromagnetic field (Klushin *et al.*, 2006; He *et al.*, 2007). Figure 8.20 shows the IV-characteristics of two bicrystal junctions arrays of 182 [001]-tilt junctions of YBCO on a 24° symmetrical bicrystal YSZ substrate with Au shunt for different angles between the electric field and the film plane.

The biepitaxial junctions can be applied in quantum measurements, qubits and π-circuitry because of their improved homogeneity and missing phase changes by meandering of the grain boundary (Tafuri *et al.*, 2004). Experimental observation of the macroscopic quantum tunnelling (MQT) in biepitaxial Josephson junctions was reported by Bauch *et al.* (2005). For qubits the intrinsic bistability of high-T_c devices resulting on the time-reversal symmetry beaking of two coupled d-wave superconductors becomes a major advantage. Amin *et al.* (2005) have demonstrated a 'silent' qubit using submicron bicrystal junctions. The symmetry of this device provides an operating point, which is intrinsically stable and protected against the external field fluctuations.

Another promising application by Schilling *et al.* (2006) is the so-called Josephson cantilever for microwave scanning microscopy where 22 bicrystal junctions are placed on a $LaAlO_3$ substrate mounted on top of a piezo-driven

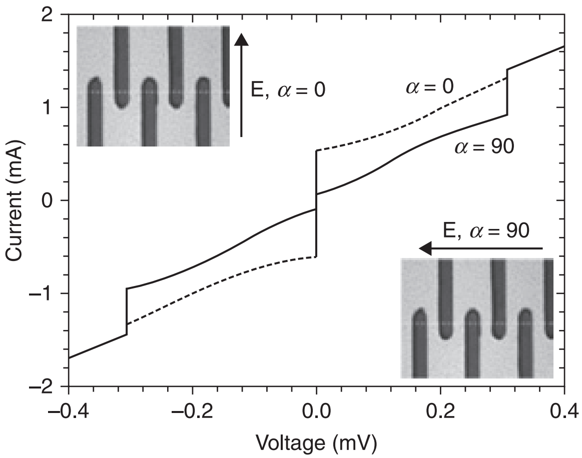

8.20 IV-characteristics of shunted series arrays of grain boundary Josephson junctions for different angle α between the electric field E and the film plane (Klushin *et al.*, 2006, Fig. 1, Copyright (2006) by the American Institute of Physics). Reprinted with permission from Klushin AM, He M, Yan SL, and Klein N (2006), 'Arrays of high-T_c Josephson junctions in open millimeter wave resonators', *Appl. Phys. Lett.* **89**, 232505, Fig. 1, Copyright (2006) by the American Institute of Physics.

spring, Fig. 8.21. The damping of the oscillation caused during the scanning of the sample is used to image the near-field microwave radiation.

8.4 Artificial barrier junctions

8.4.1 Physics of artificial barrier junctions

The selection of the barrier material plays an important role because on one side the conductivity mechanism through the barrier (normal metal, semiconductor, insulator, etc.) is different but on the other side the high-T_c superconducting electrode leads to additional requirements. The barrier materials should not interact with the high-T_c material causing a degradation of the superconducting parameters. This interacting includes chemical effects, diffusion processes and the quality of the interface. Many types of junctions require heteroepitaxial growth of the barrier material and one or even two high-T_c electrodes. Thus there are a very restricted number of barrier materials which have a small misfit in their lattice parameters and thermal expansion coefficients in comparison to the high-T_c superconductors. Perovskite-like materials like $SrTiO_3$, PrBaCuO, NdCeCuO as well as layers of high-T_c superconductors with depressed or destroyed superconducting properties are used. Additional buffer layers are used to adjust lattice mismatch and different thermal expansion coefficients as well as to act as interdiffusion barriers, e.g. CeO_2 or YSZ, but only if they do not enhance the total

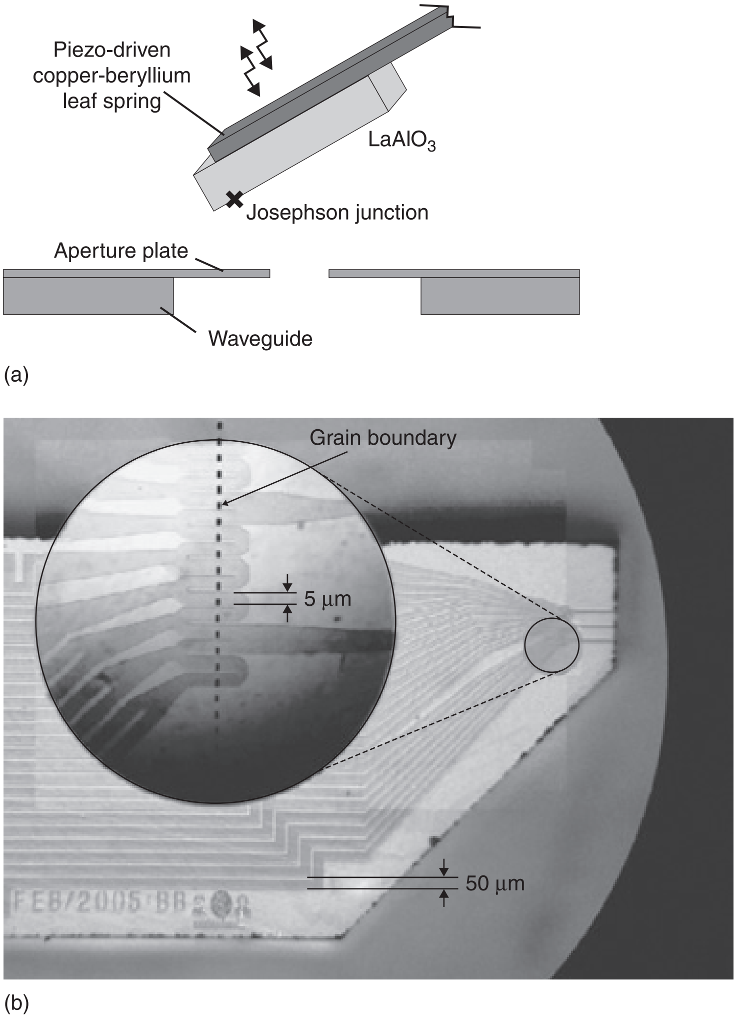
Piezo-driven
copper-beryllium
leaf spring
LaAlO$_3$
Josephson junction
Aperture plate
Waveguide
(a)
Grain boundary
5 μm
50 μm
FEB/2005 BB
(b)

8.21 (a) Schematic drawing of the setup used for microwave scanning microscopy and (b) layout of the Josephson cantilever (Schilling *et al.*, 2006, Figs 1 and 2, Copyright (2006) by the American Institute of Physics). Reprinted with permission from Schilling M, Kaestner A, and Stewing F (2006), ‘Room temperature near field microwave imaging with an $YBa_2Cu_3O_7$ Josephson cantilever’, *Appl. Phys. Lett.* **88**, 252507, Figs 1 and 2, Copyright (2006) by the American Institute of Physics.

barrier thickness too much. The use of noble elements Au und Ag for non-epitaxial types of junctions is possible but the problems with the control of the interfaces (e.g. growth and interface resistance) are a handicap to these junctions.

Very promising results were obtained for ‘native’ or ‘natural’ barriers where etched surfaces of high-T_c superconductors are used as interface-engineered barriers.

These thin parts of the superconductor show modified properties and act as normal or semiconducting barriers. An impressive TEM picture of such a ramp-edge junction with a 'native' barrier of about 2 nm thickness from Wen *et al.* (2000) is shown in Fig. 8.22. For an excellent review of TEM on ramp-edges with different materials including 'interface engineered' barriers see Merkle *et al.* (1999). The nature of the barrier material determines the transport mechanism. Tunnelling through insulators requires very thin layers which can be hardly realized in planar SIS junctions with insulating barriers. Up to now there exist only a few groups successfully working with such planar SIS junctions and it is not clear if additional current contributions like tunnelling via traps or hopping processes dominate the simple tunnelling mechanism. Kito *et al.* (2002) therefore introduced an additional $PrGaO_3$ layer and got excess-current free junctions with I_cR_N products of about 2 mV at 4.2 K. For semiconducting (Sm) barrier materials the thickness can be enhanced, but the problem with additional current contributions is enhanced too. Also the effect of induced superconductivity (proximity effect) has to be taken into account.

For some materials even an anomalous or 'gigant proximity effect' was reported, e.g. Golubov and Kuriyanov (1998), leading to barrier thicknesses of up to 200 nm. This gave a good chance to use the simple trench geometry of Sm-S bilayers (Fig. 8.9b) but problems with interface resistance as well as with microshorts across the trench appeared (Barholz *et al.*, 2000). The trench geometry

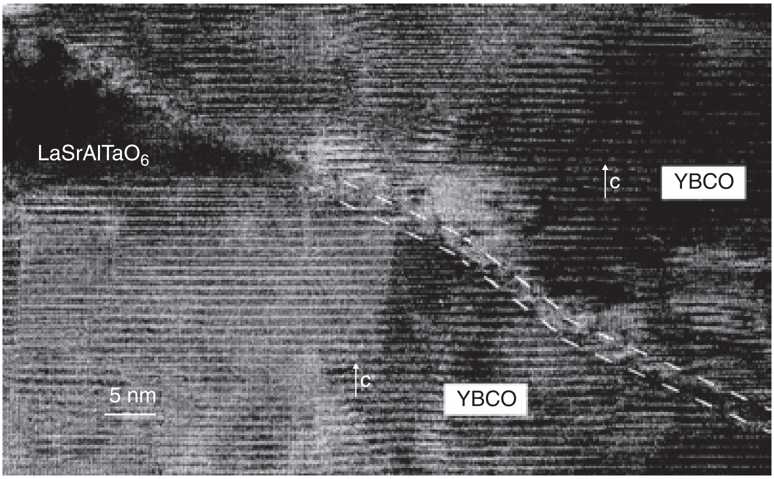

8.22 TEM picture of a ramp-edge junction with a 'native' barrier (thickness about 2 nm) indicated by dashed lines, so-called interface-engineered junction. The crystallographic c-axis direction of the YBCO films is given by arrows (Wen *et al.*, 2000, Fig. 2, Copyright (2000) by Elsevier Science Ltd). Reprinted with permission from Wen JG, Satoh T, Hidaka M, Tahara S, Koshizuka N, and Tanaka S (2000), 'TEM study on the microstructure of the modified interface junction', *Physica C* **337**, 249–255, Fig. 2, Copyright (2000) by Elsevier Science Ltd.

with a N-S bilayer also was used for MgB_2 epitaxially grown on normal conducting TiB_2 films on SiC substrate by Chen *et al.* (2006). A trench smaller than 50 nm was realized by e-beam lithography and ion milling or by focussed ion beam. The junctions show RSJ-like IV-characteristics up to 31 K.

The use of normal conducting barriers gives the chance to enhance the barrier thickness again but leads to other transport mechanisms as proximity effect and multiple Andreev reflections have to taken into account. Additional problems appear because materials usable for epitaxy often show magnetic ordering effects leading to strong influences on superconductivity and Josephson effects.

The directly written junctions or modified bridges use barrier material which is produced by electron or ion beams, thus many aspects of technology can use these materials and their properties. The changes in the material by electron beams mostly are not stable at room temperature but this can be improved by a thermal annealing step. An excellent review on these FEBI junctions was given by Pauza *et al.* (1997) and the proximity effect coupling was described by Booij *et al.* (1997). On the other side, the ion beam modified materials are stable but were dominated by complex behaviour, e.g. bridges work as Josephson junctions only in a very limited temperature range, see e.g. Schmidl *et al.* (1997), Katz *et al.* (2000), and the short review of Tinchev (2007) including the references therein.

8.4.2 Preparation and performance of artificial barrier junctions

Most of the problems in preparation of artificial barrier junctions are based on their physical problems given above. The heteroepitaxy problem is mainly solved for selected material combinations. Two examples are shown in Fig. 8.23, for details see the review of Merkle *et al.* (1999). Molecular beam epitaxy (MBE), laser MBE and pulsed laser deposition (PLD) show excellent results for multilayer systems with crystallographically fitting materials. The metal electrodes (mainly Au) are included in devices as well as passivation and protection layers.

The simple technology for modified microbridge junctions seems to be of interest for many junction circuits where the junction can be placed everywhere on the substrate, but their quite low reproducibility, large parameter spread and stability problems up to now have limited applications. The junction behaviour is strongly dependent on the barrier properties and the transport and coupling mechanisms. Instead of clear Josephson coupling these additional effects lead to differences in the IV-characteristics (often flux-flow like but RSJ-like at lower temperatures, Fig. 8.24), the microwave response, the temperature dependence of the junction parameters or additional noise. Focused electron-beam irradiated junctions with I_cR_N products of about 2 mV at 4.2 K, 650 μV at 40 K, and 120 μV at 77 K have been demonstrated by Pauza *et al.* (1997). Ion beam modified microbridges reach 200 μV at 45 K but have a spread in critical currents of up to

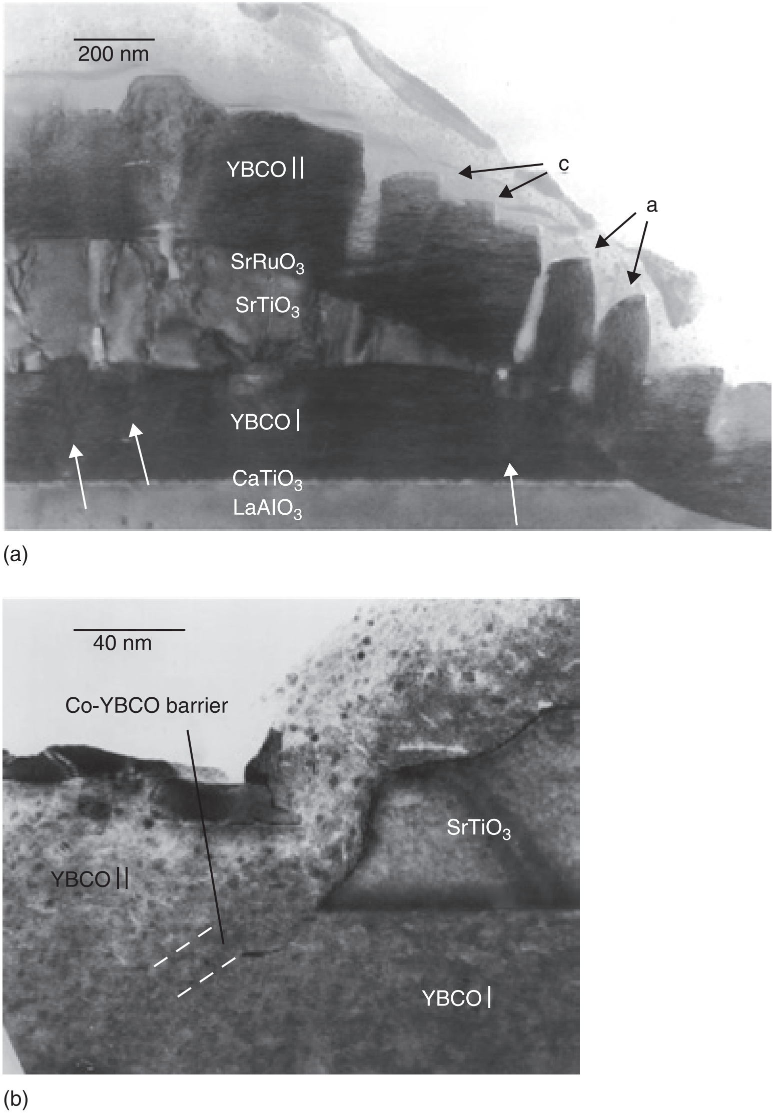
200 nm
YBCO ||
c
a
SrRuO$_3$
SrTiO$_3$
YBCO |
CaTiO$_3$
LaAlO$_3$
(a)
40 nm
Co-YBCO barrier
SrTiO$_3$
YBCO ||
YBCO |
(b)

8.23 TEM pictures of artifical barrier junctions: (a) YBCO/SrRuO$_3$/YBCO ramp-edge, (b) Co-YBCO barrier SNS ramp-edge. In (a) some a- and c-oriented grains are marked by arrows (Merkle *et al.*, 1999, Figs 9 and 16b, Copyright (1999) by Elsevier Science Ltd). Reprinted with permission from Merkle KL, Huang Y, Rozeveld S, Char K, and Moeckly BH (1999), 'Electron microscopy of high-T_c Josephson junctions formed in the epitaxial layer ramp-edge geometry: YBCO/barrier/YBCO', *Micron* **30**, 539–559, Figs 9 and 16b, Copyright (1999) by Elsevier Science Ltd.

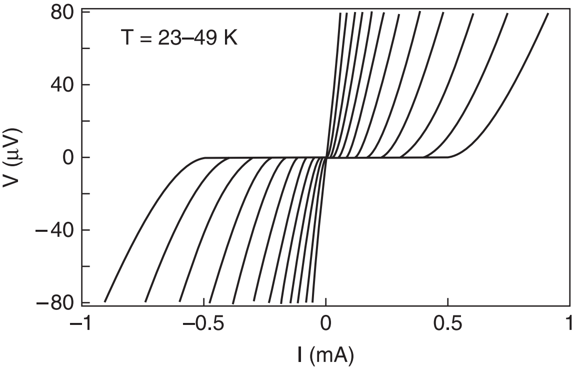

8.24 IV-characteristics of ion beam modified microbridges (film thickness 50 nm, slit width 250 nm) showing in general a flux-flow behaviour depending on preparation and working temperature. Only at lower temperatures is there an RSJ-like behaviour (Schmidl *et al.*, 1997, Fig. 7, Copyright (1997) by Springer Science and Business Media). Reprinted with permission from Schmidl F, Dörrer L, Wunderlich S, Machalett F, Hübner U, *et al.* (1997), 'Superconducting properties of ion beam modified YBCO microbridges', *J. Low Temp. Phys.* **106**, 405–416, Fig. 7, Copyright (1997) by Springer Science and Business Media.

40% (Katz *et al.*, 2000). Further improvement of the I_cR_N product was obtained by Sirena *et al.* (2007) by increasing the ion energy.

It should be mentioned that ion beam modified junctions have been realized too for MgB_2 superconductors by Cybart *et al.* (2006). Twenty-junction arrays and single junctions with an I_cR_N product of 75 μV at 37.2 K have been demonstrated.

In contrast to low-T_c devices the artificial barrier layer type is not the standard junction technology for HTS. The interface-engineered barriers will be a way out towards applications, because I_cR_N products over 5 mV at 4.2 K with a good uniformity in I_c for more than 100 junctions were obtained by Shimakage *et al.* (2001).

8.4.3 Selected applications of artificial barrier junctions

The recent progress in single flux quantum (SFQ) device technology in Japan is based mainly on the development of interface-engineered ramp-edge junctions (Tanabe and Hidaka, 2007). The spread in the critical current for one hundred junctions is smaller than 10% (Satoh *et al.*, 2001) while the I_CR_N product is larger than 1 mV at 40 K (Morimoto *et al.*, 2006). SFQ circuits with up to 200 Josephson junctions were realized. A variety of elementary SFQ circuits such as a toggle flip-flop, switches and an analog-to-digital converter have been designed for operation temperatures of 30 to 50 K, while a prototype on-chip sampler system is being developed by Maruyama *et al.* (2007) for demonstration of bandwidth over 100 GHz for optical input signals, Fig. 8.25.

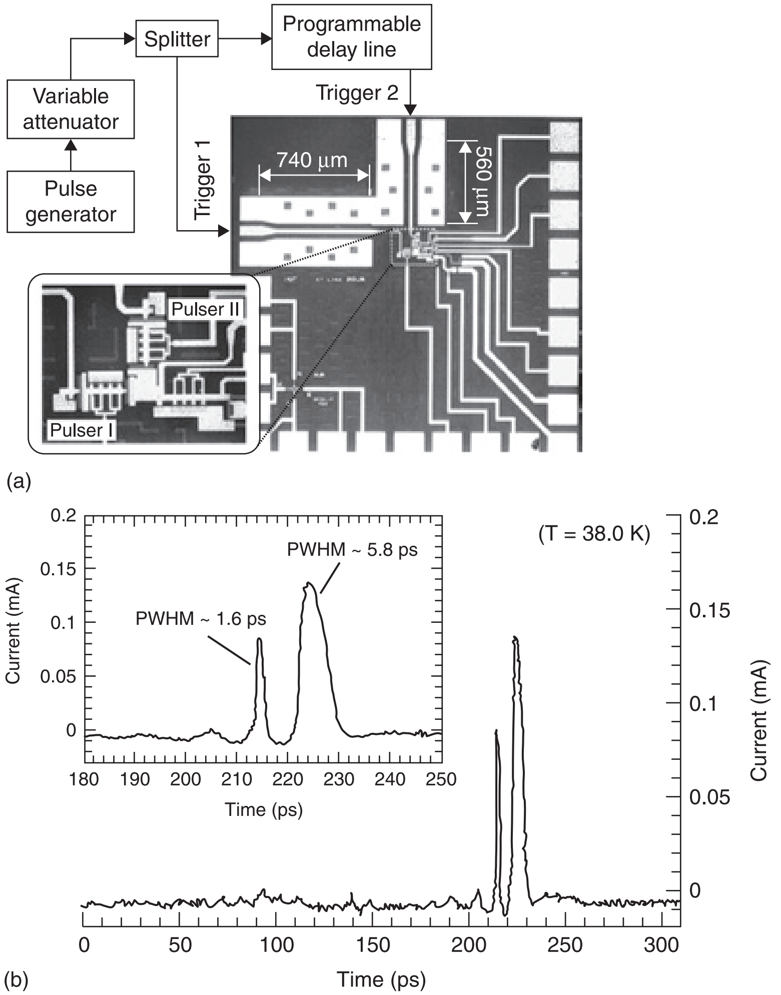

8.25 SFQ sampler system using interface-engineered ramp-edge junctions: (a) block diagram and microphotograph of the on-chip sampler for pulse measurement. The inset shows an enlargement of the circuit. (b) Measured current pulse (Maruyama *et al.*, 2007, Figs 2 and 5, Copyright (2007) by Elsevier Science Ltd). Reprinted with permission from Maruyama M, Wakana H, Hato T, Suzuki H, Tanabe K, *et al.* (2007), 'Observation of SFQ pulse using HTS sampler', *Physica C* **463–465**, 1101–1105, Figs 2 and 5, Copyright (2007) by Elsevier Science Ltd.

As one example for application of ion beam modified junctions, the superconducting quantum interference filters (SQIFs) of Cybart *et al.* (2008) should be mentioned, even if they could be included in the SQUID chapter, too. The SQIFs are SQUID-like arrays with a special variation of loop size leading to one single peak in their voltage-flux dependence with very large transfer coefficients $\partial V/\partial B$ (see e.g. Schultze *et al.*, 2003 and references therein). Series arrays of 280 such incommensurate SQUIDs from YBCO ion damage Josephson junctions show a spread of critical currents of 12% only and result in a maximum transfer function of 105 V/T.

8.5 Intrinsic Josephson junctions

8.5.1 Physics of intrinsic Josephson junctions

Since the discovery of the intrinsic Josephson effects by Kleiner *et al.* (1992) a lot of works have been published concerning the physics of the intrinsic junctions, e.g. Kleiner and Müller (1994), Kim *et al.* (1999), Yurgens (2000), Wang *et al.* (2001a, 2001b, 2005, 2009), Tachiki *et al.* (2005, 2009), Gray *et al.* (2009). Thus we will restrict ourself here to facts which are relevant for application.

The crystal structure of the high-T_c superconducting cuprates offers a natural way to realize Josephson junctions on an atomic scale. The superconducting CuO_2-planes are separated by coupling layers of some tenth of a nanometer. This leads to many differences compared to artificially prepared planar barrier junctions with quite compact superconducting electrodes and much thicker single barrier layers. For example the magnetic field dependence of the critical Josephson current is still a Fraunhofer-like dependence, eq. [8.2], but relating to the atomic size of the junction (total junction thickness is about 1.5 nm) a flux quantum requires new fields in the Tesla range. This is an advantage for some applications where stable Josephson currents even in higher fields are necessary. The other main difference to artificial junctions is that intrinsic junctions are naturally series arrays instead of single junctions. Thus the observed IV-characteristic is a sum of single junction characteristics leading to many branches up to high voltages, Fig. 8.26. For very high voltages the heat dissipation leads to non-equilibrium effects and negative differential resistance parts in the IV. While the number of junctions in the intrinsic arrays is quite easy to control by thickness of the stack of superconducting unit cells their homogeneity is still a problem. Thus there is a quite large spread in single junction parameters. If the spread can be reduced, the internal synchronization of the junctions improves the dynamic of these arrays. Additional shunting or resonance environment can further improve the synchronization leading to a collective many-junction behaviour (Grib and Seidel, 2009; Grib *et al.*, 2002; Seidel *et al.*, 2001; Wang *et al.*, 2000). This is of relevance, for example, for radiation sources realized by intrinsic arrays. The lateral dimensions of intrinsic Josephson junctions play a crucial role, too. Perpendicular to the atomic arrays there is flux-flow of Josephson vortices corresponding to these dimensions. This results in plasma waves and additional dynamic effects; for details see the reviews of Saval'ev *et al.* (2010) and Hu and Lin (2010). On the one hand, such effects can be applied for radiation sources (Gray *et al.*, 2009; Tachiki *et al.*, 2005), while on

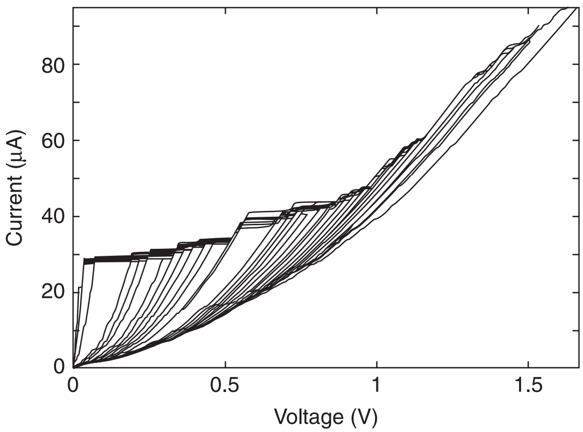

8.26 Typical IV-characteristics of an intrinsic Josepshon junction array showing multiple branches (Schmidl *et al.*, 1995, Fig. 5, Copyright (1995) by IOP Publishing Ltd). Reprinted with permission from Schmidl F, Pfuch A, Schneidewind H, Heinz E, Dörrer L, *et al.* (1995), 'Preparation and first measurements of TBCCO thin film intrinsic stacked Josephson junctions', *Supercond. Sci. Technol.* **8**, 740–743, Fig. 5, Copyright (1995) by IOP Publishing Ltd.

the other hand they lead to a complex behaviour and additional noise contributions, see e.g. Wang *et al.* (2009), Tachiki *et al.* (2009) and references therein.

8.5.2 Preparation and performance of intrinsic Josephson junctions

While the first investigations on the intrinsic junctions used single crystals like whiskers or etched parts out of them, different thin film technologies have since been developed. Thin film structures used a mesa-type geometry whereas the high-T_c film is patterned with lateral dimensions in the μm range, e.g. Schmidl *et al.* (1995), Haruta *et al.* (2009) and references therein. The problem of metal electrodes to the mesas was solved by Seidel *et al.* (1996) even for a four-point-measurement which requires two separated contacts on top of each mesa, see Fig. 8.27. A very interesting technology of preparation of quite homogeneous and well-defined junction arrays was proposed by Kim *et al.* (1999) for single crystal whiskers and later adapted by Wang *et al.* (2001b) to single crystal pieces mounted on substrates. Focussed ion beams were used to etch the small well-defined stack of junctions out of the material from two sides in a way that the remaining high-T_c materials act as electrodes to the stack. By this 'double-sided fabrication method "or" flip-chip technique' the quality and homogeneity of the intrinsic junction arrays was dramatically improved.

Other technologies were developed to realize a very small junction number down to the single junction limit, see e.g. Yurgens (2000), You *et al.* (2006), and Yurgens *et al.* (2008). Koval and co-workers (2010) showed that T_C, I_C and R_N of

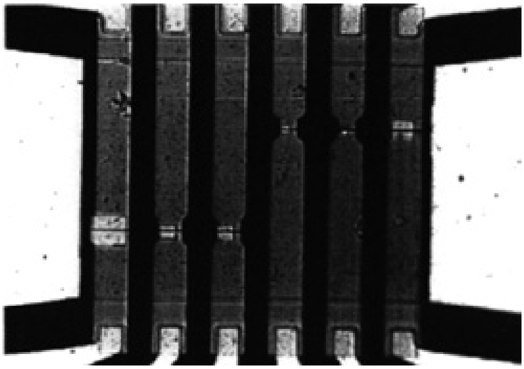

8.27 Thin film intrinsic Josephson junctions using a mesa-like geometry (six mesas from 3 × 3 to 10 × 10 μm^2) and electron beam cut Au electrodes for four-point measurements (Seidel *et al.*, 1996, Fig. 2c, Copyright (1996) by IOP Publishing Ltd). Reprinted with permission from Seidel P, Schmidl F, Pfuch A, Schneidewind H, and Heinz E (1996), 'Investigations on high-T$_c$ thin film intrinsic stacked Josephson junctions', *Supercond. Sci. Technol.* **9**, A9–A13, Fig. 2c, Copyright (1996) by IOP Publishing Ltd.

intrinsic Bi-2212 Josephson junctions can be tuned in a large range by current injection. This carrier injection effect is reversible and persistent.

An alternative way to realize a thin film intrinsic stacked junction array uses substrates with a surface not parallel to the CuO$_2$-planes (Chana *et al.*, 2000). On such vicinal cut substrates the film grows with CuO$_2$-planes tilted with respect to the surface (Fig. 8.14c). Patterning of a microbridge results in a nearly horizontal stack of junctions and the length of the microbridge corresponds to the number of junctions in series. Intrinsic Josephson behaviour of the microbridges was observed for misorientation angles equal or larger than 15 degrees (Mans *et al.*, 2006). This kind of array offers new possibilities for synchronization (Grib *et al.*, 2006).

8.5.3 Selected applications of intrinsic Josephson junctions

Wang *et al.* (2001a, 2001b) have demonstrated the impressive performance of their devices, like the response to microwaves up to the THz range. Additionally, complex 2-D arrays, 3-D arrays and artificial shunted junctions with improved synchronization have been realized leading to components and performance required for applications, see Wang *et al.* (2002, 2003). Based on the high-quality complex devices, a voltage standard using intrinsic junctions was proposed and tested by Wang *et al.* (2001b, 2002, 2003). Zero-crossing Shapiro steps with irradiation at 1.6 THz have been observed, Fig. 8.28. The 'double sided fabrication method' was extended to 3-D stack arrays with up to 2500 intrinsic junction stacks on a chip, Fig. 8.29. For a 256-stack array with about 11 000 junctions, zero-crossing steps up to a voltage of 2.4 V have been observed. The advantage

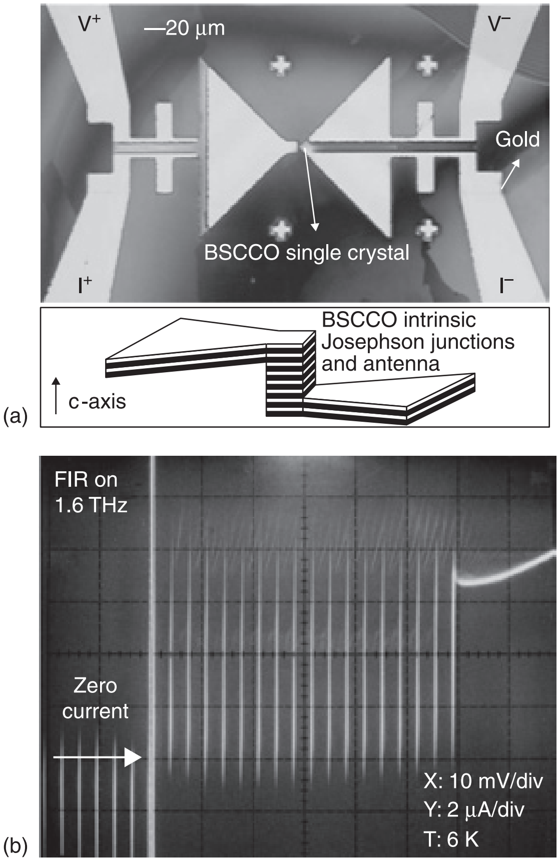

8.28 Terahertz response of intrinsic Josephson junctions: (a) optical image of a stack prepared out of a BSCCO single crystal with an integrated bow-tie antenna (schematically shown at the bottom) and r.f. filters all glued onto a silicon substrate; (b) zero-crossing Shapiro steps under microwave irradiation of 1.6 THz (Wang *et al.*, 2001a, Figs 1 and 3b, Copyright (2001) by the American Physical Society). Reprinted with permission from Wang HB, Wu PH, and Yamashita T (2001a), 'Terahertz response of intrinsic Josephson junctions in high-T_c superconductors', *Phys. Rev. Lett.* **87**, 107 002, Figs. 1 and 3b, Copyright (2001) by the American Physical Society.

would be the high working temperature which can be realized by liquid nitrogen or a cryocooler leading to very compact voltage standards.

The use of intrinsic arrays as radiation sources up to some THz, i.e. especially for the FIR range where such compact small sources can replace big CO_2-laser pumped systems, is restricted by the low power of emission of non-synchronized arrays. Even if this power was enhanced by several μW within the last few years, these sources are far from real applications.

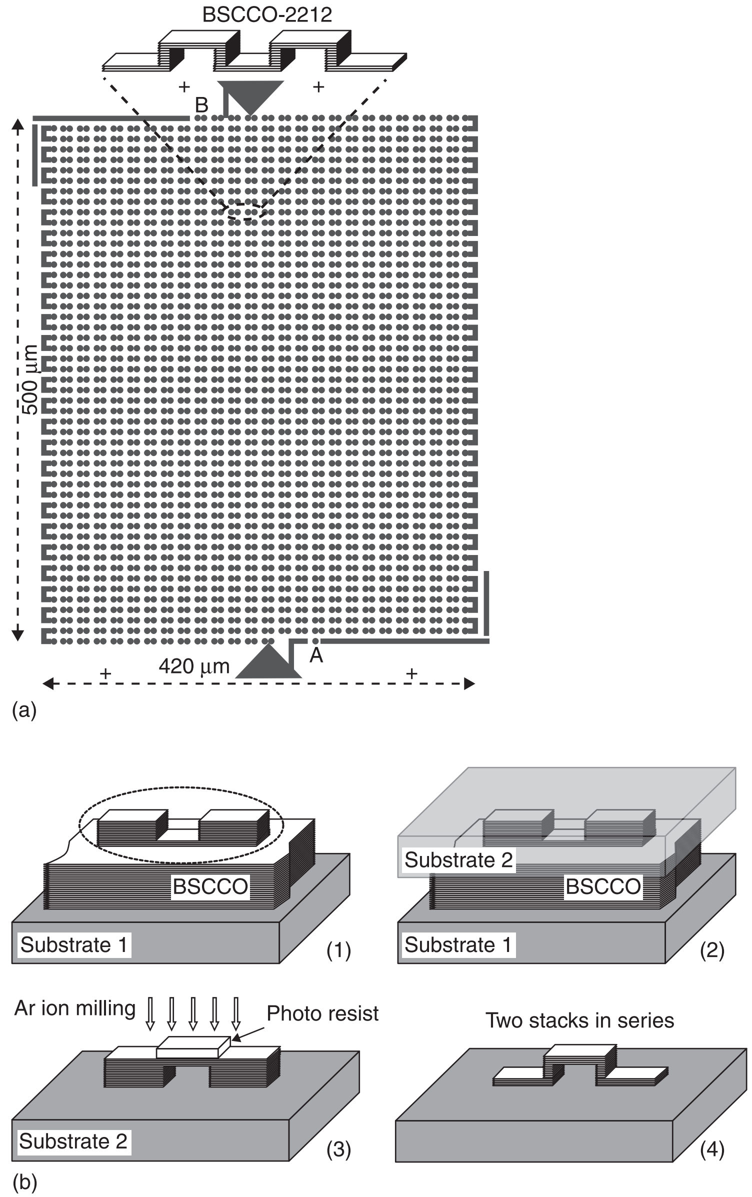
BSCCO-2212
+
B
+
500 µm
420 µm
+
A
+
(a)
BSCCO
Substrate 1
(1)
Substrate 2
BSCCO
Substrate 1
(2)
Ar ion milling
Photo resist
Substrate 2
(3)
Two stacks in series
(4)
(b)

8.29 3-D array of 2500 intrinsic Josephson junction stacks prepared by FIB etching: (a) optical photograph and schematic detail, (b) double sided fabrication process (Wang *et al.*, 2003, Figs 1 and 2, Copyright (2003) by IOP Publishing Ltd). For details of the fabrication process see Wang *et al.* (2003). Reprinted with permission from Wang HB, Chen J, Wu PH, Yamashita T, Vasyukov D, and Müller P (2003), 'Intrinsic Josephson junctions: integrated circuits and possible applications', *Supercond. Sci. Technol.* **16**, 1375–1379, Fig. 1, Copyright (2003) by IOP Publishing Ltd.

New concepts like tuning of the emitted frequency by additional d.c. currents have been proposed by Tachiki *et al.* (2005). Their simulations give emitted powers up to more than 1 mW for a 100 μm × 500 μm stack. A very promising work by Ozyuzer *et al.* (2007) offers a way out by using the flux motion without external magnetic field in these arrays with lateral dimensions in the 100 μm range, Fig. 8.30. A high power radiation of 0.5 μW at frequencies up to 0.85 THz has been observed. In analogy to a laser cavity, the excitation of a geometrical electromagnetic cavity resonance inside the sample generates a macroscopic coherent state in which a large number of junctions oscillate in phase. Even if the mechanism is up to now not clear, see for example Tachiki *et al.* (2009), Grib and Seidel (2009) and references therein, such compact solid-state sources of coherent THz radiation are being sought for sensing, imaging and spectroscopy applications across the physical and biological sciences. Kadowaki *et al.* (2008) improved the power of emission significantly to 5 μW from a single 60 μm mesa at 648 GHz.

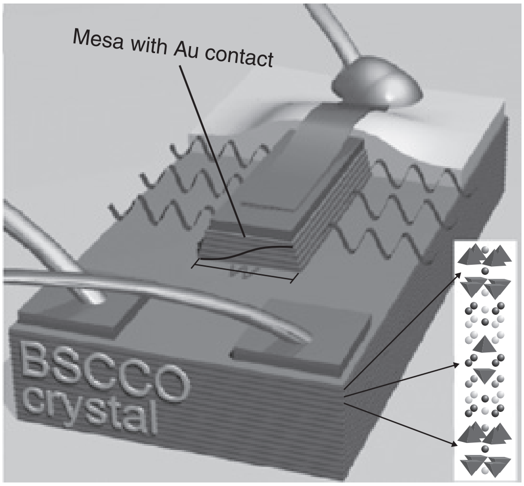

(a)

8.30 Josephson radiation source: (a) schematic of the BSCCO mesa resonator with the fundamental cavity resonance on the width w (black half wave) and the emitted THz radiation from the long side faces (grey waves); (b) temperature dependence of the IV-characteristics (dark lines, left y-axis) and voltage dependence of radiation power (grey lines, right y-axis) of a 100 μm BSCCO mesa structure. A non-monotonous temperature dependence of the radiation power (inset of panel d) results from the interplay of self-heating (back-bending of the IV-curve at high bias) and re-trapping (jumps in the IV-curve) (Gray *et al.*, 2009, Figs 1 and 2, Copyright (2009) by IEEE). Reprinted with permission from Gray KE, Ozyuzer L, Koshelev AE, Kurter C, Kadowaki K, *et al.* (2009), 'Emission of terahertz waves from stack of intrinsic junctions', *IEEE Trans. Appl. Supercond.* **19**, 886–890, Figs 1 and 2, Copyright (2009) by IEEE.

(*Continued*)

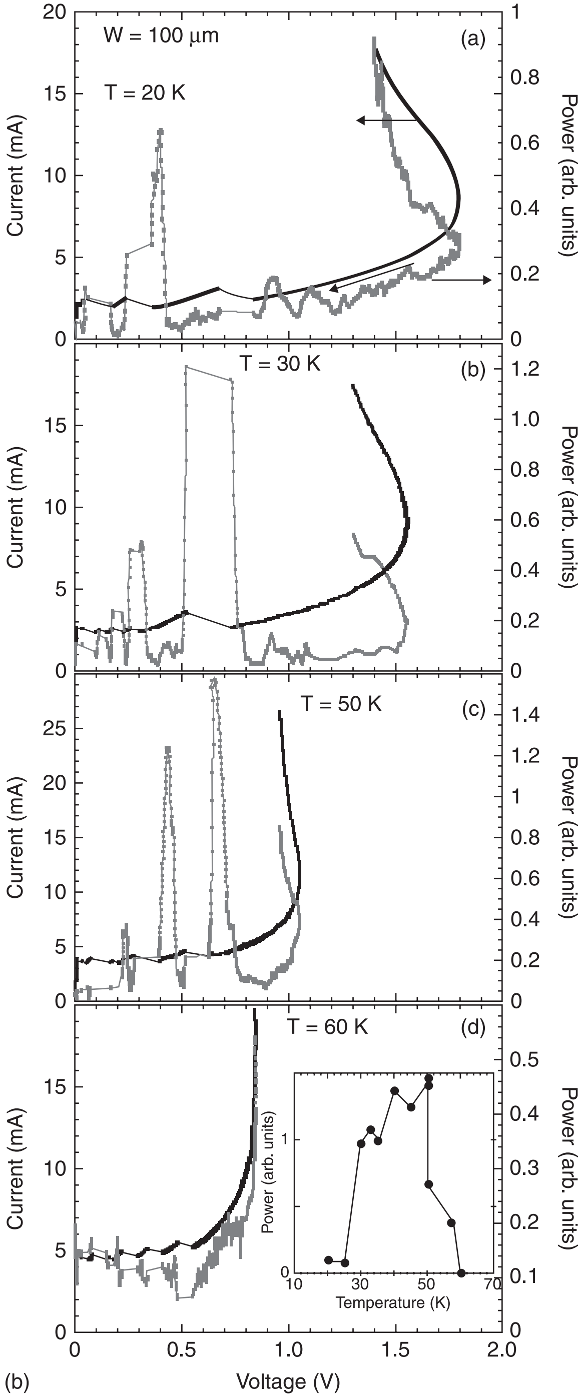

8.30 Continued.

They also observed higher harmonics up to the 4th order resulting in a frequency exceeding 2.5 THz. The geometrical resonances lead to restrictions in the emitted frequencies but Gray *et al.* (2009) have demonstrated that a proper shape of the resonator like a trapezoidal mesa cross-section yields to THz-sources with voltage-tunable emission frequencies. Computer simulations by Lin, Hu and Tachiki (2008) show that cavity resonances of the transverse plasma occur in the intrinsic Josephson junctions with frequencies up to 7 THz. The frequency as well as the energy of emission can be tuned almost continuously by the current and an external magnetic field. The emitted energy per area can go up to about 400 W/cm^2.

An additionally nanoelectrode of a thickness of 100 nm in the middle of an intrinsic Josephson junction array was realized by Wang *et al.* (2005) to investigate the self-heating effect, Fig. 8.31. This electrode provides an easy access to the

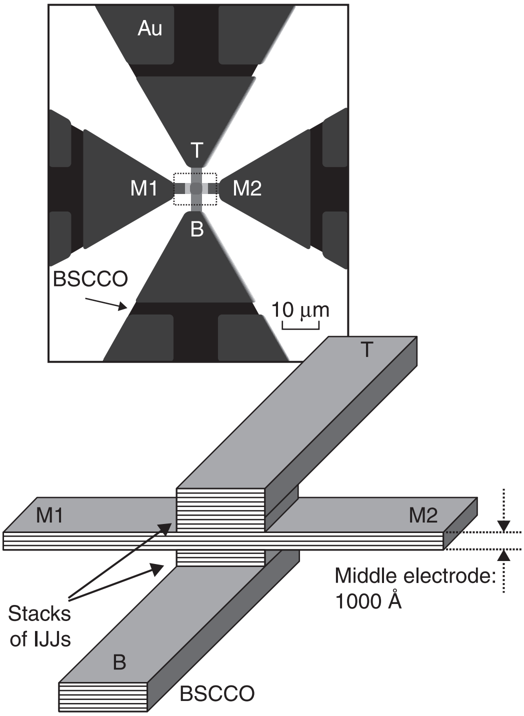

8.31 Optical microscope image and scheme of a BSCCO intrinsic Josephson junction (IJJ) with a 100-nm-thick middle electrode (Wang *et al.*, 2005, Fig. 1, Copyright (2005) by the American Institute of Physics). Reprinted with permission from Wang HB, Hatano T, Yamashita T, Wu PH, and Müller P (2005), 'Direct observation of self-heating in intrinsic Josephson junction array with a nanoelectrode in the middle', *Appl. Phys. Lett.* **86**, 023504, Fig. 1, Copyright (2005) by the American Institute of Physics.

inside of the intrinsic arrays for better understanding of their physics but it may find application in superconducting digital circuits, three-terminal devices, 3-D arrays, and other devices in superconducting electronics, too. Some possible applications of intrinsic Josephson junctions for three-terminal devices have been summarized by Yurgens (2000). Figure 8.32 shows some suggested three-terminal devices like quasiparticle-injection or electric field-effect devices as well as a vortex-flow transistor. The extreme dimensions of the intrinsic junctions will increase the sensitivity and performance of such devices compared to artificially stacked thin film structures.

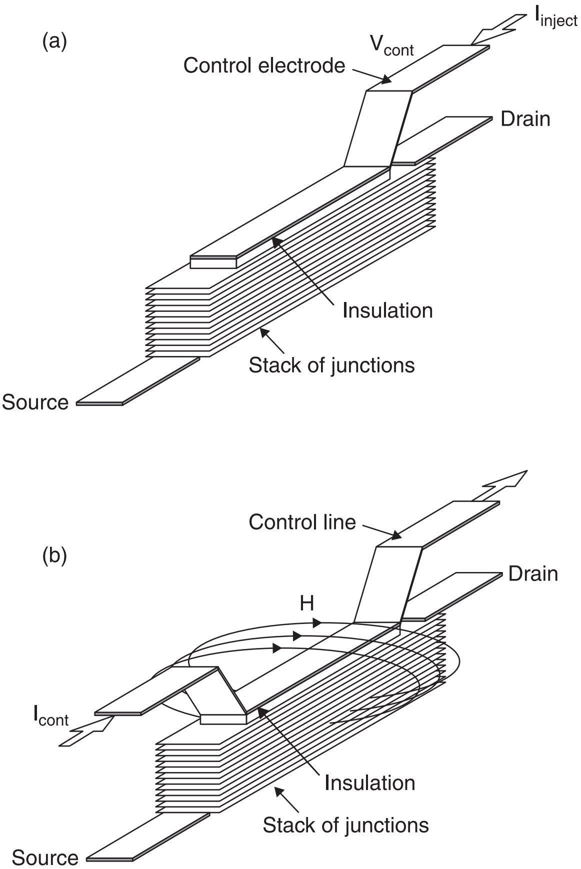
(a)
I_{inject}
V_{cont}
Control electrode
Drain
Insulation
Stack of junctions
Source
(b)
Control line
Drain
H
I_{cont}
Insulation
Stack of junctions
Source

8.32 Suggested three-terminal devices based on stacks of intrinsic Josephson junctions: (a) quasiparticle-injection or field-effect transistors, (b) vortex-flow transistor (Yurgens, 2000, Fig.17. Copyright (2000) by IOP Publishing Ltd). Reprinted with permission from Yurgens A (2000) 'Intrinsic Josephson junctions: recent developments', *Supercond. Sci. Technol.* **13**, R85–R100, Fig. 17. Copyright (2000) by IOP Publishing Ltd.

Another field of possible application for intrinsic junctions will be their use in qubits. The large superconducting gap suggests the potential advantage that they can operate at higher temperatures or for longer decoherence times. In particular, the phase qubits based on the current-biased junctions are promising since the experimental observation of the macroscopic quantum tunnelling (MQT) in intrinsic Josephson junctions (Inomata *et al.*, 2005, 2007; Maeda *et al.*, 2006; Jin *et al.*, 2006; Kashiwaya *et al.*, 2008). But the details of these experiments show the importance of multi-junction effects, d-wave symmetry, self-heating and current fluctuations. These problems have to be solved for application in quantum computing.

The nonlinear inductance of misaligned Tl-2212 thin film microbridge arrays on 20° vicinal $LaAlO_3$ substrates was applied to tunable filters with a good selectivity (Zhou *et al.*, 2007).

8.6 Hybrid junctions

8.6.1 Physics of hybrid junctions

In the beginning, the combination of a conventional superconducting electrode of s-wave order parameter symmetry with a high-T_c electrode was done to study the paring symmetry of the high-T_c superconductors. The properties of the hybrid Josephson junctions depend on the crystal orientation of the high-T_c material because the sign of the phase of the order parameter is different in the a- and b-direction within the CuO_2-planes because of d-wave symmetry. So-called corner junctions were introduced to test this behaviour, Wollman *et al.* (1993). Later, the geometry was fixed to obtain π-junctions where the phase shift of 180 degrees results in zero critical current for zero magnetic field, Kirtley *et al.* (1997). An excellent overview on π-junctions and their physics is given by Hilgenkamp (2008). It should be mentioned that π-junctions can also be obtained by the intrinsic phase shifts inside superconductor–ferromagnet–superconductor (SFS) junctions. Their operation is based on the spatial oscillations of the phase of the wave function in the ferromagnet induced by the proximity effect. Because up to now high-T_c superconductors have just started to be used for SFS junctions, see e.g. Volkov and Efetov (2009) and references therein, we will concentrate on the hybrid junctions here. The ramp-edge hybrid junction in the YBCO-Au-Nb technology is currently the most advanced technique to create π-shift structures. Chesca *et al.* (2008) have shown that these junctions have a purely sinusoidal current-phase relation which is essential to take into consideration for their implementation as qubits or π-junctions in digital circuits. Well-defined zigzag-shaped ramp-type hybrid junctions within this technology have been investigated by Smilde *et al.* (2002a). These arrays present controllable model systems to study the influences of π-facets in high-angle high-T_c grain boundaries, see section 8.3. The magnetic field dependencies of the critical currents provide evidence for the d-wave-induced alternations in the direction of the Josephson current between neighbouring sides of the zigzag structure, Fig. 8.33.

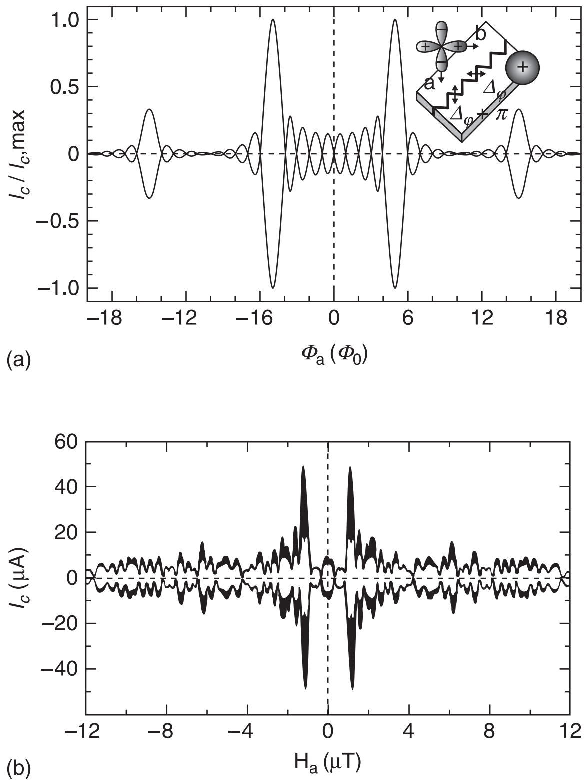

8.33 YBCO-Nb zigzag junction: (a) scheme and calculated magnetic flux dependence of critical current for an array of ten facets composed of standard and π-junctions, (b) experimental result for such an array (Smilde *et al.*, 2002a, Figs 1 and 3a, Copyright (2002) by the American Physical Society). Reprinted with permission from Smilde HJH, Ariando, Blank DHA, Gerritsma GJ, Hilgenkamp H, and Rogalla H (2002a), 'd-wave-induced Josephson current counterflow in $YBa_2Cu_3O_7$ Nb zigzag junctions', *Phys. Rev. Lett.* **88**, 057004, Figs 1 and 3a, Copyright (2002) by the American Physical Society.

8.6.2 Preparation and performance of hybrid junctions

The coupling of the s-wave niobium to the d-wave YBCO is realized via a very thin Au layer in a ramp-edge geometry (Fig. 8.15) because the etched YBCO step surface has to be covered *in situ*. In any case, the oxygen outdiffusion leads to a thick barrier region without Josephson tunnelling. It was discussed if (and how) this very thin normal layer has an influence on the junction behaviour. It is assumed that the proximity effect of the niobium–gold interface leads to a conventional superconducting order parameter at the interface to the d-wave

YBCO. The reduction of the bulk niobium order parameter amplitude leads to a reduction of the I_cR_N-product but at 4.2 K it is still about 1 mV.

The YBCO-Au-Nb technology leads to small spreads and high time stability of the devices with up to 100 Josephson junctions which allows application in simple SFQ circuits.

8.6.3 Selected applications of hybrid junctions

Beside application in basic research connected to order parameter symmetry and unusual Josephson coupling, the main interest in hybrid junctions results from the possibility of realizing standard as well as π-junctions within one well-established technology.

Superconducting loops with π-junctions produce a circulating current depending on the magnetic flux through the loop. Spontaneously generated half-flux quanta are the basis for building a bistable system in which the polarity of the flux is controllable by a current pulse. This can be used for different RSFQ circuits like a toggle-flip-flop (TFF) demonstrated by Ortlepp *et al.* (2007). In this TFF it was realized the internal states, represented by the polarity of half-flux quantum in π-rings, can be controllably toggled by applying single flux quantum pulses. Because of the natural bistability of the π-rings the symmetry of the logic devices is improved. In this way operation margins are enhanced to a level that there is no need of additional bias current lines compared to standard RSFQ circuits, Fig. 8.34. This also leads to a miniaturization of the circuits.

Kawabata *et al.* (2007) have demonstrated MQT for hybrid junctions and pointed out that due to a quasiparticle-tunnelling blockade effect the decoherence time of s/d qubits is expected to be much longer than that of the d/d qubits. This result suggests the high potential of hybrid junctions for applications in quantum information devices.

Finally, an unusual application of hybrid junctions should be mentioned. Kimura *et al.* (2008) reported on a Scanning Josephson Tunnelling Microscope (SC-STM) which uses a conventional superconducting tip (Pb with an Ag capping layer) instead of the normal conducting standard. By scanning high-T_c superconducting single crystal ($Bi_2Sr_2CaCu_2O_{8+\delta}$) the Josephson current across the surface is measured and yields local values of the I_cR_N product at 2.1 K. Corresponding energy gap measurements were also performed and a surprising inverse correlation was observed between the local I_cR_N product and the local energy gap. This result is unexpected from BCS theory but consistent with the phase fluctuation model (Emery and Kivelson, 1995).

8.7 Future trends

Within the last few years there has been impressive progress in the quality of high-T_c superconducting films, multilayers with other materials, and reduction of

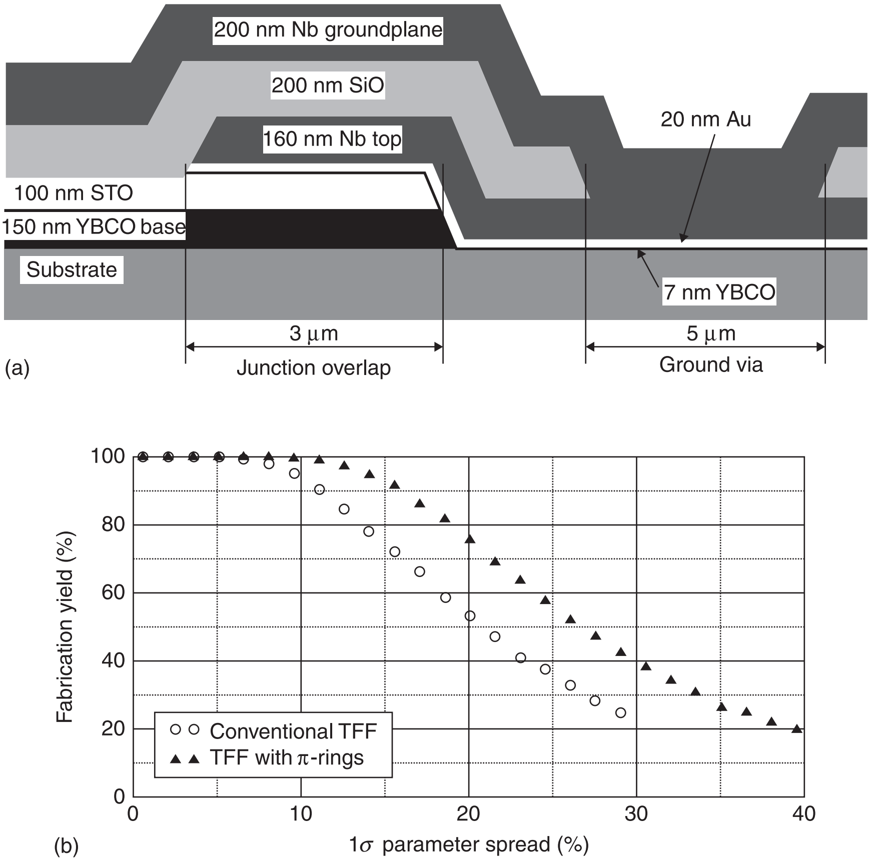

8.34 (a) Cross-section of a hybrid ramp-edge junction in YBCO/Au/Nb technology including a niobium groundplane, (b) fabrication yield on parameter spread for a toggle-flip-flop by conventional junctions compared to hybrid junctions in π-rings (Ortlepp *et al.*, 2007, Figs 6 and 8, Copyright (2007) by IEEE). Reprinted with permission from Ortlepp T, Ariando, Mielke O, Verwijs CJM, Foo KFK, *et al.* (2007), 'RSFQ circuitry using intrinsic π-phase shifts', *IEEE Trans Appl. Supercond.* **17**, 659–663, Figs 6 and 8, Copyright (2007) by IEEE.

parameter spread of Josephson junctions on a chip as well as from chip to chip. The deeper understanding of the nature of the high-T_c materials, especially their complex order parameter symmetry, the spontaneously induced currents connected to a full or a half-flux quantum state and the high asymmetry in all properties, lead to new kinds of Josephson effects like intrinsic junctions or π-junctions, respectively. Even if there is still no general microscopic theory for the high-T_c superconductors these materials offer a lot of new applications in superconductive electronics and sensor systems. The first prototypes of high-T_c Josephson junction applications have been demonstrated using specialized single junctions or arrays with up to 100 junctions. The 'SCENET roadmap for superconductor digital electronics' by ter Brake *et al.* (2006) gives an overview in status and future developments and summarizes that after the 'decade of the materials science' it is now the turn of the 'decade of the market'.

High-T_c Josephson junctions promise about a ten times higher circuit speed than low-T_c ones corresponding to their ten times larger I_cR_N product. The additional advantage of 'self-shunted' junctions requires no external normal conducting shunt resistors which leads to smaller areas for circuits on chips. The main problem up to now has been the quite large spread in junction parameters which limits the circuit complexity to 10–100 Josephson junctions. In spite of these drawbacks ter Brake *et al.* (2006) expected to have important niche applications in hand-held equipment and satellite payloads, where low weight, size and cooling power consumption (as compared to those for low-T_c Josephson circuits) is a decisive issue.

Trends in HTS JJ technology are connected to miniaturization like submicrometer junctions and use of intrinsic JJ arrays. Here the problem of spread is still unsolved but progress like the 'double-sided technology' is going on. Thus progress in voltage standards and voltage synthesizers as well as in radiation sources and THz applications have to be expected in the near future. For single junctions and spatial distributed arrays application as mixers, radiation detectors and sources up to THz range will be realized not only for astronomy but for X-ray spectroscopy and THz imaging, too.

Finally, it should be mentioned that there is rising interest in high-T_c Josephson junctions for solid-state qubits because of the new possibilities to manipulate quantum phases and their higher intrinsic stability.

Many new aspects have to be expected by other materials used for the junctions, for example for coupling barriers or metal electrodes. Even for the high-T_c superconductors there may be new materials besides MgB_2 used in the future. The discovery of the iron-pnictides (Kamihara *et al.*, 2008; Chen *et al.*, 2008) gives the possibility of replacing the standard cuprates. Up to now there have mainly been basic works to study the symmetry of the order parameter in these materials (e.g. Parish *et al.*, 2008; Hicks *et al.*, 2009) and deriving novel properties in Josephson junctions involving the pairing state of the iron-pnictides (Tsai *et al.*, 2009; Parker and Mazin, 2009), but first hybrid Josephson junctions with FeAs single crystals and Pb counter-electrodes have been demonstrated (Zhang *et al.*, 2009a). All-pnictide Josephson junctions were realized by crossing two differently doped single crystals (Zhang *et al.*, 2009b) or with thin films on bicrystal substrates resulting in grain boundary junctions (Katase *et al.*, 2010). The reported rather conventional behaviour of the pnictide Josephson junctions looks very promising as RSJ-like IV-characteristics with quite small I_cR_N products, clear Shapiro steps, and Fraunhofer-like magnetic field dependence of the critical Josephson current were reported. There may be some new kinds of Josephson junctions based on the assumed extended s-wave symmetry of some of the Fe-based superconductors.

8.8 References

Ambegaokar V and Baratoff A (1963), 'Tunneling between superconductors', *Phys. Rev. Lett.* **10**, 486–489. doi: 10.1103/PhysRevLett.10.486

Amin MHS, Smirnov AYu, Zagoskin AM, Lindström T, Charlebois SA, *et al.* (2005), 'Silent phase qubit based on d-wave Josephson junctions', *Phys. Rev. B* **71**, 064516 (5 pp.). doi: 10.1103/PhysRevB.71.064516

Barholz K-U, Kupriyanov MY, Hübner U, Schmidl F, and Seidel P (2000), 'An alternative explanation of the "long-range proximity effect" in HTS junctions', *Physica C* **334**, 175–184. doi: 10.1016/50921-4534(00)00248-3

Barone A and Paterno G (1982), *Physics and Applications of the Josephson Effect*, New York, John Wiley and Sons.

Bauch T, Lombardi F, Tafuri F, Barone A, Rotoli G, *et al.* (2005), 'Macroscopic quantum tunnelling in d-wave $YBa_2Cu_3O_{7-\delta}$ Josephson junctions', *Phys. Rev. Lett.* **94**, 087003 (4 pp.). doi: 10.1103/PhysRevLett.94.087003

Beasley MR (1995), 'Recent progress in high-T_c superconductivity: what would make a difference?' *IEEE Trans. Appl. Supercond.* **5**, 141–151. doi: 10.1109/77.402513

Booij WE, Pauza AJ, Tarte EJ, Moore DF, and Bramire MG (1997), 'Proximity coupling in high-T_c Josephson junctions produced by focused electron beam irradiation', *Phys. Rev. B* **55**, 14600–14609. doi: 10.1103/S0163-1829 (97)01821-3

Carillo F, Lombardi F, Miletto Granozio F, Punzo V, Ricci F, *et al.* (2000), 'Transport properties of Josephson junctions and SQUIDs employing different types of YBCO grain boundaries obtained through the biepitaxial technique', *Int. J. Mod. Phys. B* **14**, 3074–3079. doi: 10.1142/S 0217979200003332

Carmody M, Marks LD, and Merkle KL (2002), 'Current transport along grain boundaries in d-wave superconductors', *Physica C* **370**, 228–238. doi: 10.1016/S0921-4534(01)00946-7

Chana OS, Kuzhakhmetov AR, Warburton PA, Hyland DMC, Dew-Hughes D, and Grovenor CRM (2000), 'Alternating current Josephson effect in intrinsic Josephson bridges in $Tl_2Ba_2CaCu_2O_8$ thin films', *Appl. Phys. Lett.* **76**, 3603–3605. doi: 10.1063/1.126720

Chen GF, Liz LG, Zhon J, Wu D, Dong J, *et al.* (2008), 'Superconducting properties of the Fe-based layered superconductor $LaFeAsO_{0.9}F_{0.1-\delta}$', *Phys. Rev. Lett.* **101**, 057007 (4 pp.). doi: 10.1103/PhysRevLett.101.057007

Chen Ke, Cui Y, Li Q, Xi XX, Cybart SA, *et al.* (2006), 'Planar MgB_2 superconductor-normal metal-superconductor junctions fabricated using epitaxial MgB_2/TiB_2 bilayers', *Appl. Phys. Lett.* **88**, 222511 (3 pp.). doi: 10.1063/1.2208555

Chesca B, Smilde HJH, and Hilgenkamp H (2008), 'Coupling in untwinned $YBa_2Cu_3O_{7-x}$/Nb d-wave junctions', *J. Phys. Conf. Ser.* **97**, 012095 (6 pp.). doi: 10.1088/1742-6596/97/1/012095

Cybart SA, Chen Ke, Cui Y, Li Q, Xi XX, and Dynes RC (2006), 'Planar MgB_2 Josephson junctions and series arrays via nanolithography and ion damage', *Appl. Phys. Lett.* **88**, 012509 (3 pp.). doi: 10.1063/1.2162669

Cybart SA, Wu SM, Anton SM, Siddiqi T, Clarke J, and Dynes RC (2008), 'Series arrays of incommensurate superconducting quantum interference devices from $YBa_2Cu_3O_{7-\delta}$ ion damage junctions', *Appl. Phys. Lett.* **93**, 182502 (3 pp.). doi: 10.1063/1.3013579

Dilorio MS, Yang K-Y, and Yoshizumi S (1995), 'Biomagnetic measurements using low-noise integrated SQUID magnetometers operating in liquid nitrogen', *Appl. Phys. Lett.* **67**, 1926–1928. doi: 10.1063/1.114570

Dilorio MS, Yoshizumi S, Yang K-Y, Maung M, Zhang J, and Power B (1993), 'Low noise high-T_c DC-SQUIDS at 77 K', *IEEE Trans. Appl. Supercond.* **3**, 2011–2017. doi: 10.1109/77.233462

Divin Y, Volkov O, Pavlovskii V, Poppe U, and Urban K (2001), 'Terahertz spectral analysis by ac Josephson effect in high-T_c bicrystal junctions', *IEEE Trans. Appl. Supercond.* **11**, 582–585. doi: 10.1109/77.919412

Divin YY, Volkov OY, Liatti M, Shirotov VV, Pavlovskii VV, *et al.* (2002), 'Hilbert spectroscopy from gigahertz to terahertz frequencies by high-T_c Josephson junctions', *Physica C* **372–376**, 416–419. doi: 10.1016/S0921-4534(02)00712-8

Dmitrenko IM, Yanson IK, and Svistunov VM (1965), 'Experimental observation of the tunnel effect of Cooper pairs with the emission of photons', *Pisma ZhETF* **65**, 650–652.

Du J and Foley CP (2003), 'Trimming, stability and passivation of YBCO step-edge junctions', *Physica C*, **391**, 31–41. doi: 10.1016/S0921-4534(03)00812-8

Emry VJ and Kivelson SA (1995), 'Importance of phase fluctuations in superconductors with small superfluid density', *Nature (London)* **374**, 434–437. doi: 10.1038/374434aO

Foley CP, Mitchell EE, Lam SKH, Sankrithyan B, Wilson YM, *et al.* (1999), 'Fabrication and characterisation of YBCO single grain boundary step edge junctions', *IEEE Trans. Appl. Supercond.* **9**, 4281–4284. doi: 10.1109/77.783971

Golubov AA and Kuriyanov M Yu (1998), 'Anomalous proximity effect in d-wave superconductors', *JETP Lett.* **67**, 501–507. doi: 10.1134/1.567717

Golubov A and Tafuri F (2000), 'Andreev reflection in layered structures: implications for high-T_c grain-boundary Josephson junctions', *Phys. Rev. B* **62**, 15200–15203. doi: 10.1103/PhysRevB.62.15200

Gray KE, Ozyuzer L, Koshelev AE, Kurter C, Kadowaki K, *et al.* (2009) 'Emission of terahertz waves from stack of intrinsic Josephson junctions', *IEEE Trans. Appl. Supercond.* **19**, 886–890. doi: 10.1109/TASC.2009.2017888

Grib A and Seidel P (2009), 'Wide-band phase locking of Josephson junctions in a resonator', *Physica Status Solidi RRL* **3**, 302–304. doi: 10.1002/pssr.200903286

Grib AN, Mans M, Scherbel J, Buenfeld M, Schmidl F, and Seidel P (2006), 'Synchronization of serial intrinsic Josephson junction arrays on vicinal substrates', *Supercond. Sci. Technol.* **19**, S200–S204. doi: 10.1088/0953-2048/19/5/S07

Grib AN, Seidel P, and Scherbel J (2002), 'Synchronization of overdamped Josephson junctions shunted by a superconducting resonator', *Phys. Rev. B.* **65**, 94508 (10 pp.). doi: 10.1103/PhysRevB.65.094508

Gross R (2005), 'Grain boundaries in high temperature superconductors: A retrospective view', *Physica C* **432**, 105–115. doi: 10.1016/j.physc.2005.07.016

Gross R, Chaudhari P, Kawasaki M, and Gupta A (1990), 'Scaling behaviour in electrical transport across grain boundaries in $YBa_2Cu_3O_{7-\delta}$ superconductors', *Phys. Rev. B* **42**, 10735–10737. doi: 10.1103/PhysRevB.42. 10735

Hamilton CA (2000), 'Josephson voltage standards', *Rev. Sci. Instrum.* **71**, 3611–3623. doi: 10.1063/1.1289507

Haruta M, Kume E, and Sakai S (2009), 'Fabrication of thin-film-type $Bi_2Sr_2CaCu_2O_{8+\delta}$ intrinsic Josephson junctions by pulsed-laser-deposition', *Supercond. Sci. Technol.* **22**, 125004 (4 pp.). doi: 10.1088/0953-2048/22/12/125004

He M, Klushin AM, Yan SL, and Klein N (2007), 'Optimization of bicrystal Josephson junctions and arrays in a Fabry-Perot resonator', *IEEE Trans. Appl. Supercond.* **17**, 934–937. doi: 10.1109/TASC.2007.898140

Hicks CW, Lippmann TM, Huber ME, Ren Z-A, Zhao Z-X, and Moler KA (2009), 'Limits on the superconducting order parameter in NdFeAsO$_{1-x}$F$_y$ from scanning SQUID microscopy'. *J. Phys. Soc. Jpn.* **78**, 013708 (4 pp.). doi: 10.1143/JPSJ.78.013708

Hilgenkamp H (2008), 'Pi-phase shift Josephson structures', *Supercond. Sci. Technol.* **21**, 034011 (5 pp.). doi: 10.1188/0953-2048/21/3/034011

Hilgenkamp H and Mannhart J (2002), 'Grain boundaries in high-T$_c$ superconductors', *Rev. Mod. Phys.* **74**, 485–549. doi: 10.113/RevModPhys.74.485

Hilgenkamp H, Mannhart J, and Mayer B (1996), 'Implications of $d_{x^2-y^2}$ symmetry and faceting for the transport properties of grain boundaries in high-T$_c$ superconductors', *Phys. Rev. B* **53**, 14586–14593. doi: 10.1103/PhysRevB.53.14586

Hu X and Lin S-Z (2010), 'Phase dynamics in a stack of inductively coupled intrinsic Josephson junctions and terahertz electromagnetic radiation', *Supercond. Sci. Technol.* **23**, 053001 (29 pp.). doi: 10.1088/0953-2048/23/5/053001

Inomata K, Sato S, Kinjo M, Kitabatake N, Wang HB, *et al.* (2007), 'Study of macroscopic quantum tunnelling in $Bi_2Sr_2CaCu_2O_{8+\delta}$ intrinsic Josephson junctions', *Supercond. Sci. Technol.* **20**, S105–S109. doi: 10.1088/0953-2048/20/2/S20

Inomata K, Sato S, Nakajima K, Tanaka A, Takano Y, *et al.* (2005), 'Macroscopic quantum tunneling in a d-wave high-T$_c$ $Bi_2Sr_2CaCuO_{8+\delta}$ superconductor', *Phys. Rev. Lett.* **95**, 107005 (4 pp.). doi: 10.1103/PhysRevLett.95.107005

Jia CJ, Kabius B, Urban K, Herrmann K, Schubert J, *et al.* (1992), 'The microstructure of epitaxial YBaCuO films on steep steps in LaAlO substrates', *Physica C* **196**, 211–226. doi: 10.1016/0921-4534(92)90438-1

Jin XY, Lisenfeld J, Koval Y, Lukashenko A, Ustinov AV, and Müller P (2006), 'Enhanced macroscopic quantum tunneling in $Bi_2Sr_2CaCu_2O_{8+\delta}$ intrinsic Josephson-junction stacks', *Phys. Rev. Lett.* **96**, 177003 (4 pp.). doi: 10.1103/PhysRevLett.96.177003

Josephson BD (1962), 'Possible new effects in superconductive tunneling', *Phys. Lett.* **1**, 251–253. doi: 10.1016/0031-9163(62)91369-0

Kadin AM (1999), *Introduction to Superconducting Circuits,* New York, John Wiley & Sons.

Kadowaki K, Yamaguchi H, Kawamata K, Yamamoto T, Minami H, *et al.* (2008) 'Direct observation of tetrahertz electromagnetic waves emitted from intrinsic Josephson junctions in single crystalline $Bi_2Sr_2CaCu_2O_{8+\delta}$,' *Physica C* **468**, 634–639. doi: 10.1016/j.physc.2007.11.090

Kamihara Y, Watanabe T, Hirano M, and Hosono H (2008), 'Iron-based layered superconductor La (O$_{1-x}$F$_x$) FeAs (x = 0.05–0.12) with T$_c$ = 26 K', *J. Am. Chem. Soc.* **130**, 3296–3297. doi: 10.1021/ja800073m

Kashiwaya H, Matsumoto T, Shibata H, Kashiwaya S, Eisaki H, *et al.* (2008), 'Switching dynamics of $Bi_2Sr_2CaCu_2O_{8+\delta}$ intrinsic Josephson junctions: Macroscopic Quantum Tunneling and self-heating effect', *J. Phys. Soc. Jpn.* **77**, 104708 (8 pp.). doi: 10.1143/JPSJ.77.104708

Katase T, Ishimaru Y, Tsukamoto A, Hiramatsu H, Kamiya T, *et al.* (2010), 'Josephson junction in cobalt-doped $BaFe_2As_2$ epitaxial thin films on (La,Sr)(Al,Ta)O$_3$ bicrystal substrates', *Appl. Phys. Lett.* **96**, 142507 (3 pp.). doi: 10.1063/1.3371814

Katz AS, Woods SI, and Dynes RC (2000), 'Transport properties of high-T$_c$ planar Josephson junctions fabricated by nanolithography and ion implantation', *J. Appl. Phys.* **87**, 2978–2983. doi: 10.1063/1.372286

Kawabata S, Golubov AA, Ariando, Verwijs CJM, Hilgenkamp H, and Kirtley JR (2007), 'Macroscopic quantum tunnelling and quasiparticle-tunneling blockade effect in s-wave/d-wave hybrid junctions', *Phys. Rev. B* **76**, 064505 (6 pp.). doi: 10.1103/PhysRevB.76.064505

Kawayama I, Miyadera T, Murakami H, and Tonouchi M (2006), 'A tunable sub-terahertz wave generation and detection system with a photomixer and a high-T_c Josephson junction', *Supercond. Sci. Technol.* **19**, S403–S406. doi: 10.1088/0953-2048/19/5/S50

Kim S.-J., Latyshev YI, and Yamashita T (1999), 'Submicron stacked-junction fabrication from $Bi_2Sr_2CaCu_2O_{8+\delta}$ whiskers by focused-ion beam etching', *Appl. Phys. Lett.* **74**, 1156–1158. doi: 10.1063/1.123472

Kimura H, Barber RP, Ono S, Ando Y, and Dynes RC (2008), 'Scanning Josephson Tunneling Microscopy of single-crystal $Bi_2Sr_2CaCu_2O_{8+\delta}$ with a conventional superconducting tip', *Phys. Rev. Lett.* **101**, 037002 (4 pp.). doi: 10.1103/PhysRevLett.101.037002

Kirtley JR, Moler KA, and Scalapino DJ (1997), 'Spontaneous flux and magnetic-interference patterns in 0-π Josephson junctions', *Phys. Rev. B* **56**, 886–891. doi: 10.1103/S0163-1829(97)01726-8

Kito T, Yoshinaga Y, Izawa S, Inoue M, Fujimaki A, and Hayakawa H (2002), 'Excess-current-free stacked Josephson junctions with high I_cR_N product', *Physica C* **378–381**, 1322–1326. doi: 10.1016/S0921-4534(02)01707-0

Kleiner R and Müller P (1994), 'Intrinsic Josephson effects in high-T_c superconductors', *Phys. Rev. B* **49**, 1327–1341. doi: 10.1103/PhysRevB.49.1327

Kleiner R, Steinmeyer F, Kunkel G, and Müller P (1992), 'Intrinsic Josephson effects in $Bi_2Sr_2CaCu_2O_8$ single crystals', *Phys. Rev. Lett.* **68**, 2394–2397. doi: 10.1103/PhysRevLett.68.2394

Klushin AM, Behr R, Numssen K, Siegel M, and Niemeyer J (2002), 'Accurate measurements of quantum voltage steps on arrays of bicrystal Josephson junctions', *Appl. Phys. Lett.* **80**, 1972–1974. doi: 10.1063/1.1458072

Klushin AM, He M, Yan SL, and Klein N (2006), 'Arrays of high-T_c Josephson junctions in open milimeter wave resonators', *Appl. Phys. Lett.* **89**, 232505 (3 pp.). doi: 10.1063/1.2400401

Klushin AM, Prusseit W, Sodtke E, Borovitskii SI, Amatuni LE, and Kohlstedt H (1996), 'Shunted bicrystal Josephson junctions arrays for voltage standards', *Appl. Phys. Lett.* **69**, 1634–1636. doi: 10.1063/1.117055

Koval Y, Jin X, Bergmann C, Simsek Y, Ozyuzer L, *et al.* (2010), 'Tuning superconductivity by carrier injection', *Appl. Phys. Lett.* **96**, 082507 (3 pp.). doi: 10.1063/1.3327825

Langenberg DN, Scalapino DJ, Taylor BN, and Eck RE (1965), 'Investigation of microwave radiation emitted by Josephson junctions', *Phys. Rev. Lett.* **15**, 294–297. doi: 10.1103/PhysRevLett.15.294

Likharev KK (1986), *Dynamics of Josephson Junctions and Circuits,* Philadelphia, Gordon and Breach.

Lin S, Hu X, and Tachiki M (2008), 'Computer simulation on terahertz emission from intrinsic Josephson junctions of high-T_c superconductors', *Phys. Rev. B* **77**, 014507 (5 pp.). doi: 10.1103/PhysRevB.77.014507

Lombardi F, Tafuri F, Ricci F, Miletto Granozio F, Barone A, *et al.* (2002), 'Intrinsic d-wave effects in $YBa_2Cu_3O_{7-\delta}$ grain boundary junctions', *Phys. Rev. Lett.* **89**, 207001 (4 pp.). doi: 10.1103/PhysRevLett.89.207001

McCumber DE (1968), 'Effect of ac impedance on dc voltage-current characteristics of superconductor weak-link junctions', *Appl. Phys. Lett.* **12**, 277–280. doi: 10.1063/1.1651991

Maeda A, Kitano H, Gomez L, Kubo T, Ota K, and Ohashi T (2006), 'High-T_c Josephson junction: towards improvement of I_cR_N product and realization of phase qubits', *J. Phys.: Conf. Ser.* **43**, 1151–1154. doi: 10.1088/1742-6596/43/1/280

Mannhart J (2006), ‘Properties of grain boundaries in high-T_c superconductors – Notes on a recent presentation’, *Physica C* **450**, 152–155. doi: 10.1016/j.physc.2006.09.012

Mans M, Schneidewind H, Buenfeld M, Schmidl F, and Seidel P (2006), ‘Intrinsic Josephson junctions in misaligned $Tl_2Ba_2CaCu_2O_{8-x}$ thin films with different tilt angles’, *Phys. Rev. B* **74**, 214514. doi: 10.1103/PhysRevB.74.214514

Maruyama M, Wakana H, Hato T, Suzuki H, Tanabe K, *et al.*, (2007), ‘Observation of SFQ pulse using HTS sampler’, *Physica C* **463–465**, 1101–1105. doi: 10.1016/j.physc.2007.05.047

Merkle KL, Huang Y, Rozeveld S, Char K, and Moeckly BH (1999), ‘Electron microscopy of high-T_c Josephson junctions formed in the epitaxial layer ramp-edge geometry: YBCO/barrier/YBCO’, *Micron* **30**, 539–559. doi: 10.1016/S0968-4328(99)00053-0

Miller DJ, Roberts TA, Kang JH, Talvaccio J, Buchholz DB, and Chang RPH (1995), ‘Meandering grain boundary in $YBa_2Cu_3O_7$ bicrystal thin film’, *Appl. Phys. Lett.* **66**, 2561–2563. doi: 10.1063/1.113167

Miyadera T, Kawayama I, Kiwa T, Tsukada K, and Tonouchi M (2005), ‘Frequency detection of focused sub-THz waves using a high-T_c Josephson junction’, *Physica C* **426–431**, 1726–1730. doi: 10.1016/j.physc.2005.02.136

Morimoto Y, Tarutani Y, Wakana H, Adachi S, Tsubone K, *et al.* (2006), ‘I_CR_N product of $YBa_2Cu_3O_{7-x}$ ramp-edge junctions at temperatures higher than 30 K’, *Physica C* **445–448**, 904–907. doi: 10.1016/j.physc.2006.05.068

Ortlepp T, Ariando, Mielke O, Verwijs CJM, Foo KFK, *et al.* (2007), ‘RSFQ circuitry using intrinsic π-phase shifts’, *IEEE Trans. Appl. Supercond.* **17**, 659–663. doi: 10.1109/TASC.2007.898635

Ozyuzer L, Koshelev AE, Kurter C, Gopalsami N, Li Q, *et al.* (2007), ‘Emission of coherent THz radiation from superconductors’, *Science* **318**, 1291–1293. doi: 10.1126/science.1149802

Parish MM, Hu J, and Bernevig BA (2008), ‘Experimental consequences of the s-wave cos (k_x)cos (k_y) superconductivity in the iron pnictides’, *Phys. Rev. B.* **78**, 144514 (9 pp.). doi: 10.1103/PhysRevB.78.144514

Parker D and Mazin II (2009), ‘Possible phase-sensitive tests of pairing symmetry in pnictide superconductors’, *Phys. Rev. Lett.* **102**, 227007 (4 pp.). doi: 10.1103/PhysRevLett.102.227007

Pauza A, Booij WE, Hermann K, Moore DF, and Blamire MG (1997), ‘Electron-beam damaged high-temperature superconductor Josephson junctions’, *J. Appl. Phys.* **82**, 5612–5632. doi: 10.1063/1.366422

Poppe U, Divin YY, Faley MI, Wu JS, Jia CL, *et al.* (2001), ‘Properties of $YBa_2Cu_3O_7$ thin films deposited on substrates and bicrystals with vicinal offcut and realization of high I_cR_N junctions’, *IEEE Trans. Appl. Supercond.* **11**, 3768–3771. doi: 10.1109/77.919884

Rosenthal PA, Grossman EN, Ono RH, and Vale LR (1993) ‘High temperature superconductor-normal metal-superconductor Josephson junctions with high characteristic voltages’, *Appl. Phys. Lett.* **63**, 1984–1986. doi: 10.1063/1.106365

Ruggerio ST and Rudman DA (Eds) (1990), *Superconducting Devices*, Boston, Academic Press.

Sarnelli E and Testa G (2002), ‘Transport properties of high-temperature grain boundary junctions’, *Physica C* **371**, 10–18. doi: 10.1016/S0921-4534(01)01111-x

Satoh T, Wen J.-G., Hidaka M, Tahara S, Koshizuka, N, and Tanaka S (2001), ‘High-temperature superconducting edge-type Josephson junctions with modified interface barriers’, *IEEE Trans. Appl. Supercond.* **11**, 770–775. doi: 10.1109/77.919459

Saval'ev S, Yampol'skii VA, Rakhmanov AL, and Nori F (2010), 'Terahertz Josephson plasma waves in layered superconductors: spectrum, generation, nonlinear and quantum phenomena', *Rep. Prog. Phys.* **73**, 026501 (49 pp.). doi: 10.1088/0034-4885/73/2/026501

Schilling M, Kaestner A, and Stewing F (2006), 'Room temperature near field microwave imaging with an $YBa_2Cu_3O_7$ Josephson cantilever', *Appl. Phys. Lett.* **88**, 252507 (3 pp). doi: 10.1063/1.2214152

Schmidl F, Dörrer L, Wunderlich S, Machalett F, Hübner U, *et al.* (1997), 'Superconducting properties of ion beam modified YBCO microbridges', *J. Low Temp. Phys.* **106**, 405–416 doi: 10.1007/BF02399646

Schmidl F, Pfuch A, Schneidewind H, Heinz E, Dörrer L, *et al.* (1995), 'Preparation and first measurements of TBCCO thin film intrinsic stacked Josephson junctions', *Supercond. Sci. Technol.* **8**, 740–743. doi: 10.1088/0953-2048/8/9/007

Schneidewind H (1995), *Beiträge zum Ionenstrahlätzen von kryoelektronischen Bauelementen auf der Basis von Kupratsupraleitern*, Thesis at Friedrich-Schiller-Universität Jena. Printed in Aachen, Shaker, ISBN 3-8265-0875-0

Schultze V, IJsselsteijn R, Meyer H-G, Oppenländer J, Häussler C, and Schopohl N (2003), 'High-T_c superconducting quantum interference filters for sensitive magnetometers', *IEEE Trans. Appl. Supercond.* **13**, 775–778. doi: 10.1109/TASC.2003.814040

Seidel P, Grib AN, Shukrinov YuM, Scherbel J, Hübner U, and Schmidl F (2001), 'Quasiparticle current and phase locking of intrinsic Josephson junctions', *Physica C* **362**, 102–107. doi: 10.1016/S0921-4534(01)00654-2

Seidel P, Schmidl F, Pfuch A, Schneidewind H, and Heinz E (1996), 'Investigations on high-T_c thin film intrinsic stacked Josephson junctions', *Supercond. Sci. Technol.* **9**, A9–A13. doi: 10.1088/0953-2048/9/4A/004

Seidel P, Zakosarenko V, Schmidl F, Dörrer L, Schneidewind H, *et al.* (1995), 'Investigation of thin-film DC SQUID gradiometer using a single YBCO layer', *IEEE Trans. Appl. Supercond.* **5**, 2931–2934. doi: 10.1109/77.403206

Shimakage H, Ono RH, Vale LR, Uzawa Y, and Wang Z, (2001), 'Interface-engineered Josephson junctions with high I_cR_N products' *Physica C* **357–360**, 1416–1419. doi: 10.1016/S0921-4534(01)00605-0

Shirotov VV, Divin YY, and Urban K (2002), 'Far-infrared broadband measurements with Hilbert spectroscopy', *Physica C* **372–376**, 454–456. doi: 10.1016/S0921-4534(02)00721-9

Sirena M, Fabréges X, Bergeal N, Lesueur J, Faini G, *et al.* (2007), 'Improving the I_cR_N product and the reproducibility of high T_c Josephson junctions made by ion irradiation', *Appl. Phys. Lett.* **91**, 262508 (3 pp.). doi: 10.1063/1.2828133

Smilde HJH, Ariando, Blank DHA, Gerritsma GJ, Hilgenkamp H, and Rogalla H (2002a), 'd-wave-induced Josephson current counterflow in $YBa_2Cu_3O_7$/Nb zigzag junctions', *Phys. Rev. Lett.* **88**, 057004 (4 pp.). doi: 10.1103/PhysRevLett.88.057004

Smilde HJH, Hilgenkamp H, Rijnders G, Rogalla H, and Blank DHA (2002b), 'Enhanced transparency ramp-type Josephson contacts through interlayer deposition', *Appl. Phys. Lett.* **80**, 4579–4581. doi: 10.1063/1.1485305

Stewart WC (1968), 'Current-voltage characteristics of Josephson junctions', *Appl. Phys. Lett.* **12**, 277–280. doi: 10.1063/1.1651991

Tachiki M, Fukuya S, and Koyama T (2009), 'Mechanism of terahertz electromagnetic wave emission from intrinsic Josephson junctions', *Phys. Rev. Lett.* **102**, 127002 (4 pp.). doi: 10.1103/PhysRevLett.102.127002

Tachiki M, Iizuka M, Minami K, Tejima S, and Nakamura H (2005), 'Emission of coutinous coherent terahertz waves with tunable frequency by intrinsic Josephson junctions', *Phys. Rev. B* **71**, 134515 (5 pp.). doi: 10.1103/PhysRevB.71.134515

Tafuri F and Kitley JR (2005), 'Weak links in high critical temperature superconductors', *Rep. Prog. Phys.* **68**, 2573–2663. doi: 10.1088/0034-4885/68/11/R03

Tafuri F, Kitley JR, Lombardi F, Bauch T, and Barone A (2004), 'Vortex matter in $YBa_2Cu_3O_{7-\delta}$ grain boundary junctions: intrinsic and extrinsic d-wave effects for π-circuitry', *Physica C* **404**, 367–374. doi: 10.1016/j.physc.2003.10.028

Tanabe K and Hidaka M (2007), 'Recent progress in SFQ device technologies in Japan', *IEEE Trans. Appl. Supercond.* **17**, 494–499. doi: 10.1109/TASC.2007.898704

Tanaka Y and Kashiwaya S (1997), 'Theory of Josephson effects in anisotropic superconductors', *Phys. Rev. B* **56**, 892–912. doi: 10.1103/PhysRevB.56.892

ter Brake HJM, Buchholz F-Im, Burnell G, Cleason T, Crété D, *et al.* (2006), 'SCENET roadmap for superconductor digital electronics', *Physica C* **439**, 1–41. doi: 10.1016/j.jhysc.2005.10.017

Tinchev S (2007), 'Mechanism of operation of Josephson junctions made from HT_c materials by ion modification', *Physica C* **460–462**, 1477–1478. doi: 101016/j.physC.2007.04.001

Tsai W-F, Yao D-X, Bernevig BA, and Hu JP (2009), 'Properties in Josephson junctions involving the $\cos(k_x)$ cos (k_y) pairing state in iron pnictides', *Phys. Rev. B* **80**, 012511 (4 pp.). doi: 10.1103/PhysRevB.80.012511

van Duzer T and Turner CW (1999), *Principles of Superconductive Devices and Circuits*, 2nd edition, New Jersey, Prentice Hall PTR.

Volkov AF and Efetov KB (2009), 'Proximity effect and its enhancement by ferromagnetism in high-temperature superconductor-ferromagnet structures', *Phys. Rev. Lett.* **102**, 077002 (4 pp.). doi: 10.1103/PhysRevLett.102.077002

Wang HB, Aruga Y, Chen J, Nakajima K, Yamashita T, and Wu PH (2000), 'Individual Shapiro steps observed in resistively shunted intrinsic Josephson junctions on $Bi_2Sr_2CaCu_2O_{8+x}$ single crystals', *Appl. Phys. Lett.* **77**, 1017–1019. doi: 10.1063/1.1288601

Wang HB, Chen J, Wu PH, Yamashita T, Vasyukov D, and Müller P (2003), 'Intrinsic Josephson junctions: integrated circuits and possible applications', *Supercond. Sci. Technol.* **16**, 1375–1379. doi: 10.1088/S0953-2048(03)67114-9

Wang HB, Guénon S, Yuan J, Jishi A, Arisawa S, *et al.* (2009), 'Hot spots and waves in $Bi_2Sr_2CaCu_2O_8$ intrinsic Josephson junction stacks: A study by Low Temperature Scanning Laser Microscopy', *Phys. Rev. Lett.* **102**, 017006 (4 pp.). doi: 10.1103/PhysRevLett.102.017006

Wang HB, Hatano T, Yamashita T, Wu PH, and Müller P (2005), 'Direct observation of self-heating in intrinsic Josephson junction array with a nanoelectrode in the middle', *Appl. Phys. Lett.* **86**, 023504 (3 pp.). doi: 10.1063/1.1852077

Wang HB, Wu PH, Chen J, Maeda K, and Yamashita T (2002), 'Three-dimensional arrays of BiSrCaCuO-2212 intrinsic Josephson junctions and zero-crossing Shapiro steps at 760 GHz', *Appl. Phys. Lett.* **80**, 1604–1606. doi: 10.1063/1.1456555

Wang HB, Wu PH, and Yamashita T (2001a), 'Terahertz response of intrinsic Josephson junctions in high-T_c superconductors', *Phys. Rev. Lett.* **87**, 107 002. doi: 10.1103/PhysRevLett.87.107002

Wang HB, Wu PH, Yamashita T (2001b), 'Stacks of intrinsic Josephson junctions singled out from inside $Bi_2Sr_2CaCu_2O_{8+x}$ single crystals', *Appl. Phys. Lett.* **78**, 4010–4012. doi: 10.1063/1.1379065

Wen JG, Satoh T, Hidaka M, Tahara S, Koshizuka N, and Tanaka S (2000), 'TEM study on the microstructure of the modified interface junction', *Physica C* **337**, 249–255. doi: 10.1016/S0921-4534(00)00111-8

Wollman DA, van Harlingen DJ, Lee WC, Ginsberg DM, and Leggett AJ (1993), ‘Experimental determination of the pairing state in YBCO from the phase coherence of YBCO-Pb dc SQUIDs’, *Phys. Rev. Lett.* **71**, 2134–2137. doi: 10.1103/PhysRevLett.71.2134

Yokoyama T, Sawa Y, Tanaka Y, Golubov AA, Maeda A, and Fujimaki A (2007), ‘Quantitative model for the I_cR_N product in d-wave Josephson junctions’, *Phys. Rev. B* **76**, 052508 (4 pp.). doi: 10.1103/PhysRevB.76.052508

You LX, Torstensson M, Yurgens A, Winkler D, Lin CT, and Liang B (2006), ‘Single intrinsic Josephson junction with double-sided fabrication technique’, *Appl. Phys. Lett.* **88**, 222501 (3 pp.). doi: 10.1063/1.2207827

Yurgens A (2000) ‘Intrinsic Josephson junctions: recent developments’, *Supercond. Sci. Technol.* **13**, R85–R100. doi: 10.1088/0953-2048/13/8/201

Yurgens A, Torstensson M, You LX, Bauch T, Winkler D, *et al.* (2008), ‘Small-number arrays of intrinsic Josephson junctions’, *Physica C* **468**, 674–678. doi:10.1016/j.phys.2007.11.052

Zhang XH, Oh YS, Liu Y, Yan L, Kim KH, *et al.* (2009a), ‘Observation of the Josephson effect in Pb/$Ba_{1-x}K_xFe_2As_2$ single crystal junctions’, *Phys. Rev. Lett.* **102**, 147002 (4 pp.). doi: 10.1103/PhysRevLett.102.147002

Zhang XH, Saha SR, Butch NP, Kirshenbaum K, Paglione JP, *et al.* (2009b), ‘Josephson effect between electron-doped and hole-doped iron pnictide single crystals’, *Appl. Phys. Lett.* **95**, 062510 (3 pp.). doi: 10.1063/1.3205123

Zhou TG, Fang L, Li S, Ji L, Song FB, *et al.* (2007), ‘Nonlinear inductance of intrinsic Josephson junction arrays and its application to tunable filters’, *IEEE Trans. Appl. Supercond.* **17**, 568–589. doi: 10.11009/TASC.2007.898176

9

d-Wave YBCO dc superconductive quantum interference devices (dc SQUIDs)

F. LOMBARDI and T. BAUCH, Chalmers University of Technology, Sweden

Abstract: The discovery of High Critical Temperature Superconductors (HTS) generated great activity to develop dc Superconductive Quantum Interference Devices (SQUIDs), with operating temperatures up to the boiling point of liquid nitrogen, 77 K.

It was immediately apparent that small-scale devices, like SQUIDs, would require the development of thin-film techniques and novel Josephson junction's fabrication technologies. At present, grain-boundary junctions are the most widely used in SQUIDs. However, their properties are strongly affected by the d-wave symmetry of the order parameter. As a consequence the static and dynamic properties of HTS SQUIDs can be profoundly modified. The d-wave symmetry also offers the possibility to design π-SQUIDs showing a complementary behavior in magnetic field, compared to conventional ones, as well as dc SQUIDs with a double well potential. In this chapter the new Josephson phenomenology of HTS SQUIDs is derived, compared with experimental data available in literature, and discussed in view of future novel applications.

Key words: high critical temperature, superconductor grain boundary, Josephson junction, π-SQUID, unconventional current, phase relation, phase dynamics,'silent' quantum bit.

9.1 Introduction

The dc Superconductive Quantum Interference Devices (SQUIDs) consist of two Josephson junctions connected in parallel through a superconducting loop. When an external magnetic flux ϕ_{ext} threading the loop is changed monotonically, the maximum supercurrent the SQUID can sustain (the critical current) is modulated with a period of one flux quantum, $\phi_0 = h/2e$. Here h is Planck's constant and e is the elementary charge. SQUIDs are the most sensitive magnetic field detectors used for a large variety of applications ranging from non destructive evaluation (NDE) (Carr *et al.*, 2003) to low field magnetic resonance imaging (MRI) (Schlenga *et al.*, 1999) to magnetic nanoparticles detections (Seidel *et al.*, 2007). They are considered the most successful application of the Josephson effect and the many text books and reviews that have been written through the years provide an in-depth systematic treatment of the fundamental science, fabrication, and operation of dc SQUIDs and their many applications. The idea behind this chapter is therefore not to repeat what can be found in these excellent reviews but instead to focus on those novel aspects of the physics of High Critical Temperature Superconductor (HTS) dc SQUIDS, related to the unconventional symmetry of the order parameter that may lead in the future to new applications.

9.1.1 d-Wave symmetry of the order parameter in HTS and implications for SQUIDs design

Despite the lack of a complete microscopic theory accounting for the rich phenomenology of the superconductivity in HTS and for the pairing mechanism in these materials, there are a few well-established experimental facts which characterize the ground state of HTS; one of these is the unconventional d-wave symmetry of the superconducting order parameter which was established by various phase sensitive experiments during the early nineties (Wollman, *et al.*, 1993; Tsuei *et al.*, 1994). The two basic features of the d-wave symmetry, the 'π' shift of the phase between orthogonal directions and the presence of nodal directions, lead to a new phenomenology which characterizes the Josephson effect. We refer to the natural existence of Josephson π junctions, characterized by a stable zero current state located at a value of the phase difference between the superconductive electrodes equal to π instead of zero, as for conventional junctions; to the spontaneous nucleation of half integer flux quanta (semifluxons) in frustrated loops containing an odd number of π Josephson junctions (Tsuei *et al.*, 1994); to the existence of an unconventional Josephson current phase relation characterized by non negligible high order harmonics, for specific orientation of the d-wave order parameter in the electrodes. This last feature can dramatically change the Josephson dynamics of HTS junctions and dc SQUIDs leading to systems that in specific conditions can be characterized by a double degenerate fundamental state which can be very useful for the implementation of all HTS quantum bits (Amin *et al.*, 2005).

The existence of π Josephson junctions can be used to realize dc π-SQUIDs whose response in magnetic field, in the case of negligible loop inductance, is complementary to conventional SQUIDs (the critical current as a function of the external magnetic flux presents a minimum instead of a maximum at zero field, see Fig. 9.7(e)). In the 1990s, a very interesting theoretical proposal (Terzioglu and Beasley, 1998) of a new superconductive logic family with broad circuit margin, employing ordinary '0' junctions/conventional dc SQUIDs and the complementary 'π' junctions/dc π-SQUIDs attracted the attention of the scientific community towards π-SQUIDs made of all HTS, for the possibility they offer to operate the circuits at 77 K. Even though the implementation of such a new digital logic still appears a distant goal it remains a very interesting direction to follow once the fabrication technology of HTS Josephson junctions will be mature enough (in terms of reproducibility and performances) for the integration of a large number of devices.

9.2 Grain boundary Josephson junctions

9.2.1 Bicrystal grain boundary junctions

Most of the successful applications of HTS SQUIDs are realized by employing $YBa_2Cu_3O_{7-x}$ (YBCO) grain boundary (GB) junctions. Due to the short coherence length in HTS, grain boundaries between otherwise crystalline films present a weakened superconductivity and in certain conditions they show Josephson effect. The simplest way to create a grain boundary is the bicrystal technique where substrates of different crystallographic orientations are glued together at high temperature. A YBCO film is then deposited on top of the bicrystal. One can go from the crystallographic axis of one part of the film to those of the other by considering a rotation angle θ around a specific axis. Tilt grain boundaries (GBs) are obtained if the rotation is around an axis contained in the plane of the boundary, twist if the axis is perpendicular to the boundary plane. Figure 9.1 shows a sketch of an asymmetric θ [001] tilt grain boundary. It is also possible to realize symmetric GBs. In this case the order parameter in both electrodes are rotated by the same absolute angle but with opposite sign around the specific axis of the grain boundary.

The bicrystal junctions used for SQUID applications are generally of this type (with $0° < \theta < 45°$) and they exhibit current voltage characteristics reasonably close to the resistively shunted junction (RSJ) model, provided the grain boundary angle θ exceeds a critical value, about 10° for YBCO (Dimos *et al.*, 1990).

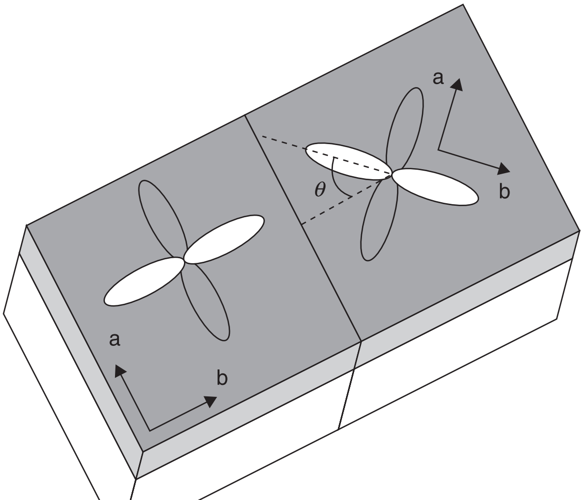

9.1 Sketch of a bicrystal substrate with an asymmetric [001] tilt GB and a YBCO film grown on top of it.

For [001] tilt YBCO GB junctions the critical-current density j_c decreases exponentially with increasing grain boundary angle (Gross and Mayer, 1991; Ivanov *et al.*, 1991). This behavior can be explained in part by the *d*-wave pairing symmetry of the order parameter (Sigrist and Rice, 1995) and in part by extrinsic effects like the faceting of the grain boundary (Hilgenkamp *et al.*, 1996); however, it is likely that a further contribution can arise from an increase of the barrier thickness with increasing grain boundary angle.

Most SQUIDs have been made on symmetric 24° or 36° bicrystals. Recently, more complicated bicrystals with grain boundaries that are a combination of tilt and twist have been used to realize SQUIDs with unconventional properties in view of novel devices. In particular, 45° [001] tilt + 45° [100] tilt (or [010] twist) have been investigated. The reason is twofold:

1 θ [001] grain boundaries usually show as RSJ current voltage characteristic with no hysteresis. While this feature is desirable for many of the most successful applications of SQUIDS, such as non destructive evaluation of structural systems, e.g. aircrafts and bio sensing of brain and heart activities, high quality factor SQUIDs with large hysteresis can give access to a regime where macroscopic quantum effects are dominant. This is fundamental in view of the possible application of HTS SQUIDs as two level systems or quantum bits (qubits). In this respect, GB with 45° [100] tilt have proven to have a specific resistance one order of magnitude higher compared with 45° [001] GB (100 $\Omega\mu m^2$ for 45° [100] compared to 0.1–10 $\Omega\mu m^2$ for 45° [001] GB) (Lombardi *et al.*, 2006; Lindström *et al.*, 2006) which leads to highly hysteretic junctions.

2 Because of the d-wave symmetry of the order parameter the Josephson effect in 45° [001] grain boundaries presents a new phenomenology which can be used to design novel devices. We refer to the existence of an unconventional current-phase relation (CPR) where the tunneling is in the node of the d-wave order parameter in one of the electrodes. This is the case of 45° [001] GB where the a-b planes in one electrode are rotated 45° with respect to the other (see Fig. 9.2).

From symmetry considerations, the first harmonics in the current-phase relation (CPR) of supercurrent is suppressed, since the tunneling of Cooper pairs from a lobe to a node of the order parameter is forbidden. Ideally, the supercurrent in this geometry should contain only higher harmonics of the CPR, mainly the second (proportional to $\sin 2\varphi$). However, in a real junction the presence of both faceting and scattering at the grain boundary plane tends to re-establish the 1st harmonic component (see Fig. 9.2). The interplay between the 1st ($\sin \varphi$, 2π periodic) and the 2nd ($\sin 2\varphi$, π periodic) harmonics has unique effects which strongly influence the dynamics of Josephson junctions and SQUIDs (Löfwander *et al.*, 2001). As will be extensively discussed later, this unconventional current phase relation may lead to a fundamental state that is double degenerate which can be used to realize an HTS silent quantum bit.

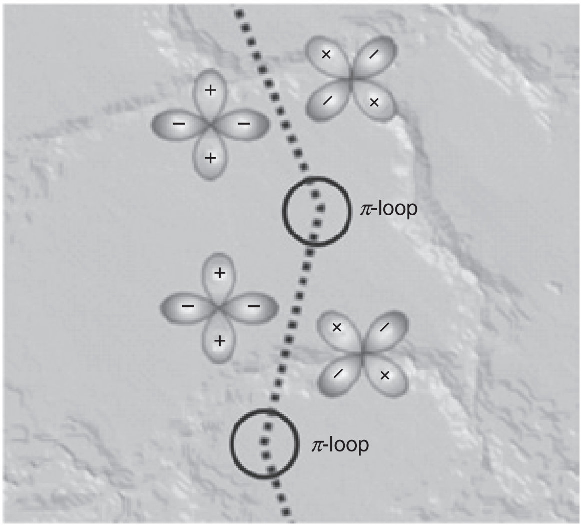

9.2 Schematic representation of a [001] YBCO 45° grain boundary. It shows the orientation of the d-wave order parameter in the two electrodes and considers the presence of faceting and π-loops.

In the beginning of the research on HTS SQUIDs, 45° [001] GBs were considered not suitable for applications. For these GBs the combination of tunnelling in the node in one electrode and the faceting of the grain boundary line gives rise to unconventional magnetic field response, a huge scatter in the junctions parameters and higher values of 1/f noise compared to 24° or 36° bicrystals (attributed to the presence of π-loops (see Fig. 9.2)). Nowadays, instead, HTS SQUIDs with grain boundaries characterized by 45° [001] tilt + 45° [100] tilt fulfill the main requirement for novel application in the quantum limit.

9.2.2 Step-edge grain-boundary junctions

The step-edge grain-boundary junction (GBJ), which is also widely used, is based on the fact that an epitaxially grown, c-axis YBCO film changes its orientation at a steep step in the substrate. This technique, initially realized by Daley *et al.* (1990), was subsequently refined by several groups (Herrmann *et al.*, 1991, 1995; Sun *et al.*, 1993; Yi *et al.*, 1996). Common substrate materials are perovskites (001) $SrTiO_3$ and (001) $LaAlO_3$. For such substrates the GB microstructure strongly depends on the step profile. For a step angle $\alpha < 45°$ there will not be GB formation, while for $\alpha \sim 45°$ GBs will be formed at the top and bottom edge and along the step profile. Only on relatively steep steps, $\alpha > 50°$, there will be the formation of two 90° [100] tilt grain boundaries at the top and bottom edge of the step (Jia *et al.*, 1991). For large step angles ($\alpha \sim 70°$) the two grain boundaries at the top and bottom edge of the step have a quite different microstructure which strongly depend on the exact morphology of the edges (Jia *et al.*, 1992; Lombardi *et al.*, 1998). In this case it has been found that only one grain boundary (the top one) is responsible for the Josephson transport in the junction. The substrate steps are aligned along major cubic axes of the substrate, and are usually patterned by standard e-beam lithography and Ar-ion milling. Often e-beam lithography in combination with hard milling masks (like amorphous carbon) is used to get steep and uniform steps. Clearly step-edge junctions can be placed at will on the substrate. This advantage over the bicrystal technique enables the fabrication of more complex circuits. Even for SQUIDs which require only one or two junctions, this flexibility in layout can be important, for example for minimizing parasitic inductances.

However the properties of step-edge junctions depend strongly on the microstructure of the milled step and on the step height/film thickness ratio (that has to be larger than 1 to avoid overgrowth) and on film-growth conditions, leading to greater spreads in parameters than for bicrystal junctions. Moreover, the unavoidable presence of two grain boundaries in series for moderately steep step may cause problems in the SQUIDs response, if their critical currents are quite close (like for step angles $\alpha > 50°$).

Step-edge YBCO SQUIDs have also been successfully implemented on poorly matched substrates like MgO. Here, for any step angle more than a few degrees (~10) there will be a formation of two grain boundaries at the top and bottom edge of the step of type θ [100] tilt, with $\theta \sim \alpha$.

Many state-of-the-art applications of HTS step-edge SQUIDs have been realized, such as systems for nondestructive evaluation (Itozaki *et al.*, 1996; Wunderlich *et al.*, 1998), magneto-cardiography (Weidel *et al.*, 1997; Krey *et al.*, 1997), scanning SQUID microscopy (Larsson *et al.*, 2001), and digital circuits (McCambridge *et al.*, 1997).

9.2.3 Biepitaxial grain boundary junctions

In the biepitaxial technique a seed layer is deposited and then patterned on top of the substrate. The seed layer has the function to change the epitaxial relations between the HTS film and the bare substrate. This technique was originally developed by Char and co-workers (1991) by employing (100) STO and (100) MgO film as seed layer. The YBCO c-axis film grows on the seed layer with the a-b planes rotated by 45° with respect to the bare STO substrate; the resulting GBs are type θ [001] tilt with θ the angle between the [001] in-plane direction of the substrate and the edge of the seed layer. Since a step between the surface of the substrate and the surface of the seedlayer is unavoidable the growth mechanisms of the GBs are much more complicated compared to the bicrystal, and often less reproducible. In the initial stage of this technique (in the early 1990s) only 45° [001] tilt GBs were investigated. They showed the same phenomenology as

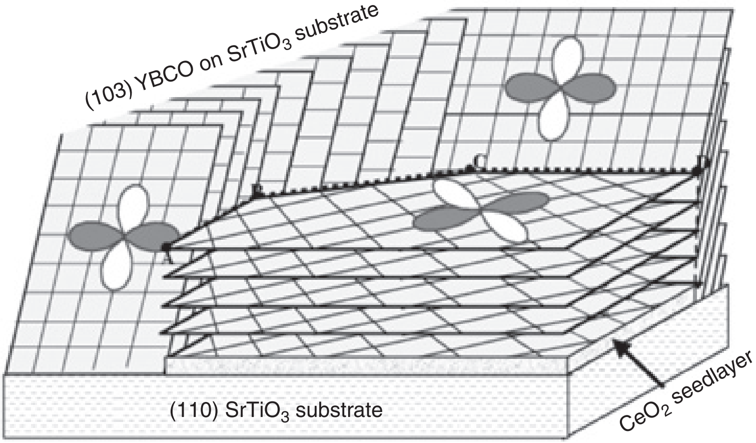

9.3 Sketch of a biepitaxial grain boundary with different interface orientations. Reported planes are a-b planes on the (001) oriented side, and a-b planes on the (103) oriented side.

45° [001] tilt bicrystal GBs with an enhanced 1/f noise (possibly due to more defects due to the complex fabrication technique). For this reason this technique was soon abandoned.

Since then there have been huge advances in the material science, structural characterization techniques and fabrication methods. The use of substrates with different orientations from the (001) and various seed layers has led to obtaining complex grain boundaries which are a combination of θ [001] tilt and 45° [100] tilt (or 45° [010] twist).

In Figure 9.3 a schematic picture of a biepitaxial sample employed in various SQUID experiments is shown. Here (110) STO is used as substrate and (110) CeO_2 as the seedlayer. The YBCO grows (103) oriented on the bare substrate and (001) oriented on the seedlayer. Different GBs can be obtained by varying the angle of the seedlayer edge with respect to the [001] in-plane direction of the substrate. More details about this technique can be found in Miletto Granozio (2003).

9.3 Dynamics of a current biased SQUID in the presence of an unconventional current phase relation

The dynamics of a current biased SQUID are described by two degrees of freedom, namely the phase differences φ_L and φ_R across the two Josephson Junctions (JJs) (see Fig. 9.4). Here a fictitious phase particle is moving in a two-dimensional potential (Lefevre-Seguin, 1992) leading to various new phenomena

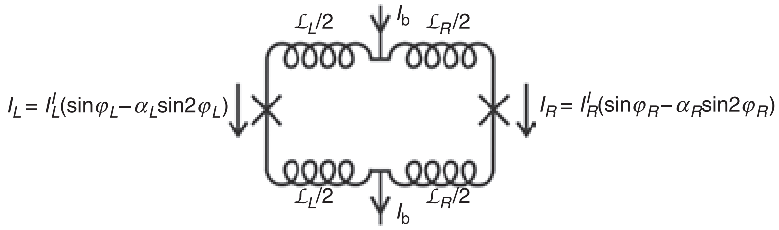
$\mathcal{L}_L/2$
I_b
$\mathcal{L}_R/2$
$I_L = I_L^I(\sin\varphi_L - \alpha_L\sin2\varphi_L)$
$I_R = I_R^I(\sin\varphi_R - \alpha_R\sin2\varphi_R)$
$\mathcal{L}_L/2$
I_b
$\mathcal{L}_R/2$

9.4 Schematic of a dc SQUID. The crosses represent the Josephson junctions having unconventional CPRs. The SQUID loop inductance is distributed between the left and right SQUID arms.

compared to the dynamics of a single JJ which is described by a one-dimensional potential. Here we assume that the magnetic area of the individual junctions is much smaller than the loop area of the SQUID. This allows us to neglect the magnetic field modulation of the junctions' critical currents. In the limit of small SQUID loop inductance the two phase differences across the two junctions are strongly coupled. In this case the dynamics of the system can be reduced to a phase particle moving in a one dimensional potential similar to a single JJ.

The expression for the total dc super-current through the SQUID, containing JJs having a second harmonic component in the CPR, as a function of applied external magnetic flux ϕ_{ext} is given by (Lindström *et al.*, 2006):

$$I(\varphi_L, \varphi_{tot}) = I_L^I \{\sin \varphi_L - \alpha_L \sin 2\, \varphi_L\} + I_R^I\{\sin(\varphi_L - \varphi_{tot}) - \alpha_R \sin 2(\varphi_L - \varphi_{tot})\} \qquad [9.1]$$

where the subscripts L and R denote the left and right arms of the SQUID, respectively. Here $\alpha_{L,R} = I_{L,R}^{II}/I_{L,R}^{I}$ are the ratios between the second and the first harmonic component in the CPR in the respective junctions. Moreover we made use of the equality

$$\varphi_R - \varphi_L = \frac{2\pi}{\phi_0}\phi_{tot} = \varphi_{tot} \qquad [9.2]$$

deduced from the fluxoid quantization in the SQUID loop (Tinkham, 2004), where $\phi_0 = h/2e$ is the superconducting flux quantum. The total magnetic flux threading the SQUID loop is given by the sum of the externally applied magnetic flux ϕ_{ext} and the self-induced magnetic flux ϕ_{self} caused by the currents flowing through the two SQUID arms, $\phi_{tot} = \phi_{ext} + \phi_{self}$. Assuming that the SQUID loop inductance $\mathcal{L}$ is equally divided between the two SQUID arms, the self-generated magnetic flux can be expressed as $\phi_{self} = \mathcal{L}(I_L - I_R)/2$. The maximum critical current of the SQUID as a function of external magnetic flux for negligible self-field ($\phi_{tot} \approx \phi_{ext}$) is given by

$$I_C(\varphi_{ext}) = \max_{-\pi<\varphi_L<\pi}\{I(\varphi_L, \varphi_{ext})\} \qquad [9.3]$$

For a SQUID with JJs having pure sinusoidal CPRs, equal values of the critical current ($I_L = I_R$), and negligible loop inductance, the SQUID critical current can be expressed as

$$I_C = 2I_L \left| \cos\left(\pi \frac{\phi_{ext}}{\phi_0} \right) \right| \qquad [9.4]$$

which is depicted in Fig. 9.7(a).

For finite junction size, the situation becomes more complicated. Faceting of the GB plays an important role and happens at two length scales: meandering creates facets that are typically 100–200 nm long (see Fig. 9.2) and there is also microfaceting which is related to the lattice structure and has a typical length scale of 1–2 nm (Chan *et al.*, 2003). Due to the d-wave symmetry the local properties of the GB depend strongly on the misorientation angle (Mannhart and Chaudhari, 2001). An important consequence of the meandering is the presence of so-called π-facets in the GB. Ideally, the 0°–45° misorientation should result in a node–lobe arrangement of the order parameter in the electrodes (see Fig. 9.1) but since the GB meanders, the exact arrangement varies. In some of these facets the arrangement will be, e.g., plus–plus and in some plus–minus. This means that the phase difference across the GB due to the d-wave symmetry will be shifted by π in some places resulting in a *negative* Josephson current density. As a result the critical current density across the junctions $j_{L,R}$ varies both in amplitude and sign as we move along the GB.

Following the usual method of deriving the equation that governs the behavior of a magnetically short junction in a perpendicular magnetic field B, we define the phase difference along the grain boundary

$$\varphi(z) = 2\pi \frac{2\lambda B}{\phi_0} z + \varphi_0 \qquad [9.5]$$

Here the barrier thickness d of the junctions is assumed negligible compared to the London penetration depth λ. Introducing $j^{I}_{L,R}(z)$, $j^{II}_{L,R}(z)$, the critical current densities of the first and second harmonic components as we move along the GB in the left and right SQUID arm, we can write the magnetic field dependence of the critical current of a SQUID as (Lindström *et al.*, 2006):

$$I_C(\varphi_{ext}) = \max_{-\pi<\varphi_0<\pi} \left\{ \begin{array}{l} w\displaystyle\int_0^{d_L} \left[j^{I}_{L}(z)\sin(\varphi(z)) - j^{II}_{L}(z)\sin(2\varphi(z)) \right] dz \\ +w\displaystyle\int_0^{d_R} \left[j^{I}_{R}(z)\sin(\varphi(z)+\varphi_{ext}) - j^{II}_{R}(z)\sin(2\varphi(z)+2\varphi_{ext}) \right] dz \end{array} \right\} \qquad [9.6]$$

where w is the film/junction thickness and $\varphi_{ext} = 2\pi\, BA/\phi_0$ is the normalized external magnetic flux threading the SQUID loop. The SQUID area is given by A, and $d_{L,R}$ is the width of the left and right junction, respectively.

For given values of I_L^I, I_R^I, α_L, α_R, and φ_{ext} the potential of the SQUID in the approximation of a negligible magnetic area of the junctions and negligible SQUID loop inductance $\mathcal{L} \to 0$ is given by

$$U(\delta) = -\frac{\phi_0}{2\pi}\left\{ I_L^I \cos\left(\delta + \frac{\varphi_{ext}}{2}\right) + I_R^I \cos\left(\delta - \frac{\varphi_{ext}}{2}\right) - \frac{\alpha_L}{2} I_L^I \cos\left(2\delta + \varphi_{ext}\right) \right\}$$
$$\left\{ -\frac{\alpha_R}{2} I_R^I \cos\left(2\delta - \varphi_{ext}\right) + I_b \delta \right\} \qquad [9.7]$$

where $\delta = (\varphi_L + \varphi_R)/2$. The particle mass is given by $m_\delta = C(\phi_0/2\pi)^2$ with C the capacitance of the junctions. The bias current I_b determines the tilt of the washboard potential. For $\varphi_{ext} = 0$ and $I_L^I = I_R^I$ we show in Fig. 9.5 the calculated SQUID potential as a function of the parameter $a = (\alpha_L + \alpha_R)/2$ and average phase difference δ at zero external applied magnetic field according to equation [9.4]. The insets show the SQUID potential for three different values of the parameter a. For $a = 0$ the potential is single welled. In the case of $a = 0.5$ we clearly see a flattening in the minimum of the well. The potential becomes double welled for $a > 0.5$ as shown in the lowest inset. This dependence is the same as for a single junction (Tzalenchuk *et al.*, 2003). The double well potential can be used to realize a 'silent' quantum bit strongly decoupled from the environment, as will be discussed later.

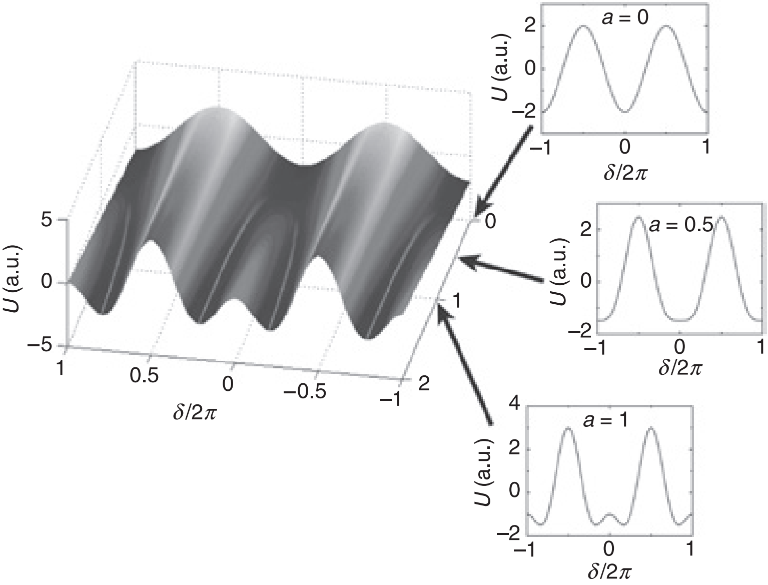

9.5 Calculated SQUID potential as a function of the parameter $a = (\alpha_L + \alpha_R)/2$ and average phase difference δ at zero external applied magnetic field and zero bias current. The insets show the SQUID potential for three different values of the parameter a.

When the bias current is ramped from $I = 0$ to $I < I_C$, the SQUID is in the zero voltage state in the absence of thermal or quantum fluctuations. At finite temperature the junction may switch into a finite voltage state for a bias current $I < I_C$. This corresponds to the phase particle escaping from the well either by a thermally activated process or by tunneling through the barrier potential (Martinis *et al.*, 1987). The time averaged voltage $\bar{V}$ across the SQUID in the resistive regime can be approximated within the resistively shunted junction model (Lindström *et al.*, 2003) and assuming a negligible SQUID loop inductance:

$$\bar{V}^{-1} = \frac{G_L + G_R}{2\pi} \int_{-\pi}^{\pi} d\varphi_L \left[I_b - I_L\left(\varphi_L + \frac{\varphi_{ext}}{2}\right) - I_R\left(\varphi_L - \frac{\varphi_{ext}}{2}\right)\right]^{-1} \qquad [9.8]$$

Here $G_{L,R}$ are the normal conductances of the junctions. In Fig. 9.6 we plot the voltage as a function of an externally applied magnetic flux at various bias currents between $I_C^{\max}/2$ and $3I_C^{\max}/2$ for two different SQUIDs, were $I_C^{\max} = \max I_C\,(\phi_{ext})$ $\phi_0/2 < \phi_{ext} < \phi_0/2$. The SQUID having JJs with pure sinusoidal CPRs shows the typical ϕ_0 periodic voltage modulations, while, the SQUID having a second harmonic component in the CPRs shows two distinct features: an offset in the voltage vs. flux characteristic with respect to the polarity of the bias current and an additional modulation superimposed to the ϕ_0 periodic modulation.

9.4 Probing the second harmonic component in the current phase relation by the magnetic field response of the SQUID

There have been several reports on the detection of an unconventional CPR in HTS systems. Most of the works refer to YBCO rf (Il'ichev *et al.*, 2001) and dc SQUIDs (Lindström *et al.*, 2003) with proper order parameter orientation in the

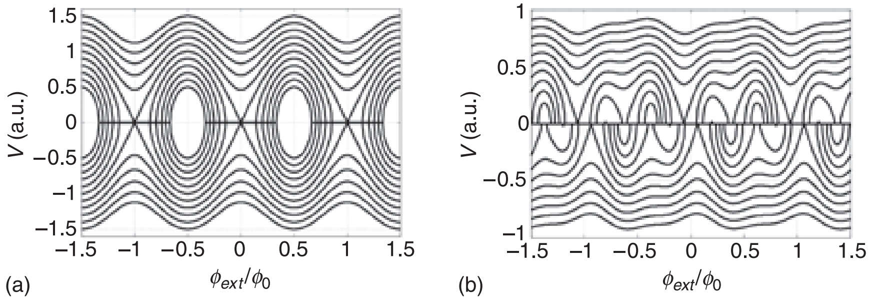

9.6 Voltage vs. externally applied magnetic flux for two dc SQUIDs with different ratios of the first and second harmonic components in the CPRs. The parameters are: (a) $I_L^I = I_R^I = 1.0$ and $\alpha_L = \alpha_R = 0$; (b) $I_L^I = 0.98$, $I_R^I = 0.19$, $\alpha_L = 0.13$ and $\alpha_R = 1.0$. The patterns are plotted for $I_b/I_C^{\max} = 0.5$ to $I_b/I_C^{\max} = 1.5$.

electrodes. Because of the $\sin(2\varphi)$ term the SQUID response to an external magnetic field is strongly modified compared to a SQUID with JJs having pure $\sin\varphi$ CPRs. In the following we will focus only on the dc SQUID response upon an admixture of second harmonic in the CPRs of the Josephson junctions. The most striking demonstration of the second harmonic component in the CPR of the JJs in a SQUID are intermediate maxima in the modulation pattern of the critical current as a function of an externally applied magnetic field. In Fig. 9.7 we show

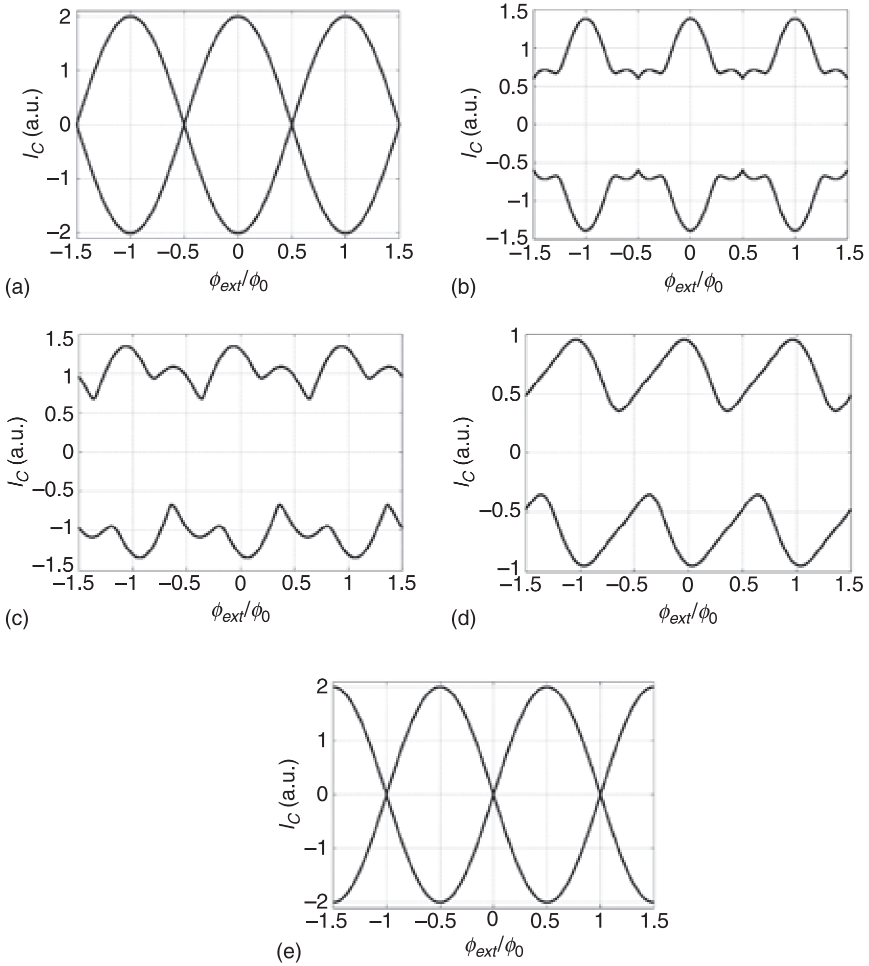

9.7 Calculated critical currents for five different dc SQUIDs. The parameters are: (a) $I_L^I = I_R^I = 1.0$ and $\alpha_L = \alpha_R = 0$; (b) $I_L^I = I_R^I = 0.5$ and $\alpha_L = \alpha_R = 0.6$; (c) $I_L^I = 0.98$, $I_R^I = 0.19$, $\alpha_L = 0.13$, and $\alpha_R = 1.0$; (d) $I_L^I = 0.28$, $I_R^I = 0.47$, $\alpha_L = 0.2$, and $\alpha_R = 0.6$; (e) $I_L = -I_R$ 1.0 and $\alpha_L = \alpha_R = 0$. The minus sign corresponds to an additional π-phase shift in the CPR of the right junction resulting in a typical π-SQUID modulation pattern.

the calculated critical current of SQUIDs with different second harmonic components in the CPR of the individual JJs using equations 9.1–9.3, and assuming a negligible SQUID loop inductance.

The typical critical current I_C of a SQUID as a function applied external magnetic flux with junctions having pure sinusoidal CPRs and equal critical currents, $I^I_L = I^I_R$ and $\alpha_L = \alpha_R = 0$, is depicted in Fig.9.7(a). One can clearly observe the ϕ_0 periodicity of the critical current modulation. By increasing the second harmonic components equally in both junctions two intermediate bumps appear between the main maxima, which is exemplified in Fig. 9.7(b) for $I^I_L = I^I_R$ and $\alpha_L = \alpha_R = 0.6$. When introducing an asymmetry in the critical currents and the second harmonic components we can distinguish two cases, as shown in Fig. 9.7(c) and (d). For $I^I_L = 0.98$, $I^I_R = 0.19$, $\alpha_L = 0.13$, and $\alpha_R = 1.0$ only one intermediate bump between the main maxima is left (see Fig. 9.7(c)). At the same time the modulation pattern becomes asymmetric with respect to, $\phi_{ext} = 0$, i.e. $I_C(\phi_{ext}) \neq I_C(-\phi_{ext})$. The intermediate bump may disappear for another set of asymmetries between the critical currents and second harmonic components as shown in Fig. 9.7(d). Here we have $I^I_L = 0.28$, $I^I_R = 0.47$, $\alpha_L = 0.2$, and $\alpha_R = 0.6$. As in the previous case the pattern is asymmetric with respect to $\phi_{ext} = 0$. It is worth noting that all magnetic field patterns are still point symmetric $I_C(\phi_{ext}) = -I_C(-\phi_{ext})$, which can be easily seen from equations 9.1 and 9.2.

9.4.1 Measurements on YBCO grain boundary Josephson junctions

Here we present measurements of the critical current as a function of an applied external magnetic field performed on YBCO SQUIDs. The junctions forming the SQUIDs were obtained by using the biepitaxial and the bicrystal technique. The grain boundaries obtained with the biepitaxial technique (STO substrate and CeO_2 seed layer) have a misorientation angle $\theta = 30°$ which is close to a configuration where the Josephson transport is in the node of the order parameter in the (103) YBCO electrode at $\theta = 35°$ (Lombardi *et al.*, 2002). Due to faceting of the grain boundary with a typical variation of the angle $\Delta\theta = \pm 15°$ we expect an admixture of both first and second harmonic component in the CPR. Dc SQUIDs were also obtained by grain boundary junctions formed on bicrystal STO substrates. The grain boundary is characterized by a [100] 45° tilt of the c-axis with respect to the interface plus a 45° tilt around the c-axis. The Josephson transport is in the node of the order parameter in the (001) YBCO electrode. The parameters for the two SQUIDs are summarized in Table 9.1.

The SQUID modulation of the bicrystal SQUID (see Fig. 9.8(a)) clearly shows the influence of the second harmonic component in the CPR. The sin 2φ term is responsible for the intermediate maxima between the main maxima in the SQUID critical current modulation.

Table 9.1 Parameters for the dc SQUIDs presented in this chapter. The effective area is calculated taking the geometry of the SQUID electrodes into account

Sample	Grain boundary	Substrate material	Seed layer	Mis-orientation angle θ	Film thickness (nm)	Junction width (μm)	Hole area (μm^2)	Critical current (μA)
S1	Biepitaxial	(110) $SrTiO_3$	CeO_2	30°	120	2	7 × 7	0.95
S2	Bicrystal	(110) $SrTiO_3$/ (001) $SrTiO_3$	–	0°	150	1	7 × 7	1.4

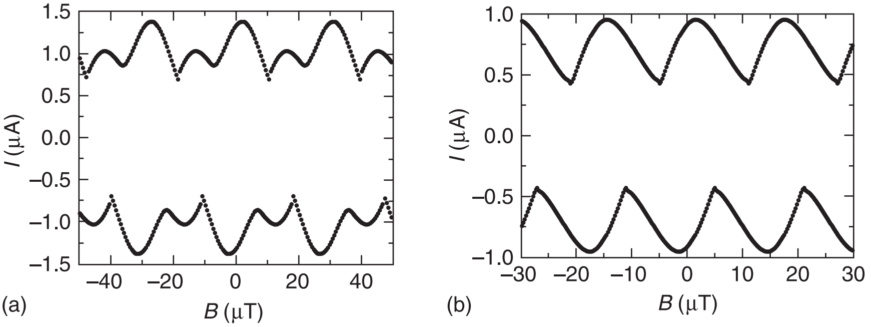

9.8 Measured critical current as a function of external applied magnetic field for a bicrystal (a) and biepitaxial (b) SQUID at $T = 20$ mK.

The critical current vs. magnetic field graph for the biepitaxial SQUID measured at $T = 20$ mK does not feature any intermediate maxima (see Fig. 9.8(b)). Instead, the magnetic field pattern shows only an asymmetry in slopes when comparing the left and right side of a lobe. This behavior is similar to the calculated critical current modulation, shown in Fig. 9.7(d), where both a first and second harmonic component was assumed in the CPRs of the two SQUID junctions. Here it is worth pointing out that a slanted critical current modulation can be also observed for SQUIDs having a pure sinusoidal CPR in the limit of a finite loop inductance $2\pi \mathcal{L} I_C > \phi_0$. In this case the slanted magnetic field pattern of the critical current is caused by an asymmetry in the critical currents of the junctions and/or an asymmetry in the inductances of the two SQUID arms. A detailed discussion about the origin of a slanted critical current modulation of a biepitaxial YBCO SQUID as function of an applied magnetic field can be found in Bauch *et al.* (2007).

9.5 Quantum circuit applications: HTS SQUIDs as 'silent' quantum bit

Recent advances in high critical temperature superconductors have allowed dramatic improvements in the performances of HTS Josephson junctions (Tafuri and Kirtley, 2005). Macroscopic quantum tunneling (Bauch *et al.*, 2005) and energy level quantization have been observed in HTS-based Josephson junctions (Bauch *et al.*, 2006), definitively opening up the way to novel quantum systems based on the HTS d-wave symmetry. This unconventional order parameter can be used to create naturally degenerate two-level systems offering significant advantages for quantum circuit applications (Amin *et al.*, 2005) and to study basic physics in previously inaccessible regimes (Bauch *et al.*, 2009). Over the past few years much progress has been achieved in the field of quantum computation and a number of groups have demonstrated that it is possible to fabricate and entangle solid state qubits (Yamamoto *et al.*, 2003; Majer *et al.*, 2007). Most of these implementations have used superconducting elements and all these structures have used low-T_c superconductors (LTS). At the same time several HTS-based phase qubit designs have been proposed (Ioffe *et al.*, 1999; Blatter *et al.*, 2001; Blais and Zagoskin, 2000; Amin, 2005). The d-wave symmetry, in fact, can be used to create a fundamental state which is naturally doubly degenerate. When compared with the low-T_c counterparts, the absence of any external bias at the operating point makes the HTS qubit protected from fluctuations of the external fields (that is why it is named 'silent' by inventors). The naturally double degenerate ground state offers significant advantages for quantum calculations and promises longer coherence times. For the description of the silent qubit implementing d-wave JJs we follow Amin *et al.*, (2005). The silent qubit consists of a superconducting loop intersected by two JJs having both a first and second harmonic component in the CPR (see Fig. 9. 9).

The shape of the 'silent' qubit potential depends both on the asymmetry $\eta = I_R^I/I_L^I$ and the relative magnitude of the second harmonic $\alpha_{L,R}$ in each junction. A single qubit is essentially a controllable two-state system and as shown in Fig. 9.10, the potential given by equation 9.7 meets these criteria. At zero external flux the potential has the familiar double-well shape which is exactly what is needed in order to make a qubit. By increasing the field we can reduce the height of the barrier and tilt the well, meaning that we can prepare the system in a known initial state. The potential has been plotted for the case $\eta = 1.5$ and $\alpha_L = \alpha_R = 2.0$ but there are many possible sets of parameters that fulfill these conditions. It is however important that the SQUID is asymmetric with respect to I_c (i.e. $\eta \neq 1$). Otherwise it is impossible to tilt the well. The two states of the qubit, which classically would correspond to two different circulating persistent currents, are separated by a flux-dependent energy barrier

$$W(\phi_{ext}) = \cos\left(\frac{\pi\phi_{ext}}{\phi_0}\right)\left(\alpha_\phi + \alpha_\phi^{-1} - 2\right) \qquad [9.9]$$

with

$$\tilde{\alpha}_\phi = \frac{2(\alpha_L + \eta\alpha_R)\cos\left(\dfrac{2\pi\phi_{ext}}{\phi_0}\right)}{(1+\eta)\cos\left(\dfrac{\pi\phi_{ext}}{\phi_0}\right)} \qquad [9.10]$$

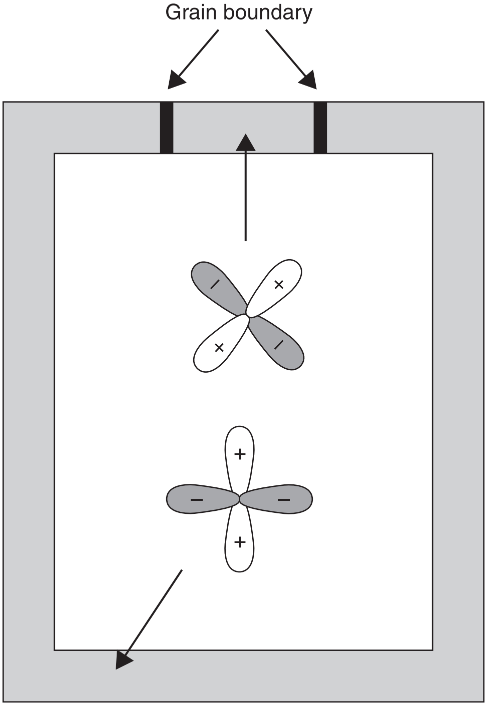

9.9 Sketch of the 'silent' qubit involving d-wave [001] tilt grain boundaries. The read-out of the circulating currents in the loop can be realized with a standard dc SQUID.

Tunneling occurs between the two minima due to the uncertain relation between charge Q and superconducting phase υ on the island. The tunneling matrix element is approximately given by ($\hbar = k_B = 1$):

$$\Delta \approx \omega_P(\phi_{ext}) e - \sqrt{\zeta W(\phi_{ext}) E_J / E_C} \qquad [9.11]$$

where ζ is a constant of the order of 1, $E_J = I_L^I\ \phi_0/2\pi$ is the Josephson energy, $E_C = e^2/2C$ the charging energy, and C is the capacitance of the junctions. The coefficient $\omega_p(\phi_{ext}) = \sqrt{\omega_p^+\ \omega_p^-}$ is determined by the frequency of small oscillations (plasma frequencies) $\omega_p^\pm$ in the right and left minimum, respectively.

Figure 9.10 also shows the positions of the energy levels in the well. The spacing between the two working qubit levels Δ is given by equation 9.11. The energy spacing separating the working levels from the next excited state is almost independent of $\tilde{\alpha}_\phi$. This means that it is possible to tune Δ using $\tilde{\alpha}_\phi$ while at the same time keeping the system effectively decoupled from the other levels of the well. Hence, despite there being many levels in the well, only the two lowest are involved in the qubit operation meaning it is effectively a two-state system. This

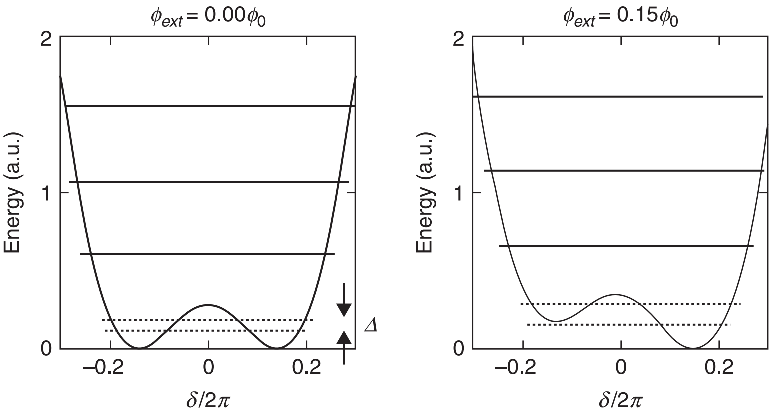

9.10 The evolution of the shape of the potential of an asymmetric dc SQUID with $\eta = 1.5$ and $\alpha_L = \alpha_R = 0.8$. As the field is increased, the barrier tends to disappear and the well is tilted, making it possible to prepare the system in a known state. The horizontal lines indicate the position of the energy levels. The two dotted lines correspond to the two working qubit levels.

qubit is in many ways similar to the flux-qubit first implemented by the Delft group (Chiorescu *et al.*, 2003). There are, however, two key differences. First of all there is no need to flux-bias the SQUID in order for the potential to have a double well shape. Secondly, this qubit is ‘silent’ in the sense that at the operating point it is almost completely decoupled from any fluctuations or the external fields, already on the classical level. The effects of the external fluctuations appear only in the third or fourth order.

9.6 Conclusions

In this chapter we have focused on the new phenomenology of HTS SQUIDs induced by the d-wave symmetry of the order parameter. For specific grain boundary configurations the combined effect of tunneling in the node and faceting of the boundary interface leads to a current phase relation of the type $I_c = I^I (\sin \varphi - \alpha \sin 2\varphi)$ which has a strong influence on the dc properties and on the dynamics of the SQUIDs. The response of a dc SQUID to an external magnetic field deviate from a conventional one; there is the appearance of bumps between main maxima whose amplitude is a function of the asymmetry of the junctions forming the SQUIDs. Moreover in certain conditions the washboard potential is double degenerate and one can lift the degeneracy of the levels in the well by applying an external magnetic field. The system can be therefore prepared in the left or right well which represent the basis for quantum information applications.

9.7 References

Amin, M. H. S., Smirnov, A. Yu., Zagoskin, A. M., Lindström, T., Charlebois, S. A., *et al.*, 2005, 'Silent phase qubit based on d-wave Josephson junctions', *Phys. Rev. B* **71**, 064516.

Bauch, T., Lombardi, F., Tafuri, F., Barone, A., Rotoli, G., *et al.*, 2005, 'Macroscopic quantum tunneling in d-wave $YBa_2Cu_3O_{7-\delta}$ Josephson junctions', *Phys. Rev. Lett.* **94**, 087003.

Bauch, T., Lindström T., Tafuri, F., Rotoli, G., Delsing, P., *et al.*, 2006, 'Quantum dynamics of d-wave Josephson junctions', *Science* **311**, 57.

Bauch, T., Cedergren, K., Johansson, J., Rotoli G., Tafuri F., and Lombardi, F., 2007, 'Dynamics of d-wave $YBa_2Cu_3O_{7-\delta}$ dc SQUIDs', *Supercond. Sci. Technol.* **20**, S98–S104.

Bauch, T., Gustafsson, D., Cedergren, K., Nawaz, S., Mumtaz Virk, M., *et al.*, 2009, 'High critical temperature superconductor Josephson junctions for quantum circuit applications', *Phys. Scr.* **T137**, 014006.

Blais A., and Zagoskin, A. M., 2000, 'Operation of universal gates in a solid-state quantum computer based on clean Josephson junctions between *d*-wave superconductors', *Phys. Rev. A* **61**, 042308.

Blatter, G., Geshkenbein, V. B., and Ioffe, L. B., 2001, 'Design aspects of superconducting-phase quantum bits', *Phys. Rev. B* **63**, 174511.

Carr, C., Graham, D., Macfarlane, J., and Donald, G. B., 2003, 'HTS SQUIDs for the nondestructive evaluation of composite structures', *Supercond. Sci. Technol.* **16**, 1387.

Chan, S. W., Jin, Q., Tsai, J., Tidrow, S., and Jiang, Q., 2003, 'Faceting and critical current densities of [001] high-angle tilt boundaries in YBCO films', *IEEE Trans. Appl. Supercond.* **13**, 2829.

Char, K., Colclough, M. S., Garrison, S. M., Newman N., and Zaharchuk, G., 1991, 'Bi-epitaxial grain boundary junctions in $YBa_2Cu_3O_7$', *Appl. Phys. Lett.* **59**, 733.

Chiorescu, I., Nakamura, Y., Harmans, C. J. P. M., and Mooij, J. E., 2003, 'Coherent quantum dynamics of a superconducting flux qubit', *Science* **299**, 1869.

Daly, K.P., Dozier, W. D., Burch, J. F., Coons, S. B., Hu, R., *et al.*, 1990, 'Substrate step-edge $YBa_2Cu_3O_7$ rf SQUIDs', *Appl. Phys. Lett.* **58**, 543.

Dimos, D., Chaudhari, P., and Mannhart, J., 1990, 'Superconducting transport properties of grain boundaries in $YBa_2Cu_3O_7$ bicrystals', *Phys. Rev. B* **41**, 4038.

Gross, R., Chaudhari, P., Dimos, D., Gupta, A., and Koren, G., 1990, 'Thermally activated phase slippage in high-T_c grain-boundary Josephson junctions', *Phys. Rev. Lett.* **64**, 228.

Herrmann, K., Zhang, Y., Mück, M., Schubert, J., and Braginski, A. I., 1991, 'Characterization of $YBa_2Cu_3O_7$ step-edge Josephson junctions', *Supercond. Sci. Technol.* **4**, 583.

Herrmann, K., Kunkel, G., Siegel, M., Schubert, J., Zander, W., *et al.*, 1995, 'Correlation of $YBa_2Cu_3O_7$ step-edge junction characteristics with microstructure', *J. Appl. Phys.* **78**, 1131.

Hilgenkamp, H., Mannhart, J., and Mayer, B., 1996, 'Implications of $d_{x^2-y^2}$ symmetry and faceting for the transport properties of grain boundaries in high-*Tc* superconductors', *Phys. Rev. B* **53**, 14586.

Il'ichev, E., M. Grajcar, M., Hlubina, R., IJsselsteijn, R. P. J., Hoenig, H. E., *et al.*, 2001, 'Degenerate ground state in a mesoscopic $YBa_2Cu_3O_{7-x}$ Grain boundary Josephson Junction', *Phys. Rev. Lett.* **86**, 5369.

Ioffe, L. B., Geshkenbein, V. B., Feigel'man, M. V., Fauchère, A. L., and Blatter, G., 1999, 'Environmentally decoupled *sds*-wave Josephson junctions for quantum computing', *Nature* **398**, 679.

Itozaki, H., Tanaka, S., Toyoda, H., Hirano, T., Haruta, Y., *et al.*, 1996, 'A multi-channel high-SQUID system and its application', *Supercond. Sci. Technol.* **9**, A38.

Ivanov, Z. G., Nilsson, P.A., Winkler, D., Alarco, J. A., Claeson, T., *et al.*, 1991, 'Weak links and dc SQUIDS on artificial nonsymmetric grain boundaries in $YBa_2Cu_3O_{7-\delta}$', *Appl. Phys. Lett.* **59**, 3030.

Jia, C. L., Kabius, B., Urban, K., Hermann, K., Cui, G.J., *et al.*, 1991, 'Microstructure of epitaxial $YBa_2Cu_3O_7$ films on step-edge $SrTiO_3$ substrates', *Physica C* **175**, 545.

Jia, C. L., Kabius, B., Urban, K., Hermann, K., Schubert, J., *et al.*, 1992, 'The microstructure of epitaxial $YBa_2Cu_3O_7$ films on steep steps in $LaAlO_3$ substrates', *Physica C* **196**, 211.

Krey, S., Subke, K. O., Reimer, D., Schilling, M., Scharnweber, R., *et al.*, 1997, 'Integrated $YBa_2Cu_3O_7$ magnetometers for biomagnetic applications', *Appl. Supercond.* **5**, 213.

Larsson, P., Tzalenchuk, A. Ya., and Ivanov, Z. G., 2001, 'Transport properties of submicron $YBa_2Cu_3O_{7-\delta}$ step-edge Josephson junctions', *J. Appl. Phys.* **90**, 3450.

Lefevre-Seguin, V., Turlot, E., Urbina, C., Esteve, D., and Devoret, M. H., 1992, 'Thermal activation of a hysteretic dc superconducting quantum interference device from its different zero-voltage states', *Phys. Rev. B* **46,** 5507.

Lindström, T., Charlebois, S. A., Tzalenchuk, A. Ya., Ivanov, Z., Amin, M. H., *et al.*, 2003, 'Dynamical effects of an unconventional current-phase relation in YBCO dc SQUIDs', *Phys. Rev. Lett.* **90**, 117002.

Lindström, T., Johansson, J., Bauch, T., Stepantsov, E., Lombardi, F., *et al.*, 2006, 'Josephson dynamics of bicrystal *d*-wave $YBa_2Cu_3O_{7-\delta}$ dc-SQUIDs', *Phys. Rev. B* **74**, 014503.

Löfwander, T., Shumeiko, V., and Wendin, G., 2001, 'Andreev bound states in high-*Tc* superconducting junctions', *Supercond. Sci. Technol.* **14**, R53.

Lombardi, F., Ivanov, Z. G., Fischer, G. M., and Claeson, T., 1998, 'Transport and structural properties of the top and bottom grain boundaries in $YBa_2Cu_3O_{7-\delta}$ step-edge Josephson junctions', *Appl. Phys. Lett.* **72**, 125.

Lombardi, F., Tafuri, F., Ricci, F., Miletto Granozio, F., Barone, A., *et al.*, 2002, 'Intrinsic *d*-wave effects in $YBa_2Cu_3O_{7-\delta}$ grain boundary Josephson junctions', *Phys. Rev. Lett.* **89**, 207001.

Lombardi, F., Bauch, T., Johansson, J., Cedergren, K., Lindström, T., *et al.*, 2006, 'Quantum properties of d-wave $YBa_2Cu_3O_{7-\delta}$ Josephson junction', *Physica C* **435**, 8.

Majer, J., Chow, J. M., Gambetta, J. M., Koch, J., Johnson, B. R., *et al.*, 2007, 'Coupling superconducting qubits via a cavity bus', *Nature* **449**, 443.

Mannhart, J., and Chaudhari, P., 2001, 'High-*Tc* bicrystal grain boundaries', *Phys. Today* **54**, 48.

Martinis, J. M., Devoret, M. H., and Clarke, J., 1987, 'Experimental tests for the quantum behavior of a macroscopic degree of freedom: The phase difference across a Josephson junction', *Phys. Rev. B* **35**, 4682.

Mc Cambridge, J. D., Forrester, M. G., Miller, D. L., Hunt, B. D., Pryzbysz, J. X., *et al.*, 1997, 'Multilayer HTS SFQ analog-to-digital converters', *IEEE Trans. Appl. Supercond.* **7**, 3622.

Miletto Granozio, F., Scotti di Uccio, U., Lombardi, F., Ricci, F., Bevilacqua, F., *et al.*, 2003, 'Structure and properties of a class of CeO_2-based biepitaxial $YBa_2Cu_3O_{7-\delta}$ Josephson junctions', *Phys. Rev. B* **67**, 184506.

Schlenga, K., McDermott, R., Clarke, J., de Souza, R. E., Wong-Foy, A., *et al.*, 1999, 'Low-field magnetic resonance imaging with a high-*Tc* dc superconducting quantum interference device', *Appl. Phys. Lett.* **75**, 3695.

Seidel, P., Becker, C., Steppke, A., Buettner, M., Schneidewind H., *et al.*, 2007, ‘Long-time stable high-temperature superconducting DC-SQUID gradiometers with silicon dioxide passivation for measurements with superconducting flux transformers’, *Supercon. Sci. Technol.* **20**, S380.

Sigrist, M., and Rice, T. M., 1995, ‘Unusual paramagnetic phenomena in granular high-temperature superconductors – A consequence of *d*-wave pairing?’, *Review of Modern Physics* **67**, 503.

Sun, J. Z., Gallagher, W. J., Callegari, A. C., Foglietti, V., and Koch, R. H., 1993, ‘Improved process for high-*Tc* superconducting step-edge junctions’, *Appl. Phys. Lett.* **63**, 1561.

Tafuri, F., and Kirtley, J., 2005, ‘Weak links in high critical temperature superconductors’, *Rep. Prog. Phys.* **68**, 2573.

Terzioglu, E., and Beasley, M. R., 1998, ‘Complementary Josephson junction devices and circuits: a possible new approach to superconducting electronics’, *IEEE Trans. Appl. Supercond.* **8**, 48.

Tinkham, M., 2004, *Introduction to Superconductivity*, 2nd ed. McGraw-Hill, New York.

Tsuei, C., Kirtley, J., Chi, C. C., Lock See Yu-Jahnes, Gupta, A., *et al.*, 1994, ‘Pairing symmetry and flux quantization in a tricrystal superconducting ring of $YBa_2Cu_3O_{7-\delta}$’, *Phys. Rev. Lett.* **73**, 593.

Tzalenchuk, A., Lindström, T., Charlebois, S., Stepantsov, E., Ivanov, Z., *et al.*, 2003, ‘Mesoscopic Josephson junctions of high-*Tc* superconductors’, *Phys. Rev. B* **68**, 100501.

Weidel, R., Brabetz, S., Schmidl, F., Klemm, F., Wunderlich, S., *et al.*, 1997, ‘Heart monitoring with high-Tc d.c. SQUID gradiometers in an unshielded environment’, *Supercond. Sci. Technol.* **10**, 95.

Wollman, D. A., Van Harlingen, D. J., Lee, W. C., Ginsberg, D. M., and Leggett, A. J., 1993, ‘Experimental determination of the superconducting pairing state in YBCO from the phase coherence of YBCO-Pb dc SQUIDs’, *Phys. Rev. Lett.* **71**, 2134.

Wunderlich, S., F. Schmidl, H. Specht, L Dorrer, H. Schneidewind, *et al.*, 1998, ‘Planar gradiometers with high-DC SQUIDs for non-destructive testing’, *Supercond. Sci. Technol.* **11**, 315.

Yamamoto, T., Pashkin, Y. A., Astafiev, O., Nakamura, Y., and Tsai, J. S., 2003, ‘Demonstration of conditional gate operation using superconducting charge qubits’, *Nature* **425**, 941.

Yi, H. R., Gustafsson, M., Winkler, D., Olsson, E., and Claeson, T., 1996, ‘Electromagnetic and microstructural characterization of $YBa_2Cu_3O_7$ step edge junctions on (001) $LaAlO_3$ substrates’, *J. Appl. Phys.* **79**, 9213.

10

Microwave filters using high-temperature superconductors

Y. S. HE and C. G. LI, Chinese Academy of Sciences, China

Abstract: This chapter discusses the applications of high-temperature superconductors (HTS) in microwave technology, particularly microwave filters. The chapter first reviews some fundamental aspects of how superconductors interact with high-frequency fields and then briefly outlines their basic elements: superconducting microwave transmission lines and related passive devices. The design and construction of superconducting filters and microwave receiver front-end subsystems will be discussed in detail. Finally the world's first superconducting meteorological radar will be introduced as a successful application example of HTS filters.

Key words: superconducting microwave technology, microwave properties, non-linearity, HTS transmission lines, HTS filters, HTS receiver front-end subsystem, superconducting meteorological radar.

10.1 Introduction

Since the discovery of superconductivity in 1911, and especially since the discovery of high-temperature superconductivity in 1986, scientists all over the world have tried very hard to understand this microscopic quantum phenomenon and to find ways of using these novel materials in practical applications. And indeed, after nearly a century of developments, superconductivity has become not only a branch of fundamental sciences, but also a branch of modern technology with ready applications. It is commonly recognized that the first application of high-temperature superconductor (HTS) thin films was in high performance microwave passive devices, especially filters.

This chapter will first summarise the fundamental concepts of superconductivity at microwave frequency and the basic elements for microwave applications, i.e., superconducting microwave transmission lines, as well as related passive devices, will be briefly outlined. Then the design and construction of superconducting filters and microwave receiver front-end subsystems will be discussed in detail. As an example of a successful application of HTS filters, the world's first superconducting meteorological radar will be introduced and, finally, conclusions will be drawn.

10.2 Superconductivity at microwave frequency

10.2.1 The surface impedance of superconductors

The study of superconductivity at microwave frequency is important, not only because the information provided by such study reveals the fundamental nature of superconductors, but also because the technology developed from such study demonstrates great potential for the application of HTS, among which filters are one of the most popular and successful passive devices in use.

In a superconductor at finite temperatures there will be normal electrons as well as Cooper pairs. This phenomenon has been successfully depicted by an empirical two-fluid model, proposed by Gorter and Casimir (1934). In this model it is simply assumed that the charge carriers can be considered as a mixture of normal and superconducting electrons, which can be expressed as $n = n_n + n_s$, where n, n_n, n_s are the numbers of total, normal and superconducting electrons, respectively, and $n_s = fn$, $n_n = (1 - f)n$. The superconducting fraction f increases from zero at T_c, to unity at zero temperature. At microwave frequencies, the effect of an alterative electromagnetic field is to accelerate both parts of the carriers or fluids. The normal component of the current will dissipate the gained energy by making collisions with the lattice. In the local limit, the conductance of a superconductor can be represented by a complex quantity

$$\sigma = \sigma_1 - j\sigma_2 \qquad [10.1]$$

where the real part σ_1 is associated with the loss response of the normal electrons, and the imaginary part is associated with responses of both the normal and superconducting electrons. Lancaster (1997) proposed a simple equivalent circuit, as shown in Fig. 10.1, to present a physical representation of complex conductivity. The total current J in the superconductor is split between the reactive inductance and the dissipative resistance. As the frequency decreases, the reactance becomes lower, and more and more of the current flows through the inductance. When the current is constant, this inductance completely shorts the resistance, allowing resistance-free current to flow. The microwave properties are determined by currents confined to skin-depth in the normal metal state, and to the penetration depth, λ, in the superconducting state. The surface impedance of a superconductor should be considered, which is defined as

$$Zs = \left(\frac{E_x}{H_y}\right)_{Z=0} = Rs + jXs \qquad [10.2]$$

where E_x and H_y are the tangential components of the electric and magnetic fields at the surface ($z = 0$). For a unit of surface current density, the surface resistance

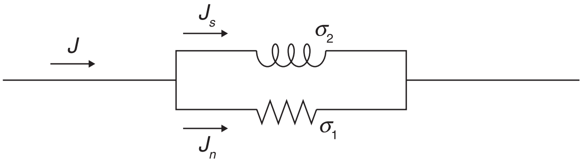

10.1 Equivalent circuit depicting complex conductivity (Lancaster, 1997).

Rs is a measure of the rate of energy dissipation in the surface, and the surface reactance *Xs* is a measure of the peak inductive energy stored in the surface. Relating to complex conductivity, surface impedance can then be written as

$$Zs = \left(\frac{j\omega\mu_0}{\sigma_1 - j\sigma_2} \right)^{\frac{1}{2}} \qquad [10.3]$$

In cases where the temperature is not too close to T_c, where more superconducting carriers are present, and σ_1 is finite but much smaller than σ_2, an approximation of $\sigma_1 << \sigma_2$ can be made. It then turns out that

$$Zs = \frac{1}{2}\omega^2\mu_0^2\lambda^3\sigma_1 + j\omega\mu_0\lambda \qquad [10.4]$$

with the frequency independent magnetic penetration depth $\lambda = (m / \mu_0 n_s e^2)^{1/2}$, where *m* is the mass of an electron and *e* is the charge on an electron.

From equation 10.4 important relations for surface resistance and reactance can easily be derived:

$$Rs = \frac{1}{2}\omega^2\mu_0^2\lambda^3\sigma_1 \qquad [10.5]$$

and

$$Xs = \omega\mu_0 \lambda \qquad [10.6]$$

It is well known that for a normal metal surface resistance increases with $\omega^{1/2}$, whereas for a superconductor it increases with ω^2. Knowledge of the frequency dependence of surface resistance is especially important to evaluate the potential microwave applications of a superconductor. Hein (1999, p.93) showed a double-logarithmic plot of surface resistance *Rs* versus frequency, depicting selected data for granular and high quality epitaxial YBCO films at 77 K. It can be seen from Fig. 10.2 that YBCO displays a lower surface resistance than Cu, up to about 100 GHz, and that the overall trend resembles that of the conventional superconductor Nb_3Sn films at 9 K. It can thus be concluded that the two-fluid formalism is capable of describing all measured data over 3 decades in frequency.

10.2.2 The non-linear microwave properties of superconductors

Non-linearity is an important phenomenon in nature, which has profound significance for modern technology. Research into nonlinear microwave properties has revealed a number of nonlinear phenomena, such as RF-vortex nucleation, annihilation and motion, etc., which will bring new understanding of fundamental sciences. The dynamics of various types of vortices behave in unique ways because the penetration of the microwave current into the superconductor is quite different to that of d.c. current. However, in this chapter we will concentrate our discussions on the effect of

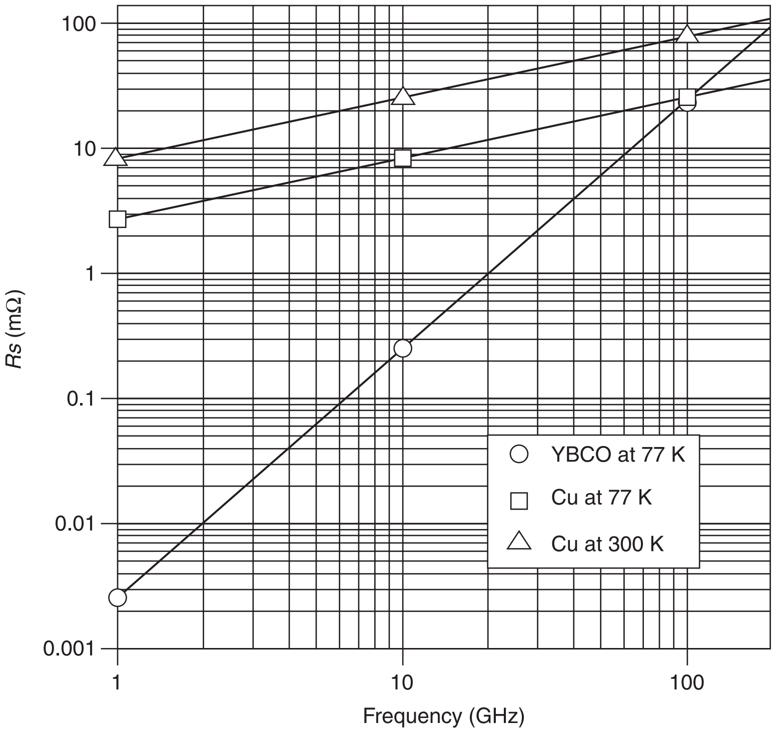

10.2 Frequency dependence of surface resistance *Rs* of high temperature superconductor YBCO at 77 K (lowest line with symbol ○) compared with normal metal Cu at 300 K (upper line with symbol △) and 77 K (lower line with symbol □).

the non-linearity of HTS materials on microwave devices, mainly in terms of the substantial restriction of their power handling ability. The superior microwave properties of HTS materials are only realized when the current density everywhere within an HTS circuit is less than the critical value. If the power level of an HTS microwave circuit is increased, the current density in the HTS material increases accordingly. When the current density exceeds the critical value, the surface resistance of the HTS material increases sharply, causing excessive loss in the circuit, and eventually the performance collapses due to the transition into the non-superconducting state. The nonlinear effects make the situation even worse. The non-optimized power handling of HTS thin films causes the performance of potentially linear devices to deteriorate greatly (e.g., filters, delay lines) and limits optimization of the properties of nonlinear devices (e.g., switches, power limiters). The power handling of HTS devices is likely to be restricted by extrinsic sources, such as growth defects and impurities within the films, but precisely what type of defects and impurities contribute to the nonlinear behaviour remains unclear for the time being. This is why nearly all modern HTS filter applications are positioned in the receiver (very low power) side. However, the demand for HTS filters with higher power handling ability, is increasing all the time (e.g., for applications of the electromagnetic compatibility of the microwave transmitter). Therefore the study of the non-linear microwave properties of superconductors, especially the HTS thin films, has drawn great attention from both scientists and engineers, and is one of the hot topics of current research. The nonlinear microwave properties of HTS thin films have most commonly been studied by investigating the power dependence of the surface impedance of un-patterned or patterned films with coplanar, microstrip or stripline arrangements. These studies can be carried out in the frequency domain or in the time domain, where the dynamic response of the test objects to excitation pulses of variable amplitude and duration can be investigated. Figure 10.3 shows a representative example of the microwave magnetic field H_{rf} dependence of R_S and X_S. The low field quadratic behaviour is usually attributed to the Ginzburg-Landau depairing mechanism, in which Cooper pairs are broken by being accelerated beyond the critical velocity in the microwave electric field. The subsequent faster increase ($\sim H_{rf}^4$) is usually dominated by hysteretic vortex penetration into the superconducting grains (Nguyen *et al.*, 1995). In this special case, the trends of the field dependencies of $R_S(H_{rf})$ and $X_S(H_{rf})$ are correlated. However, there is a wide variety of different

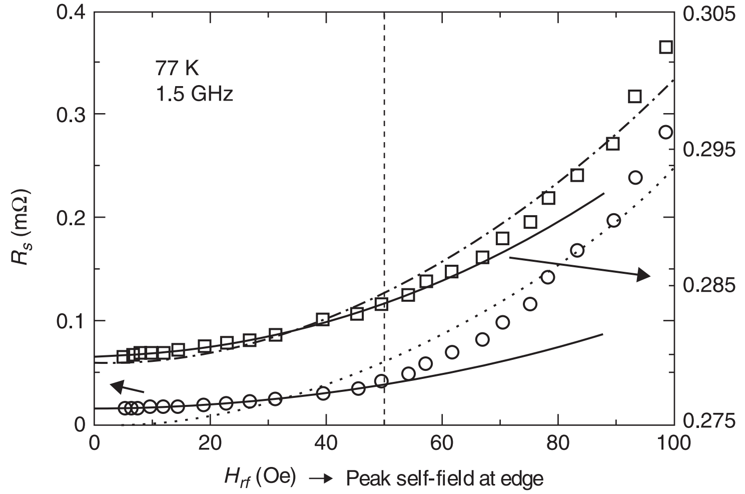

10.3 Typical power dependence of an epitaxial $YBa_2Cu_3O_7$ film measured with the help of the stripline resonator at $f = 1.5$ GHz and 77.4 K. The vertical dashed line at 50 Oe marks the approximate place where R_s and λ deviated noticeably from a quadratic dependence on H_{rf}. The solid lines are the best quadratic fits to the low field region (< 50 Oe), the dashed lines are the best general quadratic fits to the entire field range to demonstrate the nonquadratic behaviour of R_s and λ, see Nguyen *et al.* (1995).

power dependencies of $R_S(H_{rf})$ and $X_S(H_{rf})$ and, for most cases, the function behaviour of $R_S(H_{rf})$ and $X_S(H_{rf})$ are not correlated. It might be argued that the loss of correlation could result from the films being made from different substrates, growth techniques or/and heat treatments. An interesting result from Kharel *et al.* (1999) may give us a clue as to how to clarify some of the confusing results mentioned above. They showed three epitaxial co-evaporated YBCO films on MgO substrates at different temperatures, which demonstrated a great variety of behaviours, including decreasing, independent and increasing functions of $R_S(H_{rf})$, despite the function form of $X_S(H_{rf})$ being very similar for all the three films (Fig. 10.4). From Equations 10.5 and 10.6 it can be seen that $R_S \propto \sigma_1 \propto n_n\tau$, where τ is the quasiparticle scattering time, and $X_S \propto \lambda \propto \sqrt{n_S}$. Since $X_S(H_{rf})$ does not vary from film to film, this strongly suggests that there should be no profound changes in n_s from sample to sample, and hence no such

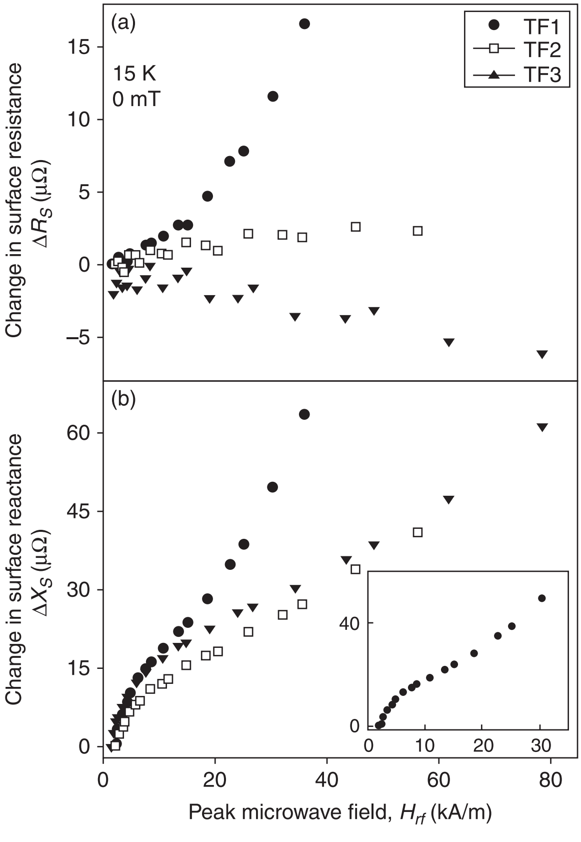

10.4 The change in R_s and X_s for three epitaxial $YBa_2Cu_3O_7$ films on MgO substrates as a function of peak microwave field H_{rf} dependencies. The measurements are made by using the coplanar resonator technique at 8 GHz and 15 K. The inset shows data for sample TF1 on an expanded scale, see Kharel *et al.* (1999).

change in n_n (since the total number of electrons is a constant). Therefore the remarkable change of $R_S(H_{rf})$ most likely originates from the power-dependent quiasiparticle conductivity σ_1 or, more precisely, from the power-dependent τ, the enhanced quasiparticle scattering due to defects and impurities. Those extrinsic mechanisms probably co-exist with intrinsic ones (such as Ginzburg-Landau depairing) and, acting together, lead to the uncorrelated behaviour.

Apart from the direct measurement of nonlinearity by studying the microwave power (H_{rf}^2) dependence of surface impedance, harmonic generation (HG) and intermodulation distortion products (IMD), measurements provide a more sensitive probe of nonlinearity at extremely low power levels, where the device response otherwise appears linear. According to the classical theory of IMD in nonlinear systems, with the impedance being proportional to H_{rf}^2, IMD products generally scale with the third power of the input power. This is usually referred to as 3:1 scaling. In IMD measurements, two microwave signals at frequencies f_1 and f_2, with a frequency separation of Δf being much less than f_1 or f_2, are placed symmetrically around the resonant frequency. The two microwave signals are combined using a power combiner and passed through a variable attenuator to the resonator loaded with film. These nonlinear effects are often expressed by a single parameter called the 'third order intercept', TOI, which is the intercept point of the two input-output power lines for the fundamental and the third harmonic in a log-log scale. The typical 3:1 behaviour of a three-pole YBCO band-pass filter with a mid-band frequency of 9.5 GHz is demonstrated by Yoshitake and Tahara (1995), where the upper line is the fundamental mode and the lower two lines are the third-order distortion products, measured at 55 and 77 K, respectively. However deviations from 3:1 are often reported from the literature. After considering a great variety of power dependencies of $Zs\ (H_{rf})$, Velichko *et al.* (2005) found that, from a theoretical point of view, the lower power slope must always be 3:1, independently of the functional form of $Zs(H_{rf})$. But, at intermediate powers, IMD slopes may indeed vary significantly and can often be less than three. Therefore, Velichko suggested that the deviation from the 3:1 scaling frequently observed in IMD measurements of HTS films has a purely technical origin, and proposed that the spectral characteristics of microwave sources do not always allow the researchers to use low enough powers to observe the 3:1 scaling. Instead, the measurements are often possible only above a certain microwave power (set by the resolution of the detection system), in which the slope is lower than 3:1.

10.3 Superconducting transmission lines and related passive devices

10.3.1 Superconducting transmission lines

In microwave circuits, a transmission line is the material medium (or structure) that forms all or part of a path for directing the transmission of electromagnetic waves from one place to another. It not only serves as an interconnection between the components in the circuits, but also often forms the basic element of components and devices. It is indeed the foundation of microwave circuits, and most microwave theories have originated directly or indirectly from transmission theory, something which is also true for superconducting devices.

The most important effect of superconducting transmission lines is their very low loss. A superconducting transmission line is dispersionless, provided the wave propagated is in a TEM mode. This is due to the fact that the penetration depth does not vary with frequency, a contrast with normal conductors, where skin depth is a function of frequency.

The realistic transmission line model represents the transmission line as an infinite series of two-port elementary components, each representing an infinitesimally short segment of the transmission line with distributed resistance R, inductance L, and capacitance C. Transmission lines which are commonly used include wires, coaxial cables, dielectric slabs, optical fibres, electric power lines, waveguides, and planar transmission lines, etc. Considering that most superconducting filters are based on superconducting films, in this chapter we will concentrate on the planar transmission lines, i.e., microstrip, coplanar, and stripline.

Microstrip is a widely used type of microwave transmission line, which consists of a conducting strip (with a width w and a thickness t) separated from a ground plane by a dielectric layer known as the substrate (with a dielectric constant ε and a thickness d). The general structure of a microstrip is shown schematically in Fig. 10.5(a). The fields in the microstrip extend within two media: air above and dielectric below. In general, the dielectric constant of the substrate will be greater than that of the air, so the wave is travelling in an inhomogeneous medium. In consequence, the propagation velocity is somewhere between the speed of microwaves in the substrate and the speed of microwaves in air. This behaviour is commonly described by stating the effective dielectric constant (or effective relative permittivity) of the microstrip, this being the dielectric constant of an equivalent homogeneous medium. Due to its inhomogeneous nature, the microstrip line will not support a pure TEM wave; both the E and H fields will have longitudinal components. However, the longitudinal components are small, so the dominant mode is referred to as quasi-TEM. The field propagation velocities will depend not only on the properties of the material, but also on the physical dimensions of the microstrip. Compared to other transmission lines, such as traditional waveguide technology, the advantage of a microstrip is that it is much less expensive, as well as being far lighter and more compact. On the other hand, the disadvantages of a microstrip compared to a waveguide are its generally lower power handling capacity, and higher losses, of which the latter can be greatly improved through the use of superconducting materials.

A coplanar line is formed from a conductor separated from a pair of ground planes, all on the same plane, at the top of a dielectric medium (Fig. 10.5(b)). In an ideal case, the thickness of the dielectric is infinite; in practice, it should be

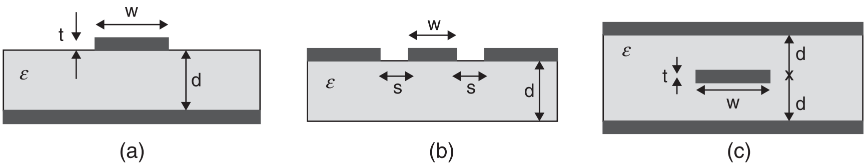

10.5 Cross-section geometries of microstrip (a), coplanar line (b), and stripline (c).

thick enough so that EM fields die out before they leave the substrate. The advantages of a coplanar line are that active devices can be mounted on top of the circuit, as on a microstrip. More importantly, it can provide an extremely high frequency response (100 GHz or more) since connecting to a coplanar line does not entail any parasitic discontinuities in the ground plane. This means that only single-side superconducting film is required for a superconducting coplanar line, which greatly reduces the difficulties in film making since double-sided films need special technology, especially for those newly discovered superconductors. One of the disadvantages of the coplanar line is the imbalance in its ground planes, although they are connected together at some points in the circuit. The potential of the ground planes can become different on each side, which may produce unwanted modes and interference. The problem can be solved to some extent by connecting the two ground planes somewhere in the circuit with a 'flying wire' (air bridge) over the conducting plane. However, it will create other problems, such as greater complexity.

A standard stripline uses a flat strip of metal, which is sandwiched between two parallel ground planes (Fig. 10.5(c)). The width of the strip, the thickness of the substrate (the insulating material between the two ground plans) and the relative permittivity of the substrate determine the characteristic impedance of the transmission line. The advantage of the stripline is that radiation losses are eliminated and a pure TEM mode can be propagated within it. The disadvantage of the stripline is the difficulty in constructing it, especially in superconducting films. It requires two pieces of superconducting films, both double-sided, or one single- plus one double-sided film. The air gap, though extremely small, will cause perturbations in impedance as well as making it very difficult to form contacts with external circuits. Besides, if two pieces of double-sided films are used, the need for precise aiming between the very fine patterns of two films creates another problem.

10.3.2 Application of transmission lines 1: superconducting delay line

A delay line consists of a long transmission line, which is used to delay incoming signals for a given amount of time, while minimizing the distortion caused by crosstalk, dispersion and loss. Conventional delay lines, such as coaxial cables and printed circuit delay lines, present the problems of large volume and unacceptable insertion loss. Superconducting delay lines with extremely small losses and compact sizes offer a promising solution for these problems.

All of the three types of superconducting transmission lines mentioned above can be used for making delay lines. However, the advantages of coplanar lines are distinctive. First, the ground planes in between the signal line provide a shield, which reduces the crosstalk. Secondly, the line width of the signal line is quite flexible since the impedance of the coplanar line is mainly determined by the ratio between the signal line width and the gap width. The disadvantage is that the unwanted odd mode can be excited by turnings, curvatures, or any asymmetry with respect to the signal line, which can be resolved by bonding crossover 'flying wires' (air bridges) between the ground planes over the top of the signal line.

Stripline is the only planar transmission line without modal dispersion. It has a longer delay per unit length, since the signal propagation velocity is slower than that of the other two lines. It also has less cross talk than the microstrip line due to the existence of the top plane. An excellent example of the application of striplines can be found in the work reported by Lyons *et al.* (1996), where the delay line was used for a chirp-response tapped filter. They used a pair of YBCO striplines to form a double spiral configuration and the chirp function was achieved by a series of $\lambda/4$ backward-wave couplers to realize the requested frequency dependent delay for different frequency components in the signal. This chirp filter was installed in a 3 GHz band width spectral analysis receiver.

10.3.3 Application of transmission lines 2: superconducting resonator

A microwave resonator is a simple structure, which can be made of cavity or transmission line, and is able to contain at least one oscillating electromagnetic field. If an oscillating field is set up within a resonator, it will gradually decay because of losses. By using superconductors, the losses can be greatly reduced and high Q-values can then be achieved. Resonators are the most fundamental building blocks in the majority of microwave circuits. By coupling a number of resonators together, a microwave filter can be constructed. A high Q-resonator forms the main feedback element in a microwave oscillator. The quality factor for a resonator is defined by

$$Q_0 = 2\pi \frac{w}{p} \qquad [10.7]$$

where w is the energy stored in the resonator, and p is the dissipated energy per period in the resonator.

Losses in a resonator occur due to a number of mechanisms. The most important are usually the losses associated with conduction currents in the conducting layer of the cavity or transmission line, the finite loss tangent of the dielectric substrate, and radiation loss from the open aperture. The total quality factor can be found by adding these losses together, resulting in

$$\frac{1}{Q_0}=\frac{1}{Q_c}+\frac{1}{Q_d}+\frac{1}{Q_r} \qquad [10.8]$$

where Q_c, Q_d, and Q_r are the conductor, dielectric and radiation quality factors, respectively. For conventional cavity or transmission line resonators at microwave frequency, Q_c usually dominates. This is why a superconductor can greatly increase the Q-value of the resonators.

For superconducting resonators, the resonant frequency and the Q-values (both loaded Q_L and unloaded Q_U values) are temperature dependent, and the variation is remarkable when close to T_c, as shown in Fig. 10.6 (Li *et al.*, 2002). It is

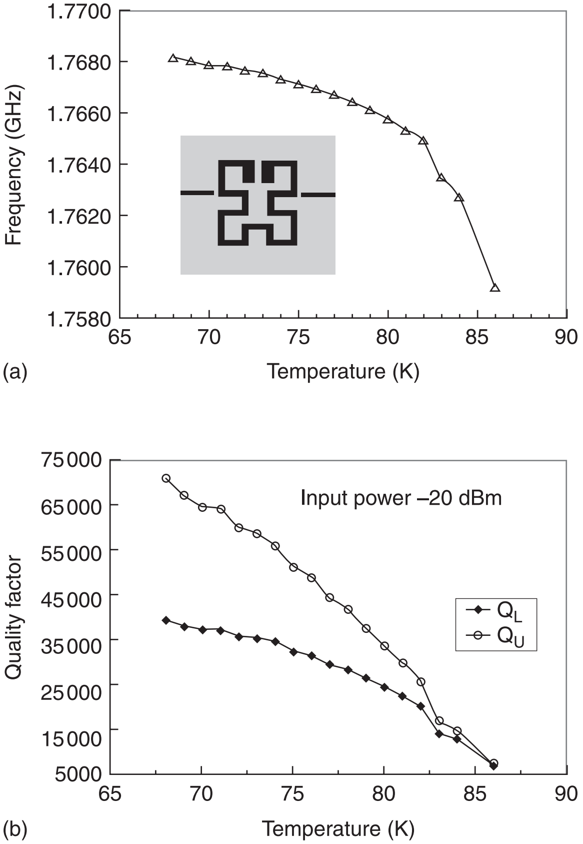

10.6 Temperature dependence of resonate frequency (a) and Q-values (b) of superconducting resonator, see Li *et al.* (2002).

therefore preferable to operate at a temperature below 80% of T_c, where a more stable resonant frequency and a high enough Q-value can be achieved.

Aside from the Q-value, size is also important in an HTS resonator, not only in terms of the commercial consideration of reducing the cost, but also because the HTS filters need to work at low temperatures and their large size will increase the burden on the cryo-cooler. However, high quality factor and minimal size are often a contradictory pair because a reduction in size always results in a reduction in the stored energy, and hence the Q-values. The quality factors and volumes of various kinds of HTS resonators are shown in Fig. 10.7 in dual-log coordinate at frequency around 5 GHz. All the data come from literature published over the last decades. Here, the volume of the planar resonators is calculated by assuming it has a height of 8 mm.

HTS cavity resonators are usually designed to resonate in the TE_{011} mode. In this mode, the current flow is circumferential, so there is no current flow across the join of the side wall and the end plates. Although such structures have very high Q-values, their volume becomes prohibitively large at low frequencies. HTS dielectric resonators usually consist of a dielectric rod of single crystal material, which is sandwiched between two planar HTS films. They can have very high Q-values (if very large area high quality superconducting films are applied), but are smaller than unloaded resonant cavities. Due to their large volume and difficulty in realizing cross couplings, HTS cavity resonators and HTS dielectric resonators are often used to construct low-phase noise oscillators and, in the case of the dielectric ones, to measure the surface resistance of HTS thin films. They are seldom used in HTS filters. Patch resonators, which are two dimensional resonators, are of interest in the design of high power handling HTS filters. An associated advantage of these resonators is their lower conductor losses compared with one dimensional line resonators. However, patch resonators tend to have stronger radiation, so they are not suitable for designing narrow band filters. The

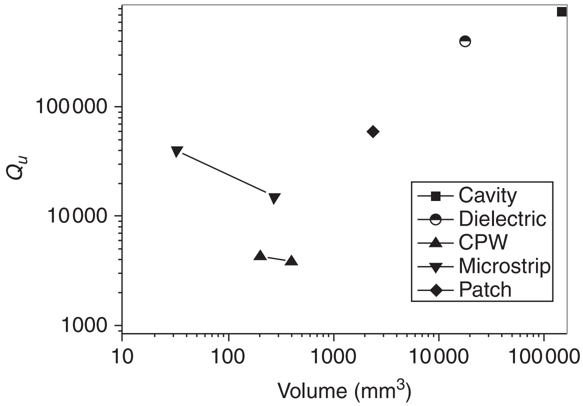

10.7 The quality factor vs. volume of different kinds of HTS resonators.

one dimensional HTS transmission line resonators frequently used in applications are coplanar waveguide (CPW) resonators and microstrip resonators. Because the circuit structure and the ground planes are fabricated on a single plane, CPW resonators offer the possibility of integration with active components. But the electromagnetic energy in the CPW resonators are more confined to a small area between the HTS line and the ground lines, so they tend to have lower quality factors compared to other types of HTS resonators. Microstrip resonators are the most popular type of resonators used in HTS microwave filters. Besides their relatively high quality factor and small size, the ease with which they can be used in a variety of coupling structures is also a big advantage. For most applications, the basic shape of an HTS microstrip resonator is a half-wavelength (Fig. 10.8(a)) line instead of a grounded quarter-wavelength ($\lambda/4$) line, due to the difficulty of realizing ground via HTS substrate. The conventional $\lambda/2$ resonator can be miniaturized by folding its straight rectangular ribbon. The height of a folded resonator, called a hairpin resonator (Fig. 10.8(b)), is usually less than $\lambda/4$. Meander-line resonators (Fig. 10.8(c)), meander-loop resonators (Fig. 10.8(d)), spiral resonators (Fig. 10.8(e)) and spiral-in-spiral-out resonators (Fig. 10.8(f)) are created as modifications of the conventional straight ribbon ($\lambda/2$) resonator by folding the ribbons several times and in different ways. In principle, $\lambda/2$ resonators can be folded or transformed to any other shape, according to the demands of miniaturization or another purpose.

10.3.4 Other related superconducting microwave passive devices: antennas and filters

As mentioned above, delay lines and resonators, which are all passive microwave devices, are ideal vehicles for demonstrating the advantages of HTS. The main advantage gained from HTS is low surface resistance, which can be directly converted into small insertion loss or high Q-values for the microwave devices. Another unique property of superconductors is their lack of dispersion due to the

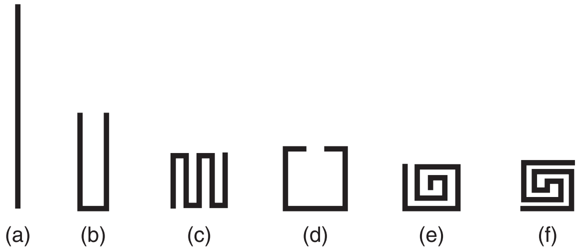

10.8 Typical one dimensional microstrip resonators: (a) half-wavelength line resonator; (b) hairpin resonator; and (c) to (f) other open loop resonators.

fact that their penetration depth does not vary with frequency. Furthermore, substrates with high dielectric constants, which are used for superconducting films, make device miniaturization possible. Based on these advantages, more HTS passive devices can be constructed for applications. Antennas can benefit in a number of ways from the use of superconductors. One obvious application of superconductors is in the improvement of radiation efficiency in small antennas. For antennas with comparable size and wavelength, their efficiency is fairly high. However, for those with dimensions that are small compared to their wavelength, which are defined as electrically small antennas, efficiency is reduced due to the increasing dominance of ohmic losses. By using extremely low loss superconductors, reasonable efficiency can be achieved. Superconductors are also useful in feeding and matching networks for super-directive antennas, which are very inefficient. High Q-value matching networks, provided by superconducting circuits, help considerably in terms of performance improvement. Another application of superconductors to antennas is in the feed networks of millimetre-wave antennas. The losses associated with long narrow microstrip feed lines can be improved considerably if superconductors are used. This is especially true for arrays with a large number of elements.

The most attractive applications of HTS in passive devices are those of filters. Due to the very small surface resistance of HTS films, filters can be constructed with remarkably high performance, i.e. with negligible insertion loss, very large out-of-band rejection, and extremely steep skirt slopes. They can reduce the band width and make ultra-narrow band filter possible. With the properties mentioned above, excellent performance HTS filters can eliminate unwanted interference, while maintaining a minimal noise figure in the system. Moreover, by using HTS films the filter can be miniaturized due to not only special substrates being employed, but also to new geometric designs being invented. In the past twenty years, various kinds of HTS filters have been constructed and successful applications in many fields have been realized, including those in direct data distribution between earth to satellite and satellite to satellite (Romanofsky *el al.*, 2000), detection of deep space radio astronomy (Wallage *et al.*, 1997; Li *et al.*, 2003), base stations for mobile communications (STI Inc., 1996; Hong *et al.*, 1999) and meteorological radars for weather forecasting (Zhang *et al.*, 2007).

10.4 Superconducting filter and receiver front-end subsystem

10.4.1 Principles and theories on filter design

Frequency-selective transmission is a property of electrical filters, which enables them to transmit energy in one or more passbands, and to attenuate energy in one or more stopbands. Filters are essential elements in many areas of RF/microwave engineering.

A filter is essentially a two port network. For linear, time-invariant two-port filter networks, the transmission and reflection function may be defined as rational functions,

$$S_{21}(p) = \frac{N(p)}{\varepsilon D(p)}; \qquad S_{11}(p) = \frac{E(p)}{D(p)} \tag{10.9}$$

where ε is a ripple constant, $N(p)$, $E(p)$ and $D(p)$ are characteristic polynomials in a complex frequency variable $p = \sigma + j\Omega$, and Ω is the normalized frequency variable. For a lossless passive network, $\sigma = 0$ and $p = j\Omega$. The horizontal axis of the p plane is called the real axis, while the vertical axis is called the imaginary axis. The values of p at which $S_{21}(p)$ becomes zero are the transmission zeros of the filter, the values at which $S_{11}(p)$ becomes zero are the reflection zeros of the filter, and the values at which $S_{21}(p)$ becomes infinite are the poles of the filter.

Filters may be classified in several ways. The main categories are defined in terms of the general response types: low-pass, bandpass, high-pass, and bandstop. Filters can also be classified by their transmission zeros and poles. The Butterworth filter is called a maximum flat response filter because its amplitude-squared transfer function has a maximum number of zero derivatives at $\Omega = 0$. The Chebyshev filter exhibits an equal-ripple passband response and maximally flat stopband response. All the transmission zeros of $S_{21}(p)$ of Chebyshev and Butterworth filters are located at infinite frequencies. When one or more transmission zeros are introduced into the stopband of a Chebyshev filter at finite frequencies the filter is known as a generalized Chebyshev filter, or as a quasi-elliptic filter. The special case where the maximum number of transmission zeros is located at finite frequencies, such that the stopbands have equal rejection level, is the well-known elliptic function filter. This is now rarely used due to problems associated with its practical realization. The Gaussian filter, unlike those mentioned above, has poor selectivity but a fairly flat group delay in the passband.

Chebyshev filters have for many years found frequent application within microwave space and terrestrial communication systems. The generic features of equal ripple passband characteristics, together with the sharp cutoffs at the edges of the passband and hence high selectivity, offer an acceptable compromise between lowest signal degradation and highest noise/interference rejection. As the frequency spectrum becomes more crowded, specifications for channel filters have tended to become very much more severe. Very high close-to-band rejections are required to prevent interference to or from closely neighbouring channels; at the same time, there is a demand for the incompatible requirements of in-band group-delay and amplitude flatness and symmetry to minimize signal degradation. With a generalized Chebyshev filter, it is easy to build-in prescribed transmission zeros for improving the close-to-band rejection slopes and/or linearizing the in-band group delay. Therefore, generalized Chebyshev filters have been extensively investigated by many researchers over the last few decades. Coupled resonator circuits are of importance for the design of generalized Chebyshev filters. This design method is based on coupling coefficients of inter-coupled resonators and the external quality factors of input and output resonators. One of the fundamental methods for the synthesis of generalized Chebyshev filters based on cross-coupled resonators was proposed by Atia and Williams (1972; Atia *et al.*, 1974), and is still commonly used. Alternative synthesis techniques were also advanced by many scientists (Cameron and Rhodes, 1981; Chambers and Rhodes, 1983; Levy, 1995; Cameron, 1999).

The first step in designing a generalized Chebyshev filter is to determine all the positions of the transmission zeros and reflection zeros of the filter that satisfy the specifications. The amplitude-squared transfer function for a lossless low-pass prototype is defined as

$$S_{21}^2(j\Omega) = \frac{1}{1+\varepsilon^2 C_N^2(\Omega)} \qquad [10.10]$$

where ε is related to the passband return loss (RL) by $\varepsilon = [10^{RL/10} - 1]^{1/2}$, and $C_N(\Omega)$ represents a filtering or characteristic function with N being the order of the filter. For a generalized Chebyshev filter, $C_N(\Omega)$ may be expressed as

$$\mathrm{C}_N(\Omega) = \cosh\left[\sum_{n=1}^{N} \cosh^{-1}(x_n)\right] \qquad [10.11]$$

where, $x_n = (\Omega - 1/\Omega)/(1 - \Omega/\Omega_n)$, and Ω_n is the position of the nth prescribed transmission zero.

It can be proved (Cameron and Rhodes, 1981) that $C_N(\Omega)$ can be expressed as a ratio of *N(p)*, *E(p)*. Given that all the transmission zeros and *RL* various methods exist for evaluating the characteristic polynomials *N(p)*, *E(p)* and *D(p)* (Cameron, 1999; Amari, 2000; Macchiarella, 2002), then the reflection zeros and poles of the filter may be found by rooting *E*(*p*) and *D(p)*, respectively. Then the complete transmission response L_A, reflection response L_R, and phase response Φ_{21}, including the group delay τ_d, can be computed by

$$\begin{cases} L_A(\Omega) = 10\log\dfrac{1}{|S_{21}(j\Omega)|^2} \quad \text{dB} \\ L_R(\Omega) = 10\log\left[1-|S_{21}(j\Omega)|^2\right] \quad \text{dB} \\ \phi_{21}(\Omega) = ArgS_{21}(j\Omega) \quad \text{radians} \\ \tau_d(\Omega) = {d\phi_{21}(\Omega)}\big/{-d\Omega} \quad \text{seconds} \end{cases} \qquad [10.12]$$

and so can the lowpass to bandpass frequency transformation: $\Omega = (1/FBW) \times (\omega/\omega_0 - \omega_0/\omega)$, where ω_0 is the centre frequency of the bandpass filter, and *FBW* is the fractional bandwidth.

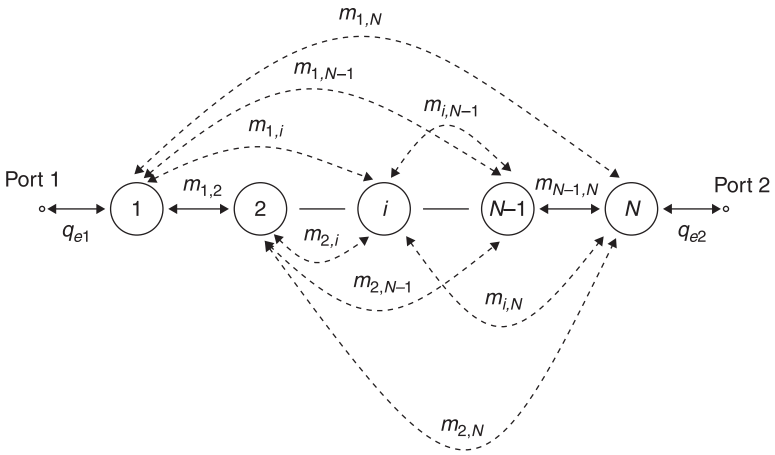

10.9 The general coupling structure of a filtering circuit of *N* coupled resonators.

Knowing all the positions of the zeros and poles, the next step of filter synthesis is to choose an appropriate topology of coupled resonators and to synthesize the coupling matrix. Figure 10.9 shows a schematic illustration of a filtering circuit of *N* coupled resonators, where each circle with a number represents a resonator, which can be of any type despite its physical structure. $m_{i,j}$ with two subscript numbers is the normalized coupling coefficient between the two (i^{th} and j^{th}) resonators and q_{e1} and q_{e2} are the normalized external quality factors of the input and output resonators. Here, we assume $\omega_0 = 1$ and $FBW = 1$. For a practical filter, the coupling coefficient $M_{i,j}$ and external quality factors Q_{e1}, Q_{e2} can be computed by

$$\begin{cases} M_{i,j} = FBW \cdot m_{i,j} \\ Q_{ei} = q_{e1} / FBW \end{cases} \qquad [10.13]$$

The transfer and reflection functions of a filter with coupling topology in Fig. 10.9 are

$$\begin{cases} S_{21} = 2\dfrac{1}{\sqrt{q_{e1} \cdot q_{e2}}}[A]_{N1}^{-1} \\ S_{11} = \pm\left(1 - \dfrac{2}{q_{e1}}[A]_{11}^{-1}\right) \\ [A] = [q] + p[U] - j[m] \end{cases} \qquad [10.14]$$

where p is the complex frequency variable as defined before, $[U]$ is the $N \times N$ identity matrix, $[q]$ is an $N \times N$ matrix with all entries zero except for $q_{11} = 1/q_{e1}$ and $q_{NN} = 1/q_{e2}$, and $[m]$ is an $N \times N$ reciprocal symmetrical matrix being named as the general coupling matrix. The non-zero values may occur in the diagonal entries of [m] for electrically asymmetric networks representing the offsets from the centre frequency of each resonance (asynchronously tuned). However, for a synchronously tuned filter, all the diagonal entries of [m] will be zero and [m] will have the form

$$\begin{bmatrix} 0 & m_{1,2} & \cdots & m_{1,i} & \cdots & m_{1,N-1} & m_{1,N} \\ m_{1,2} & 0 & \cdots & m_{2,i} & \cdots & m_{2,N-1} & m_{2,N} \\ \cdots & \cdots & \cdots & \cdots & \cdots & \cdots & \cdots \\ m_{1,i} & m_{2,i} & \cdots & 0 & \cdots & m_{i,N-1} & m_{i,N} \\ \cdots & \cdots & \cdots & \cdots & \cdots & \cdots & \cdots \\ m_{1,N-1} & m_{2,N-1} & \cdots & m_{i,N-1} & \cdots & 0 & m_{N-1,N} \\ m_{1,N} & m_{2,N} & \cdots & m_{i,N} & \cdots & m_{N-1,N-1} & 0 \end{bmatrix}$$

The minor diagonal entries of [m] all have non-zero values. They represent couplings between adjacent resonators and, in the remainder of the paper, they are called direct couplings. The other entries represent couplings between non-adjacent resonators. It is this type of couplings which create transmission zeros of filter response. Those entries may all have non-zero values in theory, which means that in the filter network that [m] represents, couplings exist between every resonator and every other non-adjacent resonator. This is clearly impractical in the case of cavity type resonators. In the case of planar resonators such as HTS microstrip resonators, couplings may exist between every resonator and every other non-adjacent resonator. However, it is still impractical to handle all those couplings as expected. So it is important to choose a realizable coupling topology to design a practical filter, which means some particular non-adjacent couplings are chosen to exist, and the others are not. Generally, the desired non-adjacent couplings are called cross-couplings, while the others are called parasitical couplings.

There are three frequently used coupling topologies in the design of generalized Chebyshev filters, as shown in Fig. 10.10, where each circle with a number represents a resonator, full lines indicate the direct couplings, and the broken lines denote cross-couplings. In the cascaded quadruplet (CQ) topology, four resonators construct a quadruplet section, as illustrated in Fig. 10.10(a), and then it can be cascaded to other resonators or quadruplets. Each quadruplet section will create a pair of transmission zeros which are symmetric with respect to the centre frequency. Similar to the CQ filter, three resonators can construct a trisection structure, as shown in Fig. 10.10(b), and this can then be cascaded to other resonators or trisections to form a cascaded trisection (CT) filter. Each trisection structure, however, will only create one transmission zero. So the frequency response in a CT filter could be asymmetrical. The cross-couplings between different CQ or CT sections are independent of each other, making the tuning of the filter relatively easy. The coupling topology shown in Fig. 10.10(c) is the

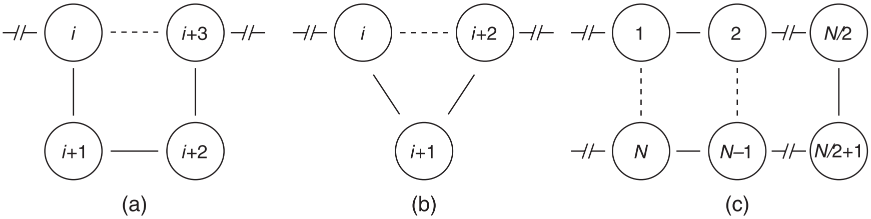

10.10 Three frequently used coupling topologies in generalized Chebyshev filters. For explanation see text.

so-called canonical fold form. The canonical fold coupling section always contains an even number of resonators. For a filter consisting of $2n$ resonators, $2n - 2$ transmission zeros can be realized. So, a given out-of-band rejection specification can meet it by fewer resonators in the canonical fold filter than in the CQ or CT structures. However, the effect of each cross-coupling in a canonical fold filter is not independent, which makes the filter tuning more difficult.

Once an appropriate coupling topology is determined, the synthesis from characteristic polynomials to coupling matrix may follow the steps of Atia *et al.* (1972, 1974). They used the orthonormalization technique to obtain a general coupling matrix with all possible cross-couplings present, and repeated similarity transformations are then used to cancel the unwanted couplings to obtain a suitable form of the prototype. Unfortunately, the processes do not always converge. In this case, an optimization technique is a good alternative to derive the sequence of transformations, allowing for annihilation of the unwanted elements and providing the matrix with the required topology (Chambers and Rhodes 1983; Atia *et al.*, 1998; Levy, 1995). Generally, the desired couplings in the optimization are evaluated by minimizing a cost function involving the values S_{11} and S_{21} at specially selected frequency points, such as those at transmission and reflection zeros. The entries of the coupling matrix are used as independent variables in the optimization process.

The final step in the design of a filter is to find an appropriate resonator and convert the coupling matrix into practical physical structures. Readers can find detailed instructions on how to establish the relationship between the values of every required coupling coefficient and the physical structure of coupled resonators in the book by Hong and Lancaster (2001). In this step it is essential to employ the help of computer-aided design (CAD), particularly full-wave electromagnetic (EM) simulation software. EM simulation software solves Maxwell equations with the boundary conditions imposed upon the RF/microwave structure to be modelled. They can accurately model a wide range of such structures.

10.4.2 Resonators for superconducting filter design

Resonators are key elements in a filter, which play a large part in deciding the performance of the filter. The HTS resonators suitable for developing narrow-band generalized Chebyshev filters should demonstrate the high-quality factors, minimized size, and convenience to realize cross couplings. For an *n*-pole bandpass filter, the quality factors of resonators directly related to the insertion loss of a filter may be described as

$$\Delta L_A = 4.343\sum_{i=1}^{n}\frac{\Omega_C}{FBW\cdot Q_{Ui}}g_i \quad \text{dB} \qquad [10.15]$$

where ΔL_A is the dB increase in insertion loss at the centre frequency of the filter, Q_{ui} is the unloaded quality factor of the i^{th} resonator evaluated at the centre frequency, and g_i is either the inductance or the capacitance of the normalized lowpass prototype.

In the design of narrow band microstrip filters, one important consideration in selecting resonators is to avoid parasitical couplings between non-adjacent resonators. Those parasitical couplings may decrease the out-of-band rejection level and/or deteriorate the in-band return loss of the filter. For example, consider a 10-pole CQ filter which has a pair of transmission zeros (the design of this filter will be detailed in the next section). The transmission zeros are created by two identical cross-couplings between resonators 2 and 5 and between resonators 6 and 9. All the other non-adjacent couplings should be zero, according to the coupling matrix. However, because all the resonators are located in one piece of dielectric substrate and in one metal housing, parasitical couplings between non-adjacent resonators are inevitable. We have performed a series of analyses by computer simulation on how parasitical couplings affect the transmission response of this 10-pole CQ filter, and the results are plotted in Fig. 10.11. In Fig. 10.11(a) different levels of the parasitical coupling between resonator 1 and 10 ($M_{1,10}$) were assumed. Its magnitude is scaled to the main coupling $M_{1,2}$. A significant degeneration of the out-of-band rejection level can be seen when $M_{1,10}$is higher than 0.1 percent of $M_{1,2}$. In Fig. 10.11(b) the effects of the parasitical coupling between resonator 1 and 9 ($M_{1,9}$) with different strengths were also simulated. It can be seen that in addition to the degeneration of

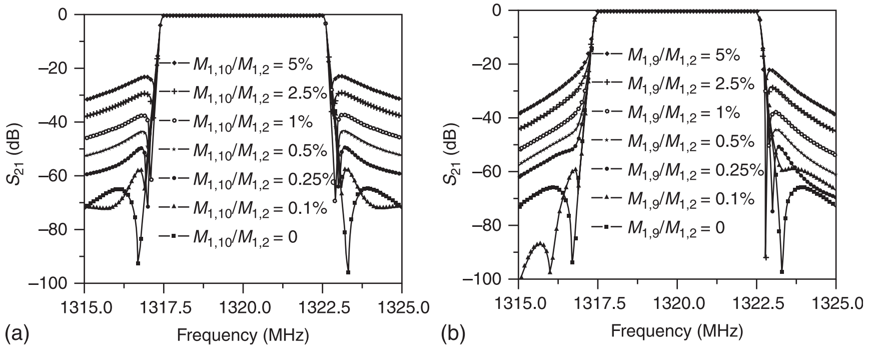

10.11 Illustration of how the parasitical couplings affect the response of a narrow band bandpass filter.

the out-of-band rejection level, the presence of $M_{1,9}$ also causes the asymmetric transmission response of the filter. To solve these parasitical coupling problems, it is necessary to employ some unique resonators. For example, the hairpin and spiral-in-spiral-out resonators (as depicted in Fig. 10.8) behave as though they have two parallel-coupled microstrips excited in the odd mode when resonating. In this case, the currents in these two microstrips are equal and opposite, resulting in the cancellation of their radiation fields. This characteristic should be of great help in reducing parasitical couplings when designing narrow band filters.

10.4.3 Superconducting filter and receiver front-end subsystem

So far, the theory and principles of HTS filter design have been discussed generally. In this section, the design, construction and integration of a real practical HTS filter and HTS receiver front-end subsystem will be introduced as an application example with one special type of meteorological radar: the wind profiler. The frequencies assigned to the wind profiler are in UHF and L band, which are very crowded and noisy with radio, TV, and mobile communication signals, and therefore the radar is often paralysed by the interference. To solve this problem, it is necessary to employ pre-selective filters. Unfortunately, due to the extremely narrow bandwidth (≤ 0.5%) there is no suitable conventional device available. The HTS filter can be designed to have very narrow bandwidth and very high rejection with very small loss, therefore it is expected that the HTS filter can help to improve the anti-interference ability of the wind profiler, without even a tiny reduction in its sensitivity. In fact, because the low noise amplifier (LNA) in the front end of the receiver is also working at a very low temperature in the HTS subsystem, the sensitivity of the radar will actually be increased.

The centre frequency of the wind profiler introduced here is 1320 MHz. In order to reject the near band interference efficiently, the filter was expected to have a bandwidth of 5 MHz and for its skirt slope to be as sharp as possible. It has been decided that the real design should employ a 10-pole generalized Chebyshev function filter with a pair of transmission zeros placed at $\Omega = \pm 1.3$ so as to produce a rejection lobe better than 60 dB on both sides of the passband. For the implementation of this filter, the CQ coupling topology shown in Fig.10.12 was

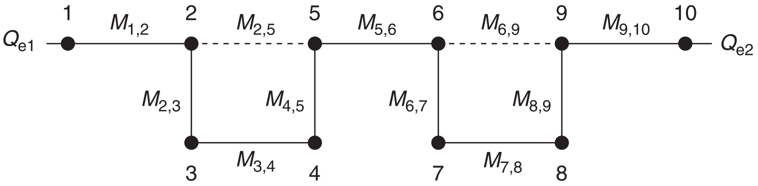

10.12 Coupling topology of the 10-pole CQ filter designed for the wind profiler.

employed. The cross couplings $M_{2,5}$ and $M_{6,9}$ in Fig.10.12 were introduced to create the desired transmission zeros. In the present design, they are set to be equal to each other to create the same pair of transmission zeros. Introducing two identical cross couplings can make the physical structure of the filter symmetric. With this strictly symmetric physical structure, only half (e.g., the left half) of the whole filter needs to be simulated in the EM simulation process, which will simplify the EM simulation and save a considerable amount of computing time.

The transfer and reflection functions and the coupling matrix can then be synthesized following the instructions in section 10.4.1. For this filter with topologic structure, shown in Fig. 10.12, the finally coupling parameters are: $Q_{e1} = Q_{e2} = 237.3812$, and

$$M = 0.01 \times \begin{bmatrix} 0 & 0.330 & 0 & 0 & 0 & 0 & 0 & 0 & 0 & 0 \\ 0.330 & 0 & 0.218 & 0 & 0.0615 & 0 & 0 & 0 & 0 & 0 \\ 0 & 0.218 & 0 & 0.262 & 0 & 0 & 0 & 0 & 0 & 0 \\ 0 & 0 & 0.262 & 0 & 0.188 & 0 & 0 & 0 & 0 & 0 \\ 0 & 0.0615 & 0 & 0.188 & 0 & 0.198 & 0 & 0 & 0 & 0 \\ 0 & 0 & 0 & 0 & 0.198 & 0 & 0.188 & 0 & 0.0615 & 0 \\ 0 & 0 & 0 & 0 & 0 & 0.188 & 0 & 0.262 & 0 & 0 \\ 0 & 0 & 0 & 0 & 0 & 0 & 0.262 & 0 & 0.218 & 0 \\ 0 & 0 & 0 & 0 & 0 & 0.0615 & 0 & 0.218 & 0 & 0.330 \\ 0 & 0 & 0 & 0 & 0 & 0 & 0 & 0 & 0.330 & 0 \end{bmatrix}$$

The synthesized response of the filter is depicted in Fig. 10.13. The designed filter shows a symmetric response which gives a rejection lobe of more than 60 dB on both sides of the passband, as expected. The passband return loss is 22 dB and the band width is 5 MHz, centred at 1320 MHz. Two transmission zeros are located at 1316.75 MHz and 1320.25 MHz, respectively.

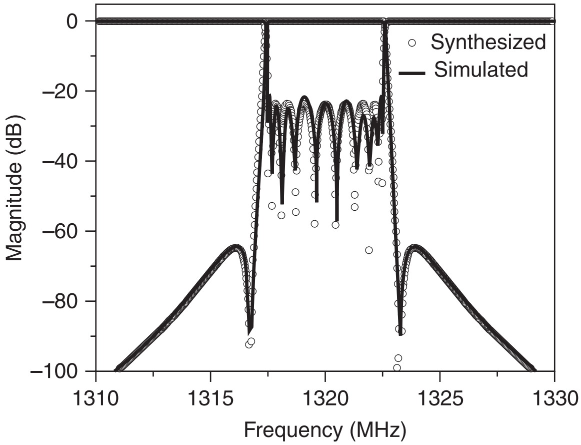

10.13 Synthesized (circles) and simulated (solid line) responses of the 10-pole CQ filter.

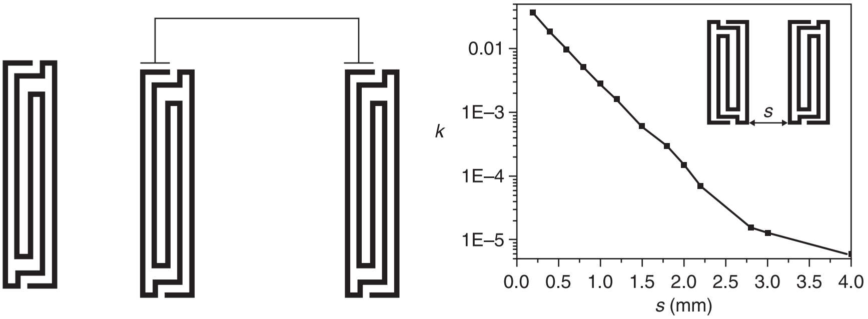

(a) (b) (c)

10.14 The resonator used in the present work (a), the introduction of cross coupling (b), and the simulated coupling coefficient *k* between two adjacent resonators as a function of the separation space *s*.

The resonator used in this filter is a spiral-in-spiral-out type resonator, as shown in Fig. 10.14(a), which is slightly different from that shown in Fig. 10.8(f). The main difference is that both ends of the microstrip line are embedded in the resonator to form capacitance loading, further constraining the electric-magnetic field. Moreover, the middle part of the microstrip line, which carries the highest currents at resonance, was widened to increase the quality factor of the resonator. The resonator with centre frequency of 1320 MHz is 10.64 mm long and 2.86 mm wide. The cross-coupling needed for the transmission zeros can be introduced by a microstrip line, as shown in Fig. 10.14(b). Figure 10.14(c) shows the simulated coupling coefficient κ between two resonators, using a full-wave EM simulation software Sonnet as a function of the space s. For the simulation, the substrate is MgO with a thickness of 0.50 mm and permittivity of 9.65. It can be seen that κ decreases rapidly with s. When s changes from 0.2 mm to 3 mm (about a resonator's width), the coupling coefficient k becomes more than 3 orders of magnitude less than its original value, making this resonator very suitable for the design of an ultra-narrow bandpass filter.

The filter layout was simulated and optimized using Sonnet, and the final layout of the filter is shown in Fig. 10.15. The final full-wave EM simulated responses of the filter are shown in Fig. 10.13 as solid lines. Comparing the full-wave EM simulated responses with the synthesized theoretical responses, the out-of-band responses are very similar. The passband response of the EM simulated return loss is 21 dB, only slightly worse than the theoretical return loss of 22 dB.

The filter was then fabricated on a 0.5 mm thick MgO wafer with double-sided YBCO films. The YBCO thin films have a thickness of 600 nm and a characteristic temperature of 87 K. Both sides of the wafer are gold-plated with 200 nm thick gold (Au) for the RF contacts. The whole dimension of the filter is 60 mm × 30 mm × 20 mm, including the brass housing. The RF measurement

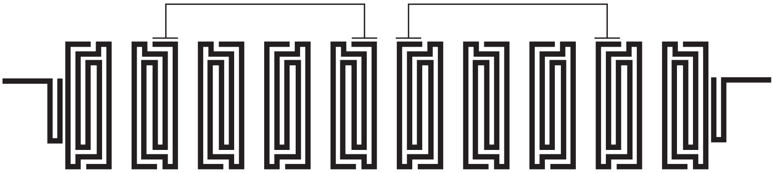

10.15 The final layout of the 10-pole quasi-elliptic filter (not to scale).

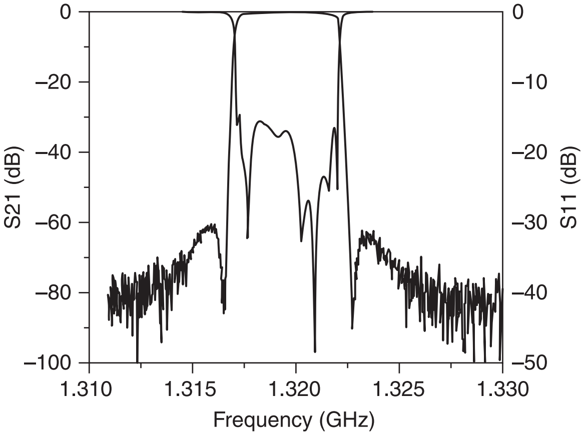

10.16 The measured response of the 10-pole filter at 70 K.

was made using an HP 8510C network analyser and in a cryogenic cooler. Figure 10.16 shows the measured results at 70 K and after tuning the filter. The measured centre frequency is 1.319 GHz, and the return loss in the passband is better than 15 dB. The insertion loss at the passband centre is 0.26 dB, which corresponds to a filter Q of about 45 000. The transmission response is very similar to the theoretically synthesized and the full-wave EM simulated responses, as shown in Fig. 10.13. The fly-back values in the S21 curve are 60.7 dB and 62 dB at the lower and upper frequency sides, respectively. Steep rejection slopes at the band edges are obtained and rejections reach more than 60 dB in about 500 kHz from the lower and upper passband edges.

Combining this filter with a low noise amplifier (LNA), as well as a Sterling cryo-cooler, an HTS subsystem was then constructed as shown schematically in Fig. 10.17 (a). There are many types of cryo-coolers on the market which are specially built for a long life under outdoor conditions in order to provide high cooling power at a cryogenic temperature. What we chose for the HTS wind profiler subsystem was Model K535 made by Ricor Cryogenic &

Vacuum Systems, Israel, for its considerably compact volume and longer life time (Fig. 10.17 (b)). The advantage of integrating the LNA with the HTS filter inside the cryo-cooler is obvious, as the noise figure of LNA is temperature dependent (Fig. 10.18 (a)). Since the cost of a cryo-cooler is inevitable for HTS filters, an extra benefit of significant reduction of the noise figure can be obtained by also putting the LNA in a low temperature without any new burden of cooling devices. The noise figure of the HTS receiver front-end subsystem, measured using an Agilent N8973A Noise Figure Analyzer at 65 K, is about 0.7 dB in the major part (80%) of the whole passband, as shown in Fig. 10.18 (b).

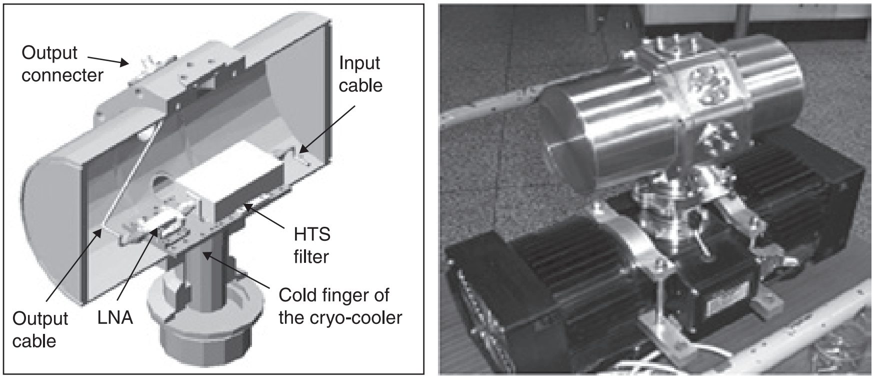

(a) (b)

10.17 Sketch (a) and photograph (b) of the HTS receiver front-end subsystem.

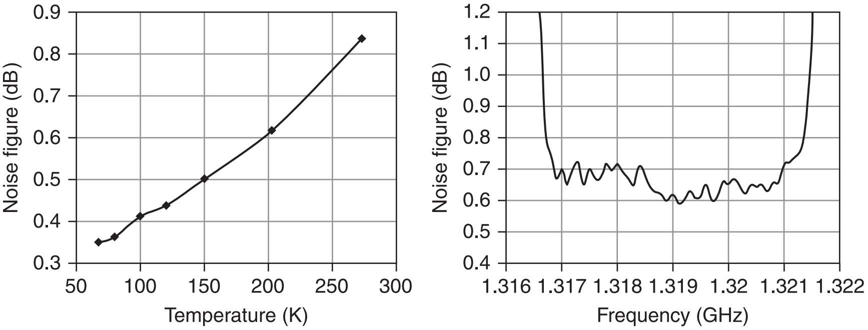

(a) (b)

10.18 Temperature dependence of the noise figure of the LNA used in the HTS subsystem (a) and the noise figure of the HTS front-end subsystem measured at 70 K (b).

10.5 Superconducting meteorological radar

10.5.1 Basic principle and configuration of wind profiler

A wind profiler is a type of meteorological radar that uses radar to measure vertical profiles of the wind, i.e., detecting the wind speed and direction at various elevations above the ground. The data synthesized from wind direction and speed is very useful in meteorological forecasting and air quality monitoring for flight planning. Pulse-Doppler radar is often used in wind profilers. In a typical profiler, the radar can sample along each of five (or at least three) beams: one is aimed vertically to measure vertical velocity, and four (or two) are tilted off-vertical and oriented orthogonal to one another to measure the horizontal components of the air's motion. The radar transmits an electromagnetic pulse along each of the antenna's pointing directions. The length of the pulse emitted by the antenna determines the volume of air illuminated by the radar beam. Small amounts of the transmitted energy are scattered back and received by the radar. Delays of fixed intervals are built into the data processing system so that the radar receives scattered energy from discrete altitudes, referred to as range gates. The Doppler frequency shift of the backscattered energy is determined and then used to calculate the velocity of the air towards or away from the radar along each beam as a function of altitude. The source of the backscattered energy is small-scale turbulent fluctuations that induce irregularities in the radio refractive index of the atmosphere. The circuit diagram of a typical wind profiler is shown in Fig 10.19. The 'transmitting system' transmits a pulse signal through the antenna, and the echoes come back to the 'downconverter' through the LNA. The 'radar receiving system' analyses the signal and produces wind profiles of the sky above the radar site.

The wind profiler measures the wind of the sky above the radar site in three directions (i.e., the roof direction, east/west direction and south/north direction), and produces corresponding wind charts. The collected wind chart data are then averaged

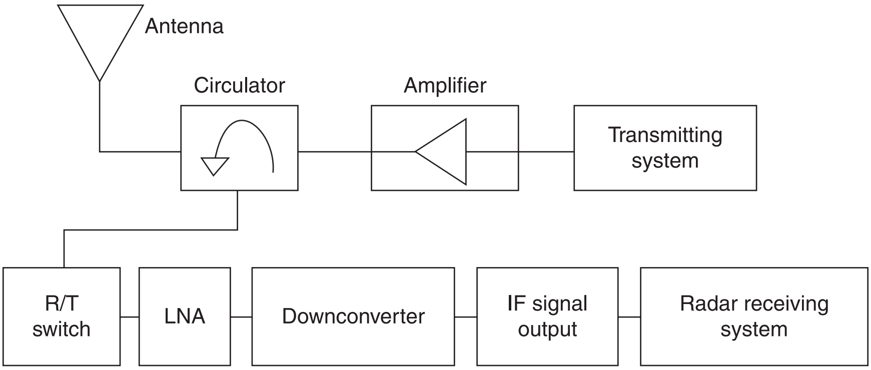

10.19 Circuit diagram of a typical wind profiler. IF, intermediate frequency.

and analyzed at 6 minute intervals so as to produce wind profiles. Typical wind profiles are shown in Plate IV in colour section between pages 244 and 245. In the profile, the horizontal axis denotes the time (from 5:42 am to 8:00 am with intervals of every 6 minutes); the vertical axis denotes the height of the sky. The arrow-like symbols denote the direction and velocity of the wind at the corresponding height and in the corresponding time interval. The arrowhead denotes the wind direction (according to the provision: up-north, down-south, left-west, right-east), and the number of the arrow feather denotes the wind velocity (please refer to the legend).

The frequencies assigned to the wind profiler are in UHF and L band, which are very crowded and noisy with radio, TV, and mobile communication signals and therefore the radar is often paralyzed by the interference. This did indeed happen, especially in or near the cities. For example, the wind profiles presented in colour Plate IV are actually real observation data recorded by a weather station in a suburb of Beijing. It is interesting to point out that the detecting range (or the height above the radar) gradually got shorter (from 3000 m down to 1700 m or so) after 6:30 am in the morning as people were getting up and more and more mobile phones were switched on, indicating that the sensitivity of the radar was affected by increasing interference (colour Plate IV (a)). Eight months later, rapid growth in the number of mobile phones in Beijing caused the electromagnetic environment to become much worse. This radar was blocked by the massive interference noise and totally lost the ability to collect any reliable data, as shown in colour Plate IV (b).

10.5.2 Laboratory tests of superconducting meteorological radar

To solve the problem outlined above, it is necessary to employ pre-selective filters. Unfortunately, due to the extremely narrow bandwidth (≤ 0.5 %), no conventional device is available. The HTS filter can be designed to have a very narrow band and very high rejection with very small loss, so it is expected that it can help to improve the anti-interference ability of the wind profiler, without even a tiny reduction of its sensitivity. In fact, because the LNA also works at a very low temperature in the HTS subsystem, the sensitivity of the whole system will actually increase. To prove this, two stages of experiments have been conducted and the performance of the conventional wind profiler was compared with the so-called HTS wind profiler, i.e., the corresponding part (the front-end, i.e., the LNA) of a conventional radar was substituted by the HTS subsystem. The first stage experiments are sensitivity comparison tests and anti-interference ability comparison tests, conducted by measuring the sensitivity and the anti-interference ability of the filters with quantitative instruments, such as a signal generator and frequency spectrometer, etc. The second stage experiments are the field trail of a superconducting meteorological radar with the conventional counterpart, which will be introduced in the next section.

Sensitivity comparison experiments

The circuit diagram for the experiment is shown in Fig. 10.20. In this experiment, an IFR2023B signal generator was used as a signal source, whose output frequency was set to the wind profiler operating frequency. The signal is emitted from a small antenna and received by the antenna of the radar system. The received signal reaches the radar receiver front-end (in Fig. 10.20 between B and C) via the R/T switch, then passes the down-converter and finally is converted as the intermediate frequency (IF) signal. The IF signal is then sent to a frequency spectrometer (HP E44118) and finally measured. The wind profiler's sensitivity is defined as the signal source output power (in dBm) when the measured signal-to-noise ratio of the intermediate frequency signal is equal to 1.

During the experiment, the sensitivity of the conventional system was measured first. Then the conventional front-end (i.e., the LNA, in Fig. 10.20 between B and C) of the wind profiler was replaced by the HTS subsystem (in Fig. 10.20 between B′ and C′). Here an 'HTS Filter + LNA' configuration was used instead of a 'LNA + HTS Filter' configuration in order to avoid saturation of the LNA. Due to the very small insertion loss of the HTS filter, this configuration should not have any noticeable effect on the dynamic range of the LNA. The measured data show that the sensitivity of the profiler employing HTS subsystem is –43.6 dBm, the sensitivity of the system employing the conventional front-end is –39.9 dBm. Thus, we find that the sensitivity of the HTS subsystem is 3.7 dB higher than that of the conventional subsystem.

Anti-interference ability comparison experiments

The circuit diagram for the experiment is similar to that shown in Fig. 10.20. The difference is that in this experiment the signal source was linked to point A, bypassing the receiving antenna and introducing an interference signal with a frequency of 1323 MHz. Similarly to the sensitivity comparison experiment, the IF signal is monitored by a spectrum analyser while the interference signal is gradually

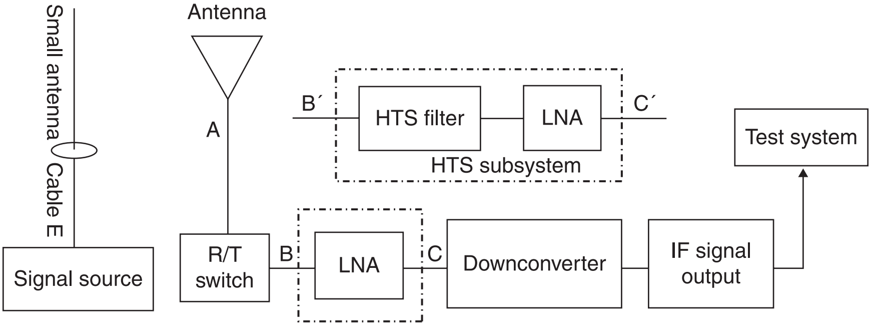

10.20 The circuit diagram for the sensitivity comparison experiment.

increased. Anti-interference ability is defined as the power of the interference signal (in dBm) when the IF output is about to increase. The measured data show that for the conventional subsystem, an interference signal as low as –92.4 dBm has an influence on the wind profiler, whereas for the HTS subsystem, the corresponding value is –44 dBm. It can thus be concluded that the anti-interference ability of the HTS subsystem is 48.4 dB higher than that of the conventional subsystem.

10.5.3 Field trail of superconducting meteorological radar

As previously mentioned, the wind profiler measures the wind in the air above the radar site in three directions and produces the wind charts correspondingly. A typical wind chart of the east/west direction is presented in Fig. 10.21, where the horizontal axis is the wind velocity (m/s, corresponding to the frequency shift due

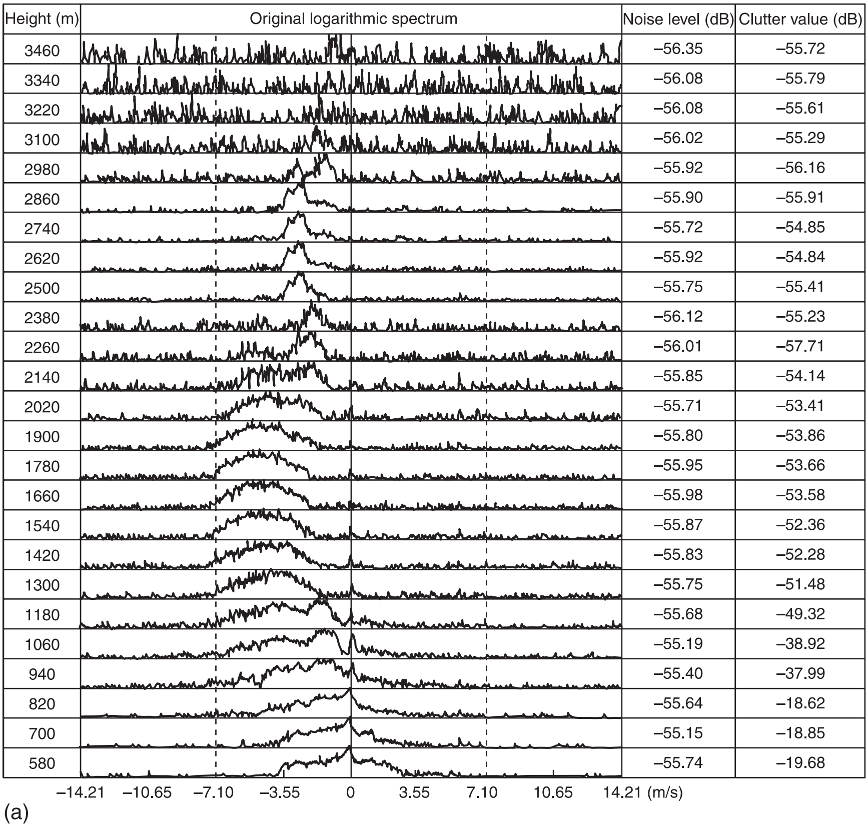

Height (m)	Noise level (dB)	Clutter value (dB)
3460	–56.35	–55.72
3340	–56.08	–55.79
3220	–56.08	–55.61
3100	–56.02	–55.29
2980	–55.92	–56.16
2860	–55.90	–55.91
2740	–55.72	–54.85
2620	–55.92	–54.84
2500	–55.75	–55.41
2380	–56.12	–55.23
2260	–56.01	–57.71
2140	–55.85	–54.14
2020	–55.71	–53.41
1900	–55.80	–53.86
1780	–55.95	–53.66
1660	–55.98	–53.58
1540	–55.87	–52.36
1420	–55.83	–52.28
1300	–55.75	–51.48
1180	–55.68	–49.32
1060	–55.19	–38.92
940	–55.40	–37.99
820	–55.64	–18.62
700	–55.15	–18.85
580	–55.74	–19.68

10.21 Wind charts produced by (a) using the conventional wind profiler without interference, (b) using the conventional wind profiler with interference (1322.5 MHz, –4.5 dBm), (c) using the HTS wind profiler with interference (1322.5 MHz, +10 dBm).

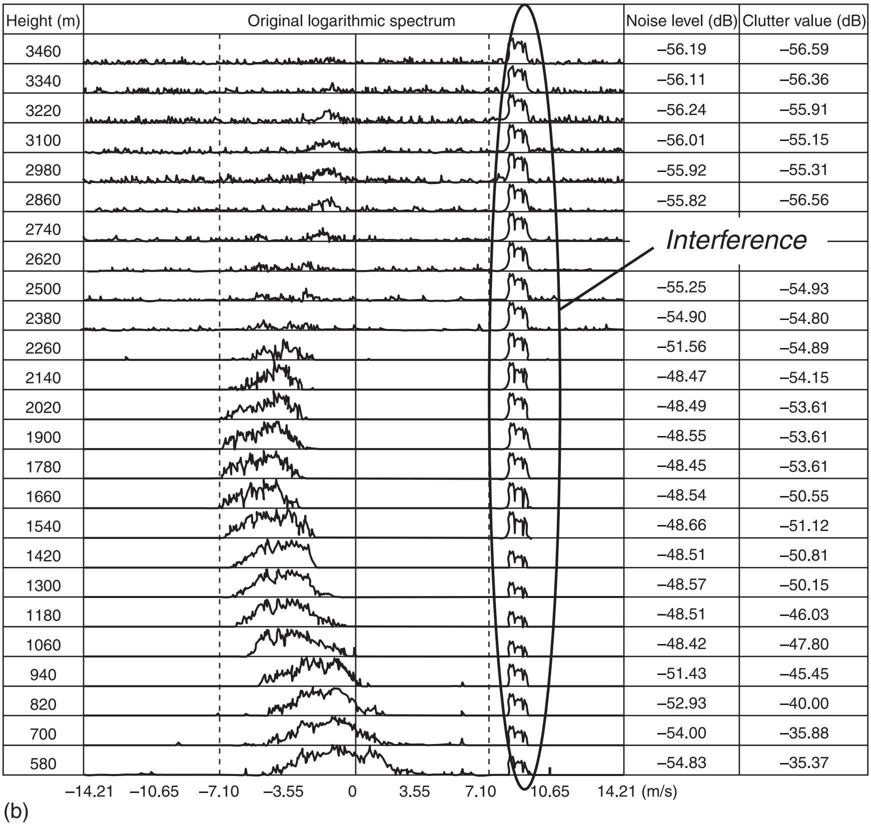

10.21 Continued.

to the Doppler effect) and the vertical axis is the height of the sky above the radar site (from 580 m to 3460 m with intervals of every 120 m) corresponding to the time at which each different echo was received. The negative values of wind velocity indicate a change in wind direction. Each curve in Fig 10.21 represents the spectrum of the corresponding echo. The radar system measures the wind charts of the sky above every 40 seconds. The collected wind chart data are then averaged and analyzed at every 6 minutes, so as to produce the wind profiles.

The procedure of the second stage experiments (field trail) is as follows: firstly, the wind charts and the wind profiles were measured using the conventional wind profiler, without any interference signal. Then an interference signal with a frequency of 1322.5 MHz and power of –4.5 dBm was applied and a new set of wind charts and wind profiles were obtained. Finally, the wind charts and wind profiles were measured using the HTS wind profiler (the LNA at the front end of the conventional wind profiler being replaced by the HTS subsystem) with the same frequency but much stronger (+10 dBm) interference signal.

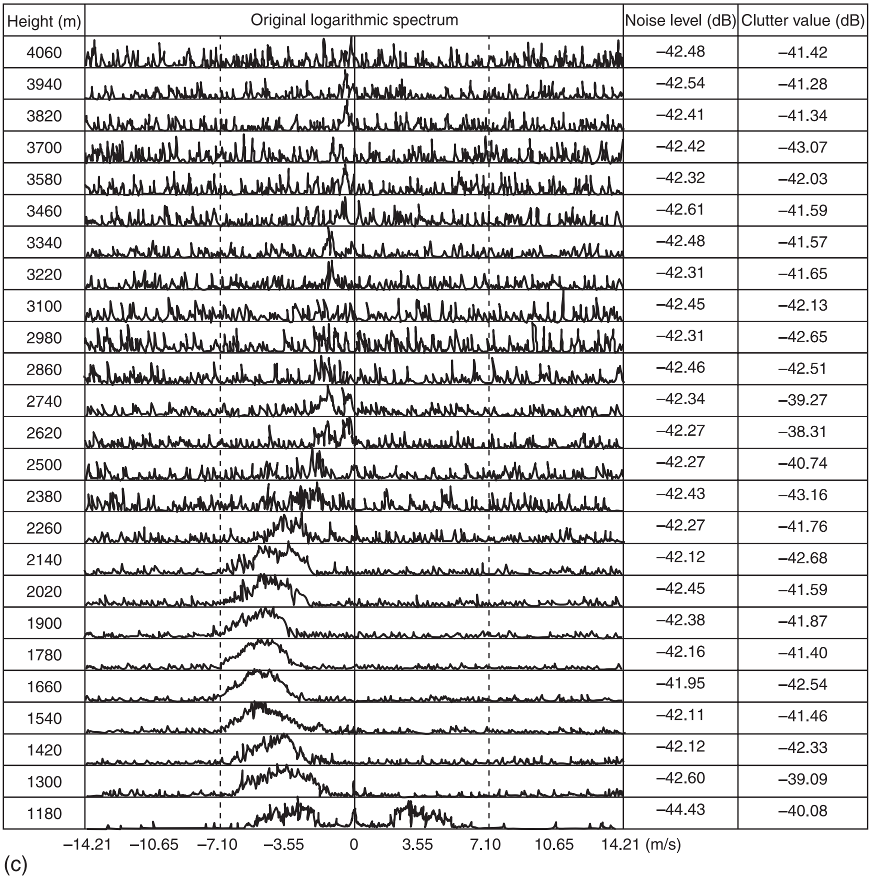

10.21 Continued.

It can be seen that a series of interference peaks appeared in the wind chart measured using the conventional wind profiler while the interference signal was introduced (Fig. 10.21 (b)). However, the wind charts produced by the HTS wind profiler show no signs of being influence by the interference at all (Fig. 10.21 (c)), even when a much stronger (up to +10 dBm) interference signal was applied. Moreover, the HTS subsystem was able to detect wind up to a maximum height of 4000 (Fig. 10.21 (c)), in contrast with more conventional systems, which reach just 3400 metres (Fig. 10.21 (a) and (b)). This is consistent with the impression that the sensitivity of the HTS radar system is higher than that of the conventional system.

Figure 10.22 shows wind profiles produced from the wind charts, measured in the same day by the conventional wind profiler and the HTS wind profiler, respectively. It can be clearly seen that the conventional wind profiler cannot

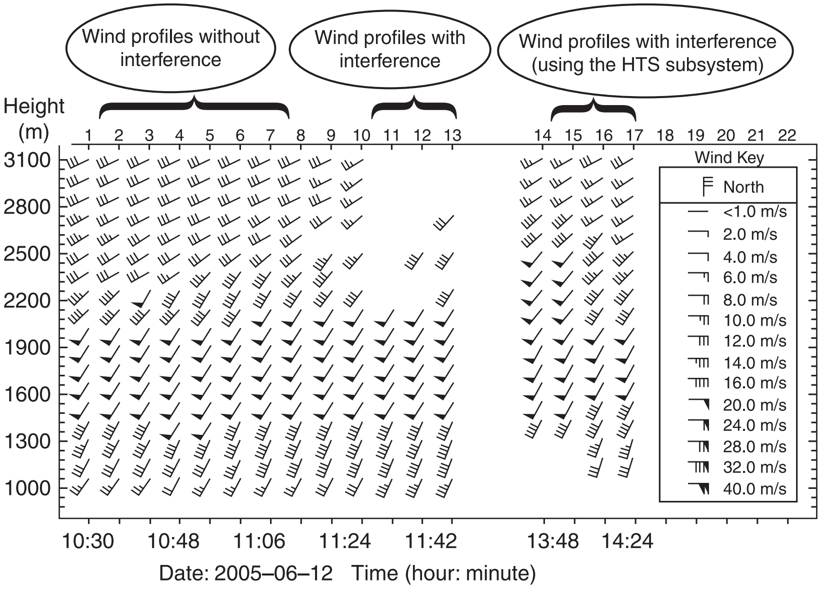

10.22 Wind profiles obtained under three different conditions by the conventional wind profiler and the HTS wind profiler, respectively

attain wind profiles above 2000 m due to the influence of the interference signal, which reproduced the phenomena observed in Fig 10.22. On the contrary, the HTS wind profiler functioned well, even with a much serious interference signal.

10.6 Summary

The study of superconductivity at microwave frequency is important, not only because of the information it provides about the fundamental nature of superconductors, but also because of the potential applications of superconductors in microwave devices.

Nowadays, the rapid developments of wireless communications, TV and radio programmes, as well as different types of radars (aviation control, weather forecast, etc.), have made the already very crowded frequency spectrum even more severe. Advanced microwave devices with excellent performances (such as better sensitivity, stronger anti-interference ability, etc.), are required to fulfil the progressive demands of everyday life and to cope with the atrocious electromagnetic environment. Due to their unique microwave properties, superconducting devices have been applied in many areas. Of these passive microwave devices, the HTS filter is the most popular and successfully used.

Based on the very small microwave surface resistance of HTS films, filters can be constructed with a negligible insertion loss, a very large out-of-band rejection, an extremely steep skirt slope, as well as a very narrow bandwidth – properties which are unachievable with conventional technology. In recent years, HTS filters and HTS receiver front-end subsystems have played important roles in mobile and satellite communications, data distribution systems between different places on earth and/or on space, the detection of extremely weak microwave signals (e.g., from deep space) and various radar systems. As an example, the demonstration HTS meteorological radar revealed its superiority in sensitivity (3.7 dB) and anti-interference ability (48.4 dB) over its conventional counterparts. Field tests of this HTS radar in weather forecasting clearly showed that whereas the conventional radar failed to detect the velocity and direction of wind above 2000 metres in the sky due to interference, the HTS radar could produce perfect and accurate wind charts and profiles.

It was generally recognized that as an emerging novel technology, HTS filters are very close to maturity in terms of application. The factor that is blocking their comprehensive application, however, is mainly the cryogenic coolers, which provide the necessary working temperature of below approximately 80 K for the devices. Enormous efforts have been made and remarkable progress has been achieved so far in providing the advanced miniature Sterling coolers and pulse-tube coolers, which made the above mentioned HTS device applications possible. Nevertheless, there are still considerable gaps in the price (the most important factor for commercial use) as well as the life-time and the volume or weight (more accurately, the ratio between volume/weight and cooling power) of these coolers for potential extensive applications. It can be predicted that, along with the development of HTS microwave technology, especially with the breakthrough in bottleneck technology (i.e. miniature cryogenic coolers), considerable far-ranging applications of HTS microwave devices will inevitably be realized in the near future.

10.7 References

Amari S (2000), 'Synthesis of cross-coupled resonator filters using an analytical gradient-based optimization technique', *IEEE Trans. Microwave Theory and Techniques*, **48**, 1559–1564.

Atia A E and Williams A E (1972), 'Narrow-bandpass waveguide filters', *IEEE Trans. Microwave Theory and Techniques*, **20**, 258–264.

Atia A E, Williams A E and Newcomb R W (1974), 'Narrow-band multiple-coupled cavity synthesis', *IEEE Trans. Microwave Theory and Techniques*, **21**, 649–656.

Atia A W, Zaki K A and Atia A E (1998), 'Synthesis of general topology multiple coupled resonator filters by optimization', *IEEE MTT-S Digest*, **2**, 821–824.

Cameron R J (1999), 'General coupling matrix synthesis methods for Chebyshev filtering functions', *IEEE Trans. Microwave Theory and Techniques*, **47**, 433–442.

Cameron R J and Rhodes J D (1981), 'Asymmetric realizations for dual-mode bandpass filters', *IEEE Trans. Microwave Theory and Techniques*, **29**, 51–59.

Chambers D S G and Rhodes J D (1983), 'A low-pass prototype network allowing the placing of integrated poles at real frequencies', *IEEE Trans. Microwave Theory and Techniques*, **33**, 40–45.

Gorter C J and Casimir H B (1934), 'On superconductivity I', *Physica*, **1**, 306.

Hein M (1999), *High Temperature Superconductor Thin Films at Microwave Frequencies*, Berlin, Springer.

Hong J S and Lancaster M J (2001), *Microstrip filters for RF/Microwave Applications*, New York, John Wiley & Sons.

Hong J S, Lancaster M J, Jedamzik D and Greed R B (1999), 'On the development of superconducting microstrip filters for mobile communications applications', *IEEE Trans. Microwave Theory and Techniques*, **47**, 1656–1663.

Kharel A P, Soon K H, Powell J R, Porch A, Lancaster M L *et al.*, (1999), 'Non-linear microwave surface impedance of epitaxial HTS thin films in low DC magnetic fields', *IEEE Trans. Appl. Supercond.*, **9**, 2121.

Lancaster M J (1997), *Passive Microwave Devices Applications of High Temperature Superconductors*, Cambridge, Cambridge University Press.

Levy R (1995), 'Direct synthesis of cascaded quadruplet (CQ) filters', *IEEE Trans. Microwave Theory and Techniques*, **43**, 2940–2945.

Li H, He Y, Li C, Hong J, Lancaster M J *et al.* (2002), 'A demonstration of HTS base station sub-system for mobile communications', *Supercond. Sci. Technol.*, **15**, 276–279.

Li Y, Lancaster M J, Huang F and Roddis, N (2003), 'Superconducting microstrip wide band filter for radio astronomy', *Microwave Symposium Pigert, 2003 IEEE MTT-S International*, 551–554.

Lyons W G, Arsenault D A, Anderson A C *et al.* (1996), 'High temperature superconductive wideband compressive receivers', *IEEE Trans. Microwave Theory and Techniques*, **44**, 1258–1278.

Macchiarella G (2002), 'Accurate synthesis of inline prototype filters using cascaded triplet and quadruplet sections', *IEEE Trans. Microwave Theory and Techniques*, **50**, 1779–1783.

Nguyen P P, Oates D E, Dresselhaus G, Dresselhaus M S and Anderson A C (1995), 'Microwave hysteretic losses in $YBa_2Cu_3O_{7-x}$ and NbN thin films', *Phys. Rev. B*, **51**, 6686–6695.

Romanofsky R R, Warner J D, Alterovitz S A *et al*. (2000), 'A cryogenic K-band ground terminal for NASA's direct-data-distribution space experiment', *IEEE Trans. Microwave Theory and Techniques*, **48**, 1216–1220.

STI Inc. (1996), 'A receiver front end for wireless base stations', *Microwave Journal,* **1966**, 116.

Velichko A V, Lancaster M J and Porch A (2005), 'Nonlinear microwave properties of high Tc thin films', *Supercond. Sci. Technol.*, **18,** R24–R49.

Wallage S, Tauritz J L, and Tan G H *et al* (1997, 'High-T_c superconducting CPW band stop filters for radio astronomy front end', *IEEE Trans. on Applied Superconductivity* **7**, 3489–3491.

Yoshitake T and Tahara S (1995), 'Intermodulation distortion measurements of a microstrip band-pass filter made from double-sided $YBa_2Cu_3O_{7-x}$ films', *Appl. Phys. Lett.,* **67,** 3963.

Zhang Q, Li C G, He Y S *et al*. (2007), 'A HTS bandpass filter for a meteorological radar system and its field tests', *IEEE Trans. on Applied Superconductivity,* **17**, 922–925.

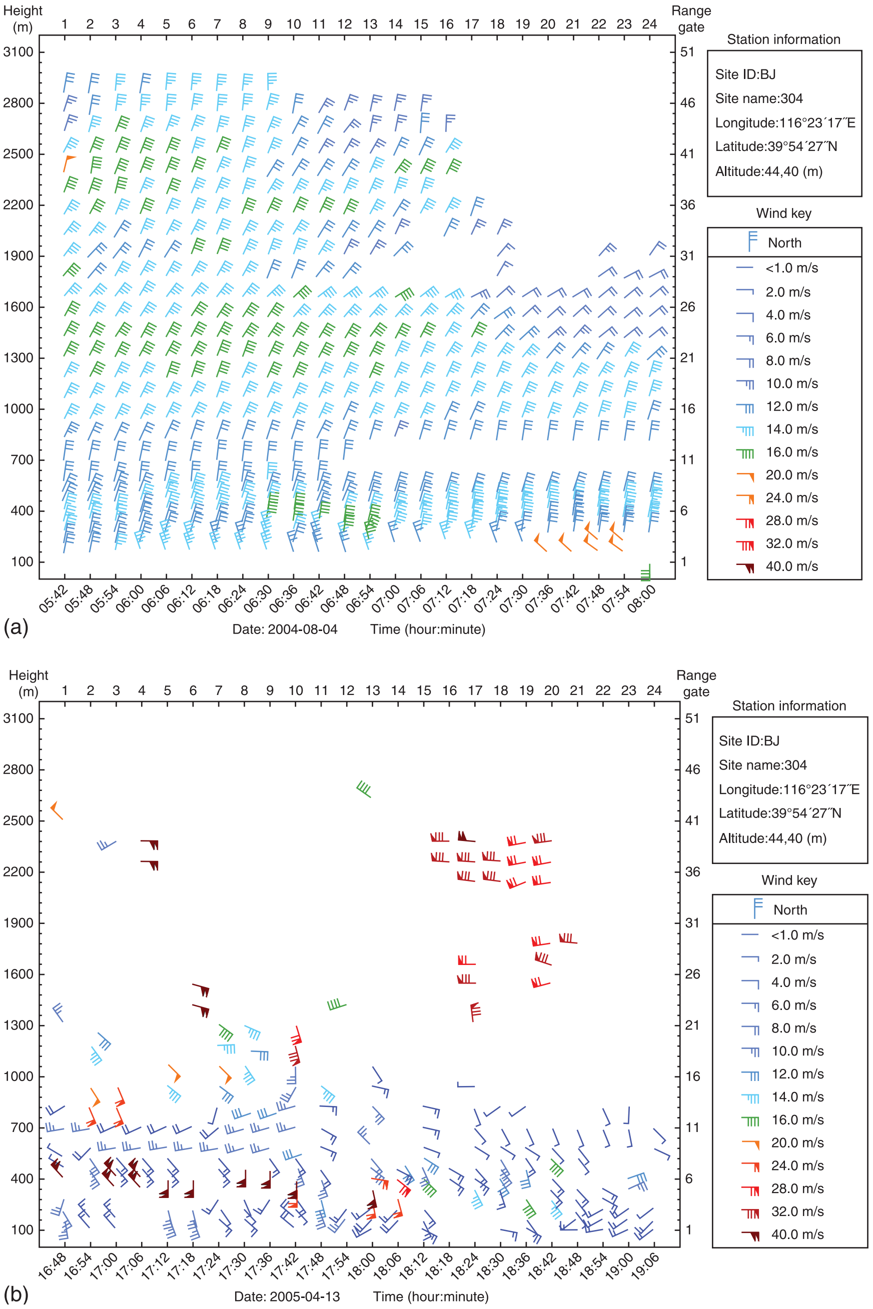

Plate IV Wind profiles produced by a wind profiler of a weather station in a suburb of Beijing. Data in (a) were collected in the morning of 4 August 2004 from 5:42 to 8:00 am at intervals of 6 minutes; data in (b) were collected in the afternoon of 13 April 2005 – no reliable data can be seen, demonstrating clearly that this radar was paralysed by interference.

Index

ablation, 14
adatom average migration, 24
adsorption rate, 24
angle-resolved photoemission spectroscopy, 260–1
anisotropy, 4, 5
antennas, 402–403
anti-interference ability, 418
APW calculation, 258, 259
arc discharge, 17–18
artificial barriers junctions, 327, 329–31, 341–48
  different SNS step-edge junctions, 330
  physics, 341–44
    ramp-edge junction, 343
  planar types, 329
  preparation and performance, 344–6
    ion beam modified microbridges IV-characteristics, 346
    TEM pictures, 345
  ramp-type junction, 331
  selected applications, 346–8
    SFG sampler system using interface-engineered ramp-edge junctions, 347
Aslamov-Larkin contribution, 59
Aslamov-Larkin fluctuations, 59
atomic layer by layer deposition-MBE, 176

band model, 258–60, 265–6
barium strontium copper calcium oxide, 174
  crystallographic structure, 175
BCS theory, 129
Bi2212
  optical conductivity, 110
  optical scattering rate, 123
  reflectivity spectra, 109
  restricted spectral weight, 131
  scattering rate for underdoped state, 122
bicrystal junctions, 339
bicrystal technique, 372, 382
biepitaxial junction, 326
biepitaxial technique, 375, 382
$Bi_2Sr_2Ca_{a-1}Cu_nO_{2n+4}$ *see* barium strontium copper calcium oxide
Bloch-Boltzmann theory, 80
Bloch theory, 38
Boltzmann equation, 56
bonding energy, 303
bosonic function, 132, 134
bosonic mode, 132–5
Bragg's law, 164
BSSCO *see* barium strontium copper
calcium oxide
BSSCO high superconducting films, 174–200
  deposition techniques, 176–9
    molecular beam epitaxy, 176–7
    pulsed laser deposition, 177
    sputtering technique, 177–9
    two chemical techniques, 179
  growth thickness, 174–82
    characterisation techniques, 180–1
    nature of the substrates, 179–80
    in situ grown thin films, 181–2
    2201 thin film deposited on SrTiO3, 181
  mixed state transport properties and anisotropy, 186–200
    angular and temperature scaling laws, 187–9
    anisotropy of the critical currents, 189–91
    critical current density field dependence, 191
    directional pinning effect, 192
    experimental phase diagram and characteristic temperatures, 197
    La-2201 superconducting-insulating transition, 198
    mixed state magnetoresistance angular variation, 188
    probing anisostropy by columnar pinning centres, 191–2
    resistive transition, 186–7
    temperature dependence of 2212 thin film resistivity, 196
  normal state properties, 192–9
    Hall effect temperature dependence, 199

    - modifying doping level, 192–4
    - resistivity vs doping and phase diagram, 194–9
    - underdoped semiconducting 2212 thin film, 193
  - physical properties of thin films and multilayers, 182–99
    - anisotropy and critical temperature, 183–6
    - 2212 film angular dependence, 190
    - 2212 film magnetic state, 184
    - normalised resistive transition, 185
    - 2212 thin films order parameter symmetry, 183
- buffer layers, 8
- bulk single crystal, 226–7
- Butterworth filters, 404

- canonical fold form, 407
- carrier concentration, 87–8
- cathodic sputtering technique, 177–9
- CeCO$_2$, 8, 10
- Chebyshev filter, 404, 405
- chemical solution deposition, 22–3, 32
  - schematic sketch, 23
- chemical vapour deposition, 20–2
- clyclotron frequency, 55
- coated conductors, 10, 151
- coincidence of reciprocal lattice points, 303, 304
- computer simulations, 355
- conductivity formula, 120
- conventional band theory, 105
- Coopers pairs, 394
- coplanar line, 397–5, 398, 399
- coplanar waveguide resonators, 402
- copper, 220
- corner junctions, 357
- Coulomb energy, 254
- Coulomb repulsion, 258
- CPR *see* current-phase relation
- CPW resonators *see* coplanar waveguide resonators
- crack formation, 30
- critical fields, 251–2
- critical thickness, 30
- CRLPs *see* coincidence of reciprocal lattice points
- crucibles, 280, 282–3
  - comparison, 282
- CSD *see* chemical solution deposition
- cuprate spin ladders, 46–9
  - two-leg ladder cuprate, 46
  - two-leg ladder ground state schematic representation, 48
- cuprate thin films *see* high-T$_c$ cuprate thin films
- current-phase relation, 373

- dark discharge, 17
- DARPES *see* Direct Angle Resolved Spectroscopy Systems
- dc superconductive quantum interference devices, 370–84
  - current biased dynamics in unconventional current phase relation, 376–8
    - calculated SQUID potential, 379
    - voltage vs magnetic flux, 380
  - grain boundary Josephson junctions, 372–4
    - bicrystal grain boundary junctions, 372–2
    - bicrystal substrate sketch, 372
    - biepitaxial grain boundary junctions, 375–4
    - biepitaxial grain boundary sketch, 376
    - 45o grain boundary representation, 374
    - step-edge grain-boundary junctions, 374–3
  - order parameter d-wave symmetry and design implications, 371
  - parameters, 383
  - quantum circuit applications, 383–4
    - asymmetric dc-SQUID potential shape evolution, 386
    - silent qubit sketch, 385
  - schematic, 377
  - second harmonic component in current phase relation, 380–81
    - critical currents, 381
    - critical current vs magnetic field graph, 383
    - measurements on YBCO grain boundary Josephson junctions, 382–3
- Debye temperature, 38, 40
- decomposition, 263
- defects, 27–30
- density of states, 59
- 2D Heisenberg model, 52, 53
- Direct Angle Resolved Spectroscopy Systems, 181
- direct couplings, 407
- dislocation lines, 28
- doped Mott insulator, 230
- DOS *see* density of states
- double-sided fabrication method, 349–50
- Drude metal, 117
- Drude model, 38, 58, 109–10, 121
  - *see also* extended Drude model
- d-wave superconductors, 247, 254

- e-beam lithography, 375
- EIES *see* electron impact emission spectroscopy
- electrical conductivity, 58
- electron-doped T$_c$ cuprates, 208–66
  - electronic phase diagram, 229–36
    - early results, 229–30
    - Nd$_2$CuO$_4$ films superconductivity, 233
    - Nd$_{2-x}$Ce$_x$CuO$_4$ films T$_c$-*versus-x*, 236
    - O$_{ap}$ impurities complete removal, 230–2
    - Pr$_2$CuO$_4$ films T$_c$ and ρ(300 K) *versus* c_0, 235
    - residual resistivity and T$_c$ reduction, 231
    - superconducting vs nonsuperconducting Sm$_2$CuO$_4$ films, 234
    - superconductivity in T′ parent compounds, 232–6

    - T_c-vs-x for MBE-grown T′-$RE_{2-x}CexCuO_4$ films, 232
    - T′-$Pr_{2-x}Ce_xCuO_4$ Ce doping dependence, 231
    - undoped T′-RE_2CuO4 and electron-doped T′-$RE_{1.85}Ce_{0.15}CuO_4$, 233
  - electronic structure, 265–6
    - band model, 265–6
    - ionic model, 265
    - spectroscopy, 266
  - electronic structure and spectroscopy, 254–63
    - angle-resolved photoemission spectroscopy, 260–1
    - band model, 258–60
    - charge transfer energy, 257
    - Cu_3dx_{2-y2}, O_2p_x and O_2p_y hybridisation, 259
    - energy diagrams based on the ionic model and band model, 257
    - energy level in oxides, 258
    - impurity effect, 255
    - ionic model, 254–7
    - $Nd_{2-x}Ce_xCuO_4$ optical conductivity, 262
    - optics, 261–3
    - T′-Nd_2CuO_4 energy bands, 259
  - low-temperature resistivity under magnetic fields
    - $Nd_{1.815}Ce_{0.185}CuO_4$, 242
    - nonsuperconducting $Pr_{1.902}Ce_{0.098}CuO_4$ and superconducting $Nd_{1.869}Ce_{0.131}CuO_4$, 241
  - materials science, 263–4
    - decomposition, 263
    - lattice parameters, 263
    - oxygen nonstoichiometry, 264
    - structure, 263
    - tolerance factor, 263
    - T′ phase stability, 263
  - NiO, CuO, and Cu_2O crystal structures, 210
  - normal state properties, 237–44
    - Hall coefficient and seebeck coefficient, 242–4
    - hole-doped T-$La_{2-x}Sr_xCuO_4$ and electron-doped T′-$Nd_{2-x}Ce_xCuO_4$, 238
    - magnetism, 237–9
    - $Pr_{2-x}Ce_xCuO_4$ ρ-T curves, 240
    - resistivity, 239–42
    - $RE_{2-x}Ce_xCuO_4$ films ρ-T curves, 240
    - R_H doping dependence, 243
    - R_H reduction dependence, 244
  - physical science, 264–5
    - electron phase diagram, 264
    - impurity effect, 265
    - magnetism, 264
    - pairing symmetry, 265
    - transport, 264–5
  - sample preparation, 226–9
    - bulk single crystal vs epitaxial thin films, 226–7
    - decomposition lines RE dependence, 223
    - metal organic decomposition, 229
    - molecular beam epitaxy system, 228
    - T′ cuprates MBE growth, 227–8
    - T′ cuprates metal organic decomposition growth, 228–9
  - solid-state chemistry, 220–6
    - decomposition lines for cuprates, 221
    - decomposition reaction thermodynamic data, 222
    - oxygen nonstoichiometry, 224–6
    - phase stability, 220–4
    - T′-$Nd_2CuO_{4-\delta}$ phase diagram, 225
  - structure, 211–20
    - bond length thermal expansion, 214–15
    - Ce doping dependence, 219
    - CuO_2 and RE_2O_2 layers, 214
    - lattice parameters, 216–20
    - lattice parameters RE dependence, 217
    - rare-earth copper oxides, 211
    - RE_2CuO_4, 211–12
    - room-temperature ionic radius, 213
    - solubility limit, 220
    - structural parameters and interstitial oxygen, 215–16
    - structural parameters and occupancy, 216
    - superconducting transition temperatures, 212
    - tolerance factor, 212–14
    - T′-RE_2CuO_4 lattice parameters, 218
  - superconducting properties, 244–54
    - critical fields, 251–2
    - Eliashberg function, 246
    - impurity effect, 252–4
    - Josephson junctions and SQUID, 250
    - magnetic penetration depth, 247–9
    - magnetic penetration depth temperature dependence, 248
    - $Nd_{1.85}Ce_{0.15}CuO_4$ point-contact spectrum, 245
    - phase-sensitive experiments, 250–1
    - superconducting parameters, 253
    - T′-$RE_{2-x}Ce_xCuO_4$ magnetic penetration depth experiments, 249
    - tunnelling, 244–7
    - tunnelling spectrum, 246
    - zigzag junction, 252
- electronic phase diagram, 229–36
- electronic structure spectroscopy, 266
- electron impact emission spectroscopy, 227
- electron lithography, 329
- electron phase diagram, 264
- Eliashberg function, 133, 245
- energy level quantisation, 384
- epitaxial thin films, 226–7
- epitaxy, 275
- evaporation, 32
- excessive reduction, 235
- excitonic effect, 255
- extended Drude model, 111–13

- Faraday’s law of induction, 81
- far-infrared optical conductivity, 137
- FEBI *see* focussed e-beam irradiation
- Ferell-Glover-Tinkham sum rule, 115
- Fermi acts, 195
- Fermi level, 258
- Fermi liquid, 41, 113
- Fermish liquid response, 106
- Fermi velocity, 120
- FGT sum rule, 130
- film crystallisation temperature, 158
- film growth, 11
- film homogeneity, 158–61
- filters, 402–403, 404
  - *see also* specific filters
- flip-chip technique, 350
- focussed e-beam irradiation, 331
- Fraunhofer pattern, 318
- full-wave electromagnetic simulation software, 408
- full width at half maximum, 162

- gallate substrate, 280–3
- Gaussion filter, 404
- Ginzburg-Landau depairing mechanism, 394
- Ginzburg-Landau free energy, 57
- Ginzburg-Landau model, 56
- glow discharge, 17
- grain boundary Josephson junctions, 372–6
- grain boundary junctions, 325–7, 328, 333–41
  - bicrystal junctions types, 326
  - biepitaxial junction types, 328
  - critical Josephson current density on grain boundary angle, 327
  - physics, 333–8, 339
    - 90o grain-boundaries types, 336
    - YBaCuO bicrystal grain boundary, 339
  - preparation and performance, 338–9
  - selected applications, 339–41, 342
    - microwave scanning microscopy set-up and Josephson cantilever layout, 342
    - shunted series arrays IV-characteristics, 341
  - step-edge junction with two grain boundaries induced in the HTS film, 328
  - YBaCuO step-edge junction
    - SEM image on MgO substrate, 338
    - TEM image on LaAlO3 substrate, 337

- Hall angle, 89
  - scaling, 94–5
- Hall coefficient, 80, 242–4
  - field induced sign reversal, 82–4
  - room temperature, 84–5
  - scaling, 92–5
  - scaling at 50 T, 94
  - temperature dependence, 85–6
- Hall conductivity, 89–92
  - linear dependence in the log-log plot, 93
  - temperature as function of doping, 92
  - T-3 scaling, 91–2
  - vs temperature, 91
- Hall constant, 80
- Hall effect, 79–96
  - *see also* Hall coefficient
  - carrier concentration, 87–8
    - hole concentration at 50 T, 87
    - hole concentration dependence, 88
  - electric field induced by motion of a vortex, 82
  - Hall angle, 89
    - cot(θ_H) vs T, 90
    - scaling of cotangent cot(θ_H) (B = 50 T), 95
  - Hall coefficient
    - field induced sign reversal, 82–4
    - Hall voltage sign reversal, 83
    - room temperature, 84–5
    - scaling, 92–5, 93–4
    - temperature dependence, 85–6
    - 50 T Hall coefficient data, 86
    - 10 T logarithmic at 300 K, 85
  - Hall conductivity, 89–92
    - low temperature behaviour, 92
    - T-3 scaling, 91–2
  - Hall mobility, 88–9
    - scaling, 92–5
  - scaling, 92–5
    - pseudogap used for scaling, 94–5
  - schematic view, 80
  - temperature dependence at various doping, 199
  - transverse Hall resistivity vs applied magnetic field, 84
- Hall mobility, 88–9
  - 50 T as a function of temperature, 89
- heteroepitaxial growth, 27–30
- heteroepitaxial nucleation, 27
- hetero-seeded growth, 296
- high-resolution transmission electron microscopy, 180
- high-T_c copper oxides, 208
  - crystal structures, 210
- high-T_c cuprates
  - *see also* electron-doped T_c cuprates
  - coordinations of oxygen ions around copper ion, 209
- high-T_c cuprate thin films
  - *see also* $La_{2-x}Sr_xCuO_4$ thin films
  - transport properties, 38–96
    - Hall effect, 79–96
    - magneto-resistivity, 54–79
    - temperature dependence of zero field resistivity, 39–54
- high-T_c Josephson junctions, 317–61
  - artificial barriers junctions, 327, 329–31, 341–48
  - future trends, 359–61
  - grain boundary junctions, 325–7, 333–9
  - hybrid junctions, 333, 335, 357–9

    intrinsic Josephson junctions, 333, 334, 348–57
    Josephson effects, 317–19
        schematic and equivalent circuit, 318
    modelling and junction parameters, 319–23
        current voltage characteristic, 320
        intrinsic Josephson junctions within the unit cell, 322
        magnetic field pattern, 323
    modified microbridges, 331–33
        High-T_c nanobridge, 332
        types, 332
    possibilities and applications, 323–4
    types, 325–33
        bicrystal junctions types, 326
        critical Josephson current density on grain boundary angle, 327
        overview, 325
high-temperature optical microscopy, 298
high-temperature superconductor films
    application areas, 3
    deposition techniques, 10–23
        CVD and MOCVD methods, 20–2
        PVD, (MO)CVD and CSD/MOD deposition technologies, 11
    deposition technologies, growth and properties, 3–32
        improvement of superconducting properties, 4
        materials and requirements, 4–6
        substrate requirements, 6–10
    growth characterisation, 23–31
        adsorption, nucleation and thin film growth, 24
        adsorption potentials, 25
        characteristic film properties, 31
        heteroepitaxial growth, stress, and defects, 27–30
        nucleation and phase formation, 23–7
        YBCO/CeO2 critical thickness, 29
    physical vapour deposition techniques, 12–20
        comparison of the different techniques, 18–20
        energy of particles leaving source, 18
        pulsed laser deposition technique and Laser MB, 14–16
        sputter techniques, 16–18
        thermal co-evaporation and MBE, 12–13
high-temperature superconductors, 276
    electron-doped cuprates, 208–66
        electronic phase diagram, 229–36
        electronic structure, 265–6
        electronic structure and spectroscopy, 254–63
        materials science, 263–4
        normal state properties, 237–44
        physical science, 264–5
        sample preparation, 226–9
        solid-state chemistry, 220–6
        structure, 211–20
        superconducting properties, 244–54
    microwave filters, 390–422
        superconducting filter and receiver front-end subsystem, 403–14
        superconducting meteorological radar, 415–21
        superconducting transmission lines and related passive devices, 396–403
        superconductivity at microwave frequency, 390–96
    optical conductivity, 103–39
        future trends, 135–9
        the normal, 117–26
        optical response, 108–17
        phase diagram of cuprate superconductors, 104–8
        superconducting state, 127–35
Hilbert spectroscopy, 340
Hooke's law, 164
HR-TEM *see* high-resolution transmission electron microscopy
HTOM *see* high-temperature optical microscopy
HTS *see* high-temperature superconductors
HTSC high-T_c superconducting films
    liquid phase epitaxy growth, 275–311
        fundamental study, 277–83
        REBCO films mechanism, 283–310
hybrid junctions, 333, 335, 357–9
    physics, 357–8
        YBCO-Nb Zigzag junction, 358
    preparation and performance, 358–79
    selected applications, 359, 360
        hybrid ramp-edge junction cross-section, 360
    YBCO/Au/Nb hybrid junction, 335

IBS *see* ion beam sputtering
ICP *see* inductively coupled plasma spectroscopy
IMD *see* intermodulation distortion products
impurity effect, 252–4, 265
inductively coupled plasma spectroscopy, 227
in-gap states, 261
in-plane resistivity, 39, 40
    high-T_c cuprates, 40
    $La_{2-x}Sr_xCuO_4$
        scaling, 44
        zero magnetic field, 43
insufficient reduction, 234
interatomic distances, 19
intermodulation distortion products, 396
interstitial oxygen, 215–16
intrinsic Josephson effects, 323
intrinsic Josephson junctions, 333, 334, 348–57
    different types, 333
    physics, 348–9
        typical IV-characteristics, 349
    preparation and performance, 349–50
        thin film intrinsic Josephson junctions, 350
    selected applications, 350–57

    BSCCO intrinsic Josephson junction image, 355
    3-D array of 2500 intrinsic Josephson junction stacks, 352
    Josephson radiation source, 353–4
    terahertz response, 351
    three-terminal devices, 356
inverse Josephson effect, 319
Ioffe-Regel criterion, 39, 41
ion beam etching, 338
ion beam sputtering, 283
ion bombardment *see* sputtering
ionic model, 254–7, 265
ionic radius, 213
iron pnictide superconductors, 136

Josephson cantilever, 340
Josephson current, 317
Josephson effects, 317–19
Josephson equation, 319

kinetic energy, 128–31
Kohler plot, 56
Kohler's rule, 55–6, 74
Kramers-Kronig causality relations, 108

La-Ba-Cu-O, 208
laser molecular beam epitaxy, 14–16, 344
  schematic sketch, 15
laser-pulsed laser deposition, 14, 15
$La_{1.8}Sr_{0.2}CuO_4$, 69
  in-plane resistivity field dependence, 70
$La_{1.9}Sr_{0.1}CuO_4$, 65
  magnetoresistivity data, 67
$La_{1.73}Sr_{0.27}CuO_4$, 72
  in-plane resistivity field dependence, 73
$La_{1.75}Sr_{0.25}CuO_4$, 69, 71, 72
  in-plane resistivity field dependence, 71
  transverse Hall resistivity vs applied magnetic field, 84
$La_{1.95}Sr_{0.05}CuO_4$, 62
  in-plane resistivity field dependence, 63
$La_{1.945}Sr_{0.06}CuO_4$, 65
  in-plane resistivity field dependence, 66
$La_{1.945}Sr_{0.055}CuO_4$, 62
  magnetoresistivity data, 64
$La_{1.955}Sr_{0.045}CuO_4$, 60–2
  in-plane magnetoresistivity data, 61
lateral growth, 277
lattice matching, 303
lattice parameters, 216–20, 263
$La_{2-x}Sr_xCuO_4$ thin films
  dimensionality of electronic transport, 45–54
    charge ordering as a function of doping, 49–51
    ^{63}Cu Knight shift, 54
    cuprate spin ladders, 46–9
    2D magnetic correlation length, 52
    quantum transport model, 51–4
    reverse inter-stripe distance, 50
    $Sr_{2.5}Ca_{11.5}Cu_{24}O_{41}$ temperature dependence of resistivity, 49
  Hall coefficient scaling at 50 T, 94
  hole concentration dependence on
  Sr doping, 88
  magnetoresistivity, 54–79
    different change order states in Cu-O planes, 79
    effective main free path decrease, 55
    Kohlers rule, 55–6
    separating fluctuation and normal state contribution, 60–78
    superconducting fluctuations, 56–60
    temperature dependence of resistivity, 78–9
  separating fluctuation and normal state contribution, 60–78
    fluctuation analysis, 76–8
    generic phase diagram including fluctuation area, 76
    influence of the normal state magnetoresistivity, 72–4
    paraconductivity as function of reduced temperature, 78
    pseudogap and pre-formed pairs, 74–6
    region where superconducting fluctuations is observed, 77
  zero field resistivity temperature dependence, 39–54
    in-plane resistivity behaviour schematic, 40
    in-plane resistivity in zero magnetic field, 43
    ρ-T dependencies identification, 40–3
    scaling of in-plane resistivity, 44
    scaling parameters, 45
    (T,x)-phase diagram, 43
    zero-field resistivity scaling, 44–5
LEED *see* low energy electron diffraction
less compatible substrates, 7
liquid phase epitaxy, 24, 174, 179, 275
  applications, 276–7
  fundamental study on growth, 277–83
    crucible and its chemical stability in the solvent, 280, 282–3
    crucibles characteristics comparison, 282
    Frank-Van der Merwe layer-by-layer growth mode, 278
    Kossel crystal growth mode, 277
    LPE grown islands slope angle, 279
    mode, 277–9
    substrate and its chemical reaction on LPE films, 279–80
    substrates properties and lattice constants, 281
  HTSC high-T_c superconducting films growth, 275–311
  method, 276
  REBCO films, 283–310
    a/c axes pinning structure and growth mechanism, 293–5
    in-plane alignment transformation, 302–10

    thermal stability, 295–302
    transition between a-axis and c-axis growth, 283–93
  vs crystal pulling method, 275–6
  vs VPE technique, 275
LNA *see* low noise amplifier
London penetration depth, 151
Lorentz force, 55, 81
low energy electron diffraction, 18
low noise amplifier, 410, 413
low-T_c superconductors, 322, 384
low-temperature superconductors, 3
LPE *see* liquid phase epitaxy
L-PLD *see* laser-pulsed laser deposition
LTS *see* low-T_c superconductors

macroscopic quantum tunnelling, 340, 384
magnesium diboride, 135
magnetic correlation lengths, 51, 52
magnetic penetration depth, 247–9
  experimental results, 249
  temperature dependence, 248
magnetism, 237–9, 264
magneto-resistivity, 54–79
  experimental results, 60–78
Maki-Thompson contribution, 59, 60
Matthews theory, 28
Maxwell-Boltzmann, 18
MBE *see* molecular beam epitaxy
McCumber parameter, 321
McMillan-Rowell method, 245
mean free path, 20
mesa-type geometry, 349
metal organic chemical vapour deposition, 20–2, 174, 179
metal organic decomposition, 22, 229
  T′ cuprates, 228–9
microstrip, 397, 398, 402
microwave filters
  high-temperature superconductors, 390–422
  superconducting filter and receiver front-end subsystem, 403–11
    design, construction and integration, 410–11
    filtering circuit coupling structure, 406
    frequently used coupling topology, 408
    HTS receiver front-end subsystem, 414
    parasitical couplings affect the narrow band bandpass filter, 409
    10-pole CQ filter coupling technology, 410
    10-pole CQ filter synthesised and stimulated responses, 411
    10-pole filter measured response, 413
    10-pole quasi-elliptic filter layout, 413
    principles and theories on filter design, 403–8
    resonators for superconducting filter design, 408–10
    resonator used in present work, 412
    temperature dependence of LNA noise figure, 414
  superconducting meteorological radar, 415–21
    anti-interference ability comparison experiments, 417–18
    circuit diagram for sensitivity comparison experiment, 417
    field trail, 418–21
    laboratory tests, 416–15
    sensitivity comparison experiments, 417
    wind charts, 418–19, 420
    wind profiler basic principle and configuration, 415–16
    wind profiler circuit diagram, 415
    wind profiles obtained by conventional and HTS wind profiler, 421
  superconducting transmission lines and related passive devices, 396–403
    antennas and filters, 402–403
    microstrip, coplanar line and stripline cross-section geometries, 398
    one dimensional microstrip resonators, 402
    resonate frequency and Q-value temperature dependence, 400
    resonators quality factors vs volume, 401
    superconducting delay line, 398–9
    superconducting resonator, 399–402
    superconducting transmission lines, 396–8
  superconductivity at microwave frequency, 390–96
  superconductors, 390–96
    epitaxial co-evaporated YBCO films on MgO substrates, 395
    epitaxial YBa2Cu3O7 film power dependence, 394
    equivalent circuit depicting complex conductivity, 391
    frequency dependence, 393
    non-linear microwave properties, 392–96
    surface impedance, 390–92
microwave resonator, 399
mixed boundaries, 334
MOCVD *see* metal organic chemical vapour deposition
MOD *see* metal organic decomposition
modified microbridges, 331–33
molecular beam epitaxy, 12–13, 176–7, 344
  schematic, 228
  T′ cuprates, 227–8
Mott-Hubbard insulators, 256
MQT *see* macroscopic quantum tunnelling

NCSL *see* near coincidence site lattice theory
near coincidence site lattice theory, 303–4
nominal lattice mismatch, 27
non-compatible substrates, 7
nucleation, 11, 23–7

off-axis geometry, 154
optical conductivity, 103–39
  future trends, 135–9

- behind the iron curtain, 135–8
  - far-infrared optical conductivity, 137
  - iron pnictide superconductors generic phase diagram, 136
  - magnesium diboride, 135
- normal state, 117–26
  - from a nodal metal to a bad metal to a fermi liquid, 123–4
  - normal state gap in electron-doped materials, 124–6
  - pseudogap in the optical response, 118–23
  - underdoped YBCO in pseudogap regime, 121
  - YBCO superconducting crystals, 119
- optical response of conducting media, 108–17
  - Drude metal, 117
  - Drude model, 109–10
  - the extended Drude model, 111–13
  - Fermi liquid frequency dependent scattering rate, 113
  - $P_4W_{14}O_{50}$ real part of optical conductivity, 114
  - real part and imaginary part, 115
  - restricted spectral weight, 116–17
  - sum rule and gaps in the excitation spectrum, 113–16
  - two component optical conductivity, 110–11
- phase diagram of cuprate superconductors, 104–8
  - electron doped and hole doped cuprate, 105
  - electron doped cuprates, 107–8
  - hole doped cuprates, 106–7
- superconducting state, 127–35
  - bosonic function, 133
  - bosonic mode, 132–5
  - Eliashberg function, 133
  - FGT sum rule violation, 130
  - gap, 127–8
  - restricted spectral weight, 131
  - sum rules and kinetic energy, 128–31

optical scattering rate, 123
optics, 261–3
optimal reduction, 235
out-of-plane site, 215
oxygen nonstoichiometry, 224–6, 264

pairing symmetry, 265
particle source, 11
particle transport, 11
Paschen’s law, 17
PCCO *see* praseodymium caesium copper oxide
perfectly compatible substrates, 6
perovskites, 8, 374
ϖ-facets, 378
phase formation, 11, 23–7
- with and without particle transport, 26

phase stability, 220–4
photons, 324
physical vapour deposition, 10, 12–20
- pulsed laser deposition technique and Laser MB, 14–16
- sputter techniques, 16–18
- thermal co-evaporation and MBE, 12–13

planar site, 215
PLD *see* pulsed laser deposition
pnictides, 138
praseodymium caesium copper oxide
- bosonic function for optimally doped states, 134
- reflectivity as a function of Ce content, 125

preferential growth phenomenon, 306
pseudogap, 74–6, 118–23, 261
pulsed laser deposition, 14–16, 32, 150, 177, 344
Pulse-Doppler radar, 415
PVD *see* physical vapour deposition

QHS model *see* quasi-hard-sphere model
quantum conductivity, 51
- model, 53

quasi-hard-sphere model, 19

Raman scattering, 305
ramp-type or ramp-edge junction, 330
rapid single flux quantum, 324
rare earth copper oxides
- crystal structures, 211
- superconducting transition temperatures, 212

REBCO films, 276
- a/c axes pinning structure and growth mechanism, 293–5
  - a/c grain boundaries morphology, 294
  - grain growth rate diagram, 295
- in-plane alignment transformation, 302–10
  - atomic configuration around REBCO/MgO interface, 307
  - films field dependence, 310
  - films melting process, 302
  - 0o grain preferential growth, 303–4
  - 45o grain preferential growth, 304–10
  - three experiment system comparison, 309
  - YBCO grains in-plane orientation in MgO substrates, 303
  - YBCO-LPE film vertical dipping region, 306
- liquid phase epitaxy growth mechanism, 283–310
  - transition between a-axis and c-axis growth, 283–93
- 45^{o}-oriented YBCO-LPE film
  - interface feature, 308
  - optical micrograph, 304
  - Raman spectrum, 305
- SmBCO, 290–3
  - Sm^{3+} and Ba^{2+} substitution influence on diffusion path, 291
  - surface migration kinetic model in LPE, 292
- thermal stability, 295–302

    - EPMA mapping images, 298
    - films thermal stability and in-plane alignments correlation, 301–2
    - hetero-seeded LPE growth mechanism using YBCO-thin-film as a seed, 296–8
    - high stability mechanism of YBCO thin film, 298–301
    - LPE process differences in YBCO and SmBCO, 296
    - sample microstructure, 299
    - specimen microstructures optical micrograph, 297
    - surface microstructures comparison between two samples, 300
  - YBCO, 283–90
    - *a*- and *c*-axis surface migration model, 290
    - *a*-axis film surface morphology, 289
    - *c*-dominated film, 286
    - *a-c* phase crossover, 287
    - *a-c* transition mechanism under different environments, 288
    - digging region with peculiar morphology, 285
    - films orientation transition, 289
    - a-phase ratio values, 284
- reciprocal space mapping, 163
- RE2CuO4, 211–12
- reflection high energy electron diffraction, 16, 18, 176
  - in-situ characterisation of oxide film growth, 15
- residual resistivity, 38
- residual stress, 164
- resistively shunted junction, 320, 372
  - model, 321
- resistivity, 239–42
- resonators, 399
- restricted spectral weight, 116–17
  - optical conductivity for a Drude metal, 117
- RHEED *see* reflection high energy electron diffraction
- RSFQ *see* rapid single flux quantum
- RSJ *see* resistively shunted junction
- RSW *see* restricted spectral weight

- Scanning Josephson Tunnelling Microscope, 359
- SDW gap *see* spin-density wave gap
- Seebeck coefficient, 242–4
- semi-coherent interface energy theory, 301
- SFQ *see* single flux quantum
- SFS *see* superconductor-ferromagnet-superconductor
- Shapiro steps, 319, 340
- silent qubit, 384, 385
- single flux quantum, 346
- SIS *see* superconductor-insulator-superconductor
- SIT *see* superconducting-insulating transition
- SmBCO, 290–3
- SNS step-edge junction, 330
- solid-state chemistry, 220–6
- solute-rich-liquid crystal-pulling method, 282
- spin-density wave gap, 261
- Spiral-Island growth mode, 277
- sputter deposition, 16–18, 32, 177–9
  - arc discharge, 17–18
  - B-2212, Bi-2201 and 2212/2201, 178
  - dark discharge, 17
  - glow discharge, 17
  - process schematic, 16
  - technique, 152–5
    - inverted cylindrical systems schematics, 154
    - sputtering system, 153
  - YBCO superconducting films, 149–69
    - challenges, 168–9
    - epitaxial YBCO thin films, 155–6
    - issues related to scale-up, 157–61
    - technique, 152–5
- sputtering, 16–18
- SQIF *see* superconducting quantum interference filters
- square planar copper oxides, 210
- SQUID *see* superconducting quantum interference device
- SRL-CP method *see* solute-rich-liquid crystal-pulling method
- step-edge technology, 328
- step-flow growth, 25
  - schematic sketch, 26
- Sterling cryo-cooler, 413
- Stewart-McCumber model, 320
- stress, 27–30
- stripline, 398, 399
- substrate materials
  - microwave applications and coated conductors, 7
  - requirements, 6–10
- *f*-sum rule, 128
- sum rules, 128–31
- superconducting delay line, 398–9
- superconducting fluctuations, 56–60
- superconducting gap, 247
- superconducting-insulating transition, 197
- superconducting meteorological radar, 415–21
- superconducting quantum interference device, 175, 183, 250, 323–4, 370
  - silent quantum bit, 383–6
    - asymmetric dc-SQUID potential shape evolution, 386
    - sketch, 385
- superconducting quantum interference filters, 347
- superconducting resonator, 399–402
- superconducting state, 127–35
- superconductor-ferromagnet-superconductor, 357
- superconductor-insulator-superconductor, 321
- superconductors, 390–96

superfluid density, 247
superheating, 295
supracurrent *see* Josephson current
surface impedance, 391–402
surface migration length, 25
surface reactance, 392
surface resistance, 391–402

T′ cuprates
  see also electron-doped T_c cuprates
  generic phase diagram, 236
  superconducting parameters, 253
TFF *see* toggle-flip-flop
theory of fracture of solids, 30
thermal co-evaporation, 12–13
  schematic sketch, 13
thermalisation, 19, 20
third order intercept, 396
Thomson relation, 18
toggle-flip-flop, 359
TOI *see* third order intercept
tolerance factor, 212–14, 263
top-seeded solution-growth, 275
Townsend discharge, 17
T′ phase stability, 263
transport, 264–5
traveling-solvent floating zone, 226
T′-RE_2CuO_4
  lattice parameters, 218
  RE dependence of the decomposition lines, 223
  thermodynamic data for decomposition reaction, 222
TSFZ *see* traveling-solvent floating zone
TSSG *see* top-seeded solution-growth
tunnelling, 244–7

unconventional order parameter, 384

van't Hoff equation, 222
vapour phase deposition, 291
vapour phase epitaxy, 275
vertical dipping method, 284
vortex dynamics Hall effect, 81
VPD *see* vapour phase deposition
VPE *see* vapour phase epitaxy

weak links, 318, 320
wind profiler, 415

YBCO *see* yttrium barium copper oxide
45° YBCO grains, 303
YBCO superconducting films
  epitaxial YBCO thin films, 155–6
    unit cell of $YBa_2Cu_3O_7$, 156
  issues related to scale-up, 156–61
    configuration with speed-modulated biaxial rotation, 157
    film homogeneity, 158–61
    in-plane wafer rotation, 157
    large-area deposition, 156–8
    pure *c*-axis oriented and good out-of-plane and in-plane epitaxy, 161
    Rutherford backscattering spectroscopy results, 159
    stoichiometric and thickness distribution, 160
    substrate and cylindrical target for biaxial rotation, 158
  residual stress, 164
    as a function film thickness, 165
    surface morphology, 166–8
    thickness-modulated films, 162–6
  sputter deposition, 149–69
    deposition parameters, 155
    epitaxial thin YBCO films, 155–6
    technique, 152–5
  thickness-dependent superconductivity, 162–8
    critical current density, 168
    film thickness dependence, 167
    FWHM of 006 peak in rocking curve, 162
    lattice parameters, strain, and residual stress, 165
    reciprocal space mapping, 163
    surface morphology, 166
    X-ray diffraction spectra, 162
yttrium barium copper oxide, 8, 20, 283–90
  critical current density of bicrystals, 5
  crystalline substrate materials suitable for preparation of thin films, 9
  frequency dependence of microwave surface resistance, 31
  in-plane orientation of grains in MgO substrates, 303
  microstructure, 299
  optical conductivity for underdoped and optimally doped states, 127
  pressure-temperature phase diagram, 21
  step-flow growth, 26
  superconducting crystals optical conductivity, 119
  underdoped in the pseudogap regime, 121

Zener diodes, 340
zero-field resistivity
  scaling for different doping levels, 44–5
  temperature dependence in $La_{2-x}Sr_xCuO_4$ thin films, 39–54